



biomedicines

Special Issue Reprint

Recent Advances in the Discovery of Novel Drugs on Natural Molecules

Edited by
Laura Quintieri, Leonardo Caputo and Orazio Nicolotti

mdpi.com/journal/biomedicines



Recent Advances in the Discovery of Novel Drugs on Natural Molecules

Recent Advances in the Discovery of Novel Drugs on Natural Molecules

Editors

Laura Quintieri

Leonardo Caputo

Orazio Nicolotti



Basel • Beijing • Wuhan • Barcelona • Belgrade • Novi Sad • Cluj • Manchester

Editors

Laura Quintieri
Italian National Council of
Research
Bari
Italy

Leonardo Caputo
Italian National Council of
Research
Bari
Italy

Orazio Nicolotti
Università degli Studi di Bari
"Aldo Moro"
Bari
Italy

Editorial Office

MDPI AG
Grosspeteranlage 5
4052 Basel, Switzerland

This is a reprint of articles from the Special Issue published online in the open access journal *Biomedicines* (ISSN 2227-9059) (available at: https://www.mdpi.com/journal/biomedicines/special-issues/novel_drugs).

For citation purposes, cite each article independently as indicated on the article page online and as indicated below:

Lastname, A.A.; Lastname, B.B. Article Title. <i>Journal Name</i> Year , <i>Volume Number</i> , Page Range.
--

ISBN 978-3-7258-1873-0 (Hbk)

ISBN 978-3-7258-1874-7 (PDF)

doi.org/10.3390/books978-3-7258-1874-7

© 2024 by the authors. Articles in this book are Open Access and distributed under the Creative Commons Attribution (CC BY) license. The book as a whole is distributed by MDPI under the terms and conditions of the Creative Commons Attribution-NonCommercial-NoDerivs (CC BY-NC-ND) license.

Contents

About the Editors ix

Laura Quintieri, Leonardo Caputo and Orazio Nicolotti

Recent Advances in the Discovery of Novel Drugs on Natural Molecules
Reprinted from: *Biomedicines* **2024**, *12*, 1254, doi:10.3390/biomedicines12061254 1

Jingjing Sun, Wei Chen, Zheng Zhou, Xin Chen, You Zuo, Jiaqian He and Hairong Liu

Tanshinone IIA Facilitates Efficient Cartilage Regeneration under Inflammatory Factors Caused Stress via Upregulating LncRNA NEAT1.2
Reprinted from: *Biomedicines* **2023**, *11*, 3291, doi:10.3390/biomedicines11123291 7

Patrik F. Schwarz, Alexander F. Perhal, Lucia N. Schöberl, Martin M. Kraus, Johannes Kirchmair and Verena M. Dirsch

Identification of the Natural Steroid Sapogenin Diosgenin as a Direct Dual-Specific ROR α / γ Inverse Agonist
Reprinted from: *Biomedicines* **2022**, *10*, 2076, doi:10.3390/biomedicines10092076 24

Kang-Hoon Kim, Ji Hoon Jung, Won-Seok Chung, Chang-Hun Lee and Hyeung-Jin Jang

Ferulic Acid Induces Keratin 6 α via Inhibition of Nuclear β -Catenin Accumulation and Activation of Nrf2 in Wound-Induced Inflammation
Reprinted from: *Biomedicines* **2021**, *9*, 459, doi:10.3390/biomedicines9050459 40

Su Cheol Baek, Sang Ah Yi, Bum Soo Lee, Jae Sik Yu, Jin-Chul Kim, Changhyun Pang, et al.

Anti-Adipogenic Polyacetylene Glycosides from the Florets of Safflower (*Carthamus tinctorius*)
Reprinted from: *Biomedicines* **2021**, *9*, 91, doi:10.3390/biomedicines9010091 60

Bruno Rizzuti, Fedora Grande, Filomena Conforti, Ana Jimenez-Alesanco, Laura Ceballos-Laita, David Ortega-Alarcon, et al.

Rutin Is a Low Micromolar Inhibitor of SARS-CoV-2 Main Protease 3CLpro: Implications for Drug Design of Quercetin Analogs
Reprinted from: *Biomedicines* **2021**, *9*, 375, doi:10.3390/biomedicines9040375 72

Maryam Ghanbari-Movahed, Tea Kaceli, Arijit Mondal, Mohammad Hosein Farzaei and Anupam Bishayee

Recent Advances in Improved Anticancer Efficacies of Camptothecin Nano-Formulations: A Systematic Review
Reprinted from: *Biomedicines* **2021**, *9*, 480, doi:10.3390/biomedicines9050480 92

Sang Keun Ha, Min Cheol Kang, Seulah Lee, Om Darlami, Dongyun Shin, Inwook Choi, et al.

Generation of Stilbene Glycoside with Promising Cell Rejuvenation Activity through Biotransformation by the Entomopathogenic Fungus *Beauveria bassiana*
Reprinted from: *Biomedicines* **2021**, *9*, 555, doi:10.3390/biomedicines9050555 117

Tzu-Hsien Chuang, Hsin-Yen Cho and Sheng-Nan Wu

Effective Accentuation of Voltage-Gated Sodium Current Caused by Apocynin (4'-Hydroxy-3'-methoxyacetophenone), a Known NADPH-Oxidase Inhibitor
Reprinted from: *Biomedicines* **2021**, *9*, 1146, doi:10.3390/biomedicines9091146 129

Nicola Gambacorta, Leonardo Caputo, Laura Quintieri, Linda Monaci, Fulvio Ciriaco and Orazio Nicolotti Rational Discovery of Antiviral Whey Protein-Derived Small Peptides Targeting the SARS-CoV-2 Main Protease Reprinted from: <i>Biomedicines</i> 2022 , <i>10</i> , 1067, doi:10.3390/biomedicines10051067	147
Rory Casey, Alessandro Adelfio, Martin Connolly, Audrey Wall, Ian Holyer and Nora Khaldi Discovery through Machine Learning and Preclinical Validation of Novel Anti-Diabetic Peptides Reprinted from: <i>Biomedicines</i> 2021 , <i>9</i> , 276, doi:10.3390/biomedicines9030276	158
Ana Rita Garizo, Lgia F. Coelho, Sandra Pinto, Tiago P. Dias, Fbio Fernandes, Nuno Bernardes and Arsnio M. Fialho The Azurin-Derived Peptide CT-p19LC Exhibits Membrane-Active Properties and Induces Cancer Cell Death Reprinted from: <i>Biomedicines</i> 2021 , <i>9</i> , 1194, doi:10.3390/biomedicines9091194	175
Rajesh Rattinam, R. Sidick Basha, Yung-Lin Wang, Zhe-Chong Wang, Ning-Shian Hsu, Kuan-Hung Lin, et al. KasQ an Epimerase Primes the Biosynthesis of Aminoglycoside Antibiotic Kasugamycin and KasF/H Acetyltransferases Inactivate Its Activity Reprinted from: <i>Biomedicines</i> 2022 , <i>10</i> , 212, doi:10.3390/biomedicines10020212	189
Corina Cheptea, Valeriu Sunel, Ana Cezarina Morosanu, Dan Gheorghe Dimitriu, Mihaela Maria Dulcescu-Oprea, Mihai-Daniel Angheluta, et al. Optimized Synthesis of New N-Mustards Based on 2-Mercaptobenzoxazole Derivatives with Antitumor Activity Reprinted from: <i>Biomedicines</i> 2021 , <i>9</i> , 476, doi:10.3390/biomedicines9050476	213
Nicolai Rgen, Timothy P. Jenkins, Natalie Wielsch, Heiko Vogel, Benjamin-Florian Hempel, Roderich D. Sssmuth, et al. Hexapod Assassins' Potion: Venom Composition and Bioactivity from the Eurasian Assassin Bug <i>Rhynocoris iracundus</i> Reprinted from: <i>Biomedicines</i> 2021 , <i>9</i> , 819, doi:10.3390/biomedicines9070819	233
Lei Peng, Prasannavenkatesh Durai, Keunwan Park, Jeong Joo Pyo and Yongsoo Choi A Novel Competitive Binding Screening Assay Reveals Sennoside B as a Potent Natural Product Inhibitor of TNF- α Reprinted from: <i>Biomedicines</i> 2021 , <i>9</i> , 1250, doi:10.3390/biomedicines9091250	258
Bernardina Scafuri, Paola Bontempo, Lucia Altucci, Luigi De Masi and Angelo Facchiano Molecular Docking Simulations on Histone Deacetylases (HDAC)-1 and -2 to Investigate the Flavone Binding Reprinted from: <i>Biomedicines</i> 2020 , <i>8</i> , 568, doi:10.3390/biomedicines8120568	271
Vedanjali Gogineni, Manal A. Nael, Narayan D. Chaurasiya, Khaled M. Elokely, Christopher R. McCurdy, John M. Rimoldi, et al. Computationally Assisted Lead Optimization of Novel Potent and Selective MAO-B Inhibitors Reprinted from: <i>Biomedicines</i> 2021 , <i>9</i> , 1304, doi:10.3390/biomedicines9101304	281
Vikas Kumar, Shraddha Parate, Gunjan Thakur, Gihwan Lee, Hyeon-Su Ro, Yongseong Kim, et al. Identification of CDK7 Inhibitors from Natural Sources Using Pharmacoinformatics and Molecular Dynamics Simulations Reprinted from: <i>Biomedicines</i> 2021 , <i>9</i> , 1197, doi:10.3390/biomedicines9091197	305

Mohamed H. Elsherbeny, Ahmed Elkamhawy, Hossam Nada, Magda H. Abdellattif, Kyeong Lee and Eun Joo Roh Development of New Meridianin/Leucettine-Derived Hybrid Small Molecules as Nanomolar Multi-Kinase Inhibitors with Antitumor Activity Reprinted from: <i>Biomedicines</i> 2021 , <i>9</i> , 1131, doi:10.3390/biomedicines9091131	328
Margarita Neganova, Alexey Semakov, Yulia Aleksandrova, Ekaterina Yandulova, Sergey Pukhov, Lada Anikina and Sergey Klochkov N-Alkylation of Anthracycline Antibiotics by Natural Sesquiterpene Lactones as a Way to Obtain Antitumor Agents with Reduced Side Effects Reprinted from: <i>Biomedicines</i> 2021 , <i>9</i> , 547, doi:10.3390/biomedicines9050547	348

About the Editors

Laura Quintieri

Laura Quintieri: Researcher at the Italian National Council of Research, Institute of Sciences of Food Production CNR-ISPA since 2018. She completed her degree in Chemistry and Pharmaceutical Technology in 2006 and her Ph.D. in Microbiology, Safety and Chemistry of Food in 2013. From 2007 to 2018, she obtained four postgraduate fellowships and started a temporary researcher position at CNR-ISPA. Her fields of research include the evaluation of biological activity (antimicrobial, anti-biofilm, and ACE-inhibitors) of peptides or other natural compounds (e.g., polyphenols) from fermented foods, microorganisms of agrifood interest (e.g., *Bacillus* spp.) and plant extracts; and phenotypic and proteomic analysis of microbial starters (e.g., *Staphylococcus* spp.), bacterial spoilers of fresh foods (e.g., *Pseudomonas* spp.) and biofilm-forming bacteria. She is an expert in food microbiology, proteomic techniques, enzymatic assays, and tools for the visualization and analysis of proteomic data. She has served as the co-leader and work package leader of European and national research projects. She is the author or co-author of more than 50 publications and nine book chapters. She has also presented more than 50 conference proceedings. H-Index: 21 Google Scholar; 20 Scopus.

Leonardo Caputo

Leonardo Caputo: Researcher at the Italian National Council of Research, Institute of Sciences of Food Production CNR-ISPA since 2001. He completed his degree in Biological Sciences in 1994 with biologist qualification in 1995. He holds a PhD in the Protection of Agricultural and Food Productions with a dissertation on oxidative stresses-related mechanisms in antagonistic yeasts controlling phytopathogenic fungi. He served as a fellowship postdoc at Gembloux Agro-Bio Tech (BE) in 2003. His main research fields are microbiology with special emphasis on fermentation and the biochemical and molecular identification and typing of yeast and bacteria concerning the agrifood chain. He is an expert in researching microbial metabolites and food-derived peptides displaying biological activities aimed at improving food processing and extending the shelf-life of fresh foods. He has worked on more than 20 competitive national R&D projects and has participated in two European projects.

To date, he is the author or co-author of more than 150 publications including 60 publications in ISI-indexed journals.

Orazio Nicolotti

Orazio Nicolotti: Full professor at the University of Bari 'Aldo Moro', Department of Pharmacy-Pharmaceutical Sciences. He completed his degree in Chemistry and Pharmaceutical Technology in 1997 and his Ph.D. in Medicinal Chemistry in 2001. He served as a two-year postdoc at the University of Sheffield (UK). He holds major skills in drug design, QSAR, chemoinformatics, predictive toxicology, combinatorial library design, evolutionary algorithms, and docking and molecular dynamics. He has served as the supervisor of 10 PhD students and 6 postdocs. He has served as the principal investigator of drug discovery projects funded with > EUR 900K. He is the founder and head of the data and molecular modeling lab Prometheus. Thus far, he is the author of 182 peer-reviewed research papers, 11 book chapters, 1 international patent, and 35 invited talks. He is the editor of the book *Computational Toxicology*, published in 2018 by Humana Press of Springer Nature. H-Index: 45 Google Scholar; 40 Scopus.



Editorial

Recent Advances in the Discovery of Novel Drugs on Natural Molecules

Laura Quintieri ^{1,*}, Leonardo Caputo ¹ and Orazio Nicolotti ²

¹ Institute of Sciences of Food Production, National Research Council (CNR), Via G. Amendola, 122/O, 70126 Bari, Italy; leonardo.caputo@ispa.cnr.it

² Dipartimento di Farmacia—Scienze del Farmaco, Università degli Studi di Bari “Aldo Moro”, Via E. Orabona, 4, 70125 Bari, Italy; orazio.nicolotti@uniba.it

* Correspondence: laura.quintieri@ispa.cnr.it

Natural products (NPs) are always a promising source of novel drugs for tackling unsolved diseases [1–3]. Natural molecules have addressed the rational design of many synthetic small-molecule drugs [4–6], despite their chemotypes having higher structural complexity, heavier molecular weights (often > 500), more sp³ carbon atoms which amplify tridimensionality and stereocenters, more oxygen atoms, fewer nitrogen and halogen atoms, more H-bond acceptors and donors, marked hydrophilicity, and greater molecular rigidity [7]. Natural molecules are likely still inspiring drug discovery due to their incredible scaffold diversity, making them extremely unique and selective in the chemistry field [8]. Thus, developing new natural bioactive compounds and repurposing approved natural drugs are hot topics in drug discovery and medicinal chemistry [9]. Since most compounds exhibit synergistic effects [10] or share multiple targets [11,12], traditional approaches to finding potential drug candidates, such as bioassay-guided fractionation, can reduce their therapeutic efficacy. As a result, new techniques are required to produce drugs with high and multi-target activity as well as improved bioavailability [13–15]. For example, molecular biological techniques can increase the availability of novel compounds produced by bacteria or yeasts [16,17], and virtual screening approaches can generate screening libraries of natural compounds resembling drug-like compounds [18–21] or predict their biological activity and related molecular targets with chemical accuracy [22,23]. Moreover, advances in metabolomics have also allowed us to identify active compounds from natural product mixtures as well as to reveal synergistic effects in complex mixtures [24,25].

We gathered twenty articles for this Special Issue that discuss the discovery of novel bioactive NPs with potential for medical purposes. The application of synthetic biology with all its multidisciplinary aspects (bioinformatics, data mining, pathway refactoring, cell factories, DNA editing, and computational chemistry) was preferred to allow the identification of novel drug molecules from microbial strains or biosources that might escape classical top-down strategies.

The plant kingdom is a significant source of molecules with potential therapeutic benefits for humans; bioactive molecules derived from plants often exhibit clear therapeutic profiles and can be employed as drugs or starting points to derive synthetic drugs [26–29]. Several recent publications on the biological activity of plant compounds are collected in this Special Issue.

In particular, Sun et al. [30] extracted and purified the lipophilic diterpene Tanshinone IIA (TAN) from *Salvia miltiorrhiza* Bunge and evaluated its role in maintaining chondrocyte viability and promoting cartilage regeneration in osteoarthritis patients. TAN was already recognized in herbal medicine for its anti-inflammatory, antioxidant, and vascular endothelial cell-protective properties. Likewise, Schwarz et al. [31] investigated the mode of action of the steroid sapogenin diosgenin, previously identified in the Chinese plant *Dioscorea rhizoma*, in dampening the autoimmune inflammatory response in T helper 17 (Th17)-driven pathologies. By combining methodological approaches including gene expression

Citation: Quintieri, L.; Caputo, L.; Nicolotti, O. Recent Advances in the Discovery of Novel Drugs on Natural Molecules. *Biomedicines* **2024**, *12*, 1254. <https://doi.org/10.3390/biomedicines12061254>

Received: 6 May 2024

Accepted: 22 May 2024

Published: 5 June 2024



Copyright: © 2024 by the authors. Licensee MDPI, Basel, Switzerland. This article is an open access article distributed under the terms and conditions of the Creative Commons Attribution (CC BY) license (<https://creativecommons.org/licenses/by/4.0/>).

analysis and in silico analyses, the authors revealed diosgenin as an inverse agonist of the key transcription factors leading to Th17 cell differentiation and metabolism. Kim and colleagues [32] demonstrated that the plant-derived ferulic acid acts as a therapeutic agent for wound healing via inhibiting β -catenin in keratinocytes and activating Nrf2 in wound-induced inflammation.

Florets of Safflower (*Carthamus tinctorius*) were identified as a source of polyacetylene glycosides, which are responsible for preventing excessive lipid accumulation in obesity through the inhibition of adipocyte differentiation, reducing the transcription levels of mature adipocyte marker genes (*Adipsin* and *Fabp4*), promoting the expression of lipolytic genes, and downregulating the expression of lipogenic genes [33].

The application of plant-derived compounds (such as polyphenols) in therapies is often hampered by several factors including structural instability; poor bioavailability, gastric solubility, and residence time; and fast metabolization in the liver [34–36]. Through the combination of experimental (spectroscopy and calorimetry) and simulation techniques (docking and molecular dynamics simulations) the glycosyl derivate of the flavonoid rutin (quercetin-3-O-rutinose) was found to exhibit comparable potency to the parental molecule rutin and an estimated higher bioavailability. Thus, the results of this work were proposed as the basis for the development of quercetin-like antiviral compounds in coronavirus infection management [37].

Like quercetin, the alkaloid antitumoral camptothecin (CPT) shows weak pharmacokinetic and pharmacodynamics properties [38]. Nanotechnology is perfect for improving CPT bioavailability; thus, the review by Ghanbari-Movahed et al. provided a comprehensive and critical evaluation of the novel, efficient nano-CPT formulations being developed for cancer therapy [38]. By contrast, biotransformation of the antioxidant resveratrol (RSV) by the entomopathogenic fungus *Beauveria bassiana* yielded a safer RSV metabolite, the stilbene glycoside resvebassianol A [39].

As widely reported, NPs can exert multiple biological activities. For example, the anti-inflammatory phenolic compound Apocynin, an inhibitor of NADPH-dependent oxidase (NOX), was suggested to interact with plasmalemmal ionic channels by perturbing ionic currents in excitable cells [40]. However, more evidence is needed to understand the molecular-level nature of interactions affecting neuroendocrine, endocrine, or cardiac function.

Food proteins from animals and plants are widely exploited for cryptic bioactive peptides exhibiting multi-target activities [41–50]. Gambacorta et al. [51] evaluated the inhibitory activity of the whey-derived bioactive small peptides MHI, IAEK, and IPAVF against the SARS-CoV-2 3C-like protease (3CLpro) for the first time. These peptides were previously obtained by the enzymatic hydrolysis of whey proteins and displayed ACE-inhibitory activity [22]. The authors integrated theoretical and experimental techniques, first performing molecular docking studies to rationally evaluate the putative chance of binding and then in vitro testing for validation. The results confirmed the highest antiviral activity for IPAVF and IAEK, providing new opportunities for the development of dual-target small peptides endowed with antiviral 3CLpro- and ACE-inhibitory activities.

Using a machine learning approach, Casey et al. [52] predicted five novel anti-diabetic peptides (pep_1E99R5, pep_37MB3O, pep_ANUT7B, pep_RTE62G and pep_QT5XGQ) from a set of 10^9 peptides. Although further work is required to elucidate their bioavailability, mechanism of action, and clinical efficacy, the authors presented pep_1E99R5 as the most active peptide, affecting blood glucose metabolism. Bioactive peptide sequences can also be re-designed to obtain novel drugs in cancer therapy, as reported by [53–55]. Thus, an in silico peptide design optimization process was applied to identify active peptides from the C-terminal of azurin, an anticancer bacterial protein produced by *Pseudomonas aeruginosa*. Due to its molecular properties, CT-p19LC was predicted to exhibit the greatest anticancer activity. This was confirmed in experimental trials and, therefore, it was suggested for the development of novel anticancer strategies.

Multidisciplinary approaches effectively reveal the synthesis pathways of NPs [56,57] or discover new molecules that might be used as templates to develop novel biotherapeutics [58,59].

Rugen et al. [60] collected venom from the assassin bug *Rhynocoris iracundus* and investigated its composition and bioactivity in vitro and in vivo to exploit it for biomedical applications. Assassin bug venom induced neurolysis, caused the paralysis and melanization of *Galleria mellonella* larvae and pupae, and exhibited antibacterial activity. The combined proteo-transcriptomic approach could successfully identify molecules responsible for biological effects (redulysins, kininogens, chitinases, hemolysins, and Ptu1 family peptide toxins).

Among 35 phytochemicals, sennoside B from *Cassia angustifolia* was predicted as a TNF- α inhibitor by a competitive binding screening assay coupled with analytical size exclusion chromatography and liquid chromatography–tandem mass spectrometry (LC-MS). Molecular docking was also performed to determine the binding mode of sennoside B to TNF- α , confirming its activity in TNF- α -induced HeLa cell toxicity assays [61]. Similarly, molecular docking revealed that flavonoids (apigenin and luteolin) bound to histone deacetylases (HDACs), with important implications in epigenetic therapy to regulate cellular gene expression [62]. In addition, computational methods were applied to design modified flavonoids endowed with high monoamine oxidase (MAO) B affinity for neurological disorder treatment [63,64], as well as to identify new potential scaffolds against Cyclin-dependent kinase 7 (CDK7) for the development of novel antitumoral strategies [65].

The bioactive compounds found in natural products are also a valuable source of inspiration for new drug synthesis [14,66–68], such as the marine-inspired potent kinase inhibitors with antiproliferative activities described by [69]. NPs can also be used to chemically modify the molecular structure of existing drugs to improve their activity or pharmacokinetics properties. For example, Neganova et al. [70] found that the conjugation of sesquiterpene lactones, extracted from *Inula helenium* L. (*Asteraceae*), reduced the side effects of antitumoral cantharacycline antibiotics.

In conclusion, the articles published in this Special Issue underline the advances and opportunities in using NPs in drug discovery. Several works show NPs' key role in a wide array of biological activities, such as maintaining tissue integrity, regulating immune responses, and influencing complex processes in human diseases. Their current limitations and promising strategies to design and identify novel molecules are also discussed.

Author Contributions: Conceptualization, L.Q., L.C. and O.N.; writing—original draft preparation, L.Q.; writing—review and editing, L.C. and O.N. All authors have read and agreed to the published version of the manuscript.

Conflicts of Interest: The authors declare no conflicts of interest.

References

1. Atanasov, A.G.; Zotchev, S.B.; Dirsch, V.M.; Supuran, C. Natural products in drug discovery: Advances and opportunities. *Nat. Rev. Drug Discov.* **2021**, *20*, 200–216. [CrossRef] [PubMed]
2. Berdigaliyev, N.; Aljofan, M. An overview of drug discovery and development. *Future Med. Chem.* **2020**, *12*, 939–947. [CrossRef] [PubMed]
3. Chopra, B.; Ashwani, K.D. Natural products: A lead for drug discovery and development. *Phytother. Res.* **2021**, *35*, 4660–4702. [CrossRef] [PubMed]
4. Gambacorta, N.; Gasperi, V.; Guzzo, T.; Di Leva, F.S.; Ciriaco, F.; Sánchez, C.; Tullio, V.; Rozzi, D.; Marinelli, L.; Topai, A.; et al. Exploring the 1,3-Benzoxazine Chemotype for Cannabinoid Receptor 2 as a Promising Anti-Cancer Therapeutic. *Eur. J. Med. Chem.* **2023**, *259*, 115647. [CrossRef] [PubMed]
5. Mangiatordi, G.F.; Trisciuzzi, D.; Alberga, D.; Denora, N.; Iacobazzi, R.M.; Gadaleta, D.; Catto, M.; Nicolotti, O. Novel chemotypes targeting tubulin at the Colchicine binding site and unbiassing P-glycoprotein. *Eur. J. Med. Chem.* **2017**, *139*, 792–803. [CrossRef] [PubMed]
6. Ma, Y.S.; Xin, R.; Yang, X.L.; Shi, Y.; Zhang, D.D.; Wang, H.M.; Wang, P.Y.; Liu, J.B.; Chu, K.J.; Fu, D. Paving the way for small-molecule drug discovery. *Am. J. Transl. Res.* **2021**, *13*, 853–870. [PubMed]

7. Dzobo, K. The role of natural products as sources of therapeutic agents for innovative drug discovery. *Compr. Pharmacol.* **2022**, *408–422*. [CrossRef]
8. Amoroso, N.; Gambacorta, N.; Mastrolorito, F.; Togo, M.V.; Trisciuzzi, D.; Monaco, A.; Pantaleo, E.; Altomare, C.D.; Ciriaco, F.; Nicolotti, O. Making sense of chemical space network shows signs of criticality. *Sci. Rep.* **2023**, *13*, 21335. [CrossRef]
9. Ciriaco, F.; Gambacorta, N.; Trisciuzzi, D.; Nicolotti, O. PLATO: A Predictive Drug Discovery Web Platform for Efficient Target Fishing and Bioactivity Profiling of Small Molecules. *Int. J. Mol. Sci.* **2022**, *23*, 5245. [CrossRef]
10. Zou, H.; Ye, H.; Kamaraj, R.; Zhang, T.; Zhang, J.; Pavek, P. A review on pharmacological activities and synergistic effect of quercetin with small molecule agents. *Phytomedicine* **2021**, *92*, 153736. [CrossRef]
11. Jha, A.K.; Sit, N. Extraction of bioactive compounds from plant materials using combination of various novel methods: A review. *Trends Food Sci. Technol.* **2022**, *119*, 579–591. [CrossRef]
12. Chemat, F.; Vian, M.A.; Fabiano-Tixier, A.S.; Nutrizio, M.; Jambak, A.R.; Munekata, P.E.; Lorenzo, J.M.; Barba, F.J.; Binello, A.; Cravotto, G. A review of sustainable and intensified techniques for extraction of food and natural products. *Green Chem.* **2020**, *22*, 2325–2353. [CrossRef]
13. Gambacorta, N.; Ciriaco, F.; Amoroso, N.; Altomare, C.D.; Bajorath, J.; Nicolotti, O. CIRCE: Web-Based Platform for the Prediction of Cannabinoid Receptor Ligands Using Explainable Machine Learning. *J. Chem. Inf. Model.* **2023**, *63*, 5916–5926. [CrossRef]
14. Najmi, A.; Javed, S.A.; Al Bratty, M.; Alhazmi, H.A. Modern approaches in the discovery and development of plant-based natural products and their analogues as potential therapeutic agents. *Molecules* **2022**, *27*, 349. [CrossRef] [PubMed]
15. Zhu, Y.; Ouyang, Z.; Du, H.; Wang, M.; Wang, J.; Sun, H.; Kong, L.; Xu, Q.; Hongyue, M.; Sun, Y. New opportunities and challenges of natural products research: When target identification meets single-cell multiomics. *Acta Pharm. Sin. B* **2022**, *12*, 4011–4039. [CrossRef] [PubMed]
16. Losurdo, L.; Quintieri, L.; Caputo, L.; Gallerani, R.; Mayo, B.; De Leo, F. Cloning and expression of synthetic genes encoding angiotensin-I converting enzyme (ACE)-inhibitory bioactive peptides in *Bifidobacterium pseudocatenulatum*. *FEMS Microbiol. Lett.* **2013**, *340*, 24–32. [CrossRef] [PubMed]
17. Yang, D.; Park, S.Y.; Park, Y.S.; Eun, H.; Lee, S.Y. Metabolic engineering of *Escherichia coli* for natural product biosynthesis. *Trends Biotechnol.* **2020**, *38*, 745–765. [CrossRef]
18. Sadybekov, A.V.; Katritch, V. Computational approaches streamlining drug discovery. *Nature* **2023**, *616*, 673–685. [CrossRef] [PubMed]
19. Vázquez, J.; López, M.; Gibert, E.; Herrero, E.; Luque, F.J. Merging Ligand-Based and Structure-Based Methods in Drug Discovery: An Overview of Combined Virtual Screening Approaches. *Molecules* **2020**, *25*, 4723. [CrossRef]
20. Oliveira, T.A.D.; Silva, M.P.D.; Maia, E.H.B.; Silva, A.M.D.; Taranto, A.G. Virtual screening algorithms in drug discovery: A review focused on machine and deep learning methods. *Drugs Drug Candidates* **2023**, *2*, 311–334. [CrossRef]
21. Parvatikar, P.P.; Patil, S.; Khaparkhantkar, K.; Patil, S.; Singh, P.K.; Sahana, R.; Kulkarni, R.V.; Raghun, A.V. Artificial intelligence: Machine learning approach for screening large database and drug discovery. *Antivir. Res.* **2023**, *220*, 105740. [CrossRef]
22. Tondo, A.R.; Caputo, L.; Mangiatordi, G.F.; Monaci, L.; Lentini, G.; Logrieco, A.F.; Montaruli, M.; Nicolotti, O.; Quintieri, L. Structure-Based Identification and Design of Angiotensin Converting Enzyme-Inhibitory Peptides from Whey Proteins. *J. Agric. Food Chem.* **2020**, *68*, 541–548. [CrossRef] [PubMed]
23. Gu, R.; Wu, F.; Huang, Z. Role of Computer-Aided Drug Design in Drug Development. *Molecules* **2023**, *28*, 7160. [CrossRef] [PubMed]
24. Vidar, W.S.; Baumeister, T.U.H.; Caesar, L.K.; Kellogg, J.J.; Todd, D.A.; Lington, R.G.M.; Kvalheim, O.; Cech, N.B. Interaction Metabolomics to Discover Synergists in Natural Product Mixtures. *J. Nat. Prod.* **2023**, *86*, 655–671. [CrossRef] [PubMed]
25. Palermo, A. Metabolomics-and systems-biology-guided discovery of metabolite lead compounds and druggable targets. *Drug Discov. Today* **2023**, *28*, 103460. [CrossRef] [PubMed]
26. Chaachouay, N.; Zidane, L. Plant-Derived Natural Products: A Source for Drug Discovery and Development. *Drugs Drug Candidates* **2024**, *3*, 184–207. [CrossRef]
27. Elshafie, H.S.; Camele, I.; Mohamed, A.A. A Comprehensive review on the biological, agricultural and pharmaceutical properties of secondary metabolites based-plant origin. *Int. J. Mol. Sci.* **2023**, *24*, 3266. [CrossRef] [PubMed]
28. Lautie, E.; Russo, O.; Ducrot, P.; Boutin, J.A. Unraveling plant natural chemical diversity for drug discovery purposes. *Front. Pharmacol.* **2020**, *11*, 397. [CrossRef] [PubMed]
29. Dias, M.C.; Pinto, D.C.; Silva, A.M. Plant flavonoids: Chemical characteristics and biological activity. *Molecules* **2021**, *26*, 5377. [CrossRef] [PubMed]
30. Sun, J.; Chen, W.; Zhou, Z.; Chen, X.; Zuo, Y.; He, J.; Liu, H. Tanshinone IIA Facilitates Efficient Cartilage Regeneration under Inflammatory Factors Caused Stress via Upregulating LncRNA EAT1_2. *Biomedicines* **2023**, *11*, 3291. [CrossRef]
31. Schwarz, P.F.; Perhal, A.F.; Schöberl, L.N.; Kraus, M.M.; Kirchmair, J.; Dirsch, V.M. Identification of the Natural Steroid Sapogenin Diosgenin as a Direct Dual-Specific ROR α/γ Inverse Agonist. *Biomedicines* **2022**, *10*, 2076. [CrossRef]
32. Kim, K.-H.; Jung, J.H.; Chung, W.-S.; Lee, C.-H.; Jang, H.-J. Ferulic Acid Induces Keratin 6 α via Inhibition of Nuclear β -Catenin Accumulation and Activation of Nrf2 in Wound-Induced Inflammation. *Biomedicines* **2021**, *9*, 459. [CrossRef]
33. Baek, S.C.; Yi, S.A.; Lee, B.S.; Yu, J.S.; Kim, J.-C.; Pang, C.; Jang, T.S.; Lee, J.; Kim, K.H. Anti-Adipogenic Polyacetylene Glycosides from the Florets of Safflower (*Carthamus tinctorius*). *Biomedicines* **2021**, *9*, 91. [CrossRef]

34. Albuquerque, B.R.; Heleno, S.A.; Oliveira, M.B.P.; Barros, L.; Ferreira, I.C. Phenolic compounds: Current industrial applications, limitations and future challenges. *Food Funct.* **2021**, *12*, 14–29. [CrossRef]
35. Zhang, Z.; Li, X.; Sang, S.; McClements, D.J.; Chen, L.; Long, J.; Jiao, A.; Jin, Z.; Qiu, C. Polyphenols as Plant-Based Nutraceuticals: Health Effects, Encapsulation, Nano-Delivery, and Application. *Foods* **2022**, *11*, 2189. [CrossRef]
36. Bertelli, A.; Biagi, M.; Corsini, M.; Bains, G.; Cappellucci, G.; Miraldi, E. Polyphenols: From Theory to Practice. *Foods* **2021**, *10*, 2595. [CrossRef]
37. Rizzuti, B.; Grande, F.; Conforti, F.; Jimenez-Alesanco, A.; Ceballos-Laita, L.; Ortega-Alarcon, D.; Vega, S.; Reyburn, H.T.; Abian, O.; Velazquez-Campoy, A. Rutin Is a Low Micromolar Inhibitor of SARS-CoV-2 Main Protease 3CLpro: Implications for Drug Design of Quercetin Analogs. *Biomedicines* **2021**, *9*, 375. [CrossRef]
38. Ghanbari-Movahed, M.; Kaceli, T.; Mondal, A.; Farzaei, M.H.; Bishayee, A. Recent Advances in Improved Anticancer Efficacies of Camptothecin Nano-Formulations: A Systematic Review. *Biomedicines* **2021**, *9*, 480. [CrossRef]
39. Ha, S.K.; Kang, M.C.; Lee, S.; Darlami, O.; Shin, D.; Choi, I.; Kim, K.H.; Kim, S.Y. Generation of Stilbene Glycoside with Promising Cell Rejuvenation Activity through Biotransformation by the Entomopathogenic Fungus *Beauveria bassiana*. *Biomedicines* **2021**, *9*, 555. [CrossRef]
40. Chuang, T.-H.; Cho, H.-Y.; Wu, S.-N. Effective Accentuation of Voltage-Gated Sodium Current Caused by Apocynin (4'-Hydroxy-3'-methoxyacetophenone), a Known NADPH-Oxidase Inhibitor. *Biomedicines* **2021**, *9*, 1146. [CrossRef]
41. Sharma, K.; Sharma, K.K.; Sharma, A.; Jain, R. Peptide-based drug discovery: Current status and recent advances. *Drug Discov. Today* **2023**, *28*, 103464. [CrossRef] [PubMed]
42. Muttenthaler, M.; King, G.F.; Adams, D.J.; Alewood, P.F. Trends in peptide drug discovery. *Nat. Rev. Drug Discov.* **2021**, *20*, 309–325. [CrossRef] [PubMed]
43. Trisciuzzi, D.; Villoutreix, B.O.; Siragusa, L.; Baroni, M.; Cruciani, G.; Nicolotti, O. Targeting protein-protein interactions with low molecular weight and short peptide modulators: Insights on disease pathways and starting points for drug discovery. *Expert Opin. Drug Discov.* **2023**, *18*, 737–752. [CrossRef] [PubMed]
44. Trisciuzzi, D.; Siragusa, L.; Baroni, M.; Cruciani, G.; Nicolotti, O. An Integrated Machine Learning Model To Spot Peptide Binding Pockets in 3D Protein Screening. *Chem. Inf. Model.* **2022**, *62*, 6812–6824. [CrossRef]
45. Trisciuzzi, D.; Siragusa, L.; Baroni, M.; Autiero, I.; Nicolotti, O.; Cruciani, G. Getting insights into structural and energetic properties of reciprocal peptide-protein interactions. *J. Chem. Inf. Model.* **2022**, *62*, 1113–1125. [CrossRef] [PubMed]
46. Quintieri, L.; Caputo, L.; Monaci, L.; Cavalluzzi, M.M.; Denora, N. Lactoferrin-Derived Peptides as a Control Strategy against Skinborne Staphylococcal Biofilms. *Biomedicines* **2020**, *8*, 323. [CrossRef] [PubMed]
47. Akbarian, M.; Khani, A.; Eghbapour, S.; Uversky, V.N. Bioactive peptides: Synthesis, sources, applications, and proposed mechanisms of action. *Int. J. Mol. Sci.* **2022**, *23*, 1445. [CrossRef] [PubMed]
48. Quintieri, L.; Fanelli, F.; Monaci, L.; Fusco, V. Milk and Its Derivatives as Sources of Components and Microorganisms with Health-Promoting Properties: Probiotics and Bioactive Peptides. *Foods* **2024**, *13*, 601. [CrossRef] [PubMed]
49. Quintieri, L.; Nitride, C.; De Angelis, E.; Lamonaca, A.; Pilolli, R.; Russo, F.; Monaci, L. Alternative Protein Sources and Novel Foods: Benefits, Food Applications and Safety Issues. *Nutrients* **2023**, *15*, 1509. [CrossRef]
50. Quintieri, L.; Zühlke, D.; Fanelli, F.; Caputo, L.; Liuzzi, V.C.; Logrieco, A.F.; Hirschfeld, C.; Becher, D.; Riedel, K. Proteomic analysis of the food spoiler *Pseudomonas fluorescens* ITEM 17298 reveals the antibiofilm activity of the pepsin-digested bovine lactoferrin. *Food Microbiol.* **2019**, *82*, 177–193. [CrossRef]
51. Gambacorta, N.; Caputo, L.; Quintieri, L.; Monaci, L.; Ciriaco, F.; Nicolotti, O. Rational Discovery of Antiviral Whey Protein-Derived Small Peptides Targeting the SARS-CoV-2 Main Protease. *Biomedicines* **2022**, *10*, 1067. [CrossRef] [PubMed]
52. Casey, R.; Adelfio, A.; Connolly, M.; Wall, A.; Holyer, I.; Khaldi, N. Discovery through Machine Learning and Preclinical Validation of Novel Anti-Diabetic Peptides. *Biomedicines* **2021**, *9*, 276. [CrossRef] [PubMed]
53. Garizo, A.R.; Coelho, L.F.; Pinto, S.; Dias, T.P.; Fernandes, F.; Bernardes, N.; Fialho, A.M. The Azurin-Derived Peptide CT-p19LC Exhibits Membrane-Active Properties and Induces Cancer Cell Death. *Biomedicines* **2021**, *9*, 1194. [CrossRef] [PubMed]
54. Jia, F.; Yu, Q.; Wang, R.; Zhao, L.; Yuan, F.; Guo, H.; Shen, Y.; He, F. Optimized antimicrobial peptide jelleine-I derivative Br-JI inhibits fusobacterium nucleatum to suppress colorectal cancer progression. *Int. J. Mol. Sci.* **2023**, *24*, 1469. [CrossRef] [PubMed]
55. Moustafa, G.O.; Shalaby, A.; Naglah, A.M.; Mounier, M.M.; El-Sayed, H.; Anwar, M.M.; Nossier, E.S. Synthesis, Characterization, In Vitro Anticancer Potentiality, and Antimicrobial Activities of Novel Peptide–Glycyrhretinic-Acid-Based Derivatives. *Molecules* **2021**, *26*, 4573. [CrossRef] [PubMed]
56. Rattinan, R.; Basha, R.S.; Wang, Y.-L.; Wang, Z.-C.; Hsu, N.-S.; Lin, K.-H.; Zadeh, S.M.; Adhikari, K.; Lin, J.-P.; Li, T.-L. KasQ an Epimerase Primes the Biosynthesis of Aminoglycoside Antibiotic Kasugamycin and KasF/H Acetyltransferases Inactivate Its Activity. *Biomedicines* **2022**, *10*, 212. [CrossRef] [PubMed]
57. Hou, S.; Du, W.; Hao, Y.; Han, Y.; Li, H.; Liu, L.; Zhang, K.; Zhou, M.; Sun, Z. Elucidation of the regulatory network of flavonoid biosynthesis by profiling the metabolome and transcriptome in tartary buckwheat. *J. Agric. Food Chem.* **2021**, *69*, 7218–7229. [CrossRef] [PubMed]
58. Cheptea, C.; Sunel, V.; Morosanu, A.C.; Dimitriu, D.G.; Dulcescu-Oprea, M.M.; Angheluta, M.-D.; Miron, M.; Nechifor, C.D.; Dorohoi, D.O.; Malancus, R.N. Optimized Synthesis of New N-Mustards Based on 2-Mercaptobenzoxazole Derivatives with Antitumor Activity. *Biomedicines* **2021**, *9*, 476. [CrossRef] [PubMed]

59. Mancini, I.; Vigna, J.; Sighel, D.; Defant, A. Hybrid Molecules Containing Naphthoquinone and Quinolinedione Scaffolds as Antineoplastic Agents. *Molecules* **2022**, *27*, 4948. [CrossRef]
60. Rügen, N.; Jenkins, T.P.; Wielsch, N.; Vogel, H.; Hempel, B.-F.; Süßmuth, R.D.; Ainsworth, S.; Cabezas-Cruz, A.; Vilcinskas, A.; Tonk, M. Hexapod Assassins' Potion: Venom Composition and Bioactivity from the Eurasian Assassin Bug *Rhynocoris iracundus*. *Biomedicines* **2021**, *9*, 819. [CrossRef]
61. Peng, L.; Durai, P.; Park, K.; Pyo, J.J.; Choi, Y. A Novel Competitive Binding Screening Assay Reveals Sennoside B as a Potent Natural Product Inhibitor of TNF- α . *Biomedicines* **2021**, *9*, 1250. [CrossRef] [PubMed]
62. Scafuri, B.; Bontempo, P.; Altucci, L.; De Masi, L.; Facchiano, A. Molecular Docking Simulations on Histone Deacetylases (HDAC)-1 and -2 to Investigate the Flavone Binding. *Biomedicines* **2020**, *8*, 568. [CrossRef] [PubMed]
63. Gogineni, V.; Nael, M.A.; Chaurasiya, N.D.; Elokely, K.M.; McCurdy, C.R.; Rimoldi, J.M.; Cutler, S.J.; Tekwani, B.L.; León, F. Computationally Assisted Lead Optimization of Novel Potent and Selective MAO-B Inhibitors. *Biomedicines* **2021**, *9*, 1304. [CrossRef] [PubMed]
64. Larit, F.; Elokely, K.M.; Chaurasiya, N.D.; Benyahia, S.; Nael, M.A.; León, F.; Abu-Darwish, M.S.; Efferth, T.; Wang, Y.H.; Belouahem-Abed, D.; et al. Inhibition of human monoamine oxidase A and B by flavonoids isolated from two Algerian medicinal plants. *Phytomedicine* **2018**, *40*, 27–36. [CrossRef] [PubMed]
65. Kumar, V.; Parate, S.; Thakur, G.; Lee, G.; Ro, H.-S.; Kim, Y.; Kim, H.J.; Kim, M.O.; Lee, K.W. Identification of CDK7 Inhibitors from Natural Sources Using Pharmacoinformatics and Molecular Dynamics Simulations. *Biomedicines* **2021**, *9*, 1197. [CrossRef] [PubMed]
66. Barba-Ostria, C.; Carrera-Pacheco, S.E.; Gonzalez-Pastor, R.; Heredia-Moya, J.; Mayorga-Ramos, A.; Rodriguez-Pólit, C.; Zúñiga-Miranda, J.; Arias-Almeida, B.; Guamán, L.P. Evaluation of Biological Activity of Natural Compounds: Current Trends and Methods. *Molecules* **2022**, *27*, 4490. [CrossRef]
67. Quintieri, L.; Mani, S.; Lentini, G.; Maisetta, G. Advances in the discovery of natural molecules and their analogues against microbial infection-related biofilms. *Front. Microbiol.* **2022**, *13*, 1092209. [CrossRef] [PubMed]
68. Guo, Z. The modification of natural products for medical use. *Acta Pharm. Sin. B* **2017**, *7*, 119–136. [CrossRef] [PubMed]
69. Elsherbeny, M.H.; Elkamhawy, A.; Nada, H.; Abdellattif, M.H.; Lee, K.; Roh, E.J. Development of New Meridianin/Leucettine-Derived Hybrid Small Molecules as Nanomolar Multi-Kinase Inhibitors with Antitumor Activity. *Biomedicines* **2021**, *9*, 1131. [CrossRef]
70. Neganova, M.; Semakov, A.; Aleksandrova, Y.; Yandulova, E.; Pukhov, S.; Anikina, L.; Klochkov, S. N-Alkylation of Anthracycline Antibiotics by Natural Sesquiterpene Lactones as a Way to Obtain Antitumor Agents with Reduced Side Effects. *Biomedicines* **2021**, *9*, 547. [CrossRef]

Disclaimer/Publisher's Note: The statements, opinions and data contained in all publications are solely those of the individual author(s) and contributor(s) and not of MDPI and/or the editor(s). MDPI and/or the editor(s) disclaim responsibility for any injury to people or property resulting from any ideas, methods, instructions or products referred to in the content.



Article

Tanshinone IIA Facilitates Efficient Cartilage Regeneration under Inflammatory Factors Caused Stress via Upregulating LncRNA NEAT1_2

Jingjing Sun ^{1,†}, Wei Chen ^{2,†}, Zheng Zhou ^{1,*}, Xin Chen ², You Zuo ¹, Jiaqian He ¹ and Hairong Liu ^{2,*}

¹ College of Biology, Hunan University, Changsha 410082, China; jingjingsun@hnu.edu.cn (J.S.); you-zuo@hotmail.com (Y.Z.); hejiaqian@hnu.edu.cn (J.H.)

² College of Material Science and Engineering, Hunan University, Changsha 410082, China; chenwei690@hnu.edu.cn (W.C.); chenxin_hnu@hnu.edu.cn (X.C.)

* Correspondence: zhouzheng@hnu.edu.cn (Z.Z.); liuhairong@hnu.edu.cn (H.L.)

† These authors contributed equally to this work.

Abstract: (1) Background: Osteoarthritis (OA) is a crippling condition characterized by chondrocyte dedifferentiation, cartilage degradation, and subsequent cartilage defects. Unfortunately, there is a lack of effective medicines to facilitate the repair of cartilage defects in OA patients. In this study, we investigated the role of lncRNA NEAT1_2 in maintaining the chondrocyte phenotype and identified tanshinone IIA (TAN) as a natural medicine that enhances NEAT1_2 levels, resulting in efficient cartilage regeneration under inflammatory cytokines. (2) Methods: The transcriptional levels of NEAT1_2 and cartilage phenotype-related genes were identified by RT-qPCR. The siRNA interference approach was utilized to silence NEAT1_2; the Alamar Blue assay was performed to determine chondrocyte viability under inflammatory conditions. To evaluate the concentrations of collagen type II and glycosaminoglycans distributed by chondrocytes in vitro and in vivo, immunohistochemical staining and Safranin O staining were used. (3) Results: IL-1 β suppresses NEAT1_2 and genes related to the chondrocytic phenotype, whereas TAN effectively upregulates them in a NEAT1_2-dependent manner. Consistently, TAN alleviated chondrocyte oxidative stress inhibited cartilage degradation by modulating the relevant genes and promoted efficient cartilage regeneration in vitro and in vivo when chondrocytes are exposed to inflammatory cytokines. (4) Conclusions: TAN enhances the expression of NEAT1_2 inhibited by IL-1 β and affects the transcription of chondrocytic phenotype-related genes, which promotes cartilage regeneration in an inflammatory environment.

Keywords: osteoarthritis; tanshinone IIA; NEAT1_2; cartilage defects repair; inflammatory

Citation: Sun, J.; Chen, W.; Zhou, Z.; Chen, X.; Zuo, Y.; He, J.; Liu, H. Tanshinone IIA Facilitates Efficient Cartilage Regeneration under Inflammatory Factors Caused Stress via Upregulating LncRNA NEAT1_2. *Biomedicines* **2023**, *11*, 3291. <https://doi.org/10.3390/biomedicines11123291>

Academic Editors: Elisa Belluzzi and Leonardo Caputo

Received: 22 October 2023

Revised: 29 November 2023

Accepted: 8 December 2023

Published: 12 December 2023



Copyright: © 2023 by the authors. Licensee MDPI, Basel, Switzerland. This article is an open access article distributed under the terms and conditions of the Creative Commons Attribution (CC BY) license (<https://creativecommons.org/licenses/by/4.0/>).

1. Introduction

Osteoarthritis (OA) is a prevalent degenerative joint disease that threatens millions of patients, and it involves various histological lesions around the infrapatellar fat pad and synovium, periarticular muscles, ligaments, subchondral bone, and especially articular cartilage [1,2]. Compared with other tissues, articular cartilage mainly consists of chondrocytes and the large amount of extracellular matrix (ECM) which they produce. Chondrocytes are responsible for maintaining the balance between ECM anabolism and catabolism. However, numerous factors such as inflammatory cytokines, abnormal mechanical stimuli, chondrocyte apoptosis, and oxidative stress disrupt chondrocyte physiology and the balance of matrix transitions, which in turn leads to matrix loss and tissue degeneration, resulting in OA [3,4]. The inflammatory cytokines, especially interleukin (IL)-1 β and tumor necrosis factor- α (TNF- α), play a dominant role in the process of chondrocyte dedifferentiation. They downregulate chondrocytic phenotype-related genes such as SRY-Box Transcription Factor 9 (SOX9) and Aggrecan (ACAN) genes as well as collagen type II (COLII), contributing to the dedifferentiation of chondrocytes and subsequent cartilage

defects [5]. Currently authorized therapies are still primarily concerned with symptomatic alleviation. Consequently, there is an urgent requirement to further comprehend the role of inflammation in the development and progression of OA, as well as to develop medical treatments to repair OA cartilage defects.

Tanshinone IIA (TAN) is a lipophilic diterpene extracted from *Salvia miltiorrhiza* Bunge, a herbal medicine with many active ingredients, which has anti-inflammatory [6], antioxidant [7], and vascular endothelial cell-protective properties [8]. It has been suggested that TAN is effective in the treatment of chronic inflammatory diseases [9–12]. For instance, the treatment of OA in SD rats with TAN resulted in a significant decrease in Mankin's score ($p < 0.002$), a significant decrease in the levels of inflammatory factors such as IL-1 β , TNF- α and inducible nitric oxide synthase (iNOS) in the serum of rats, and effective relief of OA symptoms [9]. TAN restricts the proliferation, migration, and invasion of rheumatoid arthritis (RA) fibroblast-like synoviocytes and effectively inhibits the increases in some matrix metalloproteinases and pro-inflammatory factors induced by TNF- α , thereby suppressing the inflammatory response and preventing knee joint destruction [10]. TAN resists the damage to chondrocytes by inflammatory stimuli and maintains their activities [11]. Moreover, TAN promotes the proliferation of chondrocytes and enhances the regeneration of cartilage tissue *in vitro* and *in vivo* [12]. It seems like that TAN may influence the cellular response to inflammatory-caused stress via regulating the expression of related proteins and ncRNAs.

Publications suggest that long noncoding RNAs (lncRNAs) play essential roles in OA, and bioactive small molecules, like TAN, may alter the expression of lncRNAs, including MALAT1, PVT1, HOTAIR, H19, and NEAT1 [13,14]. Nuclear-enriched abundant transcript 1 (NEAT1) plays an essential role in the advancement of several diseases, particularly inflammation [15–17]. Recently, lncRNA NEAT1 has been implicated in the regulatory processes of OA [18,19]. NEAT1_2 is one of the two heterodimeric transcripts of NEAT1, which serves a structural biological function as the core backbone of paraspeckles that participate in various cellular stress responses [20]. Hence, it is worth testing whether the bioactivity of TAN links with the expression of NEAT1_2 to maintain the cartilage phenotype.

In this study, we investigated how TAN influences the phenotype of chondrocytes in an inflammatory environment and prevents chondrocytes from oxidative stress and apoptosis induced by inflammatory stimuli. To explore the potential therapeutic implications, we also examined whether TAN affects cartilage regeneration through histological staining both *in vivo* and *in vitro*.

2. Materials and Methods

2.1. Cell Separation and Culture

The animal experiments involved in this study were approved by the Experimental Animal Ethics Committee, The Second Xiangya Hospital, Central South University, China. Rabbit chondrocytes were isolated from the articular cartilage of legs, which were obtained from New Zealand white rabbits (1-week-old, Hunan Slake Kingda Laboratory Animal Co., Changsha, China). Briefly, rabbit cartilage tissues were washed three times with PBS containing 1% antibiotics and digested with trypsin (Sangon Biotech (Shanghai) Co., Shanghai, China) at 37 °C for 30 min to remove other tissues and cells. Then, cartilage was cut into 1 mm³ pieces, and these pieces were digested with 0.2% collagenase II (Gibco, Carlsbad, CA, USA) at 37 °C for 8 h. Afterward, the digested cartilage pieces were filtered through a strainer and transferred to cell culture dishes for further incubation.

The human-derived chondrocytes were a gift from Dr Fang Bairong of the Second Xiangya Hospital of Central South University. Chondrocytes were extracted as described above. The chondrocytes and chondrosarcoma cells (SW1353) (Institute of Biochemistry and Cell Biology, Shanghai, China) were cultured in DMEM high glucose culture medium containing 10% fetal bovine serum (Gibco, Carlsbad, CA, USA) and 1% dual antibiotics (penicillin/streptomycin sulfate) at 37 °C. Cells were all treated in the exponential growth phase.

2.2. Preparation of Silk Fibroin Scaffolds and TAN-Loaded Silk Fibroin Scaffolds

Silk fibroin scaffolds and TAN-loaded silk fibroin scaffolds were prepared according to the methods in our published publications and the experimental steps were optimized [12]. Specifically, adding 0.02 M Na₂CO₃ solution over the cocoon boiling for 30 min, adding distilled water at 75 °C to wash twice, then drying the silk at 60 °C to a constant weight. LiBr solutions were added to dissolve the silk. The mixture should be dialysis and then centrifugation. Eventually, the collected silk protein supernatant was stored at 4 °C.

TAN (purity 98%, Aladdin, Shanghai, China) was dissolved in anhydrous ethanol and combined with the prepared silk fibroin solution to provide final TAN concentrations of 0, 5, 10, 20, and 40 µg/mL. The mixture was added into each well of a 96-well cell culture plate to reach the depth of 2 mm, and then frozen at −20 °C for 6 h, then transferred to −2 °C for 48 h. Following freezing, samples were lyophilized for 24 h to obtain TAN-loaded silk fibroin scaffolds and silk fibroin scaffolds. These scaffolds were named SF, SF/T5, SF/T10, SF/T20, and SF/T40, respectively, according to the concentration of TAN before mixing.

2.3. Characterization and Biocompatibility of TAN-Loaded Silk Fibroin Scaffolds

2.3.1. SEM

Scanning electron microscopy (SEM) was used to observe the microscopic morphology of tested samples (FEI Quanta 200, FEI Company, Hillsboro, OR, USA). The pore size distribution of the samples is also counted based on the microcosmograms.

2.3.2. Drug Release Properties of TAN-Loaded Silk Fibroin Scaffolds

To determine the TAN release capacity of the TAN-loaded silk fibroin scaffolds, the samples were incubated in PBS solution at pH 7.4 for 35 days and the supernatants were collected. The cumulative release of TAN was measured by UV spectrophotometry (UV2600, Shimadzu, Japan).

2.3.3. Cell Proliferation Assays

Rabbit chondrocytes (1×10^5) were inoculated on every tested sample. The proliferation of chondrocytes was evaluated by Alamar Blue assay [21], which was cultured in culture medium with different influence factors for 1, 3, 5, and 7 days. The reduction rate measured on the first day was normalized to characterize the proliferation ploidy of chondrocytes in this study.

2.4. Isolation and Extraction of Total RNA

Chondrocytes and SW1353 cells were incubated with normal culture medium and total RNA was extracted as the control samples. SW1353 cells and chondrocytes were cultured with culture medium, which contained 10 ng/mL IL-1β, for 24 h, then the proper volume of TAN solution was added into this IL-1β-containing culture medium (to obtain a final concentration of 2 µg/mL) to incubate these cells for 6 h, 12 h, 24 h, and 48 h.

We divided the TAN-loaded silk fibroin scaffolds into normal and inflammation groups according to the culture medium. The samples in the normal group were incubated with normal medium for 10 days. Samples of the inflammatory group were cultured in normal medium for 3 days and then cultured in medium containing 10 ng/mL IL-1β and 10 ng/mL TNF-α for 7 days.

We lysed the cells using Trizol (Invitrogen, Carlsbad, CA, USA) to extract total RNA and reverse transcription of total RNA with a reverse transcription kit (K1683, Thermo Scientific, Waltham, MA, USA). Following that, the samples were subjected to reverse transcription-quantitative polymerase chain reaction (RT-qPCR) and used the gene of glyceraldehyde-3-phosphate dehydrogenase (GAPDH) as the control. The relevant primer sequences are listed in Tables 1 and 2.

Table 1. Primer sequence for RT-qPCR in humans.

Gene	5'-3'	Primer
GAPDH	forward	TTCGACAGTCAGCCGCATCTTCT
	reverse	GCCCAATACGACCAAATCCGTTGA
NEAT1_2	forward	GGCCAGAGCTTTGTTGCTTC
	reverse	GGTGC GGGCACTTACTTACT
COLII	forward	TCACGTACTGCCCCTGAAG
	reverse	TGACCCTCAAACCTCATGCCTC
COLI	forward	GGCAACAGCAGGTTCACTTAC
	reverse	AGTTAGAACCCCTCCATCCC
ACAN	forward	TCGTGGTGAAAGGTGAGAGC
	reverse	CGTGGAGGAGCTGGTTTGAA
SOX9	forward	ACTCGCCCAACAGATCGCC
	reverse	GCTGGAGTCTGGTGGTTCGGTG

Table 2. Primer sequence for RT-qPCR in rabbits.

Gene	5'-3'	Primer
GAPDH	forward	TTGTCGCCATCAATGATCCAT
	reverse	GATGACCAGCTTCCC GTTCTC
SOX9	forward	GCGTCAACGGCTCCAGCAAGA
	reverse	GCGTTGTGCAAGTGCGGTAC
COLII	forward	GAGAGCCTGGGACCCCTGGAA
	reverse	CGCTCCAGCCTTCTCGTCAA
COLI	forward	CTAGCCACCTGCCAGTCTTTA
	reverse	GGACCATCATCACCATCTCTG
ACAN	forward	GCTGCTACGGAGACAAGGATG
	reverse	CGTTGCGTAAAAGACCTCACC
MMP1	forward	TTCCAAAGCAGAGAGGCAATG
	reverse	CACCTGGGTTGCTTCATCATC
MMP3	forward	GTGATACGCAAGCCCAAGGTGT
	reverse	CTCTTGGCAGATCCGGTGTGT
MMP13	forward	GTCTTCTGGCTCACGCTTTTC
	reverse	GGCAGCAACGAGAAAACAAGTT
iNOS	forward	GCTGGAGCTGAAGTGGTACGC
	reverse	CTCCGATCTCTGTGCCCATGT
APAF	forward	TCGTGGTCTGCTGATGGTGCT
	reverse	TGCTGTTACGGCCTGTTTGA
SOD2	forward	CAGAAGCACAGCCTCCCCGAC
	reverse	CCGTGGCGTTCAGGTTGTTC
COX2	forward	CCATTGACCAGAGCAGGCAGA
	reverse	CTCGGCAGCCATCTCCTTCTC
Bcl-2	forward	CGGAAGGGACTGGACCAGAGA
	reverse	GCTGTCTATGGGATCACCTCC
CASP3	forward	AAGCCACGGTGATGAAGGAGT
	reverse	TCGGCAAGCCTGAATAATGAA
Nrf 2	forward	ATTCTTTCGGCAGCATCTCT
	reverse	CTGGGTTACGCTATGAAGGCA
SOD1	forward	GCACGGATTCCATGTCCACCA
	reverse	TCACATTACCCAGGTCGCCCC

Abbreviation: *GAPDH*: glyceraldehyde-3-phosphate dehydrogenase; *COL II*: Collagen type II; *COL I*: Collagen type I; *ACAN*: Aggrecan; *SOX9*: SRY-Box Transcription Factor 9; *MMP1*: Matrix metalloproteinase 1; *MMP3*: Matrix metalloproteinase 3; *MMP13*: Matrix metalloproteinase 13; *iNOS*: Inducible nitric oxide synthase; *APAF*: Apoptotic peptidase activating factor; *SOD2*: Superoxide dismutase 2; *COX2*: Cyclooxygenase-2; *Bcl-2*: B-cell lymphoma-2; *CASP3*: Caspase 3; *Nrf 2*: Nuclear factor erythroid 2-related factor 2; *SOD1*: Superoxide dismutase 1.

2.5. Small Interfering RNA (siRNA) Transfection

To investigate how lncRNA NEAT1_2 influences the chondrogenic phenotype under the stress of inflammatory factors, SW1353 cells were transfected with a small interfering RNA targeting NEAT1_2 or with a control siRNA to silence NEAT1_2. Lipofectamine 2000 reagent (Invitrogen, Carlsbad, CA, USA) was employed to transfect SW1353 cells. After 24 h of IL-1 β stimulation, we added culture medium containing TAN and IL-1 β for 24 h and collected treated SW1353 cells. Total RNA was extracted from collected cells for further analysis.

2.6. Cartilage Regeneration Evaluation In Vitro and In Vivo

To evaluate the efficiency of cartilage regeneration, we rabbit inoculated chondrocytes (2×10^6) on the scaffolds and then cultured them for 2 or 4 weeks. Following incubation, samples were sliced and treated with hematoxylin and eosin (H&E) (Solarbio, Beijing, China) and safranin-O (SO) (Solarbio, Beijing, China) staining. The glycosaminoglycan (GAG) contained in samples was quantified using the colorimetric method of dimethyl methylene blue (DMMB).

To test the efficiency of cartilage regeneration in vivo, rabbit chondrocytes were seeded on the scaffolds and were cultured in vitro for 3 days. All tested samples were incubated with medium containing IL-1 β and TNF- α for one week. A total of 9 nude mice (6 weeks old, males, Hunan Slake Kingda Laboratory Animal Co., Changsha, China) were assigned randomly, and then the sample was implanted subcutaneously into each mouse. The implanted samples were collected 4 weeks after surgery. After a gross morphological examination was carried out, histological analysis (H&E, SO, and immunohistochemistry of type II collagen) of each sample was performed to assess the efficiency of cartilage regeneration in vivo.

2.7. Statistical Analysis

All data in this study are expressed as the standard deviation (mean \pm SD.) and are obtained from at least three independent samples or experiments ($n \geq 3$). Differences between groups were statistically assessed using one-way analysis of variance (ANOVA) or Student's *t*-test. Statistical analyses were performed by GraphPad Prism version 8.0 (GraphPad Software, San Diego, CA, USA). The significant differences were judged at the $p < 0.05$ (* $p < 0.05$, ** $p < 0.01$, *** $p < 0.001$).

3. Results

3.1. Under IL-1 β Caused Stress TAN Upregulates the Expression of NEAT1_2

It was suggested that as the backbone of paraspeckles NEAT1_2 is involved in the cellular replication stress response, possibly including the cellular response to inflammatory factors [22,23]. We speculated that the dedifferentiation of chondrocytes in OA patients may relate to the alteration of NEAT1_2. By using human chondrocytes, with incubation with IL-1 β , the level of NEAT1_2 was significantly reduced (Figure 1A). Since human chondrocytes can be cultured for limited generation, the level of NEAT1_2 significantly declined under IL-1 β -caused stress in a chondrosarcoma cell line (Figure 1B), SW1353, which will be used as the model to carry out further investigation. Based on publications, it seems likely that bioactive small molecules, which are purified from plants or herbs that are used to treat OA, may influence the expression of NEAT1_2 [24,25]. Interestingly, it has been revealed that TAN significantly upregulates NEAT1_2 in chondrocytes in response to IL-1 β -caused stress (Figure 1C,D).

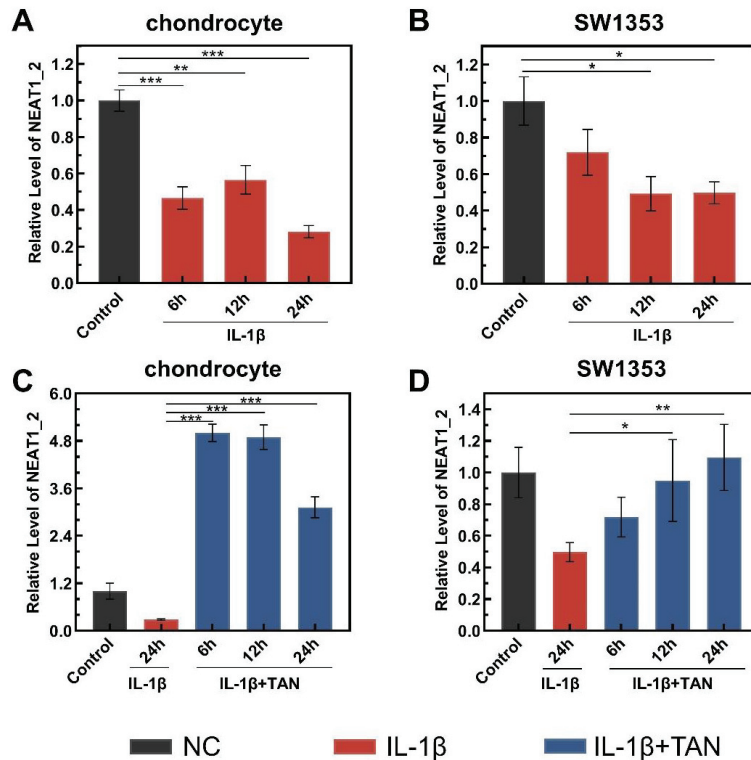


Figure 1. TAN upregulates NEAT1_2 transcription in response to IL-1 β stimulation. The relative RNA level of NEAT1_2 in chondrocytes (A) and SW1353 (B) under IL-1 β stimulation, and the relative RNA level of NEAT1_2 in chondrocytes (C) and SW1353 (D) after IL-1 β combined with TAN treatment. Values were normalized, and the RNA expression levels in untreated cells were set to 1. The data were obtained from 3 independent experiments ($n = 3$), and the error bars indicate SD. * $p < 0.05$, ** $p < 0.01$, *** $p < 0.001$, by two-tailed Student's t -test. NC: normal culture medium; IL-1 β : culture medium containing IL-1 β ; IL-1 β + TAN: culture medium containing IL-1 β and tanshinone IIA.

3.2. TAN Enhances the Transcription of Chondrocyte Phenotype Genes by Upregulating NEAT1_2 Expression under IL-1 β Caused Stress

Given that NEAT1_2 is known to be involved in cellular responses to different types of stress, it is plausible to consider that TAN may potentially upregulate NEAT1_2 under IL-1 β -induced stress, leading to an increase in the transcription of genes associated with the chondrocytic phenotype. In the case of IL-1 β -caused stress, the mRNA level of *SOX9*, *ACAN*, and the *COL II/COL I* ratio in cells were significantly increased following incubation with TAN (Figure 2A–C). To investigate whether IL-1 β caused stress in the upregulation of *SOX9*, *ACAN*, and the *COL II/COL I* ratio directly related to the TAN-induced upregulation of lncRNA NEAT1_2, an additional siRNA was used to knockdown NEAT1_2 in the same condition (Figure S1). It was displayed that with the knockdown of NEAT1_2 expression, TAN lost the capacity to upregulate *SOX9*, *ACAN*, and the *COL II/COL I* ratio under IL-1 β -caused stress (Figure 2D–F).

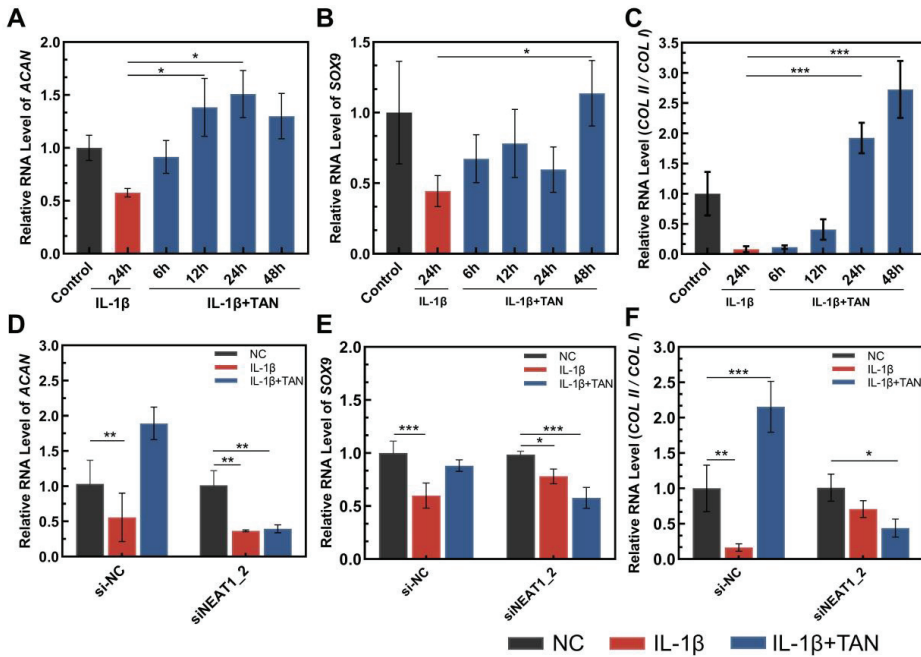


Figure 2. The relative RNA level of genes listed and the ratio of *COL II/COL I*. (A) The relative RNA level of *ACAN* in the cases indicated; (B) the relative RNA level of *SOX9* in the cases indicated; and (C) the ratio of *COL II/COL I* in the cases indicated. (D) The *ACAN* level following IL-1 β alone and IL-1 β combined with tanshinone IIA treatment in cells indicated; (E) the *SOX9* level following IL-1 β alone and IL-1 β combined with tanshinone IIA treatment in cells indicated; (F) the ratio of *COL II/COL I* following IL-1 β alone and IL-1 β combined with tanshinone IIA treatment in cells indicated. Values were normalized, and the RNA expression levels in untreated cells (control) were set to 1. The data were obtained from 3 independent experiments ($n = 3$). * $p < 0.05$, ** $p < 0.01$, *** $p < 0.001$, one-way analysis of variance. NC: normal culture medium; IL-1 β + TNF- α : culture medium containing IL-1 β and TNF- α ; IL-1 β + TNF- α + TAN: culture medium containing IL-1 β , TNF- α , and tanshinone IIA.

3.3. Preparation and Characterization of TAN-Loaded SF Scaffolds for Further Investigation

To achieve continuous exposure of chondrocytes to TAN and considering that the two-dimensional culture on cell culture plates is not suitable for long-term maintenance of the chondrocyte phenotype, which hinders the evaluation of cartilage regeneration, we established a TAN-loaded SF scaffold model to further our research. The SF and SF/T40 scaffolds revealed an internally interconnected three-dimensional porous structure in SEM images (Figure 3A). There was no significant difference in the pore size distributions of SF and SF/T40, which were all in the range of 60–120 μm (Figure 3A). It is demonstrated that the addition of TAN had no effect on the pore size of the scaffolds, and the range of the pore size was appropriate for chondrocyte migration and nutrient transport. After 35 days of cumulative drug release testing, all samples sustained TAN release; specifically, TAN release was rapid during the pre-culture period, reaching an inflection point after 7 days and a plateau TAN concentration in PBS solution after 28 days (Figure 3B). In addition, the cumulative release of TAN over time is also presented in Table S1. It is suggested that TAN-loaded SF scaffolds revealed the ability to gently release TAN while continually protecting the chondrocyte phenotype for cartilage repair during inflammatory factors incubation.

To verify the effect of inflammatory factors on chondrocyte proliferation, the culture medium containing IL-1 β and TNF- α was used to treat chondrocytes seeded on SF scaffolds

for 7 days. The data displayed that IL-1 β combined with TNF- α significantly inhibited the proliferation of chondrocytes (Figure 3C), implying that the combination of IL-1 β and TNF- α is suitable for representing the inflammatory factors of OA patients influencing chondrocytes.

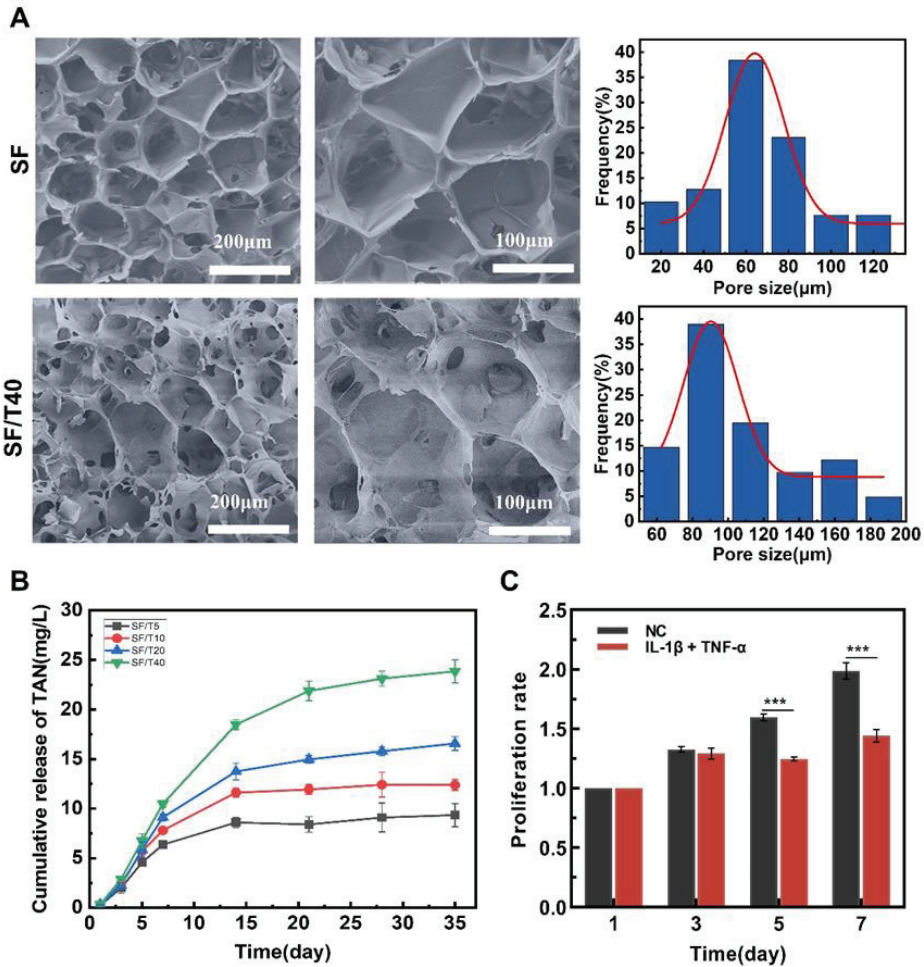


Figure 3. Preparation and characterization of SF scaffolds and TAN-loaded SF scaffolds. (A) Scanning electron microscope micrograph of SF and SF/T40. (B) Cumulative release of TAN from TAN-loaded silk fibroin scaffold in PBS (pH = 7.4) at 37 $^{\circ}\text{C}$. (C) Proliferation rates of chondrocytes grown on silk fibroin scaffolds incubated with normal culture medium and IL-1 β along with TNF- α containing culture medium, respectively ($n = 4$). The data were obtained from at least 3 independent experiments ($n = 3$). *** $p < 0.001$, by two-tailed Student's t -test.

3.4. TAN Upregulates the Transcription of Genes Facilitating Cartilage Regeneration under Inflammatory Factors Induced Stress

Whether TAN releasing from TAN-loaded SF scaffolds similarly affects adhered chondrocytes was validated by using rabbit chondrocytes, since SW1353 is a cancer cell, which is not suitable for testing cartilage regeneration. Following incubation with the culture medium containing IL-1 β and TNF- α for 7 days, *SOX9*, *ACAN*, and the *COLII/COL I* ratio were significantly downregulated, which is consistent with results obtained from cell culture plates (Figure 4A–C). Compared with chondrocytes seeded on SF scaffolds, in chondrocytes adhered on TAN-loaded SF scaffolds, the transcript levels of *SOX9*, *ACAN*, and

the *COLII*/*COLI* ratio were significantly upregulated by TAN following incubation with the culture medium containing IL-1 β and TNF- α . Within these TAN-loaded SF scaffolds, which were SF/T5, SF/T10, SF/T20, and SF/T40, the SF/T40 scaffold displayed the highest influence on genes transcriptional regulation in chondrocytes with the induction of IL-1 β and TNF- α (Figure 4A–C). Hence, the SF/T40 scaffold was selected for further investigation.

The maintenance of the chondrocyte phenotype by TAN may also be achieved by influencing the transcription of other cartilage-related genes, and the transcription of genes related to cartilage extracellular matrix degradation was detected with the same treatment applied to chondrocytes. Under IL-1 β and TNF- α caused stress, the transcription of *COX-2* was significantly upregulated, and the enhanced expression of *COX-2* subsequently promotes the secretion of matrix metalloproteinases (*MMPs*), which degrade the extracellular matrix of cartilage tissue (Figure 4D). With the induction of IL-1 β and TNF- α , the transcript levels of *MMP1*, *MMP3*, and *MMP13* in chondrocytes were significantly upregulated, and TAN significantly suppressed the transcript levels of *MMP1*, *MMP3*, and *MMP13* in cells adhered on SF/T40 scaffolds compared with those on SF scaffolds (Figure 4E–G).

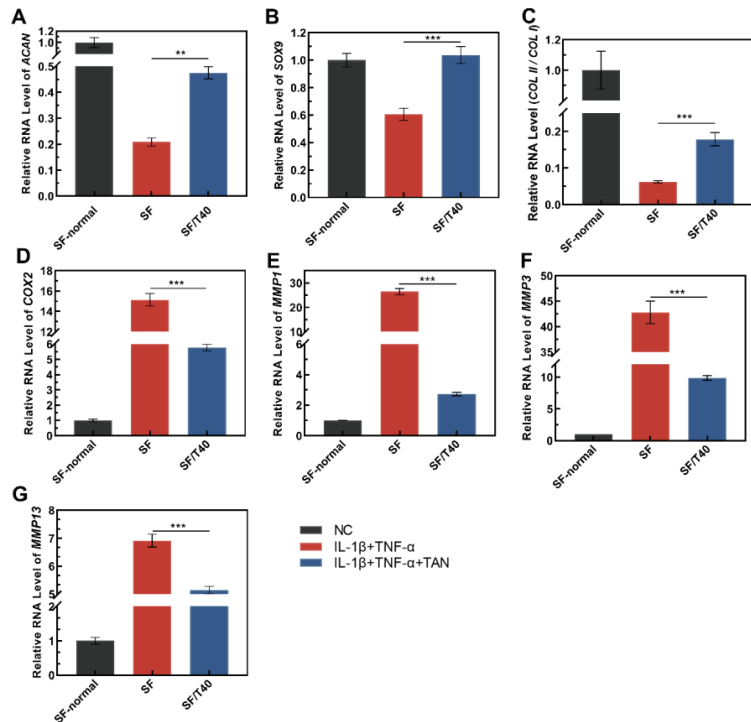


Figure 4. TAN influences the transcription of genes related to chondrogenesis and cartilage degradation in response to inflammatory stimuli. (A) *ACAN*, (B) *SOX9*, (C) the ratio of *COLII*/*COLI*, (D) *COX2*, (E) *MMP1*, (F) *MMP3*, (G) *MMP13*. The data were obtained from at least 3 independent experiments ($n = 3$), ** $p < 0.01$, *** $p < 0.001$, by two-tailed Student's t -test. NC: normal culture medium; IL-1 β + TNF- α : culture medium containing IL-1 β and TNF- α ; IL-1 β + TNF- α + TAN: culture medium containing IL-1 β , TNF- α , and tanshinone IIA.

3.5. TAN Attenuates the Aggravation of IL-1 β and TNF- α Induced Stress and Inhibits Apoptosis in Chondrocytes

Following chondrocyte exposure to IL-1 β and TNF- α , the transcription of *Nrf2*, *SOD1*, and *SOD2* were substantially repressed in chondrocytes and *iNOS* was significantly upregulated (Figure 5A). Similarly, the IL-1 β and TNF- α -caused suppression of *Nrf2*, *SOD1*, and *SOD2* was significantly reversed by TAN, which reduces the oxidative stress for cells.

The significant upregulation of *iNOS* induced by IL-1 β and TNF- α was declined by TAN, implying that it blocked the aggravation of stress in cells.

Meanwhile, TNF- α may cause apoptosis of chondrocytes, and whether TAN works in suppressing chondrocyte apoptosis in response to the stimuli of IL-1 β and TNF- α was tested with the same method. (Figure 5D–F). In contrast to chondrocytes seeded on the SF scaffold, the transcription of *Bcl-2* was upregulated by TAN in cells adhered to SF/T40 scaffolds. The transcription of *CASP3*, *CASP10*, and *APAF* was significantly upregulated in chondrocytes following IL-1 β and TNF- α induction, but in the same conditions, upregulation of *CASP3*, *CASP10*, and *APAF* was significantly reduced by TAN, which may inhibit the initiation and progress of apoptosis.

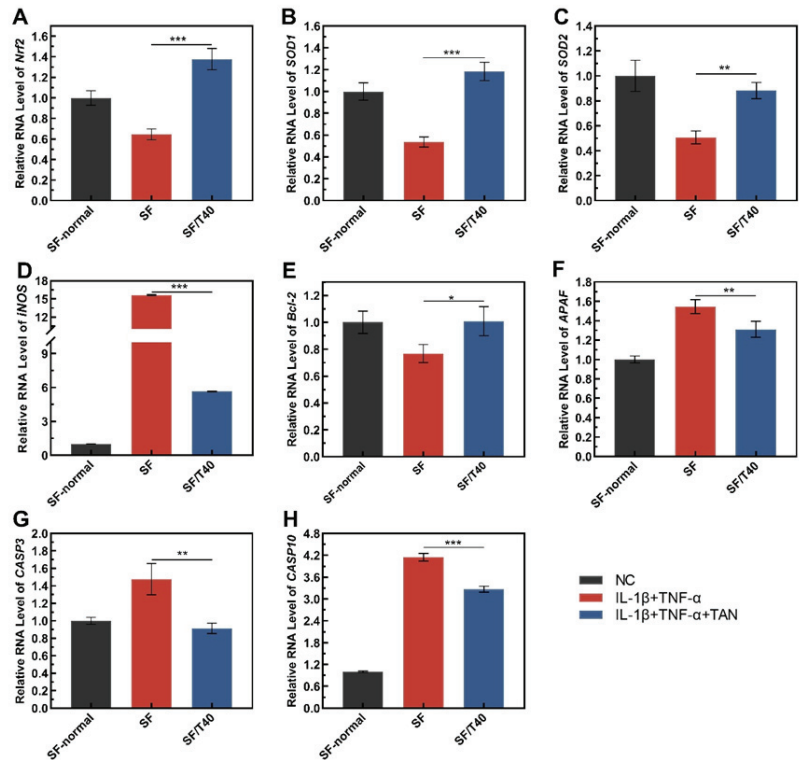


Figure 5. TAN affects the transcription of oxidative stress- and apoptosis-related genes in response to inflammatory stimuli. (A) *Nrf2*, (B) *SOD1*, (C) *SOD2*, (D) *iNOS*, (E) *Bcl-2*, (F) *APAF*, (G) *CASP3*, and (H) *CASP10*. The data were obtained from at least 3 independent experiments ($n = 3$). * $p < 0.05$, ** $p < 0.01$, *** $p < 0.001$, by two-tailed Student's *t*-test. NC: normal culture medium; IL-1 β + TNF- α : culture medium containing IL-1 β and TNF- α ; IL-1 β + TNF- α + TAN: culture medium containing IL-1 β , TNF- α , and tanshinone IIA.

3.6. TAN Promotes Cartilage Regeneration In Vitro following the Induction of IL-1 β and TNF- α

Based on all results described above, TAN maintains the chondrocytic phenotype of chondrocytes and keeps chondrocytes alive and active under IL-1 β and TNF- α caused stress, suggesting that TAN promotes cartilage regeneration even in a circumstance with the presence of inflammatory factors. To confirm this hypothesis, samples with seeded chondrocytes were incubated with a culture medium containing IL-1 β and TNF- α for 1 week, and then, two or four weeks of incubation with a normal culture medium was applied. Samples, which were SF-normal scaffolds with seeded chondrocytes, were incubated with a normal culture medium for 5 weeks and were regarded as the positive control.

After 5 weeks of incubation with a normal culture medium, many living chondrocytes and specific glycosaminoglycan (GAG) deposition were observed, indicating that cartilage tissue was regenerated (Figure 6A,D,G,J,M). With IL-1 β and TNF- α induction for 1 week, it seems that barely any cartilage tissue was generated resulting from extremely low GAG deposition (Figure 6B,E,H,K,N).

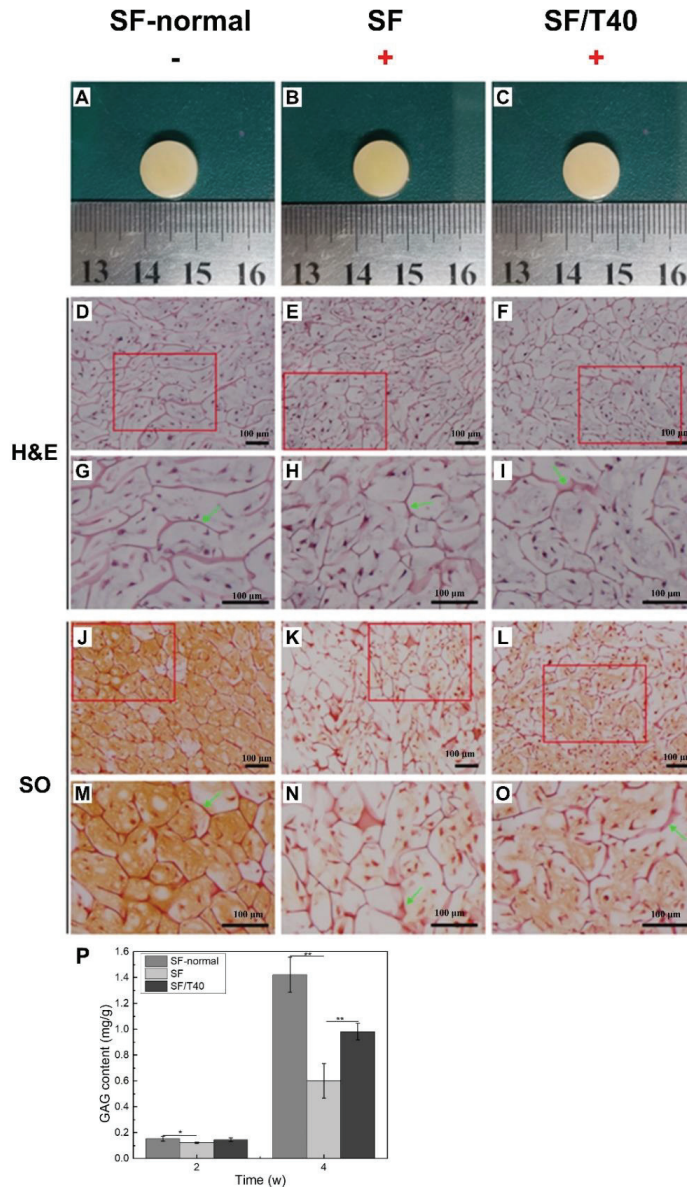


Figure 6. TAN promotes cartilage regeneration in vitro. Gross morphology (A–C), H&E staining (D–I), SO staining (J–O) and GAG content (P) of samples ($n = 3$) after 4 weeks of in vitro culture following IL-1 β and TNF- α stimuli for 1 week. (+ indicates addition of IL-1 β + TNF- α to the culture environment. Green arrows indicate scaffolds. The red box is the corresponding zoom area). The data were obtained from at least 3 independent experiments ($n = 3$). * $p < 0.05$, ** $p < 0.01$, by two-tailed Student's t -test.

With the assistance of TAN, the GAG deposition nearly covered the area of samples, demonstrating that chondrocytes maintained their phenotype and were able to generate cartilage tissue following the induction of IL-1 β and TNF- α for 1 week (Figure 6C,F,I,L,O). Furthermore, the deposition of GAG in every sample was quantified, by which the efficiency of cartilage tissue regeneration can be roughly estimated. Without disturbing with IL-1 β and TNF- α for 1 week, the GAG content was 1.42 ± 0.14 mg/g in positive control samples after 4 weeks, which was significantly higher than other samples that experienced IL-1 β and TNF- α induction (Figure 6P). The GAG content of samples was dropped to 0.60 ± 0.13 mg/g after these samples were treated with IL-1 β and TNF- α induction for 1 week, but with the assistance of TAN, the GAG content in samples significantly increased to 0.98 ± 0.06 mg/g with the same treatment. Although the GAG deposition in the two-week samples is not as high as that in the four-week samples, it demonstrates the same trend (Figure S2).

3.7. TAN Enhances Cartilage Regeneration In Vivo following IL-1 β and TNF- α Induction

To verify whether TAN regulates the transcription of genes to facilitate cartilage regeneration under IL-1 β and TNF- α -caused stress in vivo, tested scaffolds seeded with 2×10^6 chondrocytes were implanted into nude mice for 4 weeks following IL-1 β and TNF- α induction for 1 week. During the feeding period, the nude mice showed normal vital activity and no swelling or inflammation around the samples. Samples were collected after 4 weeks of subcutaneous implantation, and all samples retained their original shape (Figure 7A–C). Without IL-1 β and TNF- α treatment, chondrocytes were distributed evenly in the samples (Figure 7D), and efficient cartilage regeneration was observed everywhere in the samples (Figure 7G,J). Following IL-1 β and TNF- α treatment, living chondrocytes slightly reduced (Figure 7E), but the efficiency of cartilage regeneration dramatically declined, which is inferred from the reduced deposition of GAG and Col II (Figure 7H,K) compared with samples without IL-1 β and TNF- α treatment (Figure 7G,J). However, with TAN functioning living chondrocytes evenly distributed in samples (Figure 7F), the high intensity of SO staining and collagen II immunohistochemistry staining reflected that efficient cartilage regeneration happened in samples (Figure 7I,L) despite IL-1 β and TNF- α treatment. In conclusion, with the assistance of TAN, efficient cartilage regeneration can be achieved under the stress caused by inflammatory factors, suggesting that TAN can be applied to clinically treat OA patients to repair cartilage defects in the future.

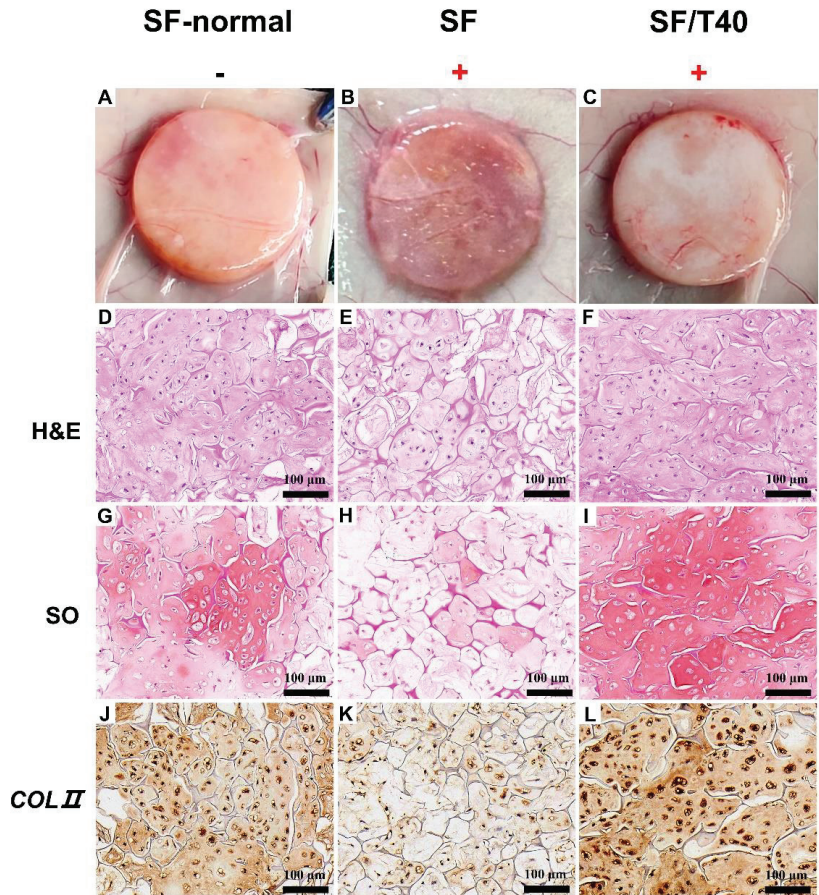


Figure 7. TAN enhances cartilage regeneration in vivo. Gross morphology (A–C), H&E staining (D–F), SO staining (G–I), and collagen II immunohistochemistry staining (J–L) of samples after 4 weeks of subcutaneous implantation in nude mice ($n = 3$) following IL-1 β and TNF- α induction for 1 week. (+' indicates addition of IL-1 β + TNF- α to the culture environment).

4. Discussion

Increased degradation of cartilage extracellular matrix leading to cartilage defects is a typical symptom in OA patients, and the key to effective treatment of degenerative OA is the progressive restoration of damaged articular cartilage [26,27]. There are currently no approved medicines that have been demonstrated to be effective in repairing defective tissue and delaying the progression of OA. There is accumulating proof that the pathogenesis of OA has been associated with the generation of pro-inflammatory mediators, cartilage matrix breakdown, chondrocyte oxidative stress, and apoptosis [28,29]. In this study, we report that TAN can upregulate the transcription of chondrocytic phenotype-related genes under inflammatory stress, and this upregulation is likely achieved through lncRNA NEAT1_2. Moreover, we found that TAN also upregulates other cartilage-related genes to alleviate chondrocyte oxidative stress and apoptosis and promote cartilage regeneration both in vitro and in vivo.

According to recent studies, long non-coding RNAs may play a crucial role in the prevention of the development of OA [5,14,30]. In particular, NEAT1 interacts with microRNAs to influence chondrocyte proliferation, migration, and apoptosis along with extracellular matrix (ECM) secretion, which in turn affects OA [25,31]. We revealed that NEAT1_2 plays

a key role in chondrocytes responding to the stress caused by inflammatory factors and dedifferentiation. Under the stress caused by IL-1 β , the level of NEAT1_2 is significantly reduced, as well as the downregulation of chondrocyte phenotype-related genes like SOX9 and ACAN and the subsequent dedifferentiation of chondrocytes. The SOX9 and ACAN genes and the collagen type II (COLII)/collagen type I (COLI) ratio as well as the matrix metalloproteinase gene (MMPs) are mainly associated with the chondrocyte phenotype, and their alteration implies an imbalance between ECM synthesis and degradation [32]. Interestingly, TAN reversed the transcription of genes related to the chondrocyte phenotype under inflammatory stress. Plant-derived active compounds have emerged in recent years as attractive pharmacological candidates for targeting lncRNAs and attaining disease treatments by altering lncRNA up- or down-regulation, and TAN is no exception [13,33,34]. Therefore, we knocked down NEAT1_2 by siRNA interference and verified that TAN's effect on cartilage phenotypes can be exerted via modifying NEAT1_2.

It has been well documented that IL-1 β and TNF- α induce oxidative stress in chondrocytes, causing chondrocyte dedifferentiation, apoptosis, and reduced proliferation, which fundamentally inhibits cartilage regeneration [35]. *Nrf2* is a major regulator of oxidative stress in chondrocytes, and its low expression links with the evolution and deterioration of OA [36]. In normal chondrocytes, *iNOS* exhibits a very low expression level, but its expression is significantly elevated in arthritic chondrocytes, catalyzing NO synthesis, and generating oxidative stress in cells, leading to further aggravation of joint inflammation [37]. Although the anti-inflammatory and antioxidant properties of TAN have been demonstrated to be effective in the treatment of neurological diseases as well as chronic diseases such as cardiovascular and nephritic diseases, only a handful of studies on the therapy of OA cartilage repair have been reported [38–40]. Our findings suggest that TAN relieved the oxidative stress by promoting the transcription of *Nrf2*, *SOD1*, and *SOD2* and repressing the transcription of *iNOS*, and initiation and TAN-blocked progress caused the upregulation of *Bcl-2* and downregulation of *CASP3*, *CASP10*, and *APAF*. Altogether, TAN may facilitate cartilage regeneration by maintaining the chondrocytic phenotype of chondrocytes and keeping chondrocytes alive and active under TNF- α and IL-1 β -caused stress. Furthermore, the results of tissue stain in vitro and in vivo demonstrated that TAN stimulated the secretion of COLII and GAGs by chondrocytes in response to IL-1 β and TNF- α -induced stress, successfully rescuing the loss of ECM degradation caused by inflammatory stimuli (Figures 6 and 7).

To sum up, TAN alleviated the imbalance between ECM synthesis and degradation caused by IL-1 β and TNF- α and inhibited the development of apoptosis and oxidative stress in cartilage chondrocytes, implying that TAN could maintain chondrocyte viability and promote cartilage regeneration in OA patients, and thus could be a promising drug for the treatment of OA in the future.

5. Conclusions

In summary, TAN upregulated the expression of lncRNA NEAT1_2 under IL-1 β -caused stress, by which the downregulation of chondrocytic phenotype-related genes caused by IL-1 β induction is significantly reversed and consequently maintains the chondrocytic phenotype of chondrocytes. Similarly, TAN inhibits the initiation and progress of apoptosis of chondrocytes and relieves the oxidative stress under IL-1 β and TNF- α -caused stress by regulating the transcription of related genes. Following IL-1 β and TNF- α induction for 1 week, TAN facilitates efficient cartilage regeneration in vitro and in vivo, suggesting that it can be an innovative strategy for treating OA patients in the future.

Supplementary Materials: The following supporting information can be downloaded at: <https://www.mdpi.com/article/10.3390/biomedicines11123291/s1>, Figure S1: The efficiency of siRNA interfering with NEAT1_2 in SW1353 indicated. *** $p < 0.001$, by two-tailed Student's *t*-test. Figure S2: TAN promotes cartilage regeneration in vitro. Gross morphology (A–C), H&E staining (D–I) and SO staining (J–O) of samples ($n = 3$) after 2 weeks of in vitro culture following IL-1 β and TNF- α stimuli for 1 week. ('+' indicates addition of IL-1 β + TNF- α to the culture environment. Green arrows

indicate scaffolds. The red box is the corresponding zoom area.) ('+' indicates addition of IL-1 β + TNF- α to the culture environment. Green arrows indicate scaffolds. The red box is the corresponding zoom area.). Table S1: Cumulative release of TAN over time, in mg/L.

Author Contributions: Z.Z. and H.L. were responsible for the conception and design of the study. J.S. acquired the lncRNA NEAT1_2 data and performed the analysis and interpretation of the data. W.C. constructed silk fibroin scaffold models for the cartilage regeneration data. X.C. is responsible for the layout of charts. X.C., Y.Z. and J.H. contributed to the animal experiments. All authors participated in the drafting, revising, and submission of the final manuscript. All authors have read and agreed to the published version of the manuscript.

Funding: The authors sincerely appreciate the support of National Natural Science Foundation of China [No. 31520103905], the Natural Science Foundation of Hunan Province [grant no. 2021JJ30095], and the Natural Science Foundation of Changsha City [grant no. kq2014040].

Institutional Review Board Statement: The animal study protocol was approved by the Experimental Animal Ethics Committee, The Second Xiangya Hospital, Central South University, China. (approval No. 2022006, approval date 28 February 2022).

Data Availability Statement: Source data are available from the corresponding author upon reasonable request.

Acknowledgments: We sincerely thank Fang Bairong of the Second Xiangya Hospital of Central South University for the gift of chondrocytes.

Conflicts of Interest: The authors have declared that no competing interest exist.

References

- Chen, D.; Shen, J.; Zhao, W.; Wang, T.; Han, L.; Hamilton, J.L.; Im, H.-J. Osteoarthritis: Toward a comprehensive understanding of pathological mechanism. *Bone Res.* **2017**, *5*, 16044. [CrossRef]
- Braun, S.; Zaucke, F.; Brenneis, M.; Rapp, A.E.; Pollinger, P.; Sohn, R.; Jenei-Lanzl, Z.; Meurer, A. The Corpus Adiposum Infrapatellare (Hoffa's Fat Pad)—The Role of the Infrapatellar Fat Pad in Osteoarthritis Pathogenesis. *Biomedicines* **2022**, *10*, 1071. [CrossRef] [PubMed]
- Belluzzi, E.; Todros, S.; Pozzuoli, A.; Ruggieri, P.; Carniel, E.L.; Berardo, A. Human Cartilage Biomechanics: Experimental and Theoretical Approaches towards the Identification of Mechanical Properties in Healthy and Osteoarthritic Conditions. *Processes* **2023**, *11*, 1014. [CrossRef]
- Pettenuzzo, S.; Arduino, A.; Belluzzi, E.; Pozzuoli, A.; Fontanella, C.G.; Ruggieri, P.; Salomoni, V.; Majorana, C.; Berardo, A. Biomechanics of Chondrocytes and Chondrons in Healthy Conditions and Osteoarthritis: A Review of the Mechanical Characterisations at the Microscale. *Biomedicines* **2023**, *11*, 1942. [CrossRef] [PubMed]
- Fathollahi, A.; Aslani, S.; Jamshidi, A.; Mahmoudi, M. Epigenetics in osteoarthritis: Novel spotlight. *J. Cell. Physiol.* **2019**, *234*, 12309–12324. [CrossRef] [PubMed]
- Li, W.; Zhang, Y.; Xing, C.; Zhang, M. Tanshinone IIA represses inflammatory response and reduces radiculopathic pain by inhibiting IRAK-1 and NF-kappaB/p38/JNK signaling. *Int. Immunopharmacol.* **2015**, *28*, 382–389. [CrossRef] [PubMed]
- Wang, P.; Zhou, S.; Xu, L.; Lu, Y.; Yuan, X.; Zhang, H.; Li, R.; Fang, J.; Liu, P. Hydrogen peroxide-mediated oxidative stress and collagen synthesis in cardiac fibroblasts: Blockade by tanshinone IIA. *J. Ethnopharmacol.* **2013**, *145*, 152–161. [CrossRef]
- Ren, J.; Fu, L.; Nile, S.H.; Zhang, J.; Kai, G. *Salvia miltiorrhiza* in Treating Cardiovascular Diseases: A Review on Its Pharmacological and Clinical Applications. *Front. Pharmacol.* **2019**, *10*, 753. [CrossRef]
- Jia, P.T.; Zhang, X.L.; Zuo, H.N.; Lu, X.; Li, L. Articular cartilage degradation is prevented by tanshinone IIA through inhibiting apoptosis and the expression of inflammatory cytokines. *Mol. Med. Rep.* **2017**, *16*, 6285–6289. [CrossRef]
- Du, H.; Wang, Y.; Zeng, Y.; Huang, X.; Liu, D.; Ye, L.; Li, Y.; Chen, X.; Liu, T.; Li, H.; et al. Tanshinone IIA Suppresses Proliferation and Inflammatory Cytokine Production of Synovial Fibroblasts from Rheumatoid Arthritis Patients Induced by TNF- α and Attenuates the Inflammatory Response in AIA Mice. *Front. Pharmacol.* **2020**, *11*, 568. [CrossRef]
- Luan, L.; Liang, Z. Tanshinone IIA protects murine chondrogenic ATDC5 cells from lipopolysaccharide-induced inflammatory injury by down-regulating microRNA-203a. *Biomed. Pharmacother.* **2018**, *103*, 628–636. [CrossRef]
- Chen, W.; Xu, Y.; Li, H.; Dai, Y.; Zhou, G.; Zhou, Z.; Xia, H.; Liu, H. Tanshinone IIA Delivery Silk Fibroin Scaffolds Significantly Enhance Articular Cartilage Defect Repairing via Promoting Cartilage Regeneration. *ACS Appl. Mater. Interfaces* **2020**, *12*, 21470–21480. [CrossRef] [PubMed]
- Chen, Y.; Li, Z.; Chen, X.; Zhang, S. Long non-coding RNAs: From disease code to drug role. *Acta Pharm. Sin. B* **2021**, *11*, 340–354. [CrossRef] [PubMed]
- Ali, S.A.; Peffers, M.J.; Ormseth, M.J.; Jurisica, I.; Kapoor, M. The non-coding RNA interactome in joint health and disease. *Nat. Rev. Rheumatol.* **2021**, *17*, 692–705. [CrossRef] [PubMed]

15. Lin, S.; Wen, Z.; Li, S.; Chen, Z.; Li, C.; Ouyang, Z.; Lin, C.; Kuang, M.; Xue, C.; Ding, Y. LncRNA Neat1 promotes the macrophage inflammatory response and acts as a therapeutic target in titanium particle-induced osteolysis. *Acta Biomater.* **2022**, *142*, 345–360. [CrossRef] [PubMed]
16. Imamura, K.; Imamachi, N.; Akizuki, G.; Kumakura, M.; Kawaguchi, A.; Nagata, K.; Kato, A.; Kawaguchi, Y.; Sato, H.; Yoneda, M.; et al. Long noncoding RNA NEAT1-dependent SFPQ relocation from promoter region to paraspeckle mediates IL8 expression upon immune stimuli. *Mol. Cell* **2014**, *53*, 393–406. [CrossRef] [PubMed]
17. Wang, S.; Zhang, Q.; Wang, Q.; Shen, Q.; Chen, X.; Li, Z.; Zhou, Y.; Hou, J.; Xu, B.; Li, N.; et al. NEAT1 paraspeckle promotes human hepatocellular carcinoma progression by strengthening IL-6/STAT3 signaling. *Oncoimmunology* **2018**, *7*, e1503913. [CrossRef] [PubMed]
18. Li, D.; Sun, Y.; Wan, Y.; Wu, X.; Yang, W. LncRNA NEAT1 promotes proliferation of chondrocytes via down-regulation of miR-16-5p in osteoarthritis. *J. Gene Med.* **2020**, *22*, e3203. [CrossRef] [PubMed]
19. Wang, Z.; Hao, J.; Chen, D. Long Noncoding RNA Nuclear Enriched Abundant Transcript 1 (NEAT1) Regulates Proliferation, Apoptosis, and Inflammation of Chondrocytes via the miR-181a/Glycerol-3-Phosphate Dehydrogenase 1-Like (GPD1L) Axis. *Med. Sci. Monit.* **2019**, *25*, 8084–8094. [CrossRef]
20. Naganuma, T.; Nakagawa, S.; Tanigawa, A.; Sasaki, Y.F.; Goshima, N.; Hirose, T. Alternative 3'-end processing of long noncoding RNA initiates construction of nuclear paraspeckles. *EMBO J.* **2012**, *31*, 4020–4034. [CrossRef]
21. Li, Y.; Chen, X.; Zhou, Z.; Fang, B.; Chen, Z.; Huang, Y.; Hu, Y.; Liu, H. Berberine oleanolic acid complex salt grafted hyaluronic acid/silk fibroin (BOA-g-HA/SF) composite scaffold promotes cartilage tissue regeneration under IL-1 β caused stress. *Int. J. Biol. Macromol.* **2023**, *250*, 126104. [CrossRef]
22. Adriaens, C.; Standaert, L.; Barra, J.; Latil, M.; Verfaillie, A.; Kalev, P.; Boeckx, B.; Wijnhoven, P.W.; Radaelli, E.; Vermi, W.; et al. p53 induces formation of NEAT1 lncRNA-containing paraspeckles that modulate replication stress response and chemosensitivity. *Nat. Med.* **2016**, *22*, 861–868. [CrossRef] [PubMed]
23. Zhang, P.; Cao, L.; Zhou, R.; Yang, X.; Wu, M. The lncRNA Neat1 promotes the activation of inflammasomes in macrophages. *Nat. Commun.* **2019**, *10*, 1495. [CrossRef]
24. Hu, Y.; Gui, Z.; Zhou, Y.; Xia, L.; Lin, K.; Xu, Y. Quercetin alleviates rat osteoarthritis by inhibiting inflammation and apoptosis of chondrocytes, modulating synovial macrophages polarization to M2 macrophages. *Free. Radic. Biol. Med.* **2019**, *145*, 146–160. [CrossRef]
25. Fu, C.; Qiu, Z.; Huang, Y.; Lin, Q.; Jin, L.; Tu, H.; Ye, J.; Zheng, C.; Zhong, W.; Ma, D. Achyranthes bidentata polysaccharides alleviate endoplasmic reticulum stress in osteoarthritis via the lncRNA NEAT1/miR-377-3p pathway. *Biomed. Pharmacother.* **2022**, *154*, 113551. [CrossRef]
26. Dai, M.; Sui, B.; Xue, Y.; Liu, X.; Sun, J. Cartilage repair in degenerative osteoarthritis mediated by squid type II collagen via immunomodulating activation of M2 macrophages, inhibiting apoptosis and hypertrophy of chondrocytes. *Biomaterials* **2018**, *180*, 91–103. [CrossRef] [PubMed]
27. Li, B.; Guan, G.; Mei, L.; Jiao, K.; Li, H. Pathological mechanism of chondrocytes and the surrounding environment during osteoarthritis of temporomandibular joint. *J. Cell. Mol. Med.* **2021**, *25*, 4902–4911. [CrossRef] [PubMed]
28. Motta, F.; Barone, E.; Sica, A.; Selmi, C. Inflammation and Osteoarthritis. *Clin. Rev. Allergy Immunol.* **2022**, *64*, 222–238. [CrossRef]
29. Rakic, R.; Bourdon, B.; Hervieu, M.; Branly, T.; Legendre, F.; Saulnier, N.; Audigié, F.; Maddens, S.; Demoor, M.; Galera, P. RNA Interference and BMP-2 Stimulation Allows Equine Chondrocytes Redifferentiation in 3D-Hypoxia Cell Culture Model: Application for Matrix-Induced Autologous Chondrocyte Implantation. *Int. J. Mol. Sci.* **2017**, *18*, 1842. [CrossRef]
30. Ghafouri-Fard, S.; Poulet, C.; Malaise, M.; Abak, A.; Mahmud Hussien, B.; Taheriazam, A.; Taheri, M.; Hallajnejad, M. The Emerging Role of Non-Coding RNAs in Osteoarthritis. *Front. Immunol.* **2021**, *12*, 773171. [CrossRef]
31. Zhang, S.; Jin, Z.; Flora, S.J.S. Bone Mesenchymal Stem Cell-Derived Extracellular Vesicles Containing Long Noncoding RNA NEAT1 Relieve Osteoarthritis. *Oxidative Med. Cell. Longev.* **2022**, *2022*, 5517648. [CrossRef] [PubMed]
32. Charlier, E.; Deroyer, C.; Ciregia, F.; Malaise, O.; Neuville, S.; Plener, Z.; Malaise, M.; de Seny, D. Chondrocyte dedifferentiation and osteoarthritis (OA). *Biochem. Pharmacol.* **2019**, *165*, 49–65. [CrossRef] [PubMed]
33. Zhang, X.; Wang, T.; Yang, Y.; Li, R.; Chen, Y.; Li, R.; Jiang, X.; Wang, L. Tanshinone IIA attenuates acetaminophen-induced hepatotoxicity through HOTAIR-Nrf2-MRP2/4 signaling pathway. *Biomed. Pharmacother.* **2020**, *130*, 110547. [CrossRef]
34. Chen, W.; Guo, S.; Li, X.; Song, N.; Wang, D.; Yu, R. The regulated profile of noncoding RNAs associated with inflammation by tanshinone IIA on atherosclerosis. *J. Leukoc. Biol.* **2020**, *108*, 243–252. [CrossRef] [PubMed]
35. Kapoor, M.; Martel-Pelletier, J.; Lajeunesse, D.; Pelletier, J.P.; Fahmi, H. Role of proinflammatory cytokines in the pathophysiology of osteoarthritis. *Nat. Rev. Rheumatol.* **2011**, *7*, 33–42. [CrossRef] [PubMed]
36. Cai, D.; Yin, S.; Yang, J.; Jiang, Q.; Cao, W. Histone deacetylase inhibition activates Nrf2 and protects against osteoarthritis. *Arthritis Res. Ther.* **2015**, *17*, 269. [CrossRef] [PubMed]
37. Ahmad, N.; Ansari, M.Y.; Haqqi, T.M. Role of iNOS in osteoarthritis: Pathological and therapeutic aspects. *J. Cell Physiol.* **2020**, *235*, 6366–6376. [CrossRef]
38. Ansari, M.A.; Khan, F.B.; Safdari, H.A.; Almatroudi, A.; Alzohairy, M.A.; Safdari, M.; Amirzadeh, M.; Rehman, S.; Equbal, M.J.; Hoque, M. Prospective therapeutic potential of Tanshinone IIA: An updated overview. *Pharmacol. Res.* **2021**, *164*, 105364. [CrossRef]

39. Ding, B.; Lin, C.; Liu, Q.; He, Y.; Ruganzu, J.B.; Jin, H.; Peng, X.; Ji, S.; Ma, Y.; Yang, W. Tanshinone IIA attenuates neuroinflammation via inhibiting RAGE/NF- κ B signaling pathway in vivo and in vitro. *J. Neuroinflamm.* **2020**, *17*, 302. [CrossRef]
40. Li, G.; Liu, Y.; Meng, F.; Xia, Z.; Wu, X.; Fang, Y.; Zhang, C.; Liu, D. Tanshinone IIA promotes the apoptosis of fibroblast-like synoviocytes in rheumatoid arthritis by up-regulating lncRNA GAS5. *Biosci. Rep.* **2018**, *38*, BSR20180626. [CrossRef]

Disclaimer/Publisher's Note: The statements, opinions and data contained in all publications are solely those of the individual author(s) and contributor(s) and not of MDPI and/or the editor(s). MDPI and/or the editor(s) disclaim responsibility for any injury to people or property resulting from any ideas, methods, instructions or products referred to in the content.



Article

Identification of the Natural Steroid Sapogenin Diosgenin as a Direct Dual-Specific ROR α / γ Inverse Agonist

Patrik F. Schwarz[†], Alexander F. Perhal^{*,†}, Lucia N. Schöberl, Martin M. Kraus, Johannes Kirchmair and Verena M. Dirsch

Department of Pharmaceutical Sciences, Division of Pharmacognosy, University of Vienna, Josef-Holaubek-Platz 2, 1090 Vienna, Austria

* Correspondence: alexander.perhal@univie.ac.at

[†] These authors contributed equally to this work.

Abstract: The steroid sapogenin diosgenin is a well-known natural product with a plethora of described pharmacological activities including the amelioration of T helper 17 (Th17)-driven pathologies. However, the exact underlying mode of action of diosgenin leading to a dampened Th17 response is still largely unknown and specific molecular targets have yet to be identified. Here, we show that diosgenin acts as a direct ligand and inverse agonist of the nuclear receptor retinoic acid receptor (RAR)-related orphan receptor (ROR) α and ROR γ , which are key transcription factors involved in Th17 cell differentiation and metabolism. IC₅₀ values determined by luciferase reporter gene assays, employing constructs for either ROR γ -Gal4 fusion proteins or full length receptors, were in the low micromolar range at around 2 μ M. To highlight the functional consequences of this ROR α / γ inverse agonism, we determined gene expression levels of important ROR target genes, i.e., *IL-17A* and glucose-6-phosphatase, in relevant cellular in vitro models of Jurkat T and HepG2 cells, respectively, by RT-qPCR (reverse transcription quantitative PCR). Thereby, it was shown that diosgenin leads to a dose-dependent decrease in target gene expressions consistent with its potent cellular ROR inverse agonistic activity. Additionally, in silico dockings of diosgenin to the ROR ligand-binding domain were performed to determine the underlying binding mode. Taken together, our results establish diosgenin as a novel, direct and dual-selective ROR α / γ inverse agonist. This finding establishes a direct molecular target for diosgenin for the first time, which can further explain reported amendments in Th17-driven diseases by this compound.

Citation: Schwarz, P.F.; Perhal, A.F.; Schöberl, L.N.; Kraus, M.M.; Kirchmair, J.; Dirsch, V.M. Identification of the Natural Steroid Sapogenin Diosgenin as a Direct Dual-Specific ROR α / γ Inverse Agonist. *Biomedicines* **2022**, *10*, 2076. <https://doi.org/10.3390/biomedicines10092076>

Academic Editors: Leonardo Caputo, Laura Quintieri, Orazio Nicolotti, Alessandra Durazzo and Konstantinos Dimas

Received: 1 June 2022

Accepted: 23 August 2022

Published: 25 August 2022

Publisher's Note: MDPI stays neutral with regard to jurisdictional claims in published maps and institutional affiliations.



Copyright: © 2022 by the authors. Licensee MDPI, Basel, Switzerland. This article is an open access article distributed under the terms and conditions of the Creative Commons Attribution (CC BY) license (<https://creativecommons.org/licenses/by/4.0/>).

Keywords: natural products; steroid sapogenin; diosgenin; anti-inflammatory; ROR γ inverse agonists; ROR α inverse agonists; retinoic acid-related orphan receptors; ROR; ROR γ ; ROR α

1. Introduction

Retinoic acid receptor (RAR)-related orphan receptors (RORs) belong to the superfamily of ligand-dependent nuclear receptors with three subtypes expressed in humans: ROR α , β and γ . While ROR α and ROR γ are widely expressed in peripheral tissues, e.g., liver, skeletal muscle or immune cells, the expression of ROR β is more restricted to the central nervous system. [1,2] Importantly, ROR γ was shown to act as a key transcription factor in proinflammatory T helper 17 (Th17) cell differentiation, which can be induced downstream of the *signal transducer and activator of transcription* (STAT) 3 signaling pathway [3,4]. Furthermore, ROR γ acts as a master regulator in hepatic gluconeogenesis, a central process in the development of metabolic disorders such as type 2 diabetes [5]. Consistent with these central roles in immunological and metabolic processes, ROR γ represents an attractive molecular drug target, and it was shown that the inhibition of ROR γ transcriptional activity is effective against Th17-mediated conditions [6–8] as well as metabolic pathologies. [5,9] Apart from ROR γ , ROR α was also shown to be indispensable for Th17 development as only deletions of both nuclear receptors completely abolished Th17 differentiation [10]. Furthermore, mice that express a truncated and, thus, dysfunctional mutant of ROR α (*Rora*^{ts8/8})

“staggerer” mice) were shown to be resistant to diet-induced obesity [11], show impaired gluconeogenesis in the liver [12], and exhibit increased insulin sensitivity and glucose uptake in skeletal muscles [13]. Notably, many target genes, such as glucose-6-phosphatase (G6PC), were shown to be mutually regulated by ROR γ and ROR α [14]. Therefore, ROR α represents a promising drug target itself and can be considered as functionally redundant to ROR γ as far as immunological [15] and metabolic [16–18] effects are concerned.

Dioscoreae rhizoma (chinese yam, shānyào, lit. “mountain medicine”) is described in traditional Chinese medicine to tonify the Qi of lung, spleen and kidney and to nourish the kidney’s essence [19]. Diosgenin was first discovered in 1937 by Tsukamoto and colleagues in *Dioscorea tokoro* (Dioscoreaceae) and can be found, along with its corresponding saponins dioscin and protodioscin, in many different *Dioscorea* species [20,21]. Chemically, diosgenin belongs to the group of steroid saponogenins consisting of a spirostan scaffold with a characteristic spiroketal in position 22 and a hydroxy group in position 3 (Figure 1, bottom), which is glycosylated in the corresponding saponins dioscin and protodioscin with a trisaccharide (Figure 1, top). The saponin protodioscin is additionally glycosylated in position 26, resulting in the formation of a hemiketal (Figure 1, top right).

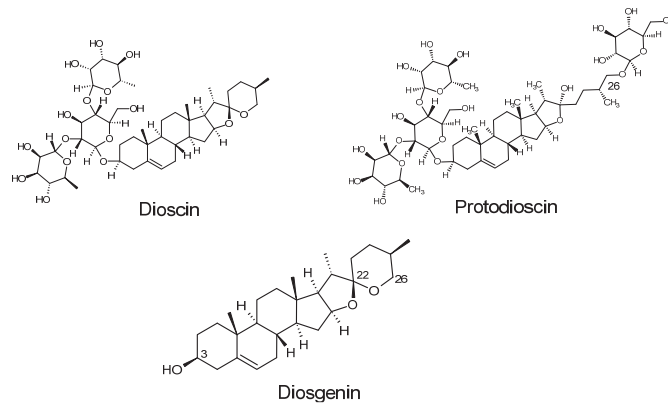


Figure 1. Structural formulas of the saponins dioscin and protodioscin (**top**) and of the saponogenin diosgenin (**bottom**).

Starting in the 1940s, diosgenin gained considerable attention due to its versatile use as a precursor compound for the synthesis of many important steroid hormones, including progesterone described by Russell Marker [22] or cortisone by Carl Djerassi [23]. Meanwhile, it became evident that diosgenin exerts many different beneficial pharmacological activities itself, including antiproliferative, anti-inflammatory, lipid-lowering and hypoglycemic activities (reviewed in [24,25]). Notably, several recent studies reported beneficial effects of diosgenin and its saponin dioscin in Th17-mediated diseases such as experimental autoimmune encephalomyelitis [26] or collagen-induced arthritis [27–29] where they could effectively suppress Th17 cell differentiation and ameliorate disease severities. Thus far, these studies attributed these beneficial effects to a reduction in STAT3 expression levels [26], its phosphorylation state [28] and/or to reduced expression levels of the downstream transcription factor ROR γ [27,29]. Furthermore, in some studies diosgenin effectively reduced the protein expression of the ROR γ target gene interleukin (IL)-17 [3] both in vitro and in vivo. [29,30] These particular studies were performed in isolated primary murine T lymphocytes from collagen-induced arthritis (CIA) or experimental autoimmune encephalomyelitis (EAE) disease models as well as in a keratinocyte (HaCaT) cell line. [29,30] Taken together, the data collected in previous studies led us to the hypothesis that diosgenin may not only act via reduction of ROR γ expression as already demonstrated before (e.g., by inhibition of STAT3 signaling) but also as a direct ligand of

ROR γ . This premise was further fueled by the high structural similarity between diosgenin and other reported natural ROR γ inhibitors (reviewed in [31]).

To answer this question and to gain a better overall understanding of the pharmacology of diosgenin, we studied its effects on ROR γ using *in vitro* and *in silico* techniques (Figure 2).

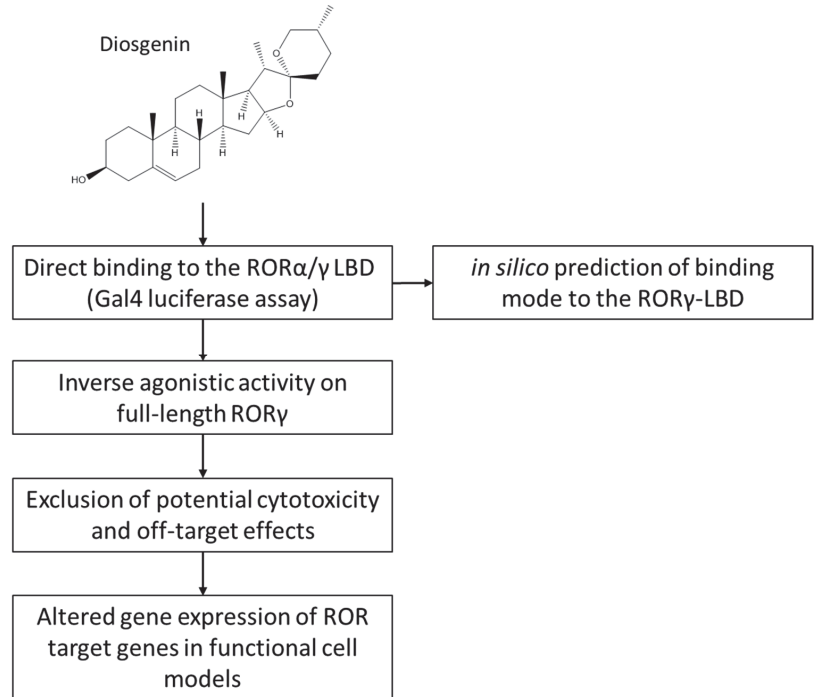


Figure 2. Graphical scheme of the study approach. First, the direct binding of diosgenin to the ROR γ (and subsequently the ROR α) LBD was examined using ROR α/γ -Gal4 luciferase assays. The inverse agonistic activity elucidated via the Gal4 assays was subsequently confirmed using full-length ROR γ luciferase assays. Then, cytotoxicity and potential off-target effects were excluded using resazurin and nuclear receptor-Gal4 assays, respectively. Finally, changes in target gene expression of ROR γ target genes in functional cellular models were studied. *In silico* prediction of diosgenin's binding mode was performed by employing molecular docking.

2. Materials and Methods

2.1. Cell Lines, Plasmids and Chemicals

Human embryonic kidney 293 (HEK293) and hepatoma G2 (HepG2) cells were purchased from the American Type Culture Collection (ATCC, Manassas, VA, USA). Jurkat T cells were a kind gift from Manfred Ogris (Department of Pharmaceutical Sciences, University of Vienna, Vienna, Austria). Dulbecco's modified Eagle medium (DMEM), Eagle's minimum essential medium (EMEM), Roswell Park Memorial Institute Medium-1640 (RPMI-1640), L-glutamine and penicillin–streptomycin mixtures were obtained from Lonza (Basel, Switzerland). Fetal bovine serum (FBS) was acquired from biowest (Nuaillé, France). Trypsin, the High-Capacity cDNA Reverse Transcription Kit, Lipofectamine LTX Reagent with PLUS Reagent, and Lipofectamin 3000 were purchased from Thermo Fisher Scientific (Waltham, MA, USA). Enhanced green fluorescent protein (pEGFP-N1) was obtained from Clontech (Mountain View, CA, USA). All other plasmids—the ROR γ -ligand-binding-domain (LBD)-Gal4-DNA-binding domain fusion construct (ROR γ -Gal4), tk(MH1000)4xLuc, farnesoid X receptor (FXR)-Gal4, liver X receptor (LXR)- α/β -Gal4,

peroxisome proliferator-activated receptor (PPAR)- γ -Gal4, retinoid X receptor (RXR)- α/β -Gal4, murine retinoic acid receptor (mRAR)- α -Gal4, ROR α/β -Gal4, full-length ROR γ transcript variant 1 (ROR γ V1) and ROR-response element (RORE)-Luc—were kindly made available by providers listed in Table S1. Primers for IL-17A and G6PC were synthesized at Microsynth (Balgach, Switzerland). Primers for Glyceraldehyde 3-phosphate dehydrogenase (GAPDH) and beta actin were acquired from Qiagen (Hilden, Germany). The Cell Activation Cocktail (without Brefeldin A) was purchased from Bio-Legend (San Diego, CA, USA). The innuPREP RNA Mini Kit 2.0 was obtained from Analytik Jena (Jena, Germany). The GoTaq Green Master Mix and the 5X reporter lysis buffer were purchased from Promega (Fitchburg, WI, USA). Ethanol (EtOH) 96% and ethylenediaminetetraacetic acid (EDTA) were obtained from Carl Roth (Karlsruhe, Germany). Diosgenin, SR2211, resazurin sodium salt, digitonin, T0901317, GW4064, GW3965, rosiglitazone, bexarotene and all-trans retinoic acid (ATRA) were acquired from Sigma-Aldrich (St. Louis, MO, USA). Dioscin and protodioscin were purchased from Biomol (Hamburg, Germany). Catalog numbers of all commercially obtained materials are listed in Table S2.

2.2. Cell Culture

HEK293 cells, Jurkat T cells and HepG2 cells were cultured in complete DMEM, RPMI-1640 and EMEM, respectively, which were supplemented with 10% FBS, 2 mM glutamine, 100 U/mL penicillin and 100 μ g/mL streptomycin at 37 °C and 5% CO₂. Cells were passaged every 2–3 days and only used up to passage number 30. Cell number and viability were determined using an automated cell counter (Vi-CELL™ XR Cell Viability Analyzer, Beckmann Coulter GmbH, Krefeld, Germany). For some experiments, media supplemented with 5% charcoal-stripped FBS (stripped media) were used.

2.3. Luciferase Assays

For luciferase assays, 6×10^6 HEK293 cells were seeded on 150 mm cell culture dishes and incubated for five hours. Afterwards, cells were transfected by calcium phosphate co-precipitation using 5 μ g of the nuclear receptor (ROR γ -Gal4 or full-length ROR γ), 5 μ g of a luciferase reporter (tk(MH1000)4xLuc for ROR γ -Gal4 experiments or RORE-Luc for full-length ROR γ experiments) and 3 μ g pEGFP-N1 (for assessing transfection efficiency) plasmid DNA and incubated overnight.

For selectivity tests, 5 μ g of different nuclear receptor-Gal4 constructs (ROR α/β , FXR, LXR α/β , PPAR γ , RXR α/β and mRAR α) were transfected together with tk(MH1000)4 \times Luc and eGFP, as described before.

On the following day, the medium was changed, and cells were further incubated for another four to five hours before adding trypsin/EDTA to detach them from dishes. Complete DMEM was added to stop trypsinization, and cell suspensions were centrifuged at $410 \times g$ for four minutes. Cell pellets were resuspended in stripped DMEM and seeded at a density of 5×10^4 viable cells per well in a 96-well plate before treatment with the vehicle control (0.096% EtOH), respective positive controls or diosgenin at the indicated concentrations for 18 h. Subsequently, cells were lysed using 5X reporter lysis buffer and luminescence and fluorescence values were measured using a spectrophotometer (Tecan Group AG, Männedorf, Switzerland). Relative luminescence units (RLU) were normalized to relative fluorescence units (RFU) and subsequently normalized to the vehicle control EtOH 0.096% (set to 1.0). Results are expressed as fold activations relative to the vehicle control.

2.4. Resazurin Conversion Assay

To check the metabolic activity of cells correlating with cell viability, cells were treated with the vehicle control (EtOH), digitonin at 50 μ g/mL (positive control for cytotoxicity) or test compounds (diosgenin, dioscin or protodioscin) at the indicated concentrations for 18 h. The next day, the medium was carefully removed and replaced with stripped DMEM

containing 10 µg/mL resazurin sodium salt. Cells were incubated for five hours before RFU values were measured at $\lambda_{em} = 590$ nm using a spectrophotometer.

2.5. Determination of Target Gene Expression by RT-qPCR

For reverse transcription quantitative PCR (RT-qPCR) experiments, 3×10^5 Jurkat T cells or 5×10^5 HepG2 cells per well were seeded on a 48 or a 6-well plate, respectively. For Jurkat T cells, 0.5 µg of full-length ROR γ plasmids were transfected using Lipofectamine LTX Reagent with PLUS Reagent according to the manufacturer's instructions. For HepG2 cells, 2.5 µg of full-length ROR γ plasmids were transfected using Lipofectamine 3000 according to the manufacturer's instructions. After 24 h incubation, transfected cells were treated with vehicle control (0.096% EtOH), positive control (1 µM SR2211 [7]) or diosgenin at the indicated concentrations. HepG2 cells were treated with compounds for 6 h. Jurkat T cells were stimulated for cytokine production after 18 h compound treatment using a cell activation cocktail containing phorbol-12-myristate-13-acetate and ionomycin at optimized concentrations for 5 h. Total RNA was extracted from cells using the innuPREP RNA Mini Kit 2.0 according to manufacturer's instructions. The concentration and purity of isolated RNA were measured using a spectrophotometer (Thermo Fisher Scientific, Waltham, MA, USA), and aliquoted RNAs were stored at -70 °C until use. 1 µg RNA was reverse transcribed into cDNA using the High-Capacity cDNA Reverse Transcription Kit according to manufacturer's instructions. Primer sequences for RT-qPCR amplifications are provided in Table 1.

Table 1. Primer used for RT-qPCR amplification.

Target Gene	Forward Primer	Reverse Primer
<i>IL-17A</i>	5'-ACCGATCCACCTCACCTTGG-3'	5'-AGTCCACGTTCCCATCAGCG-3'
<i>G6PC</i> [32]	5'-TCCATACTGGTGGGTTTTGG-3'	5'-GAGGAAAATGAGCAGCAAGG-3'
<i>GAPDH</i>	Hs_GAPDH_1_SG QuantiTect Primer Assay, GeneGlobe ID: QT00079247, Detected transcript: NM_001256799	
<i>beta actin</i>	Hs_ACTB_1_SG QuantiTect Primer Assay, GeneGlobe ID: QT00095431, Detected transcript: NM_001101	

RT-qPCR amplification reactions were performed using the GoTaq Green Master Mix with a cDNA amount of 40 ng and 10 µM primer concentration (or diluted as recommended by the manufacturer in case of QuantiTect primer) in a final reaction volume of 15 µL on a thermocycler (Roche Diagnostics, Rotkreuz, Switzerland). The PCR reaction consisted of one initial denaturation step (2 min at 95 °C) and 50 amplification cycles (denaturation step: 15 s at 95 °C, annealing/extension step: 1 min at 60 °C). Expression levels of target genes were calculated using the $2^{-\Delta\Delta C_t}$ method [33] whereby the target gene expression levels were first normalized to the expression levels of the control housekeeping genes *GAPDH* or *beta actin* before normalization to the expression levels of the vehicle control.

2.6. In Silico Docking

An X-ray structure of the ROR γ -LBD in complex with ursonic acid (PDB: 6J3N; resolution 1.99 Å) was selected for docking with GOLD (software version v2020.2.0, Cambridge Crystallographic Data Centre, Cambridge, UK) [34,35]. The protein structure was prepared with the Protein Preparation Wizard within the Maestro molecular modeling environment (software version 2021-3, Schrödinger Inc., New York, NY, USA) [36]. This preparation procedure included (i) the addition of hydrogen atoms as well as the assignment of protonation and metal charge states with Epik (a software module integrated into Maestro), (ii) the sampling of water orientations and the optimization of the hydrogen bond network and (iii) a restrained minimization using the OPLS3e force field [37] in order to converge heavy atoms to an RMSD of 0.30 Å (default settings used for all operations). A 3D structure of diosgenin was prepared with LigPrep within Maestro using default settings.

For docking with GOLD, the ligand-binding site was defined within GOLD to contain any atoms located within 6 Å of the co-crystallized ligand ursonic acid. Water molecules 701 and 756 were allowed to toggle on and off and to spin during docking. Default settings were used for the genetic algorithm, and a total of ten docking runs were executed (resulting in ten ligand poses). ChemPLP was used as scoring function.

2.7. Statistical Analysis

All data are presented as mean values \pm standard deviation (SD). Data were analyzed for normal distribution by a Shapiro–Wilk test. For normally distributed data, one-way analysis of variance (ANOVA) followed by Dunnett’s post hoc test was performed to determine statistical significance between treatment groups and the vehicle control group. For non-normally distributed data, a non-parametric Kruskal–Wallis test followed by Dunn’s post hoc test was performed. p -values ≤ 0.05 were considered to be statistically significant.

Concentration–response curves were fitted by nonlinear regression with sigmoidal dose–response curves and a standard Hill coefficient of -1.0 . Effects were considered as concentration-dependent when fitting of a sigmoidal regression curve was reasonably possible as determined by a goodness-of-fit value (R^2) close to 1.0. All statistical evaluations were performed with GraphPad Prism (software version 9.4, GraphPad Software Inc., San Diego, CA, USA).

3. Results

3.1. Diosgenin Is a Potent and Direct Inverse Agonist of the Nuclear Receptor ROR γ

In order to evaluate the potential of diosgenin as a direct ROR γ inverse agonist, luciferase assays employing ROR γ -Gal4 were performed. Thereby, diosgenin showed a potent and concentration-dependent inverse agonistic activity with a determined IC_{50} value of 1.73 μ M, which is highly comparable to that of the described ROR α/γ inverse agonist T0901317 [38] (Figure 3).

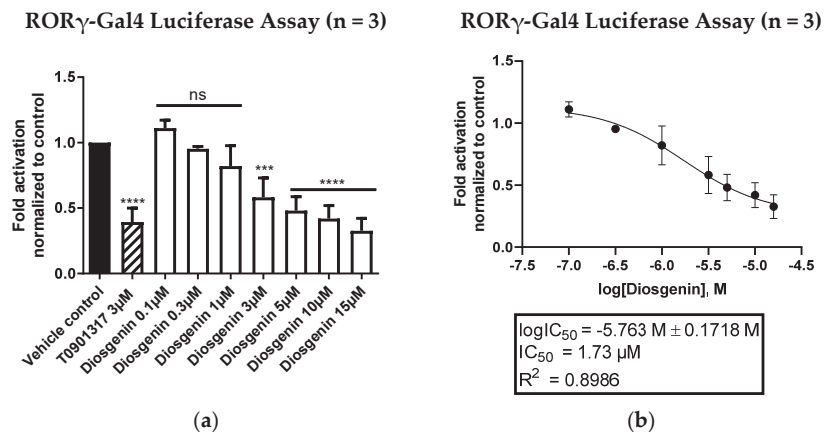
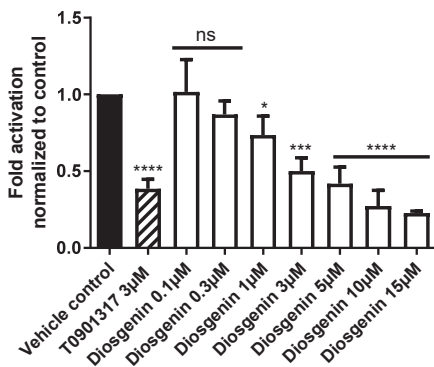


Figure 3. ROR γ -Gal4 luciferase assay of diosgenin in HEK293 cells. (a) Diosgenin was tested at different concentrations in a cell-based ROR γ -Gal4 luciferase assay to determine its inverse agonistic activity on ROR γ . The luminescence signals derived from the luciferase reporter were normalized to eGFP fluorescence and expressed as fold activation normalized to the vehicle control (0.096% EtOH). The described ROR α/γ inverse agonist T0901317 (3 μ M) was used as a positive control. Bar charts represent transactivation activities expressed as mean \pm SD of three biological replicates (n = 3) measured in technical quadruplicates. One-way ANOVA followed by Dunnett’s post hoc test were used for statistical analysis. **** $p \leq 0.0001$, *** $p \leq 0.001$, ns $p > 0.05$ compared to vehicle control. (b) Fitted concentration–response curve of the inverse agonistic activity of diosgenin on ROR γ -Gal4 with a determined IC_{50} value of 1.73 μ M. The curve was fitted by nonlinear regression using a standard

Hill coefficient of -1.0 . Data are presented as means \pm SD of three biological replicates ($n = 3$) measured in technical quadruplicates.

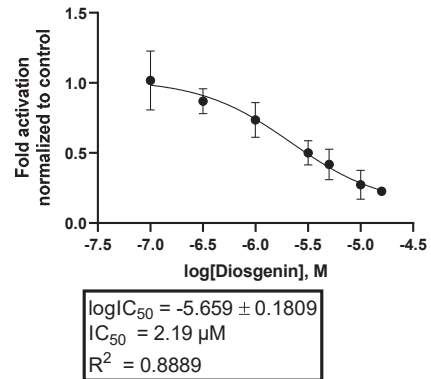
To further confirm the diosgenin-mediated reduction in RORE-dependent transcriptional activity, a luciferase assay employing full-length ROR γ (ROR γ V1) and a luciferase reporter gene under control of RORE was performed. Figure 4 shows the inverse agonistic activity of diosgenin on RORE-dependent transcriptional activity in a dose-dependent manner with a determined IC₅₀ value of 2.19 μ M.

Full-length ROR γ -RORE luciferase assay ($n = 3$)



(a)

Full-length ROR γ -RORE luciferase assay ($n = 3$)



(b)

Figure 4. Full-length ROR γ -RORE luciferase assay in HEK293 cells. (a) Diosgenin was tested at different concentrations in a cell-based full-length ROR γ luciferase assay to determine its inverse agonistic activity on full-length ROR γ . The luminescence signals derived from the luciferase reporter were normalized to eGFP fluorescence and expressed as fold activation normalized to the vehicle control (0.096% EtOH). The described ROR α / γ inverse agonist T0901317 (3 μ M) was used as a positive control. Bar charts represent transactivation activities expressed as mean \pm SD of three biological replicates ($n = 3$) measured in technical quadruplicates. One-way ANOVA followed by Dunnett's post hoc test were used for statistical analysis. **** $p \leq 0.0001$, *** $p \leq 0.001$, * $p \leq 0.05$, ns $p > 0.05$ compared to vehicle control. (b) Fitted concentration–response curve of the inverse agonistic activity of diosgenin on full-length ROR γ with a determined IC₅₀ value of 2.19 μ M. The curve was fitted by nonlinear regression using a standard Hill coefficient of -1.0 . Data are presented as means \pm SD of three biological replicates ($n = 3$) measured in technical quadruplicates.

3.2. Diosgenin Shows No Signs of Cytotoxicity in a Resazurin Conversion Assay

To exclude the possibility that the observed inverse agonistic activity of diosgenin might be biased by the cytotoxicity of the compound, we performed resazurin conversion assays in HEK293 cells treated with increasing concentrations of diosgenin. Thereby, no cytotoxicity of diosgenin could be observed up to the highest concentration (15 μ M) used for all assays (Figure 5). Additionally, no morphological signs of cytotoxicity could be observed microscopically in diosgenin-treated cells after overnight incubation (data not shown).

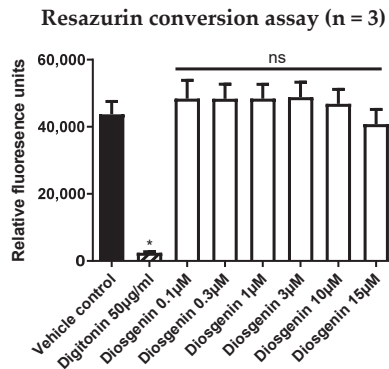


Figure 5. Resazurin conversion assay of diosgenin in HEK293 cells. To exclude potential cytotoxic effects of diosgenin in HEK293 cells, a resazurin conversion assay was performed. Cells were treated with digitonin (50 µg/mL) as a positive control or diosgenin at the indicated concentrations for 18 h. After the addition of resazurin (10 µg/mL), cells were incubated for another 5 h before RFU values were measured at $\lambda_{em} = 590$ nm. Data are presented as means \pm SD of three biological replicates (n = 3) measured in technical quadruplicates. Kruskal–Wallis tests followed by Dunn’s post hoc test were used for statistical analysis. * $p \leq 0.05$, ns $p > 0.05$ compared to the vehicle control.

3.3. The Steroid Saponins Dioscin and Protodioscin Do Not Act as ROR Inverse Agonists in Non-Toxic Concentrations

In a next step, we investigated whether the corresponding saponins of diosgenin, dioscin and protodioscin (Figure 1, top) were also able to act on ROR γ as inverse agonists. Therefore, both saponins were tested in ROR γ -Gal4 luciferase assays, as described above. Thereby, dioscin exhibited strong cytotoxicity in HEK293 cells up to a concentration of 1 µM (Figure S1), a concentration at which no inverse agonistic activity on ROR γ could be observed (Figure 6). On the other hand, protodioscin showed no apparent cytotoxicity in HEK293 cells (Figure S1) but also did not show any inverse agonistic activity on ROR γ at any of the concentrations tested (Figure 6).

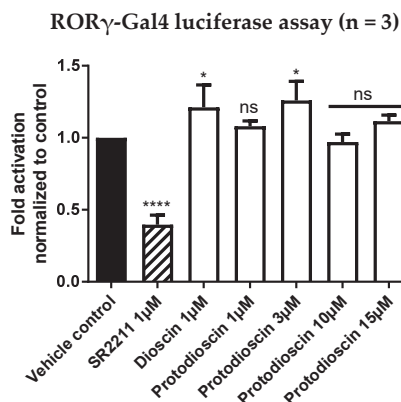


Figure 6. ROR γ -Gal4 luciferase assay of dioscin and protodioscin in HEK293 cells. Dioscin and protodioscin were tested at non-cytotoxic concentrations in a cell-based ROR γ -Gal4 luciferase assay to determine their potential activities on ROR γ . The luminescence signals derived from the luciferase reporter were normalized to eGFP fluorescence and expressed as fold activation normalized to the vehicle control (0.096% EtOH). The described ROR γ inverse agonist SR2211 (1 µM) was used as a positive control. Bar charts represent transactivation activities expressed as mean \pm SD of three biological

replicates (n = 3) measured in technical quadruplicates. One-way ANOVA followed by Dunnett's post hoc test were used for statistical analysis. **** $p \leq 0.0001$, * $p \leq 0.05$, ns $p > 0.05$ compared to vehicle control.

3.4. Diosgenin Is a Dual Specific Inhibitor of ROR α and ROR γ , but Shows No Activity on ROR β or Other Important Nuclear Receptors

To examine whether diosgenin is a selective modulator of ROR receptors, we performed additional luciferase screenings by employing several other important nuclear receptor-Gal4 constructs, including FXR, LXR α , LXR β , PPAR γ , RXR α , RXR β and mRAR α . Thereby, diosgenin showed no activities on any other nuclear receptor-Gal4 construct at the tested concentrations (Figure S2). To further investigate the ROR subtype selectivity of diosgenin, luciferase assays with ROR α and ROR β were performed as well. Notably, the results obtained showed a lack of activity on ROR β (Figure S2), while diosgenin was identified as an equipotent inverse agonist of ROR α with an IC₅₀ value of 2.17 μ M (Figure 7). This indicates that diosgenin acts as a dual specific inverse agonist of ROR α and ROR γ while showing high selectivity over ROR β and other nuclear receptors that bind ligands of the sterol metabolism, such as LXRs or FXR [39].

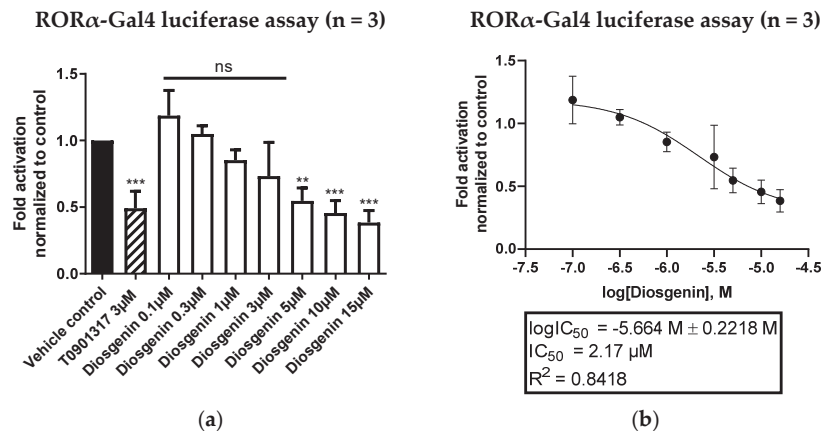


Figure 7. ROR α -Gal4 luciferase assay of diosgenin in HEK293 cells. (a) Diosgenin was tested at different concentrations in a cell-based ROR α -Gal4 luciferase assay to determine its inverse agonistic activity on ROR α . The luminescence signals derived from the luciferase reporter were normalized to eGFP fluorescence and expressed as fold activation normalized to the vehicle control (0.096% EtOH). The described ROR α / γ inverse agonist T0901317 (3 μ M) was used as a positive control. Bar charts represent transactivation activities expressed as mean \pm SD of three biological replicates (n = 3) measured in technical quadruplicates. One-way ANOVA followed by Dunnett's post hoc test were used for statistical analysis. *** $p \leq 0.001$, ** $p \leq 0.01$, ns $p > 0.05$ compared to vehicle control. (b) Fitted concentration–response curve of the inverse agonistic activity of diosgenin on ROR α -Gal4 with a determined IC₅₀ value of 2.17 μ M. The curve was fitted by nonlinear regression using a standard Hill coefficient of -1.0 . Data are presented as means \pm SD of three biological replicates (n = 3) measured in technical quadruplicates.

3.5. Diosgenin Downregulates ROR Target Gene Expression in Functional Cellular Models

In order to verify the functional consequences of ROR α / γ inhibition by diosgenin on the gene expression of important ROR-regulated target genes in suitable cell models, RT-qPCR experiments were performed. As ROR γ is a key transcription factor involved in Th17 cell differentiation and the production of their signature cytokine IL-17A [40], the expression levels of IL-17A were determined in ROR γ -transfected Jurkat T cells upon treatment with diosgenin at different concentrations. Jurkat T cells represent a human leukemia T cell line, which was shown to express ROR γ and IL-17A previously [41] and

was, therefore, chosen as a suitable cell model for investigations of altered ROR-mediated IL-17A production in this study. Concomitant with its ROR α/γ inverse agonism, the treatment with diosgenin led to a significant reduction in *IL-17A* mRNA expression in this cell model (Figure 8a).

To further confirm the functional activity of diosgenin on another important ROR target gene, mRNA transcripts of glucose-6-phosphatase (*G6PC*) [5] were quantified in ROR γ -transfected HepG2 cells by RT-qPCR. As gluconeogenesis is a metabolic process mainly occurring in the liver, the hepatocellular HepG2 cell line was chosen as a suitable cell model for these experiments. Consistently, treatment of these cells with diosgenin led to a significant reduction in *G6PC* expression levels (Figure 8b).

To further exclude potential cytotoxicity of diosgenin in these two cell lines, resazurin conversion assays were performed and no significant reductions in cell viability could be detected up to a concentration of 15 μ M (Figure S3).

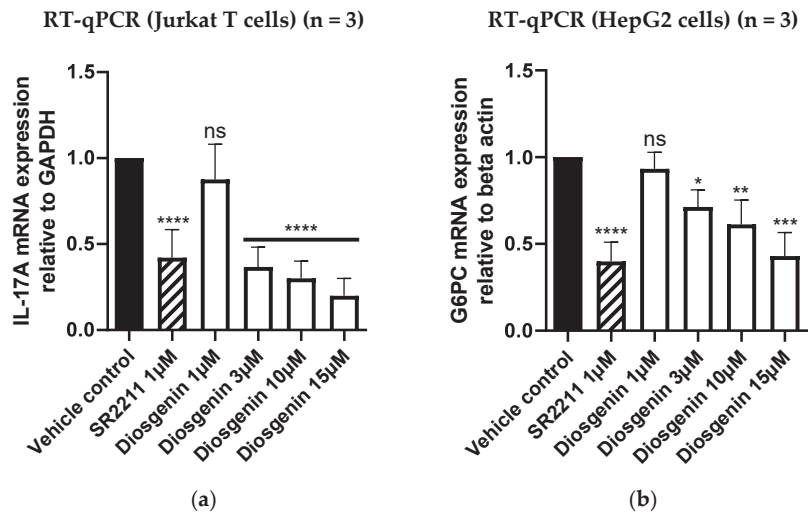


Figure 8. Determination of target gene expression in diosgenin-treated Jurkat T and HepG2 cells by RT-qPCR. To investigate the consequences of ROR inverse agonism by diosgenin, mRNA expression levels of ROR γ -regulated target genes were determined by RT-qPCR in functional cellular models (a) Downregulation of the ROR γ target gene *IL-17A* in ROR γ -transfected Jurkat T cells after treatment with diosgenin at different concentrations. The expression levels of *IL-17A* were normalized to the expression levels of the housekeeping gene *GAPDH* and subsequently normalized to the vehicle control (0.096% EtOH). The described ROR γ inverse agonist SR2211 (1 μ M) was used as a positive control. Bar charts represent expression levels relative to vehicle control expressed as mean \pm SD of three biological replicates (n = 3) measured in technical triplicates. One-way ANOVA followed by Dunnett's post hoc test were used for statistical analysis. **** $p \leq 0.0001$, ns $p > 0.05$ compared to vehicle control (b) Downregulation of the ROR γ target gene *G6PC* in ROR γ -transfected HepG2 cells after treatment with diosgenin at different concentrations. The expression levels of *G6PC* were normalized to the expression levels of the housekeeping gene *beta actin* and subsequently normalized to the vehicle control (0.096% EtOH). The described ROR γ inverse agonist SR2211 (1 μ M) was used as a positive control. Bar charts represent expression levels relative to vehicle control expressed as mean \pm SD of three biological replicates (n = 3) measured in technical triplicates. One-way ANOVA followed by Dunnett's post hoc test were used for statistical analysis. **** $p \leq 0.0001$, *** $p \leq 0.001$, ** $p \leq 0.01$, * $p \leq 0.05$, ns $p > 0.05$ compared to vehicle control.

3.6. In Silico Modelling of the Binding Mode of Diosgenin to the Ligand-Binding Domain of ROR γ

The likely binding mode of diosgenin in the ROR γ -LBD was derived by in silico docking with GOLD [34]. A total of ten docking poses were generated. All generated poses are consistent with respect to the location and orientation of the ligand, and the docking scores indicate a good geometric match of the predicted poses and the ligand-binding site (ChemPLP scores between 76.671 and 76.858). The docking poses indicate that the binding of diosgenin is likely driven by hydrophobic interactions with multiple residues forming the ligand-binding site, including Leu287, His323, Val361, Met365, Ala368, Val376, Phe388, Ile397, Ile400 and Phe401. The hydroxy moiety in position 3 of diosgenin is predicted to act as the key anchoring group by forming hydrogen bond interactions with Leu287, Arg367 and, via a water molecule, with Tyr281 (Figure 9).

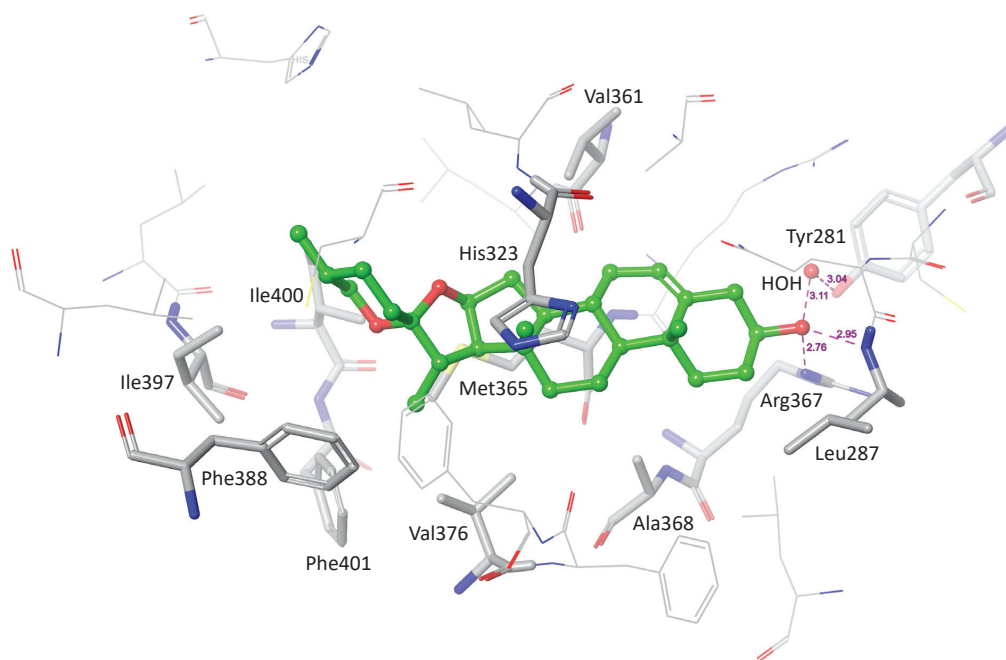


Figure 9. Predicted binding mode of diosgenin (green carbon atoms) in the ROR γ ligand-binding domain. To elucidate the binding mode of diosgenin to the ROR γ -LBD, molecular docking was employed. Protein preparation was performed using Maestro, and subsequent docking was performed with GOLD. Diosgenin is predicted to form hydrophobic interactions with residues Leu287, His323, Val361, Met365, Ala368, Val376, Phe388, Ile397, Ile400 and Phe401 of the ROR γ ligand-binding domain. The hydroxy group in position 3 forms hydrogen bonds with Leu287, Arg367 and, via a water molecule, with Tyr281. Amino acid residues forming hydrophobic interactions or hydrogen bonds with the ligand diosgenin are marked by the thick tube representation. The predicted hydrogen bonds are indicated with purple, dashed lines.

4. Discussion

Diosgenin represents a natural steroid sapogenin with a plethora of pharmacological activities, including anti-inflammatory and anti-diabetic effects demonstrated previously both in vitro and in vivo (recently reviewed in [40]). However, the specific underlying molecular targets regulated by diosgenin that are responsible for these effects remain largely unknown and have yet to be identified. In this regard, we could show, for the first time, that diosgenin acts as a direct and potent inverse agonist of the nuclear receptors ROR α and ROR γ . The activity of diosgenin could be demonstrated in this study by showing

a direct binding and transcriptional repression of ROR α / γ in both luciferase assays as well as by evaluating altered target gene expressions in functional cell models. Additionally, an *in silico* predicted binding mode of diosgenin to the ROR γ -LBD was proposed, and potentially limiting cytotoxic effects were excluded. These findings add considerable knowledge to the underlying mode of action of diosgenin, especially in the context of its previously described beneficial effects in T cell-related inflammatory diseases. Specifically, its observed beneficial effects in Th17 cell-mediated ailments such as EAE or rheumatic arthritis, can be further explained by the ROR inverse agonistic activity shown in this study. Together with previously identified effects on the STAT3 signaling pathway and observed reductions in the expression levels of ROR γ [27,29,42], the results of this study contribute to a more comprehensive understanding of diosgenin's molecular actions in these conditions. Moreover, diosgenin could be identified in this study as a dual specific inverse agonist of both ROR α and ROR γ while showing high specificity over other important nuclear receptors, including ROR β . This is of particular interest as ROR α was shown to be essential for Th17 cell differentiation on its own and was recently confirmed to be a non-redundant factor for pathogenic Th17 function [10]. Therefore, ROR α was proposed as an alternative target for the treatment of Th17-associated diseases [43].

Interestingly, we found that the steroid saponins dioscin and protodioscin showed no activity on ROR γ at non-cytotoxic concentrations in luciferase assays, limiting this activity to the aglycon diosgenin. However, it has been shown that a high proportion of ingested dioscin can become hydrolyzed to diosgenin at low pH values of gastric acid in the stomach [44]. This can also explain why dioscin was shown to be capable of inhibiting Th17 cell differentiation *in vivo* when applied orally [27,28] despite the lack of *in vitro* activity on ROR γ in our study.

In additional experiments, we could confirm that diosgenin was also able to down-regulate the expression of the ROR α / γ target genes *IL-17A* and glucose-6-phosphatase (*G6PC*) in suitable cellular models, further highlighting the functional consequences of the ROR inverse agonism. However, a potential limitation of these findings is the lack of confirmation on protein levels in this study, although other studies could already confirm such effects of diosgenin on protein levels for IL-17 in other cell models [29,30]. Moreover, alterations in mRNA expression levels represent the closest functional consequence of compounds acting as nuclear receptor modulators detectable within cells. Nevertheless, further confirmations of these effects on protein levels are needed and should be addressed in follow-up studies.

Eventually, molecular docking revealed that diosgenin binding to the ROR γ -LBD is likely driven by hydrophobic interactions as well as several anchoring hydrogen bonds formed by the hydroxyl group in position 3 of diosgenin. This might explain the observed inactivity of the steroid saponins dioscin and protodioscin on ROR γ as both of them are glycosylated at position 3. To experimentally verify the importance of the hydroxyl moiety in position 3 of diosgenin, mutagenesis of the amino acids predicted to interact with this position (Leu287, Arg367 and Tyr281) or derivatization (e.g., methylation) of the 3 hydroxyl group of diosgenin might be strategies worth pursuing in the future. Nevertheless, the information provided by the prediction of the underlying binding mode could already be used for further structural improvements in order to develop even more potent ROR inverse agonists on the basis of diosgenin. Of note, since the binding sites of ROR γ and ROR α are structurally highly conserved, it is plausible that diosgenin binds to both proteins with the same binding mode.

In addition to the aforementioned positive effects on Th17-mediated diseases, previous studies also found that diosgenin decreased plasma glucose levels in streptozotocin-induced diabetic rats [45]; reduced total cholesterol, triglyceride, and LDL levels in high-fat diet-fed Sprague–Dawley rats [46]; halted the progression of atherosclerosis by down-regulation of pro-inflammatory mediators in Wistar rats [47]; and reduced the incidence of invasive and non-invasive colon tumors in azoxymethane-induced rats by up to 60% [48] (reviewed in [49,50]). These promising activities of diosgenin, however, are highly limited

by the poor oral bioavailability of the compound, which precludes its potential therapeutic uses [51]. This issue could reportedly be overcome by employing various drug delivery strategies [52–54].

5. Conclusions

Taken together, in this study, we could demonstrate a direct inverse agonistic activity of diosgenin on the nuclear receptors ROR α and ROR γ for the first time. However, additional functional consequences of these activities on protein levels of distinct ROR α / γ target genes, the experimental validation of the *in silico* predictions, as well as overcoming pharmacokinetic obstacles should be addressed in future studies.

Collectively, our findings further extend the knowledge of the pharmacological profile of diosgenin and add to a more comprehensive picture of its beneficial effects in inflammatory and metabolic diseases reported elsewhere (reviewed in [55]) (Figure 10).

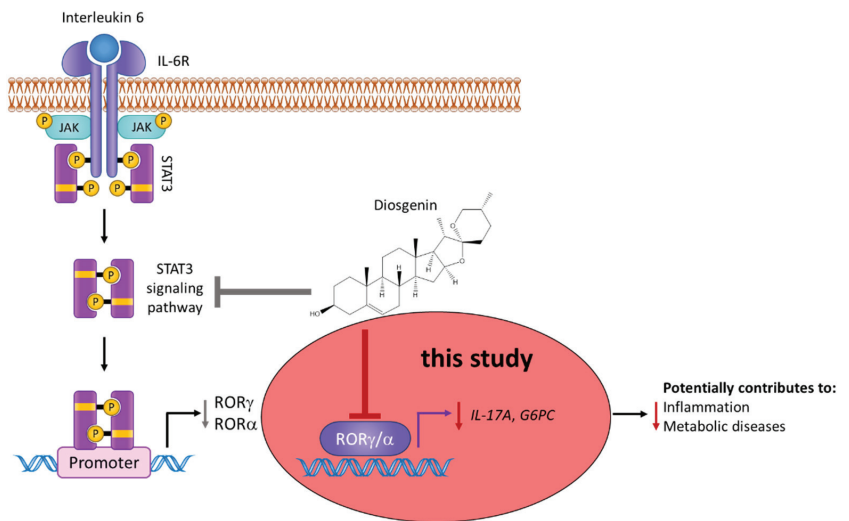


Figure 10. Overview on the updated pharmacological actions of diosgenin. Besides the already described effect of diosgenin on the expression and phosphorylation levels of STAT3 [42], this study now extends the activity profile of diosgenin to a direct and dual-specific modulation of the nuclear receptors ROR α and ROR γ (highlighted in red). The observed inverse agonistic activity on ROR α / γ was further shown to significantly decrease the expression levels of the important ROR target genes *IL-17A* and *G6PC*, which are directly involved in the pathogenesis of Th17-driven inflammatory processes and metabolic processes and thereby potentially contribute to the beneficial effects of diosgenin observed in these conditions [55].

Supplementary Materials: The following supporting information can be downloaded at: <https://www.mdpi.com/article/10.3390/biomedicines10092076/s1>, Figure S1: Resazurin conversion assay of dioscin and protodioscin in HEK293 cells; Figure S2: Nuclear receptor-Gal4 luciferase assays of diosgenin in HEK293 cells; Figure S3: Resazurin conversion assay of diosgenin in Jurkat T and HepG2 cells; Table S1: Donated plasmids and providers; Table S2: Catalog numbers and providers of commercially obtained materials.

Author Contributions: Conceptualization, P.F.S., A.F.P. and V.M.D.; formal analysis, P.F.S., A.F.P. and J.K.; funding acquisition, V.M.D.; investigation, P.F.S., A.F.P., L.N.S., M.M.K. and J.K.; methodology, P.F.S., A.F.P. and J.K.; project administration, V.M.D.; resources, V.M.D.; supervision, V.M.D.; visualization, P.F.S., A.F.P. and J.K.; writing—original draft, P.F.S. and A.F.P.; writing—review and editing, P.F.S., A.F.P., J.K. and V.M.D. All authors have read and agreed to the published version of the manuscript.

Funding: This project was funded in part (including open access publishing) by the Austrian Science Fund (FWF), project number P35241 (V.M.D.).

Institutional Review Board Statement: Not applicable.

Informed Consent Statement: Not applicable.

Data Availability Statement: The data supporting the findings of this study are available from the corresponding author upon reasonable request.

Acknowledgments: Authors would like to thank Andrea Szabo for drawing Figure 10.

Conflicts of Interest: The authors declare no conflict of interest.

Abbreviations

Ala (alanine); ANOVA (analysis of variance); Arg (arginine); ATCC (American Type Culture Collection); cDNA (complementary DNA); DMEM (Dulbecco's modified Eagle medium); DNA (deoxyribonucleic acid); EDTA (ethylenediaminetetraacetic acid); eGFP (enhanced green fluorescent protein); EMEM (Eagle's minimum essential medium); EtOH (ethanol); FBS (fetal bovine serum); FXR (farnesoid X receptor); G6PC (glucose-6-phosphatase); GAPDH (glyceraldehyde 3-phosphate dehydrogenase); HEK293 (human embryonic kidney 293); HepG2 (hepatoma G2); His (histidine); IC₅₀ (half maximal inhibitory concentration); IL (interleukin); Ile (isoleucine); LBD (ligand-binding domain); Leu (leucine); Luc (luciferase); LXR (liver X receptor); Met (methionine); OPLS (optimized potentials for liquid simulations); PCR (polymerase chain reaction); Phe (phenylalanine); PPAR (peroxisome proliferator-activated receptor); RAR (retinoic acid receptor); RFU (relative fluorescence units); RLU (relative luminescence units); RMSD (root-mean-square deviation); RNA (ribonucleic acid); ROR (retinoic acid receptor-related orphan receptor); RORE (ROR response element); RPMI-1640 (Roswell Park Memorial Institute-1640 medium); RT-qPCR (reverse transcription quantitative PCR); RXR (retinoid X receptor); SD (standard deviation); STAT (signal transducer and activator of transcription); Th (T helper); tk (thymidine kinase); Tyr (tyrosine); Val (valine); λ_{em} (emission wavelength)

References

1. Solt, L.A.; Griffin, P.R.; Burris, T.P. Ligand regulation of retinoic acid receptor-related orphan receptors: Implications for development of novel therapeutics. *Curr. Opin. Lipidol.* **2010**, *21*, 204–211. [CrossRef] [PubMed]
2. Stehlin, C.; Wurtz, J.-M.; Steinmetz, A.; Greiner, E.; Schüle, R.; Moras, D.; Renaud, J.-P. X-ray structure of the orphan nuclear receptor ROR β ligand-binding domain in the active conformation. *EMBO J.* **2001**, *20*, 5822–5831. [CrossRef] [PubMed]
3. Ivanov, I.I.; McKenzie, B.S.; Zhou, L.; Tadokoro, C.E.; Lepelley, A.; Lafaille, J.J.; Cua, D.J.; Littman, D.R. The orphan nuclear receptor ROR γ directs the differentiation program of proinflammatory IL-17+ T helper cells. *Cell* **2006**, *126*, 1121–1133. [CrossRef] [PubMed]
4. Ivanov, I.I.; Zhou, L.; Littman, D.R. Transcriptional regulation of Th17 cell differentiation. *Semin. Immunol.* **2007**, *19*, 409–417. [CrossRef]
5. Takeda, Y.; Kang, H.S.; Freudenberg, J.; DeGraff, L.M.; Jothi, R.; Jetten, A.M. Retinoic acid-related orphan receptor gamma (ROR γ): A novel participant in the diurnal regulation of hepatic gluconeogenesis and insulin sensitivity. *PLoS Genet.* **2014**, *10*, e1004331. [CrossRef]
6. Guendisch, U.; Weiss, J.; Ecoeur, F.; Riker, J.C.; Kaupmann, K.; Kallen, J.; Hintermann, S.; Orain, D.; Dawson, J.; Billich, A.; et al. Pharmacological inhibition of ROR γ suppresses the Th17 pathway and alleviates arthritis in vivo. *PLoS ONE* **2017**, *12*, e0188391. [CrossRef]
7. Kumar, N.; Lyda, B.; Chang, M.R.; Lauer, J.L.; Solt, L.A.; Burris, T.P.; Kamenecka, T.M.; Griffin, P.R. Identification of SR2211: A potent synthetic ROR γ -selective modulator. *ACS Chem. Biol.* **2012**, *7*, 672–677. [CrossRef]
8. Solt, L.A.; Kumar, N.; Nuhant, P.; Wang, Y.; Lauer, J.L.; Liu, J.; Istrate, M.A.; Kamenecka, T.M.; Roush, W.R.; Vidović, D.; et al. Suppression of TH17 differentiation and autoimmunity by a synthetic ROR ligand. *Nature* **2011**, *472*, 491–494. [CrossRef]
9. Jetten, A.M.; Kang, H.S.; Takeda, Y. Retinoic acid-related orphan receptors alpha and gamma: Key regulators of lipid/glucose metabolism, inflammation, and insulin sensitivity. *Front. Endocrinol.* **2013**, *4*, 1. [CrossRef]
10. Yang, X.O.; Pappu, B.P.; Nurieva, R.; Akimzhanov, A.; Kang, H.S.; Chung, Y.; Ma, L.; Shah, B.; Panopoulos, A.D.; Schluns, K.S.; et al. T helper 17 lineage differentiation is programmed by orphan nuclear receptors ROR alpha and ROR gamma. *Immunity* **2008**, *28*, 29–39. [CrossRef]

11. Lau, P.; Fitzsimmons, R.L.; Raichur, S.; Wang, S.C.; Lechtken, A.; Muscat, G.E. The orphan nuclear receptor, RORalpha, regulates gene expression that controls lipid metabolism: Staggerer (SG/SG) mice are resistant to diet-induced obesity. *J. Biol. Chem.* **2008**, *283*, 18411–18421. [CrossRef] [PubMed]
12. Kadiri, S.; Monnier, C.; Ganbold, M.; Ledent, T.; Capeau, J.; Antoine, B. The nuclear retinoid-related orphan receptor-alpha regulates adipose tissue glyceroneogenesis in addition to hepatic gluconeogenesis. *Am. J. Physiol. Endocrinol. Metab.* **2015**, *309*, E105–E114. [CrossRef]
13. Lau, P.; Fitzsimmons, R.L.; Pearen, M.A.; Watt, M.J.; Muscat, G.E. Homozygous staggerer (sg/sg) mice display improved insulin sensitivity and enhanced glucose uptake in skeletal muscle. *Diabetologia* **2011**, *54*, 1169–1180. [CrossRef]
14. Chopra, A.R.; Louet, J.F.; Saha, P.; An, J.; Demayo, F.; Xu, J.; York, B.; Karpen, S.; Finegold, M.; Moore, D.; et al. Absence of the SRC-2 coactivator results in a glycogenopathy resembling Von Gierke's disease. *Science* **2008**, *322*, 1395–1399. [CrossRef] [PubMed]
15. Dong, C. TH17 cells in development: An updated view of their molecular identity and genetic programming. *Nat. Rev. Immunol.* **2008**, *8*, 337–348. [CrossRef] [PubMed]
16. Huh, J.R.; Littman, D.R. Small molecule inhibitors of RORgamma: Targeting Th17 cells and other applications. *Eur. J. Immunol.* **2012**, *42*, 2232–2237. [CrossRef] [PubMed]
17. Yang, X.; Downes, M.; Yu, R.T.; Bookout, A.L.; He, W.; Straume, M.; Mangelsdorf, D.J.; Evans, R.M. Nuclear receptor expression links the circadian clock to metabolism. *Cell* **2006**, *126*, 801–810. [CrossRef]
18. Kang, H.S.; Angers, M.; Beak, J.Y.; Wu, X.; Gimble, J.M.; Wada, T.; Xie, W.; Collins, J.B.; Grissom, S.F.; Jetten, A.M. Gene expression profiling reveals a regulatory role for ROR alpha and ROR gamma in phase I and phase II metabolism. *Physiol. Genom.* **2007**, *31*, 281–294. [CrossRef]
19. Tai Lahans, L. *Integrating Conventional and Chinese Medicine in Cancer Care: A Clinical Guide*; Elsevier Health Sciences: Amsterdam, The Netherlands, 2007.
20. Yi, T.; Fan, L.L.; Chen, H.L.; Zhu, G.Y.; Suen, H.M.; Tang, Y.N.; Zhu, L.; Chu, C.; Zhao, Z.Z.; Chen, H.B. Comparative analysis of diosgenin in Dioscorea species and related medicinal plants by UPLC-DAD-MS. *BMC Biochem.* **2014**, *15*, 19. [CrossRef]
21. Tsukamoto, T.; Ueno, Y.; Ohta, Z. Diosgenin II. Glucoside of Dioscorea tokoro Makino. 3. Constitution of diosgenin. *J. Pharm. Soc. Jpn.* **1937**, *57*, 985–991. [CrossRef]
22. Marker, R.E.; Krueger, J. Sterols. CXII. Sapogenins. XLI. The Preparation of Trillin and its Conversion to Progesterone. *J. Am. Chem. Soc.* **1940**, *62*, 3349–3350. [CrossRef]
23. Lemin, A.J.; Djerassi, C. The Conversion of Diosgenin to Cortisone via 11-Ketosteroids of the 5 β -Series. *J. Am. Chem. Soc.* **1954**, *76*, 5672–5674. [CrossRef]
24. Jesus, M.; Martins, A.P.; Gallardo, E.; Silvestre, S. Diosgenin: Recent Highlights on Pharmacology and Analytical Methodology. *J. Anal. Methods Chem.* **2016**, *2016*, 4156293. [CrossRef]
25. Kim, J.K.; Park, S.U. An update on the biological and pharmacological activities of diosgenin. *EXCLI J.* **2018**, *17*, 24–28. [CrossRef]
26. Liu, W.; Zhu, M.; Yu, Z.; Yin, D.; Lu, F.; Pu, Y.; Zhao, C.; He, C.; Cao, L. Therapeutic effects of diosgenin in experimental autoimmune encephalomyelitis. *J. Neuroimmunol.* **2017**, *313*, 152–160. [CrossRef]
27. Cao, Y.J.; Xu, Y.; Liu, B.; Zheng, X.; Wu, J.; Zhang, Y.; Li, X.S.; Qi, Y.; Sun, Y.M.; Wen, W.B.; et al. Dioscin, a Steroidal Saponin Isolated from Dioscorea nipponica, Attenuates Collagen-Induced Arthritis by Inhibiting Th17 Cell Response. *Am. J. Chin. Med.* **2019**, *47*, 423–437. [CrossRef]
28. Xing, E.; Guo, Y.; Feng, G.; Song, H.; An, G.; Zhao, X.; Wang, M. Effects of dioscin on T helper 17 and regulatory T-cell subsets in chicken collagen type II-induced arthritis mice. *J. Chin. Med. Assoc.* **2019**, *82*, 202–208. [CrossRef]
29. Song, H.; Gao, Y.; Wang, Y.; Guo, Y.; Xing, E.; Zhao, X.; Li, W.; Zhang, J.; Yu, C. Effect of diosgenin on T-helper 17 cells in mice with collagen-induced arthritis. *Pharmacogn. Mag.* **2020**, *16*, 486. [CrossRef]
30. Wu, S.; Zhao, M.; Sun, Y.; Xie, M.; Le, K.; Xu, M.; Huang, C. The potential of Diosgenin in treating psoriasis: Studies from HaCaT keratinocytes and imiquimod-induced murine model. *Life Sci.* **2020**, *241*, 117115. [CrossRef]
31. Ladurner, A.; Schwarz, P.F.; Dirsch, V.M. Natural products as modulators of retinoic acid receptor-related orphan receptors (RORs). *Nat. Prod. Rep.* **2021**, *38*, 757–781. [CrossRef]
32. Karas, K.; Salkowska, A.; Karwaciak, I.; Walczak-Drzewiecka, A.; Dastyk, J.; Bachorz, R.A.; Ratajewski, M. The Dichotomous Nature of AZ5104 (an EGFR Inhibitor) Towards RORgamma and RORgammaT. *Int. J. Mol. Sci.* **2019**, *20*, 5780. [CrossRef]
33. Livak, K.J.; Schmittgen, T.D. Analysis of relative gene expression data using real-time quantitative PCR and the 2(-Delta Delta C(T)) Method. *Methods* **2001**, *25*, 402–408. [CrossRef] [PubMed]
34. Jones, G.; Willett, P.; Glen, R.C.; Leach, A.R.; Taylor, R. Development and validation of a genetic algorithm for flexible docking. *J. Mol. Biol.* **1997**, *267*, 727–748. [CrossRef] [PubMed]
35. GOLD, version v2020.2.0; Cambridge Crystallographic Data Centre (CCDC): Cambridge, UK, 2020.
36. Maestro, version 2021-3; Schrödinger Inc.: New York, NY, USA, 2021.
37. Roos, K.; Wu, C.; Damm, W.; Reboul, M.; Stevenson, J.M.; Lu, C.; Dahlgren, M.K.; Mondal, S.; Chen, W.; Wang, L.; et al. OPLS3e: Extending Force Field Coverage for Drug-Like Small Molecules. *J. Chem. Theory Comput.* **2019**, *15*, 1863–1874. [CrossRef]

38. Kumar, N.; Solt, L.A.; Conkright, J.J.; Wang, Y.; Istrate, M.A.; Busby, S.A.; Garcia-Ordenez, R.D.; Burris, T.P.; Griffin, P.R. The benzenesulfoamide T0901317 [N-(2,2,2-trifluoroethyl)-N-[4-[2,2,2-trifluoro-1-hydroxy-1-(trifluoromethyl)ethyl 1]phenyl]-benzenesulfonamide] is a novel retinoic acid receptor-related orphan receptor-alpha/gamma inverse agonist. *Mol. Pharmacol.* **2010**, *77*, 228–236. [CrossRef] [PubMed]
39. Hiebl, V.; Ladurner, A.; Latkolik, S.; Dirsch, V.M. Natural products as modulators of the nuclear receptors and metabolic sensors LXR, FXR and RXR. *Biotechnol. Adv.* **2018**, *36*, 1657–1698. [CrossRef] [PubMed]
40. Xu, T.; Wang, X.; Zhong, B.; Nurieva, R.I.; Ding, S.; Dong, C. Ursolic acid suppresses interleukin-17 (IL-17) production by selectively antagonizing the function of RORgamma t protein. *J. Biol. Chem.* **2011**, *286*, 22707–22710. [CrossRef]
41. Zhou, Q.; Qin, S.; Zhang, J.; Zhon, L.; Pen, Z.; Xing, T. 1,25(OH)2D3 induces regulatory T cell differentiation by influencing the VDR/PLC-gamma1/TGF-beta1/pathway. *Mol. Immunol.* **2017**, *91*, 156–164. [CrossRef]
42. Li, F.; Fernandez, P.P.; Rajendran, P.; Hui, K.M.; Sethi, G. Diosgenin, a steroidal saponin, inhibits STAT3 signaling pathway leading to suppression of proliferation and chemosensitization of human hepatocellular carcinoma cells. *Cancer Lett.* **2010**, *292*, 197–207. [CrossRef]
43. Wang, R.; Campbell, S.; Amir, M.; Mosure, S.A.; Bassette, M.A.; Eliason, A.; Sundrud, M.S.; Kamenecka, T.M.; Solt, L.A. Genetic and pharmacological inhibition of the nuclear receptor RORalpha regulates TH17 driven inflammatory disorders. *Nat. Commun.* **2021**, *12*, 76. [CrossRef]
44. Manda, V.K.; Avula, B.; Ali, Z.; Wong, Y.H.; Smillie, T.J.; Khan, I.A.; Khan, S.I. Characterization of in vitro ADME properties of diosgenin and dioscin from *Dioscorea villosa*. *Planta Med.* **2013**, *79*, 1421–1428. [CrossRef] [PubMed]
45. McAnuff, M.; Omoruyi, F.; Morrison, E.; Asemota, H. Changes in some liver enzymes in streptozotocin-induced diabetic rats fed saponin extract from bitter yam (*Dioscorea polygonoides*) or commercial diosgenin. *West. Indian Med. J.* **2005**, *54*, 97–101. [CrossRef]
46. Li, R.; Liu, Y.; Shi, J.; Yu, Y.; Lu, H.; Yu, L.; Liu, Y.; Zhang, F. Diosgenin regulates cholesterol metabolism in hypercholesterolemic rats by inhibiting NPC1L1 and enhancing ABCG5 and ABCG8. *Biochim. Biophys. Acta Mol. Cell Biol. Lipids* **2019**, *1864*, 1124–1133. [CrossRef] [PubMed]
47. Binesh, A.; Devaraj, S.N.; Halagowder, D. Atherogenic diet induced lipid accumulation induced NFkappaB level in heart, liver and brain of Wistar rat and diosgenin as an anti-inflammatory agent. *Life Sci.* **2018**, *196*, 28–37. [CrossRef]
48. Malisetty, V.; Patlolla, J.; Raju, J.; Marcus, L.; Choi, C.; Rao, C. Chemoprevention of colon cancer by diosgenin, a steroidal saponin constituent of fenugreek. *Proc. Amer. Assoc. Cancer Res.* **2005**, *46*, 2473.
49. Raju, J.; Rao, C.V. Diosgenin, a steroid saponin constituent of yams and fenugreek: Emerging evidence for applications in medicine. *Bioact. Compd. Phytomed.* **2012**, *125*, 143.
50. Wu, F.C.; Jiang, J.G. Effects of diosgenin and its derivatives on atherosclerosis. *Food Funct.* **2019**, *10*, 7022–7036. [CrossRef]
51. Cayen, M.N.; Ferdinandi, E.S.; Greselin, E.; Dvornik, D. Studies on the disposition of diosgenin in rats, dogs, monkeys and man. *Atherosclerosis* **1979**, *33*, 71–87. [CrossRef]
52. Okawara, M.; Tokudome, Y.; Todo, H.; Sugibayashi, K.; Hashimoto, F. Effect of beta-cyclodextrin derivatives on the diosgenin absorption in Caco-2 cell monolayer and rats. *Biol. Pharm. Bull.* **2014**, *37*, 54–59. [CrossRef]
53. Liu, C.Z.; Chang, J.H.; Zhang, L.; Xue, H.F.; Liu, X.G.; Liu, P.; Fu, Q. Preparation and Evaluation of Diosgenin Nanocrystals to Improve Oral Bioavailability. *AAPS PharmSciTech* **2017**, *18*, 2067–2076. [CrossRef]
54. Okawara, M.; Hashimoto, F.; Todo, H.; Sugibayashi, K.; Tokudome, Y. Effect of liquid crystals with cyclodextrin on the bioavailability of a poorly water-soluble compound, diosgenin, after its oral administration to rats. *Int. J. Pharm.* **2014**, *472*, 257–261. [CrossRef] [PubMed]
55. Parama, D.; Boruah, M.; Yachna, K.; Rana, V.; Banik, K.; Harsha, C.; Thakur, K.K.; Dutta, U.; Arya, A.; Mao, X.; et al. Diosgenin, a steroidal saponin, and its analogs: Effective therapies against different chronic diseases. *Life Sci.* **2020**, *260*, 118182. [CrossRef] [PubMed]



Article

Ferulic Acid Induces Keratin 6 α via Inhibition of Nuclear β -Catenin Accumulation and Activation of Nrf2 in Wound-Induced Inflammation

Kang-Hoon Kim ^{1,2}, Ji Hoon Jung ^{1,2}, Won-Seok Chung ^{2,*}, Chang-Hun Lee ^{3,*} and Hyeung-Jin Jang ^{1,2,*}

¹ Department of Science in Korean Medicine, Graduate School, Kyung Hee University, 26 Kyungheedaero, Dongdaemun-gu, Seoul 02447, Korea; poklmoo@naver.com (K.-H.K.); johnsperfume@gmail.com (J.H.J.)

² College of Korean Medicine, Kyung Hee University, 26 Kyungheedaero, Dongdaemun-gu, Seoul 02447, Korea

³ Department of New Biology, Daegu Gyeongbuk Institute of Science and Technology, Daegu 42988, Korea

* Correspondence: omduke@khu.ac.kr (W.-S.C.); leech@dgist.ac.kr (C.-H.L.); hjjang@khu.ac.kr (H.-J.J.); Tel.: +82-53-785-6612 (C.-H.L.); +82-2-961-2315 (H.-J.J.)

Abstract: Injured tissue triggers complex interactions through biological process associated with keratins. Rapid recovery is most important for protection against secondary infection and inflammatory pain. For rapid wound healing with minimal pain and side effects, shilajit has been used as an ayurvedic medicine. However, the mechanisms of rapid wound closure are unknown. Here, we found that shilajit induced wound closure in an acute wound model and induced migration in skin explant cultures through evaluation of transcriptomics via microarray testing. In addition, ferulic acid (FA), as a bioactive compound, induced migration via modulation of keratin 6 α (K6 α) and inhibition of β -catenin in primary keratinocytes of skin explant culture and injured full-thickness skin, because accumulation of β -catenin into the nucleus acts as a negative regulator and disturbs migration in human epidermal keratinocytes. Furthermore, FA alleviated wound-induced inflammation via activation of nuclear factor erythroid-2-related factor 2 (Nrf2) at the wound edge. These findings show that FA is a novel therapeutic agent for wound healing that acts via inhibition of β -catenin in keratinocytes and by activation of Nrf2 in wound-induced inflammation.

Keywords: wound healing; ferulic acid; shilajit; K6 α ; β -catenin; Nrf2; keratinocytes

Citation: Kim, K.-H.; Jung, J.H.; Chung, W.-S.; Lee, C.-H.; Jang, H.-J. Ferulic Acid Induces Keratin 6 α via Inhibition of Nuclear β -Catenin Accumulation and Activation of Nrf2 in Wound-Induced Inflammation. *Biomedicines* **2021**, *9*, 459. <https://doi.org/10.3390/biomedicines9050459>

Academic Editor: Leonardo Caputo

Received: 24 March 2021

Accepted: 20 April 2021

Published: 22 April 2021

Publisher's Note: MDPI stays neutral with regard to jurisdictional claims in published maps and institutional affiliations.



Copyright: © 2021 by the authors. Licensee MDPI, Basel, Switzerland. This article is an open access article distributed under the terms and conditions of the Creative Commons Attribution (CC BY) license (<https://creativecommons.org/licenses/by/4.0/>).

1. Introduction

Wound healing is a dynamic biological process with complex, diverse interactions at the molecular level that are only partially understood. Many studies in recent decades have contributed to a better understanding of the mechanisms of the wound repair process and the causes and results of delayed wound healing. In addition, acute wounds are still frequently reported to cause health trouble, with 11 million people suffering from wounds and approximately 300,000 patients hospitalized annually in the United States. [1]. Typically, wound healing is a well-organized process that lead to predictable tissue repair in which platelets, keratinocytes, immune surveillance cells, microvascular cells, and fibroblasts play key roles in the restoration of tissue integrity [2]. Under the conditions of injury, keratinocytes induce keratin 6 (K6) isoforms, keratin 16 (K16), and keratin 17 (K17). The expression of K6, K16, and K17 persists as wound-activated keratinocytes migrate to the site of injury [3]. This transcriptional event of keratins occurs at the expense of keratin 1 and keratin 10, and correlates with marked modulation of the morphology and other properties of keratinocytes [3,4]. The induction of K6 isoforms and K16 has functional effects on the epithelialization at the wound edge; they are essential to the homeostasis of keratin integrity in the epidermis [5]. To assist recovery from acute wounds, the development of safer therapeutic methods has been studied. The β -catenin signaling pathway has been suggested as a good candidate for wound therapy, as β -catenin is

involved in the regulation of the wound size in mesenchymal cells. The activation of β -catenin is known to contribute to chronic wounds in keratinocytes [6,7]. Furthermore, β -catenin is increased during the proliferative phase of cutaneous wound healing [8–10] and regulates the proliferation, motility, and invasiveness of mesenchymal fibroblast-like cells under wound conditions [11].

The Wnt signaling pathway plays important roles in many aspects of the control of cell proliferation, survival, adhesion, and migration through both canonical β -catenin-dependent and non-canonical β -catenin-independent signaling [12,13]. During the wound process, interestingly, epidermal keratinocytes and fibroblasts have opposite molecular patterns under canonical β -catenin-dependent signaling conditions. For example, nuclear presence of β -catenin and elevated c-myc expression showed impaired migration of keratinocytes in the human epidermis in chronic wound conditions [7]. On the other hand, valproic acid (VA), an inhibitor of glycogen synthase kinase-3 beta (GSK3 β), has demonstrated its efficacy for wound repair in dermal fibroblasts [14], as well as enhancement of hair growth [15] and the induction of hair regeneration through the activation of β -catenin through the canonical β -catenin-dependent signaling [16,17]. Given the crucial role of β -catenin signaling in normal homeostasis and repair after injury, the regulation of β -catenin as an appropriate homeostatic response may be a useful therapeutic target for the enhancement of wound healing. However, VA therapy may cause critical side effects, such as hepatotoxicity, pancreatitis, and hyper-ammonemia [18,19].

In a previous study, we screened natural resources to develop therapeutic agents for wound healing and identified biological indicators of proliferation and migration, such as the gene regulation and signaling pathways in wound healing by using microarray [20]. In the present study, to develop a safe therapeutic target for wound healing with minimal side effects, we tested the wound healing effects of shilajit (SH) in ayurvedic medicine under *in vivo* and *ex vivo* conditions and analyzed the biological signaling pathway after treatment with SH using microarray testing. SH is a blackish-brown exudate, which forms over centuries through the progressive decomposition of natural substituents by microorganisms, and is found in the Himalayans between India and Nepal [21]. In Ayurveda, the traditional medicine system of India, SH has been prescribed for centuries to patients with several diseases, including edema, tumors, epilepsy, insanity, diabetes, and skin wounds [22]. As it has been used safely and efficiently for such a long time that SH has attracted the attention of researchers for further studies. For example, researchers attempted to identify the active ingredient in SH, and found that SH contained several natural components, such as humic acid, fulvic acid, tannic acid, gallic acid, and ferulic acid (FA) [23–25]. Among the various components, studies have suggested anti-cancer effects of FA in cancer cell lines [26]. The wound healing efficacy of FA has been tested in a rat model of diabetes [27]. However, most of the previous studies did not investigate the mechanism of action of SH. In this study, to find the active compound, we performed liquid chromatography–electrospray ionization–mass spectrometry (LC-ESI-MS) on SH samples. Finally, we excavated the active compound, ferulic acid, from SH and suggested that FA promoted the re-epithelialization of wound conditions *in vivo* and inhibited β -catenin in primary keratinocytes through the enhancement of migration *ex vivo*. In the histological analysis of a full-thickness wound edge, FA inhibited translocation of β -catenin in epidermal keratinocytes. Furthermore, FA alleviated wound-induced inflammation via activation of nuclear factor erythroid-2-related factor 2 (Nrf2), which is associated with cellular protection at the wound edge. These results implied that FA induced migration by inhibiting nuclear accumulation of β -catenin and induced rapid repair by activating Nrf2.

2. Materials and Methods

2.1. Shilajit Preparation and Ferulic Acid

Purified shilajit (PRIMAVIE[®]) was purchased from Natreon Inc. (New Brunswick, NJ, USA), India. Shilajit was collected from 2400 m altitude in the rocky mountain of Beshtor, Tashkent, Uzbekistan. A sample specimen is kept in the laboratory with the specific code

number. For qualitative analysis using LC-ESI/MS, shilajit was extracted by water, acetone-trile, or methanol of 100% HPLC grade for 72 h at 45 °C in sonicated conditions (Branson, MO, USA). Ferulic acid was purchased from Sigma-Aldrich (Saint Louis, MO, USA).

2.2. Cell Cultures

Cell cultures of primary keratinocytes were harvested and purified as previously described [5]. Neonatal mouse skin was floated onto 0.25% trypsin and incubated overnight. Cells were scraped into CnT-57 media (CELLnTEC, Bern, Switzerland) and live cells were purified in Lymphoprep solution (AXIS-SHIELD, Dundee, UK) and cultured in CnT-57 media. ICR keratinocytes were harvested from newborn mice and seeded on six-well plates (TPP; Sigma-Aldrich,) for primary culture in CnT-57 media. Primary fibroblasts were purified in Lymphoprep solution (AXIS-SHIELD) and were cultured by selecting supernatants of neonatal mouse skin in DMEM media of high glucose (Lonza, Walkersville, MD, USA) containing 10% heat-inactivated fetal bovine serum (FBS; Lonza), penicillin, and streptomycin (Thermo Fisher Scientific, Vantaa, Finland). Cell cultures were incubated at 37 °C in humidified air and 5% CO₂ atmosphere [28]. The 308 cell line, which is a mouse keratinocyte cell line, was received from Pierre A. Coulombe (Bloomberg School of Public Health, Johns Hopkins University, Baltimore, MD, USA) and was described previously [29]. The 308 cell line was cultured in DMEM media of high glucose (Lonza) containing 10% heat-inactivated fetal bovine serum (Lonza), penicillin, and streptomycin. Cell cultures were incubated at 37 °C in humidified air and 5% CO₂ atmosphere [30].

2.3. Real-Time Cell Analysis (RTCA) Measurement

Growth curves were performed using the xCELLigence System (Roche, Basel, Switzerland) in 96-well plates. Cell Index was monitored every fifteen minutes throughout the experiment. For proliferation assays, cells were seeded in triplicate in 18-well culture plates and grown for 72 h after treatment of shilajit or ferulic acid at 37 °C in humidified air and 5% CO₂ atmosphere.

2.4. Real-Time Quantitative PCR

Total RNA samples from primary keratinocytes, derived from mouse back skin, were isolated. Following this, the cDNA was hybridized from 1 µg of the total RNA with a LeGene first strand cDNA synthesis system (LeGene Bioscience, San Diego, CA, USA) [31]. Several expression levels of mice keratin family (*Krt6a*, *Krt5*, and *Krt14*) were determined with a quantitative PCR test, as described in the manufacturer's protocol (Applied Biosystems, Foster City, CA, USA). The 2^{-ΔΔCt} value compared to the normal mice sample was determined with StepOne software (Applied Biosystems). Gapdh was used as a house keeping gene and endogenous control. The sequence of the forward and reverse primer was 5'-CATGGCCTTCCGTGTTCTA-3' and 5'-GCGGCACGTCAGATCCA-3' for the Gapdh gene, 5'-CCCTCTGAACCTGCAAATCG-3' and 5'-GATCTGCTCCCTCTCCTCAGT-3' for the Krt6a, 5'-TGCCCTGCCGTTTCTCTACT-3' and 5'-TGATCTGCTCCCTCTCCTCA-3' for the Krt5, and 5'-ACGAGAAGATGGCGGAGAAG-3' and 5'-CTCTGTCTTGTGAAGAACCATT-3' for the Krt14.

2.5. Western Blotting

After mouse primary keratinocytes and skin tissues were treated with shilajit or ferulic acid, the cells and tissues were lysed and the total protein concentrations were determined by Bradford reagent (Bio-Rad, Hercules, CA, USA). Equal amounts of lysates resolved using sodium dodecyl-polyacrylamide gel electrophoresis (SDS-PAGE) were transferred to a nitrocellulose membrane, then the membrane was blocked with 1 × TBS containing 0.1% Tween 20 and 5% skim milk or 2% BSA for 1 h at room temperature [32]. After the blocking, the blots were then incubated with specific primary antibodies for β-catenin (BD Bioscience, San Jose, CA, USA), K6α (Covance, Cranford, NJ, USA), or β-actin (Santa Cruz Biotechnology, Dallas, TX, USA) overnight at 4 °C. Blots were washed with TBST

and incubated HRP-conjugated anti-mouse or anti rabbit IgG secondary antibodies (Santa Cruz Biotechnology) for 1 h at room temperature. After three washes, the membranes were detected using an enhanced chemiluminescence (ECL) kit (Millipore, Burlington, MA, USA) [33].

2.6. Animals

Commercially available ICR mice purchased from DBL (Eumseong-gun, South Korea), were used for the experiments and adapted under constant conditions. The ICR littermates (0-1 day old mice) were used for skin explant culture. ICR mice (8 weeks old mice) were used for acute wound models. All studies were performed at Kyung Hee University. All animal study protocols were approved by the Institutional Animal Care and Use Committee (IACUC) of Kyung Hee University. The approval number for the animal experiment was KHUASP(SE)-14-046.

2.7. Wound Closure Test

Full-thickness excisional wounds were developed in the middle of the back skin with a 4 mm disposable biopsy punch (Kai industries, Seki, Japan) in ICR mice (8 weeks old mice). Five groups were prepared and used in the study. The control (Con) group was untreated, while the VA group was treated with only Vaseline petroleum jelly (VI-JON LABORATORIES, INC, Saint Louis, MO, USA). SH 1% and SH 10% groups received varying concentrations of the shilajit (shilajit 0.1 g and 1 g per 10 g of the Vaseline base, respectively). The FA 1% group received 1% concentration of the FA (FA 0.1 g per 10 g of the Vaseline base). In this study, Vaseline was used as the vehicle. All mice were observed for 7 days, and at 1, 3, 5, and 7 days wound images were taken with a camera (Nikon, Tokyo, Japan) and the wound closures were recorded using ImageJ software.

2.8. Skin Explant Culture

Ex vivo explant culture of 1 d old mouse skin was performed as described previously [34]. Using 4 mm punches (Kai industries, Seki, Japan), circular skin biopsies were obtained and plated with medium in 24-well dishes (SPL, Pochen-si, South Korea). A subset of explants was incubated in 24-well plates (SPL) and treated with shilajit (1 µg/mL) after 48 h. After treatment, all explants were incubated for 24 d to confirm the cellular outgrowths and mRNA levels using microarrays. Outgrowth of epithelial cells was confirmed by hematoxylin and eosin staining (H&E). The epithelial cells were fixed in 4% paraformaldehyde for 20 min. After fixation, the cells were stained with H&E solution [35]. The outgrowth of H&E-stained cells was scanned by microscope (Olympus, Tokyo, Japan) and measured using ImageJ freeware at 12 d and 24 d, respectively.

2.9. Immunofluorescence

The isolated cells were fixed in 4% paraformaldehyde for 20 min and then incubated with 3% H₂O₂ in 0.1M PBS for 30 min to remove endogenous peroxidase activity. The cells were blocked for 2 h at room temperature with a solution containing 5% normal goat serum, 2% bovine serum albumin, 2% fetal bovine serum, and 0.1% triton X-100 in PBS. The primary keratinocytes derived from skin explants (P0-P1) were first incubated overnight with rabbit anti-keratin 6α (1:200, Covance) and then incubated with Alexa Fluor 488 conjugate donkey anti-rabbit IgG secondary antibody (1:1000; Invitrogen, Carlsbad, CA, USA) for 1 h at room temperature. The primary keratinocytes and fibroblasts derived from back skin (P0-P1), were incubated overnight with mouse anti-c-Myc (1:100; Santa cruz) and with rabbit anti-beta-catenin (1:200; Cell signaling technology, Danvers, MA, USA), then incubated with Alexa Fluor 647 conjugate goat anti-mouse IgG secondary antibody and with Alexa Fluor 488 conjugate donkey anti-rabbit IgG secondary antibody for 1 h at room temperature. DAPI (Invitrogen) and Alexa Fluor 594 were visualized using a FluoView FV1000 confocal microscope (Olympus, Tokyo, Japan). Isolated wounded tissues were fixed in 4% paraformaldehyde, embedded in paraffin wax within 24 h of

removal, then deparaffinized in xylene and ethanol. The duodenal sections were incubated with 3% H₂O₂ in 0.1M PBS for 30 min to remove endogenous peroxidase activity. The sections were blocked for 2 h at room temperature with a solution containing 5% normal goat serum, 2% bovine serum albumin, 2% fetal bovine serum, and 0.1% triton X-100 in PBS. The skin sections of wounded edges were incubated overnight with mouse anti-beta-catenin (1:200; BD Bioscience) and rabbit anti-keratin 6 β , then incubated with Alexa Fluor 647 conjugate goat anti-mouse IgG secondary antibody (1:1000; Abcam, Cambridge, UK) and with Alexa Fluor 488 conjugate donkey anti-rabbit IgG secondary antibody (1:1000; Abcam, Cambridge, UK) for 1 h at room temperature. The immunofluorescence intensity values were measured using a FluoView FV1000 confocal microscope and analyzed using Mann–Whitney U tests in GraphPad Prism 5 software.

2.10. Microarray

Biotinylated cRNA samples were prepared according to the standard Affymetrix protocol from 500 ng total RNA (Expression Analysis Technical Manual, 2001, Affymetrix). Following fragmentation, 15 mg of aRNA was hybridized for 16 h at 45 °C on a GeneChip Mouse Genome Array. GeneChips were washed and stained in the Affymetrix Fluidics Station 450. GeneChips were scanned using the Affymetrix GeneChip 3000 7G scanner. The data were analyzed with RMA using Affymetrix default analysis settings with global scaling as the normalization method. The trimmed mean target intensity of each array was arbitrarily set to 100. The normalized and log-transformed intensity values were then analyzed using GeneSpring GX 12.6 (Agilent Technologies, Santa Clara, CA, USA). Fold change filters included the requirement that the genes be present in at least 200% of controls for upregulated genes and lower than 50% of controls for downregulated genes. Hierarchical clustering data were clustered groups that behaved similarly across experiments using GeneSpring GX 12.6 (Agilent Technologies). The clustering algorithm involved Euclidean distance and average linkage.

2.11. LC-ESI-MS

Chromatographic separation of shilajit using an Agilent 1290 Infinity LC (Agilent Technologies, Waldbronn, Germany) instrument was performed using a Zorbax Eclipse Plus C18 column (50 mm \times 2.1 mm i.d., 1.8 μ m, Agilent) that employed a mobile phase composed of water (A) and acetonitrile (B), each containing 0.1% formic acid (Sigma Aldrich). The gradient program was: 0–5 min (5% B in A), 5–15min (5–90% B), 15–20 min (90% B), and 20–21min (90–5% B). The column was then equilibrated with 5% B for 5 min at a flow rate of 300 μ L/min. A sample of 2 μ L was injected into the column using a thermostated HiP-ALS autosampler. The HPLC system was interfaced to the MS system using an Agilent 6550Accurate-Mass Q-TOF instrument (Agilent Technologies) equipped with a Jet Stream ESI source operating in negative ion mode. Mass spectra were acquired at a scan rate of 1.0 spectra/s, with a mass range of 100–1700 m/z .

2.12. Ethics Statement

All animal study protocols were approved by the Institutional Animal Care and Use Committee (IACUC) of Kyung Hee University. The approval number for the animal experiment was KHUASP(SE)-14-046 (13 April 2015). The 308 cell line, which is a mouse keratinocyte cell line, was received from Pierre A. Coulombe (Bloomberg School of Public Health, Johns Hopkins University, Baltimore, MD, USA).

2.13. Statistical Analysis

Data are expressed as the means \pm S.E.M. Graph Pad Prism 5 (Graph Pad software, San Diego, CA, USA.) was used for the statistical analysis. The statistical significance of each bar chart was measured using one-way ANOVA with Dunnett's post-hoc (for in vitro studies) or Tukey's post-hoc (for in vivo studies) test. For in vivo studies, two-way

ANOVA with Tukey's post-hoc (to compare more than 3 groups) or Bonferroni's post-hoc (to compare 2 groups) test was performed. Here, $p < 0.05$ was considered significant.

3. Results

3.1. SH Induces Keratinocyte Migration and Its Active Component Is FA

Although SH is used for wound tissue healing in ayurvedic medicine, the mechanism of action of SH and the active components are still unknown. To discover the biological action of SH under wound conditions, we induced an acute wound model in mice and observed wound closure with or without SH. First, we induced an epidermal wound by using a 4 mm skin punch (Experimental process, Supplementary Figure S1A) and observed wound closure in the presence or absence of SH (Figure 1a). In the treatment group with SH 10%, we observed more significant wound closure than the basal amount after day 3 (Figure 1b). The number of days needed to close 50% of the wound area was as follow: basal (BSL, 5.43 ± 0.89 day), vehicle (Ve, 5.49 ± 0.25 day), SH 1% (4.08 ± 0.107 day), and SH 10% (3.16 ± 0.09 day) (Figure 1b). To validate wound conditions for both non-wound and wound groups (basal group) on day 7, skin full-thickness was evaluated by wound-induced keratin (K6 α wound marker) using immunofluorescence staining (Supplementary Figure S2).

When wound edges healed, migration of keratinocytes contributed to rapid wound closure. Mazzalupo et al. reported that the primary keratinocytes derived from the back skin of mouse pups were used to evaluate quantitative outgrowth [34]. To further evaluate wound-healing-associated migration of keratinocytes, we prepared a primary culture derived from the back skin of explant culture in pups born within day 1 (24 h) and observed the outgrowth of epithelial keratinocytes from the back skin of explant culture on day 12 or 24 (Figure 1c). Through H&E staining, we easily distinguished the outgrowth of primary keratinocytes, measured the migrated area of primary keratinocytes, and evaluated the quantitative migration effects with or without SH. After treatment with SH (1 $\mu\text{g}/\text{mL}$), outgrowth of primary keratinocytes was significantly enhanced from day 12 to day 24. The fold changes in outgrowth of keratinocytes were 4.94 ± 0.56 at day 12 and 5.13 ± 0.58 at day 24 (Figure 1d). A schematic figure of the ex vivo skin explant culture is represented in Supplementary Figure S1B.

To cover SH-mediated migration associated with biological molecules, we performed transcriptomic analysis and a microarray of primary keratinocytes in the growth area of skin explant cultures with or without SH. In the microarray, we arranged functional categorization. The alteration of gene expression of at least two-fold was sorted into 17 categories: apoptosis, behavior, cell adhesion, cell cycle, cell differentiation, cell migration, cell proliferation, growth, homeostasis, immune response, inflammatory response, lipid metabolism, response to stress, signal transduction, transcription, and transport (Figure 1f,g). We deduced that the major alterations in mRNA expression were the upregulation of both keratins (Table 1), and junctional complex genes (Table 2) but, the downregulation of Ctnnb1 (Table 3). Next, to evaluate the preliminary mRNA expression results from the microarray analysis, we analyzed the mRNA level of Krt6a related to wound-induced keratin by using qPCR. Krt6a was increased by more than two-fold in the SH-treated group on day 12 (2.38 ± 0.17) and day 24 (2.22 ± 0.24) (Figure 1e). In addition, the mRNA expression levels of Krt6a, Krt5, and Krt14, and the protein expression of K6 α were increased by SH treatment of primary keratinocytes (Supplementary Figure S3). Under wound edges after day 7, SH treatment showed effective re-epithelialization on epidermis (Supplementary Figure S4). The SH-mediated migration suggested that an interaction between increased Krt6a and Ctnnb1 may be associated with rapid wound healing.

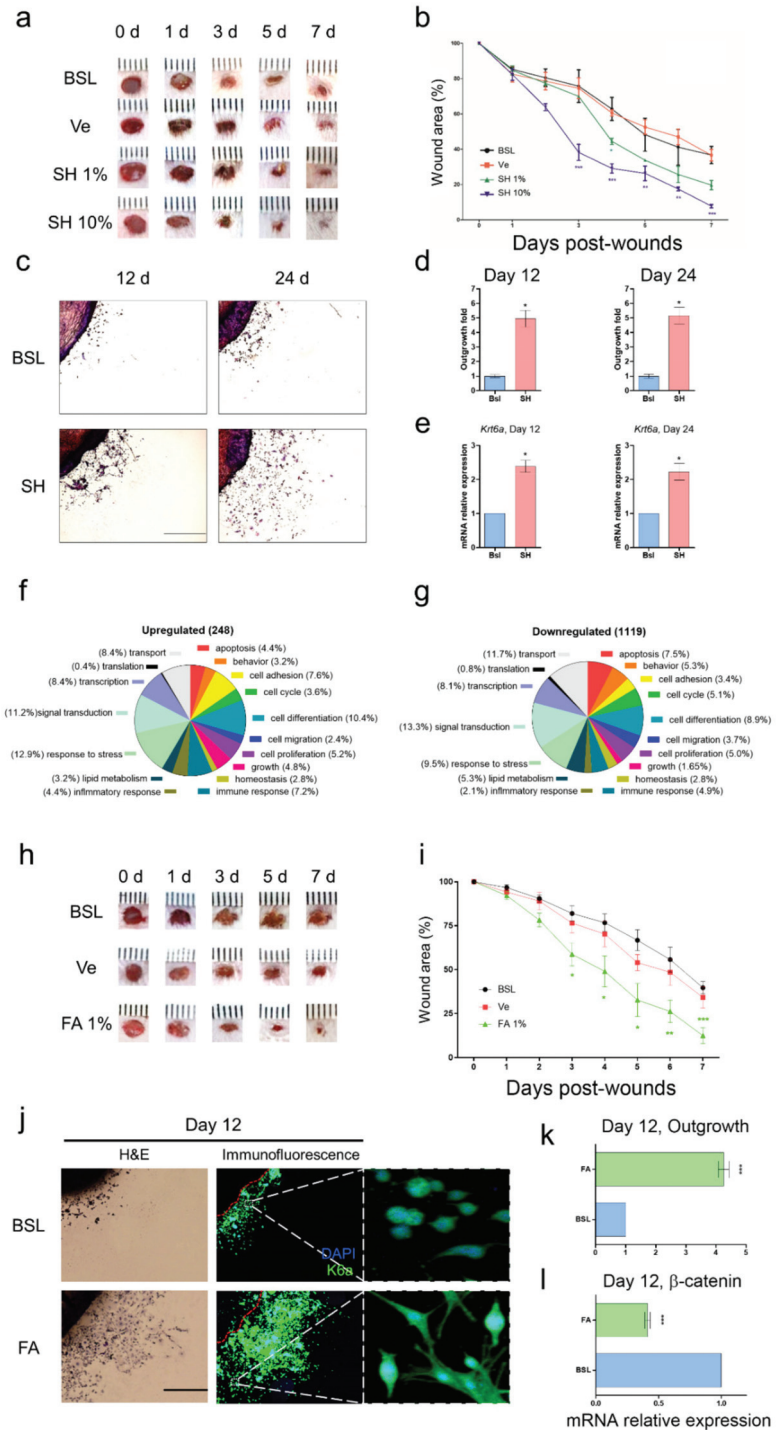


Figure 1. Wound healing of SH and FA. (a) Representative digital images of acute wounds treated with SH on days 0, 1, 3, 5, and 7 post-wounding. (b) Closure of acute wounds with SH was presented as percentage of wound area from the initial wound size. Mean \pm SEM; $n = 8$; *, $p < 0.05$; **, $p < 0.01$;

***, $p < 0.001$ compared with basal group. Statistical analysis was performed using two-way ANOVA, Bonferroni's test, or paired t -test. (c) Representative data of mouse skin explants processed for hematoxylin and eosin (H&E) staining at day 12 and day 24 in skin explant culture. The skin explant culture was analyzed in triplicate. (d) The quantitation of cellular outgrowth from explants was enhanced with SH. (e) The cells derived from skin explants were analyzed for Krt6 α using qPCR at day 12 and day 24. Mean \pm SEM; $n = 6$; *, $p < 0.05$. The significance of the outgrowth area was calculated using ImageJ software and analyzed using a paired t -test. (f,g) The classification criteria for the 17 categories were provided in the GO ontology databases (<http://www.geneontology.org>). (h) Representative digital images of acute wounds treated with SH on days 0, 1, 3, 5, and 7 post-wounding. (i) Closure of acute wounds with FA was presented as percentage of wound area from the initial wound size. Mean \pm SEM; $n = 8$; *, $p < 0.05$; **, $p < 0.01$; ***, $p < 0.001$ compared with basal group. Statistical analysis was performed using two-way ANOVA, Bonferroni's test, or paired t -test. BSL: basal, Ve: vehicle (poly petroleum jelly), FA: ferulic acid, %: (w/w). (j) Examples of mouse skin explants processed for hematoxylin and eosin (H&E) staining and immunofluorescence analyses of K6 β after day 12 in ex vivo skin explant culture. (k) The quantitation of cell outgrowth from explants was enhanced with FA. The skin explant culture was analyzed in triplicate. Mean \pm SEM; $n = 6$; ***, $p < 0.001$. The significance of outgrowth was calculated using ImageJ software and analyzed using paired t -test. (l) The cells derived from the ex vivo skin explant culture were analyzed for β -catenin using qPCR at day 12. Mean \pm SEM; $n = 6$; ***, $p < 0.001$. The significance was analyzed using paired t -test.

Table 1. Up-regulation of genes associated with wound induced keratins.

Probe Name	Description	Gene Symbol	Fold Change #
Keratins			
1422784_at	keratin 6A	<i>Krt6a</i>	14.6901
1423227_at	keratin 17	<i>Krt17</i>	7.9747
1424096_at	keratin 5	<i>Krt5</i>	7.3153
1423935_x_at	keratin 14	<i>Krt14</i>	8.1810

Fold change: BSL/SH normalized intensity ratio.

Table 2. Alteration of genes associated with extracellular matrix.

Probe Name	Description	Gene Symbol	Fold Change #
Collagen			
1455494_at	collagen, type I, alpha 1	<i>Col1a1</i>	2.5030
1423110_at	collagen, type I, alpha 2	<i>Col1a2</i>	2.6747
1427884_at	collagen, type III, alpha 1	<i>Col3a1</i>	3.4892
1418799_a_at	collagen, type XVII, alpha 1	<i>Col17a1</i>	2.4751
Tight junction			
1437932_a_at	claudin 1	<i>Cldn1</i>	2.1909
1434651_a_at	claudin 3	<i>Cldn3</i>	2.0510
Adherens junction			
1448261_at	cadherin 1	<i>Cdh1</i>	2.2079
Desmosome			
1435494_s_at	desmoplakin	<i>Dsp</i>	4.6570
1434534_at	desmocollin 3	<i>Dsc3</i>	2.1909
Gap junction			
1415801_at	gap junction protein, alpha 1	<i>Gja1</i>	−0.39884

Fold change: BSL/SH normalized intensity ratio.

Table 3. Alteration of genes associated with migration.

Probe Name	Description	Gene Symbol	Fold Change #
Oncogene			
1423240_at	Rous sarcoma oncogene	<i>Src</i>	2.1337
Integrin linked kinases			
1449942_a_at	Integrin-linked kinase	<i>Ilk</i>	2.0405
Chemokine ligand			
1417574_at	chemokine (C-X-C motif) ligand 12	<i>Cxcl12</i>	3.078
Fibroblast growth factor			
1422916_at	fibroblast growth factor 21	<i>Fgf21</i>	2.0611
A disintegrin and metallopeptidase			
1450105_at	a disintegrin and metallopeptidase domain 10	<i>Adam10</i>	−0.2529
1421857_at	a disintegrin and metallopeptidase domain 17	<i>Adam17</i>	−0.1847
Wnt signaling			
1448818_at	wingless-related MMTV integration site 5A	<i>Wnt5a</i>	−0.4180
1430533_a_at	catenin (cadherin associated protein), beta 1	<i>Ctnnb1</i>	−0.0786

Fold change: BSL/SH normalized intensity ratio.

After determining the biological evidence for SH-mediated migration associated with modulation of both *Krt6a* and *Ctnnb1*, we investigated the active compound involved in rapid wound healing. Shalini et al. reported that SH contained natural components such as tannic acid, gallic acid, caffeic acid, and ferulic acid (FA) [25]. Although a previous study reported that FA had healing effects for diabetic injuries via amelioration of hyperglycemia, our results focused on the biological and pharmacological effects of a topical skin ointment treatment during wound healing [27]. Here, we assessed whether FA as a topical medication induced wound healing or not via general blood glucoses. Before testing the FA ointment, we analyzed the SH components. Shalini et al. showed that SH contained 37.55 µg/g of ferulic acid in their study and the ratio between SH and FA was $1:2.66 \times 10^{-8}$ (shilajit: Ferulic acid). In our sample, we analyzed which SH components were involved using total ion chromatography (Supplementary Figure S5A,B), and the ratio between SH and FA was $1:1.211 \times 10^{-5}$ (Supplementary Figure S5C). FA was detected among the natural components of SH (Supplementary Figure S6).

Subsequently, to test the wound healing effects associated with wound closure and migration, we firstly observed wound closure treatment with FA 1% in an acute wound model (Figure 1h). In treatment with FA 1%, significant wound closure was observed on day 3 (Figure 1i). The numbers of days required for the closure of 50% of the wound area were as follows: BSL (5.92 ± 0.27 days), Ve (5.74 ± 0.26 days), and FA (3.99 ± 0.19 days) (Figure 1i). Next, we tested the migration of primary keratinocytes and their morphology in ex vivo cultures in the presence or absence of 100 nM FA (Figure 1j). We observed that FA treatment had three biological features in common with SH treatment. FA enhanced *K6α* expression (Figure 1j) and induced outgrowth of keratinocytes, similar to SH treatment on day 24 (Figure 1k). The change in outgrowth in the presence of FA was 3.48 ± 0.66 on day 12 (Figure 1k). FA decreased *Ctbbn1* expression (Figure 1j). The fold change of the *Ctbbn1* expression was 0.4 ± 0.02 (Figure 1l). In the histological study after treatment of SH or FA, FA treatment was the most effective wound recovery under wound edge at day 7d (Supplementary Figure S4). Moreover, qPCR analysis was performed for *Krt6a*, *Krt6b*,

Krt16, and *Nqo1* (Supplementary Figure S7). These results showed that FA derived from SH may induce wound closure and migration by modulation of *Krt6* and *Ctbbn1*.

3.2. SH and FA Induce Rapid Homeostatic Response of β -Catenin in Dermal Fibroblasts but Not in Epidermal Keratinocytes

Microarray data for cells treated with SH showed the upregulation of several keratins (Table 1) and molecules of the extracellular matrix (Table 2). However, the mRNA level of β -catenin was most downregulated in the epithelial keratinocytes of the skin explant culture (Figure 1j and Table 3). To further examine the protein expression of the genes with altered mRNA levels (i.e., the decreased *Ctbbn1* and the increased *Krt6a*) in epidermal keratinocytes of the skin explant culture, histology study using immunofluorescence staining of *K6 α* and β -catenin was performed on wound edges. In accordance with the wound closure results after treatment with SH and FA (Figure 1b,g), we observed that the significant time points of wound healing were day 3 and day 7. Then, we performed a histological study of wound edges on day 3 and day 7 after treatment with SH and FA. We measured the protein expression of β -catenin and *K6 α* in full-thickness wound edges on days 3 and 7 after treatment with SH and FA (Figure 2). The localization of β -catenin on the wound edge of the dermis was remarkably increased by treatment with SH 10% (Figure 2a). Dose-dependent increased β -catenin expression on the wounded dermis was evaluated using Western blotting on day 3. The fold change of β -catenin expression against non-treatment was 1.19 for SH 1% and 1.4 for SH 10% (Figure 2c). The localization of *K6 α* , the wound-induced marker, appeared as a thick line on the wound edge of the epidermis after treatment with SH 10% (Figure 2a). *K6 α* expression on the wounded epidermis was dose-dependently increased, as shown by western blotting on day 3. The fold change for increased expression of *K6 α* against non-treatment was 1.11 for SH 1% and 1.44 for SH 10% (Figure 2c). After post-wounding day 7, interestingly, the localization of β -catenin on the wound edge of the dermis with SH 10% seemed to be more decreased than basal group (Figure 2b). This decreasing tendency of β -catenin expression was evaluated using Western blotting. The fold change for decreasing expression of β -catenin was 0.4 for SH 10% compared with basal rates (Figure 2d). However, the localization of *K6 α* continue to increase in epidermal keratinocytes of the wound edges (Figure 2b). The state of increase of *K6 α* was evaluated using Western blotting. The fold change for increasing expression of *K6 α* was 2.2 for SH 10% compared with basal rates (Figure 2d).

To further investigate whether FA induced wound healing to modulate *K6 α* and β -catenin in common with SH, we tested the localization and quantitative expression of *K6 α* and β -catenin under wound edges on days 3 and 7 (Figure 2e–h). Similar to the modulation by treatment with SH 10%, FA increased the localization and expression of β -catenin on day 3 (Figure 2e,g) and subsequently decreased the localization and expression of β -catenin on day 7 in dermal fibroblasts (Figure 2f,h). In addition, FA treatment resulted in greater accumulation of β -catenin than basal conditions on day 7 in the epidermal keratinocytes on the wound edge (Figure 2f). During wound healing, additionally, FA treatment continued to increase the localization and expression of *K6 α* on day 3 (Figure 2e,g). These results suggested that FA exerted similar wound healing effects to SH, modulating the downregulation of β -catenin and the upregulation of *K6 α* , implying that FA modulated the expression of β -catenin and *K6 α* at the wound edge and enhanced wound healing through the promotion of keratinocyte migration. These results suggested that SH enhanced wound closure by modulating downregulation of β -catenin on the dermis and upregulation of *K6 α* on the epidermis. Additionally, FA was an active wound healing agent for modulation of both β -catenin and *K6 α* under the wound edge.

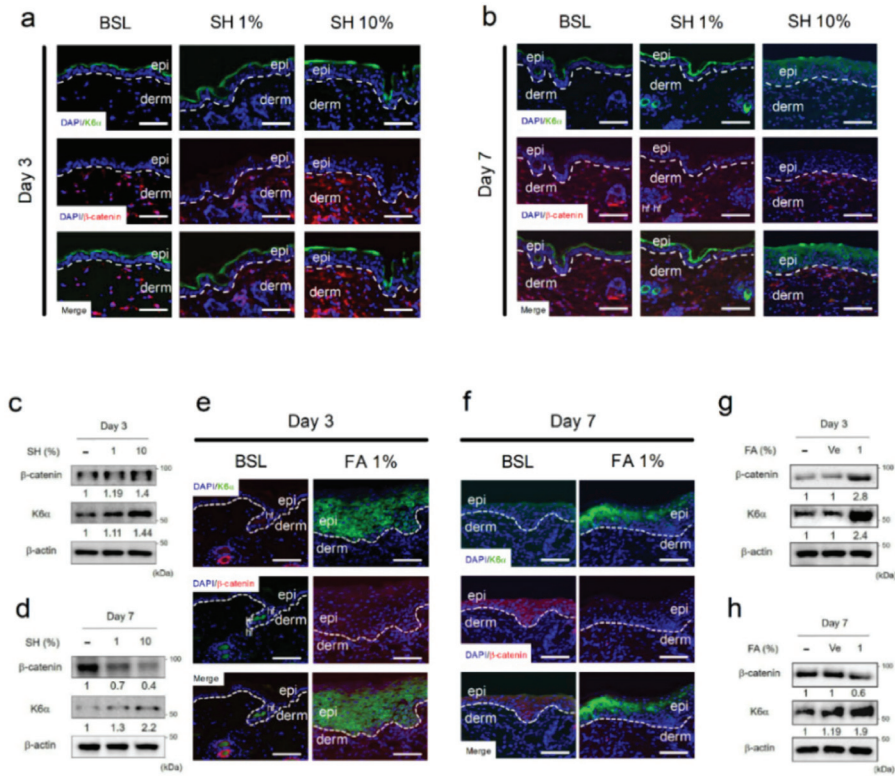


Figure 2. SH and FA induce epithelialization of keratinocytes. (a,b) Immunofluorescence (IF) staining of K6α and β-catenin in the epithelium at day 3 or 7 after wounding with or without SH. (c,d) Protein expression of K6α and β-catenin was analyzed after exposure to SH using Western blotting at day 3 and day 7. (e,f) K6α and β-catenin in the wounded epithelium at day 3 or 7 after exposure to FA. (g,h) Protein expression of K6α and β-catenin was analyzed after exposure to FA using Western blotting at day 3 and day 7. The IF and Western blots were analyzed in triplicate. Mean ± SEM; n = 5; epi: epidermis; derm: dermis.

3.3. FA Suppresses Nuclear Accumulation of β-Catenin in Epidermal Keratinocytes

As the nuclear accumulation of β-catenin caused the induction of c-myc, it contributed to the suppression of migration and the maintenance of epidermal chronic wounds in human epidermal keratinocytes [7]. Here, we hypothesized that if FA inhibited translocation of nuclear β-catenin or disturbed the accumulation of nuclear β-catenin, the delayed migration of keratinocytes might be improved. To evaluate whether FA inhibited the nuclear accumulation of β-catenin, we observed this phenomenon in primary keratinocytes treated with and without FA (Figure 3a). FA treatment significantly inhibited the nuclear translocation of β-catenin (Figure 3b) and decreased the nuclear translocation of c-myc, a downstream molecule of β-catenin (Figure 3c). To further examine the effects of FA on the inhibition of the nuclear accumulation of β-catenin, we induced the overexpression of β-catenin by using LiCl and observed the protein localization of β-catenin and c-myc (Figure 3a, white triangle). The LiCl-induced nuclear accumulation of β-catenin delayed keratinocyte migration and wound healing; if this was inhibited by FA, we would expect this to contribute to keratinocyte migration in wound healing. The IF analysis revealed that FA restricted the nuclear accumulation of β-catenin and c-myc in primary keratinocytes treated with LiCl (Figure 3a–c). In addition, FA blocked intracellular β-catenin and c-myc expression in the keratinocytes (Figure 3d–f). Our results showed that 10% SH and FA

increased localization and expression of β -catenin in dermal fibroblasts on the wound edge on day 3 (Figure 2a,e). To examine the differential effects of FA, we additionally observed localization and expression of both β -catenin and c-myc in primary fibroblasts (Figure 3g,j). FA increased translocated β -catenin and c-myc expression in primary fibroblasts, as shown by IF analysis (Figure 3g–i). Subsequently, there were no changes in β -catenin and c-myc expression in fibroblasts after LiCl treatment (Figure 3j–l). These results implied that FA’s actions of migration and wound closure resulted from the inhibition of β -catenin accumulation on epidermal keratinocytes and the translocation of β -catenin into the nucleus of dermal fibroblasts.

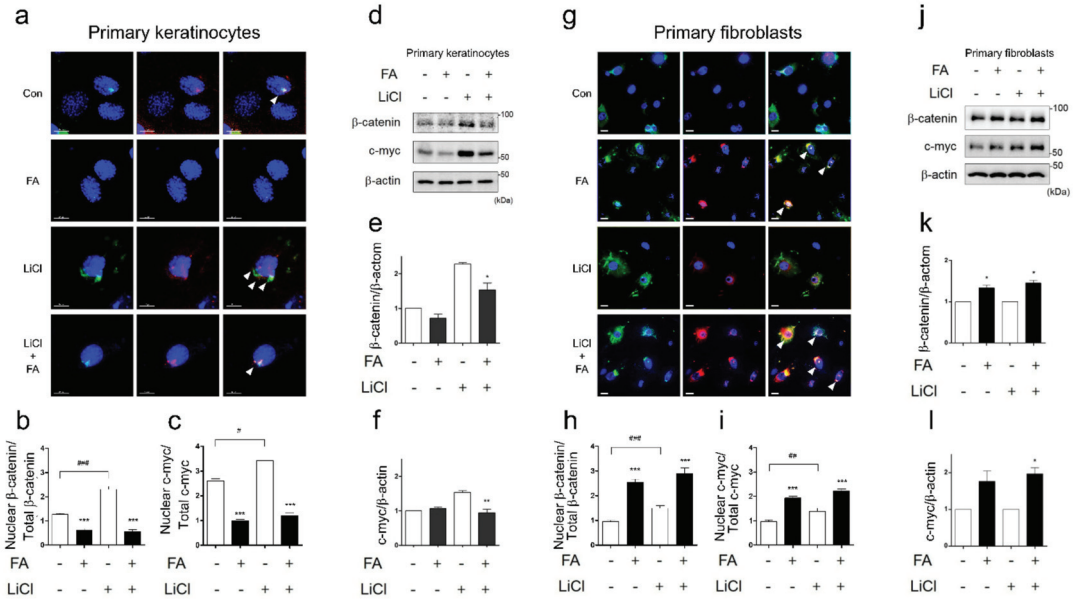


Figure 3. FA suppresses nucleus translocation of β -catenin in primary keratinocytes but induces nucleus translocation of β -catenin in primary fibroblasts. (a) After treatment with or without LiCl, immunofluorescence (IF) staining of c-myc and β -catenin was examined in primary keratinocytes. (b) The graph indicates the nucleus translocation ratio (%) of β -catenin. (c) The graph indicates the nucleus translocation ratio (%) of c-myc. Significance was measured using *t*-tests. Note: ** $p < 0.01$, scale bar: 10 μ m. The IF was analyzed in triplicate. Mean \pm SEM; $n = 100$. (d) Protein expression of c-myc or β -catenin was analyzed using Western blotting in primary keratinocytes. Significance was measured using *t*-tests. Note: ** $p < 0.01$. (e,f) Protein expression of β -catenin and c-myc was analyzed using Western blotting in primary keratinocytes. The Western blots were analyzed in triplicate. Mean \pm SEM; $n = 5$. Significance was measured using *t*-tests. Note: * $p < 0.05$, ** $p < 0.01$. (g) After treatment with or without LiCl, immunofluorescence (IF) staining of c-myc and β -catenin was examined in primary fibroblasts. (h) The graph indicates the nucleus translocation ratio (%) of β -catenin in primary fibroblasts. (i) The graph indicates the nucleus translocation ratio (%) of c-myc in primary fibroblasts. Significance was measured using *t*-tests. Note: ** $p < 0.01$, scale bar: 30 μ m. The IF was analyzed in triplicate. Mean \pm SEM; $n = 100$. (j) Protein expression of c-myc or β -catenin was analyzed using Western blotting in primary fibroblasts. (k,l) Protein expression of β -catenin and c-myc was analyzed using Western blotting in primary fibroblasts. The IF and Western blot samples were analyzed in triplicate. Mean \pm SEM; $n = 5$. Significance was measured using *t*-tests. Note: * $p < 0.05$.

3.4. FA Ameliorated Wound-Induced Inflammation by Activation of NRF2

After tissue injury, the inflammatory response plays important roles in wound healing. To evaluate whether FA had anti-inflammatory or protective effects in FA-mediated rapid wound healing, we observed major inflammatory markers, such as COX-2 and iNOS, as well as the protective marker Nrf2. In the wound edge, only iNOS localiza-

tion was significantly decreased on day 7 of FA treatment (Figure 4a). Regarding Nrf2 localization, however, FA treatment resulted in effective enhancement on both day 3 and day 7 (Figure 4b). To further evaluate the FA-mediated iNOS decrease, we tested COX-2 and iNOS expression in RAW 264.7 under LPS-mediated inflammation conditions. After 100 μ M of FA treatment, only iNOS expression was significantly decreased (Figure 4c). A previous study suggested that FA had anti-inflammatory effects via inhibition of NF- κ B and activation of Nrf2 [36]. However, the molecular interaction between iNOS and Nrf2 related to inflammatory signaling was still unknown. To investigate the mode-of-action of FA in terms of anti-inflammatory effects, we performed systemic knockdown using siRNA from Nfe2l2 and observed COX-2 and iNOS expression. Under Nfe2l2 knockdown conditions, the FA-mediated iNOS decrease disappeared in the RAW 264.7 mouse macrophage (Figure 4d). The evaluation of the knockdown of Nfe2l2 is shown in Figure 4e. These results suggested that FA alleviated wound-induced inflammation by decreasing iNOS expression, and that this iNOS decrease was mediated by FA-mediated Nrf2 activation.

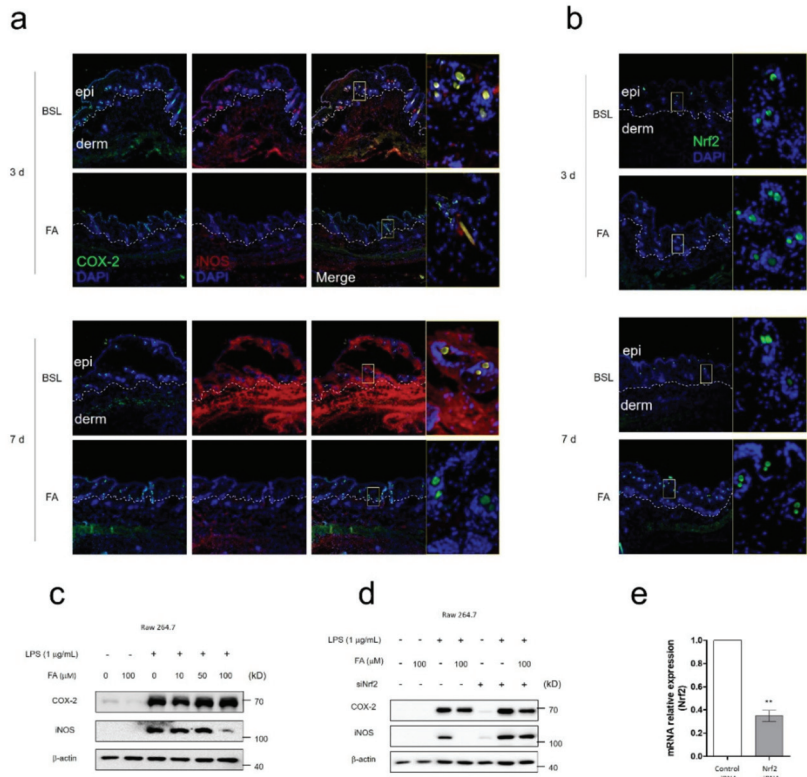


Figure 4. FA has anti-inflammatory effects via activation of NRF2. (a) Immunofluorescence (IF) staining of COX-2 and iNOS indicated in the epithelium at day 3 or 7 after wounding with or without FA. (b) Immunofluorescence (IF) staining of Nrf2 indicated in the epithelium at day 3 or 7 after wounding with or without FA. (c) Protein expression of COX-2 and iNOS was analyzed after exposure to FA using Western blotting in RAW 264.7 cells. (d) K6 α and β -catenin are indicated in the wounded epithelium at day 3 or 7 after exposure to FA. COX-2 and iNOS expression were observed using Western blotting under Nfe2l2 knockdown conditions. (e) The graph showed the knockdown ratio of Nfe2l2. The IF, Western blot and Nfe2l2 knockdown test were performed in triplicate. Mean \pm SEM; ** $p < 0.01$, $n = 5$. epi: epidermis, derm: dermis.

3.5. FA Induces Proliferation in Keratinocytes

During the regeneration of the epidermis after wounding, the proliferation of keratinocytes plays a crucial role. To determine the cellular proliferative effects of wound healing by SH and FA, we performed real-time cell analysis (RTCA). RTCA was automatically recorded by using the xCELLigence System in real time. The Kera 308 cells, a mouse keratinocyte cell line [29], were seeded at 5×10^3 cells in each E-plate. The dose curves were obtained between 1 $\mu\text{g}/\text{mL}$ to 1000 $\mu\text{g}/\text{mL}$ SH (Figure 5a) and between 1 nM and 1000 nM FA for 72 h (Figure 5b). The SH treatment group values were more increased than the basal values. The values for the area under the curve are as follows: BSL (1.02 ± 0.02), 1 (1.34 ± 0.03), 10 (1.3 ± 0.04), 100 (1.33 ± 0.03), and 1000 (1.29 ± 0.01) (Figure 5a). The FA treatment values from 1 to 100 nM were increased more than the basal values. The values for the area under the curve were as follows: BSL (1 ± 0.01), 1 (1.17 ± 0.05), 10 (1.25 ± 0.04), 100 (1.4 ± 0.03), and 1000 (1.01 ± 0.02) (Figure 5b). To further evaluate the proliferative effects of SH and FA at the wound edge, we observed the proliferation marker, Ki67, in the wound edge after treatment with SH and FA. SH and FA induced a significant increase in Ki67-positive cells in the wound epidermis 7 days after wounding. The values for Ki67-positive cells were as follow: BSL (8.6 ± 1.56), SH 10% (20.2 ± 1.56), and FA (43.8 ± 3.42) (Figure 5c). The proliferative enhancement induced by FA was more than two-fold greater than that of SH. In addition, genes associated with proliferation, such as integrin-linked kinase, chemokine ligands, and fibroblast growth factor, were altered by SH treatment (Table 3). These results suggested that keratinocytes were enhanced to proliferation in response to FA treatment in common with SH. In addition, FA treatment affected the dose-dependent increase. These results suggested that FA might be induced in wound healing as an active compound by enhancement of proliferation and Ki67-positive cells.

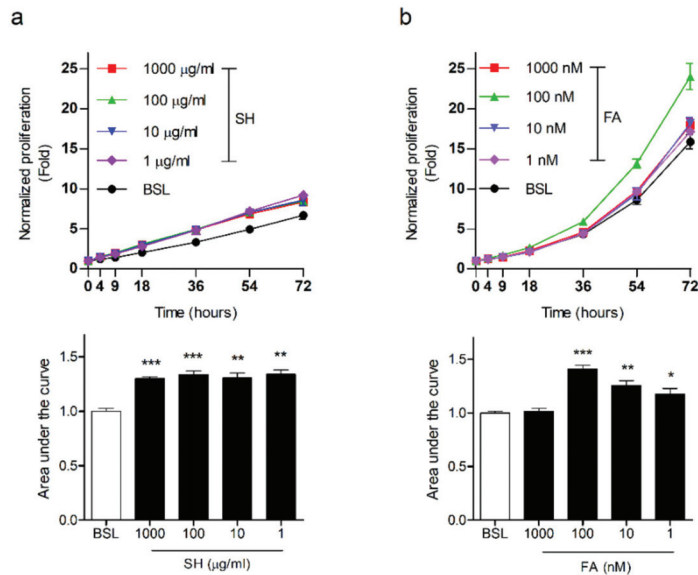


Figure 5. Cont.

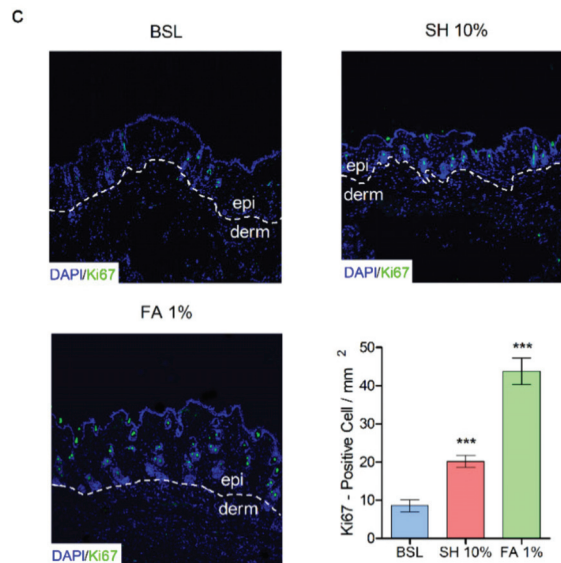


Figure 5. SH and FA enhance cellular proliferation. (a) The curves represent the course of the murine keratinocytes' (kera 308 cell line) viability with SH for 72 h. (b) FA's effects were assessed for 72 h. The RTCA was analyzed in triplicate. Each significance was measured using one-way ANOVA; $n = 3$, *** $p < 0.001$, ** $p < 0.01$, C/W; cells per well, arrow, treated point; BSL, basal; SH, shilajit; FA, ferulic acid. The graphs treated with SH or FA were compared with the area under curve using ImageJ software. (c) Immunofluorescence (IF) staining of Ki67 indicated in the wound epithelium at day 7. Significance was measured using *t*-tests. The IF was analyzed in triplicate. Mean \pm SEM; $n = 5$, * $p < 0.05$, ** $p < 0.01$.

4. Discussion and Conclusions

Under wounding conditions, the epithelial sheets of metazoans immediately trigger the repair mechanism to restore the condition and function of epithelial cells. The epidermis acts as a protective barrier; the degree of this action is dependent upon the dynamic degree of integrity of the keratin network [37–40]. Simultaneously, to repair the epidermal wound edge, epithelial stem cells from the hair follicle bulge migrate into the epidermis during wound healing [41].

In the present study, we demonstrated that SH and FA treatment induced rapid wound closure in acute wounds and the migration of epidermal keratinocytes in *ex vivo* culture. SH and FA affected the regulation of keratin genes and β -catenin (Figure 1). The induction of K6 α under wounding conditions plays an important structural role in the wound epithelialization of keratinocytes and the maintenance of keratinocyte integrity [5]. K6 α regulates homeostasis during recovery through a direct interaction with Src; thus, the interaction between K6 α and Src may be a trigger to dampen migration in the wound edge [4,42]. Paradoxically, the loss of the K6 isoform of keratinocytes resulted in enhanced epithelial migration in the wound edge [43]. Recently, the K6 isoform modulated keratinocyte migration by regulation of cell–matrix and cell–cell adhesion dynamics, which promoted essential collective cell migration and wound healing [44]. In further studies of the development of therapeutic agents in wound healing, evaluation of migration, the modulation of the K6 isoform, and its interaction proteins associated with cytoarchitecture, adhesion, and force generation should be considered at the wound edge [45,46].

Second, our results indicated that SH and FA treatment increased K6 α and β -catenin expression in the acute wound on day 3. However, on day 7, the increase in K6 α was maintained but the increase in β -catenin was dissipated by treatment with SH and FA. SH

and FA appeared to regulate protein expression in epidermal keratinocytes and dermal fibroblasts (Figure 2). In mechanical stress conditions, such as at the wound edge, β -catenin plays an essential role in the epidermal barrier function. Therefore, the loss of β -catenin in the embryonic epidermis causes neonatal lethality through the activation of K6 [47]. Wnt/ β -catenin signaling is a functional network for the regulation of keratins and is generally involved in areas such as stem cells and developmental biology [48]. When the Wnt pathway is inactivated, the key mediator of Wnt signaling, β -catenin, participates in the adherens junction, where it contributes to the stabilization of cell-to-cell interactions [49]. When the Wnt pathway is activated, β -catenin functions not only in the cytoplasm, where β -catenin levels are tightly controlled by processes regulating protein stability, but also in the nucleus, where β -catenin is involved in transcriptional regulation and chromatin interactions [50].

Third, treatment with FA, an active compound involved in wound healing, resulted in disturbed nuclear β -catenin expression after LiCl treatment in primary keratinocytes, whereas nuclear accumulation of β -catenin was activated by FA treatment in primary fibroblasts (Figure 4). In hair follicle progenitor cells, β -catenin signaling plays an important role in the active growth phase of the hair cycle [51] and contributes to proliferation, survival, and epidermal homeostasis [52]. In the continuous nucleus accumulation of β -catenin, however, keratinocyte migration and wound healing are suppressed by the induction of the c-myc activation in chronic wounds in humans [7]. The deregulation of c-myc depletes epidermal stem cells, resulting in an inability to restore wound sites and reduce β 1 integrin expression, which is involved in keratinocyte migration [53]. Thus, FA treatment suppressed nucleus accumulation of β -catenin and c-myc in primary keratinocytes, indicating wound healing via increasing migration.

Furthermore, the loss of β -catenin caused accelerated wound healing owing to reduced numbers of fibroblasts and the failure of differentiation into follicular keratinocytes [54,55]. However, in cutaneous wounds, the activation of the Wnt/ β -catenin pathway induces cutaneous wound healing in dermal fibroblasts through the inhibition of GSK3 β by valproic acid [16], because GSK3 β is involved in fibrosis through β -catenin signaling in dermal fibroblasts [56]. In addition, CXXC5, a negative feedback regulator of the Wnt/ β -catenin pathway, enhanced collagen production in cutaneous wound healing [57]. However, evidence of the therapeutic effect is limited in clinical trials of cutaneous wound healing. The problem of delivery is more tractable, as small-molecule drugs (typically <550 Da) pass through the dermal layer [58]. The side effects of small-molecule drugs include low specificity and accumulation in specific organs, which may result in severe toxic effects; for example, valproic acid affects chemicals in the body and is involved in seizures and epilepsy [59]. Although the previous study suggested that the regulation of β -catenin showed opposing mechanisms between keratinocytes and fibroblasts in wound healing [55], the development of therapeutic agents targeting both keratinocytes and fibroblasts has been poorly studied. Our results suggest that FA modulates the gene expression of β -catenin through the differential regulation of keratinocytes and fibroblasts and leads to epidermal migration and proliferation as a safe therapeutic target for wound healing. In a recent study, the wave complex, which is involved in structural organization and plays a mechanical function in cells, was essential in epidermal development by suppressing Wnt signaling [60]. In wound treatment, the control of Wnt signaling in epidermal keratinocytes may lead to well-established re-epithelization with minimal epidermal trauma. In the present study, we originally reported that FA modulated β -catenin in primary keratinocytes and fibroblasts. Our findings extend the current understanding of the pathogenesis of keratin disorders, as well as the knowledge of rapid wound healing. For example, the genetic mutation of K6a (~50% of cases), K6b, K16, or K17 causes pachyonychia congenita (PC), which is a keratinizing disorder and is a phenotypic feature of focal plantar keratoderma [61]. To treat hyperkeratotic disorders such as PC, retinoids or statins are therapeutic options. [62,63]. However, retinoids are not specific for a given keratin or keratin-related gene, and retinoids and statins may cause side effects through the inhibition of epidermal

differentiation and hepatotoxicity [64–66]. In particular, statins decrease K6a expression by downregulation of K6a promoter activity [63], and may promote neurological injury of the hippocampus and spinal cord via enhancement of the Wnt/ β -catenin signaling pathway [67,68]. Further studies to understand interaction of keratins and Wnt/ β -catenin signaling will provide treatment strategies for PC and other keratin-related disorders. Indeed, FA could be a plausible treatment option, as FA has been shown to induce compensatory keratin gene expression to overcome the effects of the mutated keratin gene and to regulate differential signaling modulation for fibroblasts and keratinocytes. Sulforaphane (SF), which is chemopreventive agent extracted from broccoli sprouts [69], regulates the induction of K16 and K17 through Nrf2-dependent and independent signaling in mouse keratinocytes [70]. In addition, SF-mediated Nrf2 signaling rescued the epidermolysis bullosa simplex (EBS), which is typified by the dysfunction of intermediated filaments in the basal keratinocytes of the epidermis [71]. Similar to the SF treatment strategy, we believe that the application of gene induction and gene repression through FA will be useful for the development of therapeutic agents for wound healing and keratinopathies via modulation of β -catenin and Nrf2, with minimal side effects.

Supplementary Materials: The following are available online at <https://www.mdpi.com/article/10.3390/biomedicines9050459/s1>: Figure S1: In vivo and ex vivo experimental processes. Figure S2: Evaluation between non-wounded and wounded skin. Figure S3: Increasing epithelial migration and mRNA expression of wound-induced keratins in primary keratinocytes. Figure S4: Histological study of wound closure in full-thickness skin. Figure S5: Total ion chromatogram of shilajit extract. Figure S6: Analysis of SIM chromatogram on total ion chromatograms. Figure S7: The qPCR analysis for *Krt6a*, *Krt6b*, *Krt16*, and *Nqo1* in kera 308 cell line.

Author Contributions: K.-H.K., W.-S.C., C.-H.L., and H.-J.J. designed the study. K.-H.K. performed all experiments and analyzed data. K.-H.K., J.H.J., W.-S.C., C.-H.L., and H.-J.J. discussed and wrote the paper. All authors have read and agreed to the published version of the manuscript.

Funding: This study was supported by the Traditional Korean Medicine R&D program funded by the Ministry of Health and Welfare through the Korea Health Industry Development Institute (KHIDI) (Grant No. HF20C0030).

Institutional Review Board Statement: The study was conducted according to the guidelines of the Declaration of Helsinki, and approved by the Institutional Animal Care and Use Committee (IACUC) of Kyung Hee University. The approval number for the animal experiment was KHUASP(SE)-14-046 (13 April 2015).

Informed Consent Statement: Not applicable.

Data Availability Statement: All data that support the findings of this study are available from the corresponding author, upon reasonable request.

Acknowledgments: We thanks to Pierre A. Coulombe for sharing 308 cell line, which is a mouse keratinocyte.

Conflicts of Interest: The authors declare no conflict of interest.

References

- Demidova-Rice, T.N.; Hamblin, M.R.; Herman, I.M. Acute and Impaired Wound Healing: Pathophysiology and current methods for drug delivery, part 1: Normal and chronic wounds: Biology, causes, and approaches to care. *Adv. Ski. Wound Care* **2012**, *25*, 304–314. [CrossRef] [PubMed]
- Elliot, S.; Wikramanayake, T.C.; Jozic, I.; Tomic-Canic, M. A Modeling Conundrum: Murine Models for Cutaneous Wound Healing. *J. Investig. Dermatol.* **2018**, *138*, 736–740. [CrossRef]
- Paladini, R.D.; Takahashi, K.; Bravo, N.S.; Coulombe, P. Onset of re-epithelialization after skin injury correlates with a reorganization of keratin filaments in wound edge keratinocytes: Defining a potential role for keratin 16. *J. Cell Biol.* **1996**, *132*, 381–397. [CrossRef]
- Takahashi, K.; Yan, B.; Yamanishi, K.; Imamura, S.; Coulombe, P.A. The Two Functional Keratin 6 Genes of Mouse Are Differentially Regulated and Evolved Independently from Their Human Orthologs. *Genomics* **1998**, *53*, 170–183. [CrossRef] [PubMed]

5. Wong, P.; Coulombe, P.A. Loss of keratin 6 (K6) proteins reveals a function for intermediate filaments during wound repair. *J. Cell Biol.* **2003**, *163*, 327–337. [CrossRef] [PubMed]
6. Cheon, S.S.; Wei, Q.; Gurung, A.; Youn, A.; Bright, T.; Poon, R.; Whetstone, H.; Guha, A.; Alman, B.A. Beta-catenin regulates wound size and mediates the effect of TGF-beta in cutaneous healing. *FASEB J.* **2006**, *20*, 692–701. [CrossRef]
7. Stojadinovic, O.; Brem, H.; Vouthounis, C.; Lee, B.; Fallon, J.; Stallcup, M.; Merchant, A.; Galiano, R.D.; Tomic-Canic, M. Molecular pathogenesis of chronic wounds: The role of beta-catenin and c-myc in the inhibition of epithelialization and wound healing. *Am. J. Pathol.* **2005**, *167*, 59–69. [CrossRef]
8. Barker, N. The Canonical Wnt/ β -Catenin Signalling Pathway. *Methods Mol. Biol.* **2008**, *468*, 5–15. [CrossRef] [PubMed]
9. Cheon, S.; Poon, R.; Yu, C.; Khoury, M.; Shenker, R.; Fish, J.; Alman, B. Prolonged β -catenin stabilization and tcf-dependent transcriptional activation in hyperplastic cutaneous wounds. *Lab. Investig.* **2005**, *85*, 416–425. [CrossRef]
10. Veltri, A.; Lang, C.; Lien, W.-H. Concise Review: Wnt Signaling Pathways in Skin Development and Epidermal Stem Cells. *Stem Cells* **2018**, *36*, 22–35. [CrossRef]
11. Cheon, S.S.; Cheah, A.Y.L.; Turley, S.; Nadesan, P.; Poon, R.; Clevers, H.; Alman, B.A. β -Catenin stabilization dysregulates mesenchymal cell proliferation, motility, and invasiveness and causes aggressive fibromatosis and hyperplastic cutaneous wounds. *Proc. Natl. Acad. Sci. USA* **2002**, *99*, 6973–6978. [CrossRef] [PubMed]
12. Chen, D.; Xie, R.; Shu, B.; Landay, A.L.; Wei, C.; Reiser, J.; Spagnoli, A.; Torquati, A.; Forsyth, C.B.; Keshavarzian, A.; et al. Wnt signaling in bone, kidney, intestine, and adipose tissue and interorgan interaction in aging. *Ann. N. Y. Acad. Sci.* **2018**, *1442*, 48–60. [CrossRef]
13. Takeichi, M. Historical review of the discovery of cadherin, in memory of Tokindo Okada. *Dev. Growth Differ.* **2017**, *60*, 3–13. [CrossRef]
14. Lee, S.-H.; Zahoor, M.; Hwang, J.-K.; Min, S.; Choi, K.-Y. Valproic Acid Induces Cutaneous Wound Healing In Vivo and Enhances Keratinocyte Motility. *PLoS ONE* **2012**, *7*, e48791. [CrossRef] [PubMed]
15. Jo, S.J.; Choi, S.-J.; Yoon, S.-Y.; Lee, J.Y.; Park, W.-S.; Park, P.-J.; Kim, K.H.; Eun, H.C.; Kwon, O. Valproic acid promotes human hair growth in in vitro culture model. *J. Dermatol. Sci.* **2013**, *72*, 16–24. [CrossRef] [PubMed]
16. Lee, S.-H.; Yoon, J.; Shin, S.H.; Zahoor, M.; Kim, H.J.; Park, P.J.; Park, W.-S.; Min, D.S.; Kim, H.-Y.; Choi, K.-Y. Valproic Acid Induces Hair Regeneration in Murine Model and Activates Alkaline Phosphatase Activity in Human Dermal Papilla Cells. *PLoS ONE* **2012**, *7*, e34152. [CrossRef] [PubMed]
17. Jo, S.J.; Shin, H.; Park, Y.W.; Paik, S.H.; Park, W.S.; Jeong, Y.S.; Shin, H.J.; Kwon, O. Topical valproic acid increases the hair count in male patients with androgenetic alopecia: A randomized, comparative, clinical feasibility study using phototrichogram analysis. *J. Dermatol.* **2014**, *41*, 285–291. [CrossRef] [PubMed]
18. Gerstner, T.; Bell, N.; König, S. Oral valproic acid for epilepsy—long-term experience in therapy and side effects. *Expert Opin. Pharmacother.* **2008**, *9*, 285–292. [CrossRef]
19. Sztajnkrzyer, M.D. Valproic Acid Toxicity: Overview and Management. *J. Toxicol. Clin. Toxicol.* **2002**, *40*, 789–801. [CrossRef]
20. Kim, K.-H.; Chung, W.-S.; Kim, Y.; Kim, K.-S.; Lee, I.-S.; Park, J.Y.; Jeong, H.-S.; Na, Y.-C.; Lee, C.-H.; Jang, H.-J. Transcriptomic Analysis Reveals Wound Healing of *Morus alba* Root Extract by Up-Regulating Keratin Filament and CXCL12/CXCR4 Signaling. *Phytother. Res.* **2015**, *29*, 1251–1258. [CrossRef]
21. Cornejo, A.; Jiménez, J.M.; Caballero, L.; Melo, F.; Maccioni, R.B. Fulvic Acid Inhibits Aggregation and Promotes Disassembly of Tau Fibrils Associated with Alzheimer’s Disease. *J. Alzheimer’s Dis.* **2011**, *27*, 143–153. [CrossRef] [PubMed]
22. Acharya, S.B.; Frotan, M.H.; Goel, R.K.; Tripathi, S.K.; Das, P.K. Pharmacological actions of Shilajit. *Indian J. Exp. Boil.* **1988**, *26*, 775–777.
23. Ozturk, E.; Ocak, N.; Coskun, I.; Turhan, S.; Erener, G. Effects of humic substances supplementation provided through drinking water on performance, carcass traits and meat quality of broilers. *J. Anim. Physiol. Anim. Nutr.* **2010**, *94*, 78–85. [CrossRef] [PubMed]
24. Vucskits, A.V.; Hullár, I.; Bersényi, A.; Andrásófszky, E.; Kulcsár, M.; Szabó, J. Effect of fulvic and humic acids on performance, immune response and thyroid function in rats. *J. Anim. Physiol. Anim. Nutr.* **2010**, *94*, 721–728. [CrossRef] [PubMed]
25. Shalini, S.R.; Srivastav, R. Antifungal Activity Screening and HPLC Analysis of Crude Extract from *Tectona grandis*, Shilajit, Valeriana wallachi. *Internet J. Altern. Med.* **2007**, *5*, 1540–2584.
26. Bouzaïene, N.N.; Jaziri, S.K.; Kovacic, H.; Chekir-Ghedira, L.; Ghedira, K.; Luis, J. The effects of caffeic, coumaric and ferulic acids on proliferation, superoxide production, adhesion and migration of human tumor cells in vitro. *Eur. J. Pharmacol.* **2015**, *766*, 99–105. [CrossRef] [PubMed]
27. Ghaisas, M.M.; Kshirsagar, S.B.; Sahane, R.S. Evaluation of wound healing activity of ferulic acid in diabetic rats. *Int. Wound J.* **2012**, *11*, 523–532. [CrossRef] [PubMed]
28. Seluanov, A.; Vaidya, A.; Gorbunova, V. Establishing Primary Adult Fibroblast Cultures from Rodents. *J. Vis. Exp.* **2010**, e2033. [CrossRef] [PubMed]
29. Strickland, J.; Greenhalgh, D.; Koceva-Chyla, A.; Hennings, H.; Restrepo, C.; Balaschak, M.; Yuspa, S.H. Development of murine epidermal cell lines which contain an activated rasHa oncogene and form papillomas in skin grafts on athymic nude mouse hosts. *Cancer Res.* **1988**, *48*, 165–169. [PubMed]
30. Oh, S.W.; Park, S.-H.; Lee, H.S.; Kang, M.; Lee, S.E.; Yoo, J.A.; Cho, J.Y.; Lee, J. Melanogenic mechanism of ethanolic extract of *Dalbergia odorifera*. *Mol. Cell. Toxicol.* **2017**, *13*, 453–459. [CrossRef]

31. Joo, S.-Y.; Ha, Y.; Seo, D.Y.; Seo, G.Y.; Kim, Y.-J.; Choi, H.-Y. Effect of *Prunus yedoensis* Matsumura extract on the gene expression in HaCaT cells. *Mol. Cell. Toxicol.* **2018**, *14*, 337–345. [CrossRef]
32. Kim, K.-H.; Park, J.Y.; Lee, I.-S.; Kim, Y.; Jang, H.-J. Proteins derived from *Prunus armeniaca* kernel are possible to cause Immunoglobulin E reactivity in human sera. *Mol. Cell. Toxicol.* **2017**, *13*, 213–220. [CrossRef]
33. An, E.-J.; Kim, K.-H.; Lee, I.-S.; Park, J.Y.; Kim, Y.; Jung, W.S.; Kwon, D.; Jang, H.-J. Identification of Possibility of Glycyrrhiza uralensis as an Allergen by Protein Analysis. *BioChip J.* **2018**, *12*, 75–82. [CrossRef]
34. Mazzalupo, S.; Wawersik, M.J.; Coulombe, P.A. An Ex Vivo Assay to Assess the Potential of Skin Keratinocytes for Wound Epithelialization. *J. Invest. Dermatol.* **2002**, *118*, 866–870. [CrossRef]
35. Lee, S.E.; Park, H.R.; Yun, H.D.; Kim, H.; Jin, Y.-H.; Ahn, H.-J.; Cho, J.-J. Effect of crotonaldehyde on the induction of HO-1 expression in A549 cells. *Mol. Cell. Toxicol.* **2017**, *13*, 221–227. [CrossRef]
36. Lampiasi, N.; Montana, G. The molecular events behind ferulic acid mediated modulation of IL-6 expression in LPS-activated Raw 264.7 cells. *Immunobiology* **2016**, *221*, 486–493. [CrossRef] [PubMed]
37. Martin, P. Wound Healing—Aiming for Perfect Skin Regeneration. *Science* **1997**, *276*, 75–81. [CrossRef] [PubMed]
38. Steinert, P.M.; Roop, D.R. Molecular and Cellular Biology of Intermediate Filaments. *Annu. Rev. Biochem.* **1988**, *57*, 593–625. [CrossRef]
39. Heins, S.; Aebi, U. Making heads and tails of intermediate filament assembly, dynamics and networks. *Curr. Opin. Cell Biol.* **1994**, *6*, 25–33. [CrossRef]
40. Jacob, J.T.; Coulombe, P.A.; Kwan, R.; Omary, M.B. Types I and II Keratin Intermediate Filaments. *Cold Spring Harb. Perspect. Biol.* **2018**, *10*, a018275. [CrossRef]
41. Ito, M.; Liu, Y.; Yang, Z.; Nguyen, J.; Liang, F.; Morris, R.J.; Cotsarelis, G. Stem cells in the hair follicle bulge contribute to wound repair but not to homeostasis of the epidermis. *Nat. Med.* **2005**, *11*, 1351–1354. [CrossRef] [PubMed]
42. Paladini, R.D.; Coulombe, P.A. Directed Expression of Keratin 16 to the Progenitor Basal Cells of Transgenic Mouse Skin Delays Skin Maturation. *J. Cell Biol.* **1998**, *142*, 1035–1051. [CrossRef]
43. Rotty, J.D.; Coulombe, P.A. A wound-induced keratin inhibits Src activity during keratinocyte migration and tissue repair. *J. Cell Biol.* **2012**, *197*, 381–389. [CrossRef]
44. Wang, F.; Chen, S.; Liu, H.B.; Parent, C.A.; Coulombe, P.A. Keratin 6 regulates collective keratinocyte migration by altering cell–cell and cell–matrix adhesion. *J. Cell Biol.* **2018**, *217*, 4314–4330. [CrossRef] [PubMed]
45. Vicente-Manzanares, M.; Choi, C.K.; Horwitz, A.R. Integrins in cell migration—The actin connection. *J. Cell Sci.* **2008**, *122*, 199–206. [CrossRef] [PubMed]
46. Simpson, C.L.; Patel, D.M.; Green, K.J. Deconstructing the skin: Cytoarchitectural determinants of epidermal morphogenesis. *Nat. Rev. Mol. Cell Biol.* **2011**, *12*, 565–580. [CrossRef] [PubMed]
47. Ray, S.; Foote, H.P.; Lechler, T. β -Catenin protects the epidermis from mechanical stresses. *J. Cell Biol.* **2013**, *202*, 45–52. [CrossRef] [PubMed]
48. Voronkov, A.; Krauss, S. Wnt/ β -catenin signaling and small molecule inhibitors. *Curr. Pharm. Des.* **2013**, *19*, 634–664. [CrossRef] [PubMed]
49. Geiger, B.; Ayalon, O. Cadherins. *Annu. Rev. Cell Biol.* **1992**, *8*, 307–332. [CrossRef] [PubMed]
50. Hecht, A.; Kemler, R. Curbing the nuclear activities of β -catenin. *EMBO Rep.* **2000**, *1*, 24–28. [CrossRef]
51. Van Mater, D.; Kolligs, F.T.; Dlugosz, A.A.; Fearon, E.R. Transient activation of β -catenin signaling in cutaneous keratinocytes is sufficient to trigger the active growth phase of the hair cycle in mice. *Genes Dev.* **2003**, *17*, 1219–1224. [CrossRef]
52. Choi, Y.S.; Zhang, Y.; Xu, M.; Yang, Y.; Ito, M.; Peng, T.; Cui, Z.; Nagy, A.; Hadjantonakis, A.-K.; Lang, R.A.; et al. Distinct Functions for Wnt/ β -Catenin in Hair Follicle Stem Cell Proliferation and Survival and Interfollicular Epidermal Homeostasis. *Cell Stem Cell* **2013**, *13*, 720–733. [CrossRef] [PubMed]
53. Waikel, R.L.; Kawachi, Y.; Waikel, P.A.; Wang, X.-J.; Roop, D.R. Deregulated expression of c-Myc depletes epidermal stem cells. *Nat. Genet.* **2001**, *28*, 165–168. [CrossRef] [PubMed]
54. Huelsken, J.; Vogel, R.; Erdmann, B.; Cotsarelis, G.; Birchmeier, W. β -Catenin controls hair follicle morphogenesis and stem cell differentiation in the skin. *Cell* **2001**, *105*, 533–545. [CrossRef]
55. Arwert, E.N.; Hoste, E.; Watt, F.M. Epithelial stem cells, wound healing and cancer. *Nat. Rev. Cancer* **2012**, *12*, 170–180. [CrossRef]
56. Bergmann, C.; Akhmetshina, A.; Dees, C.; Palumbo, K.; Zerr, P.; Beyer, C.; Zwerina, J.; Distler, O.; Schett, G.; Distler, J.H.W. Inhibition of glycogen synthase kinase 3 induces dermal fibrosis by activation of the canonical Wnt pathway. *Ann. Rheum. Dis.* **2011**, *70*, 2191–2198. [CrossRef]
57. Lee, S.-H.; Kim, M.-Y.; Kim, H.-Y.; Lee, Y.M.; Kim, H.; Nam, K.A.; Roh, M.R.; Min, D.S.; Chung, K.Y.; Choi, K.Y. The Dishevelled-binding protein CXXC5 negatively regulates cutaneous wound healing. *J. Exp. Med.* **2015**, *212*, 1061–1080. [CrossRef] [PubMed]
58. Bos, J.D.; Meinardi, M.M.H.M. The 500 Dalton rule for the skin penetration of chemical compounds and drugs. *Exp. Dermatol.* **2000**, *9*, 165–169. [CrossRef] [PubMed]
59. Davis, R.; Peters, D.H.; McTavish, D. Valproic acid. A reappraisal of its pharmacological properties and clinical efficacy in epilepsy. *Drugs* **1994**, *47*, 332–372. [CrossRef] [PubMed]
60. Cohen, J.; Raviv, S.; Adir, O.; Padmanabhan, K.; Soffer, A.; Luxenburg, C. The Wave complex controls epidermal morphogenesis and proliferation by suppressing Wnt–Sox9 signaling. *J. Cell Biol.* **2019**, *218*, 1390–1406. [CrossRef] [PubMed]

61. Leachman, S.A.; Kaspar, R.L.; Fleckman, P.; Florell, S.R.; Smith, F.J.; McLean, W.I.; Lunny, D.P.; Milstone, L.M.; Van Steensel, M.A.; Munro, C.S.; et al. Clinical and Pathological Features of Pachyonychia Congenita. *J. Investig. Dermatol. Symp. Proc.* **2005**, *10*, 3–17. [CrossRef] [PubMed]
62. De The, H.; Vivanco-Ruiz, M.D.M.; Tiollais, P.; Stunnenberg, H.; Dejean, A. Identification of a retinoic acid responsive element in the retinoic acid receptor β gene. *Nat. Cell Biol.* **1990**, *3*, 177–180. [CrossRef]
63. Zhao, Y.; Gartner, U.; Smith, F.J.; McLean, W.I. Statins Downregulate K6a Promoter Activity: A Possible Therapeutic Avenue for Pachyonychia Congenita. *J. Investig. Dermatol.* **2011**, *131*, 1045–1052. [CrossRef]
64. DiGiovanna, J.J. Fracturing Support for the Role of Systemic Retinoid Therapy as a Cause of Bone Demineralization. *Arch. Dermatol.* **2010**, *146*, 551–553. [CrossRef] [PubMed]
65. Ormerod, A.; Campalani, E.; Goodfield, M. British Association of Dermatologists guidelines on the efficacy and use of acitretin in dermatology. *Br. J. Dermatol.* **2010**, *162*, 952–963. [CrossRef] [PubMed]
66. Moctezuma-Velázquez, C.; Abalde, J.G.; Montano-Loza, A.J. The Use of Statins in Patients With Chronic Liver Disease and Cirrhosis. *Curr. Treat. Options Gastroenterol.* **2018**, *16*, 226–240. [CrossRef] [PubMed]
67. Robin, N.C.; Agoston, Z.; Biechele, T.L.; James, R.G.; Berndt, J.D.; Moon, R.T. Simvastatin promotes adult hippocampal neurogenesis by enhancing Wnt/ β -catenin signaling. *Stem Cell Rep.* **2014**, *2*, 9–17. [CrossRef]
68. Strand, N.S.; Hoi, K.K.; Phan, T.M.; Ray, C.A.; Berndt, J.D.; Moon, R.T. Wnt/ β -catenin signaling promotes regeneration after adult zebrafish spinal cord injury. *Biochem. Biophys. Res. Commun.* **2016**, *477*, 952–956. [CrossRef]
69. Zhang, Y.; Talalay, P.; Cho, C.G.; Posner, G.H. A major inducer of anticarcinogenic protective enzymes from broccoli: Isolation and elucidation of structure. *Proc. Natl. Acad. Sci. USA* **1992**, *89*, 2399–2403. [CrossRef] [PubMed]
70. Kerns, M.; DePianto, D.; Yamamoto, M.; Coulombe, P.A. Differential Modulation of Keratin Expression by Sulforaphane Occurs via Nrf2-dependent and -independent Pathways in Skin Epithelia. *Mol. Biol. Cell* **2010**, *21*, 4068–4075. [CrossRef]
71. Kerns, M.L.; DePianto, D.; Dinkova-Kostova, A.T.; Talalay, P.; Coulombe, P.A. Reprogramming of keratin biosynthesis by sulforaphane restores skin integrity in epidermolysis bullosa simplex. *Proc. Natl. Acad. Sci. USA* **2007**, *104*, 14460–14465. [CrossRef] [PubMed]



Article

Anti-Adipogenic Polyacetylene Glycosides from the Florets of Safflower (*Carthamus tinctorius*)

Su Cheol Baek ^{1,†}, Sang Ah Yi ^{1,†}, Bum Soo Lee ¹, Jae Sik Yu ¹, Jin-Chul Kim ², Changhyun Pang ³,
Tae Su Jang ⁴, Jaecheol Lee ^{1,*} and Ki Hyun Kim ^{1,*}

¹ School of Pharmacy, Sungkyunkwan University, Suwon 16419, Korea; schii513@daum.net (S.C.B.); angelna1023@hanmail.net (S.A.Y.); kosboybs@naver.com (B.S.L.); jsyu@bu.edu (J.S.Y.)

² Natural Product Informatics Research Center, KIST Gangneung Institute of Natural Products, Gangneung 25451, Korea; jckim@kist.re.kr

³ School of Chemical Engineering, Sungkyunkwan University, Suwon 16419, Korea; chpang@skku.edu

⁴ Department of Medicine, Dankook University, Cheonan, Chungnam 31116, Korea; jangts@dankook.ac.kr

* Correspondence: jaecheol@skku.edu (J.L.); khkim83@skku.edu (K.H.K.); Tel.: +82-31-290-7726 (J.L.); +82-31-290-7700 (K.H.K.)

† These authors contributed equally to this work.

Abstract: Safflower (*Carthamus tinctorius*) is an annual herb belonging to the Compositae family; it has a history of use as a food colorant, dye, and medicine in oriental countries. LC-MS-UV-based chemical analysis of extract of the florets of *C. tinctorius* led to the isolation of two new C₁₀-polyacetylene glycosides, (8Z)-decaene-4,6-diyne-1,10-diol-1-O-β-D-glucopyranoside (**1**) and (8S)-deca-4,6-diyne-1,8-diol-1-O-β-D-glucopyranoside (**2**), together with five known analogs (**3–7**). The structures of the new compounds were determined by using 1D and 2D NMR spectroscopic data and HR-MS data, as well as chemical transformations. Of compounds **1–7**, compounds **2**, **3**, and **4** inhibited the adipogenesis of 3T3-L1 preadipocytes, whereas compounds **1** and **6** promoted adipogenesis. Compounds **2**, **3**, and **4** also prevented lipid accumulation through the suppression of the expression of lipogenic genes and the increase of the expression of lipolytic genes. Moreover, compounds **3** and **4** activated AMPK, which is known to facilitate lipid metabolism. Our findings provide a mechanistic rationale for the use of safflower-derived polyacetylene glycosides as potential therapeutic agents against obesity.

Keywords: safflower; *Carthamus tinctorius*; polyacetylene glycosides; 3T3-L1 preadipocytes; AMPK

Citation: Baek, S.C.; Yi, S.A.; Lee, B.S.; Yu, J.S.; Kim, J.-C.; Pang, C.; Jang, T.S.; Lee, J.; Kim, K.H. Anti-Adipogenic Polyacetylene Glycosides from the Florets of Safflower (*Carthamus tinctorius*). *Biomedicines* **2021**, *9*, 91. <https://doi.org/10.3390/biomedicines9010091>

Received: 28 December 2020

Accepted: 15 January 2021

Published: 19 January 2021

Publisher's Note: MDPI stays neutral with regard to jurisdictional claims in published maps and institutional affiliations.



Copyright: © 2021 by the authors. Licensee MDPI, Basel, Switzerland. This article is an open access article distributed under the terms and conditions of the Creative Commons Attribution (CC BY) license (<https://creativecommons.org/licenses/by/4.0/>).

1. Introduction

Obesity is caused by energy imbalance, which leads to an excessive accumulation of body fat in adipose tissues [1]. The expansion of adipose tissue accompanies the differentiation of preadipocytes residing in adipose tissues to mature adipocytes and the generation and accumulation of lipid droplets in adipocytes [2]. Thus, the identification of compounds preventing adipogenesis and lipogenesis has been considered as an effective strategy for the alleviation of obesity and metabolic diseases.

Carthamus tinctorius L., also known as safflower, is a highly branched and thistle-like annual plant belonging to the Compositae family. *C. tinctorius* has a long history of use as a food colorant, dye, and traditional medicine for the treatment of cardiovascular diseases and gynecological symptoms [3]. The pistil of *C. tinctorius* is well-known as an edible dye agent in various European dishes, including paella, risotto, and pasta [4]. In previous studies, phytochemical investigation of this plant reported the presence of quinocalones, such as carthamin, safflower yellow, and safflomin, flavonoids, alkaloids, and polyacetylenes [5]. Further pharmacological studies demonstrated that the polyacetylenes from *C. tinctorius* inhibited LPS-induced NO (nitric oxide) release, showing its potential as an agent for treating inflammatory diseases [6]. Recent studies have shown that extracts of safflower inhibited the adipogenesis of 3T3-L1 preadipocytes and alleviated high-fat diet-induced obesity in

mice [7–10]. In addition, treatment with safflower extracts improved metabolic parameters, such as glucose metabolism and lipid profiles, in mice with diet-induced obesity [9,10]. Despite numerous evidences showing the beneficial effects of safflower on metabolism, the exact compounds responsible for the action and the mechanisms underlying their action remain undiscovered.

As a part of our continued search for natural products with novel structural and/or biological properties [11–15], seven polyacetylene glycosides (1–7), including two new C₁₀-polyacetylene glycosides, (8*Z*)-decaene-4,6-diyne-1,10-diol-1-*O*-β-D-glucopyranoside (1) and (8*S*)-deca-4,6-diyne-1,8-diol-1-*O*-β-D-glucopyranoside (2), were isolated from the extract of the florets of *C. tinctorius* by using LC-MS-UV-based chemical analysis. The structures of the new compounds were established by 1D and 2D NMR spectroscopic and high-resolution MS data analysis, and the absolute configurations of the sugar moiety were elucidated by chemical transformations followed by enzymatic hydrolysis. Herein, we have described the isolation and structural characterization of the compounds (1–7) (Figure 1) and the evaluation of their effects on de novo adipogenesis and lipid metabolism in adipocytes.

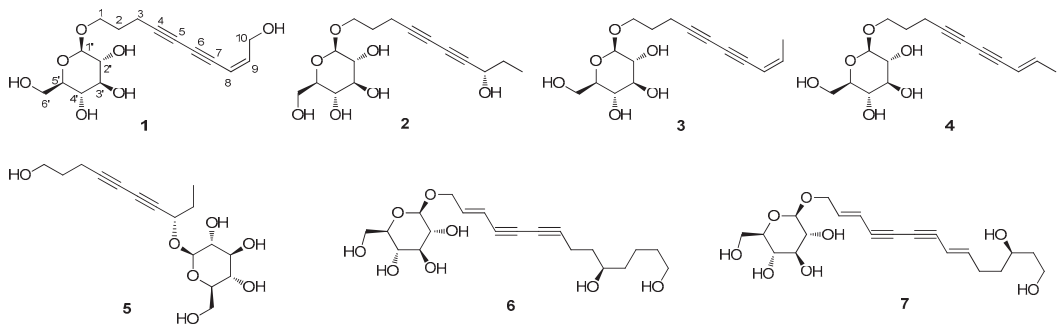


Figure 1. The chemical structures of the isolated compounds 1–7.

2. Materials and Methods

2.1. General Experimental Procedures

Optical rotations were measured using a Jasco P-2000 polarimeter (Jasco, Easton, MD, USA). IR spectra were recorded using a Bruker IFS-66/S FT-IR spectrometer (Bruker, Karlsruhe, Germany). Ultraviolet (UV) spectra were acquired using an Agilent 8453 UV-visible spectrophotometer (Agilent Technologies, Santa Clara, CA, USA). NMR spectra were recorded using a Bruker AVANCE III HD 850 NMR spectrometer with a 5-mm TCI CryoProbe, operated at 850 MHz (¹H) and 212.5 MHz (¹³C). The chemical shifts were presented in ppm (δ) for ¹H and ¹³C NMR analyses. Preparative HPLC was performed by using a Waters 1525 Binary HPLC pump with a Waters 996 photodiode array detector (Waters Corporation, Milford, MA, USA) and an Agilent Eclipse C18 column (250 × 21.2 mm, 5 μ m; flow rate: 5 mL/min; Agilent Technologies). Semi-preparative HPLC was performed on a Shimadzu Prominence HPLC System with SPD-20A/20AV Series Prominence HPLC UV-Vis detector (Shimadzu, Tokyo, Japan) and a Phenomenex Luna C18 column (250 × 10 mm, 5 μ m; flow rate: 2 mL/min; Phenomenex, Torrance, CA, USA). LC-MS analysis was performed using an Agilent 1200 Series HPLC system, equipped with a diode array detector and 6130 Series ESI mass spectrometer, and an analytical Kinetex C18 100 Å column (100 × 2.1 mm, 5 μ m; flow rate: 0.3 mL/min; Phenomenex). All HRESIMS data were obtained by using a Waters Xevo G2 quadrupole time-of-flight (QTOF) mass spectrometer and a Synapt G2 HDMS QTOF mass spectrometer (Waters). Silica gel 60 (230–400 mesh; Merck, Darmstadt, Germany) and RP-C₁₈ silica gel (Merck, 230–400 mesh) were used for column chromatography. The packing material for molecular sieve column chromatography was Sephadex LH-20 (Pharmacia, Uppsala, Sweden). Thin-layer chro-

matography was performed by using precoated silica gel F₂₅₄ plates and RP-C₁₈ F_{254s} plates (Merck) and spots were detected under UV light or by heating, after spraying with anisaldehyde–sulfuric acid.

2.2. Plant Material

The florets of *C. tinctorius* were collected in Pocheon, Gyeonggi-do, Korea, and purchased from Dongyangpharm in September 2018. The plant was identified by one of the authors (K. H. Kim). A voucher specimen (HH-18-12) was deposited in the herbarium of the School of Pharmacy, Sungkyunkwan University, Suwon, Korea.

2.3. Extraction and Isolation

The florets of *C. tinctorius* (1.8 kg) were extracted using 80% aqueous MeOH (each 20 L × 2 days) at room temperature, filtered through Whatman's filter paper No. 1, and then combined and concentrated under vacuum pressure by using a rotary evaporator, which yielded an MeOH extract (530.0 g). The MeOH extract was suspended in distilled water (700 mL, each) and then solvent-partitioned with hexane, dichloromethane, ethyl acetate, and *n*-butanol, which afforded four fractions: hexane-soluble (37.6 g), CH₂Cl₂-soluble (3.3 g), EtOAc-soluble (10.4 g), and BuOH-soluble fractions (57.3 g). After solvent partition, the residue was solvent-partitioned again with acetone, affording the acetone-soluble fraction (68.7 g). All these fractions were initially analyzed by LC-MS, which confirmed the presence of components with a distinctive UV spectrum, which was characteristic of an enediyne chromophore [16,17] in the EtOAc-soluble fraction. To identify the compounds of interest, the EtOAc fraction (10.4 g) was resolved by silica gel column chromatography [300 g; eluted using a CH₂Cl₂/MeOH (50:1→1:1, *v:v*) gradient solvent system and washed with 90% MeOH] and investigated by monitoring through LC-MS using our in-house UV library. As a result, seven fractions (E1–E7) were obtained from the column chromatography, and fraction E5 (3.2 g) was separated by MPLC, using the Yamazen UNIVERSAL Premium ODS-SM column with MeOH/H₂O (30–100% MeOH) to yield five subfractions (E51–E55). Subfraction E52 (638.7 mg) was loaded onto a Sephadex LH-20 column by using a solvent system of 100% MeOH to yield three subfractions (E521–E523). Subfraction E521 (267.2 mg) was separated by preparative reversed-phase HPLC using a gradient solvent system of MeOH/H₂O (50–100% MeOH) to yield five subfractions (E5211–E5215). Subfraction E5212 (87 mg) was subjected to silica gel column chromatography [3.0 g, eluted with CH₂Cl₂/MeOH (50:1→1:1) gradient solvent system, and washed with 90% MeOH] to yield five subfractions (E52121–E52125). Subfraction E52125 (20.7 mg) was purified by semi-preparative HPLC (36% MeOH) to furnish compound 5 (*t*_R 29.5 min, 3.0 mg). Subfraction E5215 (23.4 mg) was separated by semi-preparative HPLC (17% acetonitrile, MeCN) to yield compound 2 (*t*_R 38.0 min, 1.5 mg). Subfraction E522 (68.2 mg) was purified by using semi-preparative HPLC (35% MeOH) to yield compound 1 (*t*_R 43.0 min, 1.2 mg). Fraction E6 (1.3 g) was separated by MPLC with a gradient solvent system MeOH/H₂O (30–100% MeOH) to yield five subfractions (E61–E65). Subfraction E62 (172.7 mg) was subjected to Sephadex LH-20 column using a solvent system of 100% MeOH to yield three subfractions (E621–E623). Subfraction E622 (46.6 mg) was purified by semi-preparative HPLC (37% MeOH) to yield compounds 6 (*t*_R 42.5 min, 1.5 mg) and 7 (*t*_R 47.5 min, 3.1 mg). Subfraction E64 (299.4 mg) was separated by preparative reversed-phase HPLC with a gradient solvent system of MeOH/H₂O (70% MeOH) to yield five subfractions (E641–E645). Subfraction E643 (96.2 mg) was purified by semi-preparative HPLC (28% MeCN) to furnish compounds 3 (*t*_R 32.5 min, 12.5 mg) and 4 (*t*_R 34.0 min, 1.5 mg).

2.3.1. (8Z)-Decaene-4,6-diyne-1,10-diol-1-*O*-β-D-glucopyranoside (1)

Yellowish amorphous gum; $[a]_D^{25} - 68.0$ (c 0.06, MeOH); UV (MeOH) λ_{\max} (log ϵ) 208 (3.41), 215 (3.47), 240 (0.72), 255 (1.46), 268 (1.76), 287 (1.66) nm; IR (KBr) ν_{\max} 3396, 2976, 2265, 1655, 1610, 1365, 1116 cm⁻¹; ¹H (850 MHz) and ¹³C (212.5 MHz) NMR data, see

Table 1; ESIMS (positive-ion mode) m/z 349.1 [M + Na]⁺; HRESIMS (positive-ion mode) m/z 349.1252 [M + Na]⁺ (calculated for C₁₆H₂₂O₇Na, 349.1263).**Table 1.** ¹H and ¹³C NMR data for compounds **1** and **2** in CD₃OD. ^a

Position	1		2	
	δ_C , Type	δ_H (J in Hz)	δ_C , Type	δ_H (J in Hz)
1	68.9, CH ₂	3.98, dt (10.0, 6.0) 3.67 dt (10.0, 6.0)	69.1, CH ₂	3.95, dt (10.0, 6.0) 3.64 dt (10.0, 6.0)
2	29.5, CH ₂	1.87, m	29.6, CH ₂	1.83, m
3	16.5, CH ₂	2.52, t (7.0)	16.3, CH ₂	2.44, t (7.0)
4	85.9, C		81.4, C	
5	65.5, C		65.6, C	
6	80.3, C		70.1, C	
7	71.4, C		78.0, C	
8	109.3, CH	5.61, d (11.0)	64.0, CH	4.27, d (6.5)
9	146.6, CH	6.20, dt (11.0, 6.5)	31.7, CH ₂	1.67, m
10	60.8, CH ₂	4.32, d (6.5)	9.6, CH ₃	0.98, t (7.5)
1'	104.2, CH	4.28, d (8.0)	104.5, CH	4.25, d (8.0)
2'	74.9, CH	3.19, dd (9.0, 8.0)	74.9, CH	3.16, dd (9.0, 8.0)
3'	77.7, CH	3.28, m	77.7, CH	3.28, m
4'	71.3, CH	3.29, m	71.3, CH	3.29, m
5'	77.8, CH	3.36, m	77.8, CH	3.35, m
6'	62.5, CH ₂	3.89, dd (12.0, 2.0) 3.69, dd (12.0, 5.5)	62.6, CH ₂	3.86, dd (12.0, 2.0) 3.67, dd (12.0, 5.5)

^a Signal multiplicity and coupling constants (Hz) are in parentheses; the measurements are based on HSQC, HMBC, and ¹H-¹H COSY experiments.

2.3.2. (8S)-Deca-4,6-diyne-1,8-diol-1-O- β -D-glucopyranoside (**2**)

Colorless amorphous gum; $[\alpha]_D^{25} - 18.5$ (c 0.07, MeOH); UV (MeOH) λ_{max} (log ϵ) 210 (3.03), 222 (3.46), 242 (0.68), 255 (0.98), 270 (1.21), 285 (0.91) nm; IR (KBr) ν_{max} 3374, 2953, 2205, 1650, 1235, 1051 cm⁻¹; ¹H (850 MHz) and ¹³C (212.5 MHz) NMR data, see Table 1; ESIMS (positive-ion mode) m/z 351.1 [M + Na]⁺; HRESIMS (positive-ion mode) m/z 329.1598 [M + H]⁺ (calculated for C₁₆H₂₅O₇, 329.1600).

2.4. Enzymatic Hydrolysis and Absolute Configuration Determination of the Sugar Moiety of **1** and **2**

The absolute configuration of the sugar moiety was determined by using an LC-MS-UV-based method [18]. Compounds **1** and **2** (each 0.5 mg) were hydrolyzed with crude hesperidinase (10 mg, from *Aspergillus niger*; Sigma-Aldrich, Saint Louis, MO, USA) at 37 °C for 72 h, individually, and then, EtOAc was used for the extraction. Each aqueous layer was evaporated by using a vacuum evaporator and dissolved in anhydrous pyridine (0.5 mL) with the addition of L-cysteine methyl ester hydrochloride (1.0 mg). After the reaction mixture was heated at 60 °C for 1 h, *O*-tolyliothiocyanate (50 μ L) was added, and the mixture was incubated at 60 °C for 1 h. The reaction product was evaporated by using a vacuum evaporator and dissolved in MeOH. Subsequently, the dissolved reaction product was directly analyzed by LC-MS [MeOH/H₂O, 1:9→7:3 gradient system (0–30 min), 100% MeOH (31–41 min), 0% MeOH (42–52 min); 0.3 mL/min] using an analytical Kinetex C18 100 Å column (100 mm \times 2.1 mm i.d., 5 μ m). The sugar moiety from **1** and **2** was identified as D-glucopyranose based on the comparison of the retention time with an authentic sample (t_R : D-glucopyranose 19.3 min).

2.5. Cell Culture and Differentiation

3T3-L1 preadipocytes, purchased from the American Type Culture Collection (ATCC[®] CL-173[™], Manassas, VA, USA), were grown in Dulbecco Modified Eagle Medium (DMEM) supplemented with 10% bovine calf serum and 1% penicillin/streptomycin (P/S) [19]. For the adipogenic differentiation, 3T3-L1 cells were incubated in DMEM with 10% fetal bovine

serum (FBS), 1% P/S, 0.5 mM 3-isobutyl-1-methylxanthine (IBMX), 1 μ M dexamethasone, and 1 μ g/mL insulin. Then, the medium was replaced with DMEM containing 10% FBS, 1% P/S, and 1 μ g/mL insulin every alternate day until Day 8. To evaluate the effects of compounds 1–7 on adipogenesis, we treated 3T3-L1 cells with these compounds throughout the process of adipogenesis.

2.6. Oil Red O Staining

To observe the accumulated lipid droplets in adipocytes, Oil Red O staining was performed after the differentiation [20]. After the adipocytes were fixed in 10% formaldehyde for 1 h and washed with 60% isopropanol, mature adipocytes were incubated with the Oil Red O working solution for 1 h. Then, the cells were washed with distilled water twice, and images of the stained lipid droplets were captured with Cytation™ 5.

2.7. Cell Counting

First, 3T3-L1 cells were treated with compounds 1–7 at concentrations of 10, 20, and 40 μ M for 24 h; then, they were incubated with EDTA for 5 min for detachment. The detached cells were diluted with PBS, and the numbers of cells were counted by using a LUNA-II™ Automated Cell Counter (Logos Biosystems, Annandale, VA, USA).

2.8. Western Blotting

Proteins were extracted with Pro-Prep (Intron Biotechnology, Seoul, Korea) for 20 min on ice and then centrifuged at 13,000 rpm at 4 °C for 20 min. For Western blotting, 15 μ g of each protein in the supernatant was separated by SDS-polyacrylamide gel (10%) electrophoresis. The proteins were transferred to polyvinylidene difluoride (PVDF, Millipore, Darmstadt, Germany) membranes using a semi-dry transfer apparatus (Bio-Rad, Hercules, CA, USA). The membranes were incubated with the primary antibodies (dilution 1:2000) overnight at 4 °C, followed by incubation with horseradish peroxidase (HRP)-conjugated secondary antibodies (Abcam) for 1 h at room temperature. HRP signals reacting with chemiluminescence reagents (Abclon) were detected using AGFA X-ray films and quantified using the ImageJ software. Anti-phospho (T172) AMPK α (Abcam, ab2535) and anti-AMPK α (Abcam, ab2532S) antibodies were used for Western blotting.

2.9. Reverse Transcription and Quantitative Real-Time PCR (RT-qPCR)

Total RNA was extracted from adipocytes using Easy-Blue reagent (Intron Biotechnology) in accordance with the manufacturer's instructions. For reverse transcription (RT), cDNA was synthesized from 1 μ g of total RNA using the Maxim RT-PreMix Kit (Intron Biotechnology). For quantitative real-time PCR (qPCR), cDNA from RNA was incubated with KAPA SYBR® FAST qPCR Master Mix (Kapa Biosystems) and primers for each gene. The qPCR reaction was detected using a CFX96 Touch™ real-time PCR detector (Bio-Rad). The relative mRNA expression for each gene was normalized to the expression of β -actin. The sequences of qPCR primers used in this study are listed in Table 2.

Table 2. Sequences of primers used for RT-qPCR.

Gene	Forward	Reverse
β -Actin	5'-ACGGCCAGGTCATCACTATTG-3'	5'-TGGATGCCACAGGATTCCA-3'
Adipsin	5'-CATGCTCGGCCCTACATG-3'	5'-CACAGAGTCGTATCCGTCAC-3'
Fabp4	5'-AAGGTGAAGAGCATCATAACCCT-3'	5'-TCACGCCTTTCATAACACATTCC-3'
SREBP1	5'-AACGTCACCTCCAGCTAGAC-3'	5'-CCACTAAGGTGCCTACAGAGC-3'
ATGL	5'-TTCACCATCCGCTGTGTTGGAG-3'	5'-AGATGGTCACCCAATTTCTC-3'
HSL	5'-CACAAAGGCTGCTTCTACGG-3'	5'-GGAGAGAGTTCGAGGAACG-3'

2.10. Statistical Analysis

Statistical significance was analyzed by using a two-tailed Student's *t*-test with Excel and evaluated by using a *p*-value. The data represent the mean \pm SEM for *n* = 3 replicates. * *p* < 0.05, ** *p* < 0.01, and *** *p* < 0.001 vs. the control group.

3. Results and Discussion

3.1. Isolation of the Compounds

The crude extract of the florets of *C. tinctorius* was solvent-partitioned using water and five organic solvents of increasing polarity (hexane, dichloromethane, ethyl acetate, *n*-butanol, and acetone). The obtained fractions were primarily monitored and analyzed by LC-MS, which allowed us to identify the presence of components with a distinctive UV spectrum in the EtOAc-soluble fraction, which is characteristic of an enediyne chromophore [16,17]. To identify the compounds of interest, the LC-MS-based phytochemical analysis of the EtOAc fraction and preparative and semi-preparative HPLC were performed; the processes resulted in the isolation of two new C₁₀-polyacetylene glycosides (**1** and **2**) and five known analogs (**3**–**7**).

3.2. Structural Elucidation of Isolated Compounds

Compound **1** was obtained as yellowish amorphous gum and exhibited UV data characteristic of an enediyne chromophore (Figure S2, Supplementary Materials) [16,17]. The molecular formula was established as C₁₆H₂₂O₇ from the molecular ion peak [M + Na]⁺ at *m/z* 349.1252 (calculated for C₁₆H₂₂O₇Na, 349.1263) in the positive-ion HR-ESIMS (Figure S1) and NMR data (Table 1). The IR spectrum showed absorptions attributable to the hydroxy (3396 cm⁻¹) and acetylenic (2265 cm⁻¹) groups. The ¹H (Figure S3) and ¹³C NMR spectra of **1** (Table 1), combined with heteronuclear single quantum coherence (HSQC) and heteronuclear multiple bond correlation (HMBC) data, indicated the presence of a *cis*-configured Δ^{8,9} double bond with signals at δ_H 5.61 (1H, d, *J* = 11.0 Hz)/δ_C 109.3 and 6.20 (1H, dt, *J* = 11.0, 6.5 Hz)/δ_C 146.6, four acetylenic carbons at δ_C 65.5, 71.4, 80.3, and 85.9, and two oxygenated methylene signals at δ_H 3.98 (1H, dt, *J* = 10.0, 6.0 Hz) and 3.67 (1H, dt, *J* = 10.0, 6.0 Hz)/δ_C 68.9 and 4.32 (2H, d, *J* = 6.5 Hz)/δ_C 60.8, as well as a β-D-glucopyranosyl moiety at δ_H 4.28 (1H, d, *J* = 8.0 Hz)/δ_C 104.2 and δ_C 62.5, 71.3, 74.9, 77.7, and 77.8. Detailed NMR analysis and 2D NMR experiments (Figures S4–S6) revealed the strong similarity of **1** with bidenoside C [21], which was isolated as compound **3** in this study. The noticeable difference between the two compounds was that the NMR chemical shifts of C-10 in **1** showed a downfield shift owing to hydroxylation, which was confirmed based on the HMBC correlations between H-10 and C-8/C-9 (Figure 2). The gross structure of **1** was further established by the analysis of cross-peaks in the ¹H-¹H COSY (Figure S4) and HMBC (Figure S6) spectra (Figure 2). The absolute configuration of the sugar unit was determined by using an LC-MS-UV-based method [18], and enzymatic hydrolysis of **1** with hesperidinase resulted in the production of a glucopyranose. The β-D-glucopyranose was determined by comparing the retention time of its thiocarbamoyl-thiazolidine derivative with that of the standard sample of D-glucopyranose by LC-MS analysis and the coupling constant (*J* = 8.0 Hz) of the anomeric proton signal. Accordingly, the structure of **1** was characterized as (8*Z*)-decaene-4,6-diyne-1,10-diol-1-*O*-β-D-glucopyranoside.

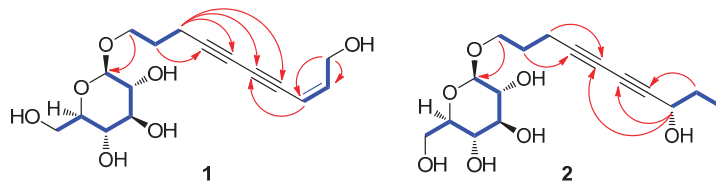


Figure 2. ¹H-¹H COSY (bold blue lines) and key HMBC (red arrows) correlations of **1** and **2**.

Compound **2** was isolated as a colorless amorphous gum, and its IR spectrum showed absorption bands for hydroxy (3374 cm^{-1}) and acetylenic (2205 cm^{-1}) groups. Its molecular formula, $\text{C}_{16}\text{H}_{14}\text{O}_7$, was established on the basis of the positive-ion HRESIMS peak at m/z 329.1598 $[\text{M} + \text{H}]^+$ (calculated for $\text{C}_{16}\text{H}_{25}\text{O}_7$, 329.1600, Figure S7) and NMR data (Table 1). The UV spectrum (Figure S8) of **2** was typical for an enediyne chromophore [16,17]. The ^1H (Figure S9) and ^{13}C NMR spectra of **2** (Table 1) showed a close resemblance to those of 8*S*-deca-4,6-diyne-1,8-diol-8-*O*- β -D-glucopyranoside [22], which was isolated as compound **5** in this study. The only slight difference in their chemical shifts was at the level of the glycosylated carbon group at C-1 and C-8, which was observed in compound **2** at δ_{C} 69.1 (C-1, $\Delta\delta_{\text{C}}$ +7.8 ppm in CD_3OD) and δ_{C} 64.0 (C-8, $\Delta\delta_{\text{C}}$ -5.6 ppm in CD_3OD) [22]. This set of data indicated that compound **2** had a glucose moiety at C-1, the position of which was confirmed by the HMBC correlation between H-1' and C-1 (Figure 2). The complete structure of **2** was determined further by the 2D NMR analysis [^1H - ^1H COSY (Figure S10), HSQC (Figure S11), and HMBC (Figure S12)] (Figure 2). The assignment of β -D-glucopyranose was also achieved by the LC-MS-UV-based method [18], which was followed by the enzymatic hydrolysis of **2** with hesperidinase. The absolute configuration of C-8 was established by the value of specific rotation of **2a** (aglycone of **2**, 4,6-decadiyne-1,8-diol) derived from the enzymatic hydrolysis of **2**. The specific rotation value of **2a** [$[\alpha]_{\text{D}}^{25} + 12.5$ (c 0.01, MeOH)] was comparable with those of the related analogs, (*S*)-panaxjapyne A [$[\alpha]_{\text{D}}^{28} + 11.0$ (c 0.1, MeOH)] [23], (2*S*)-(3*Z*,11*E*)-decadiene-5,7,9-triyn-1,2-diol [$[\alpha]_{\text{D}}^{25} + 15.8$ (c 0.1, MeOH)] [24], (6*S*)-undeca-2,4-diyne-1,6-diol [$[\alpha]_{\text{D}}^{25} + 10.74$ (c 0.37, CH_2Cl_2)] [25], (6*R*)-undeca-2,4-diyne-1,6-diol [$[\alpha]_{\text{D}}^{25} - 10.16$ (c 0.13, CH_2Cl_2)] [25], and (2*R*)-(3*E*,11*Z*)-decadiene-5,7,9-triyn-1,2-diol [$[\alpha]_{\text{D}}^{25} - 16.5$ (c 0.1, MeOH)] [24] (Figure 3), which led to the assignment of the absolute configuration of C-8 as *S*. Consequently, the structure of **2** was designated as (8*S*)-deca-4,6-diyne-1,8-diol-1-*O*- β -D-glucopyranoside.

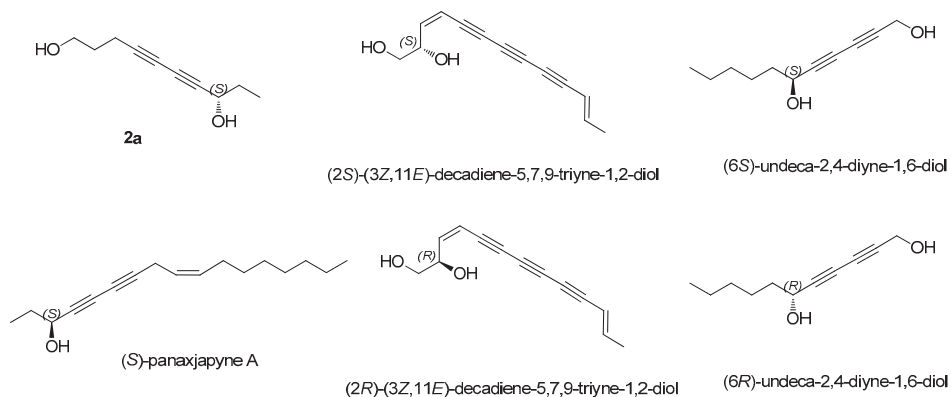


Figure 3. Structures of compound **2a** and the related analogs.

The five known compounds were identified as bidenoside C (**3**) [21], (8*E*)-decaene-4,6-diyne-1-ol-1-*O*- β -D-glucopyranoside (**4**) [26], 8*S*-deca-4,6-diyne-1,8-diol-8-*O*- β -D-glucopyranoside (**5**) [22], (2*E*)-tetradecaene-4,6-diyne-1,10,14-triol-1-*O*- β -D-glucopyranoside (**6**) [6], and (2*E*,8*E*)-tetradecadiene-4,6-diyne-1,12,14-triol-1-*O*- β -D-glucopyranoside (**7**) [6] through the comparison of their respective NMR data with previously reported data, in addition to LC-MS analysis.

3.3. Evaluation of Biological Activity of the Isolated Compounds

Prior to the assessment of the anti-adipogenic properties of the isolated compounds, we first evaluated the cytotoxic effects of compounds **1**–**7** in 3T3-L1 preadipocytes. No compounds exhibited cytotoxicity at concentrations of 10 and 20 μM , but compounds **1**,

5, and 6 decreased cell viability at a concentration of 40 μM (Figure 4). Hence, we treated 3T3-L1 cells with compounds 1–7 at a concentration of 20 μM during the entire process of adipogenesis for the evaluation of the anti-adipogenic activities of these compounds. Oil red O staining data showed that compounds 2–4 prevented the de novo generation of adipocytes and lipid accumulation within adipocytes (Figure 5A). The transcription levels of mature adipocyte marker genes (*Adipsin* and *Fabp4*) were significantly reduced by treatment with compounds 2–4 (Figure 5B). These data indicated that the new C₁₀-polyacetylene glycoside (2) and two known analogs (3 and 4) inhibited the adipogenesis of 3T3-L1 preadipocytes.

As the failure of lipid fusion was observed in the groups treated with compounds 2–4 (Figure 5A), we then investigated whether compounds 2–4 affected lipid metabolism. Upon exposure to compounds 2–4 during adipogenesis, the expression of the lipogenic gene *SREBP1* was suppressed (Figure 6A), whereas the mRNA expression of the lipolytic gene *ATGL* was increased (Figure 6B). In the case of compound 4, the expression of another lipolytic gene, *HSL*, was also markedly enhanced (Figure 6C). These results suggested that compounds 2–4 can enhance lipid metabolism through the inhibition of lipogenesis and the facilitation of lipolysis.

AMP-activated protein kinase (AMPK) is known to be a key controller of energy metabolism through the inhibition of adipogenesis and the stimulation of lipid metabolism upon its activation [27]. It has been reported that treatment of brain cells with safflower yellow B derived from *C. tinctorius* induced the phosphorylation of AMPK [28]. Thus, we assessed the effects of compounds 1–7 on AMPK activation by detecting the level of phosphorylated AMPK. Western blotting data showed that compounds 3 and 4 significantly increased the phosphorylation of AMPK compared with the total amounts of AMPK (Figure 6D).

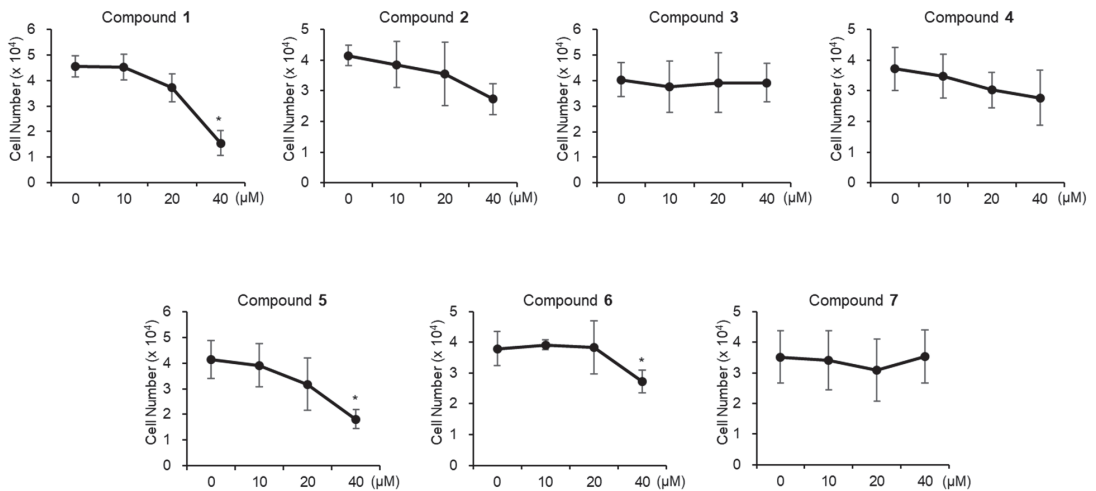


Figure 4. Cytotoxicity of compounds 1–7. Viability of 3T3-L1 cells treated with compounds 1–7 (10, 20, and 40 μM) for 24 h was determined by counting the cell number. The data are presented as the mean \pm SD for $n = 3$ replicates. * $p < 0.05$.

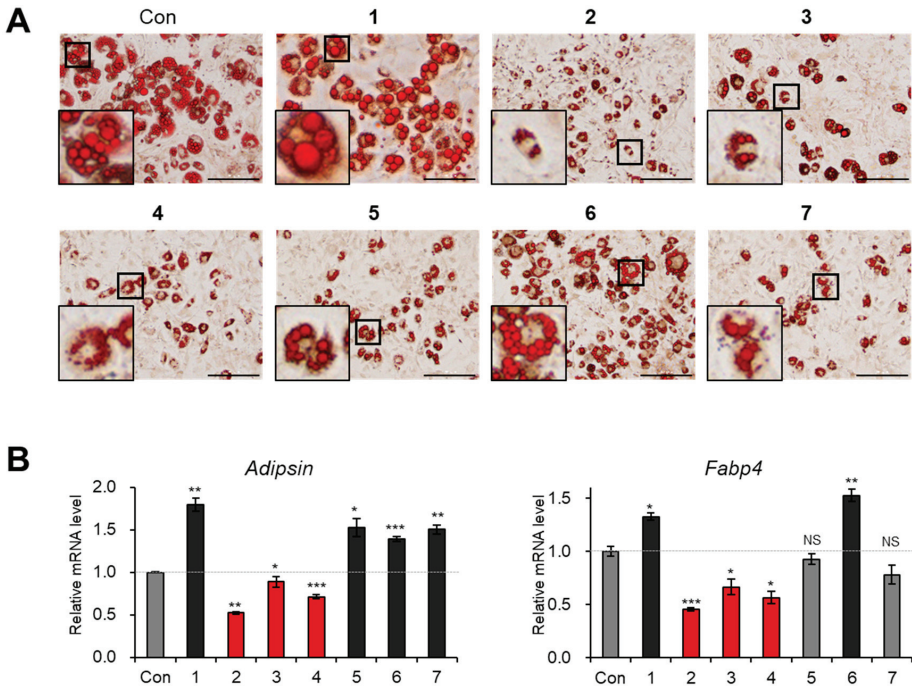


Figure 5. The inhibitory effects of compounds 1–7 on adipogenesis. (A) The Oil Red O staining of 3T3-L1 adipocytes incubated with compounds 1–7 (20 μ M) during adipogenesis. Scale bar: 200 μ m. 3 \times magnified images are indicated as black box. (B) The relative mRNA expression of *Adipsin* and *Fabp4* in 3T3-L1 adipocytes incubated with compounds 1–7 (20 μ M) during adipogenesis. The data are presented as the mean \pm SEM for $n = 3$ replicates. * $p < 0.05$, ** $p < 0.01$, *** $p < 0.001$ and NS: not significant.

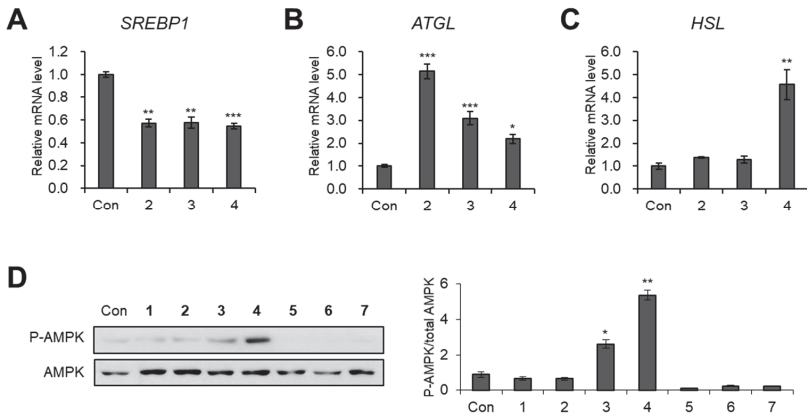


Figure 6. The inhibitory effects of compounds 1–7 on lipid metabolism. (A–C) The relative mRNA expression of *SREBP1* (A), *ATGL* (B), and *HSL* (C) in 3T3-L1 adipocytes incubated with compounds 1–7 (20 μ M) during adipogenesis. (D) Immunoblotting analysis of 3T3-L1 cells incubated with compounds 1–7 (20 μ M) for 24 h. The data are presented as the mean \pm SEM for $n = 3$ replicates. * $p < 0.05$, ** $p < 0.01$, and *** $p < 0.001$.

4. Conclusions

In this study, we identified two novel C₁₀-polyacetylene glycosides (1 and 2) and five known compounds (3–7) from the MeOH extract of the florets of *C. tinctorius*. The effects of the seven identified compounds on adipogenesis were evaluated; compounds 2–4 efficiently inhibited adipocyte differentiation from 3T3-L1 preadipocytes, reducing the mRNA expression levels of *Adipsin* and *Fabp4*. Furthermore, compounds 2–4 promoted the expression of lipolytic genes while downregulating the expression of lipogenic genes. Compounds 3 and 4 induced AMPK phosphorylation, which is known to improve energy metabolism (Figure 7); in contrast, compound 2 appeared to regulate lipid metabolism through other pathways not involved in AMPK signaling. Our findings provide experimental evidence to support the metabolic role of safflower-derived polyacetylene glycosides in the prevention of excessive lipid accumulation in obesity.

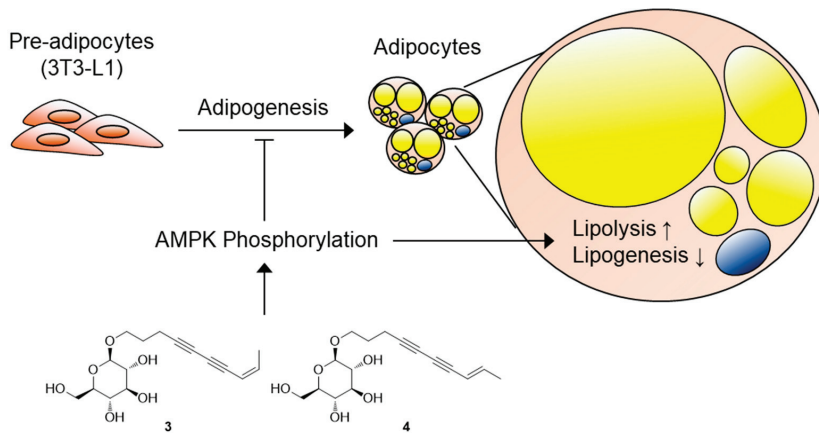


Figure 7. Molecular model explaining the mechanism of action of compounds 3 and 4. Compounds 3 and 4 inhibited the adipogenesis of 3T3-L1 preadipocytes, induced AMP-activated protein kinase (AMPK) phosphorylation, and stimulated lipid metabolism through the enhancement of lipolysis and the suppression of lipogenesis.

Supplementary Materials: The following are available online at <https://www.mdpi.com/2227-9059/9/1/91/s1>.

Author Contributions: Conceptualization, K.H.K. and J.L.; Formal Analysis, S.C.B., S.A.Y., B.S.L., J.S.Y., J.-C.K., C.P., and T.S.J.; Investigation, S.C.B., S.A.Y., B.S.L., and J.S.Y.; Resources, K.H.K.; Writing—Original Draft Preparation, S.A.Y., J.L., and K.H.K.; Writing—Review and Editing, S.A.Y., and K.H.K.; Project Administration, J.L. and K.H.K.; Funding Acquisition, J.L. and K.H.K. All authors have read and agreed to the published version of the manuscript.

Funding: This work was supported by a grant from the National Research Foundation of Korea (NRF), funded by the Korean government (MSIT) (2017R1A6A3A04001986, 2019R1A5A2027340, 2020M3A9E4037847).

Institutional Review Board Statement: Not applicable.

Informed Consent Statement: Not applicable.

Data Availability Statement: Not applicable.

Conflicts of Interest: The authors declare no conflict of interest.

References

1. Spiegelman, B.M.; Flier, J.S. Obesity and the Regulation of Energy Balance. *Cell* **2001**, *104*, 531–543. [CrossRef]
2. Smith, U.; Kahn, B.B. Adipose Tissue Regulates Insulin Sensitivity: Role of Adipogenesis, De Novo Lipogenesis and Novel Lipids. *J. Intern. Med.* **2016**, *280*, 465–475. [CrossRef] [PubMed]
3. Li, C.Y.; Yin, J.G.; Zhang, J.; Wang, X.X.; Wu, M.J.; Liu, F.; Zou, J.D.; Ju, W.Z. Pharmacokinetic Profiles of Hydroxysafflor Yellow a Following Intravenous Administration of Its Pure Preparations in Healthy Chinese Volunteers. *J. Ethnopharmacol.* **2015**, *162*, 225–230. [CrossRef] [PubMed]
4. Russo, E.; Dreher, M.C.; Mathre, M.L. *Women and Cannabis: Medicine, Science, and Sociology*, 1st ed.; Haworth Press: New York, NY, USA, 2003; p. 6.
5. Zhou, X.; Tang, L.; Xu, Y.; Zhou, G.; Wang, Z. Towards a Better Understanding of Medicinal Uses of *Carthamus Tinctorius* L. in Traditional Chinese Medicine: A Phytochemical and Pharmacological Review. *J. Ethnopharmacol.* **2014**, *151*, 27–43. [CrossRef] [PubMed]
6. He, J.; Shen, Y.; Jiang, J.; Yang, Y.; Feng, Z.; Zhang, P.; Yuan, S.; Hou, Q. New Polyacetylene Glucosides from the Florets of *Carthamus Tinctorius* and Their Weak Anti-Inflammatory Activities. *Carbohydr. Res.* **2011**, *346*, 1903–1908. [CrossRef] [PubMed]
7. Yu, S.Y.; Lee, Y.J.; Kim, J.D.; Kang, S.N.; Lee, S.K.; Jang, J.Y.; Lee, H.K.; Lim, J.H.; Lee, O.H. Phenolic Composition, Antioxidant Activity and Anti-Adipogenic Effect of Hot Water Extract from Safflower (*Carthamus Tinctorius* L.) Seed. *Nutrients* **2013**, *5*, 4894–4907. [CrossRef] [PubMed]
8. Zhu, H.J.; Wang, L.J.; Wang, X.Q.; Pan, H.; Li, N.S.; Yang, H.B.; Jin, M.; Zang, B.X.; Gong, F.Y. Hormone-sensitive Lipase is Involved in the Action of Hydroxysafflor Yellow A (HYSYA) Inhibiting Adipogenesis of 3T3-L1 cells. *Fitoterapia* **2014**, *93*, 182–188. [CrossRef]
9. Hwnag, E.Y.; Yu, M.H.; Jung, Y.S.; Lee, S.P.; Shon, J.H.; Lee, S.O. Defatted Safflower Seed Extract Inhibits Adipogenesis in 3T3-L1 Preadipocytes and Improves Lipid Profiles in C57BL/6J ob/ob Mice Fed a High-Fat Diet. *Nutr. Res.* **2016**, *36*, 995–1003. [CrossRef] [PubMed]
10. Yan, K.; Wang, X.; Pan, H.; Wang, L.; Yang, H.; Liu, M.; Zhu, H.; Gong, F. Safflower Yellow and Its Main Component HSYA Alleviate Diet-Induced Obesity in Mice: Possible Involvement of the Increased Antioxidant Enzymes in Liver and Adipose Tissue. *Front. Pharmacol.* **2020**, *11*, 482. [CrossRef]
11. Lee, S.; Ryoo, R.; Choi, J.H.; Kim, J.-H.; Kim, S.-H.; Kim, K.H. Trichothecene and tremulane sesquiterpenes from a hallucinogenic mushroom *Gymnopilus junonius* and their cytotoxicity. *Arch. Pharm. Res.* **2020**, *43*, 214–223. [CrossRef]
12. Trinh, T.A.; Park, E.J.; Lee, D.; Song, J.H.; Lee, H.L.; Kim, K.H.; Kim, Y.; Kung, K.; Kang, K.S.; Yoo, J.E. Estrogenic Activity of Sanguin H-6 through Activation of Estrogen Receptor \pm Coactivator-binding Site. *Nat. Prod. Sci.* **2019**, *25*, 28–33. [CrossRef]
13. Lee, S.; Lee, D.; Ryoo, R.; Kim, J.-C.; Park, H.B.; Kang, K.S.; Kim, K.H. Calvatianone, a sterol possessing a 6/5/6/5-fused ring system with a contracted tetrahydrofuran B-ring, from the fruiting bodies of *Calvatia nipponica*. *J. Nat. Prod.* **2020**, *83*, 2737–2742. [CrossRef] [PubMed]
14. Lee, D.; Choi, S.; Yamabe, N.; Kim, K.H.; Kang, K.S. Recent findings on the mechanism of cisplatin-induced renal cytotoxicity. *Nat. Prod. Sci.* **2020**, *26*, 28–49.
15. Lee, S.R.; Kang, H.; Yoo, M.J.; Yu, J.S.; Lee, S.; Yi, S.A.; Beemelmans, C.; Lee, J.; Kim, K.H. Anti-adipogenic pregnane steroid from a *Hydractinia*-associated fungus, *Cladosporium sphaerospermum* SW67. *Nat. Prod. Sci.* **2020**, *26*, 230–235.
16. Wang, Z.; Wen, Z.; Liu, L.; Zhu, X.; Shen, B.; Yan, X.; Duan, Y.; Huang, Y. Yanggumicins F and G, Eneidyne Congeners from *Micromonospora yangpuensis* DSM 45577. *J. Nat. Prod.* **2019**, *82*, 2483–2488. [CrossRef] [PubMed]
17. Xu, K.; Jiang, J.S.; Feng, Z.M.; Yang, Y.N.; Li, L.; Zang, C.X.; Zhang, P.C. Bioactive Sesquiterpenoid and Polyacetylene Glycosides from *Atractylodes Lancea*. *J. Nat. Prod.* **2016**, *79*, 1567–1575. [CrossRef]
18. Jo, M.S.; Yu, J.S.; Lee, J.C.; Lee, S.; Cho, Y.C.; Park, H.J.; Kim, K.H. Lobatamunsolides A-C, Norlignans From the Roots of *Pueraria lobata* and Their Nitric Oxide Inhibitory Activities in Macrophages. *Biomolecules* **2019**, *9*, 755. [CrossRef]
19. Lee, K.; Seo, Y.-J.; Song, J.-H.; Chei, S.; Lee, B.-Y. Ginsenoside Rg1 promotes browning by inducing UCP1 expression and mitochondrial activity in 3T3-L1 and subcutaneous white adipocytes. *J. Ginseng Res.* **2019**, *43*, 589–599. [CrossRef]
20. Yi, S.A.; Lee, J.; Park, S.K.; Kim, J.Y.; Park, J.W.; Lee, M.G.; Nam, K.H.; Park, J.H.; Oh, H.; Kim, S.; et al. Fermented ginseng extract, BST204, disturbs adipogenesis of mesenchymal stem cells through inhibition of S6 kinase 1 signaling. *J. Ginseng Res.* **2020**, *44*, 58–66. [CrossRef]
21. Li, S.; Kuang, H.X.; Okada, Y.; Okuyama, T. New Acetylenic Glucosides from *Bidens Bipinnata* LINNE. *Chem. Pharm. Bull.* **2004**, *52*, 439–440. [CrossRef]
22. Lie, Y.; Xue, J.; Han, H.; Yuan, T. Polyacetylenes from the florets of *Carthamus tinctorius* and their cytotoxicity. *Phytochem. Lett.* **2018**, *23*, 168–171. [CrossRef]
23. Fang, Z.; Wills, M. Asymmetric Reduction of Dinyones and the Total Synthesis of (S)-panaxjapyne A. *Org. Lett.* **2014**, *16*, 374–377. [CrossRef] [PubMed]
24. Liu, Y.; Du, D.; Liang, Y.; Xin, G.; Huang, B.Z.; Huang, W. Novel Polyacetylenes From *Coreopsis Tinctoria* Nutt. *J. Asian Nat. Prod. Res.* **2015**, *17*, 744–749. [CrossRef] [PubMed]
25. Lee, C.Y.; Yun, J.H.; Kang, K.; Nho, C.W.; Shin, D. Identification of Dialkyl Diacetylene Diols with Potent Cancer Chemopreventive Activity. *Bioorg. Med. Chem. Lett.* **2015**, *25*, 4020–4023. [CrossRef]
26. Wang, C.Z.; Yu, D.Q. Lignan and acetylenic glycosides from *Aster auriculatus*. *Phytochemistry* **1998**, *48*, 711–717. [CrossRef]

27. Daval, M.; Fougelle, F.; Ferré, P.J. Functions of AMP-activated Protein Kinase in Adipose Tissue. *J. Physiol.* **2006**, *574*, 55–62. [CrossRef]
28. Du, S.; Deng, Y.; Yuan, H.; Sun, Y. Safflower Yellow B Protects Brain Against Cerebral Ischemia Reperfusion Injury Through AMPK/NF- κ B Pathway. *Evid. Based Complement. Altern. Med.* **2019**, *2019*, 7219740. [CrossRef]



Article

Rutin Is a Low Micromolar Inhibitor of SARS-CoV-2 Main Protease 3CLpro: Implications for Drug Design of Quercetin Analogs

Bruno Rizzuti ^{1,2,*}, Fedora Grande ³, Filomena Conforti ³, Ana Jimenez-Alesanco ^{2,4}, Laura Ceballos-Laita ^{2,5}, David Ortega-Alarcon ^{2,4}, Sonia Vega ², Hugh T. Reyburn ⁶, Olga Abian ^{2,4,5,7,8,*} and Adrian Velazquez-Campoy ^{2,4,5,8,9,*}

- ¹ CNR-NANOTEC, Licryl-UOS Cosenza and CEMIFCal, Department of Physics, University of Calabria, 87036 Rende, Italy
- ² Institute for Biocomputation and Physics of Complex Systems (BIFI), Joint Units IQFR-CSIC-BIFI, and GBsC-CSIC-BIFI, University of Zaragoza, 50018 Zaragoza, Spain; ajimenez@bifi.es (A.J.-A.); ceballos.laita@gmail.com (L.C.-L.); dortega@bifi.es (D.O.-A.); svega@bifi.es (S.V.)
- ³ Department of Pharmacy, Health and Nutritional Sciences, University of Calabria, 87036 Rende, Italy; fedora.grande@unical.it (F.G.); filomena.conforti@unical.it (F.C.)
- ⁴ Department of Biochemistry and Molecular and Cell Biology, University of Zaragoza, 50009 Zaragoza, Spain
- ⁵ Institute for Health Research Aragón (IIS Aragón), 50009 Zaragoza, Spain
- ⁶ Department of Immunology and Oncology, National Centre for Biotechnology (CNB), CSIC, 28049 Madrid, Spain; htreyburn@cnb.csic.es
- ⁷ Aragón Health Sciences Institute (IACS), 50009 Zaragoza, Spain
- ⁸ Biomedical Research Network Center in Hepatic and Digestive Diseases (CIBERehd), 28029 Madrid, Spain
- ⁹ ARAID Foundation, Government of Aragón, 50018 Zaragoza, Spain
- * Correspondence: bruno.rizzuti@cnr.it (B.R.); oabifra@unizar.es (O.A.); adrianvc@unizar.es (A.V.-C.)

Citation: Rizzuti, B.; Grande, F.; Conforti, F.; Jimenez-Alesanco, A.; Ceballos-Laita, L.; Ortega-Alarcon, D.; Vega, S.; Reyburn, H.T.; Abian, O.; Velazquez-Campoy, A. Rutin Is a Low Micromolar Inhibitor of SARS-CoV-2 Main Protease 3CLpro: Implications for Drug Design of Quercetin Analogs. *Biomedicines* **2021**, *9*, 375. <https://doi.org/10.3390/biomedicines9040375>

Academic Editors: Orazio Nicolotti, Laura Quintieri and Leonardo Caputo

Received: 10 March 2021
Accepted: 30 March 2021
Published: 2 April 2021

Publisher's Note: MDPI stays neutral with regard to jurisdictional claims in published maps and institutional affiliations.



Copyright: © 2021 by the authors. Licensee MDPI, Basel, Switzerland. This article is an open access article distributed under the terms and conditions of the Creative Commons Attribution (CC BY) license (<https://creativecommons.org/licenses/by/4.0/>).

Abstract: The pandemic, due to severe acute respiratory syndrome coronavirus 2 (SARS-CoV-2), has stimulated the search for antivirals to tackle COVID-19 infection. Molecules with known pharmacokinetics and already approved for human use have been demonstrated or predicted to be suitable to be used either directly or as a base for a scaffold-based drug design. Among these substances, quercetin is known to be a potent in vitro inhibitor of 3CLpro, the SARS-CoV-2 main protease. However, its low in vivo bioavailability calls for modifications to its molecular structure. In this work, this issue is addressed by using rutin, a natural flavonoid that is the most common glycosylated conjugate of quercetin, as a model. Combining experimental (spectroscopy and calorimetry) and simulation techniques (docking and molecular dynamics simulations), we demonstrate that the sugar adduct does not hamper rutin binding to 3CLpro, and the conjugated compound preserves a high potency (inhibition constant in the low micromolar range, $K_i = 11 \mu\text{M}$). Although showing a disruption of the pseudo-symmetry in the chemical structure, a larger steric volume and molecular weight, and a higher solubility compared to quercetin, rutin is able to associate in the active site of 3CLpro, interacting with the catalytic dyad (His41/Cys145). The overall results have implications in the drug-design of quercetin analogs, and possibly other antivirals, to target the catalytic site of the SARS-CoV-2 3CLpro.

Keywords: rutin; quercetin; SARS-CoV-2; drug selection; enzyme inhibitors; antivirals; spectroscopy; molecular modeling

1. Introduction

On January 2020, the World Health Organization (WHO) announced COVID-19 as a public health emergency of international concern and, on March 2020, declared severe acute respiratory syndrome coronavirus (SARS-CoV-2) a pandemic [1]. Since then, and to date, the new coronavirus has become a major global threat, with more than 100 million reported cases and over 2 million deaths worldwide. Scientists from all over the world are

working hard in an extraordinary research mission to speed up the investigation for rapid diagnosis methods and for the development of vaccines and therapeutics to contain the spread of the infection. In less than one year, these efforts have led to the development and availability of safe and effective vaccines for COVID-19, which stimulate the immune system to produce specific antibodies able to block the spike viral protein and prevent the virus entry into the cells [2]. However, the need to cure patients already infected (or escaping from vaccination for various reasons) is a stringent necessity.

Although with little specific therapeutic indication for COVID-19, several drugs in clinical use for other disorders have been administered to patients infected with SARS-CoV-2 (for extensive reviews, see [3,4]). Many of these therapeutics belong to the class of antiviral agents, such as Remdesivir (a broad-spectrum pro-drug agent acting as a viral RNA-polymerase inhibitor), the combination Lopinavir/Ritonavir (HIV-1 protease inhibitors, which are together more efficient compared to the monotherapy of each drug), and Sofosbuvir (a nucleotide analogue targeting the hepatitis C virus (HCV) polymerase NS5B) in combination with Daclatasvir or Velpatasvir (both are potent HCV NS5A complex antagonists). However, and despite the huge number of research studies reported so far, the development of safe and effective drugs able to block the viral infection is still lacking and represents a major goal for the scientific world. Among all the possible chemical compounds, particular attention has been dedicated to molecules of natural origin [5–8], including extracts, single bioactive molecules, or entire classes of phytochemicals targeting SARS-CoV-2, and several of them are currently under investigation.

Rutin (quercetin-3-*O*-rutinose), shown in Figure 1, is a natural substance belonging to the flavonol class of flavonoids, widely distributed as secondary metabolites in several plants. Flavonoid compounds are made up by a phenylpropane-derivative and three acetyl-CoA (from malonyl-CoA) via the acetate-malonate biosynthesis pathway and cyclization via chalcones. For this reason, flavonoids possess (with only a few exceptions) an –OH group at positions C-5 and C-7. Relationships between the structure of flavonoids and their pharmacological activities have been proven so far; in particular, C-glycosidation enhances the effectiveness of antiviral and antibacterial activity [9]. Rutin is composed of one molecule of quercetin and the disaccharide rutinose. Quercetin 3-*O*-glycosides has a higher bioavailability (235%) compared to quercetin [10], and rutin is at least two times more soluble (130 mg/L) than its parent compound [11–13]. Quercetin and several of its conjugates have been approved by the U.S. Food and Drug Administration (FDA) for human use. Both quercetin and rutin are used as ingredients in numerous herbal remedies and have been extensively studied for their multiple pharmacological activities, including antiviral, antibacterial, and anti-inflammatory properties [9].

In a previous work [14], by using a combination of biophysical *in vitro* techniques, we had found that quercetin has the ability to inhibit the main protease of SARS-CoV-2, known as Mpro or 3CLpro (3C-like protease). 3CLpro is an excellent pharmacological target because it is highly conserved among the different members of the coronavirus family and no human host-cell proteases have been reported to show similar specificity. This protein is a crucial component of the viral replication machinery of SARS-CoV-2, as it is used to process the large polyproteins obtained by hijacking the host cell, to produce a number of key viral proteins that include 3CLpro itself. Quercetin was identified as the best hit in an experimental pipeline for drug screening that allowed us to identify many lead compounds against different protein targets in the recent years [15–20]. The screening library contains many drugs already approved for human administration, including natural compounds. Natural molecules bear remarkable biological qualities, and they are often found to be active against viruses [21,22].

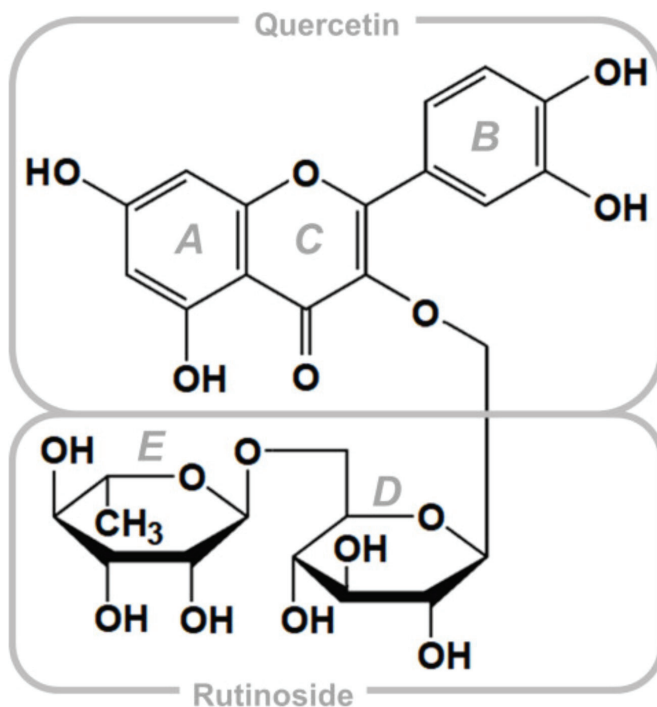


Figure 1. Chemical structure of rutin, with the quercetin scaffold (3,3',4',5,7-pentahydroxyflavone) and the rutinose moiety (α -L-rhamnopyranosyl-(1 \rightarrow 6)- β -D-glucopyranose). Rings (A–E) are labelled according to standard convention.

The molecular scaffold of quercetin has a number of interesting physico-chemical properties that are attractive for a drug design endeavor. These features include low molecular mass, the presence of chemical groups that can be easily functionalized and, in the case of the use to target 3CLpro, considerable inhibitory activity (especially when scaled with respect to its molecular weight as an inhibitory efficiency index). Major shortcomings consist of a poor solubility and a very low bioavailability due to metabolic transformations after oral administration, which convert a high percentage of quercetin to glucuronide, methyl, and sulfate conjugates [23]. In general, these issues may be tackled by resorting to different strategies, such as employing controlled drug delivery system as nanocarriers circumventing solubility/trafficking/metabolic drawbacks or designing chemical modifications such as the introduction of chemical functional groups that can increase the solubility and thus the pharmacokinetic profile of the reference compound [24–26]. Furthermore, several chemical modifications have been proposed to improve the pharmacokinetics of quercetin in other cases [27,28]. Such modifications, however, open a number of key questions in the context of the use quercetin as antiviral against SARS-CoV-2. The two most important ones are perhaps the following: does the presence of a large adduct still guarantee a quercetin analog the ability to bind into the restricted pocket that constitutes the catalytic site of 3CLpro, and will the inhibitory effect of the parent compound still be retained?

To address these questions, we have used rutin as a test case to verify that the presence of the most commonly occurring sugar adduct, naturally attached to quercetin, allows the glycoside form to retain the key bioactive features of the aglycone lead compound. Although not constituting *per se* an optimization of quercetin towards a prescription drug, such validation constitutes an important proof-of-concept that could be considered a preliminary step to embark towards a more rational and challenging campaign of drug design. Our results, obtained by combining simulation and experimental techniques,

show that rutin binds to the catalytic pocket of 3CLpro and, just like its parent compound quercetin, interacts with the dyad of protein residues responsible for the catalytic activity of the protease. More importantly, and although not being designed or optimized to this scope, rutin exerts a clear inhibitory activity with a relatively high potency against 3CLpro. These results are expected to encourage further investigations towards the development of quercetin-like antiviral compounds as a defense against coronavirus infections.

2. Materials and Methods

2.1. Protein Expression and Purification

SARS-CoV-2 3CLpro was expressed using a His-tagged construct in a pET22b plasmid transformed into BL21 (DE3) Gold *E. coli* strain. After initial cultures grown in LB/ampicillin (100 µg/mL) media at 37 °C overnight, 4 L of LB/ampicillin (100 µg/mL) were inoculated and incubated at 37 °C until reaching OD = 0.6 at a wavelength of 600 nm. Then, protein expression was induced with 1 mM isopropyl 1-thio-β-D-galactopyranoside (IPTG) at 18 °C for 5 h. Cells were harvested by centrifugation at 4 °C for 10 min at 10,000 rpm (Beckman Coulter Avanti J-26 XP Centrifuge, Barcelona, Spain) and then resuspended in lysis buffer (sodium phosphate 50 mM, pH 7, sodium chloride 500 mM). Cells were ruptured by sonication (Sonics Vibra-Cell Ultrasonic Liquid Processor, Newtown, CT) in ice, adding benzonase 20 U/mL (Merck-Millipore, Madrid, Spain) and lysozyme 0.5 mg/mL (Carbosynth, Compton, UK). Centrifugation at 4 °C for 30 min at 20,000 rpm, and filtration (0.45 µm-pore membrane) allowed removing cell debris from the extract. The protein was purified using affinity chromatography (ÄKTA FPLC System, GE Healthcare Life Sciences, Barcelona, Spain) using a cobalt HiTrap TALON column (GE-Healthcare Life Sciences), eluting by applying an imidazole 10–250 mM gradient. Purity was checked by SDS-PAGE (Figure S1), and pure protein fractions were dialyzed to remove imidazole and reach the protein storage condition (sodium phosphate 50 mM, pH 7, sodium chloride 150 mM). An extinction coefficient of 32890 M⁻¹ cm⁻¹ at 280 nm was employed for protein concentration quantification. Protein identity was assessed by mass spectrometry (LC-ESI-MS/MS).

2.2. Rutin Preparation

Rutin hydrate (purity ≥ 94%) in powder was purchased from Sigma-Aldrich (Milan, Italy). Solutions were prepared by dissolving the powder in pure DMSO at high rutin concentration (20 mM).

2.3. Circular Dichroism and Fluorescence Spectroscopy

Circular dichroism (CD) spectra were recorded in a Chirascan spectropolarimeter (Applied Photophysics, Leatherhead, UK) at 25 °C. Far-UV and near-UV spectrum were recorded at wavelengths between 190 and 250 nm in a 0.1-cm path-length cuvette, and between 250 and 310 nm in a 1 cm path-length cuvette, respectively, employing a protein concentration of 10 µM and a rutin concentration of 100 µM. Fluorescence measurements were performed in a Cary Eclipse fluorescence spectrophotometer (Agilent Technologies, Madrid, Spain), monitoring the intrinsic tryptophan fluorescence of the protein at 2 µM concentration. An excitation wavelength of 290 nm was used, with excitation and emission bandwidths of 5 nm, and recording fluorescence emission between 300 and 400 nm. All spectroscopic measurements were made in sodium phosphate 50 mM, pH 7, dimethyl sulfoxide (DMSO) 0.5%.

2.4. Proteolytic Activity Assay

In vitro catalytic activity of 3CLpro was monitored using a Förster resonance energy transfer (FRET) continuous assay with the substrate (DabcyI)KTSAVLQSGFRKME(Edans)-NH₂ (Biosyntan GmbH, Berlin, Germany) [29,30]. Briefly, the enzymatic reaction was initiated by adding substrate at 20 µM final concentration to the enzyme at 0.2 µM final concentration in a final volume of 100 µL. The reaction buffer was sodium phosphate

50 mM, pH 7, NaCl 150 mM, DMSO 2.5%. Fluorescence was measured in a FluoDia T70 microplate reader (Photon Technology International, Birmingham, NJ, USA) for 20 min (excitation wavelength, 380 nm; emission wavelength, 500 nm). Enzyme activity was quantified as the initial slope of the time evolution curve of the fluorescence signal. The Michaelis–Menten constant, K_m , and the catalytic rate constant or turnover number, k_{cat} , were estimated previously ($K_m = 11 \mu\text{M}$ and $k_{cat} = 0.040 \text{ s}^{-1}$) [14].

2.5. Inhibition Assay

To assess the *in vitro* inhibition potency of rutin, the inhibition constant was estimated from the experimental inhibition curve. The inhibition curve was obtained by measuring the enzyme activity as a function of compound concentration: enzyme at 0.2 μM final concentration was incubated with rutin concentration from 0 to 120 μM , while maintaining constant the percentage of DMSO (2.5%), and the reaction was initiated by adding substrate at 20 μM final concentration [14]. The enzymatic activity was quantitated as the initial slope of the substrate fluorescence emission time curve and was plotted as a function of compound concentration. The slope ratio between the activity in the presence and absence of rutin provides the percentage of inhibition at a certain rutin concentration. Nonlinear regression analysis employing a simple inhibition model (considering inhibitor depletion due to enzyme binding) allowed us to estimate the apparent inhibition constant for rutin, according to Equation (1), by monitoring the substrate fluorescence emission as a function of time [14]:

$$[EI] = \frac{1}{2} \left([I]_T + [E]_T + K_i^{app} - \sqrt{([I]_T + [E]_T + K_i^{app})^2 - 4[E]_T[I]_T} \right)$$

$$[I] = [I]_T - [EI] = \frac{1}{2} \left([I]_T - [E]_T - K_i^{app} + \sqrt{([I]_T + [E]_T + K_i^{app})^2 - 4[E]_T[I]_T} \right), \quad (1)$$

$$\frac{v([I])}{v([I]=0)} = 1 - \frac{[EI]}{[E]_T} = \frac{1}{1 + \frac{[I]}{K_i^{app}}}$$

where $[EI]$ is the concentration of the enzyme-inhibitor complex, $[E]_T$ and $[I]_T$ are the total concentrations of enzyme and inhibitor, K_i^{app} is the apparent inhibition constant for the inhibitor (rutin), $[I]$ is the concentration of free inhibitor, and v is the initial slope of the enzymatic activity trace at a certain (free) inhibitor concentration $[I]$ (corresponding to a total inhibitor concentration $[I]_T$). No approximation consisting of the free inhibitor concentration assumed equal to the total inhibitor concentration was made, thus having general validity for any total enzyme and inhibitor concentration and any value of the inhibition constant (even for tight binding inhibitors). If the inhibitor acts through a purely competitive mechanism, the previous equation can be substituted by Equation (2) [14]:

$$\frac{v([I])}{v([I]=0)} = \frac{1}{1 + \frac{[I]}{K_i \left(1 + \frac{[S]}{K_m}\right)}}, \quad (2)$$

where K_i is the intrinsic (i.e., substrate concentration-independent) inhibition constant, K_m is the Michaelis–Menten constant for the enzyme–substrate interaction, and $[S]$ is the substrate concentration. Because K_m and $[S]$ are known, the intrinsic inhibition constant can be determined.

2.6. Isothermal Titration Calorimetry

Target engagement for rutin against 3CLpro was further assessed by isothermal titration calorimetry (ITC). Calorimetric titrations were performed using an Auto-iTC200 calorimeter (MicroCal, Malvern-Panalytical, Malvern, UK). Protein at 10 μM , located in the calorimetric cell, was titrated with rutin at 100 μM , performing experiments in two different buffers: Tris 50 mM, pH 7, and phosphate 50 mM, pH 7, with DMSO 1%. The experimental protocol consisted of a series of 19 injections of 2 μL each, using a stirring speed of

750 rpm, maintaining a spacing between injections of 150 s, and applying a reference power of 10 μ cal/s. The association constant, K_a , the binding enthalpy, ΔH , and the binding stoichiometry, n , (or percentage of active protein in the cell) were estimated through nonlinear least-squares regression analysis of the data, by using a model considering a single ligand binding site, implemented in Origin 7.0 (OriginLab, Northampton, MA, USA). The dissociation constant, K_d , the binding Gibbs energy, ΔG , and the binding entropy, $-T\Delta S$, were obtained from basic thermodynamic relationships. By performing titrations in buffers with different ionization enthalpies, the buffer-independent enthalpic, ΔH_0 , and entropic contributions, $-T\Delta S_0$, as well as the number of protons exchanged upon complex formation, n_H , was estimated through linear regression of the observed enthalpy as a function of the ionization enthalpy of the buffer ΔH_{buf} ($\Delta H = \Delta H_0 + n_H \Delta H_{\text{buf}}$).

2.7. Molecular Docking

The simulation engine AutoDock Vina [31] and the modeling package AutoDock Tools [32] were used for docking experiments. The two reference crystallographic structures 6Y2E and 6Y2F [30] retrieved from the Protein Data Bank (PDB) were used, which contain 3CLpro in unliganded form and complexed with an α -ketoamide inhibitor bound in the catalytic protein site, respectively. Three missing residues in the latter were reconstructed in silico, and the ligand and water molecules were not considered in the docking. The structure of rutin was taken from PDB entry 1RY8 [33], and it was improved by performing an energy minimization using UCSF Chimera [34] and with the addition of the hydrogens. A blind docking search with very high exhaustiveness [35] was performed on a volume including the whole protein. The number of poses obtained for the two protein targets were reduced by performing a selection based on the binding energy (affinity within 1.5 kcal/mol from the best docking pose) and structure similarity (atomic root mean square deviations RMSD < 2 Å).

2.8. Molecular Dynamics

The 3CLpro-rutin complexes obtained after molecular docking were refined in molecular dynamics (MD) simulations performed using the GROMACS suite [36]. The complexes were solvated in a rhombic dodecahedral box with a distance of 10 Å from the closest edge, resulting in more than 20,000 water molecules added, and four Na⁺ counterions were included to neutralize the system. The force field Amber ff99SB-ILDN [37] was used for the protein, GAFF [38] for the ligand, and the TIP3P model for water [39]. Production runs were performed for 10 ns in the isobaric-isothermal ensemble, after a standard preparation routine including energy minimization, annealing, and equilibration [40]. Other simulation conditions, which include the parameters for the thermostat/barostat, the modeling of electrostatic and non-electrostatic interactions, and the use of constraints, were as previously described [41,42]. In the subsequent analysis, distances and root mean square fluctuations (RMSFs) were calculated after eliminating the protein rotation by a least-squares fit with respect to the C $^{\alpha}$ atoms. Distances from His41 and Cys145 were calculated by considering the geometric center of, respectively, the five non-hydrogen atoms in the imidazole ring and the three C $^{\alpha}$ -C $^{\beta}$ -S $^{\gamma}$ atoms in the side chain of these two residues.

3. Results

3.1. Rutin Binds and Inhibits the Main Protease 3CLpro

The far-UV CD spectrum is informative about the conformational state of a protein, providing quantitative information on its secondary structural motifs. However, in cases where protein–ligand interaction does not result in sufficiently large conformational changes, the spectrum may not reflect that interaction, as observed in 3CLpro interacting with rutin (Figure S2). On the other hand, near-UV CD is more difficult to interpret on a structural basis, but it is more sensitive to subtle changes in the tertiary structure and the environment of aromatic residues. Therefore, near-UV spectra were determined in order to provide direct evidence of 3CLpro-rutin interaction, as shown in Figure 2A. In addition,

the presence of rutin strongly affected the intrinsic tryptophan fluorescence emission, as shown in Figure 2B. Because the fluorescence of rutin is negligible, the addition of both individual fluorescence spectra was almost identical to that of the free protein. The strong quenching effect of rutin was indicative of the interaction with the protein. Rutin modified the spectroscopic properties of 3CLpro, which in turn demonstrates that the ligand (i) binds to its pharmacological target, and (ii) has the ability to alter the tertiary structure of the protein and/or the environment of aromatic protein side chains to a significant extent. The spectral distortions caused by rutin on 3CLpro are similar to those previously observed for quercetin [14], and may be ascribed in both cases to a destabilization effect of the ligand on 3CLpro.

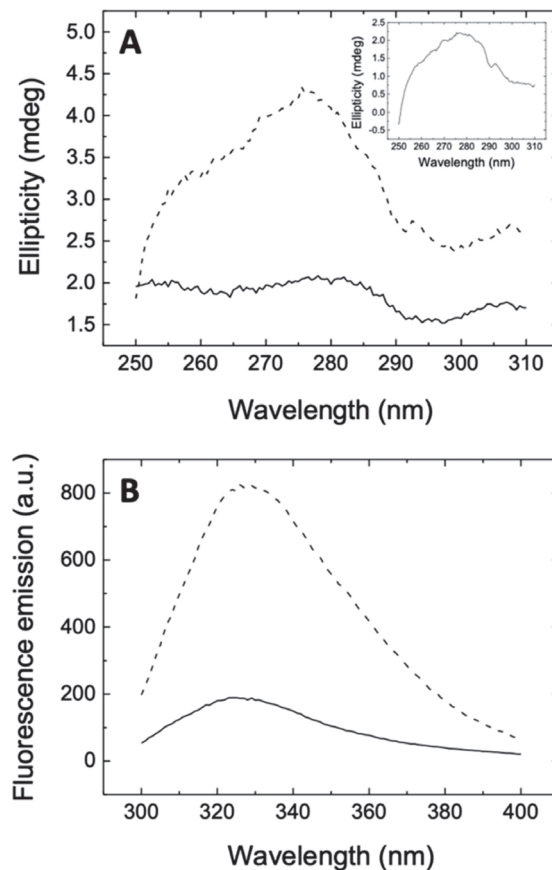


Figure 2. (A) Near-UV CD spectrum of the 3CLpro-rutin complex (continuous line) and addition of individual spectra of 3CLpro and rutin (dashed line), recorded at 10 μ M protein concentration and 100 μ M rutin concentration. Inset: Near-UV spectrum of 3CLpro. The non-equivalence of the spectrum of the complex and the addition of the spectra of free species is the result of the interaction. (B) Fluorescence emission spectrum (in arbitrary units, a.u.) of 3CLpro-rutin complex (continuous line) and addition of individual spectra of 3CLpro and rutin (dashed line), recorded at 2 μ M protein concentration and 100 μ M rutin concentration. Rutin showed negligible fluorescence emission; therefore, the dashed line also corresponds to the emission spectrum of 3CLpro.

The ability of rutin to hamper the enzymatic activity of 3CLpro was assessed by observing the inhibitory action as a function of the ligand concentration, as shown in

Figure 3. The intensity of the fluorescence signal could be monitored as a function of time (Figure 3A), by fixing the concentration of both the substrate and the protein. The curves show a more rapid and almost linear increase in the first few minutes, and afterwards the emission continues to grow more gradually up to about 1.5 h. The increase in fluorescence emission reflects the proteolytic activity of 3CLpro as a reduction in the FRET effect due to the cleavage of the substrate and the concomitant spatial separation of FRET donor and acceptor. The initial slope provides a direct quantification of the proteolytic activity of 3CLpro. Increasing the concentration of rutin (tested up to 120 μM) resulted in a reduction of the enzymatic activity of the main protease 3CLpro as a consequence of the presence of rutin, showing a concentration-dependent action. The effect is qualitatively very similar to the one previously observed for quercetin [14], indicating that conjugation with the glycoside moiety does not substantially hamper the inhibitory effect of the flavonoid molecular scaffold. This experimental finding is a first but already strong indication that the sugar region of rutin has only an auxiliary role in the binding to 3CLpro, encouraging further exploration of the potential of quercetin analogs to target this protein.

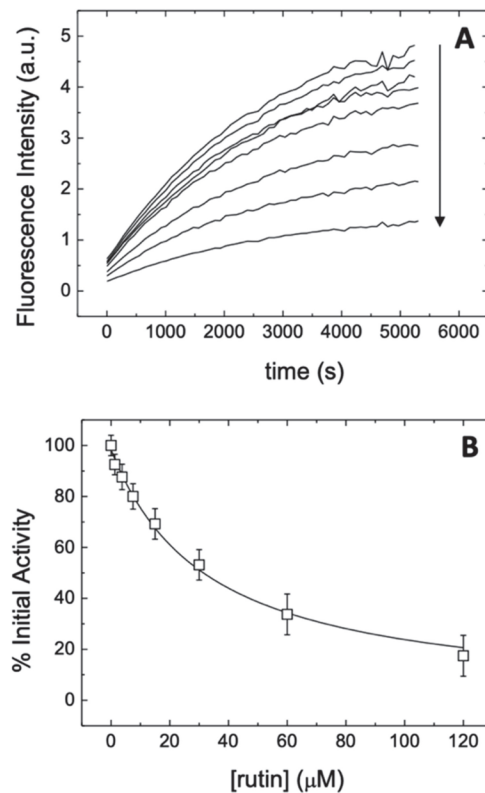


Figure 3. (A) Fluorescence emission (in arbitrary units, a.u.) of the substrate as a function of time at varying concentration of rutin. The concentration of the substrate and 3CLpro were fixed at 20 and 2 μM , respectively, while the concentration of rutin was varied from 0 to 120 μM following a two-fold serial dilution. The arrow indicates the increase in rutin concentration; (B) Experimental inhibition curve for rutin (initial slope as a function of total rutin concentration). Nonlinear least-squares regression data analysis (continuous line) according to Equations (1) and (2) provided an apparent inhibition constant K_i^{app} of 31 μM , and an intrinsic inhibition constant K_i of 11 μM .

A more direct indication of the actual potency of rutin for inhibiting the enzymatic activity of 3CLpro could be obtained by determining the initial slope of each of the fluorescence curves, to evaluate the activity as a function of the ligand concentration (Figure 3B). The inhibition curve obtained showed in a straightforward way the dose-dependent effect of the presence of this compound on the functionality of 3CLpro. More importantly, the data could be fit by using a nonlinear regression model based on a simple inhibition process (see the section Materials and Methods). The analysis yielded an apparent inhibition constant $K_i^{app} = 31 \mu\text{M}$, which can be compared with the value of $21 \mu\text{M}$ previously obtained for the parent compound quercetin [14]. Under the hypothesis that the binding of rutin takes place into a single protein site (which is later validated in the following sections), the apparent inhibition constant can be used to evaluate the so-called intrinsic inhibition constant (see again the section Materials and Methods). By using this model, which also accounts explicitly for the substrate concentration and the occurrence of a competitive inhibition, we obtained for rutin an intrinsic inhibition constant $K_i = 11 \mu\text{M}$. This value can be again directly compared with the one obtained for quercetin, $K_i = 7.4 \mu\text{M}$ [14], and is comparable with those reported for known inhibitors described in the literature for the previous coronavirus species SARS-CoV [43].

Another direct piece of evidence for the interaction of rutin with 3CLpro, as well as a quantitative determination of the dissociation constant (equivalent to the intrinsic inhibition constant), was obtained by ITC, as shown in Figure 4. ITC is the gold standard for binding affinity determination, and it also allows the determination of the binding enthalpy and stoichiometry. According to the results, the interaction of rutin with 3CLpro in Tr. is buffer is characterized by a dissociation constant $K_d = 6.9 \mu\text{M}$ and an interaction enthalpy $\Delta H = 3.4 \text{ kcal/mol}$, whereas the interaction in phosphate is characterized by a dissociation constant $K_d = 6.7 \mu\text{M}$ and an interaction enthalpy $\Delta H = -5.1 \text{ kcal/mol}$. From these data, an average dissociation constant $K_d = 6.8 \mu\text{M}$, a buffer-independent interaction enthalpy $\Delta H_0 = -5.8 \text{ kcal/mol}$, and a net number of exchanged protons $n_H = 0.8$ (protonation of complex upon binding) could be estimated. From that, a favorable albeit small buffer-independent entropic contribution ($-T\Delta S_0 = -1.3 \text{ kcal/mol}$), could be calculated. Therefore, the interaction is entropically and enthalpically favorable, but dominated by enthalpic interactions, with a Gibbs energy of binding $\Delta G = -7.0 \text{ kcal/mol}$. The dissociation constant compares fairly well with the intrinsic inhibition constant, K_i , previously measured. Compared to quercetin, there is a similar character for the binding of rutin, but the binding is driven by enthalpic effects, which may reflect a stabilization of the quercetin scaffold in the binding site due to (or in combination with) additional interactions of the glycoside moiety.

To summarize our findings on the effect of rutin towards the main protease 3CLpro from SARS-CoV2, the experimental evidence demonstrates rutin target engagement and point out a clear inhibitory action on the protein catalytic activity. The inhibition constant of rutin, although lower than that observed for its sugar-depleted parent compound, is still in the low micromolar range, indicating a sufficiently strong inhibition potency also for this ligand.

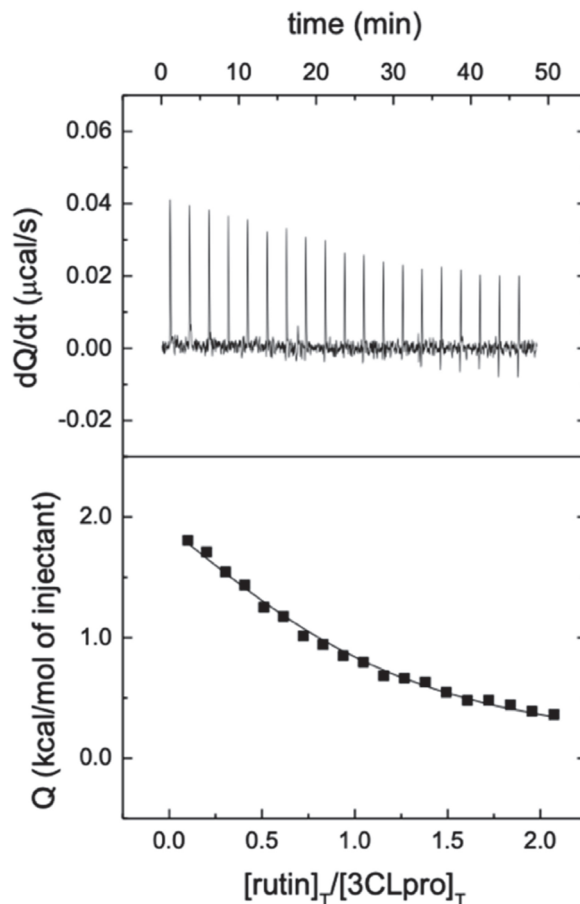


Figure 4. Interaction of rutin with 3CLpro assessed by isothermal titration calorimetry at 25 °C in Tris buffer, pH 7. The upper plot shows the thermogram (thermal power required to maintain a null temperature difference between sample and reference cells as a function of time) and the lower plot shows the binding isotherm (ligand-normalized heat effect per injection as a function of the molar ratio, the quotient between the ligand and protein concentrations in the cell). The fitting curve corresponds to the single ligand binding site model (continuous line). According to the data analysis, rutin interacts with 3CLpro with unfavorable enthalpic contribution ($\Delta H = 3.4$ kcal/mol) and favorable entropic contribution ($-T\Delta S = -10.4$ kcal/mol) to the Gibbs energy of binding ($\Delta G = -7.0$ kcal/mol), corresponding to a dissociation constant K_d of 6.9 μM . The fraction of active (or binding-competent) protein is 85% ($n = 0.85$).

3.2. 3CLpro-Rsutin Interaction Takes Place in the Catalytic Site

To investigate the binding of rutin at the catalytic site of 3CLpro, molecular docking was initially employed. Two reference crystallographic structures [30] were used, which contain 3CLpro either in unliganded form or complexed with an inhibitor in the catalytic protein site. After a blind search performed with a very high exhaustiveness on the whole surface of both (ligand-free) protein structures, the most favorable binding modes obtained with these two docking hosts were analyzed and compared. The simulation results are shown in Figure 5. The docking poses accumulated in the 3CLpro catalytic site (Figure 5A) in terms of both the number of different binding modes and the most favorable affinity scores. After clustering the poses to account for similarity in their structures, the most

favorable ones were found to belong to two sole groups (see Figure 5B,C). These two groups had in common the fact that the quercetin moiety was clearly anchored to the 3CLpro binding site, whereas rutinose interacted only through a fraction of its chemical groups with the protein pocket. Furthermore, in each group, the different binding modes had their quercetin scaffold virtually superimposed, whereas the glycoside regions were more disordered. These results suggest that the flavonoid moiety of rutin is fundamental to bind 3CLpro, whereas the rest of the molecule forms less specific interactions with the protein.

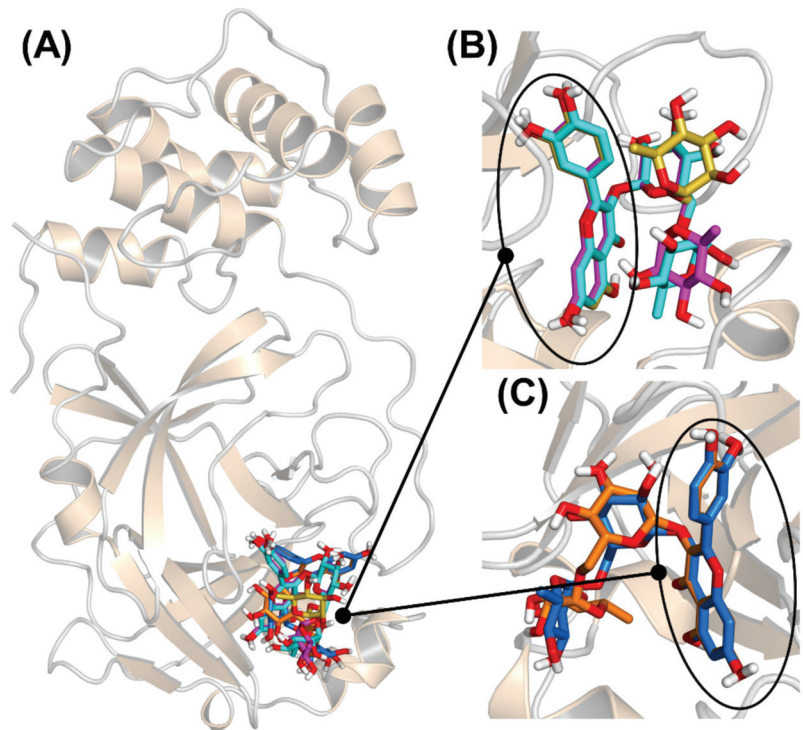


Figure 5. Docking poses of rutin in the active site of the main protease 3CLpro, shown at different rotation angles in the three panels. (A) Ribbon representation of the protein, with the most favorable docking poses superimposed; (B) Cluster of three docking poses (cyan, magenta, and yellow), with the quercetin moieties (circled) almost coincident, and the rutinose regions pointing outwards; (C) Cluster of two docking poses (blue and orange); the quercetin moieties are still almost coincident, and the rutinose regions extend on the other side with respect to the other cluster (panel B).

The binding energies calculated in our docking experiments ranged from -7.5 to -9.0 kcal/mol. These values could be considered upper bounds or even overestimations of the actual affinity, which, according to the intrinsic inhibition constant would be -6.8 kcal/mol (and could be compared to -7.0 kcal/mol for quercetin, as calculated according to its intrinsic inhibition constant). In fact, docking simulations account only implicitly for the presence of solvent, whereas, in reality, rutinose (and especially its hydroxyl groups) could be expected to interact preferentially with water molecules at the protein surface. We verified that redocking of the sole quercetin moiety of rutin (with the whole disaccharide moiety substituted in position C-3 with a single methyl group), in the same location previously found in the docking experiments and without performing any search, yielded a binding score of -6.8 kcal/mol. This result confirms that the quercetin region of rutin is essentially responsible for the binding of the whole molecule, whereas the glycoside region plays only a margin role. All these findings agree with the observation

that the parent compound quercetin has a binding free energy of about -7 kcal/mol, as we had previously measured by both isothermal titration calorimetry (ITC) experiments and docking simulations performed with the same protocol here used for rutin [14]. It is unlikely that the affinity of quercetin could be drastically improved through the addition of a bulky and largely polar chemical adduct with little specificity towards the protein surface.

An important point is the description of the molecular interactions that guarantee the binding of rutin to 3CLpro, and especially of its quercetin scaffold. In particular, it is worth clarifying whether the interaction is mediated by the two protein residues forming the catalytic dyad, His41, and Cys145. In principle, a direct involvement of these two residues in the binding is not entirely obvious because the overall active site of 3CLpro has a relatively extended shape that includes 24 amino acids and a surface area of 235 \AA^2 (as calculated by using a solvent probe with radius 1.4 \AA through the CASTp algorithm [44]). Nevertheless, as illustrated in Figure 6, the double ring A/C of the quercetin moiety forms direct interactions with the two residues His41/Cys145. The rest of the scaffold (i.e., quercetin ring B) has a higher conformational freedom, and can form hydrogen bonds as a donor with either the backbone oxygen of Leu141 or the carboxylate group in the side chain of Glu166. The disaccharide region of rutin, in sharp contrast with the flavonoid scaffold, appears to be much more exposed to the solvent.

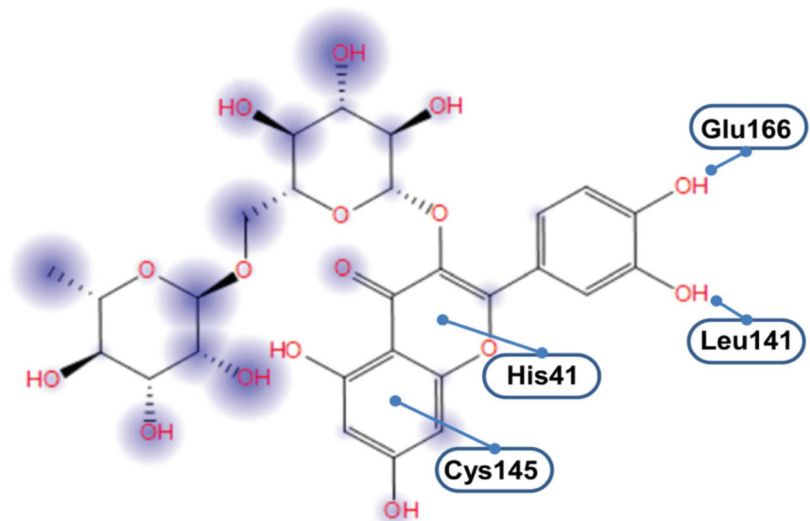


Figure 6. Schematic representation of the interactions of rutin within the active site of 3CLpro. Circular halos around rutin atoms are proportional to solvent exposure.

3.3. Binding of Quercetin Scaffold Is Not Hampered by a Bulky Adduct

Molecular docking simulations are useful to perform a blind exploration of a protein, for predicting the binding of a ligand to its host in a reasonable amount of elapsed real time. However, the docking technique has several limitations [45], which notably include the following ones: (i) the protein receptor is considered rigid to simplify the search; (ii) the solvent is accounted for in an implicit way only; and, more generally, (iii) no information can be determined on the behavior of the solvated complex as a function of time. The first point is important because it may preclude a fine accommodation of the ligand in the binding site. The second point is also particularly relevant in our specific case because of the more hydrophilic nature of the sugar region of rutin compared to the quercetin scaffold. To overcome these issues, all-atoms MD simulations in explicit solvent were performed starting from the complex structures predicted by the docking technique. The simulations were carried out for 10 ns, which is a time scale sufficient to explore the local dynamics of

the ligand in the binding pocket. Large scale modifications of 3CLpro as a consequence of the binding of rutin would require a much longer time scale and lie in the realm of state-of-the-art computations [46,47].

A direct way to confirm the interaction of rutin with the 3CLpro catalytic dyad His41/Cys145 is to estimate the distance between these two protein residues and the non-glycoside moiety of the ligand, as reported in Figure 7. In the case of the most favorable docking poses (Figure 7A), interaction with the side chain of His41 was already stable at the start of the simulation and remained so during the whole MD run, with an equilibrium distance of 4.5 ± 0.3 Å. This value can be compared with the typical ring-ring distance for π - π interactions, which is <4 Å in the most favorable cases but may increase up to 4.5 Å in many practical situations [48,49]. In our case, deviations from the ideal case could be easily ascribed to the dynamics of the protein–ligand complex. We also verified that, in a simulation run starting from a less favorable docking pose (affinity score -7.5 kcal/mol) within the catalytic pocket, the ligand took about 3.5 ns for the heterocyclic ring C to reach the equilibrium distance (again at 4.5 ± 0.3 Å, see Figure 7B) with respect to the ring of His41. In the same simulation, 2 ns were necessary for rutin to accommodate its aromatic ring A with respect to the side chain of Cys145 (equilibrium distance thereafter was 4.7 ± 0.3 Å, as visible in Figure 7C).

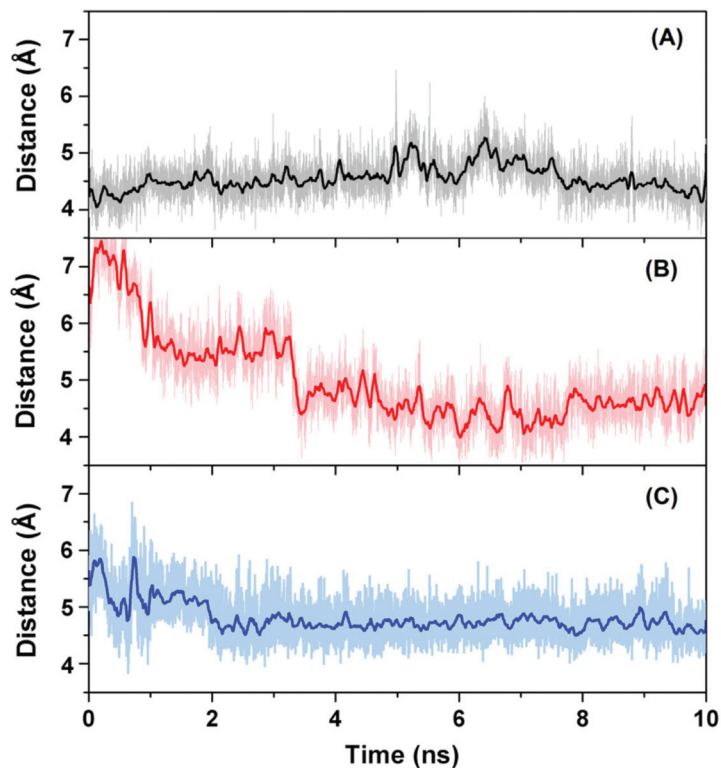


Figure 7. Distance between the double ring in the quercetin moiety of rutin and the catalytic residues His41/Cys145 of 3CLpro in MD simulation. (A) Distance with respect to the imidazole ring of His41, for the most favorable docking pose; (B) Separation from the side chain ring of His41, starting from a docking pose sub-optimally accommodated in the binding pocket; (C) Separation from the side chain of Cys145 (same simulation run as in B).

The inner dynamics of rutin were also assessed by calculating the atomic fluctuations for each of the rings in its molecular structure, after removing non-internal motions of the ligand anchored to 3CLpro due to the diffusive motion of the protein in the solvent. The results reported in Figure 8 show that fluctuations were smaller (RMSF < 1 Å) for the quercetin region of rutin, and relatively larger (RMSF > 1.5 Å) for the outmost ring in the sugar region (i.e., ring E). Movements in the latter regions led to fluctuations >2 Å for the hydroxyl O atoms, preventing the formation of stable hydrogen bonds with the protein. These findings further support the notion that the quercetin scaffold plays a prevalent role in anchoring the whole ligand to the protein, whereas the sugar region is mostly disordered. It is also interesting to note that, although the dynamics of the ligand tends to improve its accommodation within the protein site compared to the starting position, the binding affinity of rutin at the end of the MD simulations did not increase compared to the value originally estimated by applying the sole molecular docking techniques. In fact, re-docking experiments on the rutin-3CLpro complexes obtained at the end of the MD runs, performed by using the same scoring function without any search for the ligand position, showed a binding energy of -7.5 kcal/mol. As already verified in the case of molecular docking, the quercetin moiety of rutin gave the major contribution to this value, whereas the contribution of the sugar region was marginal.

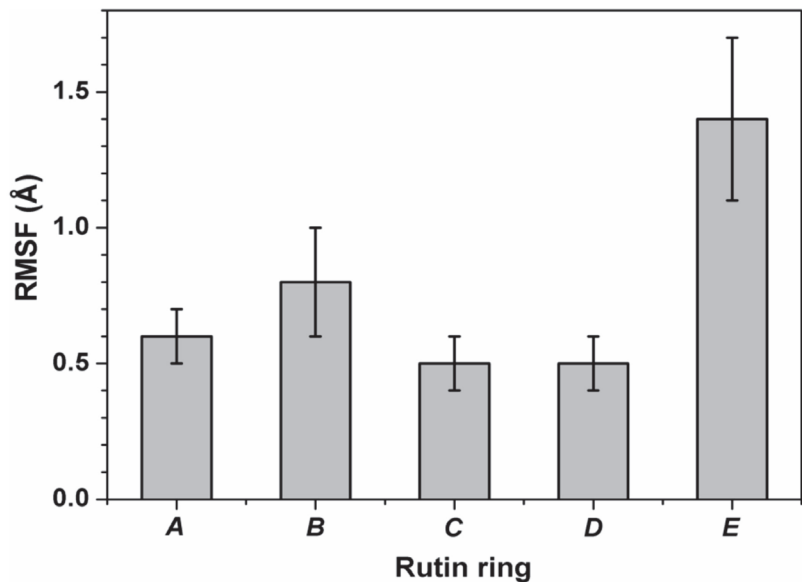


Figure 8. Root mean square fluctuations (RMSF) of the inner motion for the five rings of rutin. Rings A and C together form the connected double ring of the quercetin moiety, and rings D and E belong to the disaccharide rutinose (see also Figure 1). Values are calculated for the six non-hydrogen atoms forming each ring. Error bars indicate the uncertainties in terms of standard deviations.

4. Discussion

Pharmacological research to fight against SARS-CoV-2 is hectic at present, and large efforts are devoted to the search for antiviral agents [7]. A number of potential candidates have already been proposed [50], based on experiments and computational predictions, and many collaborations are active to find new ones [51]. However, emergence of an increasing number of mutations in SARS-CoV-2 and the necessity to prevent drug resistance calls for further attempts along this direction. Among the strategies to block SARS-CoV-2 infection, inhibiting the main protease 3CLpro is perhaps the most appealing. In fact, this protein is vital in the replication process of all coronaviruses. 3CLpro shows a high degree of

homology among different members of this family, as well as among different strains of SARS-CoV-2. Furthermore, amino acid residues in the active site are highly conserved. In addition, 3CLpro shows little homology with host–cell proteases, thus minimizing potential side-effects. Although indirect ways of inhibiting this protein could be envisioned (e.g., shifting the monomer–homodimer equilibrium toward the inactive monomeric state, or exploiting the existence of binding sites with allosteric effects), the most direct way is to tackle the catalytic binding site, and in particular the dyad of residues His41/Cys145. A number of inhibitors were found to have the ability to inhibit 3CLpro, including covalent ones. However, most of these molecules are expected to have severe side effects or other limitations that will preclude their direct use as an antiviral drug.

Among the compounds showing antiviral effects against 3CLpro, we previously demonstrated that a very active one is quercetin [14], which appears to be very interesting also because of its known pharmacokinetic properties and high tolerability. Large availability, low cost, and the absence of encumbering patents are also quite attractive features to use quercetin as a scaffold for drug design [27]. In order to prove the potential benefit in using quercetin as a starting point for such an endeavor, and before moving to more complex attempts (e.g., a modification of the central core of the structure to obtain active analogs through a scaffold hopping process), some modifications should be tested. First, quercetin has a low solubility [13]; therefore, it should be assessed whether the presence of a more hydrophilic chemical adduct still allows this compound to bind and inhibit 3CLpro. Second, quercetin has a low molecular mass (302 Da), which is very close to the threshold conventionally used to classify a compound as a chemical fragment (<300 Da), thus modifications that increase its mass and steric hindrance need to be considered. Finally, we previously noted that the pseudo-symmetry in the structure of quercetin could play a role in binding to 3CLpro [14]; therefore, the effects of the presence of a large symmetry-breaking adduct that may modify this feature should be probed.

To address all these points, we have investigated both *in vitro* and *in silico* rutin, a quercetin analog that includes a two-ring sugar moiety conjugated with the core scaffold, and with a larger solubility. Rutin is also a well-known natural product, extensively used for various pharmaceutical properties in hundreds of registered preparations [52]. It has also been proved to have no cytotoxic effects towards different healthy human cell lines, including cultured normal cells (at concentrations up to 300 μ M for 24 h), and in a variety of other cases such as for human umbilical vein endothelial (HUVE) cells, lung embryonic fibroblasts (TIG-1), and mammary fibroblasts [53,54].

The combination of our experimental and computational results points out that rutin binds to 3CLpro. This finding is demonstrated by alterations in the near-UV CD and fluorescence emission spectra, which demonstrate an engagement of the pharmacological target that produces modification in the structure of the protein. The simulation has difficulties to model these modifications due to the size of the (solvated) protein and, more importantly, due to the large timescale that needs to be probed to observe them. Therefore, a twofold computational approach was pursued. In a first step, molecular docking was employed to prove the binding of rutin in the catalytic site of 3CLpro, in blind experiments carried out considering the whole protein structure. The results showed that the protein active site, and more specifically the catalytic dyad His41/Cys145, provides an anchoring for the binding of rutin. Subsequently, MD simulation was used to refine the accommodation of the rutin, and to investigate the dynamics of the ligand. Our findings confirmed that the quercetin scaffold gives the main contribution, both from a structural and energetic point of view, whereas the rutinose moiety remains in contact with the solvent and plays a secondary role in the association. In particular, our simulation techniques provided details on how the double-ring structure of quercetin is the key binding interface with the His41/Cys145 dyad.

The resulting effect of the association of rutin on the active site of 3CLpro is an inhibitory action on 3CLpro catalytic activity that was clearly visible in our fluorescence results based on the Förster resonance energy transfer (FRET). This technique provides a

measure of the hydrolytic activity of 3CLpro on a substrate, and it is therefore useful to estimate the degree of activity for small molecules capable to block the enzymatic activity of the protein. The inhibition constants obtained for rutin were, respectively, $K_i^{app} = 31 \mu\text{M}$ (apparent) and $K_i = 11 \mu\text{M}$ (intrinsic). These values are slightly less favorable compared to those previously obtained for quercetin [14], 21 and $7.4 \mu\text{M}$, respectively, a result that is particularly encouraging for the fact that rutin was not selected with the aim to improve the molecular properties of quercetin. The corresponding concentration of rutin necessary for a 50% inhibitory effect (IC_{50}) can be readily estimated, and it has a value of $IC_{50} = 32 \mu\text{M}$, although it is important to note that this parameter may not be an appropriate inhibition potency index to measure in vitro inhibition because it is an assay-dependent value that would be different if another substrate or enzyme concentration were employed.

The inhibition constant found for rutin still compares well with the values obtained for other inhibitors specifically designed to bind 3CLpro. This constitutes an encouraging step to further explore the possibility of using other quercetin analogs to block the enzymatic activity of 3CLpro, including perhaps more radical alterations of the starting molecular scaffold. According to the inhibition constant and its molecular mass (610 Da), rutin shows a binding efficiency index ($BEI = pK_i/MW$) of 8.1, compared to 16.9 for quercetin. This reduction in binding efficiency reflects the fact that the larger molecular mass does not result in more or significantly stronger interactions, since the glycoside moiety of rutin hardly interacts with 3CLpro. However, we must consider that the overall effect of a given inhibitor will be a combination of pharmacodynamic and pharmacokinetic properties; thus, a slightly lower inhibition potency for rutin might be favorably counterbalanced by its much better solubility and bioavailability.

The use rutin and other quercetin analogs to inhibit 3CLpro had already been proposed by several studies in the vast literature on SARS-CoV-2, together with a large number of other natural compounds. To the best of our knowledge, and with the notable exception of our previous work on quercetin [14], former predictions were based solely on computational analyses. They included molecular docking [55–57], with additional insights from both classical [58,59] and more advanced MD methods [60], or machine learning approaches [57]. In some cases, the compounds identified were further examined [56,61] in terms of their quantitative structure-activity relationship (QSAR) and expected pharmacokinetics properties including absorption, distribution, metabolism, excretion, and toxicity (ADMET). Our study differs from the others in a number of key aspects. Most significantly, we obtained the first experimental evidence of the inhibitory action of rutin towards 3CLpro. We also provided an estimation of the intrinsic inhibition constant, K_i , suggesting that previous predictions were often quite inaccurate (in some cases by several order of magnitude [61]). We further demonstrated that rutin acts directly on the dyad of protein residues exerting the catalytic activity of 3CLpro, in agreement with most predictions and at variance with the hypothesis of an indirect, allosteric action [62]. More generally, we proved the importance to couple MD simulations to overcome limitations of the docking technique.

Comparison with some of the previous computational works, on the other hand, provides a number of interesting suggestions on how to further explore the potential of the quercetin scaffold to develop antiviral compounds against SARS-CoV2 main protease. Of special interest is the agreement on the potential use of glycosylated flavonoids, such as quercetin-3-*O*-rhamnoside [58], quercetin-3,5-digalactoside and quercetin-3,5-diglucoside [56]. In a more general context, this suggests that the use of quercetin and its analogs to target SARS-CoV-2 can benefit of the results already obtained for SARS-CoV and MERS-CoV, the viruses responsible for the previous coronavirus outbreak in 2002 and 2012, respectively, and which share a high sequence identity (>95%) for the main protease 3CLpro. Experiments had shown that quercetin had the ability to inhibit 3CLpro of both SARS-CoV [63] and MERS-CoV [22], and quercetin-3- β -galactoside and other synthetic derivatives were also active [64]. Thus, our findings add rutin to the list of

quercetin-derived compounds whose antiviral properties are demonstrated in vitro against the coronavirus family.

5. Conclusions

The identification and design of antiviral compounds against SARS-CoV-2 is of utmost importance as one of the main ways to reduce the impact of COVID-19 infection on public health. In particular, inhibition of the catalytic activity of the main protease 3CLpro (or Mpro) is one of the best pharmacological strategies to block the viral replication in affected patients. High similarity of the active site among different variants of SARS-CoV-2, as well as other coronaviruses, makes this approach particularly intriguing also to reduce the incidence of present and possibly future infections due to other related viral strains. After the previously reported identification of quercetin as an excellent in vitro inhibitor of 3CLpro, herein we have shown that its glycosylated conjugate rutin is also effective to this scope, and with a comparable potency. Determining the antiviral effect in vivo on human cells of this compound, and possibly of its derivatives, will give a concrete answer to the possibility of the direct use as a pharmaceutical. In the meanwhile, this adds one more natural product to the list of molecules that are potentially active against SARS-CoV-2, which is of further interest due to the high tolerability of many of these compounds for human use. More importantly, our findings suggest that there is a large amount of room for the possibility of improving the flavonoid scaffold of quercetin to design more effective analogues. The molecular features of rutin/quercetin, including the presence of many hydroxyl groups that can be readily functionalized, offer a variety of possibility for future improvements.

Supplementary Materials: The following are available online at <https://www.mdpi.com/article/10.3390/biomedicines9040375/s1>, Figure S1. SDS-PAGE showing the result of the final purification step for SARS-CoV-2 3CLpro; Figure S2. Far-UV circular dichroism spectrum of the 3CLpro-rutin complex.

Author Contributions: Conceptualization, B.R., O.A. and A.V.-C.; Methodology, B.R., O.A. and A.V.-C.; Software, B.R., O.A., and A.V.-C.; Validation, B.R., A.J.-A., L.C.-L., D.O.-A., S.V., H.T.R., O.A. and A.V.-C.; Formal Analysis, B.R., F.G., F.C., A.J.-A., L.C.-L., D.O.-A., S.V., H.T.R., O.A. and A.V.-C.; Investigation, B.R., A.J.-A., L.C.-L., D.O.-A., S.V. and H.T.R.; Resources, B.R., H.T.R., O.A. and A.V.-C.; Data Curation, B.R., F.G., F.C., H.T.R., O.A. and A.V.-C.; Writing—Original Draft Preparation, B.R., F.G., F.C., O.A. and A.V.-C.; Writing—Review and Editing, B.R., F.G., F.C., A.J.-A., L.C.-L., D.O.-A., S.V., H.T.R., O.A. and A.V.-C.; Visualization, B.R., A.J.-A., L.C.-L., D.O.-A., S.V., O.A. and A.V.-C.; Supervision, B.R., O.A. and A.V.-C.; Project Administration, B.R., O.A. and A.V.-C.; Funding Acquisition, O.A. and A.V.-C. All authors have read and agreed to the published version of the manuscript.

Funding: This work was supported by Fundación hna (to A.V.C. and O.A.); Miguel Servet Program from Instituto de Salud Carlos III (CPII13/00017 to O.A.); Fondo de Investigaciones Sanitarias from Instituto de Salud Carlos III, and European Union (ERDF/ESF, ‘Investing in your future’) (PI18/00349 to O.A. and a FIS Research Contract to L.C.-L.); Spanish Ministry of Economy and Competitiveness (BFU2016-78232-P to A.V.-C. and SAF2017-83265-R to H.T.R.); Spanish Ministry of Science, Innovation and Universities (FPI Predoctoral Research Contract BES-2017-080739 to D.O.-A.); the Spanish National Research Council (CSIC, project 202020E079); Diputación General de Aragón (Predoctoral Research Contract 2019 to A.J.-A., ‘Protein Targets and Bioactive Compounds Group’ E45_20R to A.V.-C., ‘Digestive Pathology Group’ B25_20R to O.A.); and Centro de Investigación Biomédica en Red en Enfermedades Hepáticas y Digestivas (CIBERehd).

Institutional Review Board Statement: Not applicable.

Informed Consent Statement: Not applicable.

Data Availability Statement: The data presented in this study are available from the corresponding authors upon reasonable request.

Acknowledgments: The proteomic analysis was performed in the Proteomics Facility of The Spanish National Center for Biotechnology (CNB-CSIC) that belongs to ProteoRed, PRB3-ISCIII, supported

by grant PT17/0019, and also in the Proteomics Platform from Servicios Científico Técnicos (IACS-Universidad de Zaragoza) that also belongs to ProteoRed, PRB3-ISCIII. B.R. acknowledges the use of computational resources by kind permission of the European Magnetic Resonance Center (CERM), Sesto Fiorentino (Florence), Italy.

Conflicts of Interest: The authors declare no conflict of interest. The funders had no role in the design of the study; in the collection, analyses, or interpretation of data; in the writing of the manuscript, or in the decision to publish the results.

References

- Cucinotta, D.; Vanelli, M. WHO Declares COVID-19 a Pandemic. *Acta BioMed.* **2020**, *91*, 157–160.
- Painter, E.M.; Ussery, E.N.; Patel, A.; Hughes, M.M.; Zell, E.R.; Moulia, D.L.; Scharf, L.G.; Lynch, M.; Ritchey, M.D.; Toblin, R.L.; et al. Demographic Characteristics of Persons Vaccinated During the First Month of the COVID-19 Vaccination Program—United States, December 14, 2020–January 14, 2021. *MMWR. Morb. Mortal. Wkly. Rep.* **2021**, *70*, 174–177. [CrossRef] [PubMed]
- Han, Y.J.; Lee, K.H.; Yoon, S.; Nam, S.W.; Ryu, S.; Seong, D.; Kim, J.S.; Lee, J.Y.; Yang, J.W.; Lee, J.H.; et al. Treatment of severe acute respiratory syndrome (SARS), Middle East respiratory syndrome (MERS), and coronavirus disease 2019 (COVID-19): A systematic review of in vitro, in vivo, and clinical trials. *Theranostics* **2021**, *11*, 1207–1231. [CrossRef] [PubMed]
- Peng, Y.; Tao, H.; Satyanarayanan, S.K.; Jin, K.; Su, H. A Comprehensive Summary of the Knowledge on COVID-19 Treatment. *Aging Dis.* **2021**, *12*, 155–191. [CrossRef] [PubMed]
- Muhseen, Z.; Hameed, A.; Al-Hasani, H.; Ahmad, S.; Li, G. Computational Determination of Potential Multiprotein Targeting Natural Compounds for Rational Drug Design Against SARS-CoV-2. *Molecules* **2021**, *26*, 674. [CrossRef]
- Romeo, I.; Mesiti, F.; Lupia, A.; Alcaro, S. Current Updates on Naturally Occurring Compounds Recognizing SARS-CoV-2 Druggable Targets. *Molecules* **2021**, *26*, 632. [CrossRef]
- Bhattacharya, R.; Dev, K.; Sourirajan, A. Antiviral activity of bioactive phytochemicals against coronavirus: An update. *J. Virol. Methods* **2021**, *290*, 114070. [CrossRef]
- Vougiannopoulou, K.; Corona, A.; Tramontano, E.; Alexis, M.; Skaltsounis, A.-L. Natural and Nature-Derived Products Targeting Human Coronaviruses. *Molecules* **2021**, *26*, 448. [CrossRef]
- Latos-Brozio, M.; Masek, A. Structure-Activity Relationships Analysis of Monomeric and Polymeric Polyphenols (Quercetin, Rutin and Catechin) Obtained by Various Polymerization Methods. *Chem. Biodivers.* **2019**, *16*, e1900426. [CrossRef] [PubMed]
- Magar, R.T.; Sohng, J.K. A Review on Structure, Modifications and Structure-Activity Relation of Quercetin and Its Derivatives. *J. Microbiol. Biotechnol.* **2020**, *30*, 11–20. [CrossRef]
- Gullón, B.; Lú-Chau, T.A.; Moreira, M.T.; Lema, J.M.; Eibes, G. Rutin: A review on extraction, identification and purification methods, biological activities and approaches to enhance its bioavailability. *Trends Food Sci. Technol.* **2017**, *67*, 220–235. [CrossRef]
- Lide, D.R.; Milne, G.W.A. *Handbook of data on organic compounds*, 3rd ed.; CRC Press: Boca Raton, FL, USA, 1994; pp. 1–1570.
- Srinivas, K.; King, J.W.; Howard, L.R.; Monrad, J.K. Solubility and solution thermodynamic properties of quercetin and quercetin dihydrate in subcritical water. *J. Food Eng.* **2010**, *100*, 208–218. [CrossRef]
- Abian, O.; Ortega-Alarcon, D.; Jimenez-Alesanco, A.; Ceballos-Laita, L.; Vega, S.; Reyburn, H.T.; Rizzuti, B.; Velázquez-Campoy, A. Structural stability of SARS-CoV-2 3CLpro and identification of quercetin as an inhibitor by experimental screening. *Int. J. Biol. Macromol.* **2020**, *164*, 1693–1703. [CrossRef] [PubMed]
- Abian, O.; Vega, S.; Sancho, J.; Velázquez-Campoy, A. Allosteric Inhibitors of the NS3 Protease from the Hepatitis C Virus. *PLoS ONE* **2013**, *8*, e69773. [CrossRef] [PubMed]
- Hidalgo, J.; Latorre, P.; Carrodegua, J.A.; Velázquez-Campoy, A.; Sancho, J.; Lopez-Buesa, P. Inhibition of Pig Phosphoenolpyruvate Carboxykinase Isoenzymes by 3-Mercaptopicolinic Acid and Novel Inhibitors. *PLoS ONE* **2016**, *11*, e0159002. [CrossRef]
- Neira, J.L.; Bintz, J.; Arruebo, M.; Rizzuti, B.; Bonacci, T.; Vega, S.; Lanás, A.; Velázquez-Campoy, A.; Iovanna, J.L.; Abián, O. Identification of a Drug Targeting an Intrinsically Disordered Protein Involved in Pancreatic Adenocarcinoma. *Sci. Rep.* **2017**, *7*, 39732. [CrossRef]
- Villanueva, R.; Romero-Tamayo, S.; Laplaza, R.; Martínez-Olivan, J.; Velázquez-Campoy, A.; Sancho, J.; Ferreira, P.; Medina, M. Redox- and Ligand Binding-Dependent Conformational Ensembles in the Human Apoptosis-Inducing Factor Regulate Its Pro-Life and Cell Death Functions. *Antioxid. Redox Signal.* **2019**, *30*, 2013–2029. [CrossRef]
- González, A.; Salillas, S.; Velázquez-Campoy, A.; Angarica, V.E.; Fillat, M.F.; Sancho, J.; Lanás, A. Identifying potential novel drugs against *Helicobacter pylori* by targeting the essential response regulator HsrA. *Sci. Rep.* **2019**, *9*, 1–13. [CrossRef]
- Santofimia-Castaño, P.; Xia, Y.; Lan, W.; Zhou, Z.; Huang, C.; Peng, L.; Soubeyran, P.; Velázquez-Campoy, A.; Abián, O.; Rizzuti, B.; et al. Ligand-based design identifies a potent NUPR1 inhibitor exerting anticancer activity via necroptosis. *J. Clin. Investig.* **2019**, *129*, 2500–2513. [CrossRef]
- Savov, V.M.; Galabov, A.S.; Tantcheva, L.P.; Mileva, M.M.; Pavlova, E.L.; Stoeva, E.S.; Braykova, A.A. Effects of rutin and quercetin on monooxygenase activities in experimental influenza virus infection. *Exp. Toxicol. Pathol.* **2006**, *58*, 59–64. [CrossRef]
- Jo, S.; Kim, H.; Kim, S.; Shin, D.H.; Kim, M. Characteristics of flavonoids as potent MERS-CoV 3C-like protease inhibitors. *Chem. Biol. Drug Des.* **2019**, *94*, 2023–2030. [CrossRef]
- Chen, Y.K.; Chen, S.Q.; Li, X.; Zeng, S. Quantitative regioselectivity of glucuronidation of quercetin by recombinant UDP-glucuronosyltransferases 1A9 and 1A3 using enzymatic kinetic parameters. *Xenobiotica* **2005**, *35*, 943–954. [CrossRef] [PubMed]

24. Matsumoto, M.; Matsukawa, N.; Mineo, H.; Chiji, H.; Hara, H. A Soluble Flavonoid-glycoside, α G-Rutin, Is Absorbed as Glycosides in the Isolated Gastric and Intestinal Mucosa. *Biosci. Biotechnol. Biochem.* **2004**, *68*, 1929–1934. [CrossRef]
25. Pedriali, C.A.; Fernandes, A.U.; Bernusso, L.D.C.; Polakiewicz, B. The synthesis of a water-soluble derivative of rutin as an antiradical agent. *Quim. Nova* **2008**, *31*, 2147–2151. [CrossRef]
26. Park, K.H.; Choi, J.M.; Cho, E.; Jeong, D.; Shinde, V.V.; Kim, H.; Choi, Y.; Jung, S. Enhancement of Solubility and Bioavailability of Quercetin by Inclusion Complexation with the Cavity of Mono-6-deoxy-6-aminoethylamino- β -cyclodextrin. *Bull. Korean Chem. Soc.* **2017**, *38*, 880–889. [CrossRef]
27. Iacopetta, D.; Grande, F.; Caruso, A.; Mordocco, R.A.; Plutino, M.R.; Scrivano, L.; Ceramella, J.; Muià, N.; Saturnino, C.; Puoci, F.; et al. New insights for the use of quercetin analogs in cancer treatment. *Future Med. Chem.* **2017**, *9*, 2011–2028. [CrossRef] [PubMed]
28. Nettore, I.C.; Rocca, C.; Mancino, G.; Albano, L.; Amelio, D.; Grande, F.; Puoci, F.; Pasqua, T.; Desiderio, S.; Mazza, R.; et al. Quercetin and its derivative Q2 modulate chromatin dynamics in adipogenesis and Q2 prevents obesity and metabolic disorders in rats. *J. Nutr. Biochem.* **2019**, *69*, 151–162. [CrossRef] [PubMed]
29. Lee, H.; Mittal, A.; Patel, K.; Gatuz, J.L.; Truong, L.; Torres, J.; Mulhearn, D.C.; Johnson, M.E. Identification of novel drug scaffolds for inhibition of SARS-CoV 3-Chymotrypsin-like protease using virtual and high-throughput screenings. *Bioorganic Med. Chem.* **2014**, *22*, 167–177. [CrossRef] [PubMed]
30. Zhang, L.; Lin, D.; Sun, X.; Curth, U.; Drosten, C.; Sauerhering, L.; Becker, S.; Rox, K.; Hilgenfeld, R. Crystal structure of SARS-CoV-2 main protease provides a basis for design of improved α -ketoamide inhibitors. *Science* **2020**, *368*, 409–412. [CrossRef]
31. Trott, O.; Olson, A.J. AutoDock Vina: Improving the speed and accuracy of docking with a new scoring function, efficient optimization, and multithreading. *J. Comput. Chem.* **2010**, *31*, 455–461. [CrossRef]
32. Morris, G.M.; Goodsell, D.S.; Halliday, R.S.; Huey, R.; Hart, W.E.; Belew, R.K.; Olson, A.J. Automated docking using a Lamarckian genetic algorithm and an empirical binding free energy function. *J. Comput. Chem.* **1998**, *19*, 1639–1662. [CrossRef]
33. Komoto, J.; Yamada, T.; Watanabe, K.; Takusagawa, F. Crystal Structure of Human Prostaglandin F Synthase (AKR1C3). *Biochemistry* **2004**, *43*, 2188–2198. [CrossRef] [PubMed]
34. Pettersen, E.F.; Goddard, T.D.; Huang, C.C.; Couch, G.S.; Greenblatt, D.M.; Meng, E.C.; Ferrin, T.E. UCSF Chimera—A visualization system for exploratory research and analysis. *J. Comput. Chem.* **2004**, *25*, 1605–1612. [CrossRef]
35. Santofimia-Castaño, P.; Rizzuti, B.; Pey, Á.L.; Soubeyran, P.; Vidal, M.; Urrutia, R.; Iovanna, J.L.; Neira, J.L. Intrinsically disordered chromatin protein NUPR1 binds to the C-terminal region of Polycomb RING1B. *Proc. Natl. Acad. Sci. USA* **2017**, *114*, E6332–E6341. [CrossRef]
36. Abraham, M.J.; Murtola, T.; Schulz, R.; Páll, S.; Smith, J.C.; Hess, B.; Lindahl, E. GROMACS: High performance molecular simulations through multi-level parallelism from laptops to supercomputers. *SoftwareX* **2015**, *1–2*, 19–25. [CrossRef]
37. Lindorff-Larsen, K.; Piana, S.; Palmo, K.; Maragakis, P.; Klepeis, J.L.; Dror, R.O.; Shaw, D.E. Improved side-chain torsion potentials for the Amber ff99SB protein force field. *Proteins Struct. Funct. Bioinform.* **2010**, *78*, 1950–1958. [CrossRef] [PubMed]
38. Wang, J.; Wolf, R.M.; Caldwell, J.W.; Kollman, P.A.; Case, D.A. Development and testing of a general amber force field. *J. Comput. Chem.* **2004**, *25*, 1157–1174. [CrossRef] [PubMed]
39. Jorgensen, W.L.; Chandrasekhar, J.; Madura, J.D.; Impey, R.W.; Klein, M.L. Comparison of simple potential functions for simulating liquid water. *J. Chem. Phys.* **1983**, *79*, 926–935. [CrossRef]
40. Guzzi, R.; Rizzuti, B.; Bartucci, R. Dynamics and Binding Affinity of Spin-Labeled Stearic Acids in β -Lactoglobulin: Evidences from EPR Spectroscopy and Molecular Dynamics Simulation. *J. Phys. Chem. B* **2012**, *116*, 11608–11615. [CrossRef]
41. Neira, J.L.; Rizzuti, B.; Iovanna, J.L. Determinants of the pKa values of ionizable residues in an intrinsically disordered protein. *Arch. Biochem. Biophys.* **2016**, *598*, 18–27. [CrossRef] [PubMed]
42. Guglielmelli, A.; Rizzuti, B.; Guzzi, R. Stereoselective and domain-specific effects of ibuprofen on the thermal stability of human serum albumin. *Eur. J. Pharm. Sci.* **2018**, *112*, 122–131. [CrossRef] [PubMed]
43. Bacha, U.; Barrila, J.; Velazquez-Campoy, A.; Leavitt, S.A.; Freire, E. Identification of Novel Inhibitors of the SARS Coronavirus Main Protease 3CLpro. *Biochemistry* **2004**, *43*, 4906–4912. [CrossRef]
44. Tian, W.; Chen, C.; Lei, X.; Zhao, J.; Liang, J. CASTp 3.0: Computed atlas of surface topography of proteins. *Nucleic Acids Res.* **2018**, *46*, W363–W367. [CrossRef]
45. Rizzuti, B.; Grande, F. Virtual screening in drug discovery: A precious tool for a still-demanding challenge. In *Protein Homeostasis Diseases*; Elsevier BV: Amsterdam, The Netherlands, 2020; pp. 309–327.
46. Komatsu, T.S.; Okimoto, N.; Koyama, Y.M.; Hirano, Y.; Morimoto, G.; Ohno, Y.; Taiji, M. Drug binding dynamics of the dimeric SARS-CoV-2 main protease, determined by molecular dynamics simulation. *Sci. Rep.* **2020**, *10*, 1–11. [CrossRef] [PubMed]
47. Suárez, D.; Díaz, N. SARS-CoV-2 Main Protease: A Molecular Dynamics Study. *J. Chem. Inf. Model.* **2020**, *60*, 5815–5831. [CrossRef] [PubMed]
48. Martínez, C.R.; Iverson, B.L. Rethinking the term “pi-stacking”. *Chem. Sci.* **2012**, *3*, 2191–2201. [CrossRef]
49. Avasthi, K.; Shukla, L.; Kant, R.; Ravikumar, K. Folded conformations due to arene interactions in dissymmetric and symmetric butylidene-linker models based on pyrazolo[3,4-d]pyrimidine, purine and 7-deazapurine. *Acta Crystallogr. Sect. C Struct. Chem.* **2014**, *70*, 555–561. [CrossRef] [PubMed]

50. Ghahremanpour, M.M.; Tirado-Rives, J.; Deshmukh, M.; Ippolito, J.A.; Zhang, C.-H.; De Vaca, I.C.; Liosi, M.-E.; Anderson, K.S.; Jorgensen, W.L. Identification of 14 Known Drugs as Inhibitors of the Main Protease of SARS-CoV-2. *ACS Med. Chem. Lett.* **2020**, *11*, 2526–2533. [CrossRef]
51. Chodera, J.; Lee, A.A.; London, N.; Von Delft, F. Crowdsourcing drug discovery for pandemics. *Nat. Chem.* **2020**, *12*, 581. [CrossRef]
52. Chua, L.S. A review on plant-based rutin extraction methods and its pharmacological activities. *J. Ethnopharmacol.* **2013**, *150*, 805–817. [CrossRef]
53. Matsuo, M.; Sasaki, N.; Saga, K.; Kaneko, T. Cytotoxicity of Flavonoids toward Cultured Normal Human Cells. *Biol. Pharm. Bull.* **2005**, *28*, 253–259. [CrossRef]
54. Iriti, M.; Kubina, R.; Cochis, A.; Sorrentino, R.; Varoni, E.M.; Kabała-Dzik, A.; Azzimonti, B.; Dziedzic, A.; Rimondini, L.; Wojtyczka, R.D. Rutin, a Quercetin Glycoside, Restores Chemosensitivity in Human Breast Cancer Cells. *Phytother. Res.* **2017**, *31*, 1529–1538. [CrossRef] [PubMed]
55. Al-Zahrani, A.A. Rutin as a Promising Inhibitor of Main Protease and Other Protein Targets of COVID-19: In Silico Study. *Nat. Prod. Commun.* **2020**, *15*. [CrossRef]
56. Puttaswamy, H.; Gowtham, H.G.; Ojha, M.D.; Yadav, A.; Choudhir, G.; Raguraman, V.; Kongkham, B.; Selvaraju, K.; Shareef, S.; Gehlot, P.; et al. In silico studies evidenced the role of structurally diverse plant secondary metabolites in reducing SARS-CoV-2 pathogenesis. *Sci. Rep.* **2020**, *10*, 1–24. [CrossRef]
57. Xu, Z.; Yang, L.; Zhang, X.; Zhang, Q.; Yang, Z.; Liu, Y.; Wei, S.; Liu, W. Discovery of Potential Flavonoid Inhibitors Against COVID-19 3CL Protease Based on Virtual Screening Strategy. *Front. Mol. Biosci.* **2020**, *7*, 556481. [CrossRef]
58. Cherrak, S.A.; Merzouk, H.; Mokhtari-Soulimane, N. Potential bioactive glycosylated flavonoids as SARS-CoV-2 main protease inhibitors: A molecular docking and simulation studies. *PLoS ONE* **2020**, *15*, e0240653. [CrossRef] [PubMed]
59. Kumari, A.; Rajput, V.S.; Nagpal, P.; Kukrety, H.; Grover, S.; Grover, A. Dual inhibition of SARS-CoV-2 spike and main protease through a repurposed drug, rutin. *J. Biomol. Struct. Dyn.* **2020**, 1–13. [CrossRef]
60. Huynh, T.; Wang, H.; Luan, B. Structure-based lead optimization of herbal medicine rutin for inhibiting SARS-CoV-2's main protease. *Phys. Chem. Chem. Phys.* **2020**, *22*, 25335–25343. [CrossRef] [PubMed]
61. Shivanika, C.; Kumar, S.D.; Ragunathan, V.; Tiwari, P.; Sumitha, A.; Devi, P.B. Molecular docking, validation, dynamics simulations, and pharmacokinetic prediction of natural compounds against the SARS-CoV-2 main-protease. *J. Biomol. Struct. Dyn.* **2020**, *83*, 1–27. [CrossRef]
62. Verma, S.; Pandey, A.K. Factual insights of the allosteric inhibition mechanism of SARS-CoV-2 main protease by quercetin: An in silico analysis. *3 Biotech* **2021**, *11*, 1–10. [CrossRef] [PubMed]
63. Nguyen, T.T.H.; Woo, H.-J.; Kang, H.-K.; Nguyen, V.D.; Kim, Y.-M.; Kim, D.-W.; Ahn, S.-A.; Xia, Y.; Kim, D. Flavonoid-mediated inhibition of SARS coronavirus 3C-like protease expressed in *Pichia pastoris*. *Biotechnol. Lett.* **2012**, *34*, 831–838. [CrossRef] [PubMed]
64. Chen, L.; Li, J.; Luo, C.; Liu, H.; Xu, W.; Chen, G.; Liew, O.W.; Zhu, W.; Puah, C.M.; Shen, X.; et al. Binding interaction of quercetin-3- β -galactoside and its synthetic derivatives with SARS-CoV 3CLpro: Structure–activity relationship studies reveal salient pharmacophore features. *Bioorganic Med. Chem.* **2006**, *14*, 8295–8306. [CrossRef] [PubMed]



Review

Recent Advances in Improved Anticancer Efficacies of Camptothecin Nano-Formulations: A Systematic Review

Maryam Ghanbari-Movahed^{1,2}, Tea Kaceli³, Arijit Mondal⁴, Mohammad Hosein Farzaei^{1,*} and Anupam Bishayee^{3,*}

¹ Medical Technology Research Center, Health Technology Institute, Kermanshah University of Medical Sciences, Kermanshah 6734667149, Iran; maryam.gh.movahed@gmail.com

² Department of Biology, Faculty of Science, University of Guilan, Rasht 4193833697, Iran

³ Lake Erie College of Osteopathic Medicine, Bradenton, FL 34211, USA; tkaceli1@gmail.com

⁴ Department of Pharmaceutical Chemistry, Bengal College of Pharmaceutical Technology, Dubrajpur 731123, India; juarijitmondal@gmail.com

* Correspondence: mh.farzaei@gmail.com (M.H.F.); abishayee@lecom.edu or abishayee@gmail.com (A.B.); Tel.: +98-83-3427-6493 (M.H.F.); +1-941-782-5950 (A.B.)

Abstract: Camptothecin (CPT), a natural plant alkaloid, has indicated potent antitumor activities via targeting intracellular topoisomerase I. The promise that CPT holds in therapies is restricted through factors that include lactone ring instability and water insolubility, which limits the drug oral solubility and bioavailability in blood plasma. Novel strategies involving CPT pharmacological and low doses combined with nanoparticles have indicated potent anticancer activity in vitro and in vivo. This systematic review aims to provide a comprehensive and critical evaluation of the anticancer ability of nano-CPT in various cancers as a novel and more efficient natural compound for drug development. Studies were identified through systematic searches of PubMed, Scopus, and ScienceDirect. Eligibility checks were performed based on predefined selection criteria. Eighty-two papers were included in this systematic review. There was strong evidence for the association between antitumor activity and CPT treatment. Furthermore, studies indicated that CPT nano-formulations have higher antitumor activity in comparison to free CPT, which results in enhanced efficacy for cancer treatment. The results of our study indicate that CPT nano-formulations are a potent candidate for cancer treatment and may provide further support for the clinical application of natural antitumor agents with passive targeting of tumors in the future.

Keywords: cancer; camptothecin; natural products; nano-targeted therapy

Citation: Ghanbari-Movahed, M.; Kaceli, T.; Mondal, A.; Farzaei, M.H.; Bishayee, A. Recent Advances in Improved Anticancer Efficacies of Camptothecin Nano-Formulations: A Systematic Review. *Biomedicines* **2021**, *9*, 480. <https://doi.org/10.3390/biomedicines9050480>

Academic Editor: Leonardo Caputo

Received: 10 April 2021

Accepted: 24 April 2021

Published: 27 April 2021

Publisher's Note: MDPI stays neutral with regard to jurisdictional claims in published maps and institutional affiliations.



Copyright: © 2021 by the authors. Licensee MDPI, Basel, Switzerland. This article is an open access article distributed under the terms and conditions of the Creative Commons Attribution (CC BY) license (<https://creativecommons.org/licenses/by/4.0/>).

1. Introduction

Systematic research in the tumor field has indicated that a set of multifarious processes, including quick spreading and uncontrollable multiplication of abnormal cells, results in the formation of malignant tumors with the potential for metastasis [1,2]. There are numerous diverse methods for cancer treatment, nonetheless, some might be ineffective because of the adverse side effects as well as augmented resistance to conventional antitumor drugs.

Natural compounds represent a valued resource in the discovery and development of novel drugs, mainly those used for cancer treatment [3–5], and they might act as a safe substitute for various synthetic drugs used in existing clinical therapies [6]. Evidence showed that alkaloids are important sources for developing plant-based antitumor drugs. Alkaloids are found generally in plants and are mainly present in blooming plants [7]. Screening for new agents has resulted in the detection of novel alkaloids that indicated potent apoptotic and antineoplastic capabilities in various cancer cells [8]. Alkaloids, such as vinblastine and camptothecin, have already been developed into antitumor drugs [9,10].

Camptothecin (CPT), a wide-spectrum antitumor agent, was primarily isolated from *Camptotheca acuminata* (family: Nyssaceae), a tree native to Tibet and China, which has

been widely used in traditional Chinese medicine [11]. Various analogs of CPT are used in treating colon, ovarian, and small-cell lung cancer [7,12]. CPT's mode of action involves suppression of the topoisomerase I enzyme (Topo I). Human Topo I is a critical enzyme involved in forming nonreversible and covalent Topo I-DNA complexes during replication of DNA and leads to strand breaks and subsequent apoptosis induction [13]. Additionally, several studies have shown that different synthetic analogs and semisynthetic derivatives of CPT act as topoisomerase inhibitors by changing ferment catalytic activity via stabilizing the covalent DNA-protein complexes [14–18].

The promise that CPT holds in therapy is restricted via factors that include excessive toxicity, lactone ring instability, and water insolubility, which restricts the drug oral solubility and bioavailability in blood plasma [19]. Accordingly, an efficient method for overcoming these challenges is encapsulating CPT into different nano-sized delivery vehicles [20].

Nanotechnology aims at delivering drugs more effective to their target for treating malignancies [21]. Nowadays, nanotechnology-based delivery systems have gained tremendous attention as a strategy for overcoming the challenges related to bioavailability, solubility, distribution, toxicity, and targeting of classical chemotherapeutic agents as well as antitumor natural products [22–25]. Therefore, novel approaches involving pharmacological and low doses of CPT, either alone or combined with nanoparticles, could have potent anticancer activity *in vitro* and *in vivo*.

Even though there are a small number of publications on the overview of CPT nano-formulations in cancer, these papers are narrative reviews or reviews of the antitumor activities of nano-CPT in a limited number of cancers [26]. Henceforth, a comprehensive and critical systematic review on the antitumor capability of CPT nano-formulations within different cancers has not been conducted before. Consequently, this review aims to provide an up-to-date, comprehensive, and critical assessment of the antitumor ability of nano-CPT in various cancers as a novel and more efficient natural product-based anticancer therapeutic agent.

1.1. Natural Nano-Formulations and Cancer Treatment

Natural products particularly secondary metabolites have massive chemical and structural diversity along with enduring to instigate new findings in biology, medicine, and chemistry because of their therapeutic potential [27,28]. A broad variety of anticancer properties have been attributed to these plant-derived agents, including antiproliferative, antioxidant, antimetastatic, anti-inflammatory antiangiogenic, and proapoptotic activities [29,30]. Nevertheless, several other physicochemical properties, such as weak stability, low aqueous solubility, short half-life, low bioavailability, and rapid clearance, have severely restricted their uses in clinical settings [31,32].

For achieving the maximum therapeutic profits of these natural compounds, nano-sized carriers have been used for direct delivery of parent compounds to the locations where they are required, like malignant tissues to display their potential antitumor activities. Such targeted therapy could be essential for minimizing possible systemic toxicity and optimizing efficacy to increase the clinical outcomes [33]. Various nano-formulations have been used in drug delivery research, such as liposomes, solid lipid NPs, double emulsions, protein-based systems, cyclodextrins, and chitosan [24].

Alkaloids are mostly tetracyclic, tricyclic, and bicyclic derivatives of the molecule quinolizidine, mainly found in the Leguminosae family. The tumor suppression role of alkaloids nano-formulations is indicated in multiple *in vitro* and *in vivo* studies. One study used PLGA-PEG-folate (PLGA-PEG-FOL) NPs for targeted delivery of a CPT analog, 7-ethyl-10-hydroxycamptothecin (SN-38), and demonstrated significant anticancer activity in HT-29 colon tumor-bearing nude mice [34]. In another study, albumin NPs were loaded with the antitumor drug tamoxifen (TMX). The cellular uptake of NPs was observed in HeLa and MCF-7 cell lines and TMX-loaded NPs showed greater antitumor activity com-

pared to the free drug [35]. Moreover, the cytotoxic activity of irinotecan nano-formulations against cancer has been reviewed previously [36].

Altogether, NPs derived from natural sources are considered cost-effective and more secure than synthetic NPs and offer protective and therapeutic activities with low cytotoxicity [37].

1.2. Camptothecin: Sources, Chemistry, and Pharmacology

CPT, an indole alkaloid with a pentacyclic ring (classified as pyrrolo [3,4-*b*]quinoline), was primarily isolated from *Camptotheca acuminata* (Nyssaceae) [1]. This alkaloid is also synthesized in other plants, including *Ervatamia heyeno* [38], *Nothapodytesfeotida* [39], and in several species of the genus *Ophiorrhiza* [40]. In 1966 CPT structure was determined using a combination of X-ray and Nuclear Magnetic Resonance approach (Figure 1) [41]. CPT has two remarkable chemical properties: (1) Its lack of important alkalinity makes it act as a neutral molecule, and (2) the C-20 tertiary alcohol presence imparts an uncommon electrophilicity to the lactone carbonyl group, possibly through a strong intramolecular H-bond [42].

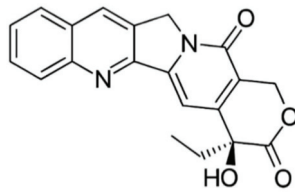


Figure 1. The chemical structure of CPT ($C_{20}H_{16}N_2O_4$, molecular weight: 348.4 g/mol).

CPT has been indicated to suppress different cancers via various mechanisms both in vitro and in vivo and rapidly entered the clinical examination (Figure 2). The most noticeable activity of CPT is the Topo I suppression which is a molecular basis of its antitumor properties [43]. The structural models show that CPT non-covalently binds to Topo I–DNA binary complex. The structure-activity relationships offer insight into a potential mechanism of Topo I suppression via CPT and its derivatives [44].

Despite the significant antineoplastic activity and an exclusive mechanism of action, CPT displays various unwanted properties which hinder its clinical application. First, the very low water solubility of CPT complicates its administration. Another challenge related to CPT is the α -hydroxy lactone ring (ring E) which opens under physiological conditions, resulting in the CPT carboxylate open form. Carboxylic acid or its sodium salt, even though soluble, has considerably lower antitumor potential as compared to CPT. Furthermore, this ionic form favorably binds to the human serum albumin, lowering the accessible drug concentration [45,46].

Even though the antitumor properties of CPT stimulated a substantial research interest, other properties of CPT including insecticidal or antiviral activities have also been investigated. Though semisynthetic CPT, such as irinotecan and topotecan, hold their position in chemotherapy, various other anticancer agents are established which are now in different phases of the preclinical or clinical development. Moreover, current research on CPT involves their novel formulations (particularly nano-formulations) for optimizing the stability, delivery, and reducing toxicity [47].

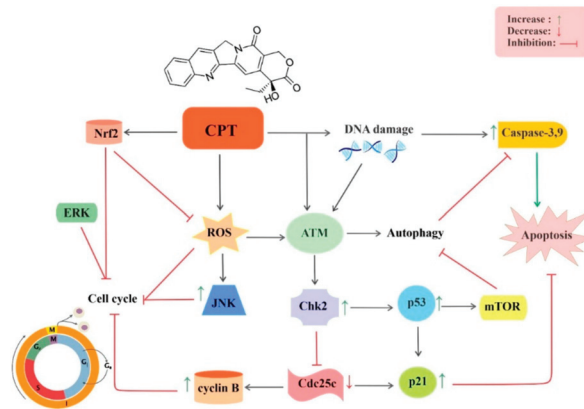


Figure 2. Molecular mechanisms underlying the anticancer effect of CPT. Abbreviations: ATM, ataxia telangiectasia mutated gene; Cdc25c, cell division cycle 25C; Chk2, checkpoint kinase 2; CPT, camptothecin; ERK, extracellular signal-regulated kinase; JNK, c-Jun N-terminal kinase; mTOR, mammalian target of rapamycin; Nfr2, nuclear factor erythroid 2-related factor 2; p21, tumor protein p53; p53, tumor protein p53; ROS, reactive oxygen species.

2. Methodology for Literature Search on Camptothecin Nano-Formulations and Cancer

The current study was conducted following the Preferred Reporting Items for Systematic Reviews and Meta-Analysis (PRISMA) guidelines [48]. The purpose of this paper is to offer a systematic review of *in vivo* studies for examining the impact of CPT nano-formulations on cancer. Various electronic scholarly databases, including Scopus, PubMed, ScienceDirect, were explored and related studies in the English language only were collected up to March 2021. The search syntax included “Camptothecin” AND “tumor” OR “cancer” OR “neoplasm” OR “malignancy” OR “carcinoma” AND “nano”. The primary search was performed by two researchers separately, and unrelated studies were excluded based upon their titles and abstracts. Review articles, meta-analyses, books, book chapters, conference abstracts, case reports, clinical trials, and non-English articles were also excluded. Between the initial 2586 studies that were collected through electronic search, 99 were excluded because of the duplicated results, 629 were omitted due to paper type, 905 review papers were ruled out, and 564 were considered unrelated based on abstract and/or title data. Besides, 4 were omitted as they were not in the English language. Out of 385 retrieved reports, 119 were omitted as they assessed other derivatives of CPT, 12 were excluded as they evaluated CPT rather than its nano-formulations, 41 were omitted because they assessed other biological effects of CPT rather than its antitumor impacts, 16 were omitted as they focused on other compounds, not CPT, and 120 were removed because they were *in vitro* studies. Finally, 82 papers were included in this systematic review as indicated in a flowchart of the selection process and literature search (Figure 3).

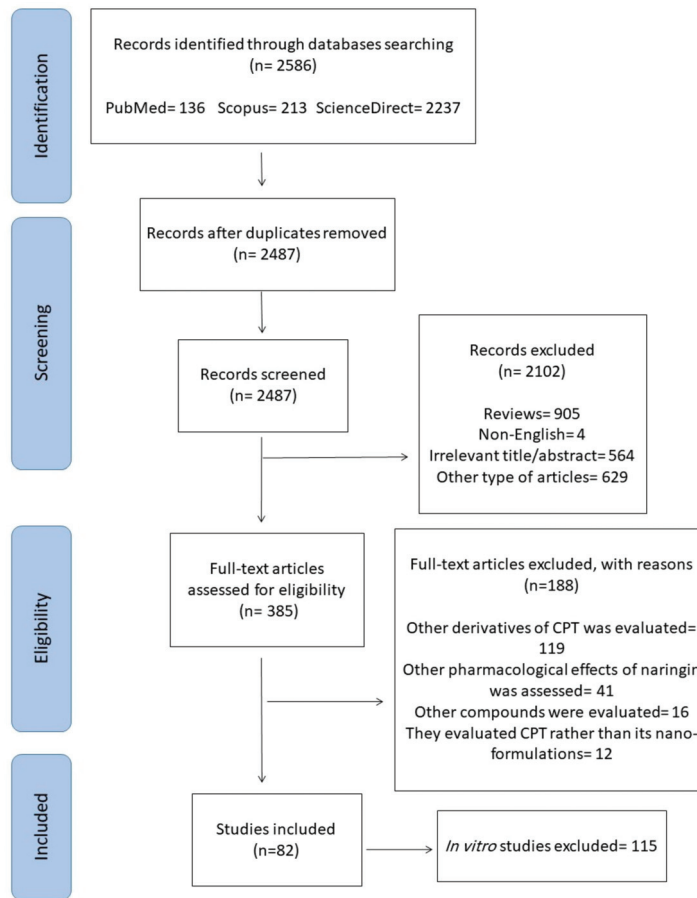


Figure 3. The PRISMA flow chart of the selection process for the included studies.

3. Anticancer Activities of Camptothecin Nano-Formulations

Nano-CPT has been indicated to suppress different cancers via various mechanisms, such as growth suppression of malignant cells, induction of apoptosis and cell cycle arrest, and modulation of oxidative stress, angiogenesis, and inflammation. The anticancer effects of CPT nano-formulations in different cancers are provided in the next sections (Table 1).

Table 1. Potential antitumor impacts of CPT nano-formulations based on in vivo studies.

Cancer Type	Animal Model	Nano-Formulation	Dose & Duration	Anticancer Effects	References
Bladder	Nude mice bearing subcutaneous AY27 xenografts	CPT-loaded micelles	5–10 mg/mL for 16 days	↑Tumor elimination, ↓tumor growth	[49]
Brain	9 L tumor-bearing mice	CPT-loaded amphiphilic β -cyclodextrin NPs	40 days	↓Tumor progression, ↓tumor growth, ↓tumor volume, ↑median survival time	[50]
Brain	GL261-luc2 tumor-bearing C57BL/6 albino mice	CPT-loaded PLGA NPs	10–20 mg/kg for 60 days	↑Tumor elimination, ↓tumor progression, ↓tumor growth	[51]
Brain	Mice bearing intracranial Luc-U87 glioma	CPC@IR780 micelles and CPD@IR780 micelles	3 mg/kg for 28 days	↑Survival time, ↓tumor growth, ↓side effects	[52]
Brain	C6 tumor-bearing rats	CPT-loaded Bom/PEG-PCL-Tat micelles	1.2 mg/kg for 60 days	↑Therapeutic efficacy, ↑tumor elimination, ↓tumor progression, ↓tumor growth	[53]
Brain	Rats bearing intracranial C6 glioma tumors	CPT-loaded MPEG-PCL and CPT-loaded MPEG-PCL-Tat micelles	1.2 mg/kg for 60 days	↑Median survival, ↓tumor growth, ↓side effects	[54]
Brain	U-87 MG tumor-bearing nude mice	CPT-TEG-ALA	4–16 mg/kg for 5 days	↑Survival time, ↓tumor progression, ↓tumor growth, ↑therapeutic efficacy	[55]
Breast	4T1 tumor-bearing BALB/c mice	CPT-ss-EB or CPT-cc-EB	3 mg/kg for 2 weeks	↓Tumor progression, ↓tumor growth, ↓side effects	[56]
Breast	4T1 tumor-bearing mice	FP-CPT/TNF micelleplexes, FP-CPT micelles	3.7 mg/kg for 25 days	↑ Animal survival, ↓tumor growth, ↓tumor volume	[57]
Breast	4T1 tumor-bearing BALB/c mice	DCPT micelles	5 mg/kg for 11 days	↓Tumor progression, ↓tumor growth, ↑therapeutic efficacy	[58]
Breast	4T1 tumor-bearing mice	HA-ss-CPT micelles	4 mg/kg for 60 days	↑Tumor elimination, ↓tumor progression, ↓tumor growth	[59]
Breast	4T1 tumor-bearing mice	DCM and DEM micelles	4 mg/kg for 60 days	↑Tumor elimination, ↓tumor progression, ↓tumor growth	[60]
Breast	4T1 tumor-bearing Balb/c mice	PM _{CPT} -co-electrospun fibers	4.0 mg/kg for 30 days	↑Therapeutic efficacy, ↑tumor elimination, ↓tumor progression, ↓tumor growth	[61]
Breast	4T1 tumor-bearing mice	NP/CPT	5 mg/kg for 16 days	↑Tumor elimination, ↓tumor progression, ↓tumor growth	[62]
Breast	4T1 tumor-bearing mice	CPT-SS-APBA, BBSA/CPT-SS-APBA NPs	5 mg/kg for 18 days	↑Tumor elimination, ↓tumor progression, ↓tumor growth	[63]

Table 1. Cont.

Cancer Type	Animal Model	Nano-Formulation	Dose & Duration	Anticancer Effects	References
Breast	4T1 tumor-bearing mic	P@CH NPs	20–65 days	↓Tumor growth, ↓tumor metastases, ↓tumor recurrence	[64]
Breast	4T1 breast tumor-bearing mice	ACI, and PCI	0.9 mg/kg for 25 days	↑Tumor elimination, ↓tumor growth, ↓tumor volume	[65]
Breast	4T1 tumor-bearing BALB/c mice	CHI-CPT-NEs	2.5 mg/kg for 4 weeks	↑Therapeutic activity, ↑tumor elimination, ↓tumor growth	[66]
Breast	4T1 tumor-bearing mice	MDNCs	1 mg/kg for 2 weeks	↑Tumor elimination, ↓tumor progression, ↓tumor growth	[67]
Breast	4T1 tumor-bearing mice	HSD NCGs	5 mg/kg for 12 days	↑Tumor accumulation, ↑apoptosis, ↓tumor progression, ↓tumor growth	[68]
Breast	MCF-7 tumor-bearing nude mice	CCO micelles	5 mg/kg for 1–14 days	↑Tumor elimination, ↓tumor progression, ↓tumor growth	[69]
Breast	MCF-7 tumor-bearing mice	CP micelles	5 mg/kg for 12 days	↑Inhibition rate, ↓tumor progression, ↓tumor growth	[70]
Breast	BALB/c nude mice bearing MCF-7 xenograft tumors	Cy@CPT or Ce@CPT micelles	1g/kg for 1–10 days	↓Tumor progression, ↓tumor growth	[71]
Breast	MCF-7 tumor-bearing nude mice	CPT@Ru-CD, VK3-CPT@RuxCD and VK3-CPT@Ru-CD	10 mg/kg for 16 days	↑ROS, ↑tumor elimination, ↓tumor progression, ↓tumor growth, ↓side effects	[72]
Breast	MCF-7 tumor-bearing mice	CPT-PGA encapsulated SNPs	13.6 mg/kg for 10 days	↑Tumor elimination, ↓tumor progression, ↓tumor growth	[73]
Breast	MCF-7 tumor-bearing nude mice	CPT/NS	5 mg/kg for 16 days	↑Tumor elimination, ↓tumor growth, ↓tumor volume	[74]
Breast	MCF-7 tumor-bearing mice	CSP-CPT	10 mg/kg for 25 days	↑Therapeutic activity, ↑tumor elimination, ↓tumor progression, ↓tumor growth	[75]
Breast	MCF-7 tumor-bearing nude mice	CCP UMIs	1 mg/mL for 15 days	↑Tumor elimination, ↓tumor progression, ↓tumor growth	[76]
Breast	MCF-7 tumor-bearing rat	CPT-loaded MrGO-AA ³ -4-HC	5 µg/kg for 6 weeks	↑Synergistic anti-tumor efficiency, ↑apoptosis, ↓tumor growth	[77]
Breast	MCF-7 tumor-bearing mouse	GNS-CB[7]-CPT	300 µg for 1–15 days	↑Tumor elimination, ↓tumor progression, ↓tumor growth	[78]
Breast	MDA-MB231 tumor-bearing nude mice	CPT-HCC NPs	10–30 mg/kg for 35 days	↑Survival rate, ↑tumor elimination, ↓tumor progression, ↓tumor growth	[79]

Table 1. Cont.

Cancer Type	Animal Model	Nano-Formulation	Dose & Duration	Anticancer Effects	References
Breast	MDA-MB-231 tumor-bearing mice	CPT-P-HA-NPs	10 mg/kg for 40 days	↑Survival rate, ↓tumor progression, ↓tumor growth	[80]
Breast	MDA-MB-231BO tumor-bearing mice	pSINP + CPT, pSINP + CPT + Ab	7.5 mg/kg for 15 weeks	↓Tumor growth, ↓metastatic spread, ↓tumor size, ↑tumor elimination	[81]
Breast	MDA-MB231 tumor-bearing mice	CPT-pH-PMs	5–10 mg/kg for 50 days	↓Tumor progression, ↓tumor growth, ↓side effects, ↑survival rate	[82]
Breast	EMT6 tumor bearing Balb/c mice	CPT/DOX-NCM ₁ and CPT/DOX-CCM	1 mg/kg for 24 days	↑Tumor elimination, ↓tumor progression, ↓tumor growth	[83]
Breast	Ehrlich Ascites Carcinoma (EAC) mice models	CPT-loaded NPs (CPT ₁ NV-P ₁ -mic)	2–3 mg/kg for 30 days	↓Necrosis, ↑tumor elimination, ↓tumor progression, ↓tumor growth	[84]
Breast	BT-474 tumor-bearing athymic nude mice	CPT encapsulated in E ₃ PA nanofibers	1.5 mg/kg for 40 days	↓Tumor growth, ↑anti-tumor activity	[85]
Cervix	Mice bearing HeLa tumors	CPT@ItS _x -PEG-FA NPs	2 mg/mL for 2 weeks	↑Tumor elimination, ↓tumor progression, ↓tumor growth	[86]
Cervix	HeLa tumor-bearing mice	PDA@PCPT NPs	9.81 mg/kg for 2 weeks	↑Therapeutic efficacy, ↑tumor elimination, ↓tumor progression, ↓tumor growth	[87]
Cervix	HeLa tumor-bearing mice	CPT/PCBn based lipoplexes	4 mg/kg for 28 days	↑Tumor suppression, ↓tumor progression, ↓tumor growth	[88]
Cervix	HeLa tumor-bearing nude mice	RLS/siPLK1+ CPT	14–26 days	↓Tumor growth, ↓tumor volumes, ↓side effects, ↑apoptosis	[89]
Cervix	HeLa tumor-bearing nude mice	EuGd-SS-CPT-FA-MSNs	23 days	↑Tumor elimination, ↓tumor progression, ↓tumor growth	[90]
Cervix	HeLa tumor-bearing BALB/c-nu nude mice	CPT-DNS-DCM	20 mg/kg for 12 days	↑Tumor elimination, ↓tumor progression, ↓tumor growth	[91]
Colon	HCT116 tumor-bearing mice	CPT-ss-EB or CPT-cc-EB	3 mg/kg for 2 weeks	↓Tumor progression, ↓tumor growth, ↓side effects	[56]
Colon	SW620 tumor-bearing nude BALB/c mice	CPT-loaded CMD NPs	10 mg/kg for 30 days	↑Tumor elimination, ↓tumor progression, ↓tumor growth, ↑anticancer efficiency	[92]

Table 1. Cont.

Cancer Type	Animal Model	Nano-Formulation	Dose & Duration	Anticancer Effects	References
Colon	HT29 tumor-bearing nude mice	CPT&Ce6, HBPTK-Ce6@CPT	8 mg/kg for 25 days	↑Tumor elimination, ↓tumor progression, ↓tumor growth, ↓tumor volume	[93]
Colon	Athymic mice bearing HCT116 xenografts	CPT-loaded NPs	1.9 mg/kg for 22 days	↑Tumor elimination, ↓tumor progression, ↓tumor growth	[94]
Colon	HCT116 tumor-bearing mice	CT MLNPs	2.4 ng/kg for 15 days	↑Tumor elimination, ↓tumor progression, ↓tumor growth	[95]
Colon	HCT-116 tumor-bearing nude mice	CPT + ICG NPs	2.5 mg/kg for 55 days	↓Tumor suppression, ↓tumor growth, ↓tumor volume	[96]
Colon	HCT 116 tumor-bearing nude BALB/c mice	CPT-DNA-Gel	1.6 mg/kg for 10-60 days	↓Tumor recurrence, ↑therapeutic efficacy, ↑apoptosis, ↓side effects, ↑tumor inhibition	[97]
Colon	HCT116 tumor-bearing mic	HRC@F127 NPs	5 mg/kg for 40 days	↓Tumor progression, ↓tumor growth, ↑therapeutic efficacy	[98]
Colon	HT-29/Fluc tumor-bearing mice	SNP-CPT and SNP-CPT-Cy5.5 NPs	0.8 mg/kg for 22 days	↑Tumor elimination, ↓tumor progression, ↓tumor growth	[99]
Colon	HCT-8 tumor-bearing BALB/c mice	Nano-CPT	1–2 mg/kg for 5 weeks	↓Tumor suppression, ↓tumor growth, ↓tumor volume	[100]
Colon	Nude mice bearing LoVo tumors	Gd(DTPA-CPT) NPs and Gd(DTPA)/CPT mixture	0.02–0.10 mmol/kg for 0.5 h–30 days	↑Tumor elimination, ↓tumor growth, ↑anticancer efficiency	[101]
Colon	HT-29 tumor-bearing BALB/c mice	CPT@Dod-ND-SPs	3 mg/kg for 18 days	↓Tumor suppression, ↓tumor growth, ↓tumor volumes	[102]
Colon	C26 tumor-bearing BALB/C mice	PEG-PAMAM-CPT and Apt-PEG-PAMAM-CPT	3 mg/kg for 20 days	↑Tumor elimination, ↓tumor progression, ↓tumor growth	[103]
Colon	BALB/c mice bearing C26 tumors	PEG-PLGA-CPT-NPs or tet-PEG-PLGA-CPT-NPs	10 mg/kg for 20 days	↑Therapeutic index, ↑tumor elimination, ↓tumor progression, ↓tumor growth	[104]
Colon	C26 tumor-bearing Balb/c mice	PEG@MSNR-CPT, PEG@MSNR-CPT/Sur and Apt-PEG@MSNR-CPT/Sur	3 mg/kg for 35 days	↑Tumor elimination, ↓tumor progression, ↓tumor growth	[105]
Colon	Colon-26 tumor-bearing mice	Fab'-siCD98/CPT-NPs	1.5 mg/kg for 1–50 days	↓Tumorigenesis, ↓tumor growth	[106]

Table 1. Cont.

Cancer Type	Animal Model	Nano-Formulation	Dose & Duration	Anticancer Effects	References
Colon	Colon-26 tumor-bearing mice	PEG-CM-NPs and iRGD-PEG-CM-NPs	3 mg/kg for 10 days	↑Therapeutic efficacy, ↓tumor progression, ↓tumor growth	[107]
Liver	BEL-7402 tumor-bearing nude mice	MGO@CD-CA-HA/CPT	0.1–1 mg/kg for 3 weeks	↑Apoptosis, ↓tumor progression, ↓tumor growth, ↑therapeutic efficacy, ↑cellular uptake	[108]
Liver	H22 tumor-bearing mice	RGD-prodrug	10 mg/kg for 2 weeks	↑Tumor elimination, ↓tumor growth, ↓tumor volume	[109]
Liver	HepG2 and H22 tumor-bearing mice	CCLM and CCLM without PBA	5 mg/kg for 25 days	↑Tumor elimination, ↓tumor progression, ↓tumor growth	[110]
Liver	balb/c mice bearing Hep1-6 tumor	IR780-LA/CPT-ss-CPT NPs	5.74 μmol/kg for 15 days	↑Synergistic chemo-photothermal therapy, ↑tumor elimination, ↓tumor growth	[111]
Liver	HepG2 tumor-bearing BALB/c nude mice	P(CPT-MAA) prodrug nanogels, P(CPT-MAA) nanogels without SeS	5–10 mg/kg for 21 days	↑Tumor elimination, ↓tumor growth, ↓side effects	[112]
Liver	H22 tumor-bearing mice	JP@EF and JNM@EF	4.0 mg/kg for 40 days	↑Tumor elimination, ↓tumor progression, ↓tumor growth	[113]
Liver	HepG2 tumor-bearing mice	UCNP@mSiO ₂ -NBCCPT/β-CD-PEG, UCNIP@mSiO ₂ -NBCCPT@DHMA/β-CD-PEG, UCNIP@mSiO ₂ -NBCCPT@DHMA/β-CD-PEG-LA	15 mg/kg for 21 days	↓Tumor progression, ↓tumor growth, ↓tumor volume, ↑median survival time	[114]
Lung	LLC tumor-bearing mice	CPT-loaded PPBS NPs	5–10 mg/kg for 25 days	↑Tumor elimination, ↓tumor progression, ↓tumor growth	[115]
Lung	A549 tumor-bearing Balb/c mice	NC _{ssG} NPs and C _{ssG} NWs	4.8 mg/kg for 16 days	↑Tumor elimination, ↓tumor progression, ↓tumor growth, ↓tumor volume	[116]
Lung	A549 tumor-bearing nude mice	CPT-loaded GCMSNs	0.1–0.4 mg for 22 days	↑Tumor elimination, ↓tumor progression, ↓tumor growth, ↑synergistic therapeutic effects	[117]
Lung	BALB/c nude mice bearing A549 tumor	PCPT-V and GOD@PCPT-NR	35 mg/kg for 1–50 days	↓Tumor progression, ↓tumor growth, ↑therapeutic efficacy	[118]
Lung	A549 tumor-bearing mice	ZTC-NMs	3 mg/kg for 1–30 days	↓Tumor progression, ↓tumor growth	[119]

Table 1. Cont.

Cancer Type	Animal Model	Nano-Formulation	Dose & Duration	Anticancer Effects	References
Lung	NCLH460 tumor-bearing nude mice	Ce6-CPT-UCNPs	2.5 mg/kg for 18 days	↓Tumor recurrence, ↓metastasis, ↓tumor progression, ↓tumor growth	[120]
Lung	NCLH460 tumor-bearing nude mice	ZnPC/CPT-TPNPs or ZnPC/CPT-NH2NPs	22.65 mg/kg for 16 days	↓Tumor recurrence, ↑tumor elimination, ↓tumor progression, ↓tumor growth	[121]
Lung	LLC tumor-bearing mice	2OA-CPT/NAs and OA-CPT/NAs	10 mg/kg for 14 days	↑Tumor elimination, ↓tumor progression, ↓tumor growth	[122]
Ovary	SKOV3 tumor-bearing nude mice	CPT-loaded NOBs	0.5 mg/kg for 25 days	↓Tumor suppression, ↓tumor growth, ↓tumor volumes	[123]
Pancreas	BxPC-3 tumor-bearing mice	GSHPTCPT, EGGTCPT, and PEGTCPT	10 mg/kg for 12 h–14 days	↓Tumor progression, ↓Tumor growth	[124]
Pancreas	PANC-1 and MIA PaCa-2 xenografts in SCID mice	CPT-loaded nude NPs and CPT-loaded αDR5-NPs	2 mg/kg for 30 days	↑Tumor regressions, ↓tumor growth	[125]
Pancreas	PANC-1 tumor-bearing nude mice	DPPSC + LL, and DPPSC + SL	5 mg/kg for 3–42 days	↓Tumor size, ↓tumor growth, ↑therapeutic efficacy	[126]
Prostate	U14 tumor-bearing mice	CPT-HA and CPT-HA@IR825	1 mg/mL for 12 days	↑Tumor elimination, ↓tumor progression, ↓tumor growth, ↓tumor volume	[127]
Prostate	DU145 tumor-bearing nude mice	P(OEGMA-co-CPT-co-G3-Cl2) or P(OEGMA-co-CPT)	0.8 mg/kg for 32 days	↓Tumor size, ↑tumor elimination, ↓tumor progression, ↓tumor growth	[128]
Skin (Melanoma)	B16 tumor-bearing nude mice	PEG-SeSe-CPT and PEG-SeSe-CPT/CUR	9.8–10 mg for 21 days	↑Tumor elimination, ↓tumor growth, ↑synergistic therapy effect	[129]

Symbols: ↓, reduction or decrease; ↑, increase.

3.1. Bladder Cancer

Bladder cancer is the tenth most frequent cancer in women and fourth in men. The primary treatment for bladder cancer includes intravesical immunotherapy and surgery. Nevertheless, these methods show several undesirable adverse effects [130,131]. Accordingly, better therapeutic approaches are vital.

Polymeric micelles enhance the drug accumulation in cancer tissues by taking advantage of the increased permeability retention (EPR) impact [132]. In a study by Yen et al. [49], strong suppression of tumor growth without toxicity was observed in the nude mice bearing AY27 xenografts after treatment with CPT-loaded micelles. Moreover, as a wide variety of therapeutic agents could be incorporated inside polymeric micelles, designing the sensitive-reduction micelles could be readily custom-made to accomplish therapeutic necessities.

3.2. Brain Cancer

Gliomas are the most frequent and aggressive brain tumors, and irrespective of progress made in treatment management, they are still limited by several barriers. Therefore, different therapeutic strategies like nano-medicines are needed for treating this disease [133,134].

One study indicated that treatment of 9L tumor-bearing mice with CPT-loaded amphiphilic β -cyclodextrin NPs inhibited tumor progression and tumor volume, and increased the median survival time. This study indicated that CPT-loaded cyclodextrin NPs arise as potential delivery systems for treating cancer which is indicated to be safe, stable, and effective formulations for CPT delivery [50].

It has been shown that high-dose CPT-loaded NPs (20 mg/kg) inhibited the growth of intracranial GL261 tumors in mice, providing important survival benefits in comparison to low-dose CPT NPs or free CPT [51]. This study indicated that CPT encapsulation can increase its activity.

Another study evaluated the anticancer effect of 3 mg/kg CPD@IR780 and CPC@IR780 micelles with or without laser toward Luc-U87 tumor-bearing mice. All the treatments inhibited tumor growth, reduced side effects, and enhanced survival time. However, CPT-S-S-PEG-iRGD@IR780 micelles with laser exhibited superior antitumor activity. Thus, these results indicated that the targeting prodrug system could not only efficiently cross different barriers to reach glioma site but also considerably increase the anticancer impact with laser [52].

Studies showed that treatment of C6 tumor-bearing rats with different CPT-loaded micelles inhibited tumor progression and growth, reduced side effects, and increased median survival rate and therapeutic efficacy [53,54]. Moreover, CPT-TEG-ALA treatment inhibited tumor growth and enhanced the survival rates and therapeutic efficacy in U-87 MG tumor-bearing nude mice. This nano-prodrug method is a versatile approach to develop therapeutic NPs enabling tumor-specific treatment [55]. The non-toxic, tumor-specific targeting properties of the nano-prodrug system make it a versatile, low-cost, and safe nano-carrier for diagnostic agents, imaging agents, and pharmaceuticals.

3.3. Breast Cancer

Breast cancer is the utmost frequently diagnosed malignancy and is the second primary cause of mortality globally. Despite these improvements, breast cancer mortality and morbidity is very high [135]. Therefore, the application of novel methods like nanotherapies is essential for the prevention and treatment of this cancer [136].

One study indicated that in 4T1 tumor-bearing mice, the albumin/CPT-ss-EB nano-complex exhibited efficient tumor accumulation, which subsequently contributed to outstanding therapeutic efficiency [56]. In a study by Zhang [137], the MOF-2 + CPT therapeutic impact was evaluated. The result of this study demonstrated that both CPT and MOF-2 can suppress tumor growth in the mouse breast cancer model. After the combination of CPT with MOF-2, the therapeutic efficiency was noticeably improved.

Several studies showed that treatment of 4T1 tumor-bearing mice with different CPT-loaded micelles (FP-CPT, DCPT, HA-ss-CPT, DCM, and DEM micelles) inhibited the tumor growth and tumor progression and resulted in enhancement of animal survival rate and therapeutic efficacy [57–60]. PM_{CPT}-co-electrospun fibers showed anticancer activity toward 4T1 tumor-bearing mice and led to the suppression of the tumor growth without toxicity [61].

Studies indicated that treating 4T1 tumor-bearing mice with various CPT-loaded NPs led to the suppression of tumor growth and reduction in tumor metastases and tumor recurrence [62–64]. Moreover, it has been shown that treatment with AmpF-CPT-IR820 (ACI), and PF + CPT + IR820 (PCI) inhibited tumor growth and volume in 4T1 breast tumor-bearing mice [65].

Treating 4T1 tumor-bearing mice with chitosan stabilized CPT nano-emulsions (CHI-CPT-NEs) led to the reduction of tumor growth and volume and enhancement of therapeutic efficacy [66]. Additionally, it has been shown that treatment with 1 mg/kg MDNCs suppressed tumor progression and tumor growth in 4T1 tumor-bearing mice and exhibited superior anticancer impact in comparison to individual drug treatment groups and free multi-drugs treatment groups [67].

In another study, the *in vivo* synergistic antitumor efficiency of HSD NGs was assessed in 4T1 tumor-bearing mice, and results indicated that HSD NGs enhanced apoptosis and tumor accumulation, and suppressed tumor growth and volume [68].

Treating MCF-7 tumor-bearing mice with various CPT-loaded micelles led to the strong inhibition of the tumor growth without toxicity [69–71]. Moreover, treatment with 10 mg/kg CPT@Ru-CD, VK3-CPT@Ru-CD, and VK3-CPT@RuxCD led to the tumor elimination, increased ROS levels and reduced side effects in MCF-7 tumor-bearing nude mice [72].

Several studies showed that treatment with different CPT-loaded nano-formulations led to tumor elimination and inhibited tumor growth and volume in MCF-7 tumor-bearing mice [73–76]. Moreover, CPT-loaded MrGO-AA-g-4-HC increased the synergistic antitumor efficacy and apoptosis in rats bearing MCF-7 tumor cells [77]. Another study showed that treating MCF-7 tumor-bearing mice with GNS-CB[7]-CPT with or without laser resulted in the elimination of the tumor. It has been shown that GNS-CB[7]-CPT with laser irradiation exhibited severe necrosis and had a greater antitumor activity [78].

Studies showed that an increase in survival rate and tumor inhibition has been observed in MDA-MB-231 tumor-bearing mice after treatment with CPT-HGC NPs [79] and CPT-P-HA-NPs [80]. Moreover, treating MDA-MB-231BO tumor-bearing mice with 7.5 mg/kg pSiNP + CPT + Ab and pSiNP + CPT led to the reduction in tumor size and inhibition of metastatic spread [81]. Another study showed that treating MDA-MB-231 tumor-bearing mice after treatment with CPT-pH-PMs, led to strong suppression of the tumor growth and reduction in side effects [82].

Treatment of EMT6 tumor-bearing mice with 1 mg/kg CPT/DOX-CCM and CPT/DOX-NCM, for 24 days led to tumor inhibition and reduced tumor size and volume [83]. CPT-loaded NPs (CPT^TNV-P_{mic}) exhibited considerable anticancer activities against the Ehrlich ascites carcinoma (EAC) mice model and reduced tumor necrosis and tumor growth [84]. In another study, the anticancer efficacy of CPT excipient formulation and CPT encapsulated in E₃ PA nanofibers was assessed in BT-474 tumor-bearing athymic nude mice, and results demonstrated that these nanofibers inhibited tumor growth and tumor progression [85]. Such nano-structures provided CPT protection from the external environment and increased CPT anticancer activity.

3.4. Cervical Cancer

Cervical cancer is the second highest cause of mortality amongst women [138]. Even though chemotherapy is the primary method for the treatment of cervical cancer, new approaches are essential for the enhancement of the efficacy of existing cervical cancer therapy [139].

Studies showed that treatment with different CPT-loaded NPs (CPT@IrS_x-PEG-FA NPs and PDA@PCPT NPs) led to the suppression of tumor progression and tumor growth and increased the therapeutic efficiency in HeLa tumor-bearing mice [86,87]. Moreover, another study showed that treating HeLa tumor-bearing mice with 4 mg/kg CPT-PCB-based lipoplexes inhibited tumor progression and tumor growth, and displayed a synergistic tumor inhibition [88].

In a study by Jiang et al. [89], the synergistic effect of RLS/siPLK1+ CPT on tumor growth suppression was evaluated in HeLa tumor-bearing nude mice. Results of this study indicated that RLS/siPLK1+ CPT has a greater anticancer activity compared to either agent alone. These data indicate that R₂SC/siPLK1 can efficiently inhibit tumor growth via silencing the siPLK1 gene and controlling the drug release and through inducing tumor cells apoptosis, contributing to a synergistic impact of siPLK1 and CPT.

In another study, the antitumor efficiency of CPT-DNS-DCM was examined on HeLa tumor-bearing nude mice. Results indicated that the prodrug considerably inhibited tumor growth and tumor progression [91]. Moreover, treating HeLa tumor-bearing nude mice with EuGd-SS-CPT-FA-MSNs led to the destruction of tumors and reduction of tumor growth and volume. EuGd-SS-CPT-FA-MSNs might offer a beneficial theranostic nano-platform for inhibiting tumor growth in vivo [90]. The results of in vivo studies indicate that the functionalized MSNs might be effectively used as a platform for targeted therapy.

3.5. Colon Cancer

Colorectal cancer (CRC) is one of the utmost common malignant tumors. The main approaches for the treatment of CRC are surgery, chemotherapy, and radiotherapy [140]. Yet, due to the difficulties resulting from drug resistance, the application of multifunctional nano-medicines could be a viable therapeutic approach [140].

One study showed that transformative CPT-ss-EB nanomedicine considerably suppressed tumor progression and drastically decreased side effects in HCT116 tumor-bearing mice [56]. Another study showed that treatment of SW620 tumor-bearing nude mice with 10 mg/kg CPT-loaded CMD NPs for 30 days resulted in the suppression of tumor growth and progression. CPT-loaded CMD NPs showed considerably higher antitumor activity than free CPT and empty CMD NPs in mouse xenograft models, indicating the synergistic therapeutic impacts of CPT with CMD [92].

In one study the antitumor activity of CPT&Ce6 and HBPTK-Ce6@CPT with or without laser irradiation in HT29 tumor-bearing nude mice has been evaluated. All the treatments inhibited tumor growth and volume. However, HBPTK-Ce6@CPT with 660 nm laser irradiation had greater anticancer activity in comparison to other groups [93].

Studies showed that treatment of HCT116 tumor-bearing mice with different CPT-loaded NPs resulted in the elimination of tumor, reduction of tumor growth and volume, tumor recurrence, and increase of therapeutic efficacy and apoptosis [94–97]. Moreover, HRC@F127 NPs indicated synergistic therapeutic efficiency and effectual tumor accumulation with minimal side effects and longer survival in mice [98].

Treatment of HT-29 tumor-bearing mice with 0.8 mg/kg SNP-CPT-Cy5.5 and SNP-CPT NPs led to the tumor elimination and inhibited tumor growth and progression, while considerably decreasing the systemic toxicity associated with CPT administration. These results demonstrate that the SNP-CPT NPs can be used as a potent drug delivery system for CPT-based anticancer treatments [99].

In a study by Yao et al. [100], the in vivo anticancer activity of nano-CPT compared with that of topotecan was assessed against HCT-8 tumor-bearing mice. Results indicated that nano-CPT had the same in vivo anticancer activity with TPT and lower toxicity. The study indicated that nano-CPT is a new promising formulation with high anticancer efficiency and low toxicity [100].

Gd(DTPA-CPT) NPs showed significant cytotoxicity against LoVo tumor-bearing nude mice and led to the tumor growth suppression with reduced adverse effects and insignificant chronic toxicity [101]. Another study showed that treatment with 3 mg/kg

CPT@Dod-ND-SPs led to suppression of tumor growth and tumor volume in HT-29 tumor-bearing mice. The results indicated that ND-SPs might serve as a nanomedicine with major therapeutic potential [102].

Several studies indicated that treating C26-tumor-bearing mice with different CPT nano-formulations resulted in the elimination of tumor growth and volume, enhancement of therapeutic efficacy, and reduction in tumor progression [103–106]. Furthermore, it has been shown that iRGD-PEG-NPs considerably increased the therapeutic efficiency of CPT via inducing tumor cell apoptosis in comparison to PEG-NPs [107]. These results indicate a promising approach for small molecular nano-drug delivery systems with noticeable antitumor efficacy for clinical applications.

3.6. Liver Cancer

Hepatocellular carcinoma (HCC) is the second leading cause of death in the world. Irrespective of the advancement in existing HCC treatments, there has been a continuous increment in the incidence rate of this cancer [141].

In a study by Wen et al. [108], the *in vivo* synergistic anticancer efficacy of MGO@CD-CA-HA/CPT with or without NIR was assessed in BEL-7402 tumor-bearing nude mice. Results showed that MGO@CD-CA-HA/CPT + NIR had a stronger inhibitory effect than MGO@CD-CA-HA/CPT, exhibiting the meliority of CPT combination therapy. Thus, this study presented a potent multiple-targeted nanocarrier for liver cancer chemo-photothermal combination therapy.

Moreover, studies showed that treatment with different CPT prodrugs (CCLM and RGD-prodrug) led to tumor elimination and suppressing tumor progression and growth in HepG2 and H22 tumor-bearing mice [109,110]. These prodrug nano-platforms showed considerable *in vivo* anticancer efficacy, without displaying considerable systemic toxicity.

In one study the antitumor activity of IR780-LA/CPT-ss-CPT NPs were investigated towards Hep1–6 tumor-bearing mice. It was noticed that the tumor volume and growth in all groups were suppressed. Nevertheless, the tumor growth in the IR780-LA/CPT-ss-CPT NPs + laser group was the most strictly suppressed. Consequently, the IR780-LA/CPT-ss-CPT NPs were indicated to be a brilliant fluorescence imaging-guided, redox-responsive, and increased synergistic chemo-photothermal therapy nanopatform toward tumors [111].

Treatment of HepG2 tumor-bearing mice with P (CPT-MAA) nanogels without SeS and P(CPT-MAA) prodrug nanogels exhibited superior antitumor activity without observed side effects. However, P(CPT-MAA) prodrug nanogels indicated the greatest efficacy in tumor growth suppression. Henceforth, the P(CPT-MAA) nanogels might be a potent delivery system for anticancer agents [112].

JP@EF and JNM@EF showed cytotoxic effects against H22 tumor-bearing mice, while the most considerable suppression of tumor growth was identified for JNM@EF treatment. It was demonstrated that the JNMs self-propelled tissue distribution and gradual release increased the tumor growth suppression [113].

In another study, the anticancer effects of UCNP@mSiO₂-NBCCPT@(DHMA)/β-CD-PEG, UCNP@mSiO₂-NBCCPT@(DHMA)/β-CD-PEG-LA, and UCNP@mSiO₂-NBCCPT/β-CD-PEG were assessed in HepG2 tumor-bearing mice. All the treatments inhibited tumor growth, while UCNP@mSiO₂-NBCCPT/β-CD-PEG-LA@DHMA had greater antitumor activity and ameliorated side effects. Therefore, it showed more beneficial for prolonging the survival of tumor-bearing mice [114]. Overall, the results indicated that the nano-drug delivery systems have the ability to overwhelming the CPT pharmacokinetic limitations, highlighting its anticancer effects.

3.7. Lung Cancer

Lung cancer is one of the leading causes of tumor-related mortality in the world [142]. The high lung cancer death rates are probably because of difficulties related to a high metastatic potential and diagnosis [143]. Accordingly, developing non-toxic alternative treatments for improving lung cancer responsiveness to chemotherapy is essential.

Even though CPT is a renowned antitumor agent, it typically needs high and multiple doses for achieving a satisfactory therapeutic impact. One study investigated the antitumor impact of CPT-loaded PPBS NPs in LLC tumor-bearing mice. Results of this study indicated that CPT-loaded PPBS NPs reduced the tumor volume and had a longer circulation time, and substantially improved anticancer efficiency *in vivo* compared to free CPT [115].

NCssG NPs and CPT-ss-GEM nanowires (CsgG NWs) showed cytotoxic effects against A549 tumor-bearing mice and suppressed tumor growth and volume. Results also showed that with the same amount of CPT-ss-GEM prodrug, NCssG NPs showed much higher *in vivo* tumor inhibition efficiency than CsgG NWs. Due to the superiority of this combination, such as EPR effect, synchronous dual drug action, prolonged blood circulation, very potent antitumor efficiency was achieved both *in vitro* and *in vivo* [116].

Studies showed that treatment of A549 tumor-bearing nude mice with different nanoformulations of CPT resulted in tumor elimination, reduction in tumor growth and volume, and enhancement of therapeutic efficacy [117,118]. These combination approaches hold great promise for the future potential application in cancer therapy.

Another study indicated that treatment with ZTC-NMs delayed tumor growth and prolonged the survival time in A549 tumor-bearing mice. Also these results showed that ZTC-NMs had a greater antitumor activity, which can be ascribed to the tumor-targeted drug delivery [119].

In one study the antitumor effect of Ce6-CPT-UCNPs with or without laser irradiation was evaluated in NCI-H460 tumor-bearing nude mice. Results showed that treatment with Ce6-CPT-UCNPs + laser irradiation inhibited tumor growth, tumor recurrence, and metastasis. In contrast, treatment with Ce6-CPT-UCNPs and no laser irradiation did not show antitumor activity, because CPT and Ce6 in the Ce6-CPT-UCNPs cannot be released out, and cannot eliminate cancer cells [120].

Treatment of NCI-H460 tumor-bearing nude mice with a new mitochondria-targeting drug delivery system, ZnPc/CPT-TPPNPs or ZnPc/CPT-NH₂NPs led to the suppression of tumor growth, tumor recurrence, and metastasis and did not result in considerable side effects *in vivo*. These results demonstrated that surface modification of the NPs with triphenylphosphine cations simplified effective subcellular delivery of the photosensitizer to mitochondria [121].

In another study, the *in vivo* anticancer efficiency of 2OA-CPT/NAs and OA-CPT/NAs was compared using the LLC tumor-bearing mice. It is found that treatments with different CPT formulations led to a considerably delayed tumor progression. However, in comparison with OA-CPT/NAs, 2OA-CPT/NA exhibited a greater potent anticancer activity. These results revealed the critical role of DHP hydrophobicity in impacting the DHP NA *in vivo* anticancer efficacy [122].

3.8. Ovarian Cancer

Ovarian cancer represents a group of neoplasms, and it is one of the utmost lethal female reproductive system tumors [144]. The conventional approaches for the treatment of this cancer are platinum-based chemotherapy and surgical cytoreduction, which have their challenges [145]. Consequently, investigating new agents with increased efficiency and reduced toxicity can open up new pathways for ovarian cancer treatment.

In one study CPT was encapsulated into plain NOBs (NOB-CPT) and ZH2-displayed NOBs (ZH-NOB-CPT) and then administered to SKOV3 tumor-bearing nude mice. Results showed that treatment with 0.5 mg/kg ZH-NOB-CPT significantly inhibited tumor growth and volume. In contrast, NOB-CPT-treated mice did not show any antitumor effects. This study indicates that ZH2-tagged NOBs selectively deliver CPT into the human epidermal growth factor receptor 2/neu-positive cancerous site. Taken together, the result shows the NOB's potential for targeted delivery of hydrophobic drugs [123].

3.9. Pancreatic Cancer

Pancreatic cancer is a disease with a high mortality rate and a very poor prognosis. Various biological and physical barriers make this tumor very hard to treat with conventional chemotherapy. Hence, more effective strategies, such as nano-therapies, are crucial to fulfill the immediate necessity for more effective pancreatic cancer treatment [146,147].

One study evaluated the therapeutic effects of EGGPTCPT, PEGPTCPT, and GSH-PTCPT in BxPC-3 tumor-bearing mice. All the treatments resulted in tumor inhibition, while GSHPTCPT displayed considerably greater anticancer activity than PEGPTCPT and EGGPTCPT. There was no considerable difference between PEGPTCPT and EGGPTCPT in terms of tumor weight and volume. This study indicates the high efficacy of an active tumor penetrating dendrimer-drug conjugate for PDA therapy [124].

Another study showed that treatment with 2 mg/kg CPT-loaded α DR5-NPs and CPT-loaded nude NPs noticeably suppressed tumor growth rates and induced tumor regressions in MIA PaCa-2 and PANC-1 xenografts in mice. The effects were more considerable in the MIA PaCa-2 cells where delivery of CPT-loaded α DR5-NPs resulted in considerable tumor regressions, whereas the CPT-loaded nude NPs only resulted in growth retardation. These results indicate the CPT-loaded α DR5-NPs potential for pancreatic cancer treatment [125].

In a study by Wang et al. [126], the DPPSC micelles *in vivo* anticancer efficiency were investigated in the pancreas cancer treatment. Results of this study showed that treatment of PANC-1 tumor-bearing nude mice with DPPSC + SL and DPPSC + LL micelles remarkably inhibited the tumor growth and tumor volume. Moreover, it has been demonstrated that the mice treated with the DPPSC + SL group led to a more significant reduction in the tumor growth, compared to the DPPSC + LL group. Hence, this system indicated a high anticancer impact in PANC-1 tumor-bearing mice because of the combination of PDT and enhanced chemotherapy. This study presents a novel approach for the design of the stepwise multiple stimuli-responsive nano-carrier with the variation of biological signals to maximize the treatment outcomes while minimizing the side effects of therapeutic agents.

3.10. Prostate Cancer

Prostate cancer is one of the most common cancers in men [148]. The combined consumption of nutraceutical agents and anticancer drugs is an excellent strategy to enhance the therapeutic antitumor effects as well as the facilitation of side effects of chemotherapy and drug resistance [149].

One study indicated that treatment of U14 tumor-bearing nude mice with CPT-HA and CPT-HA@IR825 with or without laser led to tumor elimination. *In vivo* results demonstrate that after treating tumors with CPT-HA or CPT-HA@IR825 without laser, the tumor volume was only partially inhibited. In sharp contrast, the tumor growth from the CPT-HA@IR825-treated mice upon laser irradiation has been effectively suppressed, indicating that the multifunctional polymeric prodrug NPs are very effective for cancer treatment, while having reduced cytotoxicity to the healthy organs [127].

Another study indicated that treatment with P(OEGMA-co-CPT-co-G3-C12) or P(OEGMA-co-CPT) for 32 days inhibited tumor volume and tumor growth in DU145 tumor-bearing BALB/c mice. Results of this study indicated that P(OEGMA-co-CPT-co-G3-C12) had a greater antitumor activity compared to P(OEGMA-co-CPT). Furthermore, P(OEGMA-co-CPT-co-G3-C12) indicated minimal toxicity and improved antitumor activity compared to free CPT. Henceforth, P(OEGMA-co-CPT-co-G3-C12) can be a potent drug in androgen-independent prostate cancer treatment [128].

3.11. Skin Cancer

Melanoma is the primary cause of death from skin cancer [150]. Generally, treating melanoma with chemotherapy provides very limited beneficial effects in overall survival and very low response rates. Consequently, multiple targeted therapeutic strategies have been assessed [151].

In a study by Hu et al. [129], nude mice bearing B16 tumor cells were treated with PEG-SeSe-CPT/CUR and PEG-SeSe-CPT for 21 days. In vivo assay showed that both of the treatments could inhibit B16 tumor growth and volume. This result also showed that the PEG-SeSe-CPT/CUR co-delivery system had a much better inhibition effect than either agent alone, suggesting a synergistic therapeutic effect.

4. Pharmacokinetics and Toxicity of Nano-Camptothecin

The plasma drug time-concentration profile of CPT was constructed after the oral administration of 5 mg/kg pure CPT suspension and CPT encapsulated poly (methacrylic acid-co-methyl methacrylate) nano-formulation to rats. The results demonstrated a considerable difference between the CPT nano-formulation and free CPT pharmacokinetic profiles. After oral administration of free CPT, the drug was detected rapidly in plasma in the initial hours, ascribed to the greater CPT permeability coefficient in the upper GIT. Subsequently, the drug-plasma concentration reduced rapidly to undetectable levels after 8 h. In the case of CPT nano-formulation, the maximum CPT level was reached at 12 h after oral administration as the polymer present in the nano-formulation enhanced the CPT residence time and then gradually reduced over the next 12 h, which demonstrated the released drug prolonged residence time in the colon with drug slow leaching to systemic circulation because of low permeability and compromised surface area [152,153].

After a single oral administration (1.5 mg/kg) of CPT and CPT nanocrystals in Sprague-Dawley rats, it was reported that in comparison to CPT salt solution, CPT nanocrystal's area under the curve (AUC) value was lower, but the distribution half-life ($t_{1/2\alpha}$) was higher, showing prolonged circulation via the nanocrystals. It seems to be plausible that due to the poor solubility, CPT nanocrystals gradually dissolved and released free drug molecules [154]. Therefore, concerning extending blood circulation, the CPT nanocrystals might provide considerable benefits [155].

For evaluating the subacute toxicity of CPT NPs, ICR mice were administered with 0.4 mL/20 g. body weight NPs through i.p. injection. There was no treatment-related death in the CPT NPs treated mice at any of the doses tested. Nevertheless, the free CPT group body weight was considerably lower than information from the control group and the two other CPT groups [156].

In an inorganic-organic model, CPT was primarily incorporated into micelles derived from negatively charged biocompatible surfactants, such as sodium cholate, and these negatively charged micelles were next encapsulated in NPs of magnesium-aluminum layered double hydroxides (LDHs) via an ion exchange process. Although these nano-complexes exhibited lower cytotoxicity than CPT alone, they act as a potent biocompatible model for delivering CPT, enabling the administration of drugs in a dose-controlled manner [157].

After CPT-loaded GNR@SiO₂-tLyP-1 treatment, the systemic toxicity of CPT on human mesenchymal stem cells was reduced, since the GNR@SiO₂-tLyP-1 selectively penetrated the cancer cells, and CPT was released into the blood or culture medium [158].

5. Conclusions and Future Directions

Natural products with remarkable chemical diversity have been examined in the treatment of human malignancies and particularly in cancer treatment. CPT, a natural plant alkaloid, has indicated strong antitumor activities via targeting intracellular Topo I. CPT alone or in combination with other anticancer drugs might be beneficial for cancer treatment. Studies indicated that CPT nano-formulations have higher antitumor activities in comparison to free CPT and lead to better bioefficacy for the treatment of cancer. CPT can affect different cancer types, including bladder, brain, breast, cervical, colon, leukemia, liver, lung, melanoma, and prostate cancer. It has been shown that CPT employs multiple mechanisms for suppressing cancer initiation, progression, and promotion through modulating different dysregulated signaling cascades implicated in proliferation, invasion, inflammation, cell survival, metastasis, and apoptosis (Figure 4).

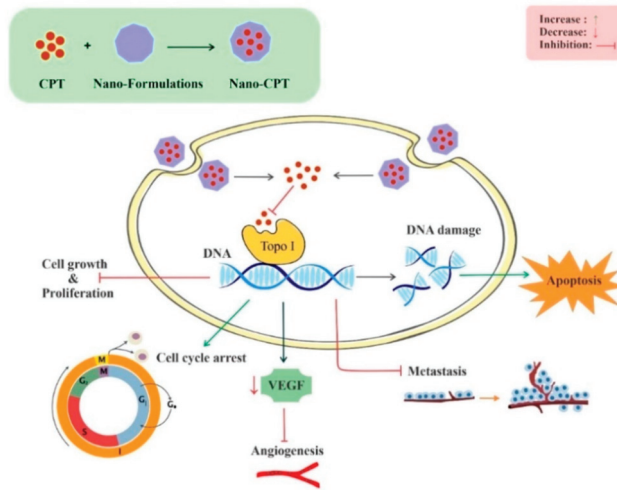


Figure 4. Molecular mechanisms underlying antitumor effects of CPT nano-formulations. Abbreviations: CPT, camptothecin; Topo I, topoisomerase I; VEGF, vascular endothelial growth factor.

The promise that CPT holds as an antitumor agent in therapy is restricted by factors that include lactone ring instability and water insolubility, which restricts the drug oral solubility and bioavailability in blood plasma. Novel approaches including pharmacological and low doses of CPT in combination with NPs have indicated potent anticancer potential in vivo. The results of our study indicate that CPT nano-formulations is a potential candidate for cancer treatment, and might provide further support for developing nano-CPT as a promising agent for cancer treatment.

Author Contributions: M.H.F. conceived and designed the study. M.G.-M. and M.H.F. collected and reviewed the literature as well as extracted and analyzed the data. M.G.-M. prepared the first draft of the manuscript and created the figures. M.G.-M. and M.H.F. collected additional literature, refined mechanistic figures, edited the manuscript. T.K. and A.M. edited the manuscript and suggested improvement. A.B. coordinated this project as well as reviewed the manuscript with final editing. All authors have read and agreed to the published version of the manuscript.

Funding: This research received no external funding.

Institutional Review Board Statement: Not applicable.

Informed Consent Statement: Not applicable.

Acknowledgments: M.G.-M. and M.H.F. are thankful to Pharmaceutical Sciences Research Center, Kermanshah University of Medical Sciences, Kermanshah, Iran, for providing the infrastructural supports for the study.

Conflicts of Interest: The authors declare no conflict of interest.

References

1. Hanahan, D.; Weinberg, R.A. Hallmarks of cancer: The next generation. *Cell* **2011**, *144*, 646–674. [CrossRef] [PubMed]
2. Seyfried, T.N.; Shelton, L.M. Cancer as a metabolic disease. *Nutr. Metab.* **2010**, *7*, 7. [CrossRef] [PubMed]
3. Newman, D.J.; Cragg, G.M. Natural Products as Sources of New Drugs over the Nearly Four Decades from 01/1981 to 09/2019. *J. Nat. Prod.* **2020**, *83*, 770–803. [CrossRef] [PubMed]
4. Cragg, G.M.; Pezzuto, J.M. Natural products as a vital source for the discovery of cancer chemotherapeutic and chemopreventive agents. *Med. Princ. Pract.* **2016**, *25*, 41–59. [CrossRef]
5. Newman, D.J.; Cragg, G.M. Natural products as sources of new drugs over the 30 years from 1981 to 2010. *J. Nat. Prod.* **2012**. [CrossRef]
6. Bishayee, A.; Sethi, G. Bioactive natural products in cancer prevention and therapy: Progress and promise. *Semin. Cancer Biol.* **2016**, *75*, 311–335. [CrossRef]

7. Mondal, A.; Gandhi, A.; Fimognari, C.; Atanasov, A.G.; Bishayee, A. Alkaloids for cancer prevention and therapy: Current progress and future perspectives. *Eur. J. Pharmacol.* **2019**, *858*, 172472. [CrossRef]
8. Habli, Z.; Toumeh, G.; Fatfat, M.; Rahal, O.N.; Gali-Muhtasib, H. Emerging cytotoxic alkaloids in the battle against cancer: Overview of molecular mechanisms. *Molecules* **2017**, *22*, 250. [CrossRef]
9. Cragg, G.M.; Newman, D.J. Plants as a source of anti-cancer agents. *J. Ethnopharmacol.* **2005**, *100*, 72–79. [CrossRef]
10. Gunasekera, S.P.; Cordell, G.; Farnsworth, N.R. Anticancer indole alkaloids of *Ervatamia heyneana*. *Phytochemistry* **1980**, *19*, 1213–1218. [CrossRef]
11. Davies, S.L.; Ferrer, E.; Moral, M.A. Chronicles in drug discovery. *Drug News Perspect.* **2006**, *19*, 295–298.
12. Bertino, J.R. Irinotecan for colorectal cancer. *Semin Oncol.* **1997**, *24*, S18–S23.
13. Hertzberg, R.P.; Caranfa, M.J.; Hecht, S.M. On the mechanism of topoisomerase I inhibition by camptothecin: Evidence for binding to an enzyme-DNA complex. *Biochemistry* **1989**, *28*, 4629–4638. [CrossRef]
14. Pommier, Y. DNA topoisomerase I inhibitors: Chemistry, biology, and interfacial inhibition. *Chem. Rev.* **2009**, *109*, 2894–2902. [CrossRef]
15. Pommier, Y. Topoisomerase I inhibitors: Camptothecins and beyond. *Nat. Rev. Cancer* **2006**, *6*, 789–802. [CrossRef]
16. D'yakov, V.A.; Dzhemileva, L.U.; Dzhemilev, U.M. Advances in the chemistry of natural and semisynthetic topoisomerase I/II inhibitors. *Stud. Nat. Prod. Chem.* **2017**, *54*, 21–86. [CrossRef]
17. Pommier, Y.; Cushman, M. The indenisoquinoline noncamptothecin topoisomerase I inhibitors: Update and perspectives. *Mol. Cancer Ther.* **2009**, *8*, 1008–1014. [CrossRef]
18. Staker, B.L.; Feese, M.D.; Cushman, M.; Pommier, Y.; Zembower, D.; Stewart, L.; Burgin, A.B. Structures of three classes of anticancer agents bound to the human topoisomerase I–DNA covalent complex. *J. Med. Chem.* **2005**, *48*, 2336–2345. [CrossRef]
19. Creaven, P.J.; PJ, C.; FM, M. Plasma camptothecin (NSC-100880) levels during a 5-day course of treatment: Relation to dose and toxicity. *Cancer Chemother. Rep.* **1972**, *56*, 573–578.
20. Cheng, J.; Khin, K.T.; Davis, M.E. Antitumor activity of β -Cyclodextrin polymer-camptothecin conjugates. *Mol. Pharm.* **2004**, *1*, 183–193. [CrossRef]
21. Orza, A.; Casciano, D.; Biris, A. Nanomaterials for targeted drug delivery to cancer stem cells. *Drug Metab. Rev.* **2014**, *46*, 191–206. [CrossRef] [PubMed]
22. Feng, L.; Mumper, R.J. A critical review of lipid-based nanoparticles for taxane delivery. *Cancer Lett.* **2013**, *334*, 157–175. [CrossRef] [PubMed]
23. Lagoa, R.; Silva, J.; Rodrigues, J.R.; Bishayee, A. Advances in phytochemical delivery systems for improved anticancer activity. *Biotechnol. Adv.* **2020**, *38*, 107382. [CrossRef] [PubMed]
24. Kashyap, D.; Tuli, H.S.; Yerer, M.B.; Sharma, A.; Sak, K.; Srivastava, S.; Pandey, A.; Garg, V.K.; Sethi, G.; Bishayee, A. Natural product-based nanoformulations for cancer therapy: Opportunities and challenges. *Semin. Cancer Biol.* **2019**, *69*, 5–23. [CrossRef]
25. Davatgaran-Taghipour, Y.; Masoomzadeh, S.; Farzaei, M.H.; Bahramsoltani, R.; Karimi-Soureh, Z.; Rahimi, R.; Abdollahi, M. Polyphenol nanoformulations for cancer therapy: Experimental evidence and clinical perspective. *Int. J. Nanomed.* **2017**, *12*, 2689. [CrossRef]
26. Gokduman, K. Strategies targeting DNA topoisomerase I in cancer chemotherapy: Camptothecins, nanocarriers for camptothecins, organic non-camptothecin compounds and metal complexes. *Curr. Drug Targets* **2016**, *17*, 1928–1939. [CrossRef]
27. Islam, M.T. Diterpenes and their derivatives as potential anticancer agents. *Phyther. Res.* **2017**, *31*, 691–712. [CrossRef]
28. Pascolutti, M.; Quinn, R.J. Natural products as lead structures: Chemical transformations to create lead-like libraries. *Drug Discov. Today* **2014**, *19*, 215–221. [CrossRef]
29. Ghanbari-Movahed, M.; Jackson, G.; Farzaei, M.H.; Bishayee, A. A Systematic Review of the Preventive and Therapeutic Effects of Naringin against Human Malignancies. *Front. Pharmacol.* **2021**, *12*, 250. [CrossRef]
30. Sak, K. Cytotoxicity of dietary flavonoids on different human cancer types. *Pharmacogn. Rev.* **2014**, *8*, 122. [CrossRef]
31. Newman, D.J.; Cragg, G.M. Natural products as sources of new drugs from 1981 to 2014. *J. Nat. Prod.* **2016**, *79*, 629–661. [CrossRef]
32. JC Furtado, N.A.; Pirson, L.; Edelberg, H.; Miranda, L.M.; Loira-Pastoriza, C.; Preat, V.; Larondelle, Y.; André, C.M. Pentacyclic triterpene bioavailability: An overview of in vitro and in vivo studies. *Molecules* **2017**, *22*, 400. [CrossRef]
33. Rahman, M.; Beg, S.; Ahmed, A.; Swain, S. Emergence of functionalized nanomedicines in cancer chemotherapy: Recent advancements, current challenges and toxicity considerations. *Recent Pat. Nanomed.* **2013**, *3*, 128–139. [CrossRef]
34. Williams, J.; Lansdown, R.; Sweitzer, R.; Romanowski, M.; LaBell, R.; Ramaswami, R.; Unger, E. Nanoparticle drug delivery system for intravenous delivery of topoisomerase inhibitors. *J. Control. Release* **2003**, *91*, 167–172. [CrossRef]
35. Martínez, A.; Benito-Miguel, M.; Iglesias, I.; Teijón, J.M.; Blanco, M.D. Tamoxifen-loaded thiolated alginate-albumin nanoparticles as antitumor drug delivery systems. *J. Biomed. Mater. Res. Part A* **2012**, *100*, 1467–1476. [CrossRef]
36. Lamb, Y.N.; Scott, L.J. Liposomal irinotecan: A review in metastatic pancreatic adenocarcinoma. *Drugs* **2017**, *77*, 785–792. [CrossRef]
37. Zhuang, X.; Deng, Z.-B.; Mu, J.; Zhang, L.; Yan, J.; Miller, D.; Feng, W.; McClain, C.J.; Zhang, H.-G. Ginger-derived nanoparticles protect against alcohol-induced liver damage. *J. Extracell. Vesicles* **2015**, *4*, 28713. [CrossRef]
38. Gunasekera, S.P.; Badawi, M.M.; Cordell, G.A.; Farnsworth, N.R.; Chitnis, M. Plant anticancer agents X. isolation of camptothecin and 9-methoxycamptothecin from *Ervatamia heyneana*. *J. Nat. Prod.* **1979**, *42*, 475–477. [CrossRef]
39. Govindachari, T.R.; Viswanathan, N. Alkaloids of *Mappia foetida*. *Phytochemistry* **1972**, *11*, 3529–3531. [CrossRef]

40. Aimi, N.; Hoshino, H.; Nishimura, M.; Sakai, S.; Haginiwa, J. Chaboside, first natural glycoamptothecin found from *Ophiorrhiza pumila*. *Tetrahedron Lett.* **1990**, *31*, 5169–5172. [CrossRef]
41. Wall, M.E.; Wani, M.C.; Cook, C.E.; Palmer, K.H.; McPhail, A.T.; Sim, G.A. Plant antitumor agents. I. The isolation and structure of camptothecin, a novel alkaloidal leukemia and tumor inhibitor from *camptotheca acuminata* 1, 2. *J. Am. Chem. Soc.* **1966**, *88*, 3888–3890. [CrossRef]
42. Cai, J.-C.; Hutchinson, C.R. Camptothecin. In *The Alkaloids: Chemistry and Pharmacology*; Elsevier: Amsterdam, The Netherlands, 1983; Volume 21, pp. 101–137. [CrossRef]
43. Hsiang, Y.-H.; Liu, L.F. Identification of mammalian DNA topoisomerase I as an intracellular target of the anticancer drug camptothecin. *Cancer Res.* **1988**, *48*, 1722–1726. [PubMed]
44. Li, Q.-Y.; Zu, Y.-G.; Shi, R.-Z.; Yao, L.-P. Review camptothecin: Current perspectives. *Curr. Med. Chem.* **2006**, *13*, 2021–2039. [CrossRef] [PubMed]
45. Soepenbergh, O.; Sparreboom, A.; Verweij, J. Clinical studies of camptothecin and derivatives. *Alkaloids Chem. Biol.* **2003**, *60*, 1–50. [CrossRef] [PubMed]
46. Adams, V.R.; Burke, T.G. *Camptothecins in Cancer Therapy*; Springer: Berlin/Heidelberg, Germany, 2005; ISBN 1592598668. [CrossRef]
47. Kacprzak, K.M. Chemistry and biology of camptothecin and its derivatives. In *Natural Products*; Springer: Berlin/Heidelberg, Germany, 2013; pp. 643–682. [CrossRef]
48. Moher, D.; Liberati, A.; Tetzlaff, J.; Altman, D.G.; Group, P. Preferred reporting items for systematic reviews and meta-analyses: The PRISMA statement. *PLoS Med.* **2009**, *6*, e1000097. [CrossRef] [PubMed]
49. Yen, H.C.; Cabral, H.; Mi, P.; Toh, K.; Matsumoto, Y.; Liu, X.; Koori, H.; Kim, A.; Miyazaki, K.; Miura, Y.; et al. Light-induced cytosolic activation of reduction-sensitive camptothecin-loaded polymeric micelles for spatiotemporally controlled in vivo chemotherapy. *ACS Nano* **2014**, *8*, 11591–11602. [CrossRef] [PubMed]
50. Çirpanlı, Y.; Allard, E.; Passirani, C.; Bilensoy, E.; Lemaire, L.; Çalıř, S.; Benoit, J.-P. Antitumoral activity of camptothecin-loaded nanoparticles in 9L rat glioma model. *Int. J. Pharm.* **2011**, *403*, 201–206. [CrossRef]
51. Householder, K.T.; DiPerna, D.M.; Chung, E.P.; Wohlleb, G.M.; Dhruv, H.D.; Berens, M.E.; Sirianni, R.W. Intravenous delivery of camptothecin-loaded PLGA nanoparticles for the treatment of intracranial glioma. *Int. J. Pharm.* **2015**, *479*, 374–380. [CrossRef]
52. Lu, L.; Zhao, X.; Fu, T.; Li, K.; He, Y.; Luo, Z.; Dai, L.; Zeng, R.; Cai, K. An iRGD-conjugated prodrug micelle with blood-brain-barrier penetrability for anti-glioma therapy. *Biomaterials* **2020**, *230*, 119666. [CrossRef]
53. Kanazawa, T.; Taki, H.; Okada, H. Nose-to-brain drug delivery system with ligand/cell-penetrating peptide-modified polymeric nano-micelles for intracerebral gliomas. *Eur. J. Pharm. Biopharm.* **2020**, *152*, 85–94. [CrossRef]
54. Taki, H.; Kanazawa, T.; Akiyama, F.; Takashima, Y.; Okada, H. Intranasal delivery of camptothecin-loaded tat-modified nanomicrospheres for treatment of intracranial brain tumors. *Pharmaceuticals* **2012**, *5*, 1092–1102. [CrossRef]
55. Lee, B.S.; Amano, T.; Wang, H.Q.; Pantoja, J.L.; Yoon, C.W.; Hanson, C.J.; Amatya, R.; Yen, A.; Black, K.L.; Yu, J.S. Reactive oxygen species responsive nanoprodrug to treat intracranial glioblastoma. *ACS Nano* **2013**, *7*, 3061–3077. [CrossRef]
56. Zhang, F.; Zhu, G.; Jacobson, O.; Liu, Y.; Chen, K.; Yu, G.; Ni, Q.; Fan, J.; Yang, Z.; Xu, F.; et al. Transformative Nanomedicine of an Amphiphilic Camptothecin Prodrug for Long Circulation and High Tumor Uptake in Cancer Therapy. *ACS Nano* **2017**, *11*, 8838–8848. [CrossRef]
57. Chen, M.; Zhang, Y.; Chen, Z.; Xie, S.; Luo, X.; Li, X. Synergistic antitumor efficacy of redox and pH dually responsive micelleplexes for co-delivery of camptothecin and genes. *Acta Biomater.* **2017**, *49*, 444–455. [CrossRef]
58. Zhang, T.; Ma, X.; Bai, S.; Wang, Y.; Zhang, X.; Lu, Y.; Wen, F.; Xue, P.; Kang, Y.; Xu, Z. Reactive oxygen species-activatable camptothecin polyprodrug based dextran enhances chemotherapy efficacy by damaging mitochondria. *J. Mater. Chem. B* **2020**, *8*, 1245–1255. [CrossRef]
59. Chen, Z.; He, N.; Chen, M.; Zhao, L.; Li, X. Tunable conjugation densities of camptothecin on hyaluronic acid for tumor targeting and reduction-triggered release. *Acta Biomater.* **2016**, *43*, 195–207. [CrossRef]
60. Luo, X.; Chen, M.; Zhang, Y.; Chen, Z.; Li, X. Pharmacokinetics and antitumor efficacy of micelles assembled from multiarmed amphiphilic copolymers with drug conjugates in comparison with drug-encapsulated micelles. *Eur. J. Pharm. Biopharm.* **2016**, *98*, 9–19. [CrossRef]
61. Luo, X.; Chen, M.; Chen, Z.; Xie, S.; He, N.; Wang, T.; Li, X. An implantable depot capable of in situ generation of micelles to achieve controlled and targeted tumor chemotherapy. *Acta Biomater.* **2018**, *67*, 122–133. [CrossRef]
62. Hao, X.; Gai, W.; Wang, L.; Zhao, J.; Sun, D.; Yang, F.; Jiang, H.; Feng, Y. 5-Boronopicolinic acid-functionalized polymeric nanoparticles for targeting drug delivery and enhanced tumor therapy. *Mater. Sci. Eng. C* **2020**, *119*, 111553. [CrossRef]
63. Hao, L.; Zhou, Q.; Piao, Y.; Zhou, Z.; Tang, J.; Shen, Y. Albumin-binding prodrugs via reversible iminoboronate forming nanoparticles for cancer drug delivery. *J. Control. Release* **2020**, *330*, 362–371. [CrossRef]
64. Raja, S.T.K.; Prakash, T.; Gnanamani, A. Redox responsive albumin autogenic nanoparticles for the delivery of cancer drugs. *Colloids Surf. B Biointerfaces* **2017**, *152*, 393–405. [CrossRef]
65. Cheng, Z.; Cheng, Y.; Chen, Q.; Li, M.; Wang, J.; Liu, H.; Li, M.; Ning, Y.; Yu, Z.; Wang, Y. Self-assembly of pentapeptides into morphology-adaptable nanomedicines for enhanced combinatorial chemo-photodynamic therapy. *Nano Today* **2020**, *33*, 100878. [CrossRef]

66. Natesan, S.; Sugumaran, A.; Ponnusamy, C.; Thiagarajan, V.; Palanichamy, R.; Kandasamy, R. Chitosan stabilized camptothecin nanoemulsions: Development, evaluation and biodistribution in preclinical breast cancer animal mode. *Int. J. Biol. Macromol.* **2017**, *104*, 1846–1852. [CrossRef]
67. Zhou, M.; Zhang, X.; Yang, Y.; Liu, Z.; Tian, B.; Jie, J.; Zhang, X. Carrier-free functionalized multidrug nanorods for synergistic cancer therapy. *Biomaterials* **2013**, *34*, 8960–8967. [CrossRef]
68. Lu, Y.; Jia, D.; Ma, X.; Liang, M.; Hou, S.; Qiu, W.; Gao, Y.; Xue, P.; Kang, Y.; Xu, Z. Reduction-Responsive Chemo-Capsule-Based Prodrug Nanogel for Synergistic Treatment of Tumor Chemotherapy. *ACS Appl. Mater. Interfaces* **2021**, *13*, 8940–8951. [CrossRef]
69. Bai, S.; Jia, D.; Ma, X.; Liang, M.; Xue, P.; Kang, Y.; Xu, Z. Cylindrical polymer brushes-anisotropic unimolecular micelle drug delivery system for enhancing the effectiveness of chemotherapy. *Bioact. Mater.* **2021**, *6*, 2894–2904. [CrossRef]
70. Bai, S.; Ma, X.; Shi, X.; Shao, J.; Zhang, T.; Wang, Y.; Cheng, Y.; Xue, P.; Kang, Y.; Xu, Z. Smart Unimolecular Micelle-Based Polyprodrug with Dual-Redox Stimuli Response for Tumor Microenvironment: Enhanced in Vivo Delivery Efficiency and Tumor Penetration. *ACS Appl. Mater. Interfaces* **2019**, *11*, 36130–36140. [CrossRef]
71. Ma, X.; Bai, S.; Zhang, X.; Ma, X.; Jia, D.; Shi, X.; Shao, J.; Xue, P.; Kang, Y.; Xu, Z. Enhanced tumor penetration and chemotherapy efficiency by covalent self-assembled nanomicelle responsive to tumor microenvironment. *Biomacromolecules* **2019**, *20*, 2637–2648. [CrossRef]
72. Yang, G.-G.; Zhang, H.; Zhang, D.-Y.; Cao, Q.; Yang, J.; Ji, L.-N.; Mao, Z.-W. Cancer-specific chemotherapeutic strategy based on the vitamin k3 mediated ros regenerative feedback and visualized drug release in vivo. *Biomaterials* **2018**, *185*, 73–85. [CrossRef]
73. Chen, K.-J.; Tang, L.; Garcia, M.A.; Wang, H.; Lu, H.; Lin, W.-Y.; Hou, S.; Yin, Q.; Shen, C.K.-F.; Cheng, J. The therapeutic efficacy of camptothecin-encapsulated supramolecular nanoparticles. *Biomaterials* **2012**, *33*, 1162–1169. [CrossRef]
74. Tang, X.-J.; Han, M.; Yang, B.; Shen, Y.-Q.; He, Z.-G.; Xu, D.-H.; Gao, J.-Q. Nanocarrier improves the bioavailability, stability and antitumor activity of camptothecin. *Int. J. Pharm.* **2014**, *477*, 536–545. [CrossRef] [PubMed]
75. Sun, R.; Luo, Q.; Li, X.; Huang, X.; Teng, L.; Shen, Z.; Zhu, W. Supramolecular PEGylation of Camptothecin for Cancer Therapy. *Mater. Today Nano* **2021**, *14*, 100115. [CrossRef]
76. Shi, X.; Hou, M.; Ma, X.; Bai, S.; Zhang, T.; Xue, P.; Zhang, X.; Liu, G.; Kang, Y.; Xu, Z. Starburst Diblock Polyprodrugs: Reduction-Responsive Unimolecular Micelles with High Drug Loading and Robust Micellar Stability for Programmed Delivery of Anticancer Drugs. *Biomacromolecules* **2019**, *20*, 1190–1202. [CrossRef] [PubMed]
77. Vinothini, K.; Rajendran, N.K.; Rajan, M.; Ramu, A.; Marraiki, N.; Elgorban, A.M. A magnetic nanoparticle functionalized reduced graphene oxide-based drug carrier system for a chemo-photodynamic cancer therapy. *New J. Chem.* **2020**, *44*, 5265–5277. [CrossRef]
78. Xu, P.; Feng, Q.; Yang, X.; Liu, S.; Xu, C.; Huang, L.; Chen, M.; Liang, F.; Cheng, Y. Near infrared light triggered cucurbit [7] uril-stabilized gold nanostars as a supramolecular nanoplatform for combination treatment of cancer. *Bioconjug. Chem.* **2018**, *29*, 2855–2866. [CrossRef]
79. Min, K.H.; Park, K.; Kim, Y.-S.; Bae, S.M.; Lee, S.; Jo, H.G.; Park, R.-W.; Kim, I.-S.; Jeong, S.Y.; Kim, K. Hydrophobically modified glycol chitosan nanoparticles-encapsulated camptothecin enhance the drug stability and tumor targeting in cancer therapy. *J. Control. Release* **2008**, *127*, 208–218. [CrossRef] [PubMed]
80. Choi, K.Y.; Yoon, H.Y.; Kim, J.H.; Bae, S.M.; Park, R.W.; Kang, Y.M.; Kim, I.S.; Kwon, I.C.; Choi, K.; Jeong, S.Y.; et al. Smart nanocarrier based on PEGylated hyaluronic acid for cancer therapy. *ACS Nano* **2011**, *5*, 8591–8599. [CrossRef]
81. Landgraf, M.; Lahr, C.A.; Kaur, I.; Shafiee, A.; Sanchez-Herrero, A.; Janowicz, P.W.; Ravichandran, A.; Howard, C.B.; Cifuentes-Rius, A.; McGovern, J.A.; et al. Targeted camptothecin delivery via silicon nanoparticles reduces breast cancer metastasis. *Biomaterials* **2020**, *240*, 119791. [CrossRef]
82. Min, K.H.; Kim, J.H.; Bae, S.M.; Shin, H.; Kim, M.S.; Park, S.; Lee, H.; Park, R.W.; Kim, I.S.; Kim, K.; et al. Tumoral acidic pH-responsive MPEG-poly(β -amino ester) polymeric micelles for cancer targeting therapy. *J. Control. Release* **2010**, *144*, 259–266. [CrossRef]
83. Zhai, S.; Hu, X.; Hu, Y.; Wu, B.; Xing, D. Visible light-induced crosslinking and physiological stabilization of diselenide-rich nanoparticles for redox-responsive drug release and combination chemotherapy. *Biomaterials* **2017**, *121*, 41–54. [CrossRef]
84. Malhotra, S.; Dumoga, S.; Joshi, A.; Mohanty, S.; Singh, N. Polymeric micelles coated with hybrid nanovesicles enhance the therapeutic potential of the reversible topoisomerase inhibitor camptothecin in a mouse model. *Acta Biomater.* **2021**, *121*, 579–591. [CrossRef] [PubMed]
85. Soukasene, S.; Toft, D.J.; Moyer, T.J.; Lu, H.; Lee, H.K.; Standley, S.M.; Cryns, V.L.; Stupp, S.I. Antitumor activity of peptide amphiphile nanofiber-encapsulated camptothecin. *ACS Nano* **2011**, *5*, 9113–9121. [CrossRef]
86. Zhang, D.Y.; Zheng, Y.; Zhang, H.; Yang, G.G.; Tan, C.P.; He, L.; Ji, L.N.; Mao, Z.W. Folate receptor-targeted theranostic IrS:X nanoparticles for multimodal imaging-guided combined chemo-photothermal therapy. *Nanoscale* **2018**, *10*, 22252–22262. [CrossRef] [PubMed]
87. Zhang, H.; Sun, Y.; Huang, R.; Cang, H.; Cai, Z.; Sun, B. pH-sensitive prodrug conjugated polydopamine for NIR-triggered synergistic chemo-photothermal therapy. *Eur. J. Pharm. Biopharm.* **2018**, *128*, 260–271. [CrossRef]
88. Li, Y.; Liu, R.; Yang, J.; Ma, G.; Zhang, Z.; Zhang, X. Dual sensitive and temporally controlled camptothecin prodrug liposomes codelivery of siRNA for high efficiency tumor therapy. *Biomaterials* **2014**, *35*, 9731–9745. [CrossRef]
89. Jiang, Q.; Chen, X.; Liang, H.; Nie, Y.; Jin, R.; Barz, M.; Yue, D.; Gu, Z. Multistage rocket: Integrational design of a prodrug-based siRNA delivery system with sequential release for enhanced antitumor efficacy. *Nanoscale Adv.* **2019**, *1*, 498–507. [CrossRef]

90. Chan, M.H.; Lin, H.M. Preparation and identification of multifunctional mesoporous silica nanoparticles for invitro and invivo dual-mode imaging, theranostics, and targeted tracking. *Biomaterials* **2015**, *46*, 149–158. [CrossRef]
91. Wang, Z.; Wu, H.; Liu, P.; Zeng, F.; Wu, S. A self-immolative prodrug nanosystem capable of releasing a drug and a NIR reporter for in vivo imaging and therapy. *Biomaterials* **2017**, *139*, 139–150. [CrossRef]
92. Yoo, W.; Yoo, D.; Hong, E.; Jung, E.; Go, Y.; Singh, S.V.B.; Khang, G.; Lee, D. Acid-activatable oxidative stress-inducing polysaccharide nanoparticles for anticancer therapy. *J. Control. Release* **2018**, *269*, 235–244. [CrossRef]
93. Jin, H.; Zhu, T.; Huang, X.; Sun, M.; Li, H.; Zhu, X.; Liu, M.; Xie, Y.; Huang, W.; Yan, D. ROS-responsive nanoparticles based on amphiphilic hyperbranched polyphosphoester for drug delivery: Light-triggered size-reducing and enhanced tumor penetration. *Biomaterials* **2019**, *211*, 68–80. [CrossRef]
94. Schmid, D.; Fay, F.; Small, D.M.; Jaworski, J.; Riley, J.S.; Tegazzini, D.; Fenning, C.; Jones, D.S.; Johnston, P.G.; Longley, D.B. Efficient drug delivery and induction of apoptosis in colorectal tumors using a death receptor 5-targeted nanomedicine. *Mol. Ther.* **2014**, *22*, 2083–2092. [CrossRef] [PubMed]
95. Ediriwickrema, A.; Zhou, J.; Deng, Y.; Saltzman, W.M. Multi-layered nanoparticles for combination gene and drug delivery to tumors. *Biomaterials* **2014**, *35*, 9343–9354. [CrossRef] [PubMed]
96. Chen, Y.; Li, H.; Deng, Y.; Sun, H.; Ke, X.; Ci, T. Near-infrared light triggered drug delivery system for higher efficacy of combined chemo-photothermal treatment. *Acta Biomater.* **2017**, *51*, 374–392. [CrossRef]
97. Zhang, J.; Guo, Y.; Pan, G.; Wang, P.; Li, Y.; Zhu, X.; Zhang, C. Injectable Drug-Conjugated DNA Hydrogel for Local Chemotherapy to Prevent Tumor Recurrence. *ACS Appl. Mater. Interfaces* **2020**, *12*, 21441–21449. [CrossRef]
98. Jiang, M.; Mu, J.; Jacobson, O.; Wang, Z.; He, L.; Zhang, F.; Yang, W.; Lin, Q.; Zhou, Z.; Ma, Y. Reactive Oxygen Species Activatable Heterodimeric Prodrug as Tumor-Selective Nanotheranostics. *ACS Nano* **2020**, *14*, 16875–16886. [CrossRef]
99. Botella, P.; Abasolo, I.; Fernández, Y.; Muniesa, C.; Miranda, S.; Quesada, M.; Ruiz, J.; Schwartz, S., Jr.; Corma, A. Surface-modified silica nanoparticles for tumor-targeted delivery of camptothecin and its biological evaluation. *J. Control. Release* **2011**, *156*, 246–257. [CrossRef]
100. Yao, L.; Zhao, X.; Li, Q.; Zu, Y.; Fu, Y.; Zu, B.; Meng, X.; Liu, C. In vitro and in vivo evaluation of camptothecin nanosuspension: A novel formulation with high antitumor efficacy and low toxicity. *Int. J. Pharm.* **2012**, *423*, 586–588. [CrossRef]
101. Ma, Y.; Mou, Q.; Sun, M.; Yu, C.; Li, J.; Huang, X.; Zhu, X.; Yan, D.; Shen, J. Cancer theranostic nanoparticles self-assembled from amphiphilic small molecules with equilibrium shift-induced renal clearance. *Theranostics* **2016**, *6*, 1703. [CrossRef]
102. Yu, Y.; Yang, X.; Liu, M.; Nishikawa, M.; Tei, T.; Miyako, E. Anticancer drug delivery to cancer cells using alkyl amine-functionalized nanodiamond supraparticles. *Nanoscale Adv.* **2019**, *1*, 3406–3412. [CrossRef]
103. Alibolandi, M.; Taghdisi, S.M.; Ramezani, P.; Shamili, F.H.; Farzad, S.A.; Abnous, K.; Ramezani, M. Smart AS1411-aptamer conjugated pegylated PAMAM dendrimer for the superior delivery of camptothecin to colon adenocarcinoma in vitro and in vivo. *Int. J. Pharm.* **2017**, *519*, 352–364. [CrossRef]
104. Alibolandi, M.; Rezvani, R.; Farzad, S.A.; Taghdisi, S.M.; Abnous, K.; Ramezani, M. Tetrac-conjugated polymersomes for integrin-targeted delivery of camptothecin to colon adenocarcinoma in vitro and in vivo. *Int. J. Pharm.* **2017**, *532*, 581–594. [CrossRef] [PubMed]
105. Babaei, M.; Abnous, K.; Taghdisi, S.M.; Taghavi, S.; Saljooghi, A.S.; Ramezani, M.; Alibolandi, M. Targeted rod-shaped mesoporous silica nanoparticles for the co-delivery of camptothecin and survivin shRNA in to colon adenocarcinoma in vitro and in vivo. *Eur. J. Pharm. Biopharm.* **2020**, *156*, 84–96. [CrossRef] [PubMed]
106. Xiao, B.; Viennois, E.; Chen, Q.; Wang, L.; Han, M.K.; Zhang, Y.; Zhang, Z.; Kang, Y.; Wan, Y.; Merlin, D. Silencing of Intestinal Glycoprotein CD98 by Orally Targeted Nanoparticles Enhances Chemosensitization of Colon Cancer. *ACS Nano* **2018**, *12*, 5253–5265. [CrossRef] [PubMed]
107. Ma, L.; Chen, Q.; Ma, P.; Han, M.K.; Xu, Z.; Kang, Y.; Xiao, B.; Merlin, D. IRGD-functionalized PEGylated nanoparticles for enhanced colon tumor accumulation and targeted drug delivery. *Nanomedicine* **2017**, *12*, 1991–2006. [CrossRef]
108. Wen, C.; Cheng, R.; Gong, T.; Huang, Y.; Li, D.; Zhao, X.; Yu, B.; Su, D.; Song, Z.; Liang, W. β -Cyclodextrin-cholic acid-hyaluronic acid polymer coated Fe₃O₄-graphene oxide nanohybrids as local chemo-photothermal synergistic agents for enhanced liver tumor therapy. *Colloids Surf. B Biointerfaces* **2021**, *199*, 111510. [CrossRef]
109. Peng, M.; Qin, S.; Jia, H.; Zheng, D.; Rong, L.; Zhang, X. Self-delivery of a peptide-based prodrug for tumor-targeting therapy. *Nano Res.* **2016**, *9*, 663–673. [CrossRef]
110. Huang, Y.; Zhang, W.; Xu, Y.; Zhu, S.; Wu, Y.; Chen, T.; Xiao, Y.; Lu, W.; Zhang, X.; Yu, J. Dynamic core crosslinked camptothecin prodrug micelles with reduction sensitivity and boronic acid-mediated enhanced endocytosis: An intelligent tumor-targeted delivery nanoplatform. *Int. J. Pharm.* **2020**, *580*, 119250. [CrossRef]
111. He, W.; Jiang, Y.; Li, Q.; Zhang, D.; Li, Z.; Luan, Y. A versatile strategy to create an active tumor-targeted chemo-photothermal therapy nanoplatform: A case of an IR-780 derivative co-assembled with camptothecin prodrug. *Acta Biomater.* **2019**, *84*, 356–366. [CrossRef]
112. Konkimalla, V.B.; Efferth, T. Inhibition of epidermal growth factor receptor-overexpressing cancer cells by camptothecin, 20-(N, N-diethyl) glycinate. *Biochem. Pharmacol.* **2010**, *80*, 39–49. [CrossRef]
113. Chen, Z.; Xia, T.; Zhang, Z.; Xie, S.; Wang, T.; Li, X. Enzyme-powered Janus nanomotors launched from intratumoral depots to address drug delivery barriers. *Chem. Eng. J.* **2019**, *375*, 122109. [CrossRef]

114. Yao, X.; Li, M.; Li, B.; Xue, C.; Cai, K.; Zhao, Y.; Luo, Z. Tumor-targeted upconverting nanoplatform constructed by host-guest interaction for near-infrared-light-actuated synergistic photodynamic-/chemotherapy. *Chem. Eng. J.* **2020**, *390*, 124516. [CrossRef]
115. Liu, J.; Jiang, Z.; Zhang, S.; Saltzman, W.M. Poly (ω -pentadecalactone-co-butylene-co-succinate) nanoparticles as biodegradable carriers for camptothecin delivery. *Biomaterials* **2009**, *30*, 5707–5719. [CrossRef]
116. Zhang, W.; Wen, Y.; He, D.-X.; Wang, Y.-F.; Liu, X.-L.; Li, C.; Liang, X.-J. Near-infrared AIEgens as transformers to enhance tumor treatment efficacy with controllable self-assembled redox-responsive carrier-free nanodrug. *Biomaterials* **2019**, *193*, 12–21. [CrossRef]
117. Lu, H.-Y.; Chang, Y.-J.; Fan, N.-C.; Wang, L.-S.; Lai, N.-C.; Yang, C.-M.; Wu, L.-C.; Ho, J.A. Synergism through combination of chemotherapy and oxidative stress-induced autophagy in A549 lung cancer cells using redox-responsive nano hybrids: A new strategy for cancer therapy. *Biomaterials* **2015**, *42*, 30–41. [CrossRef]
118. Li, J.; Li, Y.; Wang, Y.; Ke, W.; Chen, W.; Wang, W.; Ge, Z. Polymer Prodrug-Based Nanoreactors Activated by Tumor Acidity for Orchestrated Oxidation/Chemotherapy. *Nano Lett.* **2017**, *17*, 6983–6990. [CrossRef]
119. Wang, S.; Zhang, F.; Yu, G.; Wang, Z.; Jacobson, O.; Ma, Y.; Tian, R.; Deng, H.; Yang, W.; Chen, Z.Y.; et al. Zwitterionic-to-cationic charge conversion polyprodrug nanomedicine for enhanced drug delivery. *Theranostics* **2020**, *10*, 6629. [CrossRef]
120. Yue, C.; Zhang, C.; Alfranca, G.; Yang, Y.; Jiang, X.; Yang, Y.; Pan, F.; de la Fuente, J.M.; Cui, D. Near-infrared light triggered ros-activated theranostic platform based on ce6-cpt-ucnps for simultaneous fluorescence imaging and chemo-photodynamic combined therapy. *Theranostics* **2016**, *6*, 456. [CrossRef]
121. Yue, C.; Yang, Y.; Zhang, C.; Alfranca, G.; Cheng, S.; Ma, L.; Liu, Y.; Zhi, X.; Ni, J.; Jiang, W.; et al. ROS-responsive mitochondria-targeting blended nanoparticles: Chemo- and photodynamic synergistic therapy for lung cancer with on-demand drug release upon irradiation with a single light source. *Theranostics* **2016**, *6*, 2352. [CrossRef]
122. Zheng, Y.; Ying, X.; Su, Y.; Jin, X.; Xu, Q.; Li, Y. Kinetically-stable Small-molecule Prodrug Nanoassemblies for Cancer Chemotherapy. *Int. J. Pharm.* **2021**, 120369. [CrossRef]
123. Chiang, C.-J.; Lin, C.-C.; Lu, T.-L.; Wang, H.-F. Functionalized nanoscale oil bodies for targeted delivery of a hydrophobic drug. *Nanotechnology* **2011**, *22*, 415102. [CrossRef] [PubMed]
124. Wang, G.; Zhou, Z.; Zhao, Z.; Li, Q.; Wu, Y.; Yan, S.; Shen, Y.; Huang, P. Enzyme-Triggered Transcytosis of Dendrimer-Drug Conjugate for Deep Penetration into Pancreatic Tumors. *ACS Nano* **2020**, *14*, 4890–4904. [CrossRef] [PubMed]
125. Johnston, M.C.; Nicoll, J.A.; Redmond, K.M.; Smyth, P.; Greene, M.K.; McDaid, W.J.; Chan, D.K.W.; Crawford, N.; Stott, K.J.; Fox, J.P. DR5-targeted, chemotherapeutic drug-loaded nanoparticles induce apoptosis and tumor regression in pancreatic cancer in vivo models. *J. Control. Release* **2020**, *324*, 610–619. [CrossRef] [PubMed]
126. Wang, Y.; Wei, G.; Zhang, X.; Xu, F.; Xiong, X.; Zhou, S. A Step-by-Step Multiple Stimuli-Responsive Nanoplatform for Enhancing Combined Chemo-Photodynamic Therapy. *Adv. Mater.* **2017**, *29*, 1605357. [CrossRef] [PubMed]
127. Zhang, Y.; Yang, D.; Chen, H.; Lim, W.Q.; Phua, F.S.Z.; An, G.; Yang, P.; Zhao, Y. Reduction-sensitive fluorescence enhanced polymeric prodrug nanoparticles for combinational photothermal-chemotherapy. *Biomaterials* **2018**, *163*, 14–24. [CrossRef]
128. Yuan, X.; Liu, L.; Wang, W.; Gao, Y.; Zhang, D.; Jia, T.; Zeng, H.; Pan, G.; Yuan, Y. Development of (G3-C12)-mediated camptothecin polymeric prodrug targeting to Galectin-3 receptor against androgen-independent prostate cancer. *Int. J. Pharm.* **2020**, *580*, 119123. [CrossRef]
129. Hu, Y.; Wu, S.; He, Y.; Deng, L. A redox prodrug micelle co-delivering camptothecin and curcumin for synergetic B16 melanoma cells inhibition. *Chem. Eng. J.* **2019**, *362*, 877–886. [CrossRef]
130. Levi, F.; Vecchia, C.L.; Randimbison, L.; Franceschi, S. Incidence of infiltrating cancer following superficial bladder carcinoma. *Int. J. Cancer* **1993**, *55*, 419–421. [CrossRef]
131. Durán, N.; Fávoro, W.J. Nanopharmaceuticals and their applications in bladder cancer therapy: A mini review. *J. Braz. Chem. Soc.* **2018**, *29*, 973–981. [CrossRef]
132. Matsumura, Y. Preclinical and clinical studies of NK012, an SN-38-incorporating polymeric micelles, which is designed based on EPR effect. *Adv. Drug Deliv. Rev.* **2011**, *63*, 184–192. [CrossRef]
133. Tzeng, S.Y.; Green, J.J. Therapeutic nanomedicine for brain cancer. *Ther. Deliv.* **2013**, *4*, 687–704. [CrossRef]
134. Martínez-Vélez, N.; Gomez-Manzano, C.; Fueyo, J.; Patiño-García, A.; Alonso, M.M. Oncolytic Virotherapy for Gliomas: A Preclinical and Clinical Summary. In *Gene Therapy in Neurological Disorders*; Elsevier: Amsterdam, The Netherlands, 2018; pp. 357–384. [CrossRef]
135. Cadoo, K.A.; Fournier, M.N.; Morris, P.G. Biological subtypes of breast cancer: Current concepts and implications for recurrence patterns. *Q. J. Nucl. Med. Mol. Imaging Off. Publ. Ital. Assoc. Nucl. Med.* **2013**, *57*, 312–321.
136. Jain, V.; Kumar, H.; Anod, H.V.; Chand, P.; Gupta, N.V.; Dey, S.; Kesharwani, S.S. A review of nanotechnology-based approaches for breast cancer and triple-negative breast cancer. *J. Control. Release* **2020**, *326*, 628–647. [CrossRef]
137. Zhang, W.; Lu, J.; Gao, X.; Li, P.; Zhang, W.; Ma, Y.; Wang, H.; Tang, B. Enhanced Photodynamic Therapy by Reduced Levels of Intracellular Glutathione Obtained by Employing a Nano-MOF with CuII as the Active Center. *Angew. Chem. Int. Ed.* **2018**, *130*, 4985–4990. [CrossRef]
138. Fidler, M.M.; Gupta, S.; Soerjomataram, I.; Ferlay, J.; Steliarova-Foucher, E.; Bray, F. Cancer incidence and mortality among young adults aged 20–39 years worldwide in 2012: A population-based study. *Lancet Oncol.* **2017**, *18*, 1579–1589. [CrossRef]
139. Pfaendler, K.S.; Tewari, K.S. Changing paradigms in the systemic treatment of advanced cervical cancer. *Am. J. Obstet. Gynecol.* **2016**, *214*, 22–30. [CrossRef]

140. Van der Jeught, K.; Xu, H.-C.; Li, Y.-J.; Lu, X.-B.; Ji, G. Drug resistance and new therapies in colorectal cancer. *World J. Gastroenterol.* **2018**, *24*, 3834. [CrossRef]
141. Alwhibi, M.S.; Khalil, M.I.M.; Ibrahim, M.M.; El-Gaaly, G.A.; Sultan, A.S. Potential antitumor activity and apoptosis induction of *Glossostemon bruguieri* root extract against hepatocellular carcinoma cells. *Evid. Based Complement. Altern. Med.* **2017**, *2017*, 7218562. [CrossRef]
142. Jemal, A.; Thomas, A.; Murray, T.; Thun, M. Cancer statistics, 2002. *CA A Cancer J. Clin.* **2002**, *52*, 23–47. [CrossRef]
143. Sangodkar, J.; Katz, S.; Melville, H.; Narla, G. Lung adenocarcinoma: Lessons in translation from bench to bedside. *Mt. Sinai J. Med. A J. Transl. Pers. Med.* **2010**, *77*, 597–605. [CrossRef]
144. Cho, K.R.; Shih, I.-M. Ovarian cancer. *Annu. Rev. Pathol. Mech. Dis.* **2009**, *4*, 287–313. [CrossRef]
145. Jessmon, P.; Boulanger, T.; Zhou, W.; Patwardhan, P. Epidemiology and treatment patterns of epithelial ovarian cancer. *Expert Rev. Anticancer. Ther.* **2017**, *17*, 427–437. [CrossRef]
146. Manzur, A.; Oluwasanmi, A.; Moss, D.; Curtis, A.; Hoskins, C. Nanotechnologies in pancreatic cancer therapy. *Pharmaceutics* **2017**, *9*, 39. [CrossRef]
147. Sielaff, C.M.; Mousa, S.A. Status and future directions in the management of pancreatic cancer: Potential impact of nanotechnology. *J. Cancer Res. Clin. Oncol.* **2018**, *144*, 1205–1217. [CrossRef]
148. Ferlay, J.; Soerjomataram, I.; Dikshit, R.; Eser, S.; Mathers, C.; Rebelo, M.; Parkin, D.M.; Forman, D.; Bray, F. Cancer incidence and mortality worldwide: Sources, methods and major patterns in GLOBOCAN 2012. *Int. J. Cancer* **2015**, *136*, E359–E386. [CrossRef] [PubMed]
149. de Oliveira Júnior, R.G.; Adrielly, A.F.C.; da Silva Almeida, J.R.G.; Grougnet, R.; Thiéry, V.; Picot, L. Sensitization of tumor cells to chemotherapy by natural products: A systematic review of preclinical data and molecular mechanisms. *Fitoterapia* **2018**, *129*, 383–400. [CrossRef] [PubMed]
150. Siegel, R.; Naishadham, D.; Jemal, A. Cancer statistics, 2013. *CA Cancer J. Clin.* **2013**, *63*, 11–30. [CrossRef]
151. Ascierto, P.A.; Grimaldi, A.M.; Acquavella, N.; Borgognoni, L.; Calabrò, L.; Cascinelli, N.; Cesano, A.; Del Vecchio, M.; Eggermont, A.M.; Faries, M. Future perspectives in melanoma research. In *Meeting Report from the "Melanoma Bridge. Napoli, 2nd–4th December 2012"*; Springer: Berlin/Heidelberg, Germany, 2013. [CrossRef]
152. Haupt, S.M.; Rubinstein, A. The colon as a possible target for orally administered peptide and protein drugs. *Crit. Rev. Ther. Drug Carr. Syst.* **2002**, *19*. [CrossRef]
153. Hoffart, V.; Lamprecht, A.; Maincent, P.; Lecompte, T.; Vigneron, C.; Ubrich, N. Oral bioavailability of a low molecular weight heparin using a polymeric delivery system. *J. Control. Release* **2006**, *113*, 38–42. [CrossRef] [PubMed]
154. Mi, Z.; Burke, T.G. Differential interactions of camptothecin lactone and carboxylate forms with human blood components. *Biochemistry* **1994**, *33*, 10325–10336. [CrossRef] [PubMed]
155. Zhang, H.; Wang, X.; Dai, W.; Gemeinhart, R.A.; Zhang, Q.; Li, T. Pharmacokinetics and treatment efficacy of camptothecin nanocrystals on lung metastasis. *Mol. Pharm.* **2014**, *11*, 226–233. [CrossRef] [PubMed]
156. Hong, T.; Li, S.M.; Huang, Y.; Shu, K.; Li, L.X. Evaluation of the Cytotoxicity and Immune and Subacute Toxicity of Camptothecin-loaded Nanoparticles. *Pharm. Anal. Acta* **2019**, *10*, 604.
157. Tyner, K.M.; Schiffman, S.R.; Giannelis, E.P. Nanobiohybrids as delivery vehicles for camptothecin. *J. Control. Release* **2004**, *95*, 501–514. [CrossRef]
158. Xu, B.; Ju, Y.; Cui, Y.; Song, G.; Iwase, Y.; Hosoi, A.; Morita, Y. tLyP-1-Conjugated Au-Nanorod@SiO₂ Core-Shell Nanoparticles for Tumor-Targeted Drug Delivery and Photothermal Therapy. *Langmuir* **2014**, *30*, 7789–7797. [CrossRef]



Article

Generation of Stilbene Glycoside with Promising Cell Rejuvenation Activity through Biotransformation by the Entomopathogenic Fungus *Beauveria bassiana*

Sang Keun Ha^{1,2,†}, Min Cheol Kang^{3,†}, Seulah Lee^{4,5,†}, Om Darlami³, Dongyun Shin³, Inwook Choi^{1,*}, Ki Hyun Kim^{4,*} and Sun Yeou Kim^{3,*}

¹ Division of Food Functionality Research, Korea Food Research Institute, Wanju 55365, Korea; skha@kfri.re.kr

² Division of Food Biotechnology, University of Science and Technology, Daejeon 34113, Korea

³ College of Pharmacy, Gachon University, 191 Hambakmoe-ro, Yeonsu-gu, Incheon 21936, Korea; kismc0511@naver.com (M.C.K.); darlami.om@gmail.com (O.D.); dyshin@gachon.ac.kr (D.S.)

⁴ School of Pharmacy, Sungkyunkwan University, Suwon 16419, Korea; seulah@kopri.re.kr

⁵ Division of Life Sciences, Korea Polar Research Institute, KIOST, Incheon 21990, Korea

* Correspondence: choiw@kfri.re.kr (I.C.); khkim83@skku.edu (K.H.K.); sunnykim@gachon.ac.kr (S.Y.K.); Tel.: +82-63-219-9097 (I.C.); +82-31-290-7700 (K.H.K.); +82-32-820-4931 (S.Y.K.)

† These authors contributed equally to this study.

Citation: Ha, S.K.; Kang, M.C.; Lee, S.; Darlami, O.; Shin, D.; Choi, I.; Kim, K.H.; Kim, S.Y. Generation of Stilbene Glycoside with Promising Cell Rejuvenation Activity through Biotransformation by the Entomopathogenic Fungus *Beauveria bassiana*. *Biomedicines* **2021**, *9*, 555. <https://doi.org/10.3390/biomedicines9050555>

Academic Editors: Leonardo Caputo, Laura Quintieri and Orazio Nicolotti

Received: 14 April 2021

Accepted: 11 May 2021

Published: 17 May 2021

Publisher's Note: MDPI stays neutral with regard to jurisdictional claims in published maps and institutional affiliations.



Copyright: © 2021 by the authors. Licensee MDPI, Basel, Switzerland. This article is an open access article distributed under the terms and conditions of the Creative Commons Attribution (CC BY) license (<https://creativecommons.org/licenses/by/4.0/>).

Abstract: A stilbene glycoside (resvebassianol A) (1) with a unique sugar unit, 4-O-methyl-D-glucopyranose, was identified through biotransformation of resveratrol (RSV) by the entomopathogenic fungus *Beauveria bassiana* to obtain a superior RSV metabolite with enhanced safety. Its structure, including its absolute configurations, was determined using spectroscopic data, HRESIMS, and chemical reactions. Microarray analysis showed that the expression levels of filaggrin, HAS2-AS1, and CERS3 were higher, while those of IL23A, IL1A, and CXCL8 were lower in the resvebassianol A-treated group than in the RSV-treated group, as confirmed by qRT-PCR. Compound 1 exhibited the same regenerative and anti-inflammatory effects as RSV with no cytotoxicity in skin keratinocytes and TNF- α /IFN- γ -stimulated HIEC-6 cells, suggesting that compound 1 is a safe and stable methylglycosylated RSV. Our findings suggest that our biotransformation method can be an efficient biosynthetic platform for producing a broad range of natural glycosides with enhanced safety.

Keywords: *Beauveria bassiana*; resveratrol; biotransformation; microarray analysis; cell rejuvenation

1. Introduction

Resveratrol (RSV, 3,5,4'-trihydroxy-*trans*-stilbene), a natural compound commonly found in the skin of peanuts, grapes, raspberries, blueberries, and mulberries, is a physiologically active polyphenolic compound with potential antioxidant activity [1]. Naturally, RSV is present as a glycoside attached to glucose [2]. Many studies on RSV have demonstrated that it may play an important role in preventing and treating interactions involving cell signaling pathways and diseases associated with oxidative stress, inflammation, cancer, abnormal metabolism, and neurotoxicity [3].

To date, the clinical effects of RSV have not been sufficiently validated in cellular and animal studies. Additionally, there have been some limitations to its commercialization. For example, RSV is well absorbed in vivo, but it is rapidly metabolized to sulfo- or glucuronide-conjugates [4]. RSV is safe at low doses, but it may have poor bioavailability in humans due to extensive hepatic metabolism [5]. Therefore, developing a drug for clinical use using RSV has been challenging. To overcome these problems, a new micronized RSV formulation—SRT 501—has been developed [6]. However, limitations associated with the metabolism and bioavailability of RSV continue to exist, and there is a need for RSV-derived compounds with enhanced bioavailability.

Natural product drug discovery includes the process of diverting more active molecules from the original active molecules of natural products, wherein a microbial transformation is a useful approach. The use of specific microorganisms that mimic mammalian metabolism to perform selective transformation reactions is advantageous due to the economically and ecologically friendly microbial transformations [7]. Attempts have been made to produce new RSV compounds using biotransformation and biosynthesis of RSV by microorganisms. A simple method to efficiently produce RSV from polydatin (piceid) using *Bacillus safensis* has been reported [8]. Owing to the practical challenges during the microbial production of RSV, some studies have been conducted on fungal strains such as *Botrytis cinerea*, which oxidizes RSV to produce RSV dimers such as restrytisols A, B, and C [9]. RSV 3-*O*- β -D-glucoside has also been produced from RSV using *Bacillus cereus*, also known as soil bacteria [10]. Additionally, the biotransformation technique using *Aspergillus* sp. yielded a new prenylated *trans*-RSV (arahypin-16) and RSV *trans*-dehydrodimer (leachinol F) [11]. However, their biological activities are not superior to those of RSV. In our preliminary experiments, biotransformation studies were performed using several dietary Lactobacillus and fungi. Interestingly, among them, it was confirmed that newly produced substances were detected only when the experiment was performed using *Beauveria bassiana*. Therefore, to obtain superior RSV metabolites with enhanced safety using microbial co-culture, we co-cultured RSV with tissue culture seedlings of *B. bassiana*, which is an important entomopathogenic fungus currently under development as a bio-control agent for various insect pests [12]. In the present study, resvebassianol A, a stilbene glycoside with a unique sugar unit, 4-*O*-methyl-D-glucopyranose, was isolated from the whole-cell fermentation of *B. bassiana*. The bio-functional superiority of the newly produced RSV metabolite, resvebassianol A, through biotransformation of RSV by *B. bassiana*, was further investigated using microarray analysis.

2. Materials and Methods

2.1. Microorganism

Beauveria bassiana (KCCM 60248) was purchased from the Korean Culture Center of Microorganisms (Seoul, Korea). All culture and biotransformation experiments were performed in potato dextrose agar (PDA, BD, Le Pont-de-Claix, France).

2.2. Metabolites of RSV Manufactured by *B. bassiana*

B. bassiana was incubated in PDA (0.4% potato starch, 2% dextrose, and 2% agar) at 26 °C for 3 days, and subsequently, the spores were collected from the plate surface using 0.85% saline and gauze filtration. The RSV metabolites were produced at different time points (0, 1, 3, and 7 days) at 26 °C for 72 h in a 100 rpm shaking incubator with initial inoculation concentrations of 5×10^7 spores/mL and RSV concentration of 100 μ g/mL in the culture medium. The culture medium was treated with a two-fold volume of ACN, and it was vortexed, sonicated, and centrifuged at 8000 rpm for 15 min. The supernatants were filtered using a 0.2 μ m syringe. The filtrate was concentrated and chromatographically analyzed using HPLC.

2.3. HPLC Analysis of RSV Metabolites

RSV metabolites were analyzed using a reverse-phase HPLC system (Waters Corp., Milford, MA, USA) with a photodiode array detector (model 2998, Waters Corp.) and a SunFire™ analytical C18 column (4.6 \times 150 mm, 5 μ m, Waters Corp.). The solvent system consisted of a gradient of solvent A (water:tetrahydrofuran:trifluoroacetic acid, 98:2:0.1, v/v/v) and solvent B (MeCN) with an initial composition of 83% A, isocratic to 75% A from 2 to 7 min, linear gradient to 65% A from 7 to 15 min, linear gradient to 50% A from 15 to 20 min, linear gradient to 20% A from 20 to 35 min, linear gradient to 83% A from 35 to 40 min, and linear gradient to 83% A from 40 to 45 min. Following this, the column was washed and reconditioned. The solution was eluted at a flow rate of 1 mL/min, and the UV spectra were monitored at 305 nm.

2.4. Isolation of RSV Metabolites

To optimize the incubation time, the culture medium was harvested after 1, 3, and 7 days, and the biotransformation yields were monitored at each time point. After a day of incubation, the RSV metabolite reached its maximum yield. The fermentation broth was extracted using a two-fold volume of MeCN, and it was vortexed, sonicated, and filtered. The filtrate was concentrated to yield the MeCN soluble fraction, which was purified by semi-preparative HPLC using a Phenomenex Luna phenyl-hexyl column (250 × 10 mm i.d., flow rate: 2 mL/min) with a solvent system containing 40% MeOH/H₂O to yield compounds **1** (*t_R* 15.5 min, 2.1 mg) and **2** (*t_R* 34.0 min, 0.4 mg).

Resvebassianol A (**1**)

White amorphous powder; $[\alpha]_D^{25} -47.3$ (c 0.1, MeOH); IR (KBr) ν_{\max} 3039, 2866, 1551, 1210, 1076 cm⁻¹; UV (MeOH) λ_{\max} (log ϵ) 210 (2.4), 305 (4.0) nm; ¹H (700 MHz) and ¹³C (175 MHz) NMR data, see Table 1; HRESIMS (negative-ion mode): *m/z* 403.1395 [M-H]⁻ (calcd. for C₂₁H₂₃O₈, 403.1393).

Table 1. ¹H (700 MHz) and ¹³C NMR (175 MHz) Data of Resvebassianol A (**1**) in CD₃OD ^a.

Position	δ_H	δ_C
1		141.0
2	6.46 d (2.0)	106.0
3		159.8
4	6.18 t (2.0)	103.1
5		159.8
6	6.46 d (2.0)	106.0
1'		133.2
2'	7.45 d (8.5)	128.7
3'	7.07 d (8.5)	118.0
4'		158.8
5'	7.07 d (8.5)	118.0
6'	7.45 d (8.5)	128.7
1''	6.88 d (16.0)	128.7
2''	6.99 d (16.0)	129.1
1'''	4.90 d (8.0)	102.2
2'''	3.47 dd (9.0, 8.0)	75.1
3'''	3.57 t (9.0)	78.1
4'''	3.21 t (9.0)	80.7
5'''	3.43 ddd (9.0, 5.0, 2.0)	77.3
6'''	3.71 dd (12.0, 5.0); 3.86 dd (12.0, 2.0)	62.2
4'''-OCH ₃	3.59 s	61.1

^a Signal multiplicity is expressed as doublet (d), doublet of doublet (dd), doublet of doublet of doublet (ddd), and triplet (t) and coupling constants (Hz) are in parentheses.

2.5. Acid Hydrolysis of **1**

Compound **1** (1.0 mg) was hydrolyzed using 1 mL of 1N HCl under reflux conditions at 90 °C for 1 h. The hydrolysate was diluted with H₂O, extracted using CH₂Cl₂ (3 × 2 mL), and the extract was evaporated in a vacuum to yield the aglycone, RSV (0.3 mg), which was identified using ¹H NMR [13] and LC/MS analysis. The aqueous layer was neutralized by passing it through an Amberlite IRA-67 column (Rohm and Haas, Philadelphia, PA, USA), and it was repeatedly evaporated to yield the sugar unit 4-O-methyl-D-glucopyranose (0.4 mg, $[\alpha]_D^{25} +27.5$ (c 0.02, MeOH)).

2.6. Microarray

RNA labeling and hybridization were conducted in accordance with the Agilent One-Color Microarray-Based Gene Expression Analysis protocol (Agilent Technologies, V 6.5, 2010, Lexington, MA, USA). Briefly, 200 ng of total RNA from each sample was linearly amplified, and it was labeled with Cy3-dCTP. The labeled cRNAs were purified

using an RNeasy Mini Kit (Qiagen, Hilden, Germany). The concentrations and specific activities of labeled cRNAs (pmol Cy3/ μg cRNA) were measured using NanoDrop ND-1000 (NanoDrop, Wilmington, NC, USA). Subsequently, 600 ng of each labeled cRNA was fragmented by adding 1 μL of $25 \times$ fragmentation buffer and 5 μL $10 \times$ blocking agent, and they were heated at 60 °C for 30 min. Finally, 25 μL $2 \times$ GE hybridization buffer was added to dilute the labeled cRNA. Following this, 50 μL of hybridization solution was dispensed into the gasket slide, and it was placed in the SurePrint G3 Custom Gene Expression Microarrays, 8×60 K (Agilent Technologies). The slides were incubated at 65 °C for 17 h in an Agilent hybridization oven and washed at room temperature according to the Agilent One-Color Microarray-Based Gene Expression Analysis protocol (Agilent Technology, V 6.5, 2010). The hybridized array was immediately scanned using an Agilent SureScan Microarray Scanner (Agilent Technologies).

2.7. Cell Culture

HIEC-6, human small intestinal cells (ATCC, Manassas, VA, USA), were maintained in OptiMEM (Gibco, Waltham, MA, USA), 4% fetal bovine serum (FBS), 20 mM HEPES, 10 mM GlutaMAX, 10 ng/mL epidermal growth factor, 100 U/mL penicillin, and 100 $\mu\text{g}/\text{mL}$ streptomycin. HaCaT cells, spontaneously immortalized human keratinocyte cells, were obtained from the Korean Cell Line Bank. Cells were cultured in Dulbecco's modified eagle medium (Hyclone) supplemented with 10% FBS, 100 U/mL penicillin, and 100 $\mu\text{g}/\text{mL}$ streptomycin. Subsequently, cells were incubated in a humidified atmosphere of 5% CO_2 at 37 °C.

2.8. Cell Viability

To measure the cytotoxicity of compound **1** using the 3-(4,5-dimethylthiazol-2-yl)-2,5-diphenyltetrazolium bromide (MTT) assay, HIEC-6, and HaCaT cells were seeded in a 48-well plate (3×10^4 cells/well) and incubated for 24 h. Subsequently, the cells were treated with different doses of resveratrol and RSV for 24 h. After treatment, the cells were incubated with MTT solution (0.5 mg/mL, Sigma-Aldrich, St. Louis, MO, USA) at 37 °C for 1 h. The dark blue formazan crystals were solubilized using 200 μL of DMSO per well, and the absorbance was measured at 570 nm using a spectrophotometer (Molecular Devices, San Jose, CA, USA).

2.9. Enzyme-Linked Immunosorbent Assay (ELISA)

Interleukin (IL)-6 and IL-1 β levels were measured using ELISA. HIEC-6 and HaCaT cells were seeded (3×10^5 cells/well) in a 24-well plate and stimulated using TNF- α and INF- γ (10 ng/mL each) in the presence of compound **1** and RSV. After 24 h of incubation, the supernatants were collected, and the levels of IL-1 β and IL-6 were evaluated using their respective ELISA kits (R&D Systems, Minneapolis, MN, USA).

2.10. Cell Proliferation and Migration Assay

Cell proliferation was analyzed using the 5-Bromo-2-deoxyUridine (BrdU) assay. Briefly, HaCaT cells were seeded in a 24-well plate (4.0×10^4 cells/well), treated with compound **1** or RSV for 24 h or 48 h with or without IL-22 (50 ng/mL) stimulation, and incubated with a final concentration of 10 μM BrdU. After incubation, cells were fixed at room temperature for 30 min, incubated with peroxidase-linked BrdU-antibody for 1 h, washed three times, incubated with HRP-conjugated antibody for 30 min, washed three times, and incubated with 3,3',5,5'-tetramethylbenzidine solution for 30 min. Subsequently, the absorbance was measured at 450 nm. To measure the cell migration rates, cells were seeded at a density of 3.0×10^4 cells per well in 96-well ImageLock plates (Essen Bioscience, Arbor, MI, USA) and incubated to form a spatially uniform monolayer. Scratch wounds were created in monolayers of cultured cells using a Wound Maker™ (Essen Bioscience). After creating the scratch wound, cells were washed twice with phosphate-buffered saline, incubated with or without IL-22, and treated with compound **1** or RSV in fresh serum-free

media. The plate was placed in an IncuCyte® ZOOM (Essen Bioscience), and the migrating cell images were recorded after 6 h of wound creation.

2.11. Statistical Analysis

Results of the statistical analyses are expressed as mean \pm SEM. Statistical comparisons were made between the control and other groups by Bonferroni's test for multiple comparisons of one-way analysis of variance using the GraphPad Prism 5.0 software (GraphPad Software Inc., San Diego, CA, USA). A *p*-value less than 0.05 indicated statistical significance.

3. Results and Discussion

3.1. Identification of RSV Metabolite with 4-O-Methyl-D-Glucopyranose through Biotransformation by *Beauveria bassiana*

To investigate the metabolite profile of RSV obtained from biotransformation using *B. bassiana*, RSV was incubated in the culture medium with *B. bassiana* for 0, 1, 3, and 7 days. The medium samples were analyzed using HPLC, where the concentration of RSV significantly decreased with increasing incubation time, which indicates the bio-conversion of RSV (Figure S1 (Supplementary Materials)). As the biotransformation yields were monitored at each time point, the RSV metabolite reached its maximum yield after a day of incubation. Chemical analysis of the extract of the 1-day fermentation broth resulted in the isolation of a stilbene glycoside, named resvebassianol A (1) and RSV (Figure 1A) through semi-preparative HPLC purification.

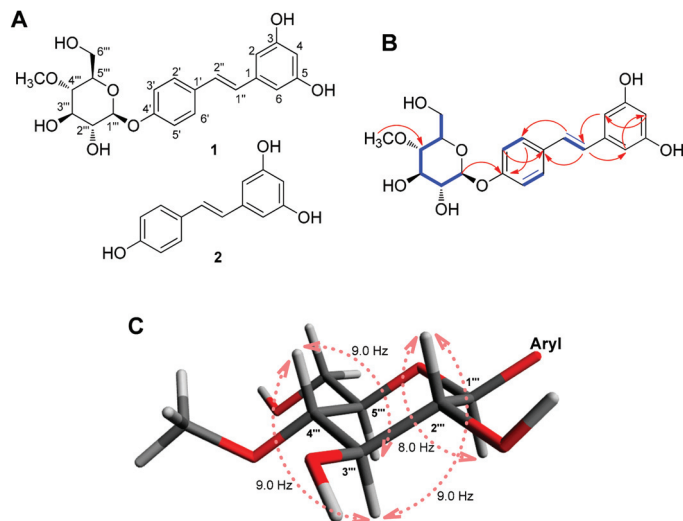


Figure 1. (A) Chemical structures of resvebassianol A (1) and RSV (2). (B) Key ¹H-¹H COSY (blue bold lines) and HMBC (red arrows) correlations of 1. (C) Coupling constant analysis of 4-O-methyl-D-glucopyranose.

3.2. Structural Elucidation of Resvebassianol A (1)

Resvebassianol A (1) was isolated as a white amorphous powder and possessed a molecular formula of C₂₁H₂₄O₈ as established by the HRESIMS ion at *m/z* 403.1395 [M-H]⁻ (calculated for C₂₁H₂₃O₈, 403.1393) and the NMR data (Table 1). The NMR data (Table 1) of 1 suggested that compound 1 shares the resveratrol skeleton by inspection and comparison of the NMR spectroscopic data with those of RSV [13], which was isolated in this study as compound 2. In addition, the signals of oxygenated protons were observed at δ_H 3.21 (1H, t, *J* = 9.0 Hz), 3.43 (1H, ddd, *J* = 9.0, 5.0, 2.0 Hz), 3.47 (1H, dd, *J* = 9.0, 8.0 Hz),

3.57 (1H, t, $J = 9.0$ Hz), 3.71 (1H, dd, $J = 12.0, 5.0$ Hz), 3.86 (1H, dd, $J = 12.0, 2.0$ Hz), and 4.90 (1H, d, $J = 8.0$ Hz), which was deduced to be attributable to the sugar unit together with the presence of a methoxyl group at δ_{H} 3.59 (3H, s). With the clear evidence of compound **1** being a resveratrol glycoside, the ^{13}C NMR spectrum (Table 1) also showed the signals for the resveratrol frame and the rest of the carbon NMR resonances corresponding to the sugar unit at δ_{C} 102.2, 80.7, 78.1, 77.3, 75.1, and 62.2, and a methoxyl group at δ_{C} 61.1.

The proton at δ_{H} 4.90 (1H, d, $J = 8.0$ Hz), attached to the downfield carbon at δ_{C} 102.2 (C-1''') with the aid of HSQC, was assigned to the anomeric proton, and its large J -value (8.0 Hz) was indicative of the β -oriented anomeric proton. A comprehensive investigation of the 2D NMR spectra of **1** allowed the establishment of its pyranose unit from C-1''' to C-6''' (Figure 1B) by ^1H - ^1H COSY correlations from H-1''' to H-6''' and HMBC correlation from methoxyl proton (δ_{H} 3.59) to C-4''' (δ_{C} 80.7). Based on this evidence and comparison of the NMR data of the sugar moiety in previous reports [14], the sugar unit was determined to be 4-*O*-methyl- β -glucopyranose. By the analysis of vicinal coupling constants of the sugar moiety ($J_{1''',2'''} = 8.0$ Hz, $J_{2''',3'''} = 9.0$ Hz, $J_{3''',4'''} = 9.0$ Hz, and $J_{4''',5'''} = 9.0$ Hz), it was confirmed that H-1''', H-2''', H-3''', H-4''', and H-5''' were all oriented in the axial positions of a pyranose ring (Figure 1C) [15]. The position of the sugar unit to the aglycone was determined by HMBC correlation between H-1''' and C-4' (δ_{C} 158.8). The assignment of the D-configuration of the sugar unit was verified by the specific optical rotation value ($[\alpha]_{\text{D}}^{25} +27.5$ (c 0.02, MeOH)) of the sugar moiety obtained from the acid hydrolysate of **1**, which was comparable to the 4-*O*-methyl-D-glucopyranose previously reported, $[\alpha]_{\text{D}}^{20} +71$ (c 0.30, MeOH) [14]. Detailed analysis of COSY and HMBC correlations confirmed the complete structure of **1** as 4'-*O*-(4'''-*O*-methyl- β -D-glucopyranosyl)-resveratrol, which we named resvebassianol A.

Interestingly, resvebassianol A is a glycosylated RSV with a unique sugar unit, 4-*O*-methyl-D-glucopyranose, and it is remarkable that natural products bearing the unique sugar moiety, including akanthol, meromusides A–B, and pyridovericin-*N*-*O*-glucopyranoside, were mostly isolated from entomopathogenic fungi [16–20]. Recently, the glycosyltransferase–methyltransferase (GT–MT) gene pair that encodes a methylglucosylation functional module has been identified in *B. bassiana* [21]. This GT–MT gene pair is unique to the entomopathogenic fungal species, leading to the characteristic methylglycosylated natural products of these organisms [21]. The GT–MT gene pair is promiscuous in conjugating methylglucose to a broad range of drug-like substrates, but it yields both *O*- and *N*-glucosides with substantial regio- and stereoselectivity. The resulting methylglycosylated products in the recent study included the production of resvebassianol A [21], yet the absolute configuration was established for the first time in the present study.

3.3. Microarray Analysis to Determine the Functional Differences between Resvebassianol A and RSV

We investigated the gene expression profiles of resvebassianol A- and RSV-treated skin keratinocytes using microarray analysis to determine the functional differences between resvebassianol A and RSV. Analyses of the gene expression data of both groups revealed 1790 differentially expressed genes with a fold-change higher than two. It was observed that 843 genes were upregulated, while 947 genes were downregulated in resvebassianol A-treated cells (Figure 2). The expression of several genes, including six upregulated genes and eight downregulated genes, was analyzed (Table 2).

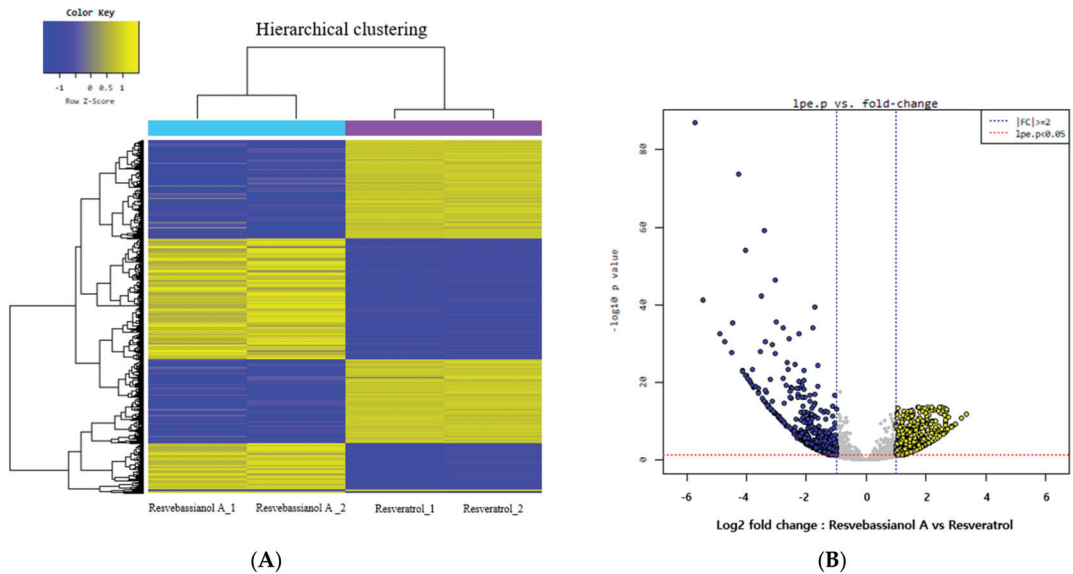


Figure 2. Differential expression of genes in resvebassianol A- and RSV-treated keratinocytes. **(A)** Hierarchical clustering of altered mRNA. Microarray analysis for mRNA expression patterns of platelet heatmap of deregulated mRNAs, which were two-fold upregulated or downregulated. **(B)** Volcano plotting microarray analysis revealed the mRNAs that were two-fold upregulated or downregulated in platelet during storage.

Table 2. Upregulated or downregulated genes in resvebassianol A-treated keratinocytes compared to those in RSV-treated cells.

Gene Symbol	RefSeq	Gene Name	Fold-Change
CCL17	NM_002987	Chemokine (C-C motif) ligand 17	4.79
FLG	NM_002016	Filaggrin	4.02
HAS2-AS1	NR_002835	HAS2 antisense RNA 1	3.43
IL17RE	NM_153483	Interleukin 17 receptor E	3.13
TLR3	NM_003265	Toll-like receptor 3	3.00
CERS3	NM_178842	Ceramide synthase 3	2.62
IL11RA	NM_001142784	Interleukin 11 receptor, alpha	-2.24
IL7R	NM_002185	Interleukin 7 receptor	-2.62
IL32	NM_001012631	Interleukin 32	-3.53
IL1A	NM_000575	Interleukin 1, alpha	-3.66
CXCL8	NM_000584	Chemokine (C-X-C motif) ligand 8	-3.90
IL23A	NM_016584	Interleukin 23, alpha subunit p19	-7.53
IL4I1	NM_152899	Interleukin 4 induced 1	-9.30
IL11	NM_000641	Interleukin 11	-13.16

To further validate the results of microarray analyses, qRT-PCR was performed to confirm the expression of differentially expressed genes. The expression levels of many selected genes (FLG, HAS2-AS1, CERS3, IL23A, IL1A, and CXCL8) were examined via qRT-PCR using the same RNA samples. The expression levels of filaggrin (FLG), HAS2-AS1, and CERS3 were higher, while those of IL23A, IL1A, and CXCL8 were lower in the resvebassianol A-treated group than in the RSV-treated group. Thus, the results of qRT-PCR were consistent with those of the microarray analysis (Figure 3). The functions of these altered genes were mainly related to the maintenance of skin barrier function, immune reaction, and cell regeneration of keratinocytes derived from the skin epidermis.

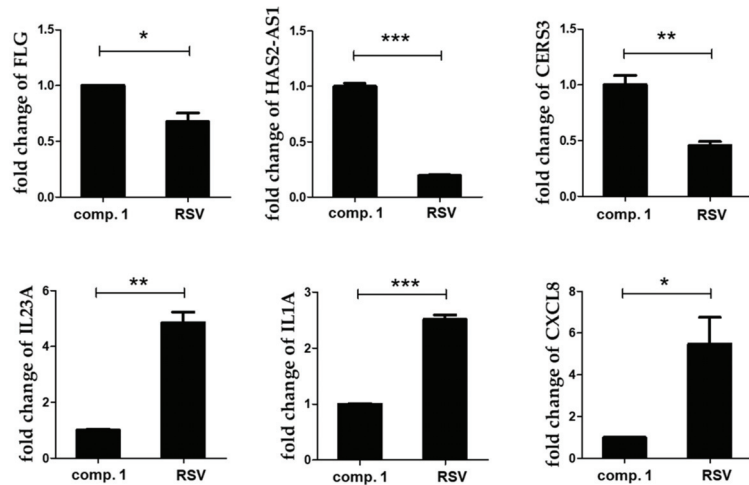


Figure 3. The key differentially expressed mRNAs identified from microarray were verified using qRT-PCR. The expression of genes in resvebassianol A (1)- and RSV-treated groups was consistent with the results of gene chip detection. Values are expressed as means \pm SD. * $p < 0.05$, ** $p < 0.01$, and *** $p < 0.001$ vs. RSV-treated group; Comp. means compound.

3.4. Effects of Resvebassianol A on the Proliferation and Migration of HaCaT Cells

Next, the proliferation effects of resvebassianol A were tested in HaCaT cells using the BrdU assay (Figure 4). Interestingly, resvebassianol A showed no cytotoxicity, whereas RSV showed cytotoxicity at 25 μ M (Figure 4A). At the cellular and animal model levels, most glycosidic compounds are safer and have higher stability than aglycones. After comparing the proliferation rates of RSV and resvebassianol A, it was observed that the latter significantly inhibited cell proliferation from 24 h to 48 h, which was similar to the activity of RSV in IL-22-induced keratinocytes without any cytotoxicity (Figure 4B). To investigate the potential effects of resvebassianol A on cell migration and rejuvenation in skin keratinocytes, we performed a cell scratch assay and wound analysis. The wound areas in IL-22-induced HaCaT cells were measured after a 6 h treatment with resvebassianol A or RSV (1, 10 μ M each, Figure 4C). Resvebassianol A inhibited cell migration; however, the same concentration of RSV showed higher inhibition (Figure 4C,D) in IL-22-induced HaCaT cells. The difference in proliferation and migration rates indicated that resvebassianol A showed effects similar to those of RSV without any cytotoxicity.

3.5. Inhibitory Effects of Resvebassianol A on the Inflammatory Cytokine Expression of TNF- α /INF- γ -Induced HIEC-6 Cells

To confirm the regenerative and anti-inflammatory effects of resvebassianol A in other tissues as well as in skin cells, we examined the inhibitory effects of resvebassianol A on inflammatory cytokine secretion in TNF- α /INF- γ -stimulated HIEC-6 cells and human intestinal epithelial cells. Treatment with resvebassianol A showed no cell death, in contrast to RSV treatment (Figure 5A). Resvebassianol A significantly inhibited both IL-6 and IL-1 β secretion in a dose-dependent manner, but the anti-inflammatory activity of RSV was higher than that of resvebassianol A (Figure 5B,C). These results suggest the inhibition of inflammatory cytokine secretion by resvebassianol A was similar to that of RSV with no cytotoxicity. Thus, resvebassianol A may maintain epithelial homeostasis and repair the damage caused by various toxic factors in skin and intestinal tissues. Based on these findings, resvebassianol A was determined to be safe for use even at high concentrations, unlike RSV, which is cytotoxic at high concentrations.

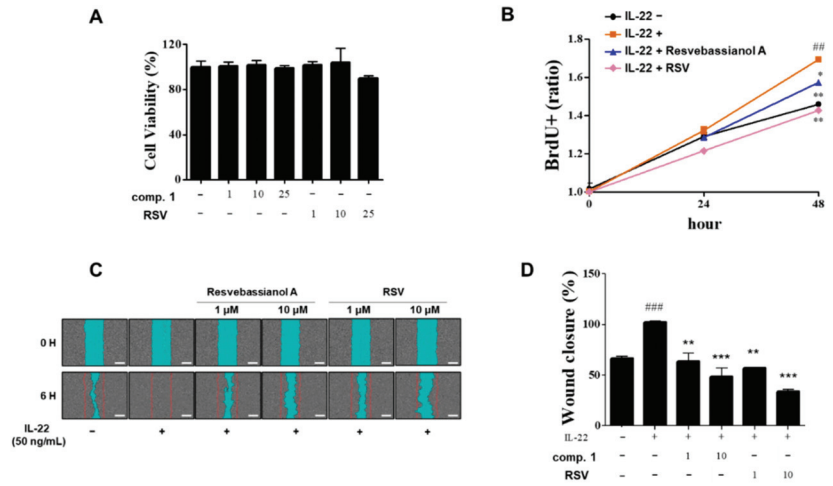


Figure 4. Effects of resvebassianol A on the proliferation and migration of HaCaT cells. (A) Cells were cultured in 96-well plates, and they were treated with resvebassianol A and RSV (1, 10, and 25 μ M). After 24 h cell viability was measured using the MTT assay. (B) HaCaT cell proliferation after 24 and 48 h of treatment with resvebassianol A and RSV was measured using BrdU incorporation assay. (C) The wound margin was photographed after 0 h and 6 h of wound scratching. (D) Quantitative analysis of wound closure was determined as the wound area at a given time relative to that of the IL-22-treated group. Values are expressed as means \pm SEM. ### $p < 0.01$ and #### $p < 0.001$ versus untreated (control) group; * $p < 0.05$, ** $p < 0.01$, and *** $p < 0.001$ vs. IL-22-treated group.

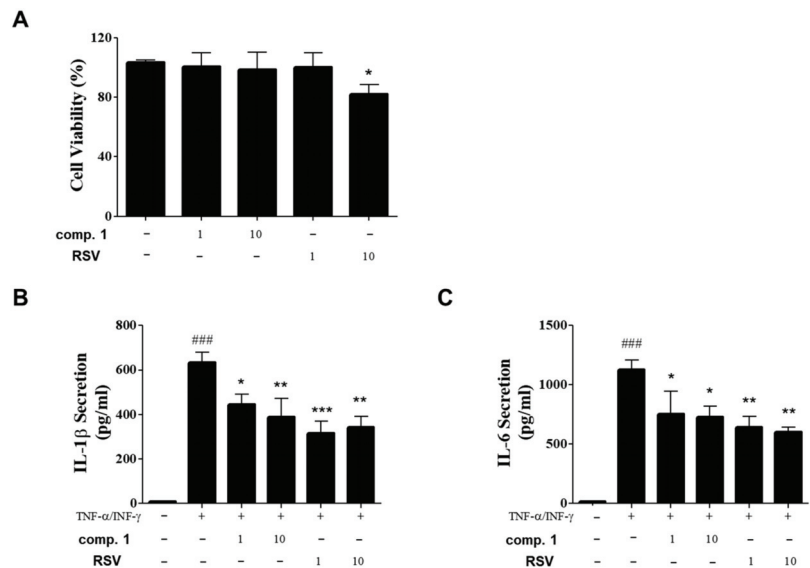


Figure 5. Inhibitory effects of resvebassianol A on the inflammatory cytokine expression of TNF- α /INF- γ -induced HIEC-6 cells. (A) Cells were cultured in 96-well plates, and they were treated with resvebassianol A and RSV at 1 and 10 μ M, respectively. After 24 h, cell viability was measured using the MTT assay. (B,C) The levels of IL-6 and IL-1 β in the supernatants were determined using ELISA. Values are expressed as means \pm SD. ### $p < 0.001$ versus control group; * $p < 0.05$, ** $p < 0.01$, and *** $p < 0.001$ vs. TNF- α /INF- γ -treated group.

RSV has various biological activities in humans [22]. Particularly, many studies have reported the effectiveness of RSV in skin photoaging, inflammation, skin whitening, and skin cancer [23–26]. Despite its various biological functions, RSV has very low structural stability and bioavailability upon oral administration [27]. Additionally, it is known to interact with other drugs [28]. We have conducted several studies to investigate the application of RSV, its synthetic derivatives, and RSV-enriched rice as functional cosmeceuticals [23,29], where RSV showed cytotoxicity in skin cells at high concentrations. Therefore, we conducted this study to establish a new method for producing RSV derivatives using biotransformation on the entomopathogenic fungus *B. bassiana*, which led to the biosynthesis of an interesting RSV derivative with enhanced stability and safety. Glycosylation is widespread among natural products and is capable of increasing the diversity of structure and function of natural products [30]. Glycosylation of natural products can be advantageous in terms of water solubility, pharmacological activities, pharmacokinetic properties, and bioavailability [30], which provides useful information for the development and application of glycosylated natural products for drug research and development.

Recently, attempts were made to use the characteristic methylglycosylated natural products from *B. bassiana* for biosynthesis, where the resulting methylglycosylated products showed increased solubility and displayed increased stability against glycoside hydrolysis [21]. Upon methylglucosidation, specific methylglycosylated products were found to exhibit enhanced bioactivities [21]. These findings support our results establishing a new method for the biosynthesis of methylglycosylated RSV with enhanced safety and stability using biotransformation by *B. bassiana*.

4. Conclusions

In this study, we suggest a practical method for the efficient biosynthesis of a wide range of natural glycosides in total biosynthetic or biocatalytic platforms. Despite many trials for the development of a drug using RSV, there have been limitations associated with the metabolism and bioavailability of RSV. Our findings introduce the method for the production of a unique RSV metabolite, resvebassianol A, which is less toxic and has higher stability upon oral administration compared to RSV, while exhibiting the biological functions that RSV possesses. Until now, most studies on biotransformation have been intensively conducted on endogenous interactions using endophytes; instead, we used edible *B. bassiana* possessing excellent pharmacological activities in the skin and other diseases [20,21,31]. The current study will establish a foothold in successfully overcoming the problems in the development of RSV-derived drugs, while introducing an economically and ecologically friendly method for producing the RSV derivatives.

Supplementary Materials: The following are available online at <https://www.mdpi.com/article/10.3390/biomedicines9050555/s1>, Figure S1: HPLC analysis of RSV metabolites obtained from biotransformation of RSV by *B. bassiana*; Figure S2: The HR-ESIMS data of compound 1; Figure S3: The ^1H NMR spectrum of compound 1 (CD_3OD , 700 MHz); Figure S4: The ^{13}C NMR spectrum of compound 1 (CD_3OD , 175 MHz); Figure S5: The ^1H - ^1H COSY spectrum of compound 1; Figure S6: The HSQC spectrum of compound 1; Figure S7: The HMBC spectrum of compound 1.

Author Contributions: Conceptualization, I.C., K.H.K., and S.Y.K.; formal analysis, S.K.H., M.C.K., S.L., O.D., and D.S.; investigation, S.K.H., M.C.K., and S.L.; writing—original draft preparation, I.C., K.H.K., and S.Y.K.; writing—review and editing, K.H.K. and S.Y.K.; visualization, S.K.H., M.C.K., and S.L.; supervision, K.H.K. and S.Y.K.; project administration, I.C., K.H.K., and S.Y.K.; funding acquisition, K.H.K. All authors have read and agreed to the published version of the manuscript.

Funding: This work was supported by a grant from the National Research Foundation of Korea (NRF), funded by the Korean government (MSIT) (2019R1A5A2027340 and 2021R1A2C2007937). This work was also supported by the Main Research Program (E0210203) of the Korea Food Research Institute (KFRI) funded by the Ministry of Science.

Institutional Review Board Statement: Not applicable.

Informed Consent Statement: Not applicable.

Conflicts of Interest: The authors declare no conflict of interest.

References

- Xia, N.; Daiber, A.; Förstermann, U.; Li, H. Antioxidant effects of resveratrol in the cardiovascular system. *Br. J. Pharmacol.* **2017**, *174*, 1633–1646. [CrossRef]
- Liu, M.; Tang, F.; Liu, Q.; Xiao, J.; Cao, H.; Chen, X. Inhibition of resveratrol glucosides (REs) on advanced glycation endproducts (AGEs) formation: Inhibitory mechanism and structure-activity relationship. *Nat. Prod. Res.* **2020**, *34*, 2490–2494. [CrossRef]
- Rauf, A.; Imran, M.; Suleria, H.A.R.; Ahmad, B.; Peters, D.G.; Mubarak, M.S. A comprehensive review of the health perspectives of resveratrol. *Food Funct.* **2017**, *8*, 4284–4305. [CrossRef] [PubMed]
- Cottart, C.H.; Nivet-Antoine, V.; Laguillier-Morizot, C.; Beaudoux, J.L. Resveratrol bioavailability and toxicity in humans. *Mol. Nutr. Food Res.* **2010**, *54*, 7–16. [CrossRef]
- Gambini, J.; Inglés, M.; Olaso, G.; Lopez-Grueso, R.; Bonet-Costa, V.; Gimeno-Mallench, L.; Mas-Bargues, C.; Abdelaziz, K.M.; Gomez-Cabrera, M.C.; Borrás, C. Properties of resveratrol: In vitro and in vivo studies about metabolism, bioavailability, and biological effects in animal models and humans. *Oxid. Med. Cell. Longev.* **2015**, *2015*, 837042. [CrossRef]
- Howells, L.M.; Berry, D.P.; Elliott, P.J.; Jacobson, E.W.; Hoffmann, E.; Hegarty, B.; Brown, K.; Steward, W.P.; Gescher, A.J. Phase I randomized, double-blind pilot study of micronized resveratrol (SRT501) in patients with hepatic metastases—Safety, pharmacokinetics, and pharmacodynamics. *Cancer Prev. Res.* **2011**, *4*, 1419–1425. [CrossRef]
- de Carvalho, C.C.C.R.; da Fonseca, M.M.R. Biotransformation of terpenes. *Biotechnol. Adv.* **2006**, *24*, 134–142. [CrossRef]
- Hu, X.; Liu, Y.; Li, D.; Feng, W.; Ni, H.; Cao, S.; Lu, F.; Li, Y. An innovative biotransformation to produce resveratrol by *Bacillus safensis*. *RSC Adv.* **2019**, *9*, 15448–15456. [CrossRef]
- Cichewicz, R.H.; Kouzi, S.A.; Hamann, M.T. Dimerization of resveratrol by the grapevine pathogen *Botrytis cinerea*. *J. Nat. Prod.* **2000**, *63*, 29–33. [CrossRef]
- Cichewicz, R.H.; Kouzi, S.A. Biotransformation of resveratrol to piceid by *Bacillus cereus*. *J. Nat. Prod.* **1998**, *61*, 1313–1314. [CrossRef]
- Wang, L.; Wu, Y.; Chen, Y.; Zou, J.; Li, X. Biotransformation of resveratrol: New prenylated *trans*-resveratrol synthesized by *Aspergillus* sp. SCS10W2. *Molecules* **2016**, *21*, 883. [CrossRef]
- Westwood, G.S.; Huang, S.-W.; Keyhani, N.O. Allergens of the entomopathogenic fungus *Beauveria bassiana*. *Clin. Mol. Allergy* **2005**, *3*, 1–8. [CrossRef] [PubMed]
- Sasikumar, P.; Lekshmy, K.; Sini, S.; Prabha, B.; Kumar, N.A.; Sivan, V.V.; Jithin, M.M.; Jayamurthy, P.; Shibi, I.G.; Radhakrishnan, K.V. Isolation and characterization of resveratrol oligomers from the stem bark of *Hopea ponga* (Dennst.) Mabb. and their antidiabetic effect by modulation of digestive enzymes, protein glycation and glucose uptake in L6 myocytes. *J. Ethnopharmacol.* **2019**, *236*, 196–204. [CrossRef] [PubMed]
- Isaka, M.; Haritakun, R.; Supothina, S.; Choowong, W.; Mongkolsamrit, S. *N*-Hydroxypyridone alkaloids, chromone derivatives, and tetrahydroxanones from the scale-insect pathogenic fungus *Orbiocrella* sp. BCC 33248. *Tetrahedron* **2014**, *70*, 9198–9203. [CrossRef]
- Bunyapairoonsri, T.; Yoiprommarat, S.; Intereya, K.; Kocharin, K. New diphenyl ethers from the insect pathogenic fungus *Cordyceps* sp. BCC 1861. *Chem. Pharm. Bull.* **2007**, *55*, 304–307. [CrossRef] [PubMed]
- Kuephadungphan, W.; Helaly, S.E.; Daengrot, C.; Phongpaichit, S.; Luangsa-Ard, J.J.; Rukachaisirikul, V.; Stadler, M. Akanthopyrones A–D, α -pyrones bearing a 4-*O*-methyl- β -D-glucopyranose moiety from the spider-associated Ascomycete *Akanthomyces novoguineensis*. *Molecules* **2017**, *22*, 1202. [CrossRef] [PubMed]
- Isaka, M.; Palasarn, S.; Supothina, S.; Komwijit, S.; Luangsa-ard, J.J. Bioactive compounds from the scale insect pathogenic fungus *Conoideocrella tenuis* BCC 18627. *J. Nat. Prod.* **2011**, *74*, 782–789. [CrossRef] [PubMed]
- Kornsakulkarn, J.; Thongpanchang, C.; Lapanun, S.; Srichomthong, K. Isocoumarin glucosides from the scale insect fungus *Torrubiella tenuis* BCC 12732. *J. Nat. Prod.* **2009**, *72*, 1341–1343. [CrossRef]
- Kornsakulkarn, J.; Saepua, S.; Srichomthong, K.; Supothina, S.; Thongpanchang, C. New mycotoxins from the scale insect fungus *Aschersonia coffeae* Henn. BCC 28712. *Tetrahedron* **2012**, *68*, 8480–8486. [CrossRef]
- Zhang, L.; Fasoyin, O.E.; Molnár, I.; Xu, Y. Secondary metabolites from hypocrealean entomopathogenic fungi: Novel bioactive compounds. *Nat. Prod. Rep.* **2020**, *37*, 1181–1206. [CrossRef] [PubMed]
- Xie, L.; Zhang, L.; Wang, C.; Wang, X.; Xu, Y.-M.; Yu, H.; Wu, P.; Li, S.; Han, L.; Gunatilaka, A.A.L.; et al. Methylglucosylation of aromatic amino and phenolic moieties of drug-like biosynthons by combinatorial biosynthesis. *Proc. Natl. Acad. Sci. USA* **2018**, *115*, E4980–E4989. [CrossRef] [PubMed]
- Fraczek, M.; Szumilo, J.; Podlodowska, J.; Burdan, F. Resveratrol—Phytophenol with wide activity. *Pol. Merkur. Lek. Organ Pol. Tow. Lek.* **2012**, *32*, 143–146.
- Kang, M.C.; Cho, K.; Lee, J.H.; Subedi, L.; Yumnam, S.; Kim, S.Y. Effect of resveratrol-enriched rice on skin inflammation and pruritus in the NC/Nga mouse model of atopic dermatitis. *Int. J. Mol. Sci.* **2019**, *20*, 1428. [CrossRef]
- Subedi, L.; Lee, T.H.; Wahedi, H.M.; Baek, S.H.; Kim, S.Y. Resveratrol-enriched rice attenuates UVB-ROS-induced skin aging via downregulation of inflammatory cascades. *Oxid. Med. Cell. Longev.* **2017**, *2017*, 8379539. [CrossRef]

25. Zhou, F.; Huang, X.; Pan, Y.; Cao, D.; Liu, C.; Liu, Y.; Chen, A. Resveratrol protects HaCaT cells from ultraviolet B-induced photoaging via upregulation of HSP27 and modulation of mitochondrial caspase-dependent apoptotic pathway. *Biochem. Biophys. Res. Commun.* **2018**, *499*, 662–668. [CrossRef]
26. Rauf, A.; Imran, M.; Butt, M.S.; Nadeem, M.; Peters, D.G.; Mubarak, M.S. Resveratrol as an anti-cancer agent: A review. *Crit. Rev. Food Sci. Nutr.* **2018**, *58*, 1428–1447. [CrossRef]
27. Chimento, A.; de Amicis, F.; Sirianni, R.; Sinicropi, M.S.; Puoci, F.; Casaburi, I.; Saturnino, C.; Pezzi, V. Progress to improve oral bioavailability and beneficial effects of resveratrol. *Int. J. Mol. Sci.* **2019**, *20*, 1381. [CrossRef]
28. Jia, Y.M.; Liu, Z.H.; Liu, K.X. Progress in regulation of drug transporters and metabolic enzymes by resveratrol. *Yao Xue Xue Bao Acta Pharm. Sin.* **2016**, *51*, 860–865.
29. Subedi, L.; Baek, S.H.; Kim, S.Y. Bioactive compounds of food: Their role in the prevention and treatment of diseases. *Oxid. Med. Cell. Longev.* **2018**, *2018*, 8092713.
30. Huang, G.; Lv, M.; Hu, J.; Huang, K.; Xu, H. Glycosylation and activities of natural products. *Mini Rev. Med. Chem.* **2016**, *16*, 1013–1016. [CrossRef]
31. Patocka, J. Bioactive metabolites of entomopathogenic fungi *Beauveria bassiana*. *Mil. Med. Sci. Lett.* **2016**, *85*, 80–88. [CrossRef]



Article

Effective Accentuation of Voltage-Gated Sodium Current Caused by Apocynin (4'-Hydroxy-3'-methoxyacetophenone), a Known NADPH-Oxidase Inhibitor

Tzu-Hsien Chuang ¹, Hsin-Yen Cho ¹ and Sheng-Nan Wu ^{1,2,*}

¹ Department of Physiology, National Cheng Kung University Medical College, No. 1, University Road, Tainan 70101, Taiwan; fytg55qq@gmail.com (T.-H.C.); lilyzhou861126@gmail.com (H.-Y.C.)

² Institute of Basic Medical Sciences, National Cheng Kung University Medical College, Tainan 70101, Taiwan

* Correspondence: snwu@ncku.edu.tw; Tel.: +886-6235-3535-5334; Fax: +886-6236-2780

Abstract: Apocynin (*aPO*, 4'-Hydroxy-3'-methoxyacetophenone) is a cell-permeable, anti-inflammatory phenolic compound that acts as an inhibitor of NADPH-dependent oxidase (NOX). However, the mechanisms through which *aPO* can interact directly with plasmalemmal ionic channels to perturb the amplitude or gating of ionic currents in excitable cells remain incompletely understood. Herein, we aimed to investigate any modifications of *aPO* on ionic currents in pituitary GH₃ cells or murine HL-1 cardiomyocytes. In whole-cell current recordings, GH₃-cell exposure to *aPO* effectively stimulated the peak and late components of voltage-gated Na⁺ current (I_{Na}) with different potencies. The EC₅₀ value of *aPO* required for its differential increase in peak or late I_{Na} in GH₃ cells was estimated to be 13.2 or 2.8 μM, respectively, whereas the K_D value required for its retardation in the slow component of current inactivation was 3.4 μM. The current–voltage relation of I_{Na} was shifted slightly to more negative potential during cell exposure to *aPO* (10 μM); however, the steady-state inactivation curve of the current was shifted in a rightward direction in its presence. Recovery of peak I_{Na} inactivation was increased in the presence of 10 μM *aPO*. In continued presence of *aPO*, further application of rufinamide or ranolazine attenuated *aPO*-stimulated I_{Na}. In methylglyoxal- or superoxide dismutase-treated cells, the stimulatory effect of *aPO* on peak I_{Na} remained effective. By using upright isosceles-triangular ramp pulse of varying duration, the amplitude of persistent I_{Na} measured at low or high threshold was enhanced by the *aPO* presence, along with increased hysteretic strength appearing at low or high threshold. The addition of *aPO* (10 μM) mildly inhibited the amplitude of erg-mediated K⁺ current. Likewise, in HL-1 murine cardiomyocytes, the *aPO* presence increased the peak amplitude of I_{Na} as well as decreased the inactivation or deactivation rate of the current, and further addition of ranolazine or esaxerenone attenuated *aPO*-accentuated I_{Na}. Altogether, this study provides a distinctive yet unidentified finding that, despite its effectiveness in suppressing NOX activity, *aPO* may directly and concertedly perturb the amplitude, gating and voltage-dependent hysteresis of I_{Na} in electrically excitable cells. The interaction of *aPO* with ionic currents may, at least in part, contribute to the underlying mechanisms through which it affects neuroendocrine, endocrine or cardiac function.

Keywords: apocynin (4'-Hydroxy-3'-methoxyacetophenone); NADPH-dependent oxidase (NOX); voltage-gated Na⁺ current; persistent Na⁺ current; erg-mediated K⁺ current; current kinetics; voltage-dependent hysteresis; electrically excitable cell

Citation: Chuang, T.-H.; Cho, H.-Y.; Wu, S.-N. Effective Accentuation of Voltage-Gated Sodium Current Caused by Apocynin (4'-Hydroxy-3'-methoxyacetophenone), a Known NADPH-Oxidase Inhibitor. *Biomedicines* **2021**, *9*, 1146. <https://doi.org/10.3390/biomedicines9091146>

Academic Editor: Leonardo Caputo

Received: 6 August 2021

Accepted: 31 August 2021

Published: 3 September 2021

Publisher's Note: MDPI stays neutral with regard to jurisdictional claims in published maps and institutional affiliations.



Copyright: © 2021 by the authors. Licensee MDPI, Basel, Switzerland. This article is an open access article distributed under the terms and conditions of the Creative Commons Attribution (CC BY) license (<https://creativecommons.org/licenses/by/4.0/>).

1. Introduction

Apocynin (*aPO*, 4'-Hydroxy-3'-methoxyacetophenone), a polyphenolic compound, is a naturally occurring ortho-methoxy-substituted catechol isolated from a variety of plant sources, including *Apocynum cannabinum*, *Pierorhiza kurroa*, and so on [1]. Of note, this compound has been widely used as a selective inhibitor of NADPH-dependent oxidase (NOX) [2–5]. Alternatively, it has been recognized to be one of the most promising drugs in

a variety of pathophysiological disorders, such as inflammatory and neurodegenerative diseases, glioma, and cardiac failure [1,3,5–11]

aPO has been recently shown to ameliorate cardiac function (e.g., structural remodeling) in heart failure [6,7,11–13]. Pituitary cells were previously demonstrated to be expressed in the activity of NOX [14,15]. *aPO* has been reported to blunt the progression of neuroendocrine alterations induced by social isolation, which were thought to be mainly through its inhibition of NOX activity [16]. However, whether *aPO* exercises any modifications on ionic currents remains largely unknown.

The voltage-gated Na⁺ (Na_V) channels, nine subtypes of which are denoted Na_V1.1 through Na_V1.9, belong to the larger protein superfamily of voltage-dependent ion channels and their activity plays an essential role in the generation and propagation of action potentials (APs) in electrically excitable cells. The Na_V channels contain four homologous domains (DI–DIV), each of which consists of a six α-helical transmembrane domain (S1–S6) and a reentry P loop between S5 and S6. Na_V1.5 channels primarily underlie AP initiation and propagation in the heart, these channels have also been shown to be critical determinants of AP duration, particularly in the setting of certain arrhythmias (e.g., LQT-3 syndrome) [17,18]. Previous studies have demonstrated the ability of *aPO* to attenuate angiotensin II-induced activation of epithelial Na⁺ channels in human umbilical vein endothelial cells as well to blunt activation of these channels caused by epidermal growth factor, insulin growth factor-1 or insulin [19,20]. However, the issue of how *aPO* or other related compounds could perturb the amplitude or kinetic gating of transmembrane ionic currents (e.g., voltage-gated Na⁺ current [I_{Na}]) still remains unmet.

Therefore, in the present study, the electrophysiological effects of *aPO* and other related compounds in pituitary GH₃ cells and in HL-1 atrial cardiomyocytes were investigated. We sought to (1) evaluate whether the *aPO* presence has any effect on the amplitude, gating and voltage-dependent hysteresis (V_{hys}) of I_{Na} residing in GH₃ cells; (2) compare the effect of other related compounds on the peak amplitude of I_{Na}; (3) study the effect of *aPO* on erg-mediated K⁺ current in GH₃ cells; and (4) investigate the effect of *aPO* on I_{Na} in HL-1 cardiomyocytes. Findings from this study, for the first time, provide distinctive evidence to show that, in addition to its effectiveness in suppressing NOX activity, the differential stimulation by *aPO* of peak and late I_{Na} may be engaged in varying ionic mechanisms underlying its perturbations on the functional activities of electrically excitable cells (e.g., GH₃ or HL-1 cells).

2. Materials and Methods

2.1. Chemicals, Drugs and Solutions Used in the Present Work

Apocynin (*aPO*, NSC 2146, NSC 209524, acetovanillone, acetoguaiacone, 4'-Hydroxy-3'-methoxyacetophenone, 1-(4-Hydroxy-3-methoxyphenyl)ethanone, C₉H₁₀O₃, CAS number: 498-02-2, <https://pubchem.ncbi.nlm.nih.gov/compound/Acetovanillone> (accessed on 16 September 2004)), methylglyoxal (MeG, acetylformaldehyde, pyruvaldehyde, pyruvic aldehyde), norepinephrine, superoxide dismutase (SOD), tefluthrin (Tef), tetraethylammonium chloride (TEA), and tetrodotoxin (TTX) were acquired from Sigma-Aldrich (Merck, Taipei, Taiwan), rufinamide (RFM, 1-[(2,6-difluorophenyl]-1H-1,2,3-triazole-4-carboxamide), E-4031 and ranolazine (Ran) were from Tocris (Union Biomed, Taipei, Taiwan), and esaxerenone (ESAX) was from MedChemExpress (Gene-chain, Kaohsiung, Taiwan). Unless noted otherwise, culture media (e.g., F-12 medium), horse serum, fetal bovine or calf serum, L-glutamine, and trypsin/EDTA were purchased from HyClone™ (Thermo Fisher Scientific, Tainan, Taiwan), while all other chemicals were of laboratory grade and taken from standard sources.

The HEPES-buffered normal Tyrode's solution used in this work had an ionic composition, comprising (in mM): NaCl 136.5, KCl 5.4, CaCl₂ 1.8, MgCl₂ 0.53, glucose 5.5, and HEPES 5.5, and the pH was adjusted with NaOH to 7.4. For measurements of I_{Na} or I_{Na(P)}, we kept GH₃ or HL-1 cells immersed in Ca²⁺-free, Tyrode's solution in attempts to avoid the contamination of Ca²⁺-activated K⁺ currents and voltage-gated currents. To record K⁺

currents, we filled up the recording pipette with a solution containing (in mM): K-aspartate 130, KCl 20, KH_2PO_4 1, MgCl_2 a, Na_2ATP 3, Na_2GTP 0.1, EGTA 0.1, HEPES 5, and the pH was titrated to 7.2 by adding KOH, while to measure I_{Na} or $I_{\text{Na(P)}}$, we substituted K^+ ions in internal pipette solution for equimolar Cs^+ ions and the pH in the solution was adjusted to 7.2 by adding CsOH. All solutions used in this study were prepared using demineralized water from Milli-Q purification system (Merck). On the day of experiments, we filtered the bathing or filling solution and culture medium by using Acrodisc[®] syringe filter with a 0.2- μm pore size (Bio-Check, Tainan, Taiwan).

2.2. Cell Preparations

These are provided in the Supplemental Materials mentioned in previous studies [21,22].

2.3. Electrophysiological Measurements

Shortly before experiments, we dispersed cells with 1% trypsin/EDTA solution and an aliquot of cell suspension was quickly placed in a custom-built chamber affixed to the stage of a CKX-41 inverted microscope (Olympus; Taiwan Instrument, Tainan, Taiwan). Ionic currents in GH₃ or HL-1 cells were measured with an RK-400 operational patch-clamp amplifier (Bio-Logic, Claix, France) or an Axopclamp-2B amplifier (Molecular Devices, Sunnyvale, CA, USA), which was equipped with a Digidata 1440A device (Molecular Devices). Ionic currents were recorded in whole-cell or cell-attached configuration of the patch-clamp technique [23,24]. By using a PP-830 vertical puller (Narishige; Taiwan Instrument, Taipei, Taiwan) or a Flaming-Brown P97 horizontal puller (Sutter, Novato, CA, USA), the recording pipettes were pulled from Kimax-51 (#34500) borosilicate glass capillaries (Kimble; Dogger, New Taipei City, Taiwan), and they had tip resistances of 3–5 M Ω in situations when filled with internal pipette solutions stated above. All measurements were undertaken at room temperature (20–25 °C) on the stage of an inverted DM-II fluorescence microscope (Leica; Major Instruments, Kaohsiung, Taiwan). Data acquisition with varying voltage-clamp waveforms (i.e., analog-to-digital and digital-to-analog) was performed using the pClamp 10.7 software suite (Molecular Devices). The liquid junction potentials were zeroed immediately before seal formation was made, and the whole-cell data were corrected.

The signals were monitored and digitally stored on-line at 10 kHz in an ASUS ExpertBook laptop computer (P2451F; Yuan-Dai, Tainan, Taiwan). During the measurements, the Digidata 1440A was operated using pClamp 10.7 software run on Microsoft Windows 7 (Redmond, WA, USA). The laptop computer was placed on the top of an adjustable Cookskin stand (Ningbo, Zhejiang, China) to enable efficient operation during the measurements.

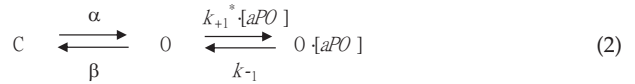
2.4. Whole-Cell Data Analyses

To determine concentration-dependent stimulation of apocynin on the transient (peak) or late I_{Na} , we kept cells bathed in Ca^{2+} -free Tyrode's solution. During the measurements, we voltage-clamped the examined cell at -80 mV and the brief depolarizing pulse to -10 mV was applied to evoke I_{Na} . The late I_{Na} in response to 100 μM *aPO* was taken as 100% and those (i.e., peak and late I_{Na}) during exposure to different *aPO* concentrations (0.3–30 μM) were thereafter compared. The concentration-response data for stimulation of peak or late I_{Na} in pituitary GH₃ cells were least-squares fitted to the Hill equation. That is,

$$\text{percentage decrease}(\%) = \frac{E_{\text{max}} \times [aPO]^{n_H}}{EC_{50}^{n_H} + [aPO]^{n_H}} \quad (1)$$

In this equation, $[aPO]$ is the *aPO* concentration used, n_H the Hill coefficient, EC_{50} the concentration needed for a 50% inhibition of peak or late I_{Na} , and E_{max} the maximal stimulation of peak or late I_{Na} caused by the addition of *aPO*.

The stimulatory effect of *aPO* on I_{Na} is thought to be explained by a state-dependent activator that binds preferentially to the open state of the Na_v channel. From a simplifying assumption, the first-order binding scheme was given as follows:



or

$$\frac{dC}{dt} = O \times \beta - C \times \alpha \quad (3)$$

$$\frac{dO}{dt} = C \times \alpha + O \cdot [aPO] \times k_{-1} - O \times \beta - O \times k_{+1}^* \cdot [aPO] \quad (4)$$

$$\frac{d(O \cdot [aPO])}{dt} = O \times k_{+1}^* [aPO] - O \cdot [aPO] \times k_{-1} \quad (5)$$

where $[aPO]$ is the *aPO* concentration applied, and α or β the voltage-gated rate constant for the opening or closing of the Na_v channels, respectively. k_{+1}^* or k_{-1} represents the forward (i.e., on or bound) or reverse (i.e., off or un-bound) rate constant of *aPO*, respectively, while C , O , or $O \cdot [aPO]$ in each term denotes the closed (resting), open, or open- $[aPO]$ state, respectively.

Forward or backward rate constants, k_{+1}^* or k_{-1} , were respectively determined from the time constants of current decay activated by the brief step depolarization from -80 to -10 mV. The time constants of I_{Na} inactivation were estimated by fitting the inactivation trajectory of each current trace with a double exponential curve (i.e., fast and slow components of current inactivation). These rate constants would be evaluated using the following equation:

$$\frac{1}{\Delta\tau} = k_{+1}^* \times [aPO] + k_{-1} \quad (6)$$

where k_{+1}^* or k_{-1} , respectively, are ascribed from the slope or from the y-axis intercept at $[aPO] = 0$ of the linear regression in which the reciprocal time constant (i.e., $1/\Delta\tau$) versus varying *aPO* concentrations was interpolated. $\Delta\tau$ indicates the difference in the slow component of current inactivation ($\tau_{inact(S)}$) obtained when the $\tau_{inact(S)}$ value during exposure to each concentration (0.03–30 μ M) was subtracted from that in the presence of 100 μ M *aPO* (Figure 1C).

The quasi-steady-state inactivation curve of peak I_{Na} with or without the *aPO* addition identified in GH₃ cells was established on the basis of a simple Boltzmann distribution (or the Fermi–Dirac distribution):

$$I = \frac{I_{max}}{1 + e^{\frac{(V-V_{1/2})qF}{RT}}} \quad (7)$$

where I_{max} is the maximal peak I_{Na} in the absence or presence of 10 μ M *aPO*; V the conditioning potential in mV; $V_{1/2}$ the half-maximal inactivation in the relationship of the curve; q the apparent gating charge; F Faraday’s constant; R the universal gas constant; and T the absolute temperature.

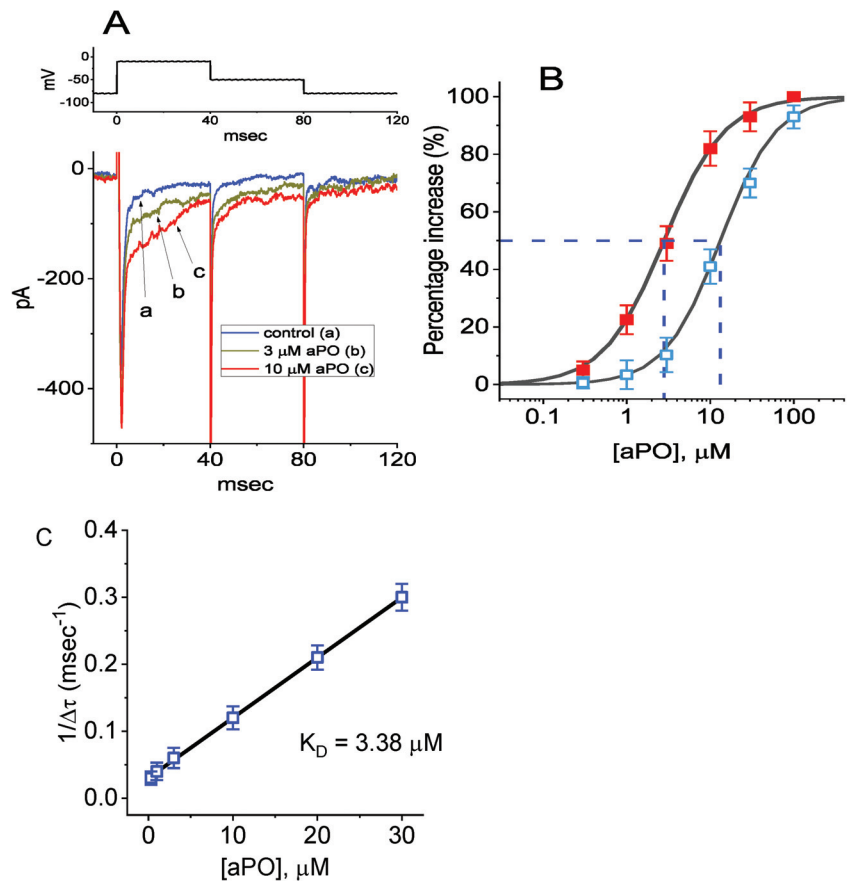


Figure 1. Effect of *aPO* on the peak and late components of voltage-gated Na^+ current (I_{Na}) identified in pituitary GH_3 cells. These experiments were undertaken in cells bathed in Ca^{2+} -free Tyrode's solution containing 10 mM tetraethylammonium chloride (TEA), whereas the recording pipette was filled up with Cs^+ -enriched solution. (A) Representative I_{Na} traces activated by brief depolarizing pulse (indicated in the upper part). a: control (i.e., *aPO* was not present); b: 3 μM *aPO*; c: 10 μM *aPO*. (B) Concentration-dependent stimulation of *aPO* on peak or late I_{Na} (mean \pm SEM; $n = 8$ for each point). The peak (\square) or late (\blacksquare) amplitude of the current was measured at the beginning or end of a 40-ms depolarizing pulse from -80 to -10 mV. Data analysis was performed by ANOVA-1 ($p < 0.05$). Each continuous line illustrates the goodness-of-fit to the Hill equation, as elaborated in Materials and Methods. The vertical broken line indicates the EC_{50} value required for 50% stimulation of the current (peak or late I_{Na}). (C) The relationship of the reciprocal to the time constant (i.e., $1/\Delta\tau$) versus the *aPO* concentration was plotted (mean \pm SEM; $n = 7$ –11 for each point). From the binding scheme (indicated under Materials and Methods), the forward (k_{+1}^*) or backward (k_{-1}) rate constant for *aPO*-accentuated I_{Na} in GH_3 cells was computed to be $0.00898 \text{ ms}^{-1}\mu\text{M}^{-1}$ or 0.0303 ms^{-1} , respectively.

2.5. Curve-Fitting Procedures and Statistical Analyses

Curve fitting (linear or non-linear (e.g., exponential or sigmoidal curve)) to various data sets was carried out with the goodness of fit by using various maneuvers, such as the Microsoft "Solver" function embedded in Excel 2019 (Microsoft) and 64-bit OriginPro[®] 2016 program (OriginLab; Scientific Formosa, Kaohsiung, Taiwan). The data are presented as the mean \pm standard error of the mean (SEM), with sample sizes (n) indicating the number

of GH₃ or HL-1 cells from which the data were collected. The Student's *t*-test (paired or unpaired) and the analyses of variance (ANOVA-1 or ANOVA-2) with or without repeated measures followed by post-hoc Fisher's least-significant different test were performed. The analyses were performed using SPSS version 20.0 (Asia Analytics, Taipei, Taiwan). A *p* value of less than 0.05 was considered to indicate the statistical difference.

3. Results

3.1. Effect of *aPO* on the Voltage-Gated Na⁺ Current (*I*_{Na}) Recorded from Pituitary GH₃ Cells

In the first stage of measurements, we kept cells immersed in a Ca²⁺-free Tyrode's solution containing 0.5 mM CdCl₂, the composition of which was stated in Materials and Methods, and we filled up the pipette by using the Cs⁺-containing solution. As the whole-cell configuration was firmly established, we voltage-clamped the tested cell at the level of −80 mV and a brief step depolarization to −10 mV was delivered to activate *I*_{Na} with a rapid activation and inactivation [23,25,26]. Of interest, one minute after cells were continually exposed to *aPO*, the peak amplitude of *I*_{Na} was progressively increased, and the concomitant inactivation time course of the current slowed (Figure 1A). In the presence of 10 μM *aPO*, the peak *I*_{Na} amplitude in response to rapid depolarizing pulse from −80 to −10 mV was significantly increased to 445 ± 31 pA (*n* = 9, *p* < 0.05) from a control value of 315 ± 22 pA. Additionally, the slow component of the inactivation time constant of *I*_{Na} activated by brief membrane depolarization was conceivably prolonged to 65.1 ± 10.2 ms (*n* = 9, *p* < 0.05) from a control value of 11.3 ± 2.3 ms (*n* = 9), although the fast component of the inactivation time constant did not differ significantly between absence and presence of *aPO*. After washout of *aPO*, the current amplitude was back to 306 ± 19 pA (*n* = 8, *p* < 0.05). Similarly, the deactivation time course of *I*_{Na} at −50 mV was prolonged in the presence of *aPO*.

The relationship between the *aPO* concentration and the peak or late component of *I*_{Na} was further analyzed and constructed in GH₃ cells. Each cell was depolarized from −80 to −10 mV and current amplitudes at different concentrations (0.3–100 μM) of *aPO* were compared. As can be seen in Figure 1B, the application of *aPO* resulted in a concentration-dependent increase in peak or late *I*_{Na} activated by a short depolarizing pulse. The EC₅₀ value for *aPO*-stimulated peak or late *I*_{Na} was 13.2 or 2.8 μM, respectively, and *aPO* at a concentration of 100 μM almost fully increased *I*_{Na}. The data, therefore, reflect that *aPO* has a specific stimulatory action on *I*_{Na} in GH₃ cells, and that the late component of *I*_{Na} was stimulated to a greater extent than the peak component of the current.

3.2. Evaluating *aPO*'s Time-Dependent Slowing of *I*_{Na} Inactivation

It needs to be mentioned that increasing *aPO* not only resulted in increased amplitude in the peak *I*_{Na} but also caused a clear and marked retardation in the magnitude of *I*_{Na} inactivation in response to rapid membrane depolarization. According to the first-order reaction scheme (indicated under Materials and Methods), the relationship between 1/Δτ and [*aPO*] turned out to be linear (Figure 1C). The forward and backward rate constants were estimated to be 0.00898 ms^{−1}μM^{−1} or 0.0303 ms^{−1}, respectively; thereafter, the apparent dissociation constant (i.e., K_D = *k*_{−1}/*k*₊₁*) for the binding of *aPO* to the Na_v channels was consequently yielded to be 3.4 μM, a value which was noticeably close to the estimated EC₅₀ value for *aPO*-mediated stimulation of late *I*_{Na} determined from the concentration-response curve (Figure 1B).

3.3. Effect of *aPO* on the Current-Voltage (*I*-*V*) Relationship or Steady-State Inactivation Curve of *I*_{Na}

We continued to examine the stimulatory effect of *aPO* at different membrane potential, and an *I*-*V* relationship of *I*_{Na} without or with the *aPO* addition was constructed. As depicted in Figure 2A, the *I*-*V* relationship of *I*_{Na} was shifted slightly to more negative potentials during cell exposure to *aPO* (10 μM). Additionally, the stimulatory effect of *aPO* on the steady-state inactivation curve of *I*_{Na} was further characterized (Figure 2B).

In this stage of experiments, a 40-ms conditioning pulse to various membrane potentials (from -120 to $+20$ mV in 10-mV steps) was delivered to precede the test pulse (40 ms in duration) to -10 mV from a holding potential of -80 mV. Under this experimental protocol, the relationship between the conditioning potentials and the normalized amplitudes of I_{Na} with or without the addition of *aPO* ($10 \mu\text{M}$) was constructed and properly fitted to a Boltzmann type sigmoidal function (indicated under Materials and Methods) by using a non-linear regression analysis. In the absence and presence of $10 \mu\text{M}$ *aPO*, the $V_{1/2}$ value was noticed to differ significantly (-62.6 ± 1.3 mV (in the control) versus -49.2 ± 1.4 mV (in the presence of *aPO*); $n = 7$, $p < 0.05$); in contrast, the value of q (apparent gating charge) did not differ significantly (2.79 ± 0.12 e (in the control) versus 2.82 ± 0.13 e (in the presence of *aPO*); $n = 7$, $p > 0.05$). Therefore, cell exposure to *aPO* not only increased the maximal conductance of I_{Na} , but also shifted the inactivation curve to the rightward direction by approximately 13 mV. However, we found no evident change in the gating charge of the inactivation curve during cell exposure to *aPO*. As such, it is reasonable to assume that the steady-state I_{Na} inactivation curve in the presence of this compound was shifted rightward, with no clear adjustment in the gating charge of this curve.

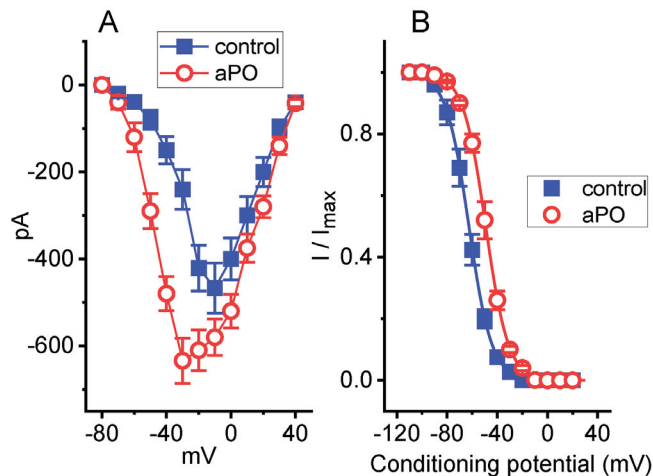


Figure 2. Stimulatory effect of *aPO* on averaged current–voltage (*I*-*V*) relationship (A) and steady-state inactivation curve (B) of I_{Na} present in GH₃ cells. Cells were kept bathed in Ca^{2+} -free Tyrode's solution containing 10 mM TEA. (A) Averaged *I*-*V* relationships of I_{Na} in the absence (■) and presence (○) of $10 \mu\text{M}$ *aPO* (mean \pm SEM; $n = 8$ for each point). The examined cell was held at -80 mV and the 40-ms voltage pulse ranging from -80 to $+40$ mV in 10-mV steps was delivered to it. The statistical analyses were undertaken by ANOVA-2 for repeated measures, p (factor 1, groups among data ken at different level of voltages) < 0.05 , p (factor 2, groups between the absence and presence of *aPO*) < 0.05 , p (interaction) < 0.05 , followed by post-hoc Fisher's least-significant difference test, $p < 0.05$. (B) Effect of *aPO* on the steady-state inactivation curve of I_{Na} taken without (■) or with (○) the addition of $10 \mu\text{M}$ *aPO*. In these experiments, the conditioning voltage pulses with a duration of 40 ms to various membrane potentials between -120 and $+20$ mV were applied from a holding potential of -80 mV. Following each conditioning potential, a test pulse to -10 mV with a duration of 40 ms was delivered to activate I_{Na} . The normalized amplitude of I_{Na} (I/I_{max}) was constructed against the conditioning potential and the sigmoidal curves were optimally fitted by the Boltzmann equation (indicated under Materials and Methods). Each point represents the mean \pm SEM ($n = 7$). The statistical analyses were undertaken by ANOVA-2 for repeated measures, p (factor 1, groups among data ken at different level of conditioning potentials) < 0.05 , p (factor 2, groups between the absence and presence of *aPO*) < 0.05 , p (interaction) < 0.05 , followed by post-hoc Fisher's least-significant difference test, $p < 0.05$.

3.4. Effect of *aPO* on the Recovery from I_{Na} Inactivation by Using Two-Step Voltage Protocol

We then examined whether the presence of *aPO* produces any effect on the recovery of I_{Na} from inactivation. In a two-step voltage protocol, a 50-ms conditioning step to -10 mV inactivated most of the current, and the recovery from current inactivation at the holding potential of -80 mV was examined at different times with a test step (-10 mV, 50 ms), as demonstrated in Figure 3A,B. In the control period (i.e., *aPO* was not present), the peak amplitude of I_{Na} nearly completely recovered from inactivation when the interpulse duration was set at 100 ms. The time constant course of recovery from current inactivation in the absence or presence of *aPO* ($10 \mu\text{M}$) was least-squares fitted to a single-exponential function with a time constant of 23.3 ± 1.1 or 11.3 ± 0.9 ms ($n = 8$, $p < 0.05$), respectively. These experimental observations indicate that cell exposure to *aPO* produces a significant shortening in the recovery from inactivation of I_{Na} in GH₃ cells.

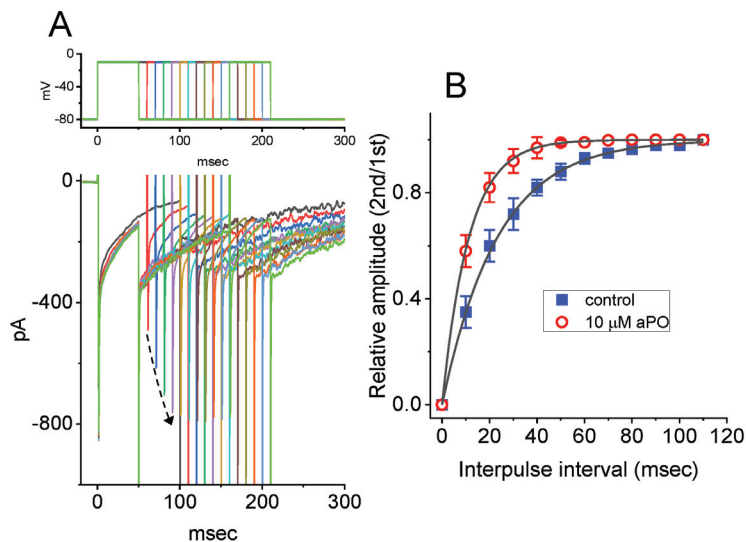


Figure 3. Effect of *aPO* on the time course of recovery from I_{Na} inactivation. The cell tested was depolarized from -80 to -10 mV with a duration of 50 ms, and voltage-clamp commands with varying durations of interpulse interval (i.e., the interval between the first and second pulses) were applied to it. (A) Superimposed I_{Na} traces in the presence of $10 \mu\text{M}$ *aPO*. The upper part shows the voltage protocol applied. The dashed arrow indicates the trajectory of current inactivation elicited by different durations of interpulse pulse. (B) Effect of *aPO* on the time course of recovery from current inactivation, as the cells examined were depolarized from -80 to -10 mV. ■: control; ○: *aPO* ($10 \mu\text{M}$). Each smooth line was optimally fitted by a single-exponential function. The relative amplitude denotes that the peak I_{Na} taken at the second pulse is divided by that at the first one. Each point represents the mean \pm SEM ($n = 8$). The statistical analyses were undertaken by ANOVA-2 for repeated measures, p (factor 1, groups among data taken at different interpulse intervals) < 0.05 , p (factor 2, groups between the absence and presence of *aPO*) < 0.05 , p (interaction) < 0.05 , followed by post-hoc Fisher's least-significant difference test, $p < 0.05$.

3.5. Comparison among Effects of *aPO*, Tefluthrin (Tef), Tef Plus *aPO*, *aPO* Plus Rufinamide (RFM), and *aPO* Plus Ranolazine (Ran) on the Peak Amplitude of I_{Na}

Tef, a type-I pyrethroid insecticide, was reported to be an activator of I_{Na} [23–25,27], Ran is recognized as a late I_{Na} blocker as well as an inhibitor of NOX activity [26,28–30], and RFM, known to be an antiepileptic agent, was previously demonstrated to perturb I_{Na} inactivation [31,32]. For these reasons, we further examined and then compared the effects of these agents on peak I_{Na} identified in GH₃ cells. As demonstrated in Figure 4, in accordance with previous studies [23], one minute after Tef ($10 \mu\text{M}$) was

applied, it was effective in stimulating peak I_{Na} . However, in the continued presence of Tef for two minutes, one minute after further addition of $10 \mu\text{M}$ *aPO*, peak I_{Na} was not increased further. In addition, as cells were continually exposed to $10 \mu\text{M}$ *aPO*, subsequent application of $10 \mu\text{M}$ RFM or $10 \mu\text{M}$ Ran was able to attenuate *aPO*-induced stimulation of I_{Na} one minute later. The results imply that *aPO* and Tef share a similarity to their stimulation of I_{Na} , and that further addition of RFM or Ran is effective in attenuating *aPO*-stimulated I_{Na} in GH₃ cells.

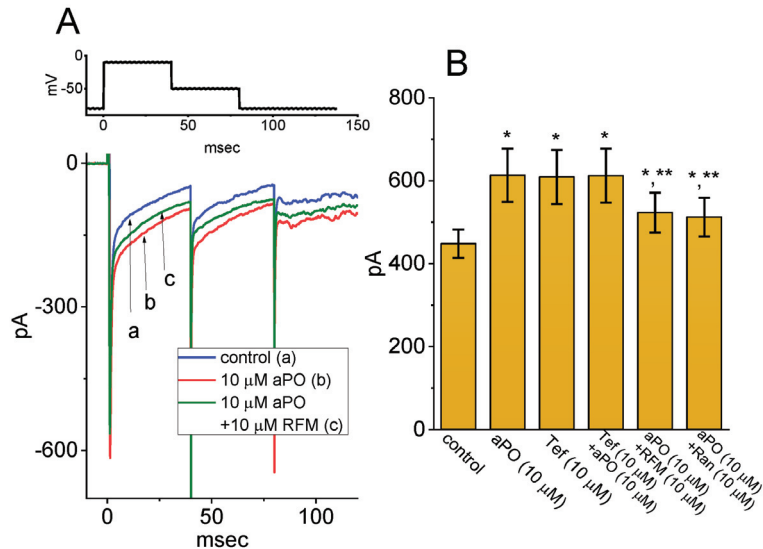


Figure 4. Effect of *aPO*, tefluthrin (Tef), Tef plus *aPO*, *aPO* plus rufinamide (RFM), and *aPO* plus ranolazine (Ran) on peak amplitude of I_{Na} identified in GH₃ cells. (A) Representative I_{Na} traces activated by depolarizing pulse (as indicated in the upper part). a: control; b: $10 \mu\text{M}$ *aPO*; c: $10 \mu\text{M}$ *aPO* plus $10 \mu\text{M}$ RFM. (B) Summary bar graph showing effect of *aPO*, Tef, Tef plus *aPO*, *aPO* plus RFM, and *aPO* plus Ran on peak I_{Na} (mean \pm SEM; $n = 8$ – 10 for each bar). The number of the control group is 10, while those in other groups are 8. Data analysis was performed by ANOVA-1 ($p < 0.05$). * Significantly different from control ($p < 0.05$) and ** significantly different from *aPO* ($10 \mu\text{M}$) alone group ($p < 0.05$).

3.6. Stimulatory Action of *aPO* on I_{Na} in Methylglyoxal- (MeG-) or Superoxide Dismutase- (SOD-) Treated Cells

One would expect that the effect of *aPO* on I_{Na} is engaged in either its inhibition of NOX activity or the reduction in the production of reactive oxygen species. The expression of NOX was previously reported to be distributed in pituitary cells [14,15]. As such, the effect of *aPO* on I_{Na} was assessed in cells preincubated with MeG or SOD for 6 h. MeG was previously recognized to be a substrate for NOX activity [33–35], while SOD, an antioxidative enzyme, was reported to reduce the production of reactive oxygen species [36]. However, in GH₃ cells preincubated with MeG for 6 h, the I-V relationship of peak I_{Na} with or without addition of *aPO* is illustrated in Figure 5. For example, in cells pretreated with MeG ($10 \mu\text{M}$), *aPO* ($10 \mu\text{M}$) could significantly increase the amplitude of I_{Na} measured at the level of -20 mV from 401 ± 31 to 511 ± 39 pA ($n = 7$, $p < 0.05$). Likewise, in SOD-preincubated cells, the addition of *aPO* ($10 \mu\text{M}$) increased I_{Na} amplitude at -20 mV from 409 ± 31 to 515 ± 41 pA ($n = 7$, $p < 0.05$). Therefore, these results allowed us to suggest that the stimulatory effect of *aPO* on I_{Na} that we obtained in these cells is unlikely to be due to changes in either the production of reactive oxygen species or cytosolic NOX activity.

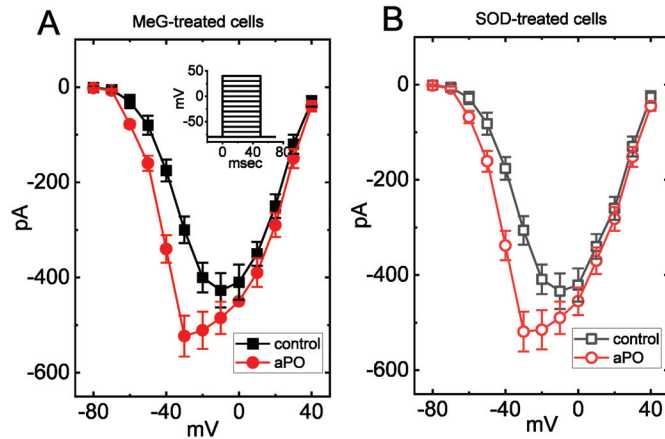


Figure 5. Stimulatory effect of *aPO* on averaged I-V relationship of I_{Na} in GH₃ cells treated with methylglyoxal (MeG) (A) or with superoxide dismutase (SOD) (B). GH₃ cells were preincubated with 10 μ M MeG for 6 h. Cells were bathed in Ca²⁺-free Tyrode's solution and the pipette was filled up with Cs⁺-containing solution. The cell tested was maintained at -80 mV and the depolarizing pulses ranging between -80 and $+40$ mV were thereafter delivered to it. Each point represents the mean \pm SEM ($n = 7$). Inset denotes the voltage-clamp protocol used. \blacksquare or \square : control; \bullet or \circ : *aPO* (10 μ M). Noticeably, in MeG- or SOD-treated cells, the stimulatory effect of *aPO* on the overall I-V relationships of peak I_{Na} was altered little. The statistical analyses were undertaken by ANOVA-2 for repeated measures, p (factor 1, groups among data taken at different levels of voltages) < 0.05 , p (factor 2, groups between the absence and presence of *aPO*) < 0.05 , p (interaction) < 0.05 , followed by post-hoc Fisher's least-significant difference test, $p < 0.05$).

3.7. Effect of *aPO* on the Amplitude and Voltage-Dependent Hysteresis (V_{hys}) of Persistent Na^+ ($I_{Na(P)}$)

The V_{hys} behavior residing in varying types of ion channels (i.e., the difference in current trajectory in response to the upsloping and the downsloping voltages) is currently a subject of extensive research, including Na_V channels [24,37,38]. We next examined whether or how the presence of *aPO* is able to modify $I_{Na(P)}$ V_{hys} activated in response to the upright isosceles-triangular ramp pulse in GH₃ cells. In this stage of our whole-cell current recordings, the tested cell was voltage-clamped at the level of -80 mV and we then applied it with a set of isosceles-triangular ramp pulses ranging between -110 and $+50$ mV (with a height of 160 mV) of varying ramp duration at a rate of 0.05 Hz through digital-to-analog conversion (Figure 6A). Consistent with previous observations [24,26], the amplitude of $I_{Na(P)}$ in response to such upright triangular ramp voltage was noticed to display a striking figure-of-eight V_{hys} (i.e., ∞) in the instantaneous I-V relationship of $I_{Na(P)}$ with two distinct peaks, i.e., low and high threshold $I_{Na(P)}$. Alternatively, there is an initial counterclockwise direction, which time goes by, in current trajectory (i.e., high-threshold loop with a peak at -0 mV) activated by the upsloping limb, and following the downsloping limb, a clockwise direction (i.e., low-threshold loop with a peak at -80 mV) ensued (Figure 6B). Of particular interest, one minute after GH₃ cells were exposed to 30 μ M *aPO* alone, the amplitude of $I_{Na(P)}$ at high or low threshold respectively activated by the upsloping triangular ramp voltage (forward or ascending) or downsloping (backward or descending) limb of upright triangular ramp voltage was increased. The augmentation of low-threshold $I_{Na(P)}$ produced by 30 μ M *aPO* was observed to be greater than that in the high-threshold one (Figure 6C), for example, as the isosceles-triangular ramp pulse with a duration of 3.2 s (or ramp speed of ± 0.1 mV/ms). In the presence of 30 μ M *aPO*, the peak $I_{Na(P)}$ amplitude measured at the level of -0 mV (i.e., high-threshold $I_{Na(P)}$) during the ascending phase of triangular ramp pulse was significantly raised to

175 ± 29 pA (n = 8, p < 0.05) from a control value (measured at the isopotential level) of 151 ± 18 pA (n = 8). Meanwhile, during cell exposure to 30 μM *aPO*, the peak $I_{Na(P)}$ amplitude measured at -80 mV during the descending phase of such a ramp concurrently increased from 285 ± 33 to 393 ± 54 pA (n = 8, p < 0.05). Alternatively, the subsequent application of 10 μM Ran, but still in the continued presence of 30 μM *aPO*, was able to attenuate the *aPO*-mediated increase of $I_{Na(P)}$ taken at either high or low threshold amplitude in the V_{phys} loop. These observations, therefore, enabled us to indicate that the V_{phys} strength of $I_{Na(P)}$ activated by isosceles-triangular ramp pulses of varying ramp duration observed in GH₃ cells was enhanced in the presence of *aPO* (Figure 6B,C).

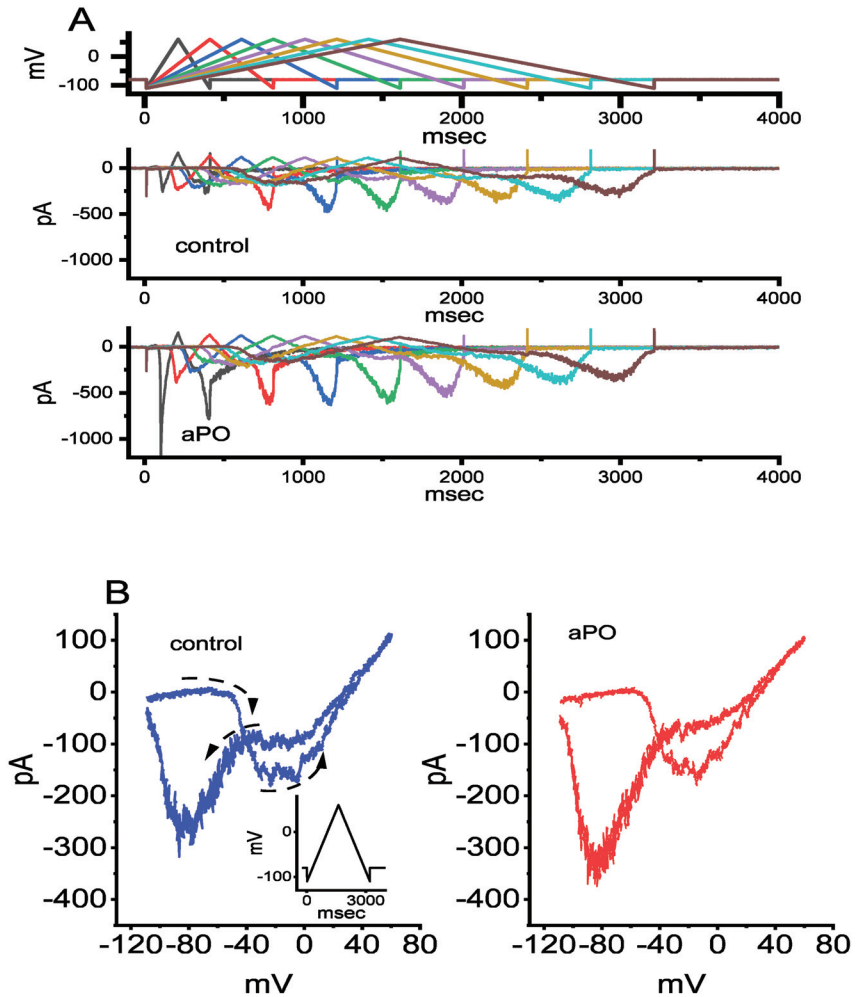


Figure 6. Cont.

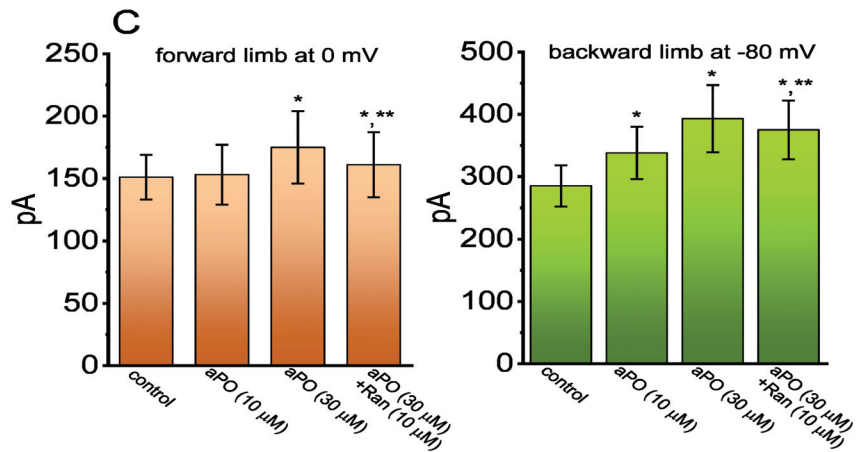


Figure 6. Effect of *aPO* on voltage-dependent hysteresis (V_{hys}) of persistent I_{Na} ($I_{Na(P)}$) activated by isosceles-triangular ramp pulses with varying ramp duration in GH_3 cells. In this series of whole-cell current recordings, we voltage-clamped the tested cell at -80 mV and the isosceles-triangular ramp voltage with varying duration of 0.4 to 3.2 s (i.e., ramp speed of ± 0.1 to 0.8 mV/ms) to activate $I_{Na(P)}$ in response to the forward (i.e., ascending from -110 to $+50$ mV) and backward (descending from $+50$ to -110 mV) that was thereafter applied to it. (A) Representative $I_{Na(P)}$ traces obtained in the control period (upper, *aPO* was not present), and during cell exposure to $10 \mu M$ *aPO* (lower). The uppermost part shows varying durations of isosceles-triangular ramp pulse applied. Of notice, the presence of *aPO* can augment the $I_{Na(P)}$ amplitude elicited by the upsloping and downsloping limbs of the triangular ramp. (B) Representative instantaneous I-V relation of $I_{Na(P)}$ in response to isosceles-triangular ramp pulse (the voltage between -100 and $+50$ mV) with a duration of 3.2 s (as indicated in the left side of panel (B)). Current trace in the left side is control, while that in the right side was acquired from the presence of $10 \mu M$ *aPO*. The dashed arrows in the left side show the direction of $I_{Na(P)}$ trajectory in which time passes during the elicitation by the upright isosceles-triangular ramp pulse. Of interest, a striking figure-of-eight (or infinity-shaped: ∞) exists in the V_{hys} trajectory responding to the triangular ramp. (C) Summary bar graph demonstrating the effect of *aPO* and *aPO* plus Ran on $I_{Na(P)}$ amplitude activated by the upsloping and downsloping limbs of 3.2-s triangular ramp pulse (mean \pm SEM; $n = 8$ for each bar). Current amplitudes in the left side were taken at the level of 0 mV in situations where the 1.6-s ascending (upsloping) end of the triangular pulse was delivered to elicit $I_{Na(P)}$ (i.e., high-threshold $I_{Na(P)}$), while those in the right side (i.e., low-threshold $I_{Na(P)}$) was at -80 mV during the descending (downsloping) end of the pulse. Current amplitude measured is illustrated in the absolute value. Data analyses were performed by ANOVA-1 ($p < 0.05$). * Significantly different from controls ($p < 0.05$) and ** significantly different from *aPO* ($30 \mu M$) alone groups ($p < 0.05$).

3.8. Effect of *aPO* on Erg-Mediated K^+ Current ($I_{K(erg)}$) in GH_3 Cells

Earlier studies have demonstrated that telmisartan, an activator of I_{Na} , can be effective in inhibiting $I_{K(erg)}$ [22]. For this reason, we decided to investigate whether *aPO* exercises any perturbations on $I_{K(erg)}$. The biophysical and pharmacological properties of $I_{K(erg)}$ in GH_3 cells have been previously reported [22,39–41]. In these whole-cell experiments, we bathed cells in high- K^+ , Ca^{2+} -free solution, and the recording pipette was filled up with K^+ -containing solution. The composition of these solutions was detailed under Materials and Methods. The examined cell was voltage-clamped at -10 mV and the linear downsloping ramp pulse from -10 to -100 mV with a duration of 1 s was applied to it. As shown in Figure 7, the addition of $10 \mu M$ *aPO* resulted in a progressive decline in the amplitude of deactivating $I_{K(erg)}$ in response to such a downsloping hyperpolarizing ramp. However, in the continued presence of *aPO*, further application of E-4031, an inhibitor of $I_{K(erg)}$, was

able to decrease the current amplitude further. Therefore, unlike I_{Na} induced by *aPO*, $I_{K(erg)}$ residing in these cells was subject to being inhibited by its presence.

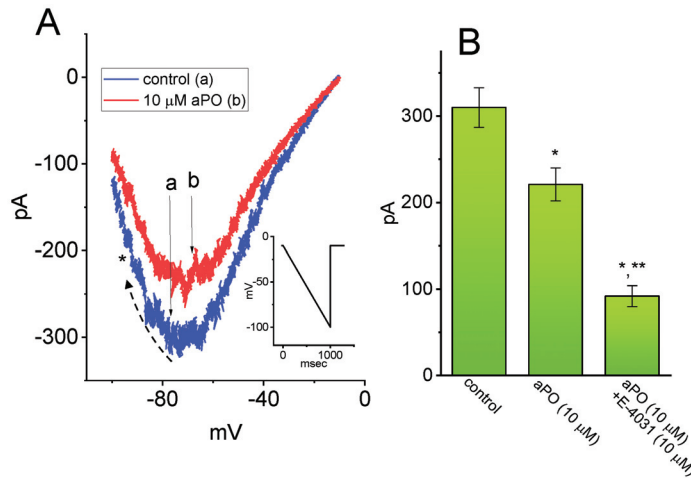


Figure 7. Effect of *aPO* on erg-mediated K^+ current ($I_{K(erg)}$) in GH₃ cells. The experiments were undertaken in cells that were bathed in high- K^+ , Ca^{2+} -free solution containing 1 μ M tetrodotoxin (TTX), and the recording pipette was filled up with K^+ -containing internal solution. **(A)** Representative $I_{K(erg)}$ traces obtained in the control (a) and during cell exposure to 10 μ M *aPO* (b). The examined cell was held at -10 mV and a downsloping ramp from -10 to -100 mV with a duration of 1 s (indicated in the inset) was applied to it. The dashed arrow indicates the direction of current trajectory in which time passes, while the asterisk shows the inwardly-rectifying property of $I_{K(erg)}$. **(B)** Summary bar graph showing effect of *aPO* and *aPO* plus E-4031 on the amplitude of $I_{K(erg)}$ (mean \pm SEM; $n = 8$ for each bar). Current amplitude (i.e., peak $I_{K(erg)}$ amplitude) was measured at the level of -70 mV. Data analyses were performed by ANOVA-1 ($p < 0.05$). * Significantly different from control ($p < 0.05$) and ** significantly different from the *aPO* (10 μ M) alone group ($p < 0.05$).

3.9. Effect of *aPO* on I_{Na} Recorded from Murine HL-1 Cardiomyocytes

aPO was previously demonstrated to be a chemo-preventive agent for cardiovascular disorders through the inhibition of NOX activity [35,42–44]. In another set of experiments, we tested whether I_{Na} inherently in heart cells (i.e., HL-1 cardiomyocytes) could still be modified by the presence of *aPO*. The preparation of these cells was described above under Materials and Methods. Cells were kept bathed in Ca^{2+} -free Tyrode's solution in which 10 mM TEA was included, and the pipette was filled with Cs^+ -enriched solution. Noticeably, as HL-1 cells were continually exposed to *aPO* at a concentration of 3 or 10 μ M, the amplitude of peak I_{Na} activated by 50-ms depolarizing pulses from -80 to -10 mV was increased; concomitantly, progressive slowing of the inactivation time course of the current was seen (Figure 8A,B). For example, cell exposure to 10 μ M *aPO* resulted in a conceivable increase of peak I_{Na} from 859 ± 56 to 1381 ± 85 pA ($n = 8$, $p < 0.05$); concomitantly, the $\tau_{inact(S)}$ value was significantly raised to 56.3 ± 7.1 ms ($n = 8$, $p < 0.05$) from a control value of 7.1 ± 1.4 ms. After washout of *aPO* (i.e., *aPO* was removed, but cells were still exposed to Ca^{2+} -free Tyrode's solution containing 10 mM TEA), current amplitude returned 892 ± 58 pA ($n = 8$, $p < 0.05$). Alternatively, in the continued presence of *aPO* (10 μ M), further application of either ranolazine (Ran, 10 μ M) or esaxerenone (ESAX, 10 μ M) was noticed to attenuate *aPO*-mediated stimulation of I_{Na} (Figure 8B). Like Ran, ESAX was recently reported to inhibit I_{Na} [24]. Therefore, consistent to some extent with the observations done in GH₃ cells, the results reflect the effectiveness of *aPO* in stimulating I_{Na} in response to the rapid depolarizing step in HL-1 cells.

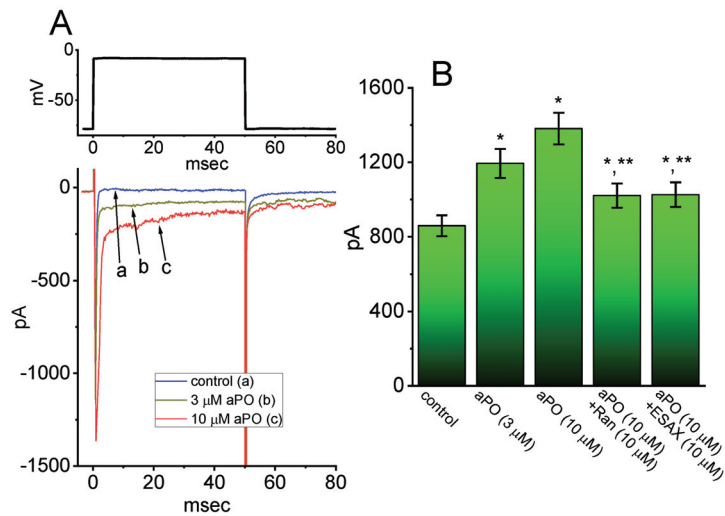


Figure 8. Effect of *aPO* on depolarization-activated I_{Na} present in HL-1 cardiomyocytes. In this set of experiments, we kept cells immersed in Ca^{2+} -free Tyrode's solution and the electrode was filled with Cs^{+} -enriched solution. When whole-cell configuration was established, we voltage-clamped the cell at -80 mV and the brief depolarization to -10 mV was delivered to it. (A) Representative I_{Na} traces activated by depolarizing command pulse (indicated in the upper part). a: control; b: $3 \mu M$ *aPO*; c: $10 \mu M$ *aPO*. (B) Summary bar graph showing effects of *aPO*, *aPO* plus ranolazine (Ran), and *aPO* plus esaxerenone (ESAX) on peak amplitude of I_{Na} in HL-1 heart cells (mean \pm SEM; $n = 8$ for each bar). Current amplitude was measured at the beginning of 50-ms depolarizing pulses from -80 to -10 mV. Data analyses were performed by ANOVA-1 ($p < 0.05$). * Significantly different from control ($p < 0.05$) and ** Significantly different *aPO* ($10 \mu M$) alone group ($p < 0.05$).

4. Discussion

The distinctive findings in the present study are that (a) GH₃-cell exposure to *aPO* could increase I_{Na} in a concentration, time-, state-, and V_{hys}-dependent fashion; (b) this agent resulted in the differential stimulation of peak or late amplitude of I_{Na} activated by abrupt step depolarization with an ineffective EC₅₀ value of 13.2 or 2.8 μM , respectively; (c) *aPO* mildly shifted the I-V curve of I_{Na} towards the depolarized potentials (i.e., a leftward shift), and it also made a rightward shift in the steady-state inactivation curve of the current towards the right side with no changes in the gating charge of the curve; (d) the recovery of the I_{Na} block was enhanced in its presence; (e) subsequent addition of rufinamide (RFM) or ranolazine (Ran) counteracted *aPO*-accentuated I_{Na} ; (f) the stimulatory effect of *aPO* on I_{Na} remained unaltered in cells preincubated with MeG or SOD; (g) *aPO* was capable of increasing the high- or low-threshold amplitude of $I_{Na(P)}$ elicited by the isosceles-triangular ramp at either upsloping (ascending) or downsloping (descending) limb, respectively; (h) the *aPO* presence mildly decreased the amplitude of $I_{K(erg)}$ activated by the downsloping ramp pulse; and (i) the exposure to *aPO* was effective at increasing the amplitude and inactivation time constant of I_{Na} in HL-1 atrial cardiomyocytes. Collectively, the present results allow us to reflect that *aPO*-stimulated changes in the amplitude, gating, and V_{hys} behavior of I_{Na} appear to be unlinked to and upstream of its inhibitory action on NOX activity, and that it would participate in the adjustments of varying functional activities in electrically excitable cells (e.g., GH₃ or HL-1 cells), presuming that similar in vivo findings exist.

From the overall I-V relationship of I_{Na} demonstrated here, there was a slight shift toward more negative potential in the presence of *aPO*. The steady-state inactivation curve of I_{Na} in its presence of *aPO* was also shifted to a rightward direction with no apparent change in the gating charge of the curve. The increased recovery of the I_{Na} block was

demonstrated in its presence. As a result, the window current of I_{Na} in GH₃ cells was expected to be increased during cell exposure to *aPO*. Such a small molecule may have higher affinity to the open/inactivated state than to the resting (closed) state residing in the Nav channels, despite the detailed ionic mechanism of its stimulatory action on the channel remaining elusive.

Several lines of clear evidence have been demonstrated to indicate that *aPO* can inhibit NOX activity and decrease the production of superoxide oxide [2–4,16]. Pituitary cells have been previously demonstrated to be expressed in the activity of NOX [14–16]. As such, the question arises as to whether the stimulatory effect of *aPO* on I_{Na} observed in GH₃ cells may actually result from either the reduction of NOX activity or the decreased level of superoxide anions [15,16]. However, this notion appears to be difficult to reconcile with the present observations disclosing that in GH₃ cells preincubated with MeG or SOD, the stimulatory effect of *aPO* on I_{Na} was indeed observed to remain effective. It is also noted that *aPO* can mildly inhibit the amplitude of $I_{K(erg)}$. Therefore, under our experimental conditions, the stimulation of I_{Na} caused by *aPO* tends to emerge in a manner largely independent of its inhibitory effect on NOX activity; hence, the *aPO* molecule can exert an interaction at binding site(s) inherently existing on Nav channels.

Perhaps more important than the issue of the magnitude of the *aPO*-induced increase in I_{Na} is that we observed the non-linear V_{hys} of $I_{Na(P)}$ in the control period (i.e., *aPO* was not present) and during cell exposure to *aPO* or *aPO* plus Ran, by use of the upright isosceles-triangular ramp voltage command of varying duration through digital-to-analog conversion. In particular, when cells were exposed to *aPO*, the peak $I_{Na(P)}$ activated by the forward (ascending or upsloping) end of the triangular ramp of varying duration was observed to be elevated, particularly at the peak level of 0 mV, whereas the $I_{Na(P)}$ amplitude at the backward (descending or downsloping) end was increased at the peak level of −80 mV. In this respect, the figure-of-eight (i.e., infinity-shaped: ∞) configuration in the V_{hys} loop activated by the triangular ramp pulse was evidently demonstrated (Figure 6A,B). Additionally, there appeared to be two types of V_{hys} loops, that is, a low-threshold loop with a peak at −80 mV (i.e., activating at a voltage range near the resting potential) and a high-threshold loop with a peak at 0 mV (i.e., activating at a voltage range near the maximal I_{Na} elicited by rectangular depolarizing step. The presence of *aPO* was capable of enhancing the V_{hys} strength of $I_{Na(P)}$ and, in its continued presence, further addition of Ran attenuated *aPO*-increased V_{hys} loop of the current. In this scenario, findings from the present observations disclosed that the triangular pulse-induced $I_{Na(P)}$ was detected to undergo striking V_{hys} change (i.e., initial counterclockwise direction followed by clockwise one) in the voltage-dependence and that such V_{hys} loops were subject to enhancement by the presence of *aPO*.

Pertinent to the stimulatory effect of *aPO* on I_{Na} is that in this study, due to its effectiveness in increasing the V_{hys} magnitude of $I_{Na(P)}$, the voltage-dependent movement of the S4 segment residing in Nav channels is probably perturbed by this agent; consequently, the coupling of the pore domain to the voltage-sensor domain, which the S1–S4 segments comprise, tended to be facilitated [45,46]. Indeed, the voltage sensor energetically coupled to channel activation, which might be influenced by the *aPO* molecule, is supposed to be a conformationally flexible region of the Nav-channel protein. Therefore, these findings can be interpreted to mean either that such $I_{Na(P)}$, particularly during exposure to *aPO*, is intrinsically and dynamically endowed with “memory” of previous (or past) events, which is encoded in the conformational (or metastable) states of the Nav-channel protein, or that there is a mode shift of channel kinetics occurring regarding the voltage sensitivity of gating charge movement, which relies on the previous state (or conformation) of the Nav channel [37,38]. Such a striking type of V_{hys} natively in Nav channels would potentially play substantial roles in interfering with electrical behavior, Na⁺ overload, and hormonal secretion in varying types of excitable cells [37]. It is also worth pointing out that the subsequent addition of Ran, still in the continued presence of *aPO*, did produce a considerable reduction in the *aPO*-mediated increase in V_{hys} responding to triangular ramp voltage.

From pharmacokinetic studies in mice [47], following intravenous injection of *aPO* (5 mg/kg), the peak plasma *aPO* level was detected at 1 min to reach around 5500 ng/mL (or 33.1 μ M). Additionally, *aPO* was reportedly a selective inhibitor of NOX2 activity with an effective IC_{50} of 10 μ M [48]. According to the data of Figure 1, the IC_{50} value required for the *aPO*-stimulated peak or late I_{Na} was 13.2 or 2.8 μ M, respectively, while the K_D value estimated on the basis of minimal reaction scheme was 3.4 μ M. It is reasonable to assume, therefore, that *aPO*-induced changes in the amplitude, gating or *Whys* behavior of I_{Na} presented herein could be highly achievable and of pharmacological relevance.

On the basis of the present experimental observations, despite the inhibitory effect on NOX activity [2–4], our results strongly suggest that the stimulatory actions of *aPO* on transmembrane ionic currents, particularly on Na_V channels, tends to be direct obligate mechanisms. Pyrethroids (e.g., permethrin and cypermethrin), known to activate I_{Na} , have also been reported to disrupt NOX activity in brain tissue (striatum) [49]. Therefore, through ionic mechanisms shown herein, pyrethroids or other structurally similar compounds are able to adjust the functional activities of varying types of neuroendocrine or endocrine cells, or heart cells, if similar *in vivo* results exist [6,7,11–13,50]. To this end, the overall findings from our study highlight an important alternative aspect that has to be taken into account, inasmuch as there is the beneficial or ameliorating effect of *aPO* in various pathologic disorders, such as inflammatory or neurodegenerative diseases, and heart failure [1,3,6,7,9–13,16,42].

Supplementary Materials: The details of cell preparation in Materials and Methods were mentioned in Supplementary Material which is available online <https://www.mdpi.com/article/10.3390/biomedicines9091146/s1>.

Author Contributions: Conceptualization, S.-N.W., H.-Y.C. and T.-H.C.; methodology, S.-N.W.; software, S.-N.W.; validation, H.-Y.C., T.-H.C. and S.-N.W.; formal analysis, S.-N.W.; investigation, H.-Y.C., T.-H.C. and S.-N.W.; resources, S.-N.W.; data curation, S.-N.W.; writing—original draft preparation, S.-N.W.; writing—review and editing, T.-H.C., H.-Y.C. and S.-N.W.; visualization, H.-Y.C., T.-H.C., and S.-N.W.; supervision, S.-N.W.; project administration, S.-N.W.; funding acquisition, S.-N.W. All authors have read and agreed to the published version of the manuscript.

Funding: This work was in part supported by a grant from the Ministry of Science and Technology (MOST-110-2320-B-006-028), Taiwan.

Institutional Review Board Statement: Not applicable.

Informed Consent Statement: Not applicable.

Data Availability Statement: The original data is available upon reasonable request to the corresponding author.

Acknowledgments: H.-Y.C. and T.-H.C. received the student assistantship from the Ministry of Science and Technology, Taiwan, while S.-N.W. received a Talent Award for the Outstanding Researchers from Ministry of Education, Taiwan.

Conflicts of Interest: The authors declare no competing interests that are directly relevant to the present study.

Abbreviations

AP, action potential; *aPO* (apocynin, 4'-Hydroxy-3'-methoxyacetophenone); EC_{50} , concentration required for 50% stimulation; *erg*, ether-à-go-go-related gene; ESAX, esaxerenone; I-V, current versus voltage; $I_{K(erg)}$, *erg*-mediated K^+ current; I_{Na} , voltage-gated Na^+ current; $I_{Na(P)}$, persistent Na^+ current; K_D , dissociation constant; MeG, methylglyoxal; NADPH oxidase, nicotinamide adenine dinucleotide phosphate oxidase; *Nav* channel, voltage-gated Na^+ channel; NADPH, nicotinamide adenine dinucleotide phosphate; NOX, NADPH oxidase; *Whys*, voltage-dependent hysteresis; Ran, ranolazine; RFM, rufinamide; SEM, standard error of the mean; SOD, superoxide dismutase; $\tau_{inact(S)}$, slow component of inactivation time constant; TEA, tetraethylammonium chloride; Tef, tefluthrin; TTX, tetrodotoxin.

References

1. Yang, T.; Zang, D.-W.; Shan, W.; Guo, A.-C.; Wu, J.-P.; Wang, Y.-J.; Wang, Q. Synthesis and Evaluations of Novel Apocynin Derivatives as Anti-Glioma Agents. *Front. Pharmacol.* **2019**, *10*, 951. [CrossRef]
2. Stefanska, J.; Pawliczak, R. Apocynin: Molecular Aptitudes. *Mediat. Inflamm.* **2008**, *2008*, 1–10. [CrossRef]
3. Petrônio, M.S.; Zeraik, M.L.; Da Fonseca, L.M.; Ximenes, V.F. Apocynin: Chemical and Biophysical Properties of a NADPH Oxidase Inhibitor. *Molecules* **2013**, *18*, 2821–2839. [CrossRef]
4. Abliz, A.; Chen, C.; Deng, W.; Wang, W.; Sun, R. NADPH Oxidase Inhibitor Apocynin Attenuates PCB153-Induced Thyroid Injury in Rats. *Int. J. Endocrinol.* **2016**, *2016*, 8354745. [CrossRef]
5. Du, Z.-D.; Yu, S.; Qi, Y.; Qu, T.-F.; He, L.; Wei, W.; Liu, K.; Gong, S.-S. NADPH oxidase inhibitor apocynin decreases mitochondrial dysfunction and apoptosis in the ventral cochlear nucleus of D-galactose-induced aging model in rats. *Neurochem. Int.* **2019**, *124*, 31–40. [CrossRef] [PubMed]
6. Qiu, J.; Zhao, J.; Li, J.; Liang, X.; Yang, Y.; Zhang, Z.; Zhang, X.; Fu, H.; Korantzopoulos, P.; Liu, T.; et al. NADPH oxidase inhibitor apocynin prevents atrial remodeling in alloxan-induced diabetic rabbits. *Int. J. Cardiol.* **2016**, *221*, 812–819. [CrossRef] [PubMed]
7. Gimenes, R.; Rosa, C.M.; Xavier, N.P.; Campos, D.H.S.; Fernandes, A.A.H.; Cezar, M.D.M.; Guirado, G.N.; Pagan, L.U.; Chaer, I.D.; Fernandes, D.D.C.; et al. Influence of apocynin on cardiac remodeling in rats with streptozotocin-induced diabetes mellitus. *Cardiovasc. Diabetol.* **2018**, *17*, 15. [CrossRef]
8. Lee, S.H.; Choi, B.Y.; Kho, A.R.; Jeong, J.H.; Hong, D.K.; Kang, D.H.; Kang, B.S.; Song, H.K.; Choi, H.C.; Suh, S.W. Inhibition of NADPH Oxidase Activation by Apocynin Rescues Seizure-Induced Reduction of Adult Hippocampal Neurogenesis. *Int. J. Mol. Sci.* **2018**, *19*, 3087. [CrossRef] [PubMed]
9. Olukman, M.; Önal, A.; Çelenk, F.G.; Uyanıkgil, Y.; Çavuşoğlu, T.; Duzenli, N.; Ülker, S. Treatment with NADPH oxidase inhibitor apocynin alleviates diabetic neuropathic pain in rats. *Neural Regen. Res.* **2018**, *13*, 1657–1664. [CrossRef]
10. Hou, L.; Sun, F.; Huang, R.; Sun, W.; Zhang, D.; Wang, Q. Inhibition of NADPH oxidase by apocynin prevents learning and memory deficits in a mouse Parkinson's disease model. *Redox Biol.* **2019**, *22*, 101134. [CrossRef]
11. Wang, K.; Zhu, Z.; Chi, R.; Li, Q.; Yang, Z.; Jie, X.; Hu, X.; Han, X.; Wang, J.; Li, B.; et al. The NADPH oxidase inhibitor apocynin improves cardiac sympathetic nerve terminal innervation and function in heart failure. *Exp. Physiol.* **2019**, *104*, 1638–1649. [CrossRef] [PubMed]
12. El-Sawalhi, M.M.; Ahmed, L.A. Exploring the protective role of apocynin, a specific NADPH oxidase inhibitor, in cisplatin-induced cardiotoxicity in rats. *Chem. Interact.* **2014**, *207*, 58–66. [CrossRef] [PubMed]
13. Liu, J.-J.; Lu, Y.; Ping, N.-N.; Li, X.; Lin, Y.-X.; Li, C.-F. Apocynin Ameliorates Pressure Overload-Induced Cardiac Remodeling by Inhibiting Oxidative Stress and Apoptosis. *Physiol. Res.* **2017**, *66*, 741–752. [CrossRef] [PubMed]
14. Bui, Q.D.; Weisz, J. Monoxygenase mediating catecholestrogen formation by rat anterior pituitary is an estrogen-4-hydroxylase. *Endocrinology* **1989**, *124*, 1085–1087. [CrossRef]
15. Dang, A.K.; Chaplin, N.L.; Murtazina, D.A.; Boehm, U.; Clay, C.M.; Amberg, G.C. Subplasmalemmal hydrogen peroxide triggers calcium influx in gonadotropes. *J. Biol. Chem.* **2018**, *293*, 16028–16042. [CrossRef]
16. Colaianna, M.; Schiavone, S.; Zotti, M.; Tucci, P.; Morgese, M.G.; Bäckdahl, L.; Holmdahl, R.; Krause, K.-H.; Cuomo, V.; Trabace, L. Neuroendocrine Profile in a Rat Model of Psychosocial Stress: Relation to Oxidative Stress. *Antioxid. Redox Signal.* **2013**, *18*, 1385–1399. [CrossRef]
17. Song, W.; Shou, W. Cardiac Sodium Channel Nav1.5 Mutations and Cardiac Arrhythmia. *Pediatr. Cardiol.* **2012**, *33*, 943–949. [CrossRef]
18. Jiang, D.; Shi, H.; Tonggu, L.; El-Din, T.M.G.; Lenaeus, M.J.; Zhao, Y.; Yoshioka, C.; Zheng, N.; Catterall, W.A. Structure of the Cardiac Sodium Channel. *Cell* **2020**, *180*, 122–134.e10. [CrossRef]
19. Ilatovskaya, D.V.; Pavlov, T.S.; Levchenko, V.; Staruschenko, A. ROS production as a common mechanism of ENaC regulation by EGF, insulin, and IGF-Am. *J. Physiol. Physiol.* **2013**, *304*, C102–C111. [CrossRef]
20. Downs, C.A.; Johnson, N.M.; Cocab, C.; Helms, M.N. Angiotensin II regulates δ -ENaC in human umbilical vein endothelial cells. *Microvasc. Res.* **2018**, *116*, 26–33. [CrossRef]
21. Bancroft, F.C.; Tashjian, A.H. Control of the production of two protein hormones by rat pituitary cells in culture. *Vitr. Cell. Dev. Biol.-Plant* **1970**, *6*, 180–189. [CrossRef]
22. Chang, W.T.; Wu, S.N. Activation of voltage-gated sodium current and inhibition of erg-mediated potassium current caused by telmisartan, an antagonist of angiotensin II type-1 receptor, in HL-1 atrial cardiomyocytes. *Clin. Exp. Pharm. Physiol.* **2018**, *45*, 797–807. [CrossRef]
23. Wu, S.N.; Wu, Y.-H.; Chen, B.-S.; Lo, Y.-C.; Liu, Y.-C. Underlying mechanism of actions of tefluthrin, a pyrethroid insecticide, on voltage-gated ion currents and on action currents in pituitary tumor (GH3) cells and GnRH-secreting (GT1-7) neurons. *Toxicology* **2009**, *258*, 70–77. [CrossRef]
24. Chang, W.-T.; Wu, S.-N. Characterization of Direct Perturbations on Voltage-Gated Sodium Current by Esaxerenone, a Nons-teroidal Mineralocorticoid Receptor Blocker. *Biomedicines* **2021**, *9*, 549. [CrossRef]
25. So, E.C.; Wu, S.-N.; Lo, Y.-C.; Su, K. Differential regulation of tefluthrin and telmisartan on the gating charges of I Na activation and inactivation as well as on resurgent and persistent I Na in a pituitary cell line (GH (3)). *Toxicol. Lett.* **2018**, *285*, 104–112. [CrossRef]

26. Chang, W.T.; Wu, S.N. Effectiveness of Columbianadin, a Bioactive Coumarin Derivative, in Perturbing Transient and Persistent I(Na). *Int. J. Mol. Sci.* **2021**, *22*, 621. [CrossRef]
27. Tan, J.; Soderlund, D.M. Actions of tefluthrin on rat Nav1.7 voltage-gated sodium channels expressed in *Xenopus* oocytes. *Pestic. Biochem. Physiol.* **2011**, *101*, 21–26. [CrossRef]
28. Chen, B.-S.; Lo, Y.-C.; Peng, H.; Hsu, T.-I.; Wu, S.-N. Effects of Ranolazine, a Novel Anti-anginal Drug, on Ion Currents and Membrane Potential in Pituitary Tumor GH3 Cells and NG108-15 Neuronal Cells. *J. Pharmacol. Sci.* **2009**, *110*, 295–305. [CrossRef]
29. Gupta, T.; Khera, S.; Kolte, D.; Aronow, W.S.; Iwai, S. Antiarrhythmic properties of ranolazine: A review of the current evidence. *Int. J. Cardiol.* **2015**, *187*, 66–74. [CrossRef] [PubMed]
30. Cappetta, D.; Esposito, G.; Coppini, R.; Piegari, E.; Russo, R.; Ciuffreda, L.P.; Rivellino, A.; Santini, L.; Rafaniello, C.; Scavone, C.; et al. Effects of ranolazine in a model of doxorubicin-induced left ventricle diastolic dysfunction. *Br. J. Pharmacol.* **2017**, *174*, 3696–3712. [CrossRef]
31. Suter, M.R.; Kirschmann, G.; Laedermann, C.J.; Abriel, H.; Decosterd, I. Rufinamide Attenuates Mechanical Allodynia in a Model of Neuropathic Pain in the Mouse and Stabilizes Voltage-gated Sodium Channel Inactivated State. *Anesthesiology* **2013**, *118*, 160–172. [CrossRef]
32. Kharatmal, S.B.; Singh, J.N.; Sharma, S.S. Rufinamide Improves Functional and Behavioral Deficits via Blockade of Tetrodotoxin-Resistant Sodium Channels in Diabetic Neuropathy. *Curr. Neurovasc. Res.* **2015**, *12*, 262–268. [CrossRef]
33. Wintergalen, N.; Thole, H.H.; Galla, H.-J.; Schlegel, W. Prostaglandin-E2 9-Reductase from Corpus Luteum of Pseudopregnant Rabbit is a Member of the Aldo-Keto Reductase Superfamily Featuring 20 α -Hydroxysteroid Dehydrogenase Activity. *JBIC J. Biol. Inorg. Chem.* **1995**, *234*, 264–270. [CrossRef] [PubMed]
34. Mukohda, M.; Okada, M.; Hara, Y.; Yamawaki, H. Methylglyoxal Accumulation in Arterial Walls Causes Vascular Contractile Dysfunction in Spontaneously Hypertensive Rats. *J. Pharmacol. Sci.* **2012**, *120*, 26–35. [CrossRef]
35. Eid, B.G.; Abu-Sharib, A.T.; El-Bassossy, H.M.; Balamash, K.; Smirnov, S.V. Enhanced calcium entry via activation of NOX/PKC underlies increased vasoconstriction induced by methylglyoxal. *Biochem. Biophys. Res. Commun.* **2018**, *506*, 1013–1018. [CrossRef] [PubMed]
36. Cannio, R.; D’Angelo, A.; Rossi, M.; Bartolucci, S. A superoxide dismutase from the archaeon *Sulfolobus solfataricus* is an extracellular enzyme and prevents the deactivation by superoxide of cell-bound proteins. *JBIC J. Biol. Inorg. Chem.* **2000**, *267*, 235–243. [CrossRef]
37. Korman, C.E.; Mayergoyz, I.D. On hysteresis of ion channels. *Math. Model. Nat. Phenom.* **2020**, *15*, 26. [CrossRef]
38. Villalba-Galea, C.A.; Chiem, A.T. Hysteretic Behavior in Voltage-Gated Channels. *Front. Pharmacol.* **2020**, *11*, 579596. [CrossRef] [PubMed]
39. Wu, S.-N.; Jan, C.-R.; Li, H.-F.; Chiang, H.-T. Characterization of Inhibition by Risperidone of the Inwardly Rectifying K⁺ Current in Pituitary GH₃ Cells. *Neuropsychopharmacology* **2000**, *23*, 676–689. [CrossRef]
40. Wu, S.N.; Yang, W.-H.; Yeh, C.-C.; Huang, H.-C. The inhibition by di(2-ethylhexyl)-phthalate of erg-mediated K⁺ current in pituitary tumor (GH₃) cells. *Arch. Toxicol.* **2012**, *86*, 713–723. [CrossRef]
41. Chang, W.-T.; Liu, P.-Y.; Wu, S.-N. High Capability of Pentagalloylglucose (PGG) in Inhibiting Multiple Types of Membrane Ionic Currents. *Int. J. Mol. Sci.* **2020**, *21*, 9369. [CrossRef]
42. Yu, J.; Weiwer, M.; Linhardt, R.J.; Dordick, J.S. The Role of the Methoxyphenol Apocynin, a Vascular NADPH Oxidase Inhibitor, as a Chemopreventative Agent in the Potential Treatment of Cardiovascular Diseases. *Curr. Vasc. Pharmacol.* **2008**, *6*, 204–217. [CrossRef] [PubMed]
43. Zhao, Z.; Fefelova, N.; Shanmugam, M.; Bishara, P.; Babu, G.J.; Xie, L.-H. Angiotensin II induces afterdepolarizations via reactive oxygen species and calmodulin kinase II signaling. *J. Mol. Cell. Cardiol.* **2011**, *50*, 128–136. [CrossRef] [PubMed]
44. Muñoz, M.; López-Oliva, M.E.; Rodríguez, C.; Martínez, M.P.; Sáenz-Medina, J.; Sánchez, A.; Climent, B.; Bedito, S.; García-Sacristán, A.; Rivera, L.; et al. Differential contribution of Nox1, Nox2 and Nox4 to kidney vascular oxidative stress and endothelial dysfunction in obesity. *Redox Biol.* **2020**, *28*, 101330. [CrossRef] [PubMed]
45. Armstrong, C.M.; Bezanilla, F. Currents Related to Movement of the Gating Particles of the Sodium Channels. *Nat. Cell Biol.* **1973**, *242*, 459–461. [CrossRef] [PubMed]
46. Stühmer, W.; Conti, F.; Suzuki, H.; Wang, X.; Noda, M.; Yahagi, N.; Kubo, H.; Numa, S. Structural parts involved in activation and inactivation of the sodium channel. *Nat. Cell Biol.* **1989**, *339*, 597–603. [CrossRef]
47. Liu, F.; Fan, L.M.; Michael, N.; Li, J. In vivo and in silico characterization of apocynin in reducing organ oxidative stress: A pharmacokinetic and pharmacodynamic study. *Pharmacol. Res. Perspect.* **2020**, *8*, e00635. [CrossRef]
48. Henriquez-Olguín, C.; Díaz-Vegas, A.; Utreras-Mendoza, Y.; Campos, C.; Arias-Calderón, M.; Llanos, P.; Contreras-Ferrat, A.; Espinosa, A.; Altamirano, F.; Jaimovich, E.; et al. NOX2 Inhibition Impairs Early Muscle Gene Expression Induced by a Single Exercise Bout. *Front. Physiol.* **2016**, *7*, 282. [CrossRef]
49. Nasuti, C.; Gabbianelli, R.; Falcioni, M.L.; Di Stefano, A.; Sozio, P.; Cantalamessa, F. Dopaminergic system modulation, behavioral changes, and oxidative stress after neonatal administration of pyrethroids. *Toxicology* **2007**, *229*, 194–205. [CrossRef]
50. Zybura, A.; Hudmon, A.; Cummins, T.R. Distinctive Properties and Powerful Neuromodulation of Na(v)1.6 Sodium Channels Regulates Neuronal Excitability. *Cells* **2021**, *10*, 1595. [CrossRef]



Article

Rational Discovery of Antiviral Whey Protein-Derived Small Peptides Targeting the SARS-CoV-2 Main Protease

Nicola Gambacorta ^{1,†}, Leonardo Caputo ^{2,†}, Laura Quintieri ^{2,*}, Linda Monaci ², Fulvio Ciriaco ³ and Orazio Nicolotti ^{1,*}

¹ Dipartimento di Farmacia Scienze del Farmaco, Università degli Studi di Bari "Aldo Moro", Via E. Orabona, 4, I-70125 Bari, Italy; nicola.gambacorta1@uniba.it

² Institute of Sciences of Food Production, National Research Council of Italy, 70126 Bari, Italy; leonardo.caputo@ispa.cnr.it (L.C.); linda.monaci@ispa.cnr.it (L.M.)

³ Dipartimento di Chimica, Università degli Studi di Bari "Aldo Moro", Via E. Orabona, 4, I-70125 Bari, Italy; fulvio.ciriaco@uniba.it

* Correspondence: laura.quintieri@ispa.cnr.it (L.Q.); orazio.nicolotti@uniba.it (O.N.)

† These authors contributed equally to this work.

Abstract: In the present work, and for the first time, three whey protein-derived peptides (IAEK, IPAVF, MHI), endowed with ACE inhibitory activity, were examined for their antiviral activity against the SARS-CoV-2 3C-like protease (3CL^{Pro}) and Human Rhinovirus 3C protease (3CP^{Pro}) by employing molecular docking. Computational studies showed reliable binding poses within 3CL^{Pro} for the three investigated small peptides, considering docking scores as well as the binding free energy values. Validation by in vitro experiments confirmed these results. In particular, IPAVF exhibited the highest inhibitory activity by returning an IC₅₀ equal to 1.21 μM; it was followed by IAEK, which registered an IC₅₀ of 154.40 μM, whereas MHI was less active with an IC₅₀ equal to 2700.62 μM. On the other hand, none of the assayed peptides registered inhibitory activity against 3CP^{Pro}. Based on these results, the herein presented small peptides are introduced as promising molecules to be exploited in the development of "target-specific antiviral" agents against SARS-CoV-2.

Keywords: antiviral peptides; protease inhibitors; molecular docking; rhinovirus; COVID-19; milk

Citation: Gambacorta, N.; Caputo, L.; Quintieri, L.; Monaci, L.; Ciriaco, F.; Nicolotti, O. Rational Discovery of Antiviral Whey Protein-Derived Small Peptides Targeting the SARS-CoV-2 Main Protease. *Biomedicines* **2022**, *10*, 1067. <https://doi.org/10.3390/biomedicines10051067>

Academic Editor: Santiago Garcia-Vallve

Received: 6 March 2022

Accepted: 30 April 2022

Published: 4 May 2022

Publisher's Note: MDPI stays neutral with regard to jurisdictional claims in published maps and institutional affiliations.



Copyright: © 2022 by the authors. Licensee MDPI, Basel, Switzerland. This article is an open access article distributed under the terms and conditions of the Creative Commons Attribution (CC BY) license (<https://creativecommons.org/licenses/by/4.0/>).

1. Introduction

On 11 March 2020, the World Health Organization (WHO) declared the novel coronavirus (COVID-19) outbreak a global pandemic for the rapid spread of severe acute respiratory syndrome coronavirus-2 (SARS-CoV-2) worldwide [1]. To date, the SARS-CoV-2 infection has caused more than 4 million deaths around the world [2].

The advent of effective vaccines and the adoption of restrictive prophylaxis measures, as well as appropriate sanitization procedures, have improved the global fight against SARS-CoV-2 [3]. However, the world still urgently needs new and affordable approaches to better counteract the spread of SARS-CoV-2 and prevent the spectrum of lethal adverse effects, especially in immunocompromised and vulnerable people. Thus, a wide range of therapies tackling the effects of COVID-19 in frail, symptomatic patients is increasingly gaining ground in clinical practice. They include both antivirals based on nucleotide analogs, such as PaxlovidTM (Nirmatrelvir and Ritonavir, Pfizer), MalnupirovirTM (Merck), Favipiravir, Remdesivir, and corticosteroids (such as Dexamethasone), and cytokine inhibitors (baricitinib and anti-IL-antibodies 6, anakinra). In addition, the use of monoclonal antibodies as an alternative to convalescent plasma is also spreading. Antivirals have been developed to block viral replication by inhibiting the RNA-dependent RNA replicase. Conversely, corticosteroids are used to avoid severe forms of the disease [4,5]. However, these drugs must be taken while under medical supervision or even in a clinical environment and they can often show serious adverse side effects. Furthermore, they all have a very

high cost, preventing their large-scale diffusion [4,6]. Thus, the discovery of new molecular entities, showing low toxicity and high specificity, to block the entry or replication of SARS-CoV-2 in host cells still represents a challenge regarding safer and more effective therapeutic solutions [7].

The SARS-CoV-2 3-chymotrypsin-like cysteine protease (3CL^{Pro}), also named the main protease (M^{Pro}), which plays an important role in the virus's life cycle, is considered an attractive target for the discovery of promising antiviral agents [8]. Importantly, 3CL^{Pro} is involved in the replication process due to its two N-terminal domains, containing two β -barrel chymotrypsin-like folds ultimately responsible for the cleavage of the viral polyproteins to yield 16 mature non-structural proteins [9,10].

Human rhinoviruses (HRV, belonging to the Picornaviridae family), etiological agents of the common cold, also show a protease (HRV 3C protease or 3C^{Pro}) involved in the viral replication process. Briefly, 3C^{Pro} and 3CL^{Pro} are cysteine proteases and share a typical chymotrypsin-like folding, a nucleophilic cysteine residue in the active site, and a preference for a glutamine or glutamic acid residue in the primary binding residue (P1 site) of the substrate proteins. Picornaviral HRV 3C protease was studied in the recent past for its degree of homology with coronaviral 3C-like proteases (3CL^{Pro}) within the 3C coding region, including the strict conservation of the active-site residues, thus providing an additional rationale for targeting drug discovery efforts [11,12]. Nevertheless, subtle differences in the active-site structures of these proteases did not allow for the identification of common inhibitors [13]. Only recently, a duplex assay based on self-assembled monolayer desorption ionization (SAMDI)-MS analysis has been developed, allowing the identification of equipotent peptides against 3CL^{Pro} and HRV 3C^{Pro} [14].

Several studies have been carried out regarding the structural and functional characterization of these proteins, to be employed for high-throughput screening for the discovery of new effective inhibitors [15–17]. The search for 3CL^{Pro} inhibitors has been pursued by exploiting FDA-approved drugs, screening the libraries of natural and chemical compounds, and considering the de novo design of novel agents [18–20]. Based on these strategies, a number of putative inhibitors, whose structures can be grouped as peptidic and non-peptidic, have been identified and are awaiting further investigations before approval [16,21–23]. Recently, the 3CL^{Pro} covalent inhibitor Nirmatrelvir (PF-07321332, purchased in combination with Ritonavir) has been authorized for emergency use for COVID-19 patients not requiring supplemental oxygen [24,25].

In order to increase the affinity and efficacy, 3CL^{Pro} inhibitor substrates have been mainly modified by introducing some reactive chemical groups, such as Michael acceptors, aldehydes, epoxy ketones, and so on [8]. However, these structural changes promote the formation of covalent bonds with the catalytic cysteine responsible for the enzyme's irreversible inhibition and, thus, for potential toxicity [14,16].

Besides synthetic compounds, other studies on promising antiviral agents are focusing on the identification of bioactive molecules from natural sources [26–28]. Among others, health-promoting - represent an attractive option. It has been reported that the role of food ingredients and active components (i.e., bioactive peptides, polysaccharides, bioactive lipids, and natural polyphenols) in supporting immune function in the prevention and treatment of COVID-19 disease is important [29,30]. Noteworthy, several peptides from milk proteins showed their ability to inhibit the main SARS-CoV-2 proteases [30,31]. Natural peptides show lower toxicity and fewer side effects: their application in adjuvant therapies is also favored by their satisfactory biological activity profiles, in which antioxidant, antimicrobial, immunomodulatory, anti-inflammatory, and/or angiotensin-converting enzyme (ACE) inhibitory activities can coexist [26,32,33]. Interestingly, peptides taken from milk proteins and endowed with ACE inhibitory activity have also been investigated recently, via *in silico* studies, for their ability to prevent interaction among the COVID-19 spike glycoproteins and the host cell dipeptidyl peptidase-4 (DPP-4, [34]); however, these promising results are still lacking validation by *in vitro* or *in vivo* studies.

Recently, we investigated ACE inhibitory activity by peptide sequences, derived from the enzymatic hydrolysis of whey proteins and predicted by molecular docking and related prioritization studies. This approach allowed us to obtain three peptides—MHI, IAEK, and IPAVF—with ACE inhibitory IC_{50} values equal to or lower than $25 \mu\text{M}$ [35]. Importantly, IPAVF and the related one-residue-longer sequence IPAVFK also exhibited DPP-4 inhibitory activity and antimicrobial activity against Gram-positive bacteria [33,34].

Building on these observations, we explored the potential of our recently studied ACE inhibitory peptides (i.e., MHI, IAEK, and IPAVF) in interfering with SARS-CoV2 3CL^{PRO} functioning. With this in mind, we carried out an integrated theoretical and experimental investigation, involving first, molecular docking studies to rationally evaluate the putative chance of binding and then, *in vitro* testing for validation. Due to the occurrence of coinfection with a common virus (influenza viruses, human metapneumovirus, and seasonal coronaviruses) in SARS-CoV-2 positive specimens [36,37], peptides were also assayed for their ability to inhibit human rhinovirus 3C protease (EC: 3.4.22.28) in order to evaluate the peptides' exploitation as broad-spectrum antiviral agents.

2. Materials and Methods

2.1. Molecular Docking

SARS-CoV-2's main protease crystal structure was fetched from the Protein Data Bank by retrieving the entry 7L0D [38]. The protein was treated with the Protein Preparation Tool [39,40] available from Schrödinger Suite (New York, NY, USA). Such a method allows for optimizing the crystal structure by removing water molecules, adjusting the side-chain conformation, and adding the missing hydrogen atoms. The peptides to be docked were processed by employing the Ligprep Tool (Schrödinger, New York, NY, USA, for more information, see [41]) to generate all possible tautomers, as well as the protonation states at the physiological pH. The grid-box was generated so as to be suitable for standard precision (SP) peptide-docking protocol and, thus, was centered on the center of mass of the cognate ligand. Satisfactorily, Glide software (Schrödinger, New York, NY, USA) [42] could properly replicate the original binding pose of the co-crystallized molecule, returning a root mean square deviation (RMSD) value as small as 1.025 \AA .

The induced-fit docking protocol [43,44] was employed, using Glide with an OPLS3e force field [45] to analyze the binding mode of the selected ligands, together with conformational changes within the receptor. Such changes are not allowed in standard docking protocols. In detail, side-chain conformation predictions were performed on residues within 6 \AA from the ligand poses, together with the Glide SP redocking of each protein–ligand complex structure within 30.0 kcal/mol from the lowest energy.

The molecular mechanics/generalized born surface area (MM-GBSA, accessed on January 2022 [46]) method was employed in the last stage of the study for the computation of the binding free energies (ΔG) between the proteins and ligands. The Prime package (Schrödinger, LLC, New York, NY, USA) [47], available in the Schrödinger 2020-4 suite (New York, NY, USA), was used for this purpose.

For completeness, -additional molecular docking analyses were carried out against the HRV 3C protease by retrieving entry 2XYA [48] from the Protein Data Bank (<https://www.rcsb.org>, accessed on 10 January 2022) and are included in the Supplementary Information.

2.2. In Vitro Screening of the Antiviral Activity

Synthetic peptides were purchased (purity $> 95\%$; GenScript, Leiden, The Netherlands) and resuspended in MQ water, then assayed at the concentrations of 2, 1, 1, 0.6 0.2 and 0.02 mg/mL (corresponding to 500 to $5 \mu\text{M}$ for MHI, from 420 to $4.2 \mu\text{M}$ for IPAVF, and from 366 to $3.6 \mu\text{M}$ for IAEK). In the case of peptides with a value of relative inhibition (RI) percentage that was higher than 40 – 50% at the lowest assayed concentration, further dilutions were made.

2.2.1. SARS-CoV-2 3CL Protease Assay

The in vitro screening of enzyme inhibition activities was evaluated by using 3CL Protease, untagged (SARS-CoV-2 Assay Kit, Catalog #: 78042-1, BPS Bioscience, Inc., Allentown, PA, USA). According to the manufacturer's protocol, a fluorescent substrate, SARS-CoV-2 3CL Protease (GenBank Accession No. YP_009725301, amino acids 1-306 (full-length), expressed in an *Escherichia coli* expression system, MW = 34 kDa) and a buffer composed of 20 mM Tris, 100 mM NaCl, 1 mM EDTA, and 1 mM DTT, pH 7.3, was used for the inhibition assay. The protease inhibitor, GC376 MW 507.5 Da, with an IC₅₀ value of 0.017 μM was used as the positive control. Initially, 30 μL of diluted SARS-CoV-2 3CL protease, at the final concentration of 15 ng, was pipetted into a 96-well plate containing pre-pipetted 10 μL quantities of each test compound (final concentrations of each peptide ranged from 2 to 0.0002 mg/mL in the wells). The mixture was incubated at room temperature for 30 min with slow shaking. Afterward, the reaction was started by adding the substrate (10 μL), dissolved in the reaction buffer to 50 μL final volume, at a concentration of 40 μM, then the plates were incubated for 4 h at room temperature with slow shaking. The plates were sealed. Fluorescence intensity (Fi) was measured with the Varioskan microtiter plate-reader (Varioskan Flash, Thermo Fisher, Milan, Italy), exciting at a wavelength of 360 nm and detecting at a wavelength of 460 nm. Each sample was assayed in triplicate.

The percentage of relative inhibitions (RI %) was calculated as follows:

$$\% \text{ Relative Inhibition} \left(\frac{\%}{RI} \right) = \left(\frac{FiC - FiT}{FiC} \right) \times 100$$

where C is the control and T is the test peptide or inhibitor.

2.2.2. HRV 3C Protease Determination Assay

The inhibition activity of synthetic peptides was assayed against human rhinovirus 3C protease (HRV 3C^{Pro}; EC:3.4.22.28), a cysteine protease that recognizes the cleavage site of Leu-Glu-Val-Leu-Phe-Gln*Gly-Pro. Protease activity in the presence or absence of peptide inhibitors was determined colorimetrically, as reported, with an HRV 3C Protease Inhibitor Screening Kit (Catalog #: ab211089, Abcam, Cambridge, UK) according to the manufacturer's instructions. The kit also included a protease inhibitor as a positive control.

Briefly, the screening sample compound wells contained 10 μL of the test compounds at each concentration (final concentration/well from 1 to 0.05 mg/mL) or 10 μL of inhibitor, or 10 μL of assay buffer in the case of enzyme control, and 50 μL of enzyme solution. After the incubation of the plate at room temperature for 15 min, 40 μL of the substrate solution was added to each reaction, and absorbance (OD = 405 nm) was measured in a kinetic mode for 1–2 h at 37 °C on the Varioskan Flash microplate reader. Each sample was assayed in triplicate.

The percentage of relative inhibitions (RI) was calculated as follows:

$$\% \text{ Relative Inhibition} (\%RI) = \left(\frac{\text{slope}C - \text{slope}T}{\text{slope}C} \right) \times 100$$

where C is the control and T is the test peptide or inhibitor.

2.3. Statistical Analyses

Results related to the 3CL protease inhibition percentage were subjected to a square root arcsin transformation in order to meet the homogeneity-of-variance assumptions, following Levene's test. The univariate general linear model (GLM) procedure, carrying out a two-way analysis of variance (ANOVA, $p < 0.05$) using the IBM SPSS Statistics release 20 (IBM, Armonk, NY, USA) to evaluate the main and interaction effects of concentration levels and the assayed peptide types on the inhibition percentage of viral protease. Whenever required, the simple main effects of peptides and the assay control inhibitor on viral

protease inhibition percentage were also examined, applying a one-way ANOVA ($p < 0.05$). Multiple comparisons among individual means for each assayed peptide and concentration level were performed using honestly significant difference (HSD)Tukey's test ($p < 0.05$). A multiple regression test was run to predict the inhibition percentage of 3CL protease activity from different peptide concentrations.

The half-maximal inhibitory concentration (IC_{50}) of peptides on SARS-CoV-2 3CL protease was calculated by using the software package SigmaPlot12 (Systat Software, Inc. SigmaPlot for Windows, San Jose, CA, USA) and referred to the micromolar range.

3. Results and Discussion

The chance of targeting SARS-CoV-2 main protease was rationally assessed by employing numerous structure-based approaches [49]. These studies were aimed at predicting the potential of the three small peptides (i.e., IAEK, IPAVF, and MHI) to act as antiviral inhibitors of SARS-CoV-2 main protease, as well as understanding the molecular interactions governing the recognition and the engagement of the binding site [50].

These sequences, endowed with high ACE inhibitor activity, were designed by the molecular pruning of longer β -lactoglobulin-derived peptides (e.g., IIAEKTKIPAVF, and MHIRL); these latter were, in turn, purified and identified after the enzymatic hydrolysis of whey, for its transformation from a by-product of cheese manufacture to a high added-value compound [33]. The assumption that IAEK, IPAVF, and MHI could be good candidates for SARS-CoV-2 3CL^{Pro} inhibition was suggested by their sequences, which contain hydrophobic and aromatic amino acids that are able to interact with the hydrophobic regions of the 3CL^{Pro} active site, such as the S2 pocket [51]. In addition, bioactive peptides, such as ACE inhibitor ones, usually exhibit multifunctional properties that, once proved, make them excellent candidates for the development of multi-target drugs [33,34]. Similarly, this latter evidence has pushed other authors into investigating their activity as inhibitors of the SARS-CoV-2 main protease [52].

We preferred to use the induced fit docking protocol instead of the standard methods, the former being suited to exploring with higher accuracy and reliability the nature and the type of molecular interactions by considering both the ligand and binding site flexibility. In this respect, the effect of the induced fit on the key binding site residues (i.e., H41, N142, C145, H161, E166, and Q189) is assessed by computing the deviations from the crystallographic pose for each protein-oligopeptide complex; the following RMSD values, equal to 1.51 Å, 1.39 Å and 1.24 Å, are measured for IPAVF, IAEK, and MHI, respectively. Interestingly, we observed that Q189 and N142 are more sensitive to the induced fit, as these two residues experienced significant conformational changes, promoting a better fit and the easier accommodation of the three small peptides through the formation of cooperative hydrogen bonds. The N142 χ_1 and Q189 χ_1 and χ_2 torsional angle shifts, due to the induced fit, were reported in Table S1 of the Supplementary Information. Furthermore, the chance of interaction with the catalytic residue H41 and, in addition, with the key residue E166 is supposed to be crucial for the effective inhibition of the target [53,54]. As shown in Figure 1, the three peptides can form a network of hydrogen bonds within the binding pocket. Specifically, IPAVF can interact with the side chains of N142, H41, and Q189, and with the backbone of E166. Furthermore, its protonated nitrogen head can trigger an electrostatic interaction with the negatively charged side-chain of E166. As far as IAEK is concerned, hydrogen bonds with H41, N142, Q189, H163, and E166 were also detected, and the protonated arm of its terminal lysine residue can engage in electrostatic interaction with the side-chain of E166. Regarding MHI, the same hydrogen bonds with E166, N142, and Q189 were observed, and, notably, π - π interactions with H41 through the imidazole ring of its histidine residue were also detected.

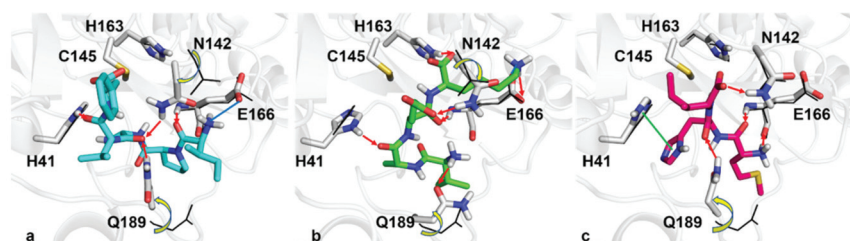


Figure 1. Panels (a–c) report the best pose returned from docking simulations for IPAVF (cyan sticks), IAEK (green sticks), and MHI (magenta sticks) peptides, respectively. Red arrows and green and blue lines depict hydrogen bonds, π - π , and electrostatic interactions, respectively. Black wireframes show the original side-chain conformation of the 7L0D crystal structures. Yellow arrows highlight the shifting of the side chains from their original positions, due to the induced fit.

From an energetic point of view, we employed the OPLS3e force field to quantify the docking scores, and the MM-GBSA method to account for the binding of free energies. Interestingly, the values of the docking scores as well as of the binding free energies calculated for the three peptides were much better than those calculated for the reference X-ray-solved cognate ligand, ML188. For the sake of comparison, all the values are reported in Table 1.

Table 1. Values of the docking score and of MM-GBSA free energy of the best poses obtained through induced-fit docking.

	Docking Score (kcal/mol)	MM-GBSA (kcal/mol)
IPAVF	−10.967	−83.43
IAEK	−10.318	−76.24
MHI	−9.338	−78.80
ML188 cognate ligand	−5.283	−68.03

In addition, a more detailed analysis of the terms of the binding free energy function indicated that the Coulomb and van der Waal energy contributions were determinants for IPAVF, with values equal to −43.15 kcal/mol and −70.55 kcal/mol, respectively. On the other hand, the strongest hydrogen bonding contribution with a value of −6.13 kcal/mol was for IAEK, due to the presence of two charged side chains within its sequence.

Taken together, all the above-described results concerning the *in silico* investigations made us confident of the potential antiviral action of these natural small peptides in contrasting SARS-CoV-2 main protease, and this encouraged us to run experimental validations.

Recently, Behzadipour et al. [31] screened several di- and tri-peptides *in silico*, resulting from the simulated digestion of bovine milk proteins, for their SARS-CoV-2 M^{Pro} inhibitory activity using molecular docking. Twenty peptides (with at least one aromatic-hydrophobic amino acid residue at the C-terminal side) showed the best binding energy but this was less than those obtained in the present work. In particular, three among these peptides, originating from the *in silico* proteolysis of β -caseins, β -lactoglobulin, and α s2-casein, were able to form at least two hydrogen bonds and achieve π -alkyl hydrophobic interactions with the catalytic residues, C145 and H41, of SARS-CoV-2 M^{Pro}, respectively. Other authors [32,34,55] have reported food-derived peptides with virtual 3CL^{Pro} inhibitory activities, showing several potential advantages in terms of high binding affinity, bioavailability, and cost-effective synthesis.

In the past, a representative group of tripeptide aldehydes (CBZ-Leu-Phe-Gln-CHO) was prepared and analyzed to demonstrate poor inhibitory activity against 3C^{Pro}. However, peptides that were modified with a primary amide (Gln- γ -CONH₂) were more active, revealing carbonyl oxygen–hydrogen bonds with the H161 and O γ of T142 [56]. Our three

small peptides were also subjected to docking simulations within the binding site of 3C^{Pro} and similar interactions were experienced, although these yielded more disappointing scoring values. Additional details are available in the Supplementary Information.

Based on the theoretical analyses, the inhibitory activity of the three investigated peptides was experimentally evaluated against SARS-CoV-2 3C^{Pro} and HRV 3C^{Pro}, both employing the catalytic dyad (His-Cys) for their functionality.

Satisfactory experimental results were observed, following the in vitro inhibition screening of the assayed peptides regarding SARS-CoV-2 3C^{Pro} activity.

The half-maximal inhibitory concentrations (IC₅₀) of the three assayed peptides against SARS-CoV-2 3C^{Pro} were measured and are shown in Table 2, confirming IPAVF and IAEK as being more active than MHI; in particular, the IC₅₀ value of IPAVF was the best and was comparable with those obtained for the ACE inhibitor peptides against SARS-CoV-2 3C^{Pro}, after in silico analyses [52]. The experimental data used to determine IC₅₀ are reported in Table S3 in the Supplementary Information.

Table 2. Experimental IC₅₀ values for the inhibition of SARS-CoV-2 3C^{Pro}.

	IC ₅₀ (μM)	95% Confidence Interval	
MHI	2700.62	1186.17	6145.84
IPAVF	1.21	0.02	9.53
IAEK	154.40	137.18	291.60
GC376 (inhibitor)	0.017	0.05	0.042

Similar inhibitory activities toward SARS-CoV2 in the μM range have been identified for synthetic tetrapeptides, pentapeptides, and octapeptides, as recently reviewed by Heydari et al. [57]. Moreover, the in silico hydrolysis of marine fish proteins by gastrointestinal enzymes released oligopeptides containing 1–3 aliphatic amino acids (A, L, V, I) with a high affinity toward SARS-CoV-2 3C^{Pro}; some of these peptides were also predicted to play a role as dual binders toward SARS-CoV-2 3C^{Pro} and monoamine oxidase A [58].

It is noteworthy that no appreciable activity was observed when testing the three small peptides against HRV 3C protease, the RI percentage being lower than a value of ca. 5% at a concentration of 1 mg/mL. A synoptic view is shown in Table 3. This finding is in agreement with our predictive docking studies. Interested readers can look at Figure S1 and Table S2 of the Supplementary Information for more details.

Table 3. The relative inhibition percentage (RI %) of HRV 3C protease by the assayed small peptides.

Peptides	Concentration for Well	Relative Inhibition (RI %)
MHI	250 μM	4.92 ± 1.02
IPAVF	210 μM	5.30 ± 1.06
IAEK	183 μM	4.54 ± 0.56

During the COVID-19 pandemic, several variants of SARS-CoV-2 emerged that, nevertheless, showed mutations in the binding domain of the spike protein receptor [59,60]. In all the variants of concern of the virus, no mutation in the M^{Pro} gene was recorded [61]. This suggests that any M^{Pro} inhibitor could also be effective against multiple variants of the same virus.

As already demonstrated for Nirmatrelvir [62], it is expected that the inhibitors studied in this work can block viral replication; therefore, they can also reduce infection. Nevertheless, unlike the currently authorized antivirals, the peptides studied could have very few or mild side effects and potentially have broad-spectrum applications. In particular, the peptides studied have been shown to have possible anti-hypertensive effects that would ameliorate the clinical conditions of COVID-19 patients. Finally, biologically active peptides would be cheaper and can be easily transformed into derivatives with improved pharmacological properties.

It is noteworthy that the three proposed peptides represent the minimum active sequences with the desired biological properties toward the SARS-CoV-2 3CL protease. This finding opens the way for the synthesis of peptides with improved activity. Their conversion into therapeutic peptides is, indeed, a further challenging task aimed firstly at tackling two intrinsic stumbling blocks: the low membrane permeability and the poor in vivo stability [63]. Inspired by consolidated medicinal chemistry strategies, backbone and side-chain modifications could be of great help. The former is normally pursued to improve the proteolytic stability of the peptides and includes, for instance, the replacement of L-amino acids with D-amino acids [64], the addition of methyl-amino acids [65], and the inclusion of β -amino acids [66] and peptoids [67]. The latter, instead, aims at exploring changes to improve the binding affinity and selectivity [68]. Together with these design approaches, targeted delivery strategies could also be exploited to overcome the inherent drawbacks of peptides [69]. These approaches could indeed be very valuable to obtain real therapeutic peptides; peptides with protease inhibitory activity have already been studied for various viruses, such as the Dengue virus, West Nile virus, and hepatitis C virus [57].

On the other hand, IAEK, IPAVF, and MHI are naturally included within whey proteins [33,35]; although their purification requires time and cost with a putative low yield, the fractionation of a mixture containing several inhibitory peptides may be an advantageous experimental design step toward the development of nutraceutical supplements with a more efficient manufacturing process and improved activity.

4. Conclusions

In this work, the inhibitory activity of the whey-derived bioactive small peptides MHI, IAEK, and IPAVF against viral proteases was evaluated for the first time, indicating their possible role in blocking the replication processes of SARS-CoV-2.

Molecular docking studies predicted the relevant interactions between the peptides and key amino acid residues of the enzyme catalytic pocket of 3CL^{PRO}. These results were validated by in vitro experiments that confirmed the highest antiviral activity for IPAVF and IAEK against 3CL^{PRO}. These peptides of natural origin were previously obtained by the enzymatic hydrolysis of whey proteins and also displayed ACE inhibitory activity. It is noteworthy that their short sequences facilitate their synthesis as well as changes to their structure to improve stability and enhance activity. The results herein open the door to new opportunities for the development of dual-target small peptides that are endowed with antiviral 3CL^{PRO} and inhibitory ACE activities.

Supplementary Materials: The following supporting information can be downloaded at: <https://www.mdpi.com/article/10.3390/biomedicines10051067/s1>, Figure S1: Panels (a), (b), and (c) report the best pose returned from docking simulations for IPAVF (cyan sticks), IAEK (green sticks) and MHI (magenta sticks) peptides, respectively. Red arrows depict hydrogen bonds. Black wireframes show the original side-chain conformation of the 2XYA crystal structures of rhinovirus 3C protease. Table S1: Docking induced-fit variation of the torsional angles χ_1 for N142 and of χ_1 and χ_2 for Q189 from the X-ray structure (PDB_ID: 7L0D) of SARS-CoV-2 3CL^{PRO}. Table S2: Comparative docking score values for SARS-CoV-2 3CL^{PRO} and HRV 3C^{PRO}. Table S3: Relative inhibition percentage (RI %) of SARS-CoV-2 3CL^{PRO} by the three small peptides assayed at different concentrations.

Author Contributions: Conceptualization, L.Q., O.N. and L.C.; methodology, L.Q., L.C., N.G., F.C., L.M. and O.N.; software, O.N., N.G. and F.C.; validation, L.Q., L.C. and N.G.; formal analysis, L.C., L.Q. and O.N.; investigation, L.C. and O.N.; resources, L.Q., L.M., N.G. and O.N.; data curation, L.Q., N.G., F.C. and O.N.; writing—original draft preparation, L.Q. and O.N.; writing—review and editing, L.Q., L.C. and O.N.; visualization, L.Q. and O.N.; supervision, L.Q. and O.N.; project administration, L.Q., L.C. and O.N.; funding acquisition, L.M. All authors have read and agreed to the published version of the manuscript.

Funding: This research was funded by the project ICONSS—Innovative Customer-Oriented Safe Solutions (ID 20431) within EIT Food 2020 program “COVID-19 Rapid Response Call for Innovation projects” and by the project “L’Evoluzione delle Produzioni Lattiero-Casearie: le Biotecnologie valorizzano la Tradizione”—ELEVATO, n. F/200112/03/X45, PON I&C 2014–2020.

Institutional Review Board Statement: The study did not require ethical approval.

Informed Consent Statement: Not applicable.

Data Availability Statement: The data presented in this study are available on request from the corresponding author. The data are not publicly available due to privacy issues.

Acknowledgments: We are grateful to Pasquale Del Vecchio (CNR-ISPAs, Bari, Italy) for data management support.

Conflicts of Interest: The authors declare no conflict of interest. The funders had no role in the design of the study; in the collection, analyses, or interpretation of data; in the writing of the manuscript; or in the decision to publish the results.

References

1. WHO. WHO Director-General's Opening Remarks at the Media Briefing on COVID-19—11 March 2020. World Health Organization (WHO): Geneva, Switzerland. 2020. Available online: <https://www.who.int/dg/speeches/detail/who-director-general-s-opening-remarks-at-the-media-briefing-on-covid-19---11-march-2020> (accessed on 22 February 2022).
2. Karlinsky, A.; Kobak, D. Tracking excess mortality across countries during the COVID-19 pandemic with the World Mortality Dataset. *eLife* **2021**, *10*, e69336. [CrossRef] [PubMed]
3. Bebenek, I.; Bannister, R.; Dubinion, J.; Fortin, M.; Liu, M.; Motter, A.L.; Rohde, C.M.; Wrzesinski, C. COVID-19 Therapeutics and Vaccines: A Race to Save Lives. *Toxicol. Sci.* **2022**, *185*, 119–127. [CrossRef] [PubMed]
4. Niknam, Z.; Jafari, A.; Golchin, A.; Danesh Pouya, F.; Nemati, M.; Rezaei-Tavirani, M.; Rasmi, Y. Potential therapeutic options for COVID-19: An update on current evidence. *Eur. J. Med. Res.* **2022**, *27*, 6. [CrossRef] [PubMed]
5. Tsai, S.C.; Lu, C.C.; Bau, D.T.; Chiu, Y.J.; Yen, Y.T.; Hsu, Y.M.; Fu, C.W.; Kuo, S.C.; Lo, Y.S.; Chiu, H.Y.; et al. Approaches towards fighting the COVID-19 pandemic. *Int. J. Mol. Med.* **2021**, *47*, 3–22. [CrossRef]
6. Chiu, M.N.; Bhardwaj, M.; Sah, S.P. Safety profile of COVID-19 drugs in a real clinical setting. *Eur. J. Clin. Pharmacol.* **2022**, *78*, 733–753. [CrossRef]
7. VanPatten, S.; He, M.; Altiti, A.; FCheng, K.; Ghanem, M.H.; Al-Abed, Y. Evidence supporting the use of peptides and peptidomimetics as potential SARS-CoV-2 (COVID-19) therapeutics. *Future Med. Chem.* **2020**, *12*, 1647–1656. [CrossRef]
8. Liu, Y.; Liang, C.; Xin, L.; Ren, X.; Tian, L.; Ju, X.; Li, H.; Wang, Y.; Zhao, Q.; Liu, H.; et al. The development of Coronavirus 3C-Like protease (3CL^{Pro}) inhibitors from 2010 to 2020. *Eur. J. Med. Chem.* **2020**, *206*, 112711. [CrossRef]
9. Needle, D.; Lountos, G.T.; Waugh, D.S. Structures of the Middle East respiratory syndrome coronavirus 3C-like protease reveal insights into substrate specificity. *Acta Crystallogr. Sect. D Biol. Crystallogr.* **2015**, *71*, 1102–1111. [CrossRef]
10. Moustaqil, M.; Ollivier, E.; Chiu, H.P.; Van Tol, S.; Rudolffi-Soto, P.; Stevens, C.; Bhumkar, A.; Hunter, D.J.B.; Freiberg, A.N.; Jacques, D.; et al. SARS-CoV-2 proteases PL^{Pro} and 3CL^{Pro} cleave IRF3 and critical modulators of inflammatory pathways (NLRP12 and TAB1): Implications for disease presentation across species. *Emerg. Microbes Infect.* **2021**, *10*, 178–195. [CrossRef]
11. Adhikari, N.; Baidya, S.K.; Saha, A.; Jha, T. Structural insight into the viral 3C-like protease inhibitors: Comparative SAR/QSAR approaches. In *Viral Proteases and Their Inhibitors*; Academic Press: Cambridge, MA, USA, 2017; pp. 317–409.
12. Ng, C.S.; Stobart, C.C.; Luo, H. Innate immune evasion mediated by picornaviral 3C protease: Possible lessons for coronavirus 3C-like protease? *Rev. Med. Virol.* **2021**, *31*, 1–22. [CrossRef]
13. Wang, H.M.; Liang, P.H. Picornaviral 3C protease inhibitors and the dual 3C protease/coronaviral 3C-like protease inhibitors. *Expert Opin. Ther. Pat.* **2010**, *20*, 59–71. [CrossRef] [PubMed]
14. Liu, C.; Boland, S.; Scholle, M.D.; Bardiot, D.; Marchand, A.; Chaltin, P.; Blatt, L.M.; Beigelman, L.; Symons, J.A.; Raboisson, P.; et al. Dual inhibition of SARS-CoV-2 and human rhinovirus with protease inhibitors in clinical development. *Antivir. Res.* **2021**, *187*, 105020. [CrossRef] [PubMed]
15. Macchiagodena, M.; Pagliai, M.; Procacci, P. Identification of potential binders of the main protease 3CL^{Pro} of the COVID-19 via structure-based ligand design and molecular modeling. *Chem. Phys. Lett.* **2020**, *750*, 137489. [CrossRef] [PubMed]
16. Chen, Y.W.; Yiu CP, B.; Wong, K.Y. Prediction of the SARS-CoV-2 (2019-nCoV) 3C-like protease (3CL pro) structure: Virtual screening reveals velpatasvir, ledipasvir, and other drug repurposing candidates. *F1000Research* **2020**, *9*, 129. [CrossRef] [PubMed]
17. Kandeel, M.; Al-Nazawi, M. Virtual screening and repurposing of FDA approved drugs against COVID-19 main protease. *Life Sci.* **2020**, *251*, 117627. [CrossRef] [PubMed]
18. Alberga, D.; Gambacorta, N.; Trisciuzzi, D.; Ciriaco, F.; Amoroso, N.; Nicolotti, O. De Novo Drug Design of Targeted Chemical Libraries Based on Artificial Intelligence and Pair-Based Multiobjective Optimization. *J. Chem. Inf. Model* **2020**, *60*, 4582–4593. [CrossRef]
19. Ciriaco, F.; Gambacorta, N.; Alberga, D.; Nicolotti, O. Quantitative Polypharmacology Profiling Based on a Multifingerprint Similarity Predictive Approach. *J. Chem. Inf. Model* **2021**, *61*, 4868–4876. [CrossRef]
20. Alberga, D.; Trisciuzzi, D.; Montaruli, M.; Leonetti, F.; Mangiardi, G.F.; Nicolotti, O. A New Approach for Drug Target and Bioactivity Prediction: The Multifingerprint Similarity Search Algorithm (MuSSEL). *J. Chem. Inf. Model* **2019**, *59*, 586–596. [CrossRef]

21. Pant, S.; Singh, M.; Ravichandiran, V.; Murty US, N.; Srivastava, H.K. Peptide-like and small-molecule inhibitors against Covid-19. *J. Biomol. Struct. Dyn.* **2021**, *39*, 2904–2913. [CrossRef]
22. Yang, H.; Yang, J. A review of the latest research on MPro targeting SARS-COV inhibitors. *RSC Med. Chem.* **2021**, *12*, 1026–1036. [CrossRef]
23. Sabbah, D.A.; Hajjo, R.; Bardaweel, S.K.; Zhong, H.A. An Updated Review on SARS-CoV-2 Main Proteinase (MPro): Protein Structure and Small-Molecule Inhibitors. *Curr. Top Med. Chem.* **2021**, *21*, 442–460. [CrossRef] [PubMed]
24. Pavan, M.; Bolcato, G.; Bassani, D.; Sturlese, M.; Moro, S. Supervised Molecular Dynamics (SuMD) Insights into the mechanism of action of SARS-CoV-2 main protease inhibitor PF-07321332. *J. Enzym. Inhib. Med. Chem.* **2021**, *36*, 1646–1650. [CrossRef] [PubMed]
25. EMA. EMA Receives Application for Conditional Marketing Authorisation Paxlovid (PF-07321332 and Ritonavir) for Treating Patients with COVID-19. European Medicines Agency (Amsterdam, The Netherlands). 2022. Available online: <https://www.ema.europa.eu/en/news/ema-receives-application-conditional-marketing-authorisation-paxlovid-pf-07321332-ritonavir-treating> (accessed on 10 February 2022).
26. Pendyala, B.; Patras, A.; Dash, C. Phycobilins as Potent Food Bioactive Broad-Spectrum Inhibitors Against Proteases of SARS-CoV-2 and Other Coronaviruses: A Preliminary Study. *Front. Microbiol.* **2021**, *12*, 1399. [CrossRef] [PubMed]
27. Kato, F.; Nakatsu, Y.; Murano, K.; Wakata, A.; Kubota, T.; Hishiki, T.; Yamaji, T.; Kidokoro, M.; Katoh, H.; Takeda, M. Antiviral Activity of CD437 Against Mumps Virus. *Front. Microbiol.* **2021**, *12*, 751909. [CrossRef]
28. Sasidharan, S.; Selvaraj, C.; Singh, S.K.; Dubey, V.K.; Kumar, S.; Fialho, A.M.; Saudagar, P. Bacterial protein azurin and derived peptides as potential anti-SARS-CoV-2 agents: Insights from molecular docking and molecular dynamics simulations. *J. Biomol. Struct. Dyn.* **2021**, *39*, 5706–5721. [CrossRef]
29. Galanakis, C.M.; Aldawoud, T.; Rizou, M.; Rowan, N.J.; Ibrahim, S.A. Food ingredients and active compounds against the coronavirus disease (COVID-19) pandemic: A comprehensive review. *Foods* **2020**, *9*, 1701. [CrossRef] [PubMed]
30. Hamid, H.; Thakur, A.; Thakur, N.S. Role of functional food components in COVID-19 pandemic: A review. *Ann. Phytomed. Int. J.* **2021**, *10*, S240–S250. [CrossRef]
31. Behzadipour, Y.; Gholampour, M.; Pirhadi, S.; Seradj, H.; Khoshneviszadeh, M.; Hemmati, S. Viral 3CL^{Pro} as a target for antiviral intervention using milk-derived bioactive peptides. *Int. J. Pept. Res. Ther.* **2021**, *27*, 2703–2716. [CrossRef]
32. Pradeep, H.; Najma, U.; Aparna, H.S. Milk Peptides as Novel Multi-Targeted Therapeutic Candidates for SARS-CoV2. *Protein J.* **2021**, *40*, 310–327. [CrossRef]
33. Brandelli, A.; Daroit, D.J.; Corrêa, A.P.F. Whey as a source of peptides with remarkable biological activities. *Food Res. Int.* **2015**, *73*, 149–161. [CrossRef]
34. Çakır, B.; Okuyan, B.; Şener, G.; Tunali-Akbay, T. Investigation of beta-lactoglobulin derived bioactive peptides against SARS-CoV-2 (COVID-19): In silico analysis. *Eur. J. Pharmacol.* **2021**, *891*, 173781. [CrossRef] [PubMed]
35. Tondo, A.R.; Caputo, L.; Mangiatordi, G.F.; Monaci, L.; Lentini, G.; Logrieco, A.F.; Montaruli, M.; Nicolotti, O.; Quintieri, L. Structure-based identification and design of angiotensin converting enzyme-inhibitory peptides from whey proteins. *J. Agric. Food Chem.* **2019**, *68*, 541–548. [CrossRef] [PubMed]
36. Nowak, M.D.; Sordillo, E.M.; Gitman, M.R.; Mondolfi, A.E.P. Coinfection in SARS-CoV-2 infected patients: Where are influenza virus and rhinovirus/enterovirus? *J. Med. Virol.* **2020**, *92*, 1699–1700. [CrossRef] [PubMed]
37. Dee, K.; Goldfarb, D.M.; Haney, J.; Amat, J.A.R.; Herder, V.; Stewart, M.; Szemiel, A.M.; Baguelin, M.; Murcia, P.R. Human rhinovirus infection blocks SARS-CoV-2 replication within the respiratory epithelium: Implications for COVID-19 epidemiology. *J. Infect. Dis.* **2021**, *224*, 31–38. [CrossRef] [PubMed]
38. Lockbaum, G.J.; Reyes, A.C.; Lee, J.M.; Tilvawala, R.; Nalivaika, E.A.; Ali, A.; Kurt Yilmaz, N.; Thompson, P.R.; Schiffer, C.A. Crystal Structure of SARS-CoV-2 Main Protease in Complex with the Non-Covalent Inhibitor ML188. *Viruses* **2021**, *13*, 174. [CrossRef]
39. Madhavi Sastry, G.; Adzhigirey, M.; Day, T.; Annabhimoju, R.; Sherman, W. Protein and Ligand Preparation: Parameters, Protocols, and Influence on Virtual Screening Enrichments. *J. Comput. Aided. Mol. Des.* **2013**, *27*, 221–234. [CrossRef]
40. Schrödinger Release 2020-4: *Protein Preparation Wizard*; Epik, Schrödinger, LLC.: New York, NY, USA, 2016; Impact, Schrödinger, LLC.: New York, NY, USA, 2016; Prime, Schrödinger, LLC.: New York, NY, USA, 2020.
41. Schrödinger Release 2020-4: *LigPrep*; Schrödinger, LLC.: New York, NY, USA, 2020.
42. Friesner, R.A.; Banks, J.L.; Murphy, R.B.; Halgren, T.A.; Klicic, J.J.; Mainz, D.T.; Repasky, M.P.; Knoll, E.H.; Shelley, M.; Perry, J.K.; et al. Glide: A New Approach for Rapid, Accurate Docking and Scoring. 1. Method and Assessment of Docking Accuracy. *J. Med. Chem.* **2004**, *47*, 1739–1749. [CrossRef]
43. Schrödinger Release 2020-4: *Induced Fit Docking Protocol*; Glide, Schrödinger, LLC.: New York, NY, USA, 2016; Prime, Schrödinger, LLC.: New York, NY, USA, 2020.
44. Sherman, W.; Day, T.; Jacobson, M.P.; Friesner, R.A.; Farid, R. Novel Procedure for Modeling Ligand/Receptor Induced Fit Effects. *J. Med. Chem.* **2006**, *49*, 534–553. [CrossRef]
45. Harder, E.; Damm, W.; Maple, J.; Wu, C.; Reboul, M.; Xiang, J.Y.; Wang, L.; Lupyan, D.; Dahlgren, M.K.; Knight, J.L.; et al. OPLS3: A Force Field Providing Broad Coverage of Drug-like Small Molecules and Proteins. *J. Chem. Theory Comput.* **2016**, *12*, 281–296. [CrossRef]
46. Genheden, S.; Ryde, U. The MM/PBSA and MM/GBSA Methods to Estimate Ligand-Binding Affinities. *Expert Opin. Drug Discov.* **2015**, *10*, 449–461. [CrossRef]

47. Schrödinger Release 2020-4; Prime, Schrödinger, LLC.: New York, NY, USA, 2020.
48. Baxter, A.; Chambers, M.; Edfeldt, F.; Edman, K.; Freeman, A.; Johansson, C.; King, S.; Morley, A.; Petersen, J.; Rawlins, P.; et al. Non-covalent inhibitors of rhinovirus 3C protease. *Bioorganic Med. Chem. Lett.* **2011**, *21*, 777–780. [CrossRef] [PubMed]
49. Piacentini, S.; La Frazia, S.; Riccio, A.; Pedersen, J.Z.; Topai, A.; Nicolotti, O.; Rossignol, J.F.; Santoro, M.G. Nitazoxanide inhibits paramyxovirus replication by targeting the Fusion protein folding: Role of glycoprotein-specific thiol oxidoreductase ERp57. *Sci. Rep.* **2018**, *8*, 10425. [CrossRef] [PubMed]
50. Trisciuzzi, D.; Siragusa, L.; Baroni, M.; Autiero, I.; Nicolotti, O.; Cruciani, G. Getting Insights into Structural and Energetic Properties of Reciprocal Peptide–Protein Interactions. *J. Chem. Inf. Model* **2022**, *62*, 1113–1125. [CrossRef] [PubMed]
51. Hernández González, J.E.; Eberle, R.J.; Willbold, D.; Coronado, M.A. A Computer-Aided Approach for the Discovery of D-Peptides as Inhibitors of SARS-CoV-2 Main Protease. *Front. Mol. Biosci.* **2021**, *8*, 816166. [CrossRef]
52. Yathisha, U.G.; Srinivasa, M.G.; Siddappa Bc, R.; PMandal, S.; Dixit, S.R.; Pujar, G.V.; Bangera Sheshappa, M. Isolation and characterization of ACE-I inhibitory peptides from ribbonfish for a potential inhibitor of the main protease of SARS-CoV-2: An in silico analysis. *Proteins* **2022**, *90*, 982–992. [CrossRef]
53. Jin, Z.; Du, X.; Xu, Y.; Deng, Y.; Liu, M.; Zhao, Y.; Zhang, B.; Li, X.; Zhang, L.; Peng, C.; et al. Structure of M^{Pro} from SARS-CoV-2 and Discovery of Its Inhibitors. *Nature* **2020**, *582*, 289–293. [CrossRef]
54. Huff, S.; Kummetha, I.R.; Tiwari, S.K.; Huante, M.B.; Clark, A.E.; Wang, S.; Bray, W.; Smith, D.; Carlin, A.F.; Endsley, M.; et al. Discovery and Mechanism of SARS-CoV-2 Main Protease Inhibitors. *J. Med. Chem.* **2022**, *65*, 2866–2879. [CrossRef]
55. Chourasia, R.; Padhi, S.; Chiring Phukon, L.; Abedin, M.M.; Singh, S.P.; Rai, A.K. A potential peptide from soy cheese produced using *Lactobacillus delbrueckii* WS4 for effective inhibition of SARS-CoV-2 main protease and S1 glycoprotein. *Front. Mol. Biosci.* **2020**, *7*, 601753. [CrossRef]
56. Webber, S.E.; Okano, K.; Little, T.L.; Reich, S.H.; Xin, Y.; Fuhrman, S.A.; Matthews, D.A.; Love, R.A.; Hendrickson, T.F.; Patick, A.K.; et al. Tripeptide aldehyde inhibitors of human rhinovirus 3C protease: Design, synthesis, biological evaluation, and cocrystal structure solution of P1 glutamine isosteric replacements. *J. Med. Chem.* **1998**, *41*, 2786–2805. [CrossRef]
57. Heydari, H.; Golmohammadi, R.; Mirnejad, R.; Tebyanian, H.; Fasihi-Ramandi, M.; Moghaddam, M.M. Antiviral peptides against Coronaviridae family: A review. *Peptides* **2021**, *139*, 170526. [CrossRef]
58. Yao, Y.; Luo, Z.; Zhang, X. In silico evaluation of marine fish proteins as nutritional supplements for COVID-19 patients. *Food Funct.* **2020**, *11*, 5565–5572. [CrossRef] [PubMed]
59. Gupta, R.K. Will SARS-CoV-2 variants of concern affect the promise of vaccines? *Nat. Rev. Immunol.* **2021**, *21*, 340–341. [CrossRef] [PubMed]
60. Planas, D.; Veyer, D.; Baidaliuk, A.; Staropoli, I.; Guivel-Benhassine, F.; Rajah, M.M.; Planchais, C.; Porrot, F.; Robillard, N.; Puech, J.; et al. Reduced sensitivity of SARS-CoV-2 variant Delta to antibody neutralization. *Nature* **2021**, *596*, 276–280. [CrossRef] [PubMed]
61. Jukić, M.; Škrlić, B.; Tomšić, G.; Pleško, S.; Podlipnik, Č.; Bren, U. Prioritisation of compounds for 3CL^{Pro} inhibitor development on SARS-CoV-2 variants. *Molecules* **2021**, *26*, 3003. [CrossRef]
62. Owen, D.R.; Allerton, C.M.N.; Anderson, A.S.; Aschenbrenner, L.; Avery, M.; Berritt, S.; Boras, B.; Cardin, R.D.; Carlo, A.; Coffman, K.J.; et al. An oral SARS-CoV-2 M^{Pro} inhibitor clinical candidate for the treatment of COVID-19. *Science* **2021**, *374*, 1586–1593. [CrossRef]
63. Wang, L.; Wang, N.; Zhang, W.; Cheng, X.; Yan, Z.; Shao, G.; Wang, X.; Wang, R.; Fu, C. Therapeutic peptides: Current applications and future directions. *Sig. Transduct. Target Ther.* **2022**, *7*, 48. [CrossRef]
64. Werner, H.M.; Cabaltea, C.C.; Horne, W.S. Peptide Backbone Composition and Protease Susceptibility: Impact of Modification Type, Position, and Tandem Substitution. *Chembiochem* **2016**, *17*, 712–718. [CrossRef]
65. Chatterjee, J.; Rechenmacher, F.; Kessler, H. N-methylation of peptides and proteins: An important element for modulating biological functions. *Angew. Chem. Int. Ed. Engl.* **2013**, *52*, 254–269. [CrossRef]
66. Cheloha, R.W.; Watanabe, T.; Dean, T.; Gellman, S.H.; Gardella, T.J. Backbone Modification of a Parathyroid Hormone Receptor-1 Antagonist/Inverse Agonist. *ACS Chem. Biol.* **2016**, *11*, 2752–2762. [CrossRef]
67. Schneider, J.A.; Craven, T.W.; Kasper, A.C.; Yun, C.; Haugbro, M.; Briggs, E.M.; Svetlov, V.; Nudler, E.; Knaut, H.; Bonneau, R.; et al. Design of Peptoid-peptide Macrocycles to Inhibit the β -catenin TCF Interaction in Prostate Cancer. *Nat. Commun.* **2018**, *9*, 4396. [CrossRef]
68. Masri, E.; Ahsanullah Accorsi, M.; Rademann, J. Side-Chain Modification of Peptides Using a Phosphoranylidene Amino Acid. *Org. Lett.* **2020**, *22*, 2976–2980. [CrossRef] [PubMed]
69. Mitragotri, S.; Burke, P.A.; Langer, R. Overcoming the challenges in administering biopharmaceuticals: Formulation and delivery strategies. *Nat. Rev. Drug Discov.* **2014**, *13*, 655–672. [CrossRef] [PubMed]



Article

Discovery through Machine Learning and Preclinical Validation of Novel Anti-Diabetic Peptides

Rory Casey, Alessandro Adelfio, Martin Connolly, Audrey Wall *, Ian Holyer and Nora Khaldi

Nuritas Ltd., Joshua Dawson House, D02 RY95 Dublin, Ireland; casey.rory@nuritas.com (R.C.); adelfio.alessandro@nuritas.com (A.A.); connolly.martin@nuritas.com (M.C.); info@nuritas.com (I.H.); n.khaldi@Nuritas.com (N.K.)

* Correspondence: wall.audrey@nuritas.com; Tel.: +353-1-430-1290

Abstract: While there have been significant advances in drug discovery for diabetes mellitus over the past couple of decades, there is an opportunity and need for improved therapies. While type 2 diabetic patients better manage their illness, many of the therapeutics in this area are peptide hormones with lengthy sequences and a molecular structure that makes them challenging and expensive to produce. Using machine learning, we present novel anti-diabetic peptides which are less than 16 amino acids in length, distinct from human signalling peptides. We validate the capacity of these peptides to stimulate glucose uptake and Glucose transporter type 4 (GLUT4) translocation in vitro. In obese insulin-resistant mice, predicted peptides significantly lower plasma glucose, reduce glycated haemoglobin and even improve hepatic steatosis when compared to treatments currently in use in a clinical setting. These unoptimised, linear peptides represent promising candidates for blood glucose regulation which require further evaluation. Further, this indicates that perhaps we have overlooked the class of natural short linear peptides, which usually come with an excellent safety profile, as therapeutic modalities.

Citation: Casey, R.; Adelfio, A.; Connolly, M.; Wall, A.; Holyer, I.; Khaldi, N. Discovery through Machine Learning and Preclinical Validation of Novel Anti-Diabetic Peptides. *Biomedicines* **2021**, *9*, 276. <https://doi.org/10.3390/biomedicines9030276>

Academic Editor: Jean A. Boutin

Received: 4 February 2021

Accepted: 7 March 2021

Published: 9 March 2021

Publisher's Note: MDPI stays neutral with regard to jurisdictional claims in published maps and institutional affiliations.



Copyright: © 2021 by the authors. Licensee MDPI, Basel, Switzerland. This article is an open access article distributed under the terms and conditions of the Creative Commons Attribution (CC BY) license (<https://creativecommons.org/licenses/by/4.0/>).

Keywords: drug discovery; peptide; type 2 diabetes; machine learning

1. Introduction

Type 2 diabetes mellitus (T2DM) is a chronic condition which accounts for over 90% of all diabetes mellitus (DM) incidences. In T2DM, cells fail to respond to the hormone insulin, or a relative lack of insulin is produced by the beta cells of the pancreas, which normally allows glucose to enter cells from the blood, reducing blood glucose levels. This condition has long-term implications, affecting several organs in the body, such as nephropathy of the kidney and retina, and hepatic steatosis, all of which contribute to poor quality of life and a high burden on healthcare systems [1]. Major risk factors for T2DM include obesity, lack of exercise and sedentary lifestyle, all of which are increasingly common in the West. Currently, the global incidence of DM continues to grow at an inexorable rate, currently affecting over 450 million people, and is expected to afflict almost 700 million by 2045 [2]. While DM drug discovery has seen some important advances over the last two decades [3,4], in light of such widespread disease prevalence, there is an evident and urgent need for novel, effective anti-diabetic treatments that have improved safety profiles and are well tolerated for chronic use in the DM population [5,6].

Pharmacological interventions for T2DM include metformin, a small-molecule drug known to work via several mechanisms, including AMP-activated protein kinase (AMPK) [7] and mitochondrial activity [8,9]; it is a well-established first line treatment for T2DM, both as a monotherapy and in combination with other medications, and has been routinely shown to have glucose-lowering effects [10]. Thiazolidinediones are cyclic compounds that act as ligands to peroxisome proliferator-activated receptors (PPARs), reducing circulating fatty acids and increasing the expression of glucose transporter Glucose transporter type 4 (GLUT4), allowing cells to take up more glucose from the blood for energy, reducing blood

glucose levels [11,12]. More recently, sodium glucose transporter 2 (SGLT2) inhibitors have been developed, which work to prevent the action of the transporters in the proximal tubule of the kidney from reabsorbing glucose to the body, thereby allowing excretion and reducing blood glucose [13]. Indeed, SGLT2 inhibitors are often used in combinational therapy with other medications to help manage the complex pathophysiology of T2DM [14].

An important and efficacious group of T2DM therapeutics includes a group of peptides such as insulin analogues, and, more recently, incretin mimetics, acting as either agonists (e.g., Glucagon-like peptide-1 (GLP-1) and glucose-dependent insulinotropic polypeptide (GIP) analogues) or antagonists (e.g., GLP-1 receptor antagonists) of endogenous human hormones, with modifications [15]. These therapeutics form a significant number of the modern anti-diabetic drugs and also those in the development pipeline [16]. This group has been shown to suppress glucagon and hepatic glucose production, slow gastric emptying and reduce appetite [17], with two approved members of the class, Exenatide and Liraglutide, having long-term weight loss effects on patients over a 1–2-year period [18]. Both Exenatide and Liraglutide are relatively shorter compared to 51-amino-acid-long insulin, at 39 amino acids and 32 amino acids in length, respectively. Both medications are administered as subcutaneous injectables and have presented with some adverse effects, including vomiting and nausea [19,20].

An alternative class of peptides which may offer good safety profiles and toleration for chronic use, but have been largely underexplored, are short linear peptides with few modifications. Linear endogenous and synthetic peptides have been shown to be capable of modulating intracellular signalling, without modifications [21]. As such, these advantages position this class as an attractive addition to the diabetes armamentarium. Indeed, peptides can be highly selective, having multiple points of contact with their target, which may result in decreased side effects and toxicity [22]. Furthermore, as they comprise amino acids, peptides are easily metabolised over time, thereby avoiding the tolerance issues that can be associated with chronic administration of many drugs [22,23]. A possible advantage of short linear peptides includes lower manufacturing costs and offers a flexible base for modifications [24,25]. However, presently, a major drawback of these peptides is that they are readily broken down during gastrointestinal digestion (GID); therefore, issues with low bioavailability via oral administration remain problematic [26]. This has resulted in a turn towards developing optimised peptides to enhance therapeutic properties, such as cyclisation [27], although there are instances where anti-cancer linear peptides outperform their cyclic counterparts [25], indicating that this class of peptides should not be so readily dismissed.

Biology is an extremely data-rich discipline owing to various “omics” technologies producing increasingly larger volumes of heterogeneous data [28]. In recent years, integration of such data has facilitated a greater understanding of the molecular basis of disease [29], but with continued escalation in terms of scale and complexity, human-directed interpretation is rendered increasingly impractical [27,30]. When considering peptides, deciphering scale and complexity becomes a major hurdle; for example, proteins can be broken down into peptides at a rate of 36 million per minute [21]. However, Artificial Intelligence (AI) and deep learning techniques are perfectly primed to extract previously indecipherable knowledge from disparate biological data streams; as such, machine learning is increasingly seen as a discovery tool in life science, with bioactive peptides being successfully predicted in the areas of inflammation and skin aging [31–34]. Here, similar machine learning methods were employed to identify a short linear novel peptide therapeutics for use in T2DM. The goal of this project was to identify (a) peptide(s) which could modulate an effect on blood glucose levels, GLUT4 expression and/or glycated haemoglobin (HbA1c) levels, while being both non-toxic and showing no off-target effects. The peptide candidates were validated in both *in vitro* and *in vivo* assays to ensure these properties.

2. Materials and Methods

2.1. Cell Line

Human skeletal muscle cells (HskMCs; Cell Applications Inc., San Diego, CA, USA) were cultured at 37 °C, 5% CO₂ in HskMC growth medium (Cell Applications Inc., San Diego, CA, USA). HskMCs cultured for, at most, 10 passages were used for all experiments described.

2.2. Animals

All animal procedures were carried out in accordance with Institutional Animal Care and Use (IACUC) guidelines in an Association for Assessment and Accreditation of Laboratory Animal Care International-accredited facility. Ethical approval was granted by the International Association of Religious Freedom (IARF #:MLR-101, IARF #:MLR-115) Studies were performed with 12-week-old male KK.Cg-A^y/J (KK-A^y) mice obtained from the Jackson Laboratory, which were randomly assigned to treatment groups according to baseline fasting blood glucose (IARF #: MLR-101, 1 May 2018). Mice were housed with no more than 4 per cage on a 12-h light/dark cycle with ad libitum access to standard rodent chow and water. Mice were subcutaneously (sc) administered either indicated doses of peptide or saline (untreated vehicle control) once daily for 2 weeks. Bodyweight was measured at baseline and once per week thereafter. Fasting (overnight) blood glucose was measured at baseline, day 5, day 7 and day 13 of dosing (cohort 1). In a second, independent *in vivo* study (IARF #: MLR-151; 13 January 2020), mice (n = 11/group) were sc administered either indicated dose of peptide, Liraglutide or saline for 6 weeks. Glycated haemoglobin was measured at 6 weeks, and liver sectioning via microtome, staining with haematoxylin and eosin (H&E) and scoring were performed on snap-frozen tissues.

2.3. Prediction Workflow

A similar predictive model to that used by Kennedy et al., 2020 [33] was utilised here; briefly, the model was developed using an ensemble of neural networks. To build the training set for the model, we used structured data from public databases (bioactivity annotations, biological pathways and structural annotations) and unstructured data extracted from peer-reviewed scientific papers and patents (Figure 1). Initial descriptors used to query these data sources were “diabetes”, “blood glucose regulation” and “GLUT4”. A combination of graph-based techniques and manual curation was used to process the structured data, while, concurrently, Natural Language Processing (NLP) techniques, such as word and sentence embedding and named entity recognition, were applied to the unstructured data. The high-level information extracted was assembled and formatted into a bespoke peptide representation format.

The resulting dataset of peptides with a known effect on blood glucose regulation was used to train our predictive architecture for bioactivity in fold cross-validation. The fully trained model was used to predict novel peptides’ glucose uptake efficacy from a large input set of peptide sequences.

Additional testing and refinement of the predictive architecture was achieved by incorporating a predict–test–refine loop. The predict–test–refine loop is an example of active learning. Uncertainty sampling was performed where peptides that the model was least certain as to what their activity should be were selected for experimental testing. This strategy was mixed with the selection of the best predicted peptides, which were tested concurrently. Uncertainty sampling was prevalent in the first iterations and progressively reduced to be completely replaced by the identification of the most promising peptides in the latest iteration. The results of *in vitro* testing were additionally integrated into the model to bias it towards the prediction of peptides with specific GLUT4 translocation activity. In this framework, a set of peptides, which the model found most difficult to classify (i.e., those with an efficacy prediction close to 50%), were selected for experimental testing *in vitro*, with resultant data being fed back to the predictive model. This predict–test–refine loop was completed three times. Across the multiple iterations, *in vitro* activity

was measured in 74% of cases, where peptides tested in glucose regulation assays would show what was internally classified as “medium to high activity”. A similar active learning paradigm was used in Kennedy et al., 2020 [33]. In that case, a lower ratio of in vitro activity was measured across the multiple lab tests, with only 40% of peptides tested in extra cellular matrix development assays displaying “medium to high activity”.

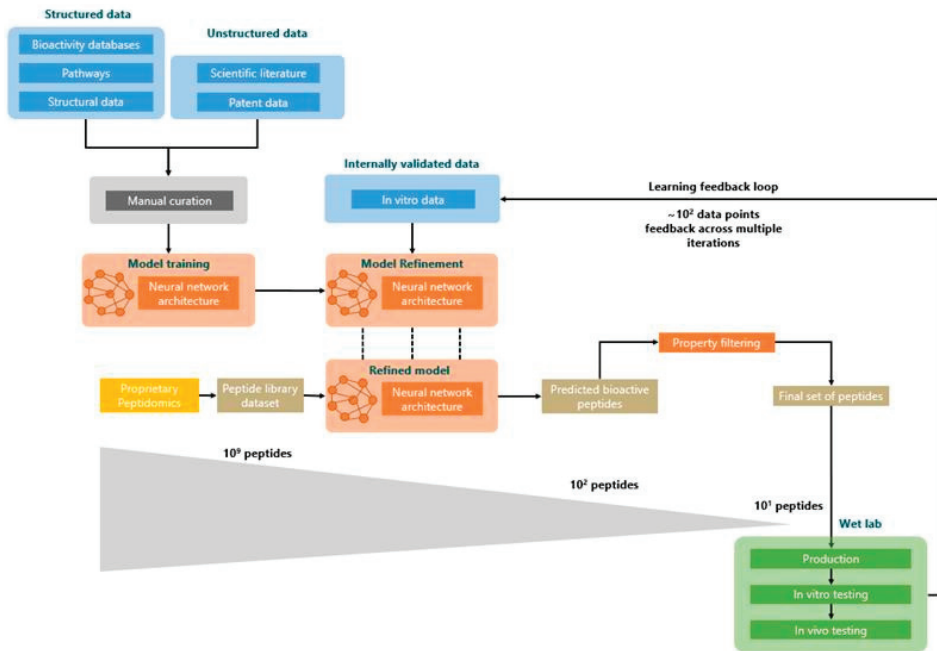


Figure 1. Peptide prediction. Workflow for predictive models adapted from Corrochano et al., 2021 [35].

At the end of the refinement process, a set of 10^9 peptides was fed into the model, which returned an output set of 10^2 peptides classed as “active.”

Next, a further collection of internally built tools was used to filter out sequences exhibiting undesirable properties. To narrow down the number of relevant peptides to be tested at each iteration (from hundreds to tens), predicted peptides were ranked using different internal predictive models. Specifically, peptides predicted as cell-penetrant, stable in blood and not toxic were prioritised. Additionally, other filters were applied, removing peptides with an odd number of cysteines or with sequence longer than 30 residues, to facilitate synthesis. Finally, all peptides exhibiting high homology against peptides contained known to have a role in glucose regulation were discarded. This final stage ultimately left a set of 5 distinct, novel peptides suitable for experimental validation.

2.4. Homology Searching and Synthesis of Predicted Peptides

To determine the true novelty of our 5 predicted peptides, we measured their homology to (1) each other and (2) to analogues or antagonists of endogenous human hormones. All searches were performed using BLASTP from the BLAST+ (BLAST+, v2.2.31) suite of programs using the following parameters: word size = 2; matrix = PAM30, E-value = 10,000. Predicted peptides were chemically synthesised by GenScript Corporation (Piscataway, New Jersey, United States). For all peptides screened at initial stages, theoretical molecular weight (MW) was checked, and all were confirmed to have HPLC purity of $\geq 95.0\%$. pep_1E99R5 had a theoretical MW of 1270.48 with a HPLC purity of $\geq 98.0\%$.

2.5. Glucose Uptake Assay

HSkMCs were plated on collagen-coated 96-well plates (1×10^4 /well) and allowed to adhere overnight at 37 °C, 5% CO₂ in 100 µL of HSkMC growth medium. The medium was then changed to HSkMC differentiation medium (Promocell, Heidelberg, Germany) and cells were allowed to differentiate for 7 days, with fresh medium added every 2 days. The day prior to the experimentation, cells were starved overnight in basal medium. Glucose uptake was measured using a glucose uptake assay kit (Abcam, Cambridge, MA, USA) as per the manufacturer's instructions. Briefly, cells were rinsed three times in Dulbecco's phosphate-buffered saline (DPBS; Lonza, Basel, Switzerland) and then starved of glucose by incubating with 100 µL of Krebs-Ringer-Phosphate-Hepes (KRPH) buffer for 40 min at 37 °C. KRPH buffer was made with 20 mM HEPES, 5 mM monopotassium phosphate, 1 mM magnesium sulphate, 1mM calcium chloride, 136 mM sodium chloride, 4.7 mM potassium chloride, adjusted to pH 7.4, all compounds were purchased from Sigma-Aldrich (St. Louis, MO, USA). Cells were treated with HSkMC basal medium containing 0.5 µg/mL (~0.4 µM) of peptide or 1 µM of human insulin solution (Sigma-Aldrich, St. Louis, MO, USA) for 20 min, followed by incubation with 10 µL of 2-deoxyglucose (2-DG; Glucose uptake assay kit; Abcam, Cambridge, UK) for 20 min at 37 °C. Subsequently, cells were washed 3 times with PBS and lysed with 80 µL of extraction buffer, after which cell lysates were freeze-thawed once before heating at 85 °C for 40 min. Following cooling on ice for 5 min, lysates were neutralised by adding 10 µL of neutralisation buffer and then diluted with assay buffer to a total volume of 50 µL (5 µL lysate + 45 µL assay buffer). After two amplification reactions, absorbance of the samples was measured at 412 nm with a microplate spectrophotometer.

2.6. GLUT4 Translocation Assay

HSkMCs aliquots (2×10^5 /well) were seeded in muscle growth medium in collagen-coated 6-well plates and differentiated in differentiation medium for 7 days. The day prior to the experimentation, cells were starved overnight in basal medium. The cells were treated with peptide (0.5 µg/mL (~0.4 µM)) or 1 µM human insulin solution for 20 min. Membrane proteins were then solubilised and isolated from cytosolic proteins using a MemPER™ Plus Membrane Protein Extraction Kit (ThermoFisher, Waltham, Mass, USA) as per the manufacturer's instructions. A 1-µM treatment with insulin to investigate glucose uptake and the associated downstream signalling is widely used in the literature, in both rat and human cell line models [36,37]. GLUT4 concentration was subsequently measured via a commercially available Human GLUT4 Sandwich ELISA kit (Abbexa, Cambridge, UK). Briefly, 100 µL of standard, blank or sample was loaded into individual wells of a 96-well plate and incubated at 37 °C for 2 h. Liquid was then aspirated and 100 µL of detection reagent A was added for 1 h at 37 °C. Subsequently, liquid was aspirated from each well, which was then washed 3 times using 350 µL of wash buffer before detection reagent B was added for 30 min at 37 °C. Wells were washed 5 times, as before, following which 90 µL of 3,3',5,5'-Tetramethylbenzidine substrate was added to each well and incubated at 37 °C for 10 min while protecting from light. Then, 50 µL of Stop solution was then added, after which the optical density of the sample was determined using a microplate reader (SpectraMax M3, Molecular Devices, Sunnyvale, CA 94089, USA) set to 450 nm.

2.7. Microarrays

HSkMCs aliquots (2×10^5 /well) were seeded in muscle growth medium in collagen-coated 6-well plates and differentiated in differentiation medium for 7 days. The day prior to the experimentation, cells were starved overnight in basal medium. The cells were treated, in triplicate, with peptide (0.5 µg/mL (~0.4 µM)) or 1 µM or human insulin solution for 20 min, at which point the treatment medium was removed and the cells were scraped in 1 mL of PBS. The cell suspension was pelleted in a microcentrifuge at 1500 rpm for 5 min, and the supernatant was removed. The cells were immediately flash-frozen in liquid nitrogen and transferred to a -80 °C freezer for storage prior to RNA extraction. RNA

was extracted in accordance with standard operating procedures for RNA extraction from tissue/cell pellets using a RNeasy mini kit (Qiagen, Manchester, UK). RNA quality and integrity were determined via bioanalyser. For each microarray experiment, 100 ng of total RNA was used. To study the whole genome expression with a comprehensive coverage of genes and transcripts, 26,083 Entrez Genes and 30,606 lncRNA, SurePrint G3 Human Gene Expression v3, 8×60 K Microarrays (Agilent, Santa Clara, CA, USA) were used. Microarray gene expression experiment was performed according to the manufacturer's protocol (One-Color Microarray-Based Gene Expression Analysis—Low Input Quick Amp Labeling v6.9). After the experiment, the arrays were scanned by SureScan Microarray Scanner (Agilent, Santa Clara, CA, USA) and data were extracted using Feature Extraction Software (Agilent, Santa Clara, CA, USA). The samples were prepared for array hybridisation according to the manufacturer's protocol. Briefly, labelled cRNA was hybridised to the microarray for 16 h before the array slides were washed and scanned using an Agilent G2565CA Microarray Scanner System.

2.8. Transcriptomics and Pathway Enrichment

Microarray data analysis was conducted using the R Bioconductor package limma [38]. Intensities were background corrected using the normexp method with an offset of 50 [39]. Quantile normalisation was then applied. Due to the use of several arrays, subsequent batch effect was identified and removed using ComBat (sva R package) [40]. Each treated group was compared to the negative untreated control using linear modelling, from which an empirical Bayesian analysis was then performed using the function ebyes from limma.

To initiate the pathway enrichment analysis, significant gene lists were filtered using raw p -value < 0.01 and fold-change > 1.3 . Enrichment was performed on Kyoto Encyclopedia of Genes and Genomes (KEGG) pathways using a hypergeometric test. Pathways were considered enriched at raw p -value < 0.01 . Enrichment was assessed for each treatment insulin and pep_1E99R5, respectively, considering up- and downregulated gene lists. All analysis was performed internally and by third-party Fios Genomics Ltd. (Edinburgh, UK).

2.9. Statistical Analyses

All data are presented as mean \pm SEM. Replicate numbers for each experiment are indicated in figure legends. Results of in vitro experiments were assessed by one-way ANOVA followed by Dunnett's post-hoc test. Comparisons between different peptide treated and untreated KK-A^y groups were assessed by one-way ANOVA followed by Dunnett's post-hoc test. Statistical significance was defined as $p < 0.05$. Graphs were generated using the "ggplot2" R package [41].

3. Results

3.1. Novel Peptide Prediction and Validation

Using a machine learning approach similar to Kennedy et al., 2020 [33], one hundred peptide candidates were predicted as potentially possessing anti-diabetic functionality via blood glucose regulatory activity. This set of peptides was further refined using a collection of tools to filter out the sequences with undesirable physiochemical properties. Taking into account the significant costs involved in peptide drug manufacturing [42], all predicted peptides were to be less than 20 amino acids in length and linear with no major structures. Ultimately, this resulted in a final set of five peptides that interestingly exhibited no homology to each other or to any known patented or published bioactive peptides. These peptides are referred to hereafter as pep_1E99R5, pep_37MB3O, pep_ANUT7B, pep_RTE62G and pep_QT5XGQ. To validate the bioactivity of these predicted peptides, an in vitro glucose uptake method was employed.

Insulin-stimulated uptake of blood glucose by skeletal muscle plays a fundamental role in the maintenance of glucose homeostasis, accounting for 75% of glucose utilisation in the body [43]. Accordingly, the predicted bioactivity of our predicted peptides was first validated in a cell-based glucose uptake assay, where insulin was used as a positive control.

Three predicted peptides, pep_1E99R5, pep_37MB3O and pep_ANUT7B, demonstrated the ability to significantly increase glucose uptake in human skeletal muscle cells (HSkMCs), with pep_37MB3O and pep_ANUT7B displaying a stronger effect than that of insulin (Figure 2A). No significant glucose uptake activity was reported for pep_RTE62G and pep_QT5XGQ; thus, these peptides were not progressed further in our in vitro and in vivo validation studies. Cumulatively, these results indicate an in vitro validation success rate of 60% for the predictive model and suggest that these sequences should be further examined in relevant models. Of note, a more comprehensive absorption, distribution, metabolism, and excretion (ADMET) prediction could be incorporated for further development of the presented peptides.

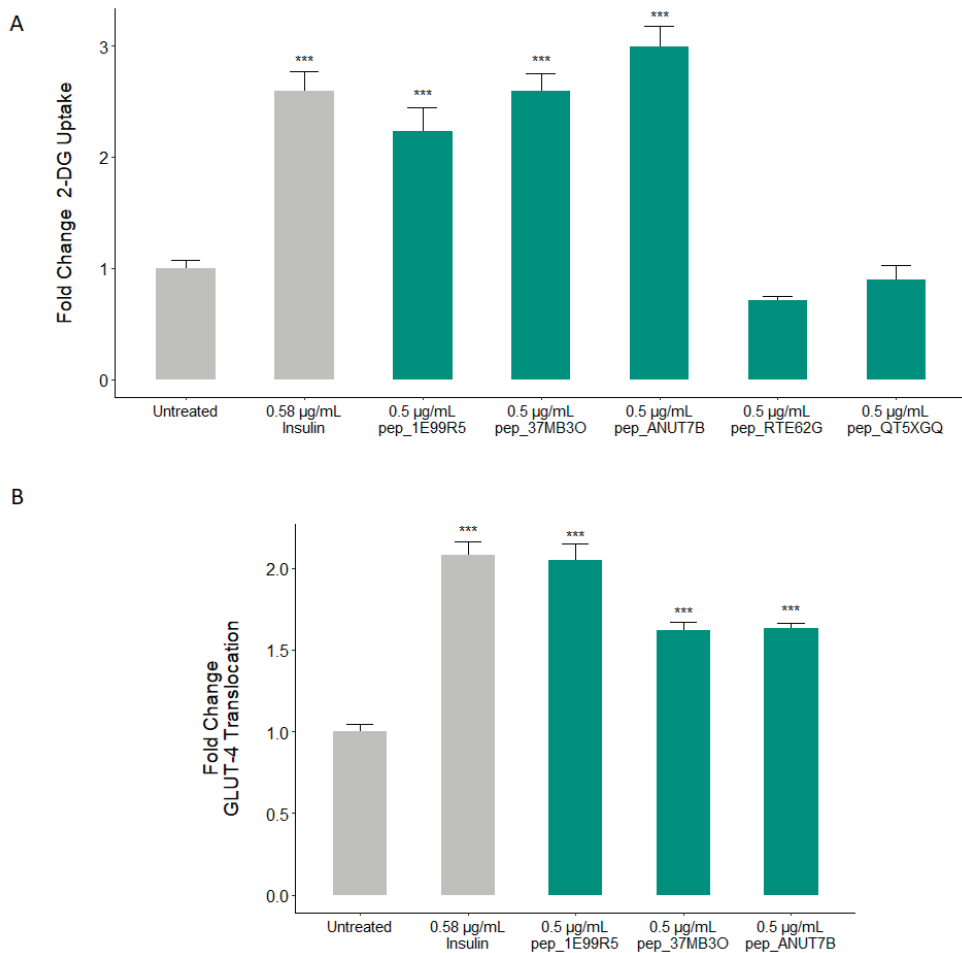


Figure 2. In vitro validation of predicted peptides as potent stimulators of glucose uptake and Glucose transporter type 4 (GLUT4) translocation. Skeletal muscle cells were stimulated with either insulin or predicted natural peptides at the indicated concentrations for 15 min. (A) The effect on glucose uptake is measured, while in (B), the extent of GLUT4 translocation is assessed (one-way ANOVA analysis with Dunnett's test; *** $p < 0.001$; data presented are the mean \pm SEM of at least 3 independent replicates).

The key mediator of glucose uptake into skeletal muscle cells is the protein GLUT4 [44]. Skeletal muscle accounts for the majority of glucose uptake in the body [45]. While glucose uptake efficacy was used as an initial experimental validation of our predicted peptides,

the ultimate objective of the predictor was to identify peptides capable of stimulating GLUT4 translocation to the plasma membrane, which is known to be decreased in type 2 diabetics [46]. Indeed, interventions to promote the expression and translocation of GLUT4 in appropriate cells such as skeletal muscle fibres are of clear benefit to those with T2DM [47]. The HSkMC model used for this study allows for measurement of GLUT4 translocation, which, in turn, allows for a specific molecular mechanism to be identified as the cause of these peptides' ability to modulate glucose levels. Accordingly, we evaluated the ability of these peptides to initiate GLUT4 translocation in HSkMCs. At a test dose of 0.5 µg/mL, we found that all three predicted peptides stimulated a highly significant increase in GLUT4 translocation (Figure 2B). Of the three positively predicted peptides, pep_1E99R5 is seen to demonstrate the most potent effect, eliciting an approximately equivalent response to insulin (Figure 2B).

3.2. Validation of Peptides in a Diabetic Mouse Model

The therapeutic potential of our in-vitro-validated anti-diabetic peptides was evaluated in the KK-*A^y* model of obese insulin-resistant DM. In KK-*A^y* mice, fasting blood glucose and HbA1c levels are elevated, and when fed a normal diet, obesity and DM are observed by 12 weeks. Peptides pep_37MB3O, pep_1E99R5 and pep_ANUT7B at 127 mg/kg (100 µM) or vehicle were dosed subcutaneously (sc) once daily for 14 days. All animals tolerated treatment well and body weight did not change per treatment throughout the study (Figure S1). At day 5 post-baseline, all three predicted peptides significantly reduced fasting blood glucose compared to the vehicle control group (Figure 3), with pep_1E99R5 demonstrating the most significant reduction. The effect of pep_ANUT7B was tempered by day 7 ($p = 0.07$) and day 13, with pep_1E99R5 and pep_37MB3O both exhibiting a significant reduction in fasting blood glucose at these time points. However, the effect of pep_1E99R5 was slightly reduced at day 13 (Figure 3), a trend that is in line with what is observed for known anti-diabetic therapies in several animal studies [48,49]. While pep_1E99R5 and pep_37MB3O's effects were maintained throughout the study period, pep_1E99R5 treatment resulted in the most potent effects on fasting blood glucose levels in vivo; therefore, this peptide was chosen for a longer in vivo study to measure HbA1c.

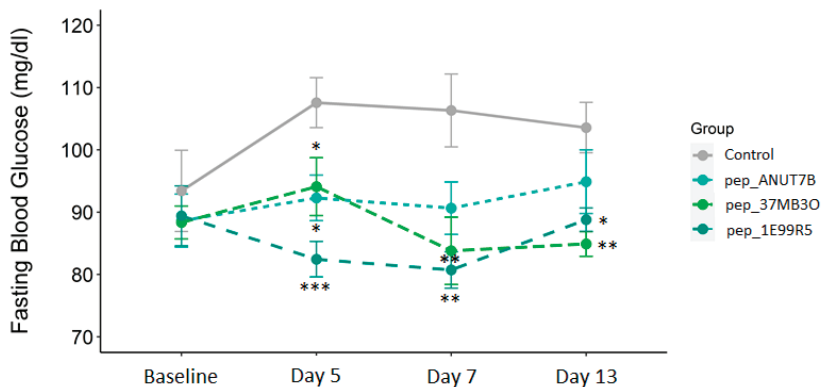


Figure 3. Predicted peptides in a mouse model of type 2 diabetes. Fasting glucose levels (overnight) of all mice were measured as indicated. Data are mean \pm SEM ($n = 8$ per group; aged 12 weeks at baseline) and analysed by Dunnett's test to compare the differences between the peptide treatment groups and the vehicle control group (* $p < 0.05$ ** $p < 0.01$ *** $p < 0.001$).

As a decrease of $>1\%$ HbA1c is considered to be of significant clinical benefit [50], the effects of pep_1E99R5 on HbA1c % were measured in a trial over 6 weeks. In KK-*A^y* mice, pep_1E99R5 (12.7 mg/kg (10 µM) or 63.5 mg/kg (50 µM)) was administered daily via sc injection and compared to control groups of vehicle or Liraglutide (250 µg/kg), previously

shown to have a positive effect on HbA1c [51]. HbA1c levels are a long-term indicator of blood glucose regulation [52]; previous studies have shown significant treatment effects on HbA1c at 8 weeks in similar KK-*A^y* models [53]. However, Liraglutide treatment did not significantly reduce HbA1c percentage compared to vehicle control following 6 weeks of treatment (Figure 4); it is possible that a significant drop in HbA1c levels would have been recorded if the study duration were extended. In contrast, pep_1E99R5 (63.5 mg/kg)-treated mice showed a significant reduction of approximately 1.3% in HbA1c compared to vehicle control, suggesting a sustained effect of pep_1E99R5 in the animals. No effect was noted in the 10- μ M-treated mice, which suggests a dose-dependent effect of the peptide.

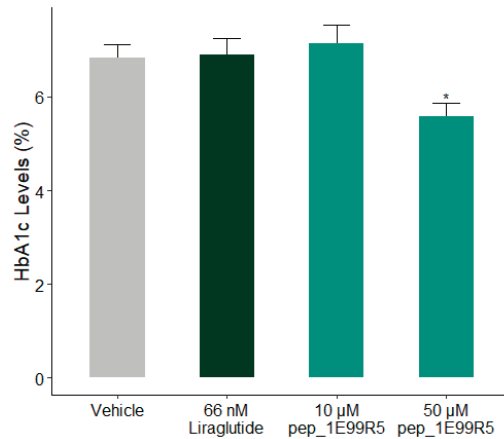


Figure 4. Effect of pep_1E99R5 on HbA1c levels. HbA1c levels (%) of all mice were measured as indicated. Data are mean \pm SEM ($n = 11$ per group; aged 12 weeks at baseline) and analysed by Dunnett's test to compare the differences between peptide treatment groups, Liraglutide group and vehicle control (* $p < 0.05$).

A common complication associated with T2DM is hepatic steatosis (HS), a condition in which fatty deposits accumulate in the liver, affecting up to 75% of T2DM patients, often leading to non-alcohol fatty liver disease (NAFLD) [54]. Moreover, HS among the prediabetic population is considered to be a predictor of conversion to DM [55]. In a study by Fiorentino et al., a subset of HbA1c-defined prediabetic individuals with 1-h postload glucose ≥ 155 mg/dL were at higher risk of developing HS [56]. Furthermore, the prevalence of prediabetes and DM was found to be six-fold higher in NAFLD patients compared to healthy controls. [57] Therefore, a decrease in HS, alongside the HbA1c decrease, would be of significant clinical interest.

Consequently, levels of hepatic steatosis (HS) in the mice were measured via sectioning and H&E staining. Histological NAFLD scoring was performed by an independent third-party reviewer. Features were scored according to a murine liver scoring system devised by [58] (Figure 5A). Vehicle control and Liraglutide-treated mice exhibited signs of NAFLD; however, these were reduced significantly in 50- μ M pep_1E99R5 and trended to a decrease in 10- μ M pep_1E99R5 treatment, suggesting a dose-dependent effect (Figure 5B).

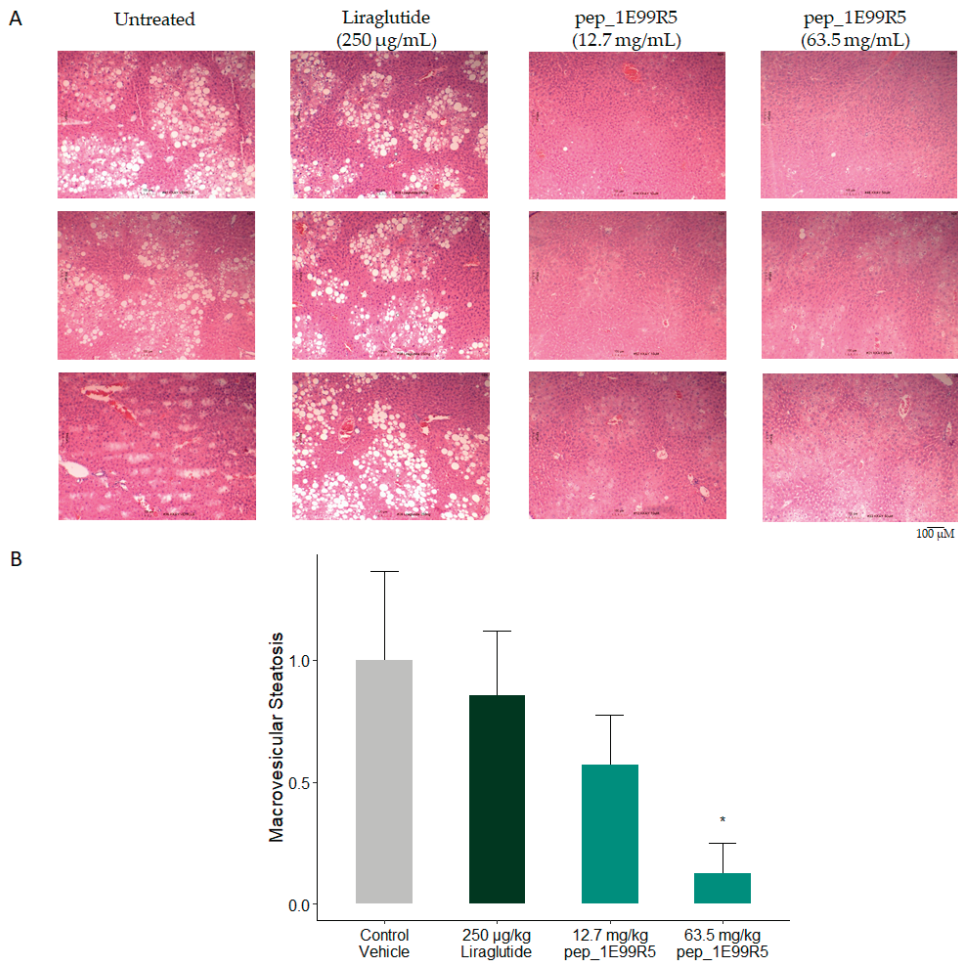


Figure 5. Effect of pep_1E99R5 on hepatic steatosis. **(A)** Livers of all mice were excised and sectioned before staining with H&E. Images were taken using a Motic BA310E trinocular compound microscope at 10x magnification. Histological non-alcohol fatty liver disease (NAFLD) scoring was performed by an independent third-party reviewer. **(B)** Features were scored according to a murine liver scoring system devised by Liang et al., 2014. Data are mean ± SEM ($n = 6$ per group; aged 12 weeks at baseline) and analysed by Dunnett's test to compare the differences between the two peptide treatment groups and vehicle control and Liraglutide groups (* $p < 0.05$).

3.3. Characteristics of Predicted Peptides

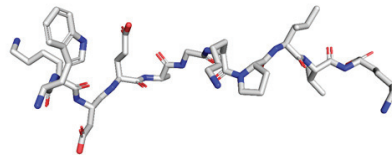
As short linear peptides offer an intriguing therapeutic option due to decreased side effects and toxicity [22], the predictive model focused on peptides <20 amino acids (AA) in length. Of note, pep_1E99R5 consists of 11 AA, WKDEAGKPLVK, with no major structures (Table 1; Figure 6A). While this specific sequence of amino acids was predicted due to desirable features identified through the predictive model, further work is being carried out on derivatives of pep_1E99R5 to assess bioactivity retention. Apart from structure and length, an important consideration often overlooked when describing predictions of functional compounds is the level of true novelty offered by the de-novo-discovered compounds. Accordingly, focusing our most promising candidate peptide, pep_1E99R5, presented in Table 1, we assessed the extent to which it was truly novel in light of (1) key

human peptide hormones involved in glucose regulation and (2) the larger set of 1550 known endogenous human peptides (Figure 6B). To achieve this, we calculated three major peptide properties: charge, molecular weight and hydrophobicity. Here, pep_1E99R5's charge (+1) and hydrophobicity (45.5%) are no different to most human endogenous peptides, with an average charge of +2.9 (50% of the peptides between -1 and $+7$) and an average hydrophobicity of 46.4 (50% of the peptides between 42.9% and 50.4%) (Figure S2). However, pep_1E99R5 (1.3 kDa) is substantially smaller than 99.6% of human endogenous peptides and smaller than both insulin (5.8 kDa) and GLP-1 (3.3 kDa), as well as on-the-market DM-treatment peptides Exenatide (4.1 kDa) and Liraglutide (3.7 kDa), which offers a considerable advantage in terms of production cost. pep_1E99R5 was further assessed against the natural glucose-regulating hormones in terms of homology, where, even at a very lenient e-value threshold, no sequence similarity was reported.

Table 1. pep_1E99R5 characteristics.

Sequence	Length (Amino Acid)	Molecular Weight (Da)	Charge	Isoelectric Point	Hydrophobicity
WKDEAGKPLVK	11	1270.48	1	8.5	45.5%

A



B

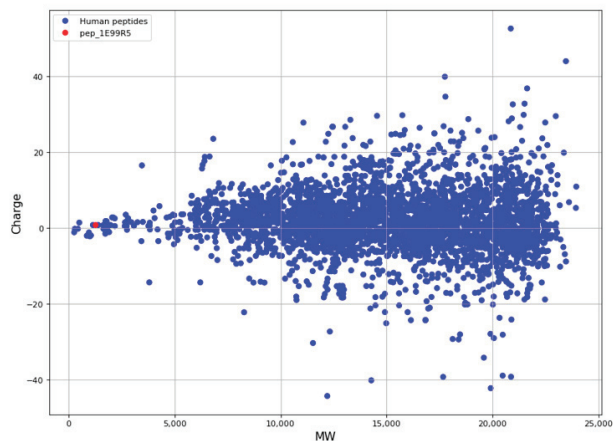


Figure 6. Linear representation of pep_1E99R5 and molecular weight and charge dispersion of pep_1E99R5 compared to endogenous human peptides. (A) Representation of the linear structure for pep_1E99R5 generated using PyMol, Version 2.3.5, Schrödinger, LLC (stick visualisation). (B) Dispersion of molecular weight and charge of human endogenous peptides (blue) and pep_1E99R5 (red). The human peptides were retrieved from UniprotKB (<https://www.uniprot.org/statistics/Swiss-Prot>) (Accession date: 8 March 2021) and filtered with a threshold of 200 amino acids. The average molecular weight of the human peptides is 14.4 kDa (Q1 = 11.3 kDa, Q3 = 18.1 kDa) while pep_1E99R5 is 1.3 kDa. The average charge of the human peptides is +2.9 (Q1 = -1 , Q3 = $+7$) while pep_1E99R5's charge is +1.

3.4. Molecular Mechanisms Modulated by pep_1E99R5

To elucidate the molecular pathways modulated by pep_1E99R5 *in vitro*, HSkMCs treated with the peptide underwent a full transcriptomic screen. HSkMCs treated with insulin were screened in parallel. To determine gene expression, RNA was extracted from the cells, fluorescently labelled and run in triplicate on SurePrint G3 Human Gene Expression v3 8 × 60 K Microarrays. Microarray technology simultaneously measures the expression of large numbers of transcripts in treated and untreated samples.

A 20-min stimulation of HSkMCs with 0.5 µg/mL (0.4 µM) pep_1E99R5 changed the expression, up or down (>1.3 fold; $p < 0.01$) of 625 transcripts, compared to untreated cells. A 1-µM insulin treatment of HSkMCs was run in parallel and changed the expression, up or down (>1.3 fold; $p < 0.01$) of 540 transcripts, compared to untreated cells (data not shown). KEGG analysis was used to obtain a biochemical overview of the pathways differentially expressed under the influence of pep_1E99R5 and insulin [59].

Pathways related to glycolysis, oxidative phosphorylation and the citrate cycle were among the most highly ranked of the 21 KEGG pathways enriched by our peptide (all $p < 0.01$) (Figure 7). These pathways are typically downregulated in T2DM patients [60]. The pentose phosphate pathway, an alternative pathway to glycolysis, and the citrate cycle for oxidation of glucose also showed a trend toward enrichment when treated with pep_1E99R5, as did the TGF-β pathway, shown to stimulate the glucose uptake through GLUT1 [61]. Stimulation of these key glucose metabolism pathways with pep_1E99R5 may be key to its efficacy in enhancing glucose uptake in skeletal muscle cells. Nineteen KEGG pathways were downregulated by pep_1E99R5 ($p < 0.01$), including the PI3k-Akt pathway, the primary pathway for insulin-stimulated glucose uptake. This is further evidence that our peptide stimulates glucose uptake independent of the insulin pathway. The p53 signalling pathway was also downregulated by pep_1E99R5; typically, a tumour suppressing pathway, this mechanism has the added ability to mediate metabolic changes in cells through the regulation of energy metabolism and has been shown to disrupt glucose uptake into cells [62]; hence, downregulation of this pathway will promote glucose uptake into cells.

The transcriptomic profile of cells treated with 1 µM insulin showed minimal KEGG pathway enrichment related to T2DM. This may be due to the relatively high insulin dose that the cells were exposed to, promoting upregulation in genes related to insulin resistance, including SOCS3, which was significantly upregulated by the insulin treatment and has been shown to be key to the physiological regulation of insulin signalling [63]. Conversely the KEGG pathway related to type 1 DM (T1DM) was among the pathways decreased by insulin treatment ($p < 0.01$). This finding is easier to interpret as the deficiency of bioavailable insulin is the primary mechanism by which T1DM arises. Furthermore, while the oxidative phosphorylation pathway showed a trend towards enrichment in the insulin-treated cells, this enrichment was less than that observed in the pep_1E99R5-treated samples. Comparison of significant gene enrichment in this pathway when the cells are stimulated with insulin ($n = 3$ genes) versus pep_1E99R5 ($n = 9$ genes) suggests that pep_1E99R5 has a greater effect in activating this key glucose metabolism pathway. While these data indicate different transcriptomic profiles for pep_1E99R5 and insulin, further work is underway to elucidate specific targets of pep_1E99R5.

Peptides represent the largest class of signalling molecules in animals, acting as hormones, neurotransmitters and growth factors to perform many critical physiological functions. Given that peptides have evolved to interact with specific biological targets, they offer great promise as selective, potent therapeutics that are less likely to suffer from issues of tolerability and toxicity [22,23]. Although beyond the scope of the current study, it is expected that natural peptides in their current form, due to their linear nature and absence of modifications, can circumvent issues with safety [64]. Indeed, no tolerability concerns were noted in any animals during both *in vivo* studies in this project with doses as high as 127 mg/kg.

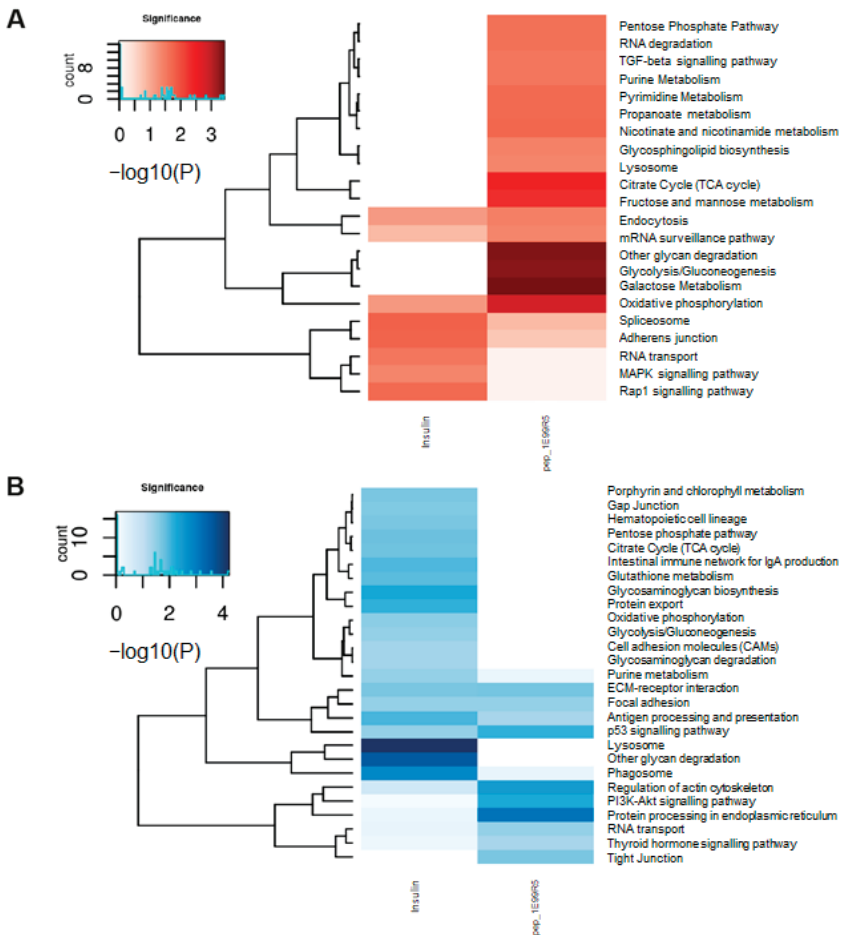


Figure 7. Kyoto Encyclopedia of Genes and Genomes (KEGG) pathway enrichment analyses of pep_1E99R5 and insulin. Representation of the KEGG pathway enrichment of significantly differentially expressed genes for insulin and pep_1E99R5 compared to untreated. Gene lists were filtered using raw p -value < 0.05 and fold change ≥ 1.3 . The significance of a given KEGG pathway is assessed with raw p -value < 0.05 . (A) Heatmap showing significantly downregulated (red) enrichment in KEGG pathways and (B) heatmap showing significantly upregulated (blue) enrichment in KEGG pathways (deeper colour indicates increased significance). Heatmaps present log-transformed raw p -values. Enrichment analyses were performed for each treatment (insulin and pep_1E99R5) separately and then brought together for comparison. Colour gradients indicate significance; the darker the colour, the more significant the result is.

To date, linear peptides as therapeutics have been largely underexplored. By their nature, they usually have an excellent safety profile and are easier to manufacture, with reduced loss of yield during synthesis [65]. Given their simple structure, a linear peptide can, in many cases, be optimised for bioavailability and stability more easily [42] than more structured, “difficult” peptides where optimisation alters efficacy [27,66,67]. Our aim here was to find a novel short natural linear peptide that can improve glucose modulation *in vivo*. When taking molecule size into account in current T2DM therapeutics, pep_1E99R5 is demonstrably smaller than current peptide therapeutics, which creates the potential for improved precision at the target site and reduced manufacture scale-up costs [68]. This coupled with the reduced economic burden observed following improved glycaemic control in T2DM of up to 13% [69], indicates further potential for such a peptide.

Understanding the mechanism of action (MOA) of pep_1E99R5 might reveal new mechanisms of glucose regulation *in vivo*; our results indicate that its MOA is different to that of insulin and further work is underway to elucidate this. Our initial study is a first step in investigating the world of natural linear peptides which, combined with good stability and bioavailability profiles, could become a repository for future therapeutic development.

The exploration of a diverse class of linear peptides and their association with glucose metabolism could not have been possible without the use of AI and machine learning. The predicted peptide, pep_1E99R5, is capable of modulating GLUT4 translocation, thereby affecting glucose uptake *in vitro*. Preclinical studies suggest that this peptide is biologically functional, leading to potential clinically relevant changes in both blood glucose and glycated haemoglobin, as well as a concomitant reduction in hepatic steatosis. Furthermore, analysis of the peptide itself, along with KEGG pathway analysis compared to insulin, suggests a unique, novel function of pep_1E99R5 in modulating blood glucose metabolism. An interesting application would be to integrate these machine learning approaches to explore the bioavailability and stability of linear peptides, which could give rise to candidates with not only good safety and efficacy profiles but also desirable pharmacokinetic properties for future therapeutic development in metabolic disorders such as T2D or others.

4. Conclusions

In undertaking this study, we aimed to explore short linear peptides with glucose-regulating activity and present experimental evidence that machine learning methods can reveal truly novel molecules capable of demonstrating meaningful and clinically relevant biological effects—in this case, in the context of T2DM. Of note, efficacious short linear peptides with good tolerability *in vivo* also present an opportunity for the pharmaceutical industry, with reduced manufacturing costs. Although further work is required to elucidate bioavailability, mechanism of action and clinical efficacy, we show initial evidence that unoptimised predicted peptides can display enhanced bioactivity *in vitro* than insulin and outperform Liraglutide in a hyperinsulinemic *in vivo* model. Ultimately, we highlight the capabilities of AI in discovery and present pep_1E99R5 as a short, linear bioactive peptide capable of affecting blood glucose metabolism *in vitro* and *in vivo* via robust modulation of a unique network of several key signalling pathways.

Supplementary Materials: The following are available online at <https://www.mdpi.com/2227-9059/9/3/276/s1>, Figure S1: AI predicted peptides in a mouse model of type 2 diabetes, Figure S2: Property dispersion of AI predicted peptides relative to known endogenous human peptides.

Author Contributions: R.C.: Validation, Investigation, Methodology, Writing—Original Draft. A.A.: Software, Visualisation, Formal Analysis, Data Curation, Writing—Original Draft. M.C.: Formal Analysis, Writing—Original Draft, Writing—Review and Editing. A.W.: Formal Analysis, Project administration, Visualisation, Writing—Original Draft, Writing—Review and Editing. I.H.: Conceptualisation, Writing—Original Draft, Writing—Review and Editing. N.K.: Conceptualisation, Writing—Review and Editing, Supervision. All authors have read and agreed to the published version of the manuscript.

Funding: This research received no external funding.

Institutional Review Board Statement: Ethical approval was granted by the International Association of Religious Freedom (IARF #:MLR-101 (1 May 2018), IARF #:MLR-115 (13 January 2020)) and, therefore, experiments were performed in accordance with the ethical standards laid out by the Institutional Animal Care and Use Committee (IACUC).

Informed Consent Statement: Not applicable.

Data Availability Statement: Publicly available datasets were analyzed in this study. This data can be found here (<https://www.uniprot.org/statistics/Swiss-Prot>).

Acknowledgments: The authors wish to acknowledge Cyril Lopez. for his guidance on the AI performed during the prediction of novel peptide targets. We appreciate the contributions of Brendan

Molloy, Tim Considine, Therese Holton, Hansel Gomez and Brian Keogh in the planning and structuring of the data and manuscript. We also appreciate the guidance of Vivian Cong (Melior Discovery Inc., Exton, PA, USA) for animal study design and execution.

Conflicts of Interest: All authors are employees of Nuritas Ltd. (Dublin, Ireland).

References

1. Trikkalinou, A.; Papazafropoulou, A.K.; Melidonis, A. Type 2 diabetes and quality of life. *World J. Diabetes* **2017**, *8*, 120–129. [CrossRef]
2. Cho, N.; Shaw, J.; Karuranga, S.; Huang, Y.; Fernandes, J.D.R.; Ohlogge, A.; Malanda, B. IDF Diabetes Atlas: Global estimates of diabetes prevalence for 2017 and projections for 2045. *Diabetes Res. Clin. Pract.* **2018**, *138*, 271–281. [CrossRef]
3. Tahrani, A.A.; Bailey, C.J.; Del Prato, S.; Barnett, A.H. Management of type 2 diabetes: New and future developments in treatment. *Lancet* **2011**, *378*, 182–197. [CrossRef]
4. Nicholson, G.; Hall, G.M. Diabetes mellitus: New drugs for a new epidemic. *Br. J. Anaesth.* **2011**, *107*, 65–73. [CrossRef] [PubMed]
5. Bhatt, H.B. Thoughts on the progression of type 2 diabetes drug discovery. *Expert Opin. Drug Discov.* **2014**, *10*, 107–110. [CrossRef]
6. Turner, N.; Zeng, X.-Y.; Osborne, B.; Rogers, S.; Ye, J.-M. Repurposing Drugs to Target the Diabetes Epidemic. *Trends Pharmacol. Sci.* **2016**, *37*, 379–389. [CrossRef]
7. Zhou, G.; Myers, R.; Li, Y.; Chen, Y.; Shen, X.; Fenyk-Melody, J.; Wu, M.; Ventre, J.; Doebber, T.; Fujii, N.; et al. Role of AMP-activated protein kinase in mechanism of metformin action. *J. Clin. Investig.* **2001**, *108*, 1167–1174. [CrossRef] [PubMed]
8. Fontaine, E. Metformin-Induced Mitochondrial Complex I Inhibition: Facts, Uncertainties, and Consequences. *Front. Endocrinol.* **2018**, *9*, 753. [CrossRef]
9. Madiraju, A.K.; Erion, D.M.; Rahimi, Y.; Zhang, X.-M.; Braddock, D.T.; Albright, R.A.; Prigaro, B.J.; Wood, J.L.; Bhanot, S.; Macdonald, M.J.; et al. Metformin suppresses gluconeogenesis by inhibiting mitochondrial glycerophosphate dehydrogenase. *Nat. Cell Biol.* **2014**, *510*, 542–546. [CrossRef] [PubMed]
10. Nasri, H.; Rafieian-Kopaei, M. Metformin: Current knowledge. *J. Res. Med. Sci.* **2014**, *19*, 658–664. [PubMed]
11. Hauner, H. The mode of action of thiazolidinediones. *Diabetes/Metab. Res. Rev.* **2002**, *18*, S10–S15. [CrossRef] [PubMed]
12. Smith, U. Pioglitazone: Mechanism of action. *Int. J. Clin. Pract. Suppl.* **2001**, *121*, 13–18.
13. Wright, E.M.; Loo, D.D.F.; Hirayama, B.A. Biology of Human Sodium Glucose Transporters. *Physiol. Rev.* **2011**, *91*, 733–794. [CrossRef] [PubMed]
14. Clar, C.; Gill, J.A.; Court, R.; Waugh, N. Systematic review of SGLT2 receptor inhibitors in dual or triple therapy in type 2 diabetes. *BMJ Open* **2012**, *2*, e001007. [CrossRef] [PubMed]
15. Gupta, V. Glucagon-like peptide-1 analogues: An overview. *Indian J. Endocrinol. Metab.* **2013**, *17*, 413–421. [CrossRef] [PubMed]
16. Kahn, S.E.; Cooper, M.E.; Del Prato, S. Pathophysiology and treatment of type 2 diabetes: Perspectives on the past, present, and future. *Lancet* **2014**, *383*, 1068–1083. [CrossRef]
17. Tasyurek, H.M.; Altunbas, H.A.; Balci, M.K.; Sanlioglu, S. Incretins: Their physiology and application in the treatment of diabetes mellitus. *Diabetes/Metab. Res. Rev.* **2014**, *30*, 354–371. [CrossRef] [PubMed]
18. Astrup, A.; Carraro, R.; Finer, N.N.; Harper, A.; Kunesova, M.; Lean, M.E.J.; Niskanen, L.; Rasmussen, M.F.; Rissanen, A.; Rössner, S.; et al. Safety, tolerability and sustained weight loss over 2 years with the once-daily human GLP-1 analog, liraglutide. *Int. J. Obes.* **2011**, *36*, 843–854. [CrossRef] [PubMed]
19. Astrup, A.; Rössner, S.; Van Gaal, L.; Rissanen, A.; Niskanen, L.; Al Hakim, M.; Madsen, J.; Rasmussen, M.F.; Lean, M.E. Effects of liraglutide in the treatment of obesity: A randomised, double-blind, placebo-controlled study. *Lancet* **2009**, *374*, 1606–1616. [CrossRef]
20. Rosenstock, J.; Klaff, L.J.; Schwartz, S.; Northrup, J.; Holcombe, J.H.; Wilhelm, K.; Trautmann, M. Effects of Exenatide and Lifestyle Modification on Body Weight and Glucose Tolerance in Obese Subjects With and Without Pre-Diabetes. *Diabetes Care* **2010**, *33*, 1173–1175. [CrossRef]
21. Zucconelli, C.R.; Brock, R.; Adjobo-Hermans, M.J. Linear Peptides in Intracellular Applications. *Curr. Med. Chem.* **2017**, *24*. [CrossRef] [PubMed]
22. Craik, D.J.; Fairlie, D.P.; Liras, S.; Price, D. The Future of Peptide-based Drugs. *Chem. Biol. Drug Des.* **2013**, *81*, 136–147. [CrossRef] [PubMed]
23. Fosgerau, K.; Hoffmann, T. Peptide therapeutics: Current status and future directions. *Drug Discov. Today* **2015**, *20*, 122–128. [CrossRef] [PubMed]
24. Radermecker, R.P.; Scheen, A.J. Continuous subcutaneous insulin infusion with short-acting insulin analogues or human regular insulin: Efficacy, safety, quality of life, and cost-effectiveness. *Diabetes/Metab. Res. Rev.* **2004**, *20*, 178–188. [CrossRef] [PubMed]
25. Roxin, A.; Zheng, G. Flexible or fixed: A comparative review of linear and cyclic cancer-targeting peptides. *Futur. Med. Chem.* **2012**, *4*, 1601–1618. [CrossRef]
26. Aungst, B.J.; Saitoh, H.; Burcham, D.L.; Huang, S.-M.; Mousa, S.A.; Hussain, M.A. Enhancement of the intestinal absorption of peptides and nonpeptides. *J. Control. Release* **1996**, *41*, 19–31. [CrossRef]
27. Lee, A.C.-L.; Harris, J.L.; Khanna, K.K.; Hong, J.-H. A Comprehensive Review on Current Advances in Peptide Drug Development and Design. *Int. J. Mol. Sci.* **2019**, *20*, 2383. [CrossRef]
28. Marx, V. The big challenges of big data. *Nature* **2013**, *498*, 255. [CrossRef]

29. Schadt, E.E.; Friend, S.H.; Shaywitz, D.A. A network view of disease and compound screening. *Nat. Rev. Drug Discov.* **2009**, *8*, 286–295. [CrossRef]
30. Mamoshina, P.; Vieira, A.; Putin, E.; Zhavoronkov, A. Applications of Deep Learning in Biomedicine. *Mol. Pharm.* **2016**, *13*, 1445–1454. [CrossRef]
31. Rein, D.; Ternes, P.; Demin, R.; Gierke, J.; Helgason, T.; Schön, C.; Gierke, J. Artificial intelligence identified peptides modulate inflammation in healthy adults. *Food Funct.* **2019**, *10*, 6030–6041. [CrossRef]
32. Wall, A.; Kennedy, K.; Cal, R.; Casey, R.; Holton, T.; Adelfio, A.; Khaldi, N. pep_35E7UW, a natural peptide with cutaneous anti-ageing effects discovered within the *Oryza sativa* proteome through machine learning. *J. Dermatol. Cosmetol.* **2020**, *4*, 109–116. [CrossRef]
33. Kennedy, K.; Keogh, B.; Lopez, C.; Adelfio, A.; Molloy, B.; Kerr, A.; Wall, A.M.; Jalowicki, G.; Holton, T.A.; Khaldi, N. An Artificial Intelligence Characterised Functional Ingredient, Derived from Rice, Inhibits TNF- α and Significantly Improves Physical Strength in an Inflammaging Population. *Foods* **2020**, *9*, 1147. [CrossRef] [PubMed]
34. Kennedy, K.; Cal, R.; Casey, R.; Lopez, C.; Adelfio, A.; Molloy, B.; Wall, A.M.; Holton, T.A.; Khaldi, N. The anti-ageing effects of a natural peptide discovered by artificial intelligence. *Int. J. Cosmet. Sci.* **2020**, *42*, 388–398. [CrossRef] [PubMed]
35. Corrochano, A.R.; Cal, R.; Kennedy, K.; Wall, A.M.; Murphy, N.; Trajkovic, S.; O'Callaghan, S.; Adelfio, A.; Khaldi, N. Characterising the efficacy and bioavailability of bioactive peptides identified for attenuating muscle atrophy within a *Vicia faba*-derived functional ingredient. *Curr. Res. Food Sci.* **2021**, in press.
36. Guigas, B.; Sakamoto, K.; Taleux, N.; Reyna, S.M.; Musi, N.; Viollet, B.; Hue, L. Beyond AICA riboside: In search of new specific AMP-activated protein kinase activators. *IUBMB Life* **2009**, *61*, 18–26. [CrossRef] [PubMed]
37. Freymond, D.; Guignet, R.; Lhote, P.; Passaquin, A.-C.; Rüegg, U.T. Calcium homeostasis and glucose uptake of murine myotubes exposed to insulin, caffeine and 4-chloro-m-cresol. *Acta Physiol. Scand.* **2002**, *176*, 283–292. [CrossRef] [PubMed]
38. Smyth, G.K. Linear Models and Empirical Bayes Methods for Assessing Differential Expression in Microarray Experiments. *Stat. Appl. Genet. Mol. Biol.* **2004**, *3*, 1–25. [CrossRef] [PubMed]
39. Silver, J.D.; Ritchie, M.E.; Smyth, G.K. Microarray background correction: Maximum likelihood estimation for the normal-exponential convolution. *Biostatistics* **2008**, *10*, 352–363. [CrossRef] [PubMed]
40. Leek, J.T.; Johnson, W.E.; Parker, H.S.; Jaffe, A.E.; Storey, J.D. *sva: Surrogate Variable Analysis*, R package version 3.10; Bioconductor: New York, NY, USA, 2014.
41. Wickham, H. *ggplot2*; Springer: New York, NY, USA, 2009.
42. Di, L. Strategic Approaches to Optimizing Peptide ADME Properties. *AAPS J.* **2015**, *17*, 134–143. [CrossRef]
43. Ehrenborg, E.; Krook, A. Regulation of Skeletal Muscle Physiology and Metabolism by Peroxisome Proliferator-Activated Receptor δ . *Pharmacol. Rev.* **2009**, *61*, 373–393. [CrossRef]
44. Zisman, A.; Peroni, O.D.; Abel, E.D.; Michael, M.D.; Mauvais-Jarvis, F.; Lowell, B.B.; Wojtaszewski, J.F.; Hirshman, M.F.; Virkamaki, A.; Goodyear, L.J.; et al. Targeted disruption of the glucose transporter 4 selectively in muscle causes insulin resistance and glucose intolerance. *Nat. Med.* **2000**, *6*, 924–928. [CrossRef]
45. Vargas, E.; Podder, V.; Sepulveda, M.A.C. Physiology, Glucose Transporter Type 4 (GLUT4). In *StatPearls*; StatPearls Publishing: Treasure Island, FL, USA, 2020.
46. Kennedy, J.W.; Hirshman, M.F.; Gervino, E.V.; Ocel, J.V.; Forse, R.A.; Hoening, S.J.; Aronson, D.; Goodyear, L.J.; Horton, E.S. Acute exercise induces GLUT4 translocation in skeletal muscle of normal human subjects and subjects with type 2 diabetes. *Diabetes* **1999**, *48*, 1192–1197. [CrossRef] [PubMed]
47. Alam, F.; Islam, A.; Khalil, I.; Gan, S.H. Metabolic Control of Type 2 Diabetes by Targeting the GLUT4 Glucose Transporter: Intervention Approaches. *Curr. Pharm. Des.* **2016**, *22*, 3034–3049. [CrossRef] [PubMed]
48. Lotfy, M.; Singh, J.; Rashed, H.; Tariq, S.; Zilahi, E.; Adeghate, E. Mechanism of the beneficial and protective effects of exenatide in diabetic rats. *J. Endocrinol.* **2013**, *220*, 291–304. [CrossRef] [PubMed]
49. Chen, L.-N.; Lyu, J.; Yang, X.-F.; Ji, W.-J.; Yuan, B.-X.; Chen, M.-X.; Ma, X.; Wang, B. Liraglutide ameliorates glycometabolism and insulin resistance through the upregulation of GLUT4 in diabetic KKAY mice. *Int. J. Mol. Med.* **2013**, *32*, 892–900. [CrossRef] [PubMed]
50. Stratton, I.M.; Adler, A.I.; Neil, H.A.W.; Matthews, D.R.; Manley, S.E.; Cull, C.A.; Hadden, D.; Turner, R.C.; Holman, R.R. Association of glycaemia with macrovascular and microvascular complications of type 2 diabetes (UKPDS 35): Prospective observational study. *BMJ* **2000**, *321*, 405–412. [CrossRef] [PubMed]
51. Ostwal, A.; Mocevic, E.; Kragh, N.; Xu, W. Clinical Effectiveness of Liraglutide in Type 2 Diabetes Treatment in the Real-World Setting: A Systematic Literature Review. *Diabetes Ther.* **2016**, *7*, 411–438. [CrossRef] [PubMed]
52. Sherwani, S.I.; Khan, H.A.; Ekhzaimy, A.; Masood, A.; Sakharkar, M.K. Significance of HbA1c Test in Diagnosis and Prognosis of Diabetic Patients. *Biomark. Insights* **2016**, *11*, 95–104. [CrossRef] [PubMed]
53. Liu, Q.; Liu, S.; Gao, L.; Sun, S.; Huan, Y.; Li, C.; Wang, Y.; Guo, N.; Shen, Z. Anti-diabetic effects and mechanisms of action of a Chinese herbal medicine preparation JQ-R in vitro and in diabetic KKAY mice. *Acta Pharm. Sin. B* **2017**, *7*, 461–469. [CrossRef]
54. Angulo, P. Nonalcoholic Fatty Liver Disease. *N. Engl. J. Med.* **2002**, *346*, 1221–1231. [CrossRef]
55. Franch-Nadal, J.; Caballeria, L.; Mata-Cases, M.; Mauricio, D.; Giraldez-García, C.; Mancera, J.; Goday, A.; Mundet-Tuduri, X.; Regidor, E. For the PREDAPS Study Group Fatty liver index is a predictor of incident diabetes in patients with prediabetes: The PREDAPS study. *PLoS ONE* **2018**, *13*, e0198327. [CrossRef]

56. Fiorentino, T.V.; Andreozzi, F.; Mannino, G.C.; Pedace, E.; Perticone, M.; Sciacqua, A.; Perticone, F.; Sesti, G. One-Hour Postload Hyperglycemia Confers Higher Risk of Hepatic Steatosis to HbA1c-Defined Prediabetic Subjects. *J. Clin. Endocrinol. Metab.* **2016**, *101*, 4030–4038. [CrossRef]
57. Singh, S.P.; Pati, G.K.; Misra, B.; Kar, S.K.; Panigrahi, M.K.; Meher, C.; Agrawal, O.; Rout, N.; Pattnaik, K.; Bhuyan, P.; et al. A Study of Prevalence of Diabetes and Prediabetes in Patients of Non-Alcoholic Fatty Liver Disease and the Impact of Diabetes on Liver Histology in Coastal Eastern India. *J. Diabetes Mellit.* **2014**, *4*, 290–296. [CrossRef]
58. Liang, W.; Menke, A.L.; Driessen, A.; Koek, G.H.; Lindeman, J.H.; Stoop, R.; Havekes, L.M.; Kleemann, R.; Hoek, A.M.V.D. Establishment of a General NAFLD Scoring System for Rodent Models and Comparison to Human Liver Pathology. *PLoS ONE* **2014**, *9*, e115922. [CrossRef] [PubMed]
59. Kanehisa, M. From genomics to chemical genomics: New developments in KEGG. *Nucleic Acids Res.* **2006**, *34*, D354–D357. [CrossRef] [PubMed]
60. Bouché, C.; Serdy, S.; Kahn, C.R.; Goldfine, A.B. The Cellular Fate of Glucose and Its Relevance in Type 2 Diabetes. *Endocr. Rev.* **2004**, *25*, 807–830. [CrossRef]
61. Kitagawa, T.; Masumi, A.; Akamatsu, Y. Transforming growth factor-beta 1 stimulates glucose uptake and the expression of glucose transporter mRNA in quiescent Swiss mouse 3T3 cells. *J. Biol. Chem.* **1991**, *266*, 18066–18071. [CrossRef]
62. Schwartzberg-Bar-Yoseph, F.; Armoni, M.; Karnieli, E. The Tumor Suppressor p53 Down-Regulates Glucose Transporters GLUT1 and GLUT4 Gene Expression. *Cancer Res.* **2004**, *64*, 2627–2633. [CrossRef]
63. Shi, H.; Tzameli, I.; Bjørbaek, C.; Flier, J.S. Suppressor of Cytokine Signaling 3 Is a Physiological Regulator of Adipocyte Insulin Signaling. *J. Biol. Chem.* **2004**, *279*, 34733–34740. [CrossRef]
64. Uhlig, T.; Kyprianou, T.; Martinelli, F.G.; Oppici, C.A.; Heiligers, D.; Hills, D.; Calvo, X.R.; Verhaert, P. The emergence of peptides in the pharmaceutical business: From exploration to exploitation. *EuPA Open Proteom.* **2014**, *4*, 58–69. [CrossRef]
65. Tovi, A.; Eidelman, C.; Shushan, S.; Elster, S.; Hagi, A.; Ivchenko, A.; Butilca, G.M.; Zaoui, G.; Alterman, E.; Bar-Oz, L. High Purity Peptides. U.S. Patent PCT/US2008/002869, 12 September 2008.
66. Paradis-Bas, M.; Tulla-Puche, J.; Albericio, F. The road to the synthesis of “difficult peptides.” *Chem. Soc. Rev.* **2015**, *45*, 631–654. [CrossRef] [PubMed]
67. Werner, H.M.; Cabaltea, C.C.; Horne, W.S. Peptide Backbone Composition and Protease Susceptibility: Impact of Modification Type, Position, and Tandem Substitution. *ChemBioChem* **2016**, *17*, 712–718. [CrossRef] [PubMed]
68. Ghosh, S. Peptide therapeutics market. *Chim. Oggi-Chem. Today* **2016**, *34*, 3.
69. Lage, M.J.; Boye, K.S. The relationship between HbA1c reduction and healthcare costs among patients with type 2 diabetes: Evidence from a U.S. claims database. *Curr. Med. Res. Opin.* **2020**, *36*, 1–7. [CrossRef] [PubMed]



Article

The Azurin-Derived Peptide CT-p19LC Exhibits Membrane-Active Properties and Induces Cancer Cell Death

Ana Rita Garizo ^{1,2}, Lígia F. Coelho ^{1,2}, Sandra Pinto ^{1,2}, Tiago P. Dias ^{1,2}, Fábio Fernandes ^{1,2,3}, Nuno Bernardes ^{1,2,3} and Arsénio M. Fialho ^{1,2,3,*}

- ¹ iBB-Institute for Bioengineering and Biosciences, Biological Sciences Research Group, Instituto Superior Técnico, University of Lisbon, Av. Rovisco Pais, 1, 1049-001 Lisbon, Portugal; anagarizo@tecnico.ulisboa.pt (A.R.G.); ligiapcoelho@gmail.com (L.F.C.); sandrapinto@ist.utl.pt (S.P.); tiagompdias@tecnico.ulisboa.pt (T.P.D.); fernandesf@tecnico.ulisboa.pt (F.F.); nuno.bernardes@tecnico.ulisboa.pt (N.B.)
- ² Associate Laboratory i4HB—Institute for Health and Bioeconomy, Instituto Superior Técnico, University of Lisbon, Av. Rovisco Pais, 1, 1049-001 Lisbon, Portugal
- ³ Department of Bioengineering, Instituto Superior Técnico, University of Lisbon, Av. Rovisco Pais, 1, 1049-001 Lisbon, Portugal
- * Correspondence: afialho@tecnico.ulisboa.pt; Tel.: +351-21-8417684

Abstract: Peptides have been thoroughly studied as new therapeutic strategies for cancer treatment. In this work, we explored in vitro the anticancer potential of three novel peptides derived from the C-terminal of azurin, an anticancer bacterial protein produced by *Pseudomonas aeruginosa*. CT-p26, CT-p19 and CT-p19LC peptides were previously obtained through an in silico peptide design optimization process, CT-p19LC being the most promising as it presented higher hydrophobicity and solubility, positive total charge and, most importantly, greater propensity for anticancer activity. Therefore, in this study, through proliferation and apoptosis assays, CT-p19LC was tested in four cancer cell lines—A549, MCF-7, HeLa and HT-29—and in two non-cancer cell lines—16HBE14o- and MCF10A. Its membrane-targeting activity was further evaluated with zeta potential measurements and membrane order was assessed with the Laurdan probe. The results obtained demonstrated that CT-p19LC decreases cell viability through induction of cell death and binds to the plasma membrane of cancer cells, but not to non-cancer cells, making them less rigid. Overall, this study reveals that CT-p19LC is an auspicious selective anticancer peptide able to react with cancer cell membranes and cause effective action.

Citation: Garizo, A.R.; Coelho, L.F.; Pinto, S.; Dias, T.P.; Fernandes, F.; Bernardes, N.; Fialho, A.M. The Azurin-Derived Peptide CT-p19LC Exhibits Membrane-Active Properties and Induces Cancer Cell Death. *Biomedicines* **2021**, *9*, 1194. <https://doi.org/10.3390/biomedicines9091194>

Academic Editor: Leonardo Caputo

Received: 11 August 2021

Accepted: 6 September 2021

Published: 10 September 2021

Publisher's Note: MDPI stays neutral with regard to jurisdictional claims in published maps and institutional affiliations.



Copyright: © 2021 by the authors. Licensee MDPI, Basel, Switzerland. This article is an open access article distributed under the terms and conditions of the Creative Commons Attribution (CC BY) license (<https://creativecommons.org/licenses/by/4.0/>).

Keywords: anticancer peptide; azurin; peptide-based drug development; cytotoxic effect; membrane-based anticancer therapy

1. Introduction

The use of membranolytic anticancer peptides (ACPs) has become a potential strategy for the development of new cancer therapies [1]. ACPs (<10 kDa), either from eukaryotes or of bacterial origin, are small linear or cyclic molecules (5–50 amino acids), rich in cationic and hydrophobic amino acids that give them an overall positive charge (at pH 7) and an amphipathic behavior. These peptides can adopt α -helix or β -pleated sheet configurations, but random coil structures have also been described in the literature [2].

There are two different classifications for ACPs considering their selectivity properties. The first is the ACP_T class, which includes non-selective peptides with identical activities against several cell types, such as mammalian, bacterial and cancer cells [3,4]. The second category, named ACP_{AO}, corresponds to those that selectively target bacterial and cancer cells while showing residual activity against normal cells. The reason for this behavior is not fully clear yet but the differences at the membrane level between normal and cancer cells may explain, at least in part, this selectivity. In fact, the plasma membrane of cancer

cells is characterized as having some unique features, from which a larger surface area, a net negative charge and an abnormal fluidity stand out. This may be due to a high number of microvilli, with the negative charge in the outer layer resulting from the abnormal presence of anionic phospholipid phosphatidylserine, O-glycosylated mucins, sialylated gangliosides and heparin sulfate [3–6].

The mechanism of action for ACPs leads to the irreparable disruption of the plasma membrane of tumor cells [7] through pore formation, followed by cell lysis (direct-acting mechanism) [8,9]. Both the structure they adopt when in contact with the plasma membrane of these cells as well as their intrinsic characteristics mean that these peptides are capable of associating with this cellular barrier mainly through electrostatic interactions [4,10]. Apart from the plasma membrane, other internal membranes may be targeted by the membranolytic effects of ACPs, such as the mitochondrial membrane, where their effects can trigger apoptosis (indirect-acting mechanism) [8,11].

The development of cancer therapies with the use of ACPs presents advantages for clinical applications compared to conventional chemotherapy. In particular, ACPs act both in metabolically active tumor cells and in slow-growing or multidrug-resistant cancer cells [12]. Additionally, ACPs have a relatively high tissue penetration, the cost for producing them is low and they can be easily modified by solid-phase synthesis technology [13].

Currently, the database of the National Library of Medicine (NLM) at the National Institutes of Health (NIH) in the PubMed.gov platform displays a total of 463 clinical trials with the application of ACPs in several types of cancer, being the most common studies in melanomas, breast and lung cancer [9,14]. As examples, LTX-3158, a human lactoferrin-derived oncolytic peptide, is currently in a phase I clinical trial and bryostatin 1, a peptide within the bryostatin family composed of marine natural products, is at phase II [15,16]. In addition to them, there is p28, a cell-penetrating peptide derived from the anticancer protein azurin (14 kDa) produced by the bacterium *Pseudomonas aeruginosa* [17]. This peptide has already completed two phase I clinical trials in cancer patients [18,19] and received approval as an orphan drug by the Food and Drug Administration (FDA) [20]. Overall, these studies show promising results for the treatment of cancer with ACPs not only as sole drugs but also in combination with other therapeutic approaches [21].

The aim of this study was to evaluate the anticancer potential of new peptides derived from azurin. Evidence from our previous work and from others suggests that azurin may therapeutically act on cancer cell membranes through a lipid raft/*caveolae*-mediated pathway [22–24]. By specifically targeting such plasma membrane microdomain sites, azurin promotes a multivalent action accelerating the endocytosis of receptors and the disruption of signaling pathways hyperactivated in cancer cells [25,26]. In addition, it is known that p28, derived from this protein, is a protein transduction domain (PTD), in part responsible for mediating the entrance of azurin into cells, and it also has anticancer properties [25,27]. Beyond this, it has become clear that the anticancer activity exerted by azurin depends on other domains (azurin C-terminal 88–128 amino acids) besides the p28 domain (azurin 50–77 amino acids). In fact, the C-terminal peptide has anticancer activity through its binding with the cell surface EphB2 receptor and interfering in cancer growth promotion, which has been explored to design peptides to improve radiotherapy efficacy in lung cancer [28,29]. On the other hand, the phenylalanine residue at position 114 was found to be critical for azurin uptake by cancer cells [30]. Based on this, in a previous study, our group used a region of 26 amino acid residues of azurin close to its C-terminal (CT-p26 peptide) as a template for the discovery of new bioactive peptides against cancer cells. Bioinformatics tools used in peptide design studies have enabled the assessment of the bioactivity of this native peptide. First, by reducing its length, and then by changing some residues in its amino acid sequence, it was possible to improve the parameters for solubility, hydrophobicity, overall charge and anticancer potential, giving rise to two new peptides, CT-p19 (shorter than CT-p26) and CT-p19LC (three amino acid residues altered compared to CT-p19) [31]. In the present work, we evaluated in vitro the anticancer activity

of these peptides and compared it with the anticancer activity of full-length azurin and its derived native peptides.

2. Materials and Methods

2.1. Azurin-Derived Peptides

The four azurin-derived peptides used, namely p28, CT-p26, CT-p19 and CT-p19LC, were chemically synthesized by Pepmic Co., Ltd., Suzhou, China, with a minimal purity of 95.0%. CT-p19 and CT-p19LC peptides labeled with 5,6-FAM were commercially synthesized by CASLO ApS, Kongens Lyngby, Denmark. Lyophilized samples of the peptides were resuspended in 10 mM sodium phosphate buffer (pH 7.4) or in phosphate buffer saline (PBS; pH 7.4), divided into aliquots and stored at $-20\text{ }^{\circ}\text{C}$.

2.2. Circular Dichroism Spectroscopy

The secondary structure of the CT-p19LC peptide was analyzed through spectroscopic analysis. UV-visible and far-UV circular dichroism (CD) spectra were traced. UV-visible spectra between 250 and 800 nm were obtained using a PharmaSpec UV-1700 (Shimadzu, Kyoto, Japan) UV-visible spectrophotometer. Far-UV CD spectra were traced using a PI*-180 spectropolarimeter from Applied Photophysics using default parameters. Ten measurements were made with an integration time of 1 sec, a cuvette path length of 10 mm, a wavelength ranged of 190 to 250 nm and a step size of 1 nm. The obtained spectra were analyzed using the online DICHROWEB server (<http://dichroweb.cryst.bbk.ac.uk/html/home.shtml>, accessed on 1 July 2019) to predict the secondary structure of the peptide [32].

2.3. Human Cancer Cell Lines and Cell Culture Conditions

The A549 (lung), MCF-7 (breast), HeLa (cervix) and HT-29 (colorectal) human cancer cell lines (European Collection of Authenticated Cell Cultures (ECACC), Public Health England, Salisbury, United Kingdom), the 16HBE14o- human bronchial cell line [33] and the MCF10A human mammary gland cell line (American Type Culture Collection (ATCC), Manassas, VA, United States) were used. The cancer cells were seeded and maintained in Dulbecco's Modified Eagle Medium (DMEM; Gibco[®] by Life Technologies, Carlsbad, CA, United States). The medium was supplemented with 10% heat-inactivated fetal bovine serum (FBS; Gibco[®] by Life Technologies, Carlsbad, CA, United States), 100 IU/mL penicillin and 100 mg/mL streptomycin (Pen-Strep, Invitrogen, Waltham, MA, United States). The 16HBE14o- cells were grown in MEM medium without earls' salts and supplemented with 10% FBS, 1% L-glutamine and 10,000 U/mL penicillin and 10,000 mcg/mL streptomycin (PenStrep, Invitrogen, Waltham, MA, United States). The MCF10A cells were cultured in 50% DMEM/50% F12 nutrient mix, supplemented with 5% equine serum, EGF (20 ng/mL), insulin (10 $\mu\text{g}/\text{mL}$), hydrocortisone (0.5 $\mu\text{g}/\text{mL}$), cholera toxin (100 ng/mL) and 10,000 U/mL penicillin and 10,000 mcg/mL streptomycin (PenStrep, Invitrogen, Waltham, MA, United States). The culture conditions for all cell lines were $37\text{ }^{\circ}\text{C}$ in a humidified chamber containing 5% CO_2 (binder CO_2 incubator C150, Keison products, Chelmsford, United Kingdom).

2.4. MTT Cell Proliferation Assays

Cell proliferation after treatment with the peptides was measured by MTT (3-(4,5 dimethylthiazol-2-yl)-2,5 tetrazolium bromide) assay. The A549, MCF-7, HeLa and HT-29 human cancer cells were seeded in 96-well plates at a density of 10^4 cells/well (three replicates) and were left to adhere and grow overnight in a CO_2 incubator (5%) at $37\text{ }^{\circ}\text{C}$. The 16HBE14o- and MCF10A cells were seeded at densities of 7.5×10^4 and 4.5×10^4 cells/well (three replicates), respectively, and left to adhere and grow overnight in the same conditions. The next day, the medium was collected and the cells were treated with the peptides (concentrations from 0 μM to 100 μM). Proliferation was determined after 48 h. Following the incubation period, 20 μL of MTT (5 mg/mL) was added to

each well and incubated at 37 °C for 3.5 h. The reaction was stopped with the addition of 150 µL of a solution of 40 mM HCL in isopropanol. The MTT formazan formed was spectrophotometrically read at 590 nm in a microplate reader (SpectroStarNano, BMG LABTECH, Aylesbury, United Kingdom). Untreated cells were used as controls (0% of viability decrease) to determine the relative cell viability of treated cells.

2.5. LDH Release Assays

The Invitrogen™ CyQUANT™ LDH Cytotoxicity Assay Kit (Invitrogen, Waltham, MA, United States) was used to determine the LDH release of non-cancer cells treated with CT-p19LC, according to the manufacturer's instructions. Briefly, 16HBE14o- and MCF10A cells were seeded at densities of 7.5×10^4 and 4.5×10^4 cells/well (three replicates), respectively, and left to adhere and grow overnight in the same conditions. The next day, the medium was collected and the cells were treated with the peptides (100 µM). After 48 h, the medium was collected and analyzed. Untreated cells were used as controls to compare the spontaneous LDH release and to normalize the data. Additional controls used were the maximum LDH activity release by lysing the cells with the lysis buffer provided in the kit, as well as the LDH positive control.

2.6. Quantitative Cellular Interaction

In order to evaluate the cell-peptide interaction, A549, MCF-7, HeLa and HT-29 cell lines were plated in 6-well plates with 5×10^5 cells/well, respectively, and left to adhere and grow overnight in a CO₂ incubator (5%) at 37 °C. The following day, the medium was removed, and the cells were washed twice with PBS and treated with 5 µM of CT-p19 and CT-p19LC labeled with 5,6-FAM over 2 h at 37 °C. After treatment, cells were washed twice with PBS, detached with TrypLE™ Express (Gibco® by Life Technologies, Carlsbad, CA, United States) at 37 °C and resuspended in medium. Then, cells were collected by centrifugation at 1200 rpm over 3 min, washed once with PBS and re-dispersed in 350 µL of PBS for cytometry analysis.

The quantification of the peptides' interaction with the cells was done using a BD Accuri™ C6 Plus Flow Cytometer (BD Biosciences, Devon, England), where peptides were detected through the fluorescein isothiocyanate (FITC) channel (FL1 detector, 533/563 nm; laser configuration of 3-blue 1-red, 640 nm laser). Measurements were carried out in triplicate and 20,000–50,000 events were acquired in the gated region of the forward-scatter/side-scatter plot per sample. A control based only on cells without treatment was also performed to exclude the possible cellular autofluorescence. The results were analyzed using the software FlowJo v10 by gating out cellular debris and doublets and expressed as the geometric mean fluorescence intensity (Geo MFI).

2.7. CT-p19LC Cellular Uptake

In order to characterize the cellular uptake of CT-p19LC, cells were cultured on µ-Slide 8-well glass-bottom chambers (ibidi®, Munich, Bavaria, Germany) with 5×10^4 cells/well and left to adhere overnight before being treated with 5 µM of CT-p19LC-5,6-FAM peptide for 2 h. After this time, the medium was collected and the cells were washed twice with phosphate buffer saline (PBS) pH 7.4. Then, Alexa Fluor® 633 WGA (Invitrogen™, Waltham, MA, United States; 1:200) and Hoechst 33342 (Invitrogen™, Waltham, MA, United States; 1:500) were added to stain the plasma membrane and the nucleus, respectively, followed by 15 min of incubation. Finally, the samples were observed on a Leica TCS SP5 (Leica Microsystems CMS GmbH, Mannheim, Germany) inverted confocal microscope (model DMI6000) with a 63.3× water-immersion (1.2-numerical-aperture) apochromatic objective [34].

2.8. Apoptosis Assay

The FITC-Annexin V Apoptosis Detection Kit I (BD Pharmingen™, BD Biosciences, Devon, England) was used to study the apoptosis of cancer cell lines and non-cancer cell

lines under study after treatment with CT-p19LC peptide. Briefly, A549, MCF-7, HeLa, HT-29 and the 16HBE14o- and MCF10A cell lines were plated in 6-well plates with 5×10^5 and 7.5×10^5 cells/well, respectively, and left to adhere and grow overnight in a CO₂ incubator (5%) at 37 °C. The following day, the medium was removed and the cells were washed once with PBS pH 7.4 and treated with 20 µM of CT-p19LC over 48 h at 37 °C. After treatment, the cells were washed twice with PBS pH 7.4, detached with Accutase® (Merck KGaA, Darmstadt, Germany) at 37 °C and resuspended in cell culture medium. After that, 1×10^5 cell/mL was collected and centrifuged at 1200 rpm for 3 min. The supernatant was discarded, and cells were resuspended in 100 µL of 1X annexin V binding buffer. Then, FITC-annexin and PI (5 µL each) were added, and the cells were incubated at room temperature in the dark for 15 min. Finally, 400 µL of 1X annexin V binding buffer was added, and cells were analyzed on a BD Accuri™ C6 Plus Flow Cytometer (BD Biosciences, Devon, England). Untreated cells were used as a control. Cell death induction was considered by adding quadrant 2 (Q2) to quadrant 4 (Q4). At least 20,000 events were acquired and analyzed per sample.

2.9. Zeta Potential Measurements of Live A549, MCF-7, HeLa and HT-29 Cancer Cells and 16HBE14o- and MCF10A Non-Cancer Cells in the Presence of CT-p19LC

Zeta potential measurements through laser Doppler anemometry (LDA) were performed to assess the surface charge density of cancer and non-cancer cells and the electrostatic attraction of CT-p19LC toward them. For this, cells were diluted to 1×10^5 cells/mL in DMEM and washed with PBS pH 7.4 twice (1200 rpm; 5 min). Then, cellular suspensions were incubated with different peptide concentrations (5, 10 and 20 µM) in serum-free medium for 30 min at 37 °C and dispensed into disposable zeta cells with gold electrodes. A set of 10 measurements (≈ 40 runs each) were performed at 37 °C with a voltage of 48 V (Malvern Instruments Ltd., Worcestershire, United Kingdom). Control values were obtained by measuring the surface charge of each cellular suspension in the absence of CT-p19LC (0 µM, untreated condition).

2.10. GP Determination for Membrane Order Evaluation

The membrane order evaluation of the A549, MCF-7, HeLa and HT-29 human cancer cell lines after CT-p19LC treatment was investigated with the probe Laurdan using two-photon excitation microscopy. Cells were treated for 2 h with 20 µM of CT-p19LC after seeding with 5×10^4 cells on µ-Slide 8-well glass-bottom chambers (ibidi®, Munich, Bavaria, Germany). Subsequently, two washing steps with PBS pH 7.4 were performed followed by incubation at 37 °C for 15 min with medium containing 5 µM of Laurdan [35]. Untreated cells were used as controls. Following incubation, samples were examined on a Leica TCS SP5 inverted confocal microscope (model DMI6000) with a 63.3× water-immersion (1.2-numerical-aperture) apochromatic objective. Fluorescence microscopy data was obtained by using a titanium-sapphire laser as the excitation light source (the wavelength was set to 780 nm and the fluorescence emission was collected at 400–460 nm and 470–550 nm to calculate the GP images). Fluorescence imaging data was processed through homemade software based on a MATLAB environment, with the GP value defined as $GP = (I_{400-460} - G \cdot I_{470-530}) / (I_{400-460} + G \cdot I_{470-530})$. The parameter G was a calibration factor calculated from imaging Laurdan in DMSO (GP = 0.01 in this solvent) using the same experimental conditions.

2.11. Statistical Analysis




Statistical analysis was performed using GraphPad Prism 8.0.1 (GraphPad Software Inc., San Diego, CA, USA). Statistical significance of the difference between two groups was evaluated by with Student's *t*-test. Differences between groups were compared using one-way analysis of variance (ANOVA) and Tukey's multiple comparisons test. Results are expressed as means \pm standard deviation (SD) and geometric means with 95% confidence intervals.

3. Results and Discussion

3.1. CT-p26 Peptide Effect on Cell Viability Confirms the Anticancer Potential of C-Terminal Azurin

The CT-p26 peptide comprises amino acid residues 95 to 120, close to the C-terminal region of the bacterial protein azurin (Table 1), which is known to contribute to its anticancer activity as well as to its ability to enter cancer cells [28–30].

Table 1. Overview of the characteristics of azurin and its derived peptides.

PROTEIN/ PEPTIDE	STRUCTURE	AMINO ACID SEQUENCE	AZURIN POSITION	HYDROPHOBICITY	CHARGE	ISOELECTRIC POINT	WATER SOLUBILITY	SMV SCORE	VIABILITY DECREASE AFTER 100 μ M OF PROTEIN/ PEPTIDE TREATMENT	REFERENCES
Azurin		128 aa	n.a.	n.a.	n.a.	n.a.	n.a.	n.a.	20–40%	[30]
p28		LSTAADMQGVVTDG- MASGLDKDYLPDD	50–77 aa	n.a.	n.a.	n.a.	n.a.	n.a.	0–25%	[21]
CT-p26		VTFDVSKLKEGEQYMFF- CTFPGHSAL	95–120 aa	−0.03	−0.5	5.3	Poor	0.76	n.a.	[31]
CT-p19	n.a.	VSKLKEGEQYMFFCTFPGH	99–117 aa	−0.08	0.5	7.0	Poor	0.90	n.a.	[31]
CT-p19LC	n.a.	VSKLRKGEKYMFFCTFPGH	n.a.	−0.16	3.5	10.0	Good	0.99	n.a.	[31]

SMV: Support vector machine score; aa: amino acids; n.a.: not applicable

Taking this into account, MTT cell proliferation assays were performed to evaluate the effect of this peptide on A549 lung and MCF-7 breast cancer cell lines. Parallel assays, under the same conditions, have also been carried out with the p28 peptide, also derived from azurin and mentioned previously for its anticancer properties [17,21,25]. These assays were performed with increasing concentrations of both peptides, from 0 to 100 μ M. As shown in Figure 1, the two peptides exhibited cytotoxic activity against both cancer cell lines, and a dose–response effect is evident in the A549 lung cancer cell line. Moreover, treatment with CT-p26 leads to a higher decrease in cell viability than treatment with p28: by about two- to seven-fold in the case of A549 cells and one- to four-fold in the case of MCF-7 cells. These results confirmed that the C-terminal region of the azurin protein can be used as an anticancer functional peptide, thereby making it an interesting lead peptide.

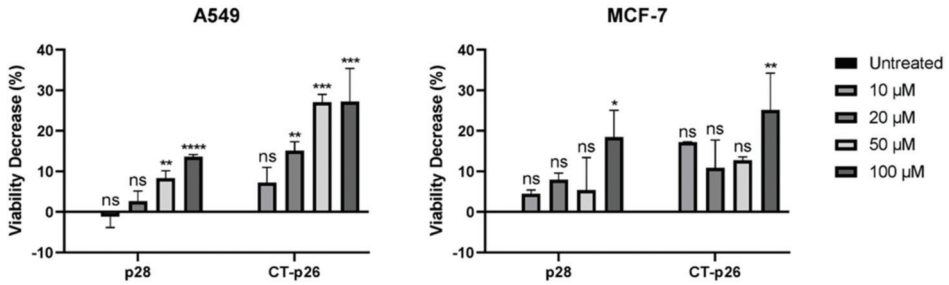


Figure 1. Comparison of cell viability after treatment with p28 and CT-p26 peptides (0 to 100 μ M) in A549 (lung) and MCF-7 (breast) cancer cells incubated over 48 h. Untreated condition (control) consisted of cells incubated with medium only. Values represent the means \pm SD, and each condition had at least $n = 3$. *, **, ***, **** and ns denote significant differences of $p < 0.1$, $p < 0.01$, $p < 0.001$ and $p < 0.0001$ and differences that were not statistically significant, respectively, when comparing control with treatments.

3.2. CT-p19 Peptide Decreases Cancer Cell Viability and Has Selective Property

The *in silico* study previously performed by our group made it possible to design a new peptide with a shorter length, and with a higher propensity to demonstrate anticancer activity, from the C-terminal peptide (support vector machine (SVM) score: 0.76 vs. 0.90; Table 1) [31]. This parameter and the possible selectivity of this peptide, as seen in azurin and the other peptides derived therefrom [25,36], were evaluated through an MTT cell proliferation assay on the cancer cell lines under study and on two matching-tissue non-cancer cell lines, 16HBE14o- and MCF10A (Figure 2). After treatment with 10, 20, 50 and 100 μ M of CT-p19, decreases in cell viability of 10%, 14%, 22% and 28% were observed in the case of the A549 cancer cell line. The same concentrations of CT-p19 induced decreases of 9%, 9%, 30% and 27% on the viability of MCF-7 cells. Regarding non-cancer cell lines, the viability decrease did not exceed 3% in 16HBE14o- and 8% in MCF10A. Thus, the results showed that the CT-p19 peptide is able to decrease the viability of cancer cells but not of non-cancer cells, which demonstrates that this peptide has the desired selectivity. These results provided a smaller version of the CT-p26 peptide while maintaining its anticancer activity.

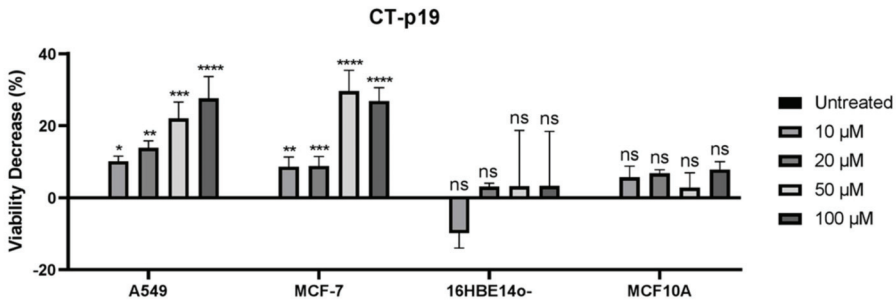


Figure 2. Viability decrease (100% of proliferation in untreated condition—% of proliferation for each treatment condition) of A549 (lung) and MCF-7 (breast) cancer cells and 16HBE14o- (bronchial) and MCF10A (mammary gland) non-cancer cells when incubated with different concentrations of CT-p19 peptide (0 to 100 μ M) over 48 h. Untreated condition (control) consisted of cells incubated with medium only. Values represent the means \pm SD, and each condition had at least $n = 3$. *, **, ***, **** and ns denote significant differences of $p < 0.1$, $p < 0.01$, $p < 0.001$ and $p < 0.0001$ and differences that were not statistically significant, respectively, when comparing control with treatments.

3.3. The Newly Designed CT-p19LC Peptide Reduces Proliferation and Induces Cell Death in Cancer Cell Lines

After the development of CT-p19 in silico, our group re-designed a new peptide based on single substitutions of amino acid residues that made it possible to not only increase the SMV score to 0.99 but also improve its solubility (Table 1). Thus, this new peptide, designated CT-p19LC, contained 19 amino acids (VSKLRKGEKYMFFCTPFGH) and represented an iterative peptide optimization from a region close to the C-terminal of the anticancer protein azurin. It had a molecular weight of 2275.7 g/mol (2.3 kDa), a pI of pH 10 and a net charge of +3.5 at pH 7 (Table 1) [31].

In this work, circular dichroism (CD) spectral measurements (Figure 3A) indicated that the peptide adopted a randomly coiled structure in solution.

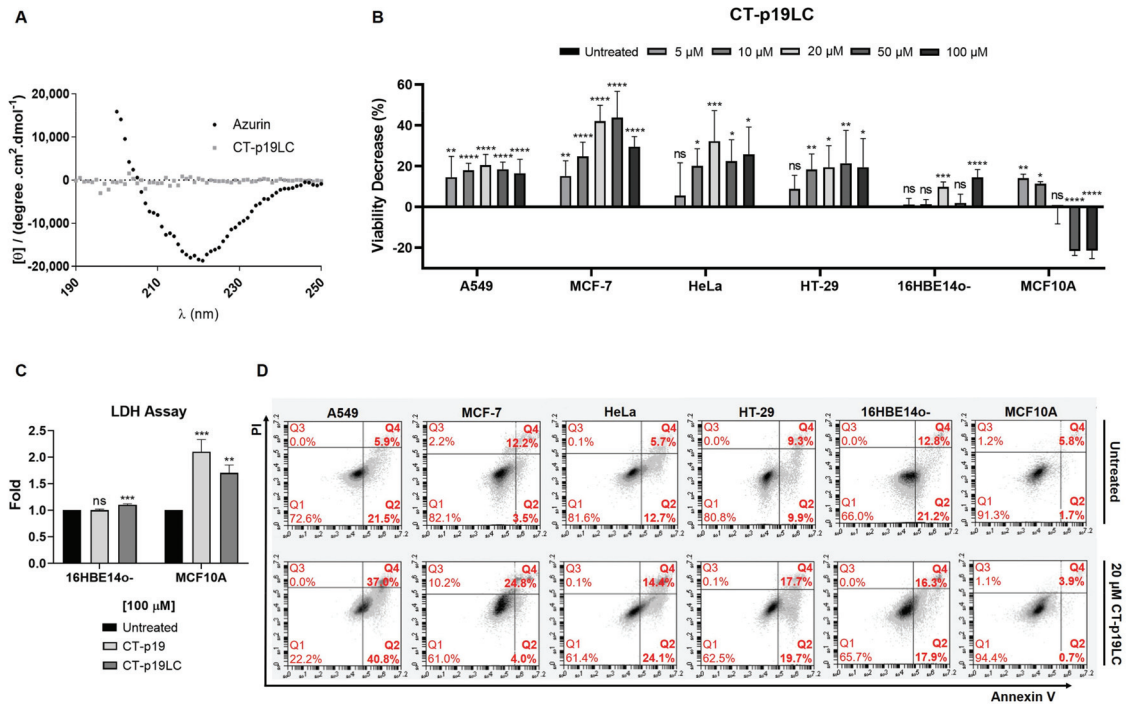


Figure 3. Cytotoxic effect of newly designed CT-p19LC peptide: (A) circular dichroism spectra of azurin and CT-p19LC (5 μM) in sodium phosphate buffer 10 mM, pH 7.4, at 25 °C; (B) viability decrease (100% of proliferation in untreated condition—% of proliferation for each treatment condition) of A549 (lung), MCF-7 (breast), HeLa (cervix) and HT-29 (colorectal) cancer cells and 16HBE14o- (bronchial) and MCF10A (mammary gland) non-cancer cells when incubated with different concentrations of CT-p19LC peptide (0 to 100 μM) over 48 h. Untreated condition (control) consisted of cells incubated with medium only. Values represent the means ± SD, and each condition had at least n = 3. *, **, ***, **** and ns denote significant differences of $p < 0.1$, $p < 0.01$, $p < 0.001$ and $p < 0.0001$ and differences that were not statistically significant, respectively, when comparing control with treatments; (C) LDH assay in non-cancer cell lines treated with 100 μM of CT-p19 and CT-p19LC. Values represent the means ± SD (n = 3). **, *** and ns denote significant differences of $p < 0.01$ and $p < 0.001$ and differences that were not statistically significant, respectively, when comparing treatments with control; (D) apoptosis assay in cancer and non-cancer cells treated with 20 μM of CT-p19LC for 48 h, assessed by flow cytometry. Representative figures showing a population of viable cells in the left lower quadrant (Q1; annexin V − /PI −), early apoptotic cells in the right lower quadrant (Q2; annexin V + /PI −), necrotic cells in the left upper quadrant (Q3; annexin V − /PI +) and advanced apoptotic or necrotic cells in the right upper quadrant (Q4; annexin V + /PI +).

To evaluate the anticancer potential of the CT-p19LC peptide, MTT cell proliferation and apoptosis assays were carried out. For this, the spectrum of cell lines used was expanded by adding the HeLa (cervix) and HT-29 (colorectal) cancer cell lines to the A549 (lung) and MCF-7 (breast) cancer cells, and the 16HBE14o- (bronchial) and MCF10A (mammary gland) non-cancer cell lines.

First, the MTT cell proliferation assays were performed with increasing doses of CT-p19LC (0 to 100 μM ; Figure 3B). Comparing it with the CT-p19 treatment that led to a dose–response effect on the lung and breast cancer cell lines (Figure 2), this same effect was only observed at the lowest concentrations of 5, 10 and 20 μM in the case of the CT-p19LC treatment. At higher concentrations of 50 and 100 μM , a stabilization of the decrease in viability was observed. However, we observed that for the concentration of 20 μM of CT-p19LC, the values for the decrease in viability were similar to those obtained with higher concentrations of CT-p19. These results confirmed the anticancer potential predicted *in silico* for CT-p19LC (0.90 vs. 0.99 SMV score; Table 1). The CT-p19LC treatment in the cervix and colorectal cancer cell lines demonstrated that this peptide can exert its anticancer action on a wide spectrum of cancer lines, since a decrease in cell viability of 20–30% was observed (Figure 3B). It is interesting to note that the values of the decrease in viability for the concentration of 20 μM of CT-p19LC in all cancer cell lines were around 20–40%, and to achieve the same decrease with the azurin (Table 1) or p28 peptide treatment (Figure 1), 100 μM would be needed. Furthermore, it was also found that CT-p19LC does not have a cytotoxic effect on the non-cancer cell lines under study (in all concentrations tested, less than a 14% decrease in viability was observed; Figure 3B), which indicates that this peptide also demonstrates selectivity for cancer cells, an important and desired characteristic in the development of new anticancer compounds. The non-toxic effect on non-cancer cells was also supported by the low levels of spontaneous LDH release in cells treated with 100 μM of peptide, in particular for CT-p19LC (Figure 3C).

Second, the apoptosis assays supported the MTT cell proliferation assays. Treating cancer cells with a single dose of CT-p19LC at 20 μM strongly promoted cell death. This concentration was chosen as it corresponded to the maximum anticancer potential, since higher concentrations had no additional impact on cell viability. In A549 cells, there was induction of cell death in 77.8% of the cells, in MCF-7 in 28.8%, in HeLa in 38.5% and in HT-29 in 37.4%, which were comparable to the values in their controls (untreated condition) of 27.4%, 15.7%, 18.4% and 19.2%, respectively (Figure 3D). Importantly, the same was not observed in non-cancer cell lines, since in 16HBE14o- (34.0% control condition vs. 34.2% treatment condition) and MCF10A (7.5% control condition vs. 4.6% treatment condition), cell death was similar to the control condition (untreated), again demonstrating the selectivity of this peptide (Figure 3D). Overall, these results indicate that CT-p19LC induces a decrease in cell viability in part through the induction of cell death.

3.4. CT-p19LC Peptide Targets Cellular Plasma Membrane

It is known that the plasma membrane of cancer cells is more anionic at their surface than for non-cancer cells due to its constitution based on negatively charged components [3–5]. In addition, one of the mechanisms by which it has been proposed that there is an electrostatic attraction of ACPs towards this cellular barrier of cancer cells is related to the positive charge of these peptides [4,10]. In the case of the CT-p19LC peptide, the *in silico* approach established a charge of +3.5 at pH 7 (Table 1) [31]. Therefore, we evaluated the capacity of CT-p19 and CT-p19LC to associate to the cancer cell lines using flow cytometry. Cells were treated with 5,6-FAM labeled peptides (5 μM) and left to interact with the cells for 2 h. A stronger association of CT-p19LC was observed for all cell lines compared to CT-p19, which may have contributed to its higher anticancer activity (Figure 4A). We then proceeded to analyze the cellular distribution of this peptide in both cancer and non-cancer cells using fluorescence confocal microscopy (Figure 4B). The peptide was detected both in the plasma membrane and intracellularly distributed, suggesting its capacity to pene-

trate the plasma membrane and even reach the nucleus, but only in cancer cells. In the non-cancer cell line MCF10A, almost no peptide was detected.

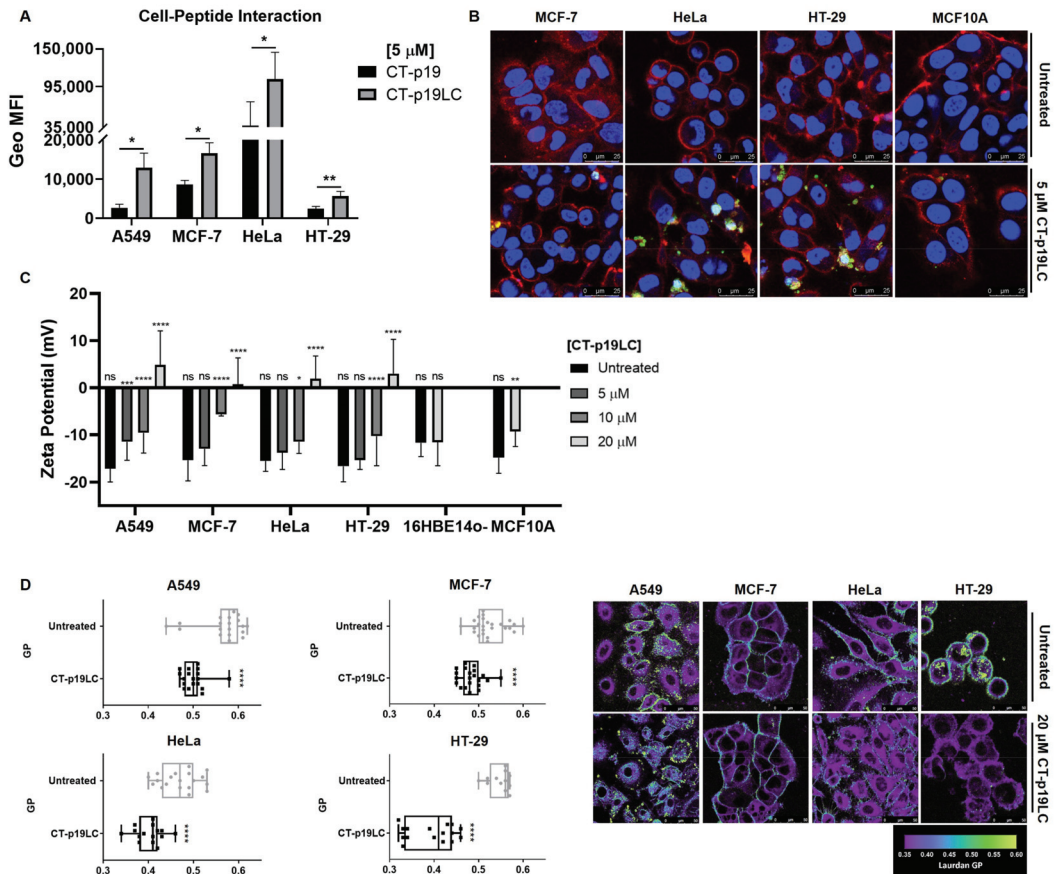


Figure 4. CT-p19LC membrane-active properties: (A) flow cytometry quantitative analysis of cancer cell–peptides interaction. Results are reported as the means \pm SD, and each condition had at least $n = 3$. * and ** denote significant differences of $p < 0.1$ and $p < 0.01$, respectively, when comparing CT-p19LC treatment with CT-p19 treatment; (B) representative confocal microscopy qualitative analysis of CT-p19LC cellular uptake by MCF-7, HeLa and HT-29 cancer cells and MCF10A non-cancer cells incubated with PBS pH 7.4 as control and 5 μ M of peptide labeled with 5,6-FAM (green color) for 2 h. WGA Alexa Fluor® 633 and Hoechst 33342, for staining the plasma membrane and nucleus, respectively, are shown in red and blue colors. Scale bars represent 25 μ m; (C) zeta potential of A549, MCF-7, HeLa and HT-29 cancer cells and 16HBE14o- and MCF10A non-cancer cells in the presence of CT-p19LC peptide. A total of 1.5×10^5 cells/mL were incubated and stabilized for 30 min at 37 °C with different peptide concentrations, and the zeta potential was measured. Data are represented as means \pm SD. *, **, ***, **** and ns denote significant differences of $p < 0.1$, $p < 0.01$, $p < 0.001$ and $p < 0.0001$ and differences that were not statistically significant, respectively, when comparing the untreated condition (0 μ M) with increasing concentrations of CT-p19LC (5, 10 and 20 μ M); (D) the effects of CT-p19LC on the cell’s membrane order for A549, MCF-7, HT-29 and HeLa cancer cell lines and their respective GP values. All represented cell lines were seeded on μ -Slide 8-well glass-bottom chambers and treated with 20 μ M of CT-p19LC for 2 h. For each condition, 5 μ M of Laurdan was used. Untreated cells were used as the control. Homemade software built in a MATLAB environment was used to measure the GP values. Representative Laurdan GP images are shown. Scale bars represent 50 μ m. Average GP values are expressed as means \pm SD from at least 15 individual cells in each condition. Results are compared to the untreated population with equal variance (****, $p < 0.0001$).

We also evaluated the zeta potential of the live non-cancer and cancer cell lines under study in the presence of increasing concentrations of CT-p19LC peptide (0 to 20 μM). The measurements of the zeta potential allowed the assessment of the electrostatic potential that is triggered after a particle with a certain charge is placed in solution with others [37]. This concept can be applied to evaluate the interaction of peptides with cell membranes, which results in the alteration of the cell surface electropotential [38]. As the concentration of CT-p19LC exposed to cancer cells increased, an increase in the zeta potential was obtained in all cancer cell lines, with this potential reaching positive values for the highest concentration of the peptide (Figure 4C).

After treatment with 20 μM of CT-p19LC, the potential of the lung cancer cell line increased from -17.2 ± 2.8 mV to 4.8 ± 7.3 mV; in the case of the breast cancer cell line, it increased from -15.4 ± 4.4 mV to 0.8 ± 5.5 mV; in the cervix cancer cell line, it increased from -15.5 ± 2.2 mV to 1.9 ± 4.8 mV; and, finally, in the colorectal cancer cell line, it increased from -16.6 ± 3.3 mV to 3.0 ± 7.3 mV. These results indicate that this peptide targets the plasma membrane of cancer cells. In the case of the non-cancer cell lines, at the highest concentration used (20 μM), it was found that the potential remained negative and close to the value obtained in the untreated condition (Figure 4C). For 16HBE14o-, before treatment the zeta potential was -11.7 ± 2.9 mV, and it did not change with the treatment (-11.6 ± 4.9 mV). In the case of MCF10A, before treatment the zeta potential was -14.8 ± 3.3 mV, and after treatment it increased only moderately to -9.3 ± 3.2 mV, remaining more negative than that obtained in the same concentration of peptide in cancer cells. Thus, these results show that the CT-p19LC peptide directs itself towards the cancer cell membranes much more strongly than towards non-cancer cell membranes.

To further characterize the effect on the membranes of cancer cells, the membrane order of the plasma membranes subjected to treatment with the CT-p19LC peptide was investigated with the Laurdan probe using two-photon excitation microscopy. To do this, the cancer cells (A549, MCF-7, HT-29 and HeLa) were treated over 2 h with CT-p19LC at 20 μM . To quantify the degree of lipid packing (the measured mean of the GP value) in both conditions (untreated and treated cancer cells), homemade software created in a MATLAB environment was used. The GP value varies between -1 and 1 ; a GP value higher than 0.5 indicates the existence of very compact and ordered membranes. In contrast, a GP value lower than 0.5 is typically observed for more fluid membranes [35,39]. As shown in Figure 4D, for the four cancer cell lines the GP values decreased after CT-p19LC treatment, making the cell membranes more fluid (A549: 0.57 to 0.50 ; MCF-7: 0.53 to 0.48 ; HeLa: 0.47 to 0.40 ; HT-29: 0.55 to 0.39). This common pattern indicates that the CT-p19LC peptide acts efficiently at the plasma-membrane level. Fluorescence microscopy images of the cells showed that treated cells suffered a variety of morphological modifications; i.e., the cell shape became irregular and the fragmentation of the plasmatic membrane and the nucleus was visible (Figure 4D).

In general, these results indicate that the CT-p19LC peptide engaged with the plasma membrane, which could trigger the apoptotic events. However, it remains to clarify the possible membrane components that could be targets of CT-p19LC. Further studies with biophysical approaches such as atomic force microscopy (AFM) or leakage studies using model membranes (liposomes) are necessary to unravel the mode of action of this peptide against cancer cells.

4. Conclusions

The CT-p19LC anticancer potential explored in this work reinforces the relevance of studies in other domains of azurin that contain anticancer properties of their own. In an initial approach, a region of the C-terminal domain of azurin, which was studied in the form of a peptide with 26 residues, CT-p26, was shown to have a similar anticancer potential to the p28 peptide and azurin. From here, the *in silico* redesign of this region made it possible to decrease the length of its peptide chain and increase its anticancer potential, as well as its selectivity for cancer cells through changes in hydrophobicity and net charge, giving

rise to a new peptide called CT-p19LC. The results of this work suggest that the CT-p19LC application induced a decrease in the cell viability, in part through the triggering of cell death, in all the cancer cell lines under study, without affecting the non-cancer cell lines. In addition to this, it was also demonstrated that this peptide selectively binds to the plasma membranes of cancer cells, since its electrostatic potential is altered, and changes occur at the level of lipid packing. All in all, this study characterizes CT-p19LC as a synthetic ACP with improved and selective anticancer potential and with membrane-active properties.

Author Contributions: N.B. and A.M.F. conceived, designed and supervised the experiments; A.R.G., L.F.C. and N.B. performed the experiments and analyzed the data; S.P., T.P.D. and F.F. contributed reagents/materials/analysis tools in confocal and two-photon microscopy experiments; writing—original draft preparation, A.R.G. and L.F.C.; writing—review and editing, A.R.G., N.B. and A.M.F. All authors have read and agreed to the published version of the manuscript.

Funding: The work was supported by scientific projects PTDC/BTM-SAL/30034/2017_LISBOA-01-0145-FEDER-030034 and SAICTPAC/0019/2015. This work was financed by national funds from Fundação para a Ciência e a Tecnologia (FCT), I.P., in the scope of the projects UIDB/04565/2020 and UIDP/04565/2020 of the Research Unit Institute for Bioengineering and Biosciences (iBB) and the project LA/P/0140/2020 of the Associate Laboratory Institute for Health and Bioeconomy (i4HB). The PPBI-Portuguese Platform of BioImaging (POCI-01-0145-FEDER-022122) is also acknowledged. A.R.G. acknowledges a FCT PhD fellowship (SFRH/BD/122636/2016).

Institutional Review Board Statement: Not applicable.

Informed Consent Statement: Not applicable.

Data Availability Statement: The data presented in this study are available on request from the corresponding author.

Conflicts of Interest: The authors declare no conflict of interest.

References

- Gabernet, G.; Müller, A.T.; Hiss, J.A.; Schneider, G. Membranolytic anticancer peptides. *Med. Chem. Commun.* **2016**, *7*, 1–14. [CrossRef]
- Hoskin, D.W.; Ramamoorthy, A. Studies on Anticancer Activities of Antimicrobial Peptides. *Biochim. Biophys. Acta—Biomembr.* **2008**, *1778*, 357–375. [CrossRef]
- Harris, F.; Dennison, S.R.; Singh, J.; Phoenix, D.A. On the Selectivity and Efficacy of Defense Peptides with Respect to Cancer Cells. *Med. Res. Rev.* **2013**, *33*, 190–234. [CrossRef]
- Gaspar, D.; Veiga, A.S.; Castanho, M.A.R.B. From Antimicrobial to Anticancer Peptides. A Review. *Front. Microbiol.* **2013**, *4*, 1–16. [CrossRef]
- Leuschner, C.; Hansel, W. Targeting Breast and Prostate Cancers Through Their Hormone Receptors. *Biol. Reprod.* **2005**, *73*, 860–865. [CrossRef]
- Bernardes, N.; Fialho, A.M. Perturbing the Dynamics and Organization of Cell Membrane Components: A New Paradigm for Cancer-Targeted Therapies. *Int. J. Mol. Sci.* **2018**, *19*, 3871. [CrossRef]
- Ehrenstein, G.; Lecar, H. Electrically gated ionic channels in lipid bilayers. *Q. Rev. Biophys.* **1977**, *10*, 1–34. [CrossRef] [PubMed]
- Hilchie, A.L.; Hoskin, D.W. Application of cationic antimicrobial peptides in cancer treatment: Laboratory investigations and clinical potential. In *Proceedings of the Emerging Cancer Therapy: Microbial Approaches and Biotechnological Tools*; Wiley: Hoboken, NJ, USA, 2010; pp. 309–332.
- Chiangjong, W.; Chutipongtanat, S.; Hongeng, S. Anticancer peptide: Physicochemical property, functional aspect and trend in clinical application (Review). *Int. J. Oncol.* **2020**, *57*, 678–696. [CrossRef] [PubMed]
- Teixeira, V.; Feio, M.J.; Bastos, M. Role of Lipids in the Interaction of Antimicrobial Peptides with Membranes. *Prog. Lipid Res.* **2012**, *51*, 149–177. [CrossRef] [PubMed]
- Hetz, C.; Bono, M.R.; Barros, L.F.; Lagos, R. Microcin E492, a Channel-Forming Bacteriocin from *Klebsiella Pneumoniae*, Induces Apoptosis in Some Human Cell Lines. *Proc. Natl. Acad. Sci. USA* **2002**, *99*, 2696–2701. [CrossRef] [PubMed]
- Xie, M.; Liu, D.; Yang, Y. Anti-cancer peptides: Classification, mechanism of action, reconstruction and modification. *Biol. Open* **2020**, *10*, 200004. [CrossRef]
- Hilchie, A.L.; Hoskin, D.W.; Power Coombs, M.R. Anticancer Activities of Natural and Synthetic Peptides. *Adv. Exp. Med. Biol.* **2019**, *1117*, 131–147. [CrossRef] [PubMed]
- Pubmed, Keyword: Anticancer Peptides in Clinical Trials. 2021. Available online: <https://pubmed.ncbi.nlm.nih.gov/?term=anticancer+peptide&filter=pubt.clinicaltrial&filter=years.2000-2021&sort=date> (accessed on 13 March 2021).

15. Haug, B.E.; Camilio, K.A.; Eliassen, L.T.; Stensen, W.; Svendsen, J.S.; Berg, K.; Mortensen, B.; Serin, G.; Mirjolet, J.-F.; Bichat, F.; et al. Discovery of a 9-Mer Cationic Peptide (LTX-315) as a Potential First in Class Oncolytic Peptide. *J. Med. Chem.* **2016**, *59*, 2918–2927. [CrossRef] [PubMed]
16. Wali, A.F.; Majid, S.; Rasool, S.; Shehada, S.B.; Abdulkareem, S.K.; Firdous, A.; Beigh, S.; Shakeel, S.; Mushtaq, S.; Akbar, I.; et al. Natural products against cancer: Review on phytochemicals from marine sources in preventing cancer. *Saudi Pharm. J.* **2019**, *27*, 767–777. [CrossRef] [PubMed]
17. Yamada, T.; Christov, K.; Shilkaitis, A.; Bratescu, L.; Green, A.; Santini, S.; Bizzarri, A.R.; Cannistraro, S.; Gupta, T.K.D.; Beattie, C.W. P28, A First in Class Peptide Inhibitor of Cop1 Binding to P53. *Br. J. Cancer* **2013**, *108*, 2495–2504. [CrossRef]
18. Lulla, R.R.; Goldman, S.; Yamada, T.; Beattie, C.W.; Bressler, L.; Pacini, M.; Pollack, I.F.; Fisher, P.G.; Packer, R.J.; Dunkel, I.J.; et al. Phase I Trial of P28 (NSC745104), a Non-HDM2-Mediated Peptide Inhibitor of P53 Ubiquitination in Pediatric Patients with Recurrent or Progressive Central Nervous System Tumors: A Pediatric Brain Tumor Consortium Study. *Neuro. Oncol.* **2016**, *18*, 1319–1325. [CrossRef] [PubMed]
19. Warso, M.A.; Richards, J.M.; Mehta, D.; Christov, K.; Schaeffer, C.; Rae Bressler, L.; Yamada, T.; Majumdar, D.; Kennedy, S.A.; Beattie, C.W.; et al. A First-in-Class, First-in-Human, Phase I Trial of P28, a Non-HDM2-Mediated Peptide Inhibitor of P53 Ubiquitination in Patients with Advanced Solid Tumours. *Br. J. Cancer* **2013**, *108*, 1061–1070. [CrossRef]
20. Chakrabarty, A.M.; Bernardes, N.; Fialho, A.M. Bacterial Proteins and Peptides in Cancer Therapy: Today and Tomorrow. *Bioengineered* **2014**, *5*, 234–242. [CrossRef]
21. Yamada, T.; Das Gupta, T.K.; Beattie, C.W. P28-Mediated Activation of P53 in G2-M Phase of the Cell Cycle Enhances the Efficacy of DNA Damaging and Antimitotic Chemotherapy. *Cancer Res.* **2016**, *76*, 2354–2365. [CrossRef]
22. Bernardes, N.; Ribeiro, A.S.; Abreu, S.; Vieira, A.F.; Carreto, L.; Santos, M.; Seruca, R.; Paredes, J.; Fialho, A.M. High-Throughput Molecular Profiling of a P-Cadherin Overexpressing Breast Cancer Model Reveals New Targets for the Anti-Cancer Bacterial Protein Azurin. *Int. J. Biochem. Cell Biol.* **2014**, *50*, 1–9. [CrossRef] [PubMed]
23. Bernardes, N.; Ribeiro, A.S.; Abreu, S.; Mota, B.; Matos, R.G.; Arraiano, C.M.; Seruca, R.; Paredes, J.; Fialho, A.M. The bacterial protein azurin impairs invasion and FAK/Src signaling in P-cadherin-overexpressing breast cancer cell models. *PLoS ONE* **2013**, *8*, e69023. [CrossRef]
24. Mehta, R.R.; Yamada, T.; Taylor, B.N.; Christov, K.; King, M.L.; Majumdar, D.; Lekmine, F.; Tirupathi, C.; Shilkaitis, A.; Bratescu, L.; et al. A Cell Penetrating Peptide Derived from Azurin Inhibits Angiogenesis and Tumor Growth by Inhibiting Phosphorylation of VEGFR-2, FAK Akt. *Angiogenesis* **2011**, *14*, 355–369. [CrossRef] [PubMed]
25. Yamada, T.; Mehta, R.R.; Lekmine, F.; Christov, K.; King, M.L.; Majumdar, D.; Shilkaitis, A.; Green, A.; Bratescu, L.; Beattie, C.W.; et al. A Peptide Fragment of Azurin Induces a P53-Mediated Cell Cycle Arrest in Human Breast Cancer Cells. *Mol. Cancer Ther.* **2009**, *8*, 2947–2958. [CrossRef] [PubMed]
26. Bernardes, N.; Abreu, S.; Carvalho, F.A.; Fernandes, F.; Santos, N.; Fialho, A.M. Modulation of Membrane Properties of Lung Cancer Cells by Azurin Enhances the Sensitivity to EGFR-Targeted Therapy and Decreased. β 1 *Integrin.—Mediat. Adhesion. Cell Cycle* **2016**, *15*, 1415–1424. [CrossRef]
27. Taylor, B.N.; Mehta, R.R.; Yamada, T.; Lekmine, F.; Christov, K.; Chakrabarty, A.M.; Green, A.; Bratescu, L.; Shilkaitis, A.; Beattie, C.W.; et al. Noncationic peptides obtained from azurin preferentially enter cancer cells. *Cancer Res.* **2009**, *69*, 537–546. [CrossRef]
28. Chaudhari, A.; Mahfouz, M.; Fialho, A.M.; Yamada, T.; Granja, A.T.; Zhu, Y.; Hashimoto, W.; Schlarb-Ridley, B.; Cho, W.; Das Gupta, T.K.; et al. Cupredoxin—Cancer Interrelationship: Azurin Binding with EphB2, Interference in EphB2 Tyrosine Phosphorylation, and Inhibition of Cancer Growth. *Biochemistry* **2007**, *46*, 1799–1810. [CrossRef]
29. Micewicz, E.D.; Jung, C.; Shaue, D.; Ewa, D.; Luong, H.; McBride, W.H.; Ruchala, P. Small Azurin Derived Peptide Targets Ephrin Receptors for Radiotherapy. *Int. J. Pept. Res. Ther.* **2011**, *17*, 247–257. [CrossRef]
30. Bernardes, N.; Garizo, A.R.; Pinto, S.N.; Caniço, B.; Perdigão, C.; Fernandes, F.; Fialho, A.M. Azurin Interaction with the Lipid Raft Components Ganglioside GM-1 and Caveolin-1 Increases Membrane Fluidity and Sensitivity to Anti-Cancer Drugs. *Cell Cycle* **2018**, *17*, 1649–1666. [CrossRef]
31. Coelho, L.F. Anticancer Activity of CT-p19LC, a Synthetic Peptide Derived from the Bacterial Protein Azurin. Master’s Thesis, Instituto Superior Técnico, University of Lisbon, Lisbon, Portugal, 2017.
32. Whitmore, L.; Wallace, B.A. DICHROWEB, an Online Server for Protein Secondary Structure Analyses from Circular Dichroism Spectroscopic Data. *Nucleic Acids Res.* **2004**, *32*, W668–W673. [CrossRef] [PubMed]
33. Cozens, A.L.; Yezzi, M.J.; Kunzelmann, K.; Ohri, T.; Chin, L.; Eng, K.; Finkbeiner, W.E.; Widdicombe, J.H.; Gruenert, D. CFTR Expression and Chloride Secretion in Polarized Immortal Human Bronchial Epithelial Cells. *Am. J. Respir. Cell. Mol. Biol.* **1994**, *10*, 38–47. [CrossRef] [PubMed]
34. Pinto, S.N.; Silva, L.C.; de Almeida, R.F.M.; Prieto, M. Membrane Domain Formation, Interdigitation, and Morphological Alterations Induced by the Very Long Chain Asymmetric C24:1 Ceramide. *Biophys. J.* **2008**, *95*, 2867–2879. [CrossRef] [PubMed]
35. Owen, D.M.; Rentero, C.; Magenau, A.; Abu-Siniyeh, A.; Gaus, K. Quantitative Imaging of Membrane Lipid Order in Cells and Organisms. *Nat. Protoc.* **2012**, *7*, 24–35. [CrossRef]
36. Yamada, T.; Fialho, A.M.; Punj, V.; Bratescu, L.; Das Gupta, T.K.; Chakrabarty, A.M. Internalization of bacterial redox protein azurin in mammalian cells: Entry domain and specificity. *Cell. Microbiol.* **2005**, *7*, 1418–1431. [CrossRef] [PubMed]
37. Freire, J.M.; Domingues, M.M.; Matos, J.; Melo, M.N.; Veiga, A.S.; Santos, N.C.; Castanho, M.A.R.B. Using zeta-potential measurements to quantify peptide partition to lipid membranes. *Eur. Biophys. J.* **2011**, *40*, 481–487. [CrossRef] [PubMed]

38. Domingues, M.M.; Santiago, P.S.; Castanho, M.A.; Santos, N.C. What can light scattering spectroscopy do for membrane-active peptide studies? *J. Pept. Sci.* **2008**, *14*, 394–400. [CrossRef] [PubMed]
39. Pinto, S.N.; Fernandes, F.; Fedorov, A.; Futerman, A.H.; Silva, L.C.; Prieto, M. A Combined Fluorescence Spectroscopy, Confocal and 2-Photon Microscopy Approach to Re-Evaluate the Properties of Sphingolipid Domains. *BBA—Biomembr.* **2013**, *1828*, 2099–2110. [CrossRef] [PubMed]



Article

KasQ an Epimerase Primes the Biosynthesis of Aminoglycoside Antibiotic Kasugamycin and KasF/H Acetyltransferases Inactivate Its Activity

Rajesh Rattinam^{1,2,3}, R. Sidick Basha¹, Yung-Lin Wang¹, Zhe-Chong Wang¹, Ning-Shian Hsu¹, Kuan-Hung Lin¹, Saeid Malek Zadeh^{1,2,3}, Kamal Adhikari¹, Jin-Ping Lin¹ and Tsung-Lin Li^{1,2,4,*}

- ¹ Genomics Research Center, Academia Sinica, Taipei 115, Taiwan; rajeshbuibt@gmail.com (R.R.); sidickchem@gmail.com (R.S.B.); hcvns3@hotmail.com (Y.-L.W.); mournermind@gmail.com (Z.-C.W.); kevin320@gate.sinica.edu.tw (N.-S.H.); cardboy19821022@hotmail.com (K.-H.L.); saeid.malekzadeh@gmail.com (S.M.Z.); arsonkamal@yahoo.com (K.A.); jpl0815@gate.sinica.edu.tw (J.-P.L.)
- ² Chemical Biology and Molecular Biophysics Program, Taiwan International Graduate Program, Academia Sinica, Taipei 115, Taiwan
- ³ Institute of Bioinformatics and Structural Biology, National Tsing Hua University, Hsinchu 300, Taiwan
- ⁴ Biotechnology Center, National Chung Hsing University, Taichung City 402, Taiwan
- * Correspondence: tlli@gate.sinica.edu.tw

Citation: Rattinam, R.; Basha, R.S.; Wang, Y.-L.; Wang, Z.-C.; Hsu, N.-S.; Lin, K.-H.; Zadeh, S.M.; Adhikari, K.; Lin, J.-P.; Li, T.-L. KasQ an Epimerase Primes the Biosynthesis of Aminoglycoside Antibiotic Kasugamycin and KasF/H Acetyltransferases Inactivate Its Activity. *Biomedicines* **2022**, *10*, 212. <https://doi.org/10.3390/biomedicines10020212>

Academic Editors: Leonardo Caputo, Laura Quintieri and Orazio Nicolotti

Received: 19 November 2021

Accepted: 17 January 2022

Published: 19 January 2022

Publisher's Note: MDPI stays neutral with regard to jurisdictional claims in published maps and institutional affiliations.



Copyright: © 2022 by the authors. Licensee MDPI, Basel, Switzerland. This article is an open access article distributed under the terms and conditions of the Creative Commons Attribution (CC BY) license (<https://creativecommons.org/licenses/by/4.0/>).

Abstract: Kasugamycin (KSM), an aminoglycoside antibiotic, is composed of three chemical moieties: D-*chiro*-inositol, kasugamine and glycine imine. Despite being discovered more than 50 years ago, the biosynthetic pathway of KSM remains an unresolved puzzle. Here we report a structural and functional analysis for an epimerase, KasQ, that primes KSM biosynthesis rather than the previously proposed KasF/H, which instead acts as an acetyltransferase, inactivating KSM. Our biochemical and biophysical analysis determined that KasQ converts UDP-GlcNAc to UDP-ManNAc as the initial step in the biosynthetic pathway. The isotope-feeding study further confirmed that ¹³C, ¹⁵N-glucosamine/UDP-GlcNH₂ rather than glucose/UDP-Glc serves as the direct precursor for the formation of KSM. Both KasF and KasH were proposed, respectively, converting UDP-GlcNH₂ and KSM to UDP-GlcNAc and 2-N'-acetyl KSM. Experimentally, KasF is unable to do so; both KasF and KasH are instead KSM-modifying enzymes, while the latter is more specific and reactive than the former in terms of the extent of resistance. The information gained here lays the foundation for mapping out the complete KSM biosynthetic pathway.

Keywords: kasugamycin; kasugamine; antibiotic biosynthesis; epimerase and acetyltransferase

1. Introduction

Kasugamycin (KSM), an aminoglycoside antibiotic produced by *Streptomyces kasugaensis*, was discovered in 1965. KSM is composed of three structurally distinct sub-components: a glycine imine, an unusual amino-sugar kasugamine and D-*chiro*-inositol (Figure 1) [1,2]. It has long been known that KSM binds specially to the interface between E- and P-site of the 30S ribosomal subunit to control fungal and bacterial protein translation [3]. KSM was used as an agricultural supplement to protect rice from fungus-derived diseases [4]. Beyond that, a number of new findings revealed that KSM possesses several unexpected biological activities effectively countering some recalcitrant human diseases: (i) an in vitro and in vivo study showed that the combination of KSM with rifamycin is in a position to control *Mycobacterium tuberculosis*, [5] (ii) KSM was recently shown to be capable of inhibiting herpes simplex virus-2 (HSV-2), [6] and (iii) KSM has also been shown to have a promising activity against COVID-19 by inhibiting 3 α -channel [7] and chitinase 3-like-1 (CHI3L1) proteins [8]. We were attracted by these new findings and thus eager to investigate the biosynthetic pathway of KSM in the hope of generating new and useful KSM analogs in the future.

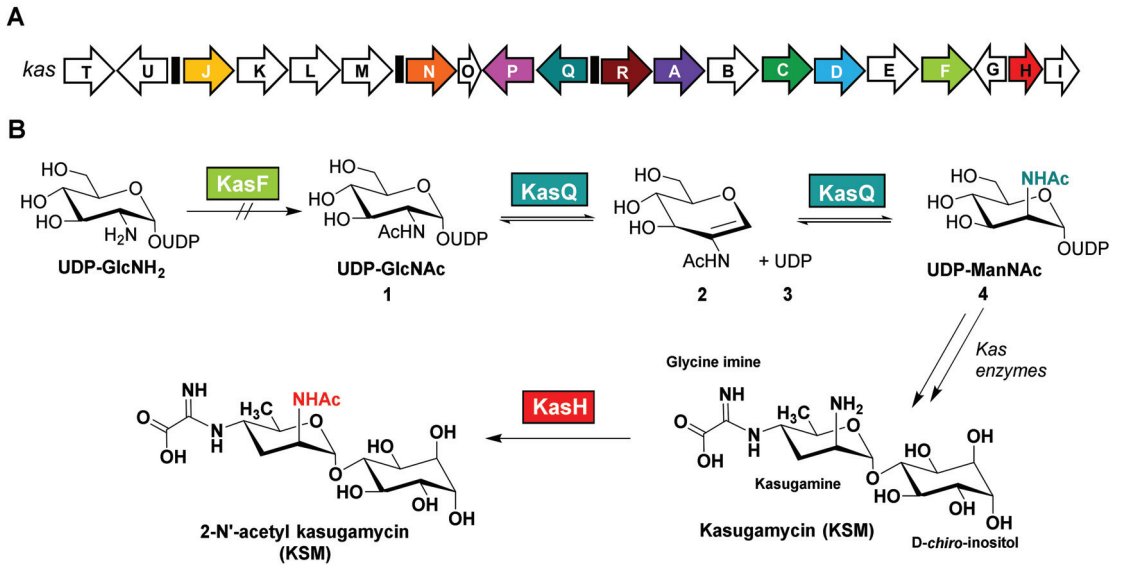


Figure 1. (A) The biosynthetic gene cluster (BGC) sequenced and identified from *Streptomyces kasugaensis*. (B) The proposed biosynthetic pathway of KSM based on the results revealed in this study. KasF is unable to acetylate UDP-GlcNH₂ to UDP-GlcNAc. KasQ initiates the KSM biosynthesis by converting UDP-GlcNAc 1 to UDP-ManNAc 4 through AAG 2 and UDP 3 intermediates. KasH acts as a self-resistance enzyme to acetylate kasugamycin (KSM) to 2-N'-acetyl kasugamycin (Ac-KSM).

The KSM biosynthetic pathway was proposed on the basis of the gene sequence similarity of each gene encoded in its biosynthetic gene cluster (BGC) [9–11]. However, the gene products responsible for the formation of UDP-N-acetyl-glucosamine (UDP-GlcNAc) and *myo*-inositol, the possible starting units for the formation of the kaugamine moiety, were still unclear (Figure S1). Five enzymes (KasF codes for an acetyltransferase, KasD codes for a NAD-dependent dehydratase, KasR codes for a PLP-dependent dehydratase, KasP codes for an oxidoreductase, and KasC codes for an aminotransferase) were proposed to act on UDP-GlcNAc in sequence to form the UDP-kasugamine precursor. Two downstream gene products—KasN, a glycine oxidase, and KasQ, an epimerase—may drive reactions toward UDP-kasugamine and UDP-carboxyformimidoyl-kasugamine sequentially. KasA, a glycosyltransferase, could couple UDP-carboxyformimidoyl-kasugamine and *myo*-inositol to form a KSM disaccharide precursor, then KasJ, an epimerase, could complete the synthetic pathway by epimerizing the equatorial C1-OH of *myo*-inositol to *D-chiro*-inositol (with an axial C1-OH) to afford KSM (Figure S1) [9–11]. KasH was reported as a self-resistance enzyme inactivating KSM by N2'-acetylation [12]. F. Kudo et al. recently came up with a new biosynthetic pathway for KSM [13], whereas no intrinsic *in vitro* biochemical evidence was provided therein unequivocally delineating the actual roles of the enzymes designated in the biosynthesis of KSM. With the aim of determining the roles of these enzymes, our *in silico* analysis revealed that KasQ shares a high sequence similarity with many UDP-GlcNAc 2-epimerases, especially RffE (also referred to as WecB, 47% identity) and to SecA (44% identity). RffE converts UDP-GlcNAc to UDP-ManNAc in the early stage of enterobacterial common antigen (ECA) biosynthesis [14]. Likewise, SecA performs the same reaction in the first step of the capsular polysaccharide (CPS) biosynthesis [15]. L. Zhang et al. further examined the substrate specificity of SecA with a group of C2 N-acyl-modified UDP-GlcNAc and UDP-ManNAc derivatives, concluding that the C2 N-acyl group in the UDP-acylhexosamines is critical for molecular recognition [16]. Of these facts, we speculated that KasQ should stand in the early stage of the biosynthetic

pathway (converting UDP-GlcNAc 1 to UDP-ManNAc 4; Figures 1 and S2) instead of the reported pathway where UDP-deoxy aminosugar is epimerized to UDP-kasugamine (Figure S1) [9–11]. This viewpoint, however, conflicted with the roles assigned for KasH and KasF; namely, they were proposed to prime and regulate the biosynthesis of KSM. We were thus prompted to resolve this long-standing issue by employing in vitro biochemical and biophysical analyses alongside in vivo isotope feeding assays, whereby we concluded that KasQ is the starter enzyme rather than KasF, and both KasF and KasH are self-resistant enzymes in the biosynthesis of KSM.

2. Materials and Methods

2.1. Cloning, Expression, and Purification

For the expression of KasQ, a gene was amplified from *Streptomyces kasugaensis* and cloned into expression vector pET28a+ to generate the protein with an N-terminal His₆ tag. The recombinant plasmid was transformed into *Escherichia coli* BL21 competent cells for protein overexpression. The transformed BL21 cells were used to inoculate LB medium (1000 mL) containing 1 mM kanamycin and the culture was grown at 37 °C. After reaching the OD at A600 nm of 0.6–0.8, the culture was induced by the addition of 1 mM IPTG, followed by incubation at 16 °C overnight. Cells were harvested by centrifugation at 6000 rpm using a JLA8.1 rotor in a Beckman Coulter centrifuge for 25 min at 4 °C. The harvested (1000 mL) cells were resuspended in 20 mL of binding buffer (50 mM Tris pH 7.5, 500 mM NaCl, 10% glycerol, and 10 mM imidazole). Resuspended cells were lysed using a sonicator (time, 4 min, pulse, 3 s on and 2 s off). The resulting lysate was centrifuged at 18,000 rpm (JA20.50 rotor, Beckman Coulter, Brea, CA, USA) for 30 min at 4 °C. The supernatant was added to a Ni-agarose affinity column equilibrated with binding buffer. The unbound proteins were washed off using varied imidazole concentrations (10 mM, 25 mM, and 50 mM). The protein was then eluted with elution buffer (50 mM Tris pH 7.5, 500 mM NaCl, 10% glycerol, and 250 mM imidazole). The eluted protein samples were concentrated and injected into a Superdex S-200 column equilibrated with gel filtration buffer (50 mM HEPES pH 8.0, 100 mM NaCl). The peak fractions were collected and the purity of the KasQ protein was analyzed by 10% SDS-PAGE.

For the expression of KasH, a gene was amplified from *Streptomyces kasugaensis* and cloned into the expression vector pET28a+ to generate the protein with an N-terminal His₆ tag. The recombinant plasmid was transformed into *E. coli* BL21 competent cells and the protein was overexpressed. The purification steps of the above procedure were followed with the different gel filtration buffer (50 mM MOPS pH 7.5, 100 mM NaCl). The purity of the KasH protein was analyzed by 10% SDS-PAGE and confirmed by mass spectrometry (peptide mass fingerprinting).

For the expression of KasF, the gene was amplified from *Streptomyces kasugaensis* and cloned into the expression vector pET28a+ to generate the protein with an N-terminal His₆ tag. The recombinant plasmid was transformed into *E. coli* BL21 competent cells and the protein was overexpressed. The purification steps were followed by the above procedure with the different gel filtration buffer (50 mM HEPES pH 7.5, 200 mM NaCl). The purity of the KasF protein was analyzed by 10% SDS-PAGE and confirmed by mass spectrometry (peptide mass fingerprinting).

2.2. Crystallization and Data Collection

KasQ wild type (WT) and complex crystals were crystallized using the hanging drop vapor diffusion method at 20 °C. KasQ wild type (WT) protein was crystallized (7 mg mL⁻¹) in a buffer (50 mM HEPES pH 8.0, 100 mM NaCl) using a reservoir solution (0.2 M potassium/sodium tartrate, 0.1 M Bis-Tris propane pH 7.5 and 20% PEG 3350). KasQ–WT crystals were formed after 7 days of incubation. The enzyme (10 mg mL⁻¹) was co-crystallized with 2 mM UDP or 2 mM UDP-Glc in the presence of 2 mM MgCl₂ with a reservoir solution containing 0.2 M lithium sulfate, 0.1 M Bis-Tris pH 5.5 and 25% PEG 3350 to obtain the KasQ–UDP or KasQ–UDP-Glc complex crystals. The complex crystals

were formed after 15 days. Prior to the data collection, the crystals were transformed into the mother liquor containing 20% glycerol as a cryoprotectant and flash-frozen using liquid nitrogen. All the crystal data were collected in beamline 15A1 and 05A equipped with an ADSC Quantum-315 or MX300HE CCD detector (Rayonix, L.L.C., Evanston, IL, USA) at an operating temperature of 100K in National Synchrotron Radiation Research Center (NSRRC), Taiwan. The raw data were indexed and processed using the HKL2000 package (HKL Research, Inc., Charlottesville, VA, USA) [17]. The KasQ–WT crystal belongs to the C2 space group; the KasQ–UDP and KasQ–UDP-Glc complex crystals belong to the P1 space group. Detailed data collection statistics are shown in Table 1.

Table 1. Summary of crystal data-collection statistics.

	KasQ–WT			KasQ–UDP			KasQ–UDP-Glc		
PDB code	7VYY			7VZA			7VZ6		
Wavelength (Å)	1.0			1.0			1.0		
Space group	C2			P1			P1		
Cell dimensions									
<i>a</i> , <i>b</i> , <i>c</i> (Å)	112.4	106.1	94.3	81.8	104.7	106.3	82.8	104.9	106.8
α , β , γ (°)	90	124.9	90	74.5	73.0	68.4	74.9	72.9	68.1
Resolution (Å)	25.45–2.44 (2.55–2.46)			19.89–2.60 (2.68–2.60)			21.56–2.10 (2.18–2.10)		
<i>R</i> _{merge}	0.031 (0.387)			0.023 (0.365)			0.035 (0.296)		
<i>I</i> / <i>I</i>	26.6 (2.4)			23.8 (1.9)			19.7 (2.7)		
Completeness (%)	85.9 (86)			93.9 (94.1)			95.2 (95.1)		
Redundancy	3.6 (3.9)			2.4 (2.5)			2.2 (2.1)		
Refinement									
Resolution (Å)	25.45–2.44 (2.55–2.44)			19.9–2.58 (2.68–2.58)			21.5–2.09 (2.14–2.09)		
No. reflections	28,957			91,395			176,474		
<i>R</i> _{work} / <i>R</i> _{free}	0.22/0.27			0.21/0.24			0.20/0.22		
R.m.s deviations									
Bond lengths (Å)	0.66			0.66			0.70		
Bond angles (°)	0.77			0.79			0.84		

2.3. Structure Determination and Refinement

The KasQ–WT and its complex crystal structures were determined by molecular replacement (MR) with Phaser-MR from the CCP4 program suit [18]. The *E. coli* UDP-GlcNAc epimerase (PDB entry 1vqv) was used as a search model to solve the initial phase [19]. The protein structures were built and refined using REFMAC [20], COOT [21], and PHENIX [22]. PyMOL as used to construct the protein structures and electron density maps [23].

2.4. Site-Directed Mutagenesis

Site-directed mutagenesis was performed using QuikChange (Stratagene), following the manufacturer's protocol. The sequences of primers used in this study to create KasQ mutants are shown in Table 2. The wild-type KasQ plasmid (BCRC12349) was used as the template for the single mutation. All mutations were confirmed by DNA sequencing. KasQ mutants were expressed and purified with the same protocol as used for the wild-type protein.

Table 2. The sequences of primers used in this study to create KasQ mutants.

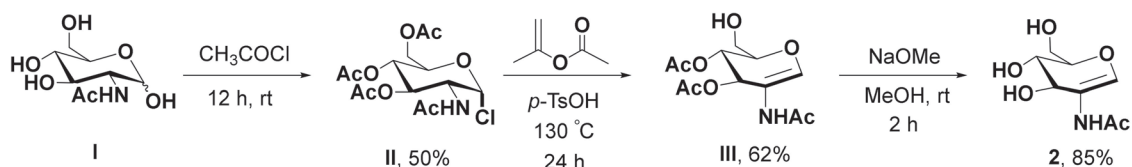
Mutants	Primers
Q95A	Forward 5'-TGGTGTCTCCCGCTACCACGGCGACGTCC-3' Reverse 5'-GGACGTCGCCGTGGTAGCGGGAGACACCA-3'
Q95E	Forward 5'-TGTCTCCCTTACCACGGCGACGTCCA-3' Reverse 5'-TGGACGTCGCCGTGGTAGAGGGAGACA-3'
E308A	Forward 5'-CCTCGGGGCGCGCGGTGCCGTCC-3' Reverse 5'-GGACCGCACGGCGCGCCCGAGG-3'
E308Q	Forward 5'-CTCGGGGCGCTGCGGTGCCGTCC-3' Reverse 5'-GGACCGCACGACGCGCCCGAG-3'

2.5. Isothermal Titration Calorimetry (ITC)

ITC analyses were carried out at 25 °C using an ITC200 microcalorimeter (MicroCal Inc., Northampton, MA, USA). The buffer solution (50 mM HEPES pH 8.0, 100 mM NaCl) was used to prepare protein and substrates for ITC analysis. Each titration contained 0.1 mM KasQ in the sample cell (250 μ L), and 1 mM substrates was loaded into the syringe (40 μ L). The titration experiment contains 18 injections (2 μ L for a duration of 4 s) and each injection was separated by 120 s. The distilled water was filled in the reference cell throughout all titrations. The cell stirring speed was 1000 rpm. The collected raw data were processed in Origin 7.0 (provided by MicroCal) by a non-linear least square method to a single-site binding model. KasH ITC analyses were followed using the above procedure with a buffer solution of 50 mM MOPS pH 7.5, 100 mM NaCl.

2.6. Synthesis of 2-Acetamidoglucal (AAG)

AAG **2** was synthesized as shown in Scheme 1. GlcNAc **I** reacts with acetyl chloride to yield glycosyl chloride **II**. Further reaction with isopropenyl acetate affords glucal **III**. Deacetylation of **III** using sodium methoxide provides **2**.



Scheme 1. The synthetic steps for AAG **2**.

2.6.1. General Information

^1H and ^{13}C NMR spectra were recorded on a Bruker 600 spectrometer with tetramethylsilane as the internal reference. ^{31}P NMR was performed in Bruker Avance 500 AV NMR. Chemical shifts (δ scale) were reported in parts per million (ppm). ^1H NMR spectra were reported in the order: multiplicity, number of protons, and coupling constant (J value) in hertz (Hz); signals were characterized as s (singlet), d (doublet), dd (doublet of doublet), and m (multiplet). Saturation transfer difference nuclear magnetic resonance (^1H -STD NMR) was performed using a Bruker 600 MHz spectrometer, with KasQ and UDP-GlcNAc in a ratio of 1:100 recorded within 0–5 min. A saturation time of 2 s was employed. UDP-GlcNAc-relative STD (saturation transfer difference) effects were determined by $(I_0 - I_{\text{sat}})/I_0$. $(I_0 - I_{\text{sat}})$ is the signal intensity in the STD NMR spectrum, whereas I_0 is the signal intensity of the reference spectrum. Column chromatography was performed on silica gel (70–230 mesh). TLC analysis was carried out on Merck Silica gel 60 F254 plates using MOSTAIN/ p -anisaldehyde sugar staining. Compound **2** was synthesized by following a slight modification of the procedure described in the literature [16].

2.6.2. Procedure for the Synthesis of 2-Acetamidoglucal (AAG)

Acetyl chloride (6 mL), GlcNAc **I** (2.00 g, 9.04 mmol) was added and stirred for up to 12 h. After that, CHCl_3 (20 mL) was added and the mixture was poured into ice-cold water. The organic layer was washed with an aqueous sodium bicarbonate solution (20 mL) and concentrated under reduced pressure. The crude residue was purified by flash column chromatography to obtain the pure glycosyl chloride **II** (1.65 g, 50%). ^1H NMR (600 MHz, CDCl_3) δ 6.18 (d, $J = 3.7$ Hz, 1H), 5.88 (d, $J = 8.7$ Hz, 1H), 5.31 (dd, $J = 10.8, 9.4$ Hz, 1H), 5.20 (dd, $J = 11.0, 8.6$ Hz, 1H), 4.53 (ddd, $J = 10.7, 8.8, 3.7$ Hz, 1H), 4.27 (m, 2H), 4.13 (m, 1H), 2.09 (s, 3H), 2.04 (s, 6H), 1.98 (s, 3H). ^{13}C NMR (150 MHz, CDCl_3) δ 171.7, 170.8, 170.3, 169.3, 93.8, 71.1, 70.3, 67.1, 61.3, 53.7, 23.3, 20.9, 20.7. The resulting chloride **II** (1.40 g, 3.83 mmol) was treated with isopropenyl acetate (28 mL) and $p\text{-TsOH}$ (45 mg) and was refluxed at $130\text{ }^\circ\text{C}$ for 24 h. Then, the mixture was concentrated under reduced pressure and the crude

residue was purified by flash column chromatography to attain the pure glucal product **III** (0.682 g, 62%). $^1\text{H NMR}$ (600 MHz, CDCl_3) δ 6.60 (s, 1H), 5.56 (d, $J = 4.8$ Hz, 1H), 5.25 (m, 1H), 4.51 (m, 1H), 4.47 (m, 1H), 4.19 (dd, $J = 12.0, 3.0$ Hz, 1H), 2.09 (s, 6H), 2.01 (s, 3H). $^{13}\text{C NMR}$ (150 MHz, CDCl_3) δ 170.7, 170.0, 169.7, 148.0, 113.5, 74.9, 67.4, 67.1, 61.1, 20.9, 20.8. To a glucal **III** (0.600 g, 2.09 mmol), dry methanol (14 mL) was added and dissolved, then sodium methoxide was added (pH \sim 8.5) and the mixture was stirred for up to 2 h. The mixture was neutralized with Amberlite IR-120 (H+), filtered, and concentrated. The crude residue was purified by flash column chromatography and the pure solid product **2** (0.360 g, 85%) was obtained. $^1\text{H NMR}$ (600 MHz, D_2O) δ 6.61 (s, 1H), 4.18 (d, $J = 6.6$ Hz, 1H), 3.91 (m, 1H), 3.79 (d, $J = 4.0$ Hz, 2H), 3.69 (dd, $J = 9.2, 6.8$ Hz, 1H), 1.97 (s, 3H). $^{13}\text{C NMR}$ (150 MHz, D_2O) δ 174.5, 141.7, 113.2, 78.5, 68.8, 68.4, 59.9, 21.9.

2.7. Construction of pMKBAC08-KAS and pWZC07-PrpsJ-kasT

The *E. coli-Streptomyces* spp. shuttle BAC plasmid, pMKBAC08, was designed by amplifying the DNA segments containing the origin of transfer region (*oriT*) and the integrase and apramycin resistance gene, *aacIII(IV)*, within the primer set P325 and P326 from plasmid pGUSRolRPA3 [24], and inserted into the BAC plasmid pBeloBAC11 (New England Biolabs, NEB).

pMKBAC08-KAS-Int, which carries an intact kasugamycin BGC, was constructed via sequentially cloning partial segments from the kasugamycin BGC into the pMKBAC08 plasmid as reported in previous studies [11]. Briefly, the DNA fragments containing the *kasT* gene, *kasU-kasM*, *kasN-kasQ*, *kasR-kasB*, and *kasC-kasI* were amplified with the primer sets P115/P116, P117/P118, P119/120, P121/P122m and P123/P124 (Table 3). After digesting the amplicons by different restriction enzymes and individually introducing them into the pMKBAC08 vector using T4 DNA ligase, the BAC-containing kasugamycin BGC, pMKBAC08-KAS, was obtained.

Table 3. The sequences of primers used to construct pMKBAC08-KAS and pWZC07-PrpsJ-kasT.

Primers	Sequence
P303	TAACCGTTTAAACTTAATTAAGAAGATCCTTTGATCTTTTCTACGG
P304	AAGCCCTGGATCCAATTCCTCAATGTCGAAGCACTT
P115	ATTATATTATCATATGCGCGTCATCGACGGGATGCACCCGGCT
P116	ACCTGTGTTCAACCAAGGAAATTCCTGGGTTGAACACCCG
P117	AAGATCAGATCCCCCGGTGACGTAGTACGAGAT
P118	ACAGCGTCATGACGTGAAGTTCAGCGACCCGAT
P119	ATTATATTCAATTGCACTACAAGTTCGGCTGGGTGTACCTGAATTT
P120	ATTATATTTTAATTAAGCTTATTCGACGAGCTCTCGATGACGAAGACA
P121	CAGGAAATTCGAGGCGGAATTCGCCGAATCCTT
P122	TGCCTTGTCGTCGTAGGTGTGGAGGCTTT
P123	TTCGACATCGGCATGATCACCCACGGTCTGCTCT
P124	ATTATATTAAGCTTAACAACGTGACGGGTTACGCCAGTTACCGTTCATGCTT

The *E. coli-Streptomyces* spp. shuttle plasmid, pWZC07, was constructed by replacing the apramycin resistant gene, *aacIII(IV)*, in the plasmid pGUSRolRPA3 [24] with the neomycin resistant gene, *neo (Tn5)*. To activate the expression of kasugamycin, the pWZC07-PrpsJ-kasT plasmid was constructed by cloning the *rpsJ* promoter fused with the *kasT* activator gene into the pWZC07 vector as reported previously [11].

2.8. In Vivo Isotope Incorporation Assay

For investigating the incorporation of the isotope-labeled compounds, *Streptomyces lividans* TK64 was introduced with pMKBAC08-KAS and pWZC07-PrpsJ-kasT. After being grown on an MS agar plate at 28 °C for 7 days [25], the grown spores were inoculated into flasks (50 mL volume) containing 10 mL of KPMb medium (maltose monohydrate, 15 g/L; bacto-yeast extract, 4.0 g/L; phytone-peptone, 15 g/L; $\text{MgSO}_4 \cdot 7\text{H}_2\text{O}$, 0.5 g/L; KH_2PO_4 , 1.0 g/L; and NaCl, 3.0 g/L.) and incubated at 28 °C for 5 days [11]. After 24 h of incubation,

isotope-labeled precursors (^{13}C -glucose; ^{13}C -glucosamine; ^{13}C - ^{15}N -glucosamine; ^{15}N -glycine; ^{15}N -aspartic acid; and ^{15}N -glutamic acid) were prepared and added into the culture individually every 24 h until 72 h (17 mg/mL). After shaking for 96 h, the mycelium was removed from the culture broth and the filtrate was adjusted to pH 4.0 with oxalic acid. The treated samples were incubated at 70 °C for 20 min and then the supernatant was collected and analyzed after removing the debris by centrifuge. Supernatants were injected into the HPLC-TQ-MS and separated by the method described below.

HPLC method A:

The supernatant was subjected to HPLC-TQ-MS with a Bridge BEH amide column (250 mm \times 4.6 mm, 5 μm). The mobile phase was set up with a linear gradient, 30% H_2O + 0.1 formic acid (FA) and 70% acetonitrile, at a flow rate of 1.0 mL min^{-1} over 30 min.

2.9. Disc Diffusion Assay

KSM susceptibility and production were confirmed by disc diffusion assay. An *E. coli* culture was grown at 37 °C overnight and spread on an LB agar plate (pH 7.0). About 5 μL of extracted samples from *Streptomyces lividans* TK64 (from days 2–5) were loaded onto the paper disc. The disc was placed onto the surface of an LB agar plate and incubated at 37 °C overnight to visualize the zone of inhibition (ZOI).

For the KSM resistant assay, BL21 cells with/without the *kasH* or *kasF* gene were individually expressed and seeded on LB agar plates (pH 7.0). About 5 μL of different aminoglycoside antibiotics (amikacin, gentamicin, sisomicin, streptothricin-F, or tobramycin) were loaded onto each paper disc and placed on the surface of the LB plates. The plates were incubated 37 °C overnight to visualize the appearance of the zone of inhibition (ZOI). Note: this is a standard protocol for evaluating the effectiveness of common antibiotics, including aminoglycosides; there is no apparent impact concerning the structural integrity or biological deterioration of the selected aminoglycosides at pH 7.0 during the examining course.

2.10. HPLC Activity Assay

The epimerization reaction was carried out in a 100 μL reaction mixture containing 0.1 mg freshly purified KasQ, 1 mM UDP-GlcNAc, and 1 mM MgCl_2 in 25 mM Tris buffer, pH 8.0. The reactions were incubated at 37 °C for 12 h and quenched by adding equal volumes of chloroform. The precipitated protein was removed from the reaction mixture by centrifugation at 15,000 rpm for 20 min. For the screening of different NDP-sugar substrates, the enzymatic reactions were carried out in a 100 μL reaction mixture containing 0.1 mg KasQ, 1 mM NDP-Sugars (UDP-GalNAc, UDP-Glc, TDP-Glc, GDP-Glc, and UDP-Gal) in the presence of 1 mM MgCl_2 in 25 mM Tris buffer, pH 8.0. The reactions were incubated at 37 °C for 12 h and quenched by adding equal volumes of chloroform. The precipitated protein was removed from the reaction mixture by centrifugation at 15,000 rpm for 20 min. Supernatants were injected into the HPLC-LTQ-MS and separated by the method described below.

HPLC method A:

The supernatant was subjected into HPLC-LTQ-MS with a Hypercarb Porous Graphitic Carbon Column (100 mm \times 4.6 mm, 5 μm , Thermo Fisher Scientific, USA). The solvents used in the mobile phases were: solvent A: 50 mM ammonium formate; solvent B: 100% acetonitrile. A gradient started at 0–5 min (solvent A: 95%; solvent B: 5%) and progressed to 18 min (solvent A: 60%; solvent B: 40%) and 24–26 min (solvent A: 2%; solvent B: 98%) and ended at 28–32 min (solvent A: 95%; solvent B: 5%) at a flow rate of 1.0 mL min^{-1} .

The acetylation reactions were carried out in a 100 μL reaction mixture containing 0.1 mg KasH or KasF, 1 mM KSM or UDP-GlcNH₂, and 0.5 mM AcCoA in 25 mM Tris buffer, pH 8.0. The reactions were incubated 12 h at 37 °C and quenched by adding equal volumes of chloroform. Supernatants were injected into the HPLC-LTQ-MS and separated by the method described below.

HPLC method B:

The supernatant was subjected into HPLC-LTQ-MS with a Phenomenex Prodigy C-18 column (250 mm × 4.6 mm, 5 μm). The solvents used in the mobile phases were: solvent A: H₂O + 0.1% trifluoroacetic acid (TFA); solvent B: acetonitrile (ACN) + 0.1% TFA. A gradient started at 0–5 min (solvent A: 98%; solvent B: 2%) and progressed to 18 min (solvent A: 60%; solvent B: 40%) and 24–32 min (solvent A: 2%; solvent B: 98%) and ended at 35–41 min (solvent A: 98%; solvent B: 2%) at a flow rate of 1.0 mL min⁻¹.

2.11. Thin Layer Chromatography (TLC) Analysis

About 1–2 μL of AAG 2 and reaction mixture of KasQ with UDP-GlcNAc and MgCl₂ were spotted onto a TLC plate (Merck Silica gel 60 F254 plates). For aminoglucal detection, TLC was soaked with *p*-anisaldehyde stain solution and, upon gentle heating on a hot plate, the red color spot was visualized.

2.12. HPLC Kinetic Analysis

Kinetic analysis was performed in a 100 μL reaction mixture containing 0.1 mg freshly purified KasQ, six different concentrations of UDP-GlcNAc (0.25, 0.50, 0.75, 1.00, 1.25, and 1.50 mM) and 1 mM MgCl₂ in 25 mM Tris buffer, pH 8.0. The reaction mixture was mixed by vortex and incubated at 37 °C. Reactions were stopped at six different time points (10, 30, 60, 120, 180, and 240 min) by adding equal volumes of chloroform. Precipitation was removed by centrifugation and analyzed by HPLC-LTQ-MS using HPLC method B as described above. Substrate (UDP-GlcNAc 1) peaks were eluted at 10.69 min and products were (UDP-ManNAc 4) eluted at 9.90 min, whereas the intermediates UDP 3 and AAG 2 were eluted at 9.51 min and 8.99 min, respectively. The Michaelis–Menten curve of the KasQ activity was derived from the integrated peak area of each reaction.

2.13. NMR Activity Assay

Enzymatic reactions were performed in 25 mM Tris pH 8.0 with 1 mg freshly purified KasQ, 15 mM UDP-GlcNAc, and 5 mM MgCl₂ in a total reaction volume of 600 μL, incubated at 37 °C for 4 h. After incubation, the reaction was quenched by adding an equal volume of chloroform, and the supernatant was collected by centrifugation. The supernatant was filtered through a 3 kDa cut-off filter membrane (Millipore) and freeze-dried using a lyophilizer. The lyophilized product was dissolved in D₂O (500 μL) and analyzed by NMR. For standards, a pure UDP-GlcNAc 1, AAG 2, and UDP 3 were dissolved in D₂O (500 μL) and analyzed by NMR.

Similarly, time course NMR samples were prepared. The enzymatic reactions were stopped at six different time points (10 min, 30 min, 60 min, 120 min, 180 min, and 12 h) by adding an equal volume of chloroform, and supernatants were collected by centrifugation. The supernatants were filtered through a 3 kDa cut-off filter membrane (Millipore) and freeze-dried using a lyophilizer. The lyophilized product was dissolved in D₂O (500 μL) and analyzed by ¹H and ³¹P NMR spectroscopy.

HPLC method C:

Each enzymatic reaction was performed in a 100 μL reaction mixture containing 1 mM UDP-GlcNAc and 1 mM MgCl₂, incubated with or without KasQ in D₂O. Deuterium incorporation was stopped at nine different time points (0 min, 2 min, 5 min, 10 min, 15 min, 20 min, 25 min, 30 min, and 12 h) by adding equal volumes of chloroform. Supernatants were injected into the HPLC-LTQ-MS and separated by the method described below.

HPLC method D:

The supernatant was subjected to HPLC-LTQ-MS with a Phenomenex Prodigy C-18 column (250 mm × 4.6 mm, 5 μm). The solvents used in the mobile phase were: solvent A: 50 mM ammonium formate; solvent B: 100% acetonitrile. A gradient started at 0–6 min (solvent A: 92%; solvent B: 8%) and progressed to 7–10 min (solvent A: 70–50%; solvent B: 30–50%) and 11–21 min (solvent A: 98%; solvent B: 2%) at a flow rate 0.3 mL min⁻¹.

2.14. Computational Analysis

For sequence alignment, KasQ homologue protein sequences were retrieved from the National Center for Biotechnology Information (NCBI). Multiple sequence alignment was performed with Clustal Omega and the *aln* format file was uploaded into EsPript to construct the final image (Figure S21) [26]. KasQ homologue selected active sites were uploaded to the Weblogo server to build the KasQ active site sequence logo [27].

3. Results and Discussion

3.1. Biochemical Investigation of an Epimerase

In an attempt to validate the biochemical function of KasQ, N-terminally His-tagged KasQ was purified, which exists in solution as dimeric proteins (Figure S3). At first, potential substrates/intermediates UDP-GlcNAc 1, 2-acetamidoglucal 2 (AAG), and UDP 3 were analyzed by HPLC-MS. Next, enzymatic reactions of KasQ incubated with UDP-GlcNAc and MgCl₂ were examined at various time points (Figures 2A,B and S4). At 10 min, the expected product, UDP-ManNAc 4 (*m/z* 605.15 [M-H]), appeared at the retention time of 9.90 min. On an elevated timeline, AAG 2 and UDP 3 (*m/z* 402.20 [M-H]) emerged, respectively, at 8.99 and 9.51 min, and then increased over time (Figure S5). The generation of UDP-ManNAc 4 stagnated after 10 min and slightly increased at 12 h. The optimum temperature for KasQ epimerization activity was 37–42 °C. (Figure S6). Next, the efficiency of the epimerase reaction was investigated. UDP-ManNAc formation was 6.8% at 10 min and marginally increased to 9.2% at 12 h. On the other hand, at 10 min AAG and UDP were formed at 0.2% and 1.1%, respectively. At 12 h, the conversion of AAG was 23.8% and that of UDP was 64.4%. UDP-ManNAc concentration was 2.6-fold lower than that of AAG and seven-fold lower than that of UDP, which indirectly suggested that the intermediates formed are thermodynamically stable, consistent with previous studies (Figures 2C and S7) [14].

The KasQ epimerase reaction was parallelly probed by NMR spectrometry. The reaction of UDP-GlcNAc in the presence of KasQ and MgCl₂ emanated the peak of a singlet at 6.60 ppm corresponding to an alkenyl proton of AAG and an appreciable amount of UDP-ManNAc was determined by its anomeric proton at 5.35 ppm. In contrast, a lesser number of UDP-GlcNAc anomeric protons at 5.41 ppm was observed (Figure S8). Extensive studies at various time intervals of the enzymatic reaction were executed (Figure 3). AAG formed at 10 min and increased consistently with respect to time (Figure 3B), whereas UDP-ManNAc formation from 10–120 min remained almost the same and slightly increased at 12 h (Figure 3C). The equilibrated existence of phosphorus in the epimerase reaction was tracked at various time periods by P³¹ NMR spectrometry. At 10 min, UDP extrusion was observed with P_α at −8.7 ppm and P_β at −4.5 ppm, along with UDP-GlcNAc P_α at −11.7 ppm and P_β at −10.0 ppm. At a wider timespan, the UDP-GlcNAc peak was reduced and the UDP peak was intensified, whereas UDP-ManNAc P_α and P_β at −12.8 and −12.7 ppm moderately increased with respect to time (Figure 3D). Enzymatic isotope labeling studies of UDP-GlcNAc were scantily documented [14,28]. To gain further insight into the KasQ epimerization reaction, a reversibility experiment was performed. UDP-GlcNAc with or without KasQ in the presence of MgCl₂ was incubated in D₂O at different time intervals and the reaction mixtures were subjected to HPLC-MS analysis (Figure S9). No deuterium scrambling was observed when UDP-GlcNAc was incubated in D₂O without KasQ up to 12 h (*m/z* 605.98 [M-H]) (Figures 3E and S9A). Moreover, in the presence of KasQ with UDP-GlcNAc and MgCl₂ in D₂O, deuterium was labeled from 2 min to 12 h (*m/z* 606.96 [M-H]) (Figures 3E and S9B). To validate the position of the deuterium incorporation, NMR studies were performed (Figure 3F,G). The C2 position of the UDP-GlcNAc was deuterated (97%) and appeared as a doublet at 5.36 ppm with minor traces of C2-deuterated UDP-ManNAc (<1%). Heavily incorporated deuterium at the C2 position of the UDP-GlcNAc clearly suggests that the abstraction of protons at the C2 position is highly reversible with the surrounding active-site residues of KasQ. It also postulates that first step of the reaction mechanism is highly reversible. A control experiment was

performed to recognize the ability of thermodynamically stable AAG with UDP to generate UDP-ManNAc or UDP-GlcNAc. KasQ incubated with AAG and UDP in the presence of MgCl_2 was monitored by ^1H NMR (Figure S12). The absence of anomeric proton signals of UDP-ManNAc or UDP-GlcNAc concluded that the enzymatic reaction was ultimately futile. A similar finding was also noticed with SacA [16]. An ITC experiment for AAG with KasQ showed unfavored binding in the medium (Table 4). This implies that, thermodynamically, there is no binding affinity with KasQ for AAG. Enzyme binding interactions of UDP-GlcNAc were determined by saturation transfer difference (STD) NMR (Figure 3H). The proton binding epitope of UDP-GlcNAc with KasQ suggested that the ribose framework accumulated a major zone of interactions, whereas the GlcNAc and uridine moieties occupied a minor zone with KasQ. Both uridine H13 (the alkenyl group) and ribose H7 bind closely with KasQ, acquiring major STD effects. Moderate binding was attained on H8 and H9 of the ribose ring. GlcNAc H5, H14, and ribose H11 formed weak binding interactions with KasQ. Based on these binding studies of STD NMR and ITC analyses, we propose that the KasQ epimerase may proceed through a kinetically favorable or an enzyme-bound reaction mechanism. The proposed pathway for this epimerization reaction is from UDP-GlcNAc which undergoes an *anti*-elimination to generate AAG and UDP. Then, it undergoes subsequent *syn*-addition to afford an epimer UDP-ManNAc **4**. Overall, our biochemical investigations indicate that KasQ converts UDP-GlcNAc **1** to UDP-ManNAc **4** in a shorter reaction time, whereas in a prolonged reaction it releases a higher amount of AAG **2** and UDP **3**.

3.2. Biochemical Characterization of Acetyltransferases

The primary sequence analysis revealed that both KasF and KasH belong to enzymes of the acetyltransferase superfamily, while both share very low sequence identity (<10%) (Figure S13). Purified KasF forms monomers but KasH forms dimers in solution (Figure S3). The *in vivo* acetylation (resistance) activity of KasF and KasH versus KSM was evaluated with a disc diffusion assay (Figure S14). Individually, we introduced the pET28a+ plasmid carrying the *kasF* or *kasH* gene into the BL21 (DE3) *E. coli* cells. The *E. coli* cells (carrying the empty pET28a+ plasmid without the given acetyltransferase gene) were used as a control. We observed a clear zone of inhibition (ZOI) in the *E. coli* cells (not carrying the acetyltransferase gene) representing the cells' inability to grow in the presence of KSM (the disc contained ~5 μL of 7.6 mg/mL of KSM). The growth of *E. coli* that carried the *kasH* gene was not affected in the presence KSM, whereas moderate growth of *E. coli* was observed in the cells carrying the *kasF* gene (Figures 4A and S14). This phenomenon indicated that KasH serves as a resistance gene specific to KSM. Whether KasF is a resistance gene against other aminoglycoside antibiotics was further examined (Figures 4B,C and S15). The activities of these two acetyltransferases against a number of commonly used aminoglycoside antibiotics (amikacin, gentamicin, kanamycin B, sisomicin, streptothricin-F, and tobramycin) were examined. The appearance of ZOI in all conditions strongly suggested that neither KasH nor KasF are active towards these aminoglycoside antibiotics (Figures 4B,C and S15). Based on this *in vivo* assay we concluded that KasH serves as a self-resistance gene, while KasF partially acts as a self-resistance gene to KSM. To support this finding, an *in vitro* assay was performed. KasF or KasH were incubated with 1 mM KSM and 0.5 mM AcCoA at 37 °C for 12 h. KasH completely acetylated KSM (m/z 380.16 [M+H]) to produce 2'*N*-acetyl-kasugamycin (Ac-KSM; m/z 422.38 [M+H]). Consistent with the *in vivo* analysis, KasF partially acetylated KSM (m/z 380.10 [M+H]) to form Ac-KSM (m/z 422.07 [M+H]) (Figure 4J–M). As a result, KasH is the main self-resistance enzyme in the biosynthesis of KSM, but *KasF* may play a supportive role in the overall resistance system. Additionally, both KasF and KasH that are unable to acetylate the generally used aminoglycoside antibiotics (Figure 4D–I) suggested that the two enzymes are a pair of resistance enzymes specific to KSM, the latter stronger than the former in terms of antimicrobial effectiveness. The specificity of KasF and KasH is due likely to their regioselectivity on KSM because it is an atypical aminoglycoside antibiotic, thereby incapable of acetylating other aminoglycosides.

Isothermal titration calorimetry (ITC) was used to quantify the binding affinity of KasH versus CoA ($K_d = 96.1 \mu\text{M}$), AcCoA ($K_d = 160.7 \mu\text{M}$), and KSM ($K_d = 56.1 \mu\text{M}$). Among these binding affinity parameters, KasH and KSM concentrations are 2.9- and 1.7-fold higher than AcCoA and CoA, respectively (Figure S17 and Table S1). Although KasF is capable of partially acetylating KSM, it may not be a direct substrate. In the proposed biosynthetic pathway, KasF catalyzes the first step of reactions by converting UDP-GlcNH₂ to UDP-GlcNAc. To check this proposition, KasF was incubated with 1 mM UDP-GlcNH₂ and 0.5 mM AcCoA at 37 °C for 12 h. We could not observe the formation of UDP-GlcNAc, thus ruling out the possibility that KasF primes the KSM biosynthesis (Figure S18). The origin of UDP-GlcNH₂ or UDP-GlcNAc may be directly from the first metabolism, as they are fundamental metabolites. To test whether KasF carries out the deacetylation reaction in the KSM biosynthesis pathway (given UDP-GlcNAc the precursor, a deacetylase is required but not found in the KSM BGCs), KasF was incubated with 1 mM UDP-GlcNAc and 0.1 mM divalent ion (Zn^{2+}). We found that neither KasF nor KasH was able to catalyze the deacetylation reaction (Figure S19).

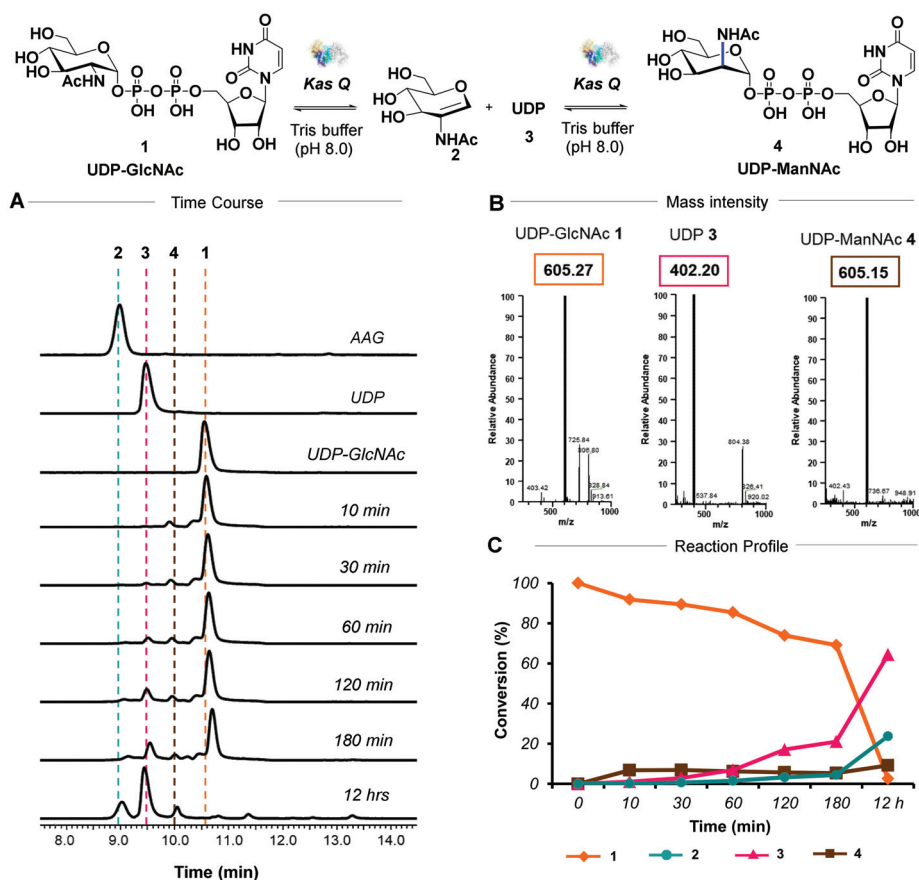


Figure 2. Biochemical investigation of KasQ by HPLC-LTQ-MS. (A) Time course assay for the KasQ-mediated reaction in the presence of UDP-GlcNAc. The assay scheme is shown at the top: 1. UDP-GlcNAc, 2. AAG, 3. UDP, and 4. UDP-ManNAc. (B) The m/z of UDP-GlcNAc, UDP-ManNAc, and UDP for the reaction carried out by KasQ in the presence of UDP-GlcNAc and MgCl_2 for 180 min. (C) The conversion rate of UDP-GlcNAc (orange) to UDP-ManNAc (brown), UDP (pink), and AAG (cyan) over 12 h time course.

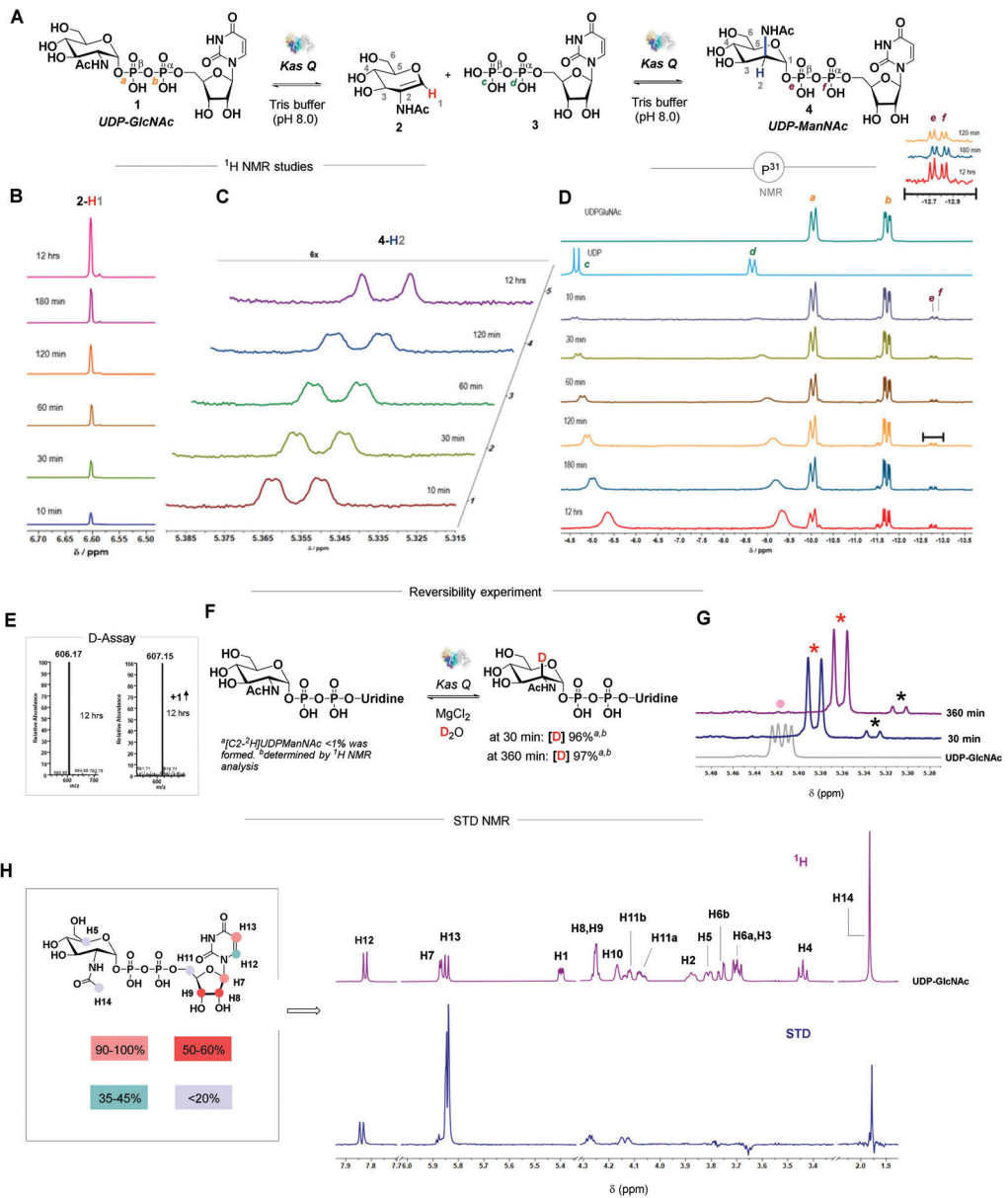


Figure 3. Biochemical investigation of KasQ by NMR and mass spectrometry. (A) Scheme of the KasQ-mediated epimerization reaction. Proton and phosphorous labels are shown in structural formulas. (B) The ¹H NMR stack plot of AAG evolution. (C) Time course ¹H NMR spectra during UDP-ManNAc formation. (D) The ³¹P NMR stack plot of varied time intervals. (E) The deuterium incorporation assay with or without KasQ was incubated with UDP-GlcNAc and MgCl₂ in D₂O. (F,G) Reversibility experiment. The pink circle denotes anomeric protons of UDP-GlcNAc; red and black asterisks are the C2 deuterated UDP-GlcNAc and UDP-ManNAc anomeric protons. (H) ¹H-STD NMR analysis of UDP-GlcNAc in the presence of KasQ and the relative STD effects are shown in appropriate colors. The highest intensity of the STD signal signifies 100%, according to which the other signals were respectively calculated.

Table 4. Thermodynamic parameters of KasQ versus different substrates.

S.No	KasQ with	n	K_d (μM)	ΔG (kcal mol^{-1})	ΔH (kcal mol^{-1})	ΔS ($\text{cal mol}^{-1} \text{K}^{-1}$)
1	AMP	NBD	NBD	NBD	NBD	NBD
2	ADP	NBD	NBD	NBD	NBD	NBD
3	ATP	NBD	NBD	NBD	NBD	NBD
4	GMP	NBD	NBD	NBD	NBD	NBD
5	GDP	NBD	NBD	NBD	NBD	NBD
6	GTP	NBD	NBD	NBD	NBD	NBD
7	TTP	1.1 \pm 0.1	174.5 \pm 20.2	-5.128 \pm 1.221	-7.612 \pm 1.221	-8.33
8	UMP	1.0 \pm 0.0	123.9 \pm 70.9	-13.19 \pm 1.245	-9.254 \pm 1.245	13.2
9	UDP 3	1.0 \pm 0.0	32.2 \pm 6.8	-6.128 \pm 0.5523	-4.130 \pm 0.5523	6.70
10	UTP	1.0 \pm 0.0	71.4 \pm 5.7	-5.645 \pm 1.340	-9.104 \pm 1.340	-11.6
11	UDP-GlcNAc 1	NBD	NBD	NBD	NBD	NBD
12	UDP-GlcNAc/Mg ²⁺	NBD	NBD	NBD	NBD	NBD
13	UDP-GalNAc	1.8 \pm 0.4	334.4 \pm 133.7	-4.742 \pm 1.700	-3.418 \pm 1.700	4.44
14	UDP-Glc	0.5 \pm 0.0	9.5 \pm 0.3	-6.834 \pm 0.0375	-0.3944 \pm 0.0375	21.6
15	TDP-Glc	0.3 \pm 0.0	25.1 \pm 0.2	-6.273 \pm 0.2773	-4.568 \pm 0.2773	5.72
16	GDP-Glc	NBD	NBD	NBD	NBD	NBD
17	UDP-Gal	1.0 \pm 0.2	273.3 \pm 54.6	-4.862 \pm 1.926	-6.636 \pm 1.926	-5.95
18	UDP-GlcA	1.5 \pm 0.2	76.3 \pm 15.2	-5.61 \pm 0.5751	-1.376 \pm 0.5751	14.2
19	GDP-Man	NBD	NBD	NBD	NBD	NBD
20	UDP-GlcNH ₂	NBD	NBD	NBD	NBD	NBD
21	GlcNAc	NBD	NBD	NBD	NBD	NBD
22	GalNAc	NBD	NBD	NBD	NBD	NBD
23	GlcNH ₂	NBD	NBD	NBD	NBD	NBD
24	GlcA	NBD	NBD	NBD	NBD	NBD
25	GalA	NBD	NBD	NBD	NBD	NBD
26	D-Glucose	NBD	NBD	NBD	NBD	NBD
27	D-Mannose	NBD	NBD	NBD	NBD	NBD
28	D-Galactose	NBD	NBD	NBD	NBD	NBD
29	AAG 2	NBD	NBD	NBD	NBD	NBD

NBD: No binding detected.

A number of studies revealed that modified aminoglycoside antibiotics carried encouraging antimicrobial activity to inhibit some human pathogens [29–32]. For example, the enzymatically modified isepamicin (ISP), 6'-N-acetylated ISP analogs, manifested stronger antimicrobial activity but less cytotoxicity than ISP against ISP-resistant Gram-negative pathogens [33]. This fact prompted us to examine KasH for its ability to generate 2-N'-acylated KSM analogs. KasH was examined in the presence of AcCoA, isovaleryl-CoA, β -hydroxybutyryl-CoA, acetoacetyl-CoA, and propionyl-CoA alongside KSM, whereby new 2-N'-acyl substituted KSM analogs were generated (Figure 5). The binding affinity of KasH versus isovaleryl-CoA ($K_d = 199.2 \mu\text{M}$), acetoacetyl-CoA ($K_d = 98.0 \mu\text{M}$), and propionyl-CoA ($K_d = 35.0 \mu\text{M}$) was further determined (Figure S17 and Table S1), indicating that KasH has considerable substrate promiscuity when it comes to forming new analogs.

3.3. Crystal Structure of KasQ in Complex with UDP and UDP-Glc

To better understand the catalytic mechanism of KasQ, we solved crystal structures of KasQ for the wild type (WT) and its complexes with UDP or UDP-Glc in resolutions of 2.44 Å, 2.58 Å, and 2.09 Å, respectively. Concerning the structure in complex with UDP-GlcNAc—the structure that was most wanted—it was not obtainable from all our co-crystallization conditions. Despite this, the structures, not least the one with UDP-Glc, are still in a position to provide a structural basis to help elucidate the mechanism of the epimerization reaction mediated by KasQ. Figures 6A and S20, respectively show the ribbon diagram of the tertiary structure and the topology diagram of the secondary structure of KasQ-WT. In consistency with homodimers in solution, an asymmetric unit contains two monomers colored in rainbow (N-terminal blue, C-terminal red) and gray. Superimposition of these two monomers with an RMSD of 0.86 Å for 317 C α atoms indicated no significant conformational differences. In brief, each monomer consists of two domains (N-terminal and C-terminal domains), in which each subdomain is made of a typical sandwich ($\alpha\beta\alpha$) architecture of a Rossmann fold (Figure 6A). Two fragments marked in dashed lines

(residues 40–45 in the N-terminal domain and residues 184–190 in the C-terminal domain) are missing from the model due to lack of electron density, likely a consequence of structural disorder/flexibility in loop regions. The N-terminal domain is constituted by residues 1–170 that fold into a central seven-strand β -sheet (β 1– β 7) sandwiched by α -helices (α 1– α 7) on each side along with a stand-alone α 16 helix (residues 357–370). The C-terminal domain is formed by residues 201–359 composed of a central six-strand β -sheet (β 8– β 13) sandwiched α -helices (α 9– α 16) on each side. The N-terminal and C-terminal domains are connected by two helices, α 7– α 8 (residues 173–199). The cleft between these two domains provides the substrate binding pocket.

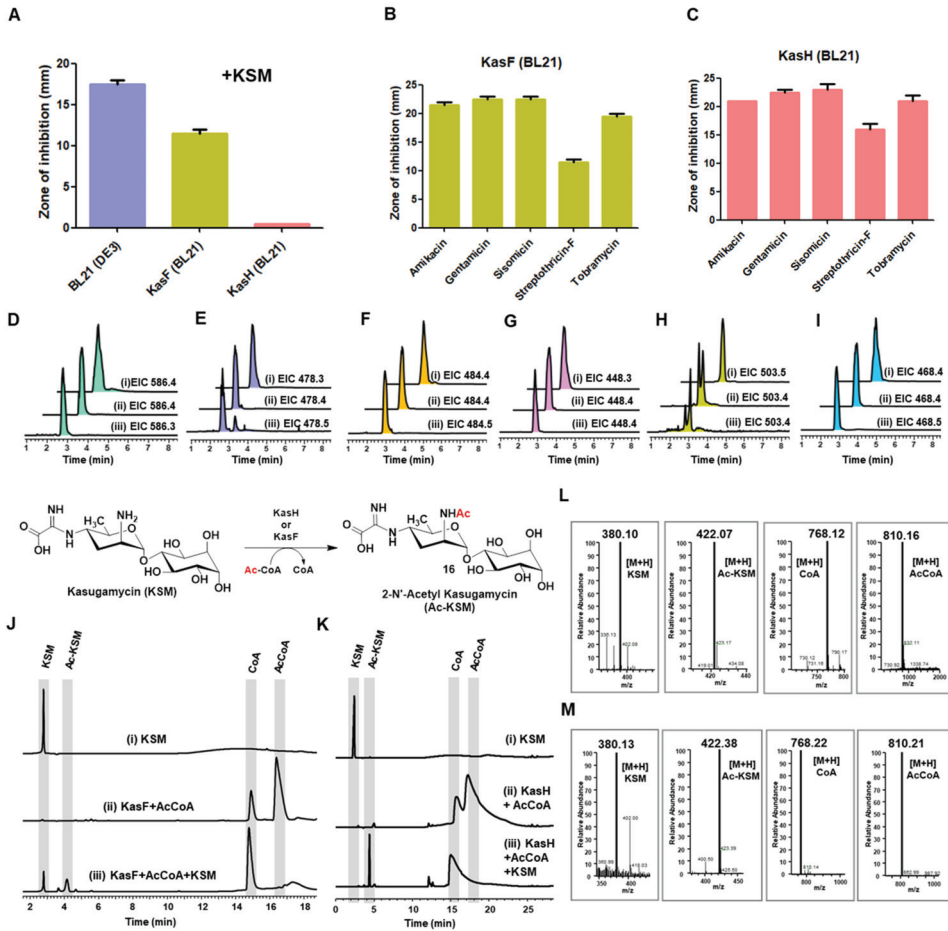


Figure 4. Biochemical characterization of acetyltransferases KasF and KasH. (A) Disc diffusion assay with or without KSM. The *E. coli* BL21 (DE3) strain was used as a control. (B,C) The in vivo resistance activity of KasF and KasH was assayed against amikacin, gentamicin, sisomicin, streptothricin-F, and tobramycin. (D–I) The acetylation reactions of KasF and KasH were examined in the presence of AcCoA and different aminoglycoside antibiotics, (D) amikacin, (E) gentamicin, (F) kanamycin B, (G) sisomicin, (H) streptothricin-F, and (I) tobramycin. The EICs of (i) the antibiotic alone, (ii) KasF with the selected antibiotic and AcCoA, (iii) KasH with the selected antibiotic and AcCoA are displayed. (J,K) The acetylation reactions of KasF and KasH were examined in the presence of KSM and AcCoA, indicating that both KasF and KasH are specific to KSM. (L,M) MS spectra for the substrates and products (in *m/z*) of the KasF- and KasH-mediated reactions.

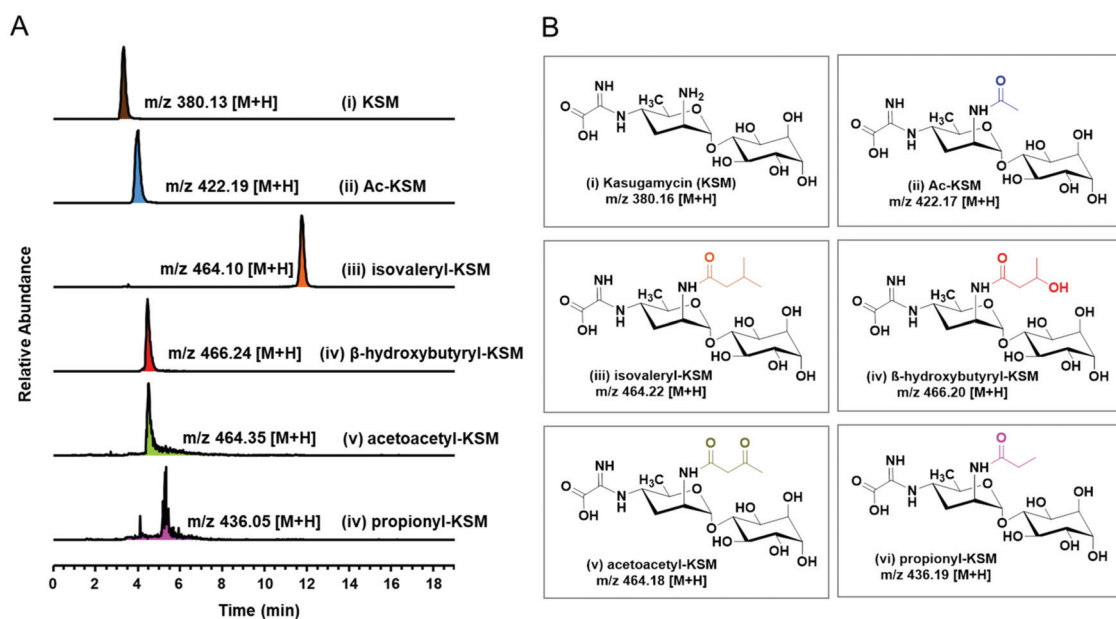


Figure 5. HPLC-LTQ-MS analysis for 2-*N'*-acyl substituted KSM analogs generated using KasH. (A) EIC spectra of (i) KSM at m/z 380.13 [M+H], (ii) Ac-KSM at m/z 422.19 [M+H], (iii) isovaleryl-KSM at m/z 464.10 [M+H], (iv) β -hydroxybutyryl-KSM at m/z 466.24 [M+H], (v) acetoacetyl-KSM at m/z 464.35 [M+H], (vi) propionyl-KSM at m/z 436.05 [M+H]. (B) Chemical structures of 2-*N'*-acyl substituted KSM analogs with calculated m/z [M+H].

As revealed above, UDP or UDP-Glc is bound to its binding site at the interface of the two domains. The superimposition of KasQ-UDP and KasQ-UDP-Glc with an RMSD of 0.29 Å for 332 C α atoms suggested no apparent conformational differences as a result of binding from different ligands (Figure 6B). The electron density of UDP or UDP-Glc is well defined and consistent in the substrate binding site (Figure 6C,D). The UDP binding site is highly conserved among all non-hydrolyzing UDP-GlcNAc 2-epimerases (Figure S21): the guanidino side chain of Arg12 and the backbone of Leu267 are in close contact with the uracil O2 atom, likely due to hydrogen bonding (3.1 Å and 3.4 Å, respectively). The backbone of Leu267 is also in a hydrogen-bonding distance to the O4 atom (3.1 Å) and the N3 atom (2.7 Å) of the uracil base. The two hydroxyl groups of the ribose moiety are associated with Glu292 (2.8 Å and 2.6 Å) by hydrogen bonds. His209 may play a role in stabilizing UDP by interacting with its α -phosphate (3.1 Å) and β -phosphate (2.6 Å). Ser286, Gly287, and Gly289 are three highly conserved residues for molecular recognition, in which Ser286 interacts with α/β phosphate (2.7 Å/3.2 Å, respectively), Gly287 is in contact with the O1/O2 atom of β -phosphate (3.3 Å/3.1 Å, respectively), and Gly289 is associated with the O1 atom of β -phosphate (2.9 Å) (Figure 6C).

In view of the KasQ-UDP-Glc complex, the UDP portion is well defined as it is surrounded by an array of highly conserved residues, His209, Leu267, Ser286, Gly287, and Gly289. The hexose moiety is held in place by a group of highly conserved residues for its recognition and epimerization, except for Arg12, which differs from the corresponding residues in other homologs pointing away from the uracil O2 atom (4.6 Å); the guanidino group of Arg309, which is associated with Glu291 (2.9 Å), is in close proximity to the C2 hydroxyl group (4.1 Å), and the terminal carboxyl group of Asp97 is in close proximity to the C2 atom (3.8 Å). These residues may act as a set of the interlinking acids/bases triggering the elimination/addition reaction for the epimerization of UDP-GlcNAc to UDP-

ManNAc. The C3 hydroxyl group of the hexose moiety is also within hydrogen-bonding distances to both the guanidino group of Arg309 (2.7 Å/2.9 Å) and the carboxyl group of Glu119 (3.3 Å). The C4 hydroxyl group is interacting with both Lys17 and Gln95 through hydrogen bonding (3.5 Å and 3.1 Å, respectively). The C6 hydroxyl group is likewise interacting with the carboxyl and amino groups of Asp97 through hydrogen bonding (2.5 Å and 2.8 Å, respectively). Importantly, the carboxyl group of Asp97 that is located on top of the sugar plane relative to the C2 atom (3.8 Å) likely serves as the general base to deprotonate C2 in the first half of the reaction, yielding AAG and UDP; the Arg309/Glu291 dyad, on the other hand, acts as the general acid, likely protonating AAG to afford UDP-ManNAc, thus completing the epimerization reaction (Figure 6D). Samuel et al. created five mutants of catalysis-related residues K15A, D95Q, E117Q, E131Q, and H213N to evaluate their biochemical importance [34]: they observed that all the mutants can release the AAG intermediate. The activity of mutants D95Q and E131Q was 100-fold slower than that of the wild type. Although non-hydrolyzing UDP-GlcNAc 2-epimerases have been extensively studied, the catalytic residues that engage in the *anti*-elimination and *syn*-addition to form the product remain unclear. On the basis of the KasQ structural complexes, we highlighted the importance of two residues, Q95 and E308, which were mentioned less frequently in all UDP-GlcNAc 2-epimerases reported thus far (Figure S21). To confirm their importance, we prepared four mutants, Q95A, Q95E, E308A and E308Q, and performed biochemical assays by incubating them with UDP-GlcNAc and MgCl₂ at 37 °C for 12 h. For mutants E308A and E308Q, both HPLC and TLC analyses did not show the appearance of the intermediates, thereby confirming their importance in the catalysis (Figure S22). Moreover, given their special and geographic position relative to the AAG intermediate, we propose that Asp97 acts as the active site general base to trigger the elimination reaction, resulting in the formation of UDP and AAG. In contrast, both mutants Q95A and Q95E performed equally well, as did the wild type in terms of biochemical reactions, thus negating their direct participation in the epimerization reactions. To this end, obtaining the UDP-Glc or UDP bound complexes along with the mutagenesis studies allowed us to summarize the catalytic mechanism of KasQ: Asp97 may serve as the first base to abstract the C2 proton from GlcNAc, resulting in the formation of AAG and the neglect of UDP that is stabilized by nearby Arg210. Since the *anti*-elimination and *syn*-addition follow different electron-configuration courses, an oxocarbenium intermediate may be transiently present for buffering the transition state as well as helping change the reaction path. The positively charged oxocarbenium intermediate may be stabilized by the negatively charged UDP nearby [35]. In the UDP-addition course, the Arg309/Glu291 dyad opposite to Asp97 may serve as the general acid to protonate AAG so that UDP-ManNAc is derived in a *syn*-addition manner, completing the epimerization reaction.

3.4. Structural Comparison

The primary sequence and tertiary structural analysis revealed that KasQ is a homolog to many non-hydrolyzing UDP-GlcNAc 2-epimerases in bacteria (Figure S21), for example, 2-epimerase from *E. coli* (PDB entry 1vgv; 47% identity [19]), *Neisseria meningitidis* (PDB entry 6v1c; 44% identity [36]), *Burkholderia vietnamiensis* (PDB entry 5dld; 44% identity), and *Bacillus subtilis* (PDB entry 4fkz; 42% identity). Despite the fact that KasQ exists as dimers in solution as well as asymmetric units, only one UDP-Glc molecule is bound to one protomer of the dimer. The superimposition of the KasQ-UDP-Glc complex with that from *E. coli* (PDB entry 1vgv) shows high structural similarity (RMSD of 1.0 Å for 286 C α), UDP-glucose and UDP-ManNAc well overlapping each other in the active site, suggesting that both substrate-binding environments are comparable (Figure 7A). In light of the residue sequence of the substrate/active site of KasQ, it is highly conserved except for Q95 when aligned against other homologs (Figure 7B). Q95 was found interacting with the C4-OH of UDP-Glc (Figure 6D) in contrast to the histidine (H) counterpart in homologous 2-epimerases, which is at a distance from C4-OH of 4.5 Å. The close-up view out of these active sites suggests that there is adequate space for KasQ to accommodate

UDP-GlcNAc or UDP-ManNAc (Figure S23). Residue R214 of that in *E. coli* is missing due to a lack of electron density (Figure 7C), while both structures fit well (*E. coli* epimerase bound with UDP, PDB entry 1f6d; 47% identity [37]) with an RMSD as low as 2.0 Å for 298 C α (Figure 7D). The UDP binding sites among all the selected epimerases are conserved (Figure 7E) where residues SGG are highly conserved, likely to stabilize UDP by interacting with its α/β -phosphates through hydrogen bonds (Figure 7F).

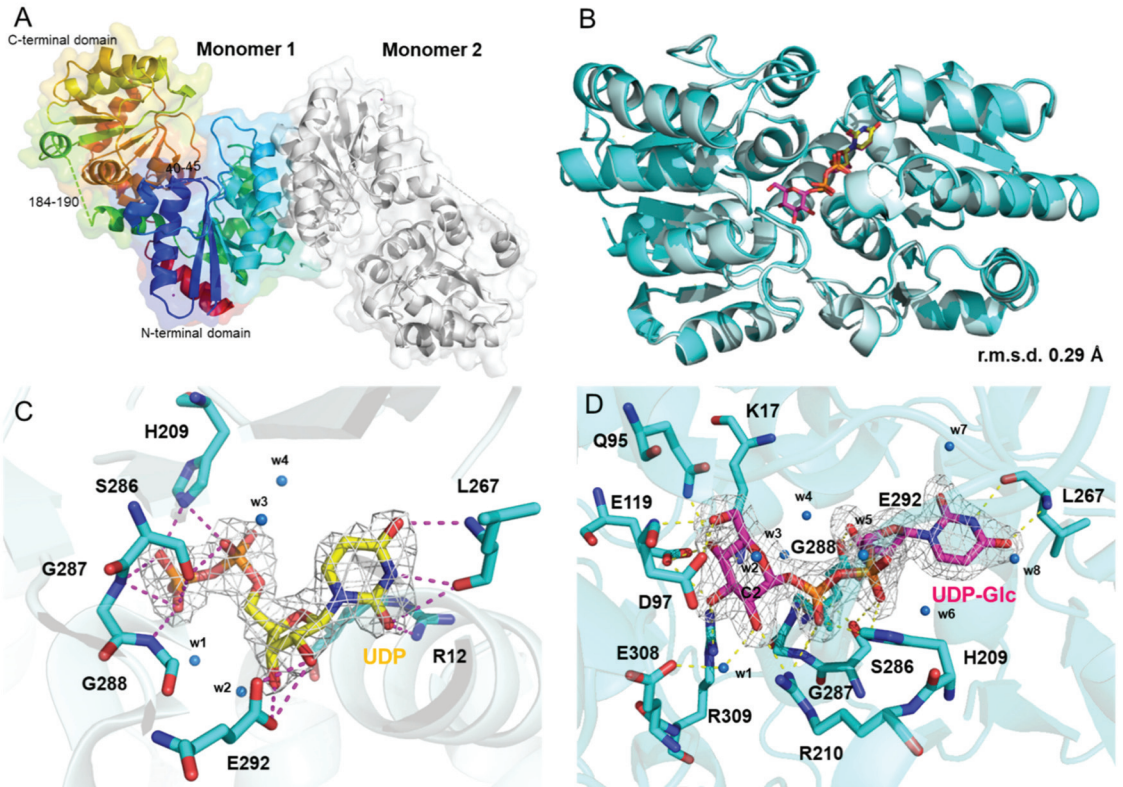


Figure 6. Crystal structures of KasQ in complex with UDP or UDP-Glc. (A) KasQ-WT structure. Monomer 1 is displayed in rainbow colors (N-terminal blue/C-terminal domain in red) and monomer 2 is displayed in gray. The missing residues 40–45 and 184–190 are designated by dashed lines. (B) Superimposition of the KasQ-UDP monomer (pale cyan) with the KasQ-UDP-Glc monomer (cyan) gives an RMSD of 0.29 Å. UDP and UDP-GlcNAc are displayed as yellow and pink sticks, respectively. (C) The UDP model fits well into its $2F_o-F_c$ electron density map (contoured at 1σ). (D) The UDP-Glc model fits well into its $2F_o-F_c$ electron density map (contoured at 1σ).

A sodium ion was observed in coordination with the carbonyl backbone of N-terminal residues Leu25, Asp26, Asp28, and Phe31 (Figure S24). In the KasQ-UDP complex, the carboxyl group of Glu32 makes an additional interaction with the Na^+ ion. Moreover, we found that the C-terminal residues Pro298, Ser250, and Ala352 of a KasQ homolog (PDB entry 1f6d) are associated with a Na^+ ion (Figure S24D). These metal-ion binding sites, however, are ~ 25 Å away from the substrate binding region (Figure S24E), suggesting that they have little or no influences on the substrate-binding and enzymatic activity (Figure S24F).

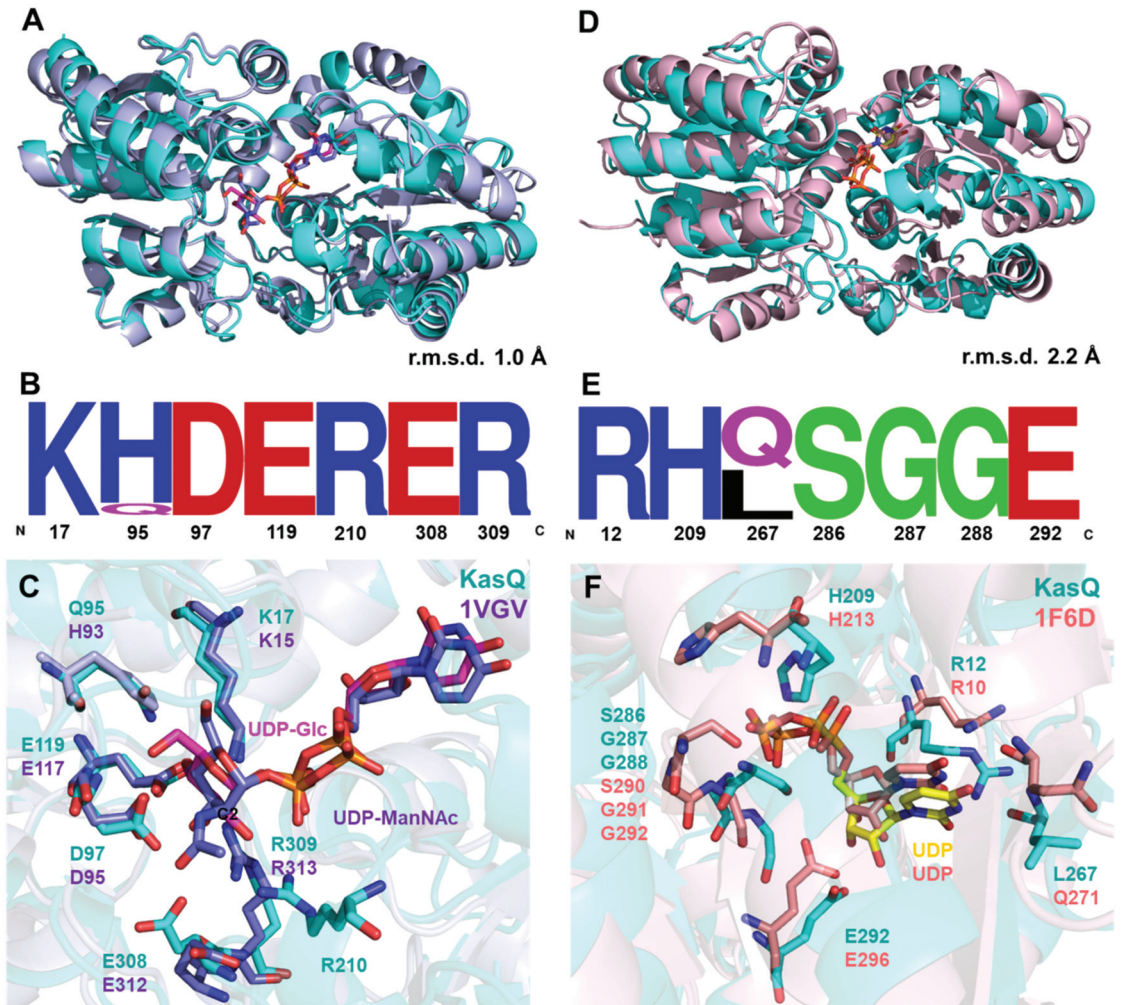


Figure 7. Sequence and structural comparison of KasQ with reported UDP-GlcNAc 2-epimerases. (A) Superimposition of KasQ–UDP-Glc monomer (cyan) with UDP-GlcNAc 2-epimerases of *E. coli* bound with UDP-ManNAc colored blue (PDB entry 1vqv, crystal structure modeled with UDP-ManNAc, mistakenly named UDP-GlcNAc) gives an RMSD of 1.0 Å. UDP-Glc and UDP-GlcNAc are colored as pink and blue sticks, respectively. (B) Sequence logo of sugar binding-site residues amid KasQ homologs. (C) The active site of KasQ–UDP-Glc superimposed with that of *E. coli* bound with UDP-ManNAc. (D) Superimposition of the KasQ–UDP monomer (cyan) with the *E. coli* counterpart bound with UDP (PDB entry 1f6d) gives an RMSD of 2.2 Å. (E) Sequence logo of UDP binding sites amid KasQ homologs. (F) Active sites of KasQ–UDP superimposed with the *E. coli* counterpart bound with UDP.

3.5. KasQ Substrate Specificity

To investigate the substrate specificity, KasQ was assayed against an array of NDP-sugars. In brief, KasQ was incubated with NDP-sugars (UDP-GlcNAc, UDP-GalNAc, UDP-Glc, TDP-Glc, GDP-Glc, and UDP-Gal) in the presence of MgCl₂ at 37 °C for 12 h and then subjected to HPLC analysis. In comparison with standards (both retention time and molecular weight, *m/z*), we concluded that KasQ can only convert UDP-GlcNAc 1 to UDP-

ManNAc 4. The consumption of a considerable amount of UDP-GlcNAc and release of AAG 2 and UDP 3 in solution were observed in a 12 h reaction. The fact is that none of the other NDP-sugars can be hydrolyzed by KasQ, suggesting that UDP-GlcNAc is the only valid substrate (Figure S25). The kinetic parameters for KasQ in the presence of UDP-GlcNAc and $MgCl_2$ were determined: k_{cat} $1.33\ s^{-1}$, K_M 40.28 mM, and $k_{cat}/K_M = 0.032\ s^{-1}mM^{-1}$ (Figure S26 and Table S2). In addition, the dissociation constants (K_d) of KasQ versus nucleosides, (mono/di/tri) phosphates, NDP-sugars, and monosaccharides were examined using ITC, as summarized in Table 4 and Figures S27–S29. Neither UDP-GlcNH₂ that was enzymatically synthesized using the published procedure [38] nor AMP, ADP, ATP, GMP, GDP, or GTP shows detectable binding affinity with KasQ. We nevertheless observed some binding affinity in a micromolar range when KasQ was titrated with UMP ($K_d = 123.9\ \mu M$), UDP ($K_d = 32.2\ \mu M$), UTP ($K_d = 71.4\ \mu M$), and TTP ($K_d = 174.5\ \mu M$) (Table 4 and Figure S27). Of these, the binding affinity of UDP versus KasQ was shown to be 2–5-fold higher than that of the others, suggesting that UDP-sugar is most likely the physiological substrate for KasQ. In contrast, UDP-Glc showed the highest binding affinity ($K_d = 9.5\ \mu M$) in contrast to UDP-GlcNAc, which, for some reason, could not be determined (Table 4 and Figure S28). We speculated that divalent ions (Mg^{2+}) may influence the binding but cannot conclude this from the ITC assay. Interestingly, both mutants Q95A and Q95E showed high binding affinity versus UDP-GlcNAc ($K_d = 45.2\ \mu M$ and $K_d = 14.2\ \mu M$, respectively) comparable to that of WT versus UDP-Glc (Figure S30 and Table S3). In addition, we performed time course assays for KasQ in the presence of UDP-Glc and $MgCl_2$, while we could not observe the formation of 2-hydroxyglucal and UDP-mannose, thereby concluding that UDP-Glc is not a substrate (Figure S31). Given these facts, we summarized that Q95 interacts with the C4 hydroxyl group of UDP-Glc (Figure 6D), while mutants Q95A and Q95E are not able to bind with UDP-Gal (C4-axial hydroxyl group). We propose that Q95 may play a critical role in the control of the reaction rate, directionality, and product release. Our mutagenic study may have shed new light on this subtle regulation in KSM biosynthesis while the actuality may depend on future detailed kinetic and biochemical/biophysical examinations.

3.6. In Vivo Isotope Incorporation Analysis

The origin of the main chemical components of KSM has previously been examined using isotopically labeled sugars, glycine, or ammonia. These results as a whole revealed that glucose or mannose is the precursor of kasugamine, that the D-inositol moiety is derived from *myo*-inositol, and that the glycine imine side chain comes directly from glycine [39–43]. This information, however, is insufficient to shed light on the real roles of KasF, H, and Q in the biosynthesis of KSM. To address the insufficiency, we used *Streptomyces lividans* TK64 harboring pMKBAC08-KAS as a model system to produce KSM, for which the susceptibility of *E. coli* to KSM was gauged by disc diffusion assay to profile its production. The inhibition zone appeared in agar plates on the third day, suggesting that KSM had been produced to a considerable quantity by manifesting a significant inhibition zone against *E. coli* (Figures 8A and S33). Samples collected from the culture medium were subjected to HPLC-TQ-MS (positive mode), whereby the molecular weight of KSM was determined with m/z at 380.1 [M+H] as a reference. To see if KSM directly derived from glucose or glucosamine, we fed three precursors, ¹³C1-D-glucose, ¹³C1-D-glucosamine, and ¹³C1,¹⁵N2-D-glucosamine, to the culture of *Streptomyces lividans* TK64. We found that only ¹³C1-D-glucose is partially incorporated into KSM, as shown by the isotopic profile of KSM with m/z at 380.1 [M+H], 381.2 [M+1+H], and 382.1 [M+2+H], in which the latter two displayed a ratio close to unit, likely as a result of D-glucose that serves as the precursor for both kasugamine and inositol in the KSM biosynthetic pathway (Figures 8B, S1 and S32). Given ¹³C1-D-glucosamine, the isotopic profile is dissimilar to ¹³C1-D-glucose, where it showed a dominant m/z at 381.2 [M+1+H] and a second dominant m/z at 382 [M+2+H] with a ratio close to 2 in contrast to the almost vanished native KSM (m/z at 380.1 [M+H]), suggesting that glucosamine instead of glucose is the main or direct precursor of kasugamine and is readily convertible back to glucose at a high rate, an

alternative source to *myo*-inositol (Figures 8B and S32). Given $^{13}\text{C}_1,^{15}\text{N}_2$ -D-glucosamine, the isotopic profile showed the dominant m/z at 382.2 [M+2+H] and 383 [M+3+H] with a ratio close to unit confirming the above reasoning. D-glucose is an indirect substrate, while glucosamine is the “direct” substrate in terms of utilization efficiency towards incorporation into KSM. On the other hand, given ^{15}N -glycine, the molecular weight of KSM increased by one mass unit (m/z 381.2 [M+1+H]), indicating that glycine is the key precursor for the carboxyformidoyl group at C4-NH₂ of KSM. Although UDP-N-Glc derivatives are the key precursors for KSM, the origin of the C4 amino group was parallelly investigated using ^{15}N -aspartic acid or ^{15}N -glutamic acid. An equal isotopic increment at M+H and M+1+H and a relatively minor extent of M+2+H for KSM were observed, suggesting that both ^{15}N -aspartic acid and ^{15}N -glutamic acid are the C4-NH₂ donor of KSM and a minor C2-NH₂ donor of glucosamine (Figure 8B,C). Based on our bioinformatics analysis, we put forward that KasC, the committed transaminase (28% similarity to PDB entry 5ghg, ω -Transaminase), may transfer the amino group given by either of these two amine donors to the precursor of KSM [44]; KasN, the committed glycine oxidase (42% similarity to fms14), may oxidatively add the glycine to the kasugamine precursor, forming carboxyformimidoyl-kasugamine [45].

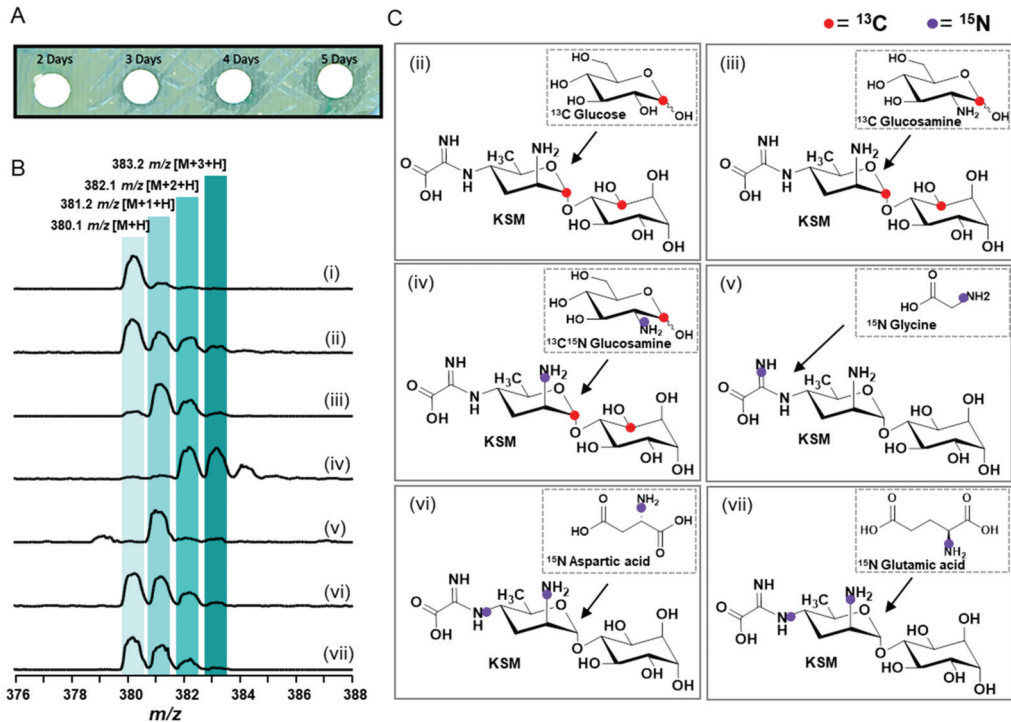


Figure 8. Disc diffusion and in vivo isotope incorporation assay. (A) Disc diffusion assay shows the zone of inhibition (ZOI) determining the optimal course of kasugamycin production against *E. coli*. (B) Isotope incorporation analysis: (i) KSM isolated from the producing strain fed without isotopes, (ii) KSM isolated from the producing strain fed with $^{13}\text{C}_1$ -glucose, (iii) KSM isolated from the producing strain fed with $^{13}\text{C}_1$ -glucosamine, (iv) KSM isolated from the producing strain fed with $^{13}\text{C}_1^{15}\text{N}_2$ -glucosamine, (v) KSM isolated from the producing strain fed with ^{15}N -glycine, (vi) KSM isolated from the producing strain fed with ^{15}N -aspartic acid, and (vii) KSM isolated from the producing strain fed with ^{15}N -glutamic acid. Increments of m/z are colored in light to dark green. (C) Schematic diagram of isotope incorporation in KSM.

4. Conclusions

In summary, KSM is produced by *Streptomyces kasugaensis*, isolated in 1965 [2]. It has been widely used in agriculture because of good activities against a plethora of plant bacterial diseases, for example, to control rice bacterial grain and seedling rot [4]. Beyond this, a number of new findings have highlighted that KSM is a promising drug lead, as it effectively counters some recalcitrant human diseases [5–8]. Unlike other aminoglycosides, KSM is composed of two unusual sugars, a *D*-*chiro*-inositol and a kasugamine with a glycine imine appendage. Whereas KSM has been discovered more than 50 years, its biosynthetic pathway remains still elusive due to lack of biochemical evidence. Based on the previous hypothesis, KasF was proposed as a starter enzyme involved in the formation of UDP-GlcNAc to initiate the biosynthesis of KSM, KasH as a self-resistance enzyme to regulate its biosynthesis, and KasQ as an enzyme standing in the middle of the pathway for the formation of kasugamine. In this study, we took advantage of in vitro biochemical and biophysical analyses alongside in vivo isotope feeding assays to solve these outstanding issues. First, we biochemically characterized the function of KasQ, which indeed is an epimerase converting UDP-GlcNAc to UDP-ManNAc, likely serving as the first step in the KSM biosynthesis. Mechanistically, we made use of NMR, stable isotope labelling, and synthetic AAG to ascertain that KasQ belongs to the un-hydrolyzing 2-epimerase protein family, in which the 2-epimerization reaction is carried out following the *anti*-elimination and *syn*-addition dual mechanisms. Structurally, we determined three crystal structures of KasQ for the wild type and its complex with UDP or UDP-Glc, thus allowing insights into the molecular recognition and catalytic mechanism at the molecular level. KasF was previously proposed as an enzyme that primes the biosynthesis of KSM; our in vivo and in vitro biochemical assays, however, ruled out this possibility. The fact is that UDP-GlcNH₂ cannot be converted to UDP-GlcNAc in the presence of KasF alongside AcCoA. KasF, nevertheless, shares the KSM-inactivation activity to some extent. By contrast, KasH is literally the aminoglycoside-modifying enzyme transferring the acetyl group from AcCoA specific to KSM to form 2-*N'*-acetyl KSM. Finally, the isotope-feeding study confirmed that ¹³C,¹⁵N-glucosamine/UDP-GlcNH₂ rather than glucose/UDP-Glc is the direct precursor in the formation of KSM. To this end, we have addressed several long-standing unresolved issues, which should be conducive toward mapping out the correct KSM biosynthetic pathway. The information garnered should also pave the way for developing novel KSM-based medicines using chemoenzymatic and synthetic biology approaches.

Supplementary Materials: The following supporting information can be downloaded at: <https://www.mdpi.com/article/10.3390/biomedicines10020212/s1>, Figure S1: Previous biosynthetic proposals for kasugamycin (KSM), Figure S2: The proposed biosynthetic pathway of KSM from this study, Figure S3: Protein overexpression and purification for KasQ, KasF and KasH, Figure S4: The mass spectra (in m/z) of UDP-GlcNAc 1, UDP-ManNAc 4 and UDP 3 for the reactions carried out by KasQ in the presence of UDP-GlcNAc and MgCl₂, Figure S5: The determination of the AAG 2 intermediate in time-course enzymatic reactions, Figure S6: Effects of different temperatures on the enzymatic activity of KasQ, Figure S7: The conversion rate of substrates to products, Figure S8: Trapping the intermediate and product formation by ¹H NMR spectroscopy, Figure S9: Determination of deuterated water incorporated into UDP-GlcNAc, Figure S10: The mass spectra of UDP-GlcNAc incubated with D₂O at different time points, Figure S11: The mass spectra of KasQ incubated with UDP-GlcNAc and MgCl₂ in D₂O at different time points, Figure S12: ¹H NMR spectra, Figure S13: The sequence alignment of KasH and KasF, Figure S14: Disc diffusion assay of KasF and KasH with or without KSM, Figure S15: Disc diffusion assay of KasF and KasH with some commonly used aminoglycoside antibiotics, Figure S16: The mass spectra of the substrates and products (in m/z) of the KasF, Figure S17: Isothermal Titration Calorimetry (ITC) analysis, Figure S18: Acetylation assay of KasF with UDP-GlcNH₂ and AcCoA, Figure S19: Deacetylation assay for KasH or KasF with UDP-GlcNAc and Zn²⁺, confirming that both enzymes are lack of the deacetylation activity, Figure S20: Topology diagram of the protein fold of the KasQ protomer, Figure S21: Sequence alignment of KasQ with different UDP-GlcNAc 2-epimerases, Figure S22: Biochemical assay of KasQ mutants E308A and E308Q, Figure S23: The active site and the binding pocket of KasQ, Figure S24: The metal-ion

binding site of KasQ, Figure S25: Enzymatic reactions of KasQ with different NDP sugars, Figure S26: The kinetic curve of KasQ for the epimerization reactions, Figure S27: ITC analyses of KasQ with different nucleosides (mono/di/tri) phosphates, Figure S28: ITC analyses of KasQ with different NDP sugars, Figure S29: ITC analyses of KasQ with different monosaccharides, Figure S30: ITC analyses of KasQ mutants with different NDP sugars, Figure S31: ^1H NMR spectra of KasQ in time course reactions, Figure S32: Relative intensity of isotopes in mass spectra from different labeled sugar donors in order to probe the correct kasugamycin biosynthetic pathway, Figure S33: Disc diffusion test and mass spectrum of KSM, Figure S34: ^1H and ^{13}C NMR spectra, Figure S35: ^1H and ^{13}C NMR spectra, Figure S36: ^1H and ^{13}C NMR spectra, Table S1: Thermodynamic parameters of KasH for its binding affinity with testing ligands, Table S2: Kinetics of KasQ_WT in reaction with UDP-GlcNAc and MgCl_2 , Table S3: Thermodynamic parameters of KasQ mutants in the binding affinity assay.

Author Contributions: Conceptualization, R.R. and T.-L.L.; methodology, R.R., R.S.B., Y.-L.W., Z.-C.W., N.-S.H., K.-H.L. and T.-L.L.; software, R.R., Y.-L.W. and T.-L.L.; validation, all authors.; formal analysis, all authors.; investigation, R.R., R.S.B., Y.-L.W., Z.-C.W., N.-S.H., K.-H.L. and T.-L.L.; resources, T.-L.L.; data curation, R.R., R.S.B., Y.-L.W., Z.-C.W. and T.-L.L.; writing—original draft preparation, R.R. and T.-L.L.; writing—review and editing, all authors.; visualization, R.R., R.S.B., Y.-L.W., Z.-C.W. and T.-L.L.; supervision, T.-L.L.; project administration, R.R. and T.-L.L.; funding acquisition, T.-L.L. All authors have read and agreed to the published version of the manuscript.

Funding: This work was supported by funds from the Ministry of Science and Technology (MOST), Taiwan (MOST-108-2113-M-001-021-MY3 and MOST 110-0210-01-22-02) and Academia Sinica (AS-KPQ-109-BioMed, 109-0210-01-18-02 and AS-IA-109-L06).

Institutional Review Board Statement: Not applicable.

Informed Consent Statement: Not applicable.

Data Availability Statement: All the data described in this article can be found in the text and supplementary information; protein data bank (PDB) ID: 7VYY, 7VZA and 7VZ6.

Acknowledgments: We would like to acknowledge National Synchrotron Radiation Research Center (NSRRC), a national user facility supported by MOST of Taiwan, ROC. We thank NSRRC for beam time allocations at beam lines 13B, 05A, and 15A.

Conflicts of Interest: The authors declare no conflict of interest.

References

- Ikekawa, T.; Umezawa, H.; Iitaka, Y. The structure of kasugamycin hydrobromide by x-ray crystallographic analysis. *J. Antibiot.* **1966**, *19*, 49–50.
- Umezawa, H.; Hamada, M.; Suhara, Y.; Hashimoto, T.; Ikekawa, T. Kasugamycin, a new antibiotic. *Antimicrob. Agents Chemother.* **1965**, *5*, 753–757. [PubMed]
- Schuwirth, B.S.; Day, J.M.; Hau, C.W.; Janssen, G.R.; Dahlberg, A.E.; Cate, J.H.; Vila-Sanjurjo, A. Structural analysis of kasugamycin inhibition of translation. *Nat. Struct. Mol. Biol.* **2006**, *13*, 879–886. [CrossRef] [PubMed]
- Ishiyama, T.; Hara, I.; Matsuoka, M.; Sato, K.; Shimada, S.; Izawa, R.; Hashimoto, T.; Hamada, M.; Okami, Y.; Takeuchi, T.; et al. Studies on the preventive effect of kasugamycin on rice blast. *J. Antibiot.* **1965**, *18*, 115–119.
- Chaudhuri, S.; Li, L.; Zimmerman, M.; Chen, Y.; Chen, Y.X.; Toosky, M.N.; Gardner, M.; Pan, M.; Li, Y.Y.; Kawaji, Q.; et al. Kasugamycin potentiates rifampicin and limits emergence of resistance in *Mycobacterium tuberculosis* by specifically decreasing mycobacterial mistranslation. *elife* **2018**, *7*, e36782. [CrossRef] [PubMed]
- Gopinath, S.; Kim, M.V.; Rakib, T.; Wong, P.W.; van Zandt, M.; Barry, N.A.; Kaisho, T.; Goodman, A.L.; Iwasaki, A. Topical application of aminoglycoside antibiotics enhances host resistance to viral infections in a microbiota-independent manner. *Nat. Microbiol.* **2018**, *3*, 611–621. [CrossRef]
- Tomar, P.P.S.; Krugliak, M.; Arkin, I.T. Blockers of the SARS-CoV-2 3a Channel Identified by Targeted Drug Repurposing. *Viruses* **2021**, *13*, 532. [CrossRef]
- Kamle, S.; Ma, B.; He, C.H.; Akosman, B.; Zhou, Y.; Lee, C.M.; El-Deiry, W.S.; Huntington, K.; Liang, O.; Machan, J.T.; et al. Chitinase 3-like-1 is a therapeutic target that mediates the effects of aging in COVID-19. *JCI Insight* **2021**, *6*, e148749. [CrossRef] [PubMed]
- Flatt, P.M.; Mahmud, T. Biosynthesis of aminocyclitol-aminoglycoside antibiotics and related compounds. *Nat. Prod. Rep.* **2007**, *24*, 358–392. [CrossRef] [PubMed]

10. Ikeno, S.; Aoki, D.; Hamada, M.; Hori, M.; Tsuchiya, K.S. DNA sequencing and transcriptional analysis of the kasugamycin biosynthetic gene cluster from *Streptomyces kasugaensis* M338-M1. *J. Antibiot.* **2006**, *59*, 18–28. [CrossRef]
11. Kasuga, K.; Sasaki, A.; Matsuo, T.; Yamamoto, C.; Minato, Y.; Kuwahara, N.; Fujii, C.; Kobayashi, M.; Agematu, H.; Tamura, T.; et al. Heterologous production of kasugamycin, an aminoglycoside antibiotic from *Streptomyces kasugaensis*, in *Streptomyces lividans* and *Rhodococcus erythropolis* L-88 by constitutive expression of the biosynthetic gene cluster. *Appl. Microbiol. Biotechnol.* **2017**, *101*, 4259–4268. [CrossRef] [PubMed]
12. Ikeno, S.; Tsuji, T.; Higashide, K.; Kinoshita, N.; Hamada, M.; Hori, M. A 7.6 kb DNA region from *Streptomyces kasugaensis* M338-M1 includes some genes responsible for kasugamycin biosynthesis. *J. Antibiot.* **1998**, *51*, 341–352. [CrossRef]
13. Kudo, F. 2.22—Biosynthesis of Aminoglycoside Antibiotics. In *Comprehensive Natural Products III*; Liu, H.-W., Begley, T.P., Eds.; Elsevier: Oxford, UK, 2020; pp. 588–612. [CrossRef]
14. Morgan, P.M.; Sala, R.F.; Tanner, M.E. Eliminations in the Reactions Catalyzed by UDP-N-Acetylglucosamine 2-Epimerase. *J. Am. Chem. Soc.* **1997**, *119*, 10269–10277. [CrossRef]
15. Swartley, J.S.; Liu, L.J.; Miller, Y.K.; Martin, L.E.; Edupuganti, S.; Stephens, D.S. Characterization of the gene cassette required for biosynthesis of the (α 1 \rightarrow 6)-linked N-acetyl-D-mannosamine-1-phosphate capsule of serogroup A *Neisseria meningitidis*. *J. Bacteriol.* **1998**, *180*, 1533–1539. [CrossRef]
16. Zhang, L.; Muthana, M.M.; Yu, H.; McArthur, J.B.; Qu, J.; Chen, X. Characterizing non-hydrolyzing *Neisseria meningitidis* serogroup A UDP-N-acetylglucosamine (UDP-GlcNAc) 2-epimerase using UDP-N-acetylmannosamine (UDP-ManNAc) and derivatives. *Carbohydr. Res.* **2016**, *419*, 18–28. [CrossRef]
17. Otwinowski, Z.; Minor, W. Processing of X-ray diffraction data collected in oscillation mode. *Methods Enzymol.* **1997**, *276*, 307–326.
18. McCoy, A.J.; Grosse-Kunstleve, R.W.; Adams, P.D.; Winn, M.D.; Storoni, L.C.; Read, R.J. Phaser crystallographic software. *J. Appl. Crystallogr.* **2007**, *40*, 658–674. [CrossRef] [PubMed]
19. Badger, J.; Sauder, J.M.; Adams, J.M.; Antonysamy, S.; Bain, K.; Bergseid, M.G.; Buchanan, S.G.; Buchanan, M.D.; Batiyenko, Y.; Christopher, J.A.; et al. Structural analysis of a set of proteins resulting from a bacterial genomics project. *Proteins* **2005**, *60*, 787–796. [CrossRef] [PubMed]
20. Vagin, A.A.; Steiner, R.A.; Lebedev, A.A.; Potterton, L.; McNicholas, S.; Long, F.; Murshudov, G.N. REFMAC5 dictionary: Organization of prior chemical knowledge and guidelines for its use. *Acta Crystallogr. Sect. D Biol. Crystallogr.* **2004**, *60*, 2184–2195. [CrossRef] [PubMed]
21. Emsley, P.; Lohkamp, B.; Scott, W.G.; Cowtan, K. Features and development of Coot. *Acta Crystallogr. Sect. D Biol. Crystallogr.* **2010**, *66*, 486–501. [CrossRef] [PubMed]
22. Afonine, P.V.; Grosse-Kunstleve, R.W.; Echols, N.; Headd, J.J.; Moriarty, N.W.; Mustyakimov, M.; Terwilliger, T.C.; Urzhumtsev, A.; Zwart, P.H.; Adams, P.D. Towards automated crystallographic structure refinement with phenix.refine. *Acta Crystallogr. Sect. D Biol. Crystallogr.* **2012**, *68*, 352–367. [CrossRef]
23. DeLano, W.L. The PyMOL Molecular Graphics System. 2002. Available online: <http://www.pymol.org> (accessed on 18 November 2021).
24. Horbal, L.; Fedorenko, V.; Luzhetskyy, A. Novel and tightly regulated resorcinol and cumate-inducible expression systems for *Streptomyces* and other actinobacteria. *Appl. Microbiol. Biot.* **2014**, *98*, 8641–8655. [CrossRef] [PubMed]
25. Kieser, T.; Hopwood, D.A. Genetic Manipulation of *Streptomyces*—Integrating Vectors and Gene Replacement. *Methods Enzymol.* **1991**, *204*, 430–458.
26. Robert, X.; Gouet, P. Deciphering key features in protein structures with the new ENDscript server. *Nucleic Acids Res.* **2014**, *42*, W320–W324. [CrossRef] [PubMed]
27. Crooks, G.E.; Hon, G.; Chandonia, J.M.; Brenner, S.E. WebLogo: A sequence logo generator. *Genome Res.* **2004**, *14*, 1188–1190. [CrossRef] [PubMed]
28. Salo, W.L. The incorporation of tritium from tritium-enriched water into UDP-N-Acetylglucosamine and UDP-N-Acetyl Mannosamine catalyzed by UDP-N-Acetylglucosamine 2-Epimerase from *Escherichia coli*. *Biochim. Biophys. Acta (BBA) Enzymol.* **1976**, *452*, 625–628. [CrossRef]
29. Bellucci, M.C.; Volontero, A. Aminoglycosides: From Antibiotics to Building Blocks for the Synthesis and Development of Gene Delivery Vehicles. *Antibiotics* **2020**, *9*, 504. [CrossRef] [PubMed]
30. Litovchick, A.; Lapidot, A.; Eisenstein, M.; Kalinkovich, A.; Borkow, G. Neomycin B—Arginine Conjugate, a Novel HIV-1 Tat Antagonist: Synthesis and Anti-HIV Activities. *Biochemistry* **2001**, *40*, 15612–15623. [CrossRef]
31. Llewellyn, N.M.; Spencer, J.B. Chemoenzymatic acylation of aminoglycoside antibiotics. *Chem. Commun.* **2008**, *32*, 3786–3788. [CrossRef] [PubMed]
32. Thamban Chandrika, N.; Garneau-Tsodikova, S. Comprehensive review of chemical strategies for the preparation of new aminoglycosides and their biological activities. *Chem. Soc. Rev.* **2018**, *47*, 1189–1249. [CrossRef]
33. Ban, Y.H.; Song, M.C.; Kim, H.J.; Lee, H.; Wi, J.B.; Park, J.W.; Lee, D.G.; Yoon, Y.J. Development of 6'-N-Acylated Isepamicin Analogs with Improved Antibacterial Activity Against Isepamicin-Resistant Pathogens. *Biomolecules* **2020**, *10*, 893. [CrossRef] [PubMed]
34. Samuel, J.; Tanner, M.E. Active site mutants of the “non-hydrolyzing” UDP-N-acetylglucosamine 2-epimerase from *Escherichia coli*. *Biochim. Biophys. Acta* **2004**, *1700*, 85–91. [CrossRef] [PubMed]

35. Whitworth, G.E.; Macauley, M.S.; Stubbs, K.A.; Dennis, R.J.; Taylor, E.J.; Davies, G.J.; Greig, I.R.; Vocadlo, D.J. Analysis of PUGNAc and NAG-thiazoline as transition state analogues for human O-GlcNAcase: Mechanistic and structural insights into inhibitor selectivity and transition state poise. *J. Am. Chem. Soc.* **2007**, *129*, 635–644. [CrossRef]
36. Hurlburt, N.K.; Guan, J.; Ong, H.; Yu, H.; Chen, X.; Fisher, A.J. Structural characterization of a nonhydrolyzing UDP-GlcNAc 2-epimerase from *Neisseria meningitidis* serogroup A. *Acta Crystallogr. Sect. F Struct. Biol. Commun.* **2020**, *76*, 557–567. [CrossRef] [PubMed]
37. Campbell, R.E.; Mosimann, S.C.; Tanner, M.E.; Strynadka, N.C. The structure of UDP-N-acetylglucosamine 2-epimerase reveals homology to phosphoglycosyl transferases. *Biochemistry* **2000**, *39*, 14993–15001. [CrossRef]
38. Huang, C.M.; Lyu, S.Y.; Lin, K.H.; Chen, C.L.; Chen, M.H.; Shih, H.W.; Hsu, N.S.; Lo, I.W.; Wang, Y.L.; Li, Y.S.; et al. Teicoplanin Reprogrammed with the N-Acyl-Glucosamine Pharmacophore at the Penultimate Residue of Aglycone Acquires Broad-Spectrum Antimicrobial Activities Effectively Killing Gram-Positive and -Negative Pathogens. *ACS Infect. Dis.* **2019**, *5*, 430–442. [CrossRef]
39. Fukagawa, Y.; Sawa, T.; Takeuchi, T.; Umezawa, H. Studies on biosynthesis of kasugamycin. I. Biosynthesis of kasugamycin and the kasugamine moiety. *J. Antibiot.* **1968**, *21*, 50–54. [CrossRef]
40. Fukagawa, Y.; Sawa, T.; Takeuchi, T.; Umezawa, H. Biosynthesis of kasugamycin. II. Biosynthesis of the two-carbon-side chain of kasugamycin. *J. Antibiot.* **1968**, *21*, 182–184. [CrossRef]
41. Fukagawa, Y.; Sawa, T.; Takeuchi, T.; Umezawa, H. Studies on biosynthesis of kasugamycin. 3. Biosynthesis of the d-inositol moiety. *J. Antibiot.* **1968**, *21*, 185–188. [CrossRef] [PubMed]
42. Sawa, T.; Fukagawa, Y.; Homma, I.; Takeuchi, T.; Umezawa, H. Studies on biosynthesis of kasugamycin. VI. Some relationships between the incorporation of ¹⁴C-compounds and the production of kasugamycin. *J. Antibiot.* **1968**, *21*, 413–420. [CrossRef] [PubMed]
43. Fukagawa, Y.; Sawa, T.; Homma, I.; Takeuchi, T.; Umezawa, H. Studies on biosynthesis of kasugamycin. V. Biosynthesis of the amidine group. *J. Antibiot.* **1968**, *21*, 410–412. [CrossRef] [PubMed]
44. Han, S.-W.; Kim, J.; Cho, H.-S.; Shin, J.-S. Active Site Engineering of ω -Transaminase Guided by Docking Orientation Analysis and Virtual Activity Screening. *ACS Catal.* **2017**, *7*, 3752–3762. [CrossRef]
45. Dairi, T.; Yamaguchi, K.; Hasegawa, M. N-formimidoyl fortimicin A synthase, a unique oxidase involved in fortimicin A biosynthesis: Purification, characterization and gene cloning. *Mol. Gen. Genet. MGG* **1992**, *236*, 49–59. [CrossRef] [PubMed]



Article

Optimized Synthesis of New N-Mustards Based on 2-Mercaptobenzoxazole Derivatives with Antitumor Activity

Corina Cheptea ¹, Valeriu Sunel ², Ana Cezarina Morosanu ³, Dan Gheorghe Dimitriu ^{3,*}, Mihaela Maria Dulcescu-Oprea ⁴, Mihai-Daniel Angheluta ⁵, Mihaela Miron ⁶, Cristina Delia Nechifor ⁷, Dana Ortansa Dorohoi ³ and Razvan Nicolae Malancus ⁸

- ¹ Department of Biomedical Sciences, Faculty of Biomedical Engineering, "Grigore T. Popa" University of Medicine and Pharmacy, 700115 Iasi, Romania; corina.cheptea@umfiasi.ro
 - ² Faculty of Chemistry, Alexandru Ioan Cuza University, 700506 Iasi, Romania; vsunel@uaic.ro
 - ³ Faculty of Physics, Alexandru Ioan Cuza University, 700506 Iasi, Romania; cezarina_morosanu@yahoo.com (A.C.M.); ddorohoi@uaic.ro (D.O.D.)
 - ⁴ Regional Institute of Oncology, 700483 Iasi, Romania; opreamihaelamaria@yahoo.com
 - ⁵ Faculty of Medicine, "Tuliu Hateganu" University of Medicine and Pharmacy, 400012 Cluj-Napoca, Romania; mihai.daniel.angheluta@gmail.com
 - ⁶ Faculty of Medicine, "Grigore T. Popa" University of Medicine and Pharmacy, 700115 Iasi, Romania; mihaela-miron@email.umfiasi.ro
 - ⁷ Department of Physics, Faculty of Machine Manufacturing and Industrial Management, 700050 Iasi, Romania; cd13_nechifor@yahoo.com
 - ⁸ Department of Physiology and Pathophysiology, Faculty of Veterinary Medicine, "Ion Ionescu de la Brad" University of Agricultural Sciences and Veterinary Medicine, 700490 Iasi, Romania; razvanmalancus@uaiasi.ro
- * Correspondence: dimitriu@uaic.ro; Tel.: +40-232-201-183

Citation: Cheptea, C.; Sunel, V.; Morosanu, A.C.; Dimitriu, D.G.; Dulcescu-Oprea, M.M.; Angheluta, M.-D.; Miron, M.; Nechifor, C.D.; Dorohoi, D.O.; Malancus, R.N. Optimized Synthesis of New N-Mustards Based on 2-Mercaptobenzoxazole Derivatives with Antitumor Activity. *Biomedicines* **2021**, *9*, 476. <https://doi.org/10.3390/biomedicines9050476>

Academic Editors: Leonardo Caputo, Laura Quintieri and Orazio Nicolotti

Received: 18 March 2021

Accepted: 23 April 2021

Published: 26 April 2021

Publisher's Note: MDPI stays neutral with regard to jurisdictional claims in published maps and institutional affiliations.



Copyright: © 2021 by the authors. Licensee MDPI, Basel, Switzerland. This article is an open access article distributed under the terms and conditions of the Creative Commons Attribution (CC BY) license (<https://creativecommons.org/licenses/by/4.0/>).

Abstract: New di-(β -chloroethyl)-amides of some acids derived from 2-mercaptobenzoxazole were prepared by reaction of the corresponding pivalic mixed anhydrides with di-(β -chloroethyl)-amine. A study regarding the optimization of the chemical reactions was made for the case of di-(β -chloroethyl)-amines. The quantum chemical analysis by Spartan'14 was made in order to establish the most stable configuration of the ground electronic states for the obtained chemical structures and some physico-chemical parameters of N-mustards reported in this paper. Mercaptobenzoxazoles substituted in the side chain with the cytotoxic group show antitumor activity and they inhibit *Ehrlich Ascites* in an appreciable proportion compared to the drug I.O.B.-82, as our studies evidenced.

Keywords: 2-mercaptobenzoxazole; N-mustards; anti-inflammatory activity

1. Introduction

Cancer can be considered one of the most pressing concerns of research in medicine, chemotherapy, phytochemistry, and biology. Chemotherapy alone or in combination with radio-immunosurgical treatment is the major strategy in the fight against cancer.

In addition to drugs that support the current possibilities of clinical treatment, the range of antitumor compounds is constantly growing [1–10].

However, there are some drawbacks in the administration of various chemicals used as cytostatic drugs. First, their poor selectivity towards cancer cells, they also act on normal cells and are, therefore, toxic for the body. Second, there are concerns about the installation of the resistance of malignant tumors against the used drugs [11]. Nowadays, the most active and widely used class of cytostatics is that of alkylating substances. The cytostatics containing the di-(β -chloroethyl)-amine group in their structure have the widest utility.

When the active group is attached to a radical of an aliphatic hydrocarbon, those N-mustards have a reduced selective action against cancer cells and a high toxicity to the normal cells [12].

N-mustards chemotherapy has taken a step forward in the use of aromatic and heterocyclic di-(β -chloroethyl)-amines. Their lower toxicity is due to the action of the aromatic or heterocyclic support, which causes a decrease in the basicity of the nitrogen atoms and the rate of alkylation, respectively. The main mode of action of di-(β -chloroethyl)-amines consists in the possibility of an intramolecular cyclization with the formation of an immonium cation consisting of an ethylene ring of three atoms, which, being unstable, easily breaks and can react through carbon as an alkylating agent for substances possessing active groups: NH_2 , SH , and so forth.

It is assumed that, through the alkylating group, the N-mustards bind to the active groups NH_2 , SH , and so forth, from two protein macromolecules, nucleoproteins, deoxyribonucleic acids that participate in the multiplication process of the neoplastic cells and, by forming cross-links, forms a bridge between two nucleoprotein macromolecules or protein molecules and enzymes (cross-linking), preventing them from participating in accelerated biosynthesis, stopping the anarchic division of malignant cells [13].

The specialized literature offers synthesis techniques for some N-mustards in which, by varying the support of the cytotoxic group, alkylated substances with advantageous chemotherapeutic indices and lower toxicity were obtained [4,5,13–18].

Benzoxazole and its derivatives constitute an important class of compounds that possess a wide range of pharmacological properties [19–28]. In addition, some of the benzoxazoles also show cytotoxic activity against malignant cells [29,30].

The aim of the present study is to propose new N-mustard compounds for biomedical applications in cancer therapy. As new compounds, they are studied both for the optimization of their obtaining reactions and for establishing some characteristics based on quantum mechanical analysis. Their very low toxicity and the results provided after testing on experimental animals recommend them as potential candidates for antitumor drugs development.

2. Materials and Methods

The chemical reactants were provided by Merck Company (Darmstadt, Germany) and Fluka (Darmstadt, Germany) and used without any purification.

The purity of the obtained substances was checked by quantitative elemental analysis, as well as Fourier-transform infrared (FT-IR) and nuclear magnetic resonance (NMR) spectroscopy. Quantitative elemental analysis was performed by using the Exeter Analytical CE 440 (Exeter Analytical UK Ltd., Coventry, UK). BRUKER Tensor-27 FT-IR (ATR) spectrophotometer (Bruker Optik GmbH, Ettlingen, Germany) was used to record the FT-IR spectra. ^1H -NMR spectra (DMSO-d_6 , 400 MHz) were recorded using a BRUKER ARX 400 spectrometer (Bruker BioSpin GmbH, Rheinstetten, Germany) equipped with 5 mm QNP $^1\text{H}/^{13}\text{C}/^{31}\text{P}/^{19}\text{F}$ samples and Silicon Graphics INDIGO² workstation (Silicon Graphics, Inc., Mountain View, CA, USA).

Statistical models based on the factorial design [31–33] were applied to establish the best conditions in which the reaction rates can be maximized. To decide the situations for which the reaction yield does not depend on a given variable, the Student's *t*-test [32] was applied.

The quantum mechanical analysis was performed by the help of Spartan'14 software (Wavefunction, Inc., Irvine, CA, USA) [34,35], using the density functional method (Density Functional EDF2, 6-31 G*).

The acute toxicity was established by evaluation of produced mortality. The toxicity degree indicates the maximum bearable dose LD_0 , minimum lethal dose LD_{100} , and the killing dose that kills 50% of the experimental animals LD_{50} , these representing the best clues in the interpretation of the results. In the determination of the acute toxicity of the compounds, mice weighing 20 ± 2 g were used, the experimental groups consisting of 10 animals of both sexes. The substances were administered intraperitoneally as a suspension in Tween 80 (Sigma-Aldrich, Darmstadt, Germany) and the mortality was recorded at 24 h, 48 h, and 7 days. The general condition, the appearance of the hair, the

behavior, the appearance of the tremors, and so forth were observed. The Spearman–Kärber method [36] allowed for the quick determination of LD₅₀ on a small number of animals, using the next calculation method:

$$LD_{50} = LD_{100} - \sum \frac{a \times b}{n} \quad (1)$$

where a is the difference between two successive doses of the administered substance, b is the average number of dead animals in two successive doses, and n is the total number of animals in the group.

To study the cytostatic action, the A₂G mice weighing 25–30 g (± 2 g) were used as experimental animals and *Ascita Ehrlich* has been used as an experimental tumor. The transplantation was performed intraperitoneally. The substances were administered as suspensions in 1% methylcellulose, by single injections on the 7th day after transplantation. The concentrations of 400, 200, and 40 mg/kg body weight were used. The experimental groups included 20 animals for each concentration, while the control groups had 10 tumored animals. The inhibition was calculated according to the methods from the literature [37], 7 days after the administration of the substances.

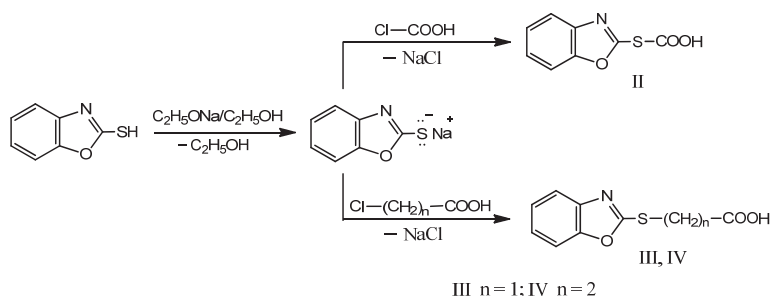
3. Results and Discussion

3.1. Chemical Reactions

The pharmacodynamic action of various chemicals is the result of their interaction with substances from the biological substrate, under the influence of biochemical factors. Consequently, the synthesis and study of a wide range of chemical compounds that contain bioactive groups in the molecule will allow the establishment of a more accurate correlation between structure and biological activity.

Based on the previous research [13–17,38,39], the synthesis of new N mustard derivatives containing the benzoxazole heterocycle and the di-(β -chloroethyl)-amine group in their molecules was made. Thus, it becomes interesting to study the mutual influence of these components that are present in the same molecule, as well as their contribution to the overall biological activity of the substance.

In our research, we aimed to graft the di-(β -chloroethyl)-amine group in different positions on the side chain of the oxazole ring within the 2-mercapto benzoxazole substrate. For this purpose, by the hot dissolution of 2-mercaptobenzoxazole in alcoholic solution containing sodium ethoxide, the sodium salt of 2-mercaptobenzoxazole (I) was obtained, which, treated in water-acetone solution, with chloroformic acid, chloroacetic acid and β -chloropropionic acid, led to benzoxazole-2-yl-mercapto-formic (II), acetic (III), and β -propionic (IV) acids (Scheme 1).



Scheme 1. Synthesis of the benzoxazole-2-yl-mercapto-(II–IV) acids.

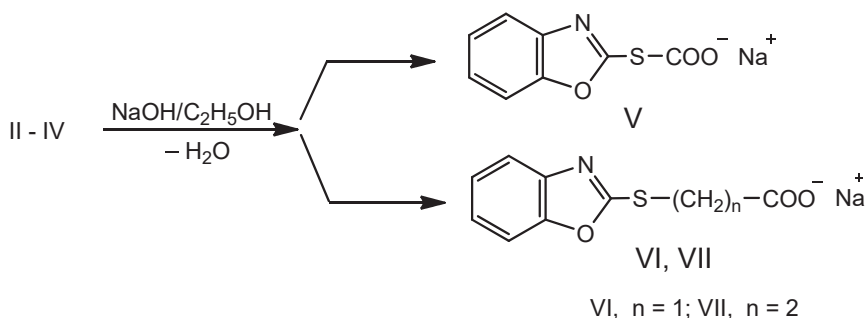
The synthesis of the compounds I–IV was confirmed by elemental and spectral analysis (FT-IR, ¹H-NMR).

The IR spectra of the compound (I) show a characteristic band of the aromatic ring at 3000 cm^{-1} . The band attributed to the valence vibration of the cyclic $\text{C}=\text{N}$ group can be noticed at 1481 cm^{-1} . The $\text{C}-\text{S}$ group gives absorption at 685 cm^{-1} . In the $^1\text{H-NMR}$ spectra, the signal of the aromatic protons appears in the form of a doublet in the range $6.94\text{--}7.47\text{ ppm}$.

The IR spectra of the derivatives (II–IV) show a band at $3356\text{--}3368\text{ cm}^{-1}$ corresponding to the valence vibrations of the COOH group and in the immediate proximity, at $2982\text{--}3060\text{ cm}^{-1}$, an intense absorption band given by the vibrations of the aromatic CH group. The cyclic $\text{C}=\text{N}$ group is highlighted by the band at $1638\text{--}1644\text{ cm}^{-1}$. The bands specific to the valence vibration of the $\text{C}-\text{S}$ connection appear at $720\text{--}752\text{ cm}^{-1}$. The band at $1076\text{--}1080\text{ cm}^{-1}$ is assigned to the cyclic $\text{C}-\text{O}$ group. In the $^1\text{H-NMR}$ spectra of the compounds (II–IV), the proton of the COOH group is highlighted at $11.56\text{--}11.76\text{ ppm}$, while signals of the aromatic protons are present at $7.13\text{--}7.69\text{ ppm}$. For compounds (III) and (IV), due to the nucleophilic nature of the COOH group and the two heteroatoms (N and O) of the benzoxazole heterocycle, the peak values for the protons of the CH_2 group are found close to the protons in the benzene nucleus, namely at $7.6\text{--}7.11\text{ ppm}$.

It is known [13,40–45] that the functionalization of di-(β -chloroethyl)-amine is performed in the presence of an inert solvent, using anhydrides, acid chlorides or other acylating agents. The use of the mixed anhydride method [46] allowed us to functionalize the di-(β -chloroethyl)-amine with acids derived from 2-mercaptobenzoxazole and to obtain, with good yield, some di-(β -chloroethyl)-new benzoxazole amides.

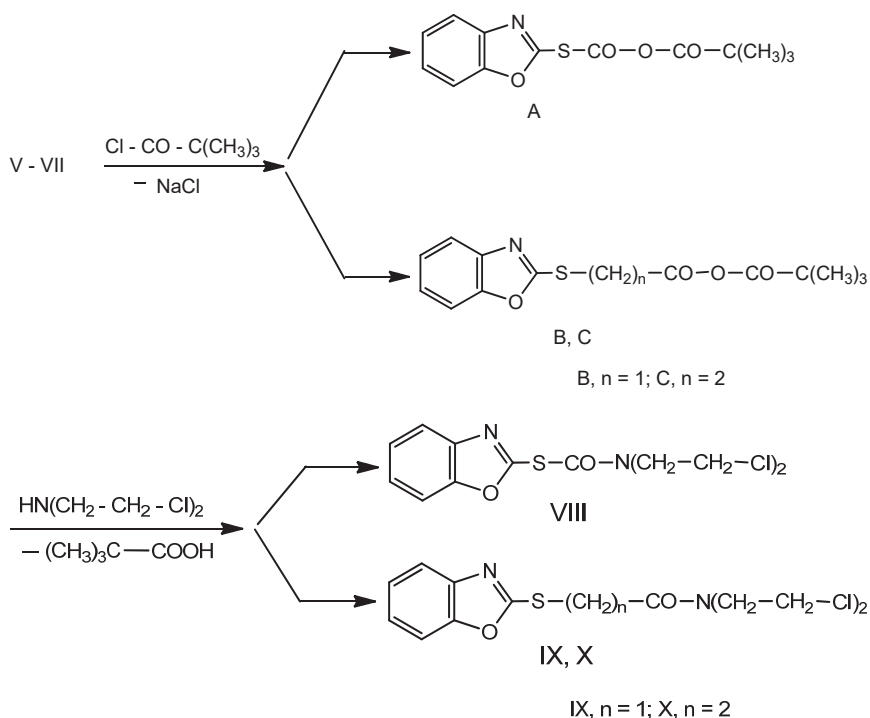
Initially, the sodium salts of the benzoxazole-2-yl-mercapto-formic, acetic, and β -propionic (V–VII) acids were synthesized by refluxing a mixture of acid (II–IV) in alcoholic solution with sodium hydroxide (Scheme 2).



Scheme 2. Synthesis of the sodium salts of benzoxazole-2-yl-mercapto-formic, acetic, and β -propionic acids (V–VII), respectively.

The structure of the compounds V–VII was also investigated by elemental and spectral analysis (FT-IR, $^1\text{H-NMR}$). The IR spectra for the compounds V–VII show absorption at $1608\text{--}1640\text{ cm}^{-1}$, specific to the COO^- group. The $^1\text{H-NMR}$ spectra of the compounds V–VII show the aromatic protons as a doublet at $7.12\text{--}7.68\text{ ppm}$ and the protons of the CH_2 group (in the compounds VI and VII) as a multiplet in the region of $7.05\text{--}7.12\text{ ppm}$.

In order to increase the reactivity of the carboxyl group in sodium salts (V–VII), they were converted by treatment with pivaloyl chloride (trimethylacetic acid chloride) to mixed anhydrides (A–C), capable of reacting rapidly and under mild conditions with di-(β -chloroethyl)-amine. The mixed anhydrides (A–C) are unstable and it is difficult to isolate them, so we chose for their in situ use a dichloromethane solution in which di-(β -chloroethyl)-amine is dissolved as a free base. The reaction mixture was stirred for three hours, filtered, and recrystallized from the anhydrous dioxane precipitate to give N-mustards (VIII–X) (Scheme 3).



Scheme 3. Reactions for obtaining di-(β -chloroethyl)-amides of benzoxazole-2-yl-mercapto-formic (VIII), acetic (IX) and β -propionic (X) acids, respectively.

The structure of the compounds VIII–X was established by elemental and spectral analysis (FT-IR, $^1\text{H-NMR}$). The IR spectra show characteristic bands of the three N-mustards. In the area $3094\text{--}3097\text{ cm}^{-1}$, there are the bands corresponding to the vibration of the aromatic CH group. The C = O amide bond produces a well-highlighted band at 1623 cm^{-1} and 1624 cm^{-1} . The vibration of the C = N group appears at $1490\text{--}1493\text{ cm}^{-1}$. In the IR absorption spectra of N-mustards VIII–X, the C–N stretching frequency was identified at $1283\text{--}1306\text{ cm}^{-1}$, while the C–Cl stretching frequency was identified between $747\text{--}789\text{ cm}^{-1}$. In the $^1\text{H-NMR}$ spectra of the compounds VIII–X, multiplets between $\delta = 3.16\text{--}3.41\text{ ppm}$ (VIII), $\delta = 3.55\text{--}3.57\text{ ppm}$ (IX) and $\delta = 2.55\text{--}3.39\text{ ppm}$, respectively, whose integrated surface satisfactorily coincides, in all cases, with the eight existing protons, were obtained for the protons from the N-mustard group.

3.2. Experimental Procedure

3.2.1. Sodium Salt of the 2-Mercaptobenzoxazole (I)

First, 0.2 mol 2-mercaptobenzoxazole were treated with 0.2 mol metal sodium dissolved in 120 mL anhydrous ethyl alcohol. The obtained solution was refluxed for 90 min on a water bath, then hot filtered to remove any impurities. Excess of alcohol was removed by distillation under reduced pressure, then, after cooling, the precipitate was separated, filtered in vacuum, and then dried.

Light gray solid (32.76 g; yield 95%); M.p. = $298\text{--}300\text{ }^\circ\text{C}$.

Elemental analysis calculated for $\text{C}_7\text{H}_4\text{NOSNa}$ (%): C, 48.55; H, 2.31; N, 8.09; S, 18.49. Found: (%): C, 48.67; H, 2.65; N, 8.31; S, 18.90.

IR; ν_{max} (cm^{-1}): 3000 (CHAr); 1481 (C = N); 685 (C–S).

$^1\text{H-NMR}$ (DMSO- d_6 , 400 MHz), δ (ppm): 6.94–7.14 (d, 2H, CHAr); 7.31–7.47 (d, 2H, CHAr).

3.2.2. Benzoxazole-2-Yl-Mercapto-Formic, Acetic, β -Propionic Acids, Respectively (II–IV)

Next, 0.05 mol of sodium salt of 2-mercaptobenzoxazole (I) were dissolved in 60 mL of water-acetone (1:1) to give a clear gray solution. Then, 0.05 mol of acid (chloroformic, chloroacetic and β -chloropropionic) were added in portions, under vigorous stirring. The reaction mixture was heated at 40–45 °C, stirring for 100–120 min. Towards the end, an abundant white-yellow precipitate appeared instantly. It was filtered by vacuum, dried, and purified by recrystallization from boiling water.

3.2.3. Benzoxazole-2-Yl-Mercapto-Formic Acid (II)

White, crystalline solid (6.24 g; yield, 64%); M.p. = 111–112 °C.

Elemental analysis calculated for C₈H₅NO₃S (%): C, 49.23; H, 2.56; N, 7.17; S, 16.41. Found: (%): C, 49.57; H, 2.78; N, 7.36; S, 16.68.

IR; ν_{\max} (cm⁻¹): 2988 (CHAr); 1644 (C = N); 1076 (C–O); 720 (C–S); 3360 (COOH).

¹H-NMR (DMSO-d₆, 400 MHz), δ (ppm): 7.26–7.39 (d, 2H, CHAr); 7.41–7.69 (d, 2H, CHAr); 11.76 (s, 1 H, COOH).

3.2.4. Benzoxazole-2-YL-Mercapto-Acetic Acid (III)

White, crystalline solid (8.04 g; yield, 77%); M.p. = 113–114 °C.

Elemental analysis calculated for C₉H₇NO₃S (%): C, 51.67; H, 3.34; N, 6.69; S, 15.31. Found: (%): C, 52.02; H, 3.51; N, 6.97; S, 15.64.

IR; ν_{\max} (cm⁻¹): 2982 (CHAr); 1641 (C = N); 1076 (C–O); 760 (C–S); 784 (–CH₂–S); 3356 (COOH).

¹H-NMR (DMSO-d₆, 400 MHz), δ (ppm): 7.06–7.08 (m, 2H, CH₂); 7.13–7.16 (d, 2H, CHAr); 7.24–7.32 (d, 2H, CHAr); 11.60 (s, 1 H, COOH).

3.2.5. Benzoxazole-2-Yl-Mercapto- β -Propionic Acid (IV)

White, crystalline solid (7024 g; yield, 63%); M.p. = 120–122 °C.

Elemental analysis calculated for C₁₀H₉NO₃S (%): C, 53.01; H, 4.03; N, 6.27; S, 14.34. Found: (%): C, 53.35; H, 4.22; N, 6.65; S, 14.61.

IR; ν_{\max} (cm⁻¹): 3060 (CHAr); 1638 (C = N); 1080 (C–O); 752 (C–S); 788 (–CH₂–S); 3360 (COOH).

¹H-NMR (DMSO-d₆, 400 MHz), δ (ppm): 7.09–7.11 (m, 4H, CH₂); 7.27–7.28 (d, 2H, CHAr); 7.60 (d, 2H, CHAr); 11.51 (s, 1 H, COOH).

3.2.6. Sodium Salts of Benzoxazole-2-Yl-Mercapto-Formic, Acetic, β -Propionic Acids (V–VII)

0.02 moles of sodium hydroxide p.a. are introduced into 100 mL of anhydrous ethyl alcohol with 0.02 moles of acid (II–IV). The mixture is stirred until the acids are completely dissolved, then is refluxed for 60 min. The alcoholic solution is filtered and then concentrated by distillation under reduced pressure to a volume of 25–30 mL. The content of the flask still hot is transferred to a crystallizer in which, by cooling, the sodium salt (V–VII) precipitates in the form of crystals in an abundant layer.

3.2.7. Sodium Salt of Benzoxazole-2-Yl-Mercapto-Formic Acid (V)

White, crystalline solid (4.07 g; yield, 94%); M.p. = 188–190 °C.

Elemental analysis calculated for C₈H₄NO₃SNa (%): C, 44.23; H, 1.84; N, 6.45; S, 14.74. Found: (%): C, 44.38; H, 2.07; N, 6.78; S, 15.03.

IR; ν_{\max} (cm⁻¹): 720 (C–S); 1610 (COO⁻).

¹H-NMR (DMSO-d₆, 400 MHz), δ (ppm): 7.25–7.68 (d, 2H, CHAr).

3.2.8. Sodium Salt of Benzoxazole-2-Yl-Mercapto-Acetic Acid (VI)

White, crystalline solid (4.48 g; yield, 97%); M.p. = 206–208 °C.

Elemental analysis calculated for C₉H₆NO₃SNa (%): C, 46.75; H, 2.59; N, 6.06; S, 13.85. Found: (%): C, 46.96; H, 2.77; N, 6.43; S, 14.18.

IR; ν_{\max} (cm^{-1}): 784 (S-CH₂); 1608 (COO⁻).
¹H-NMR (DMSO-d₆, 400 MHz), δ (ppm): 7.05–7.07 (m, 2H, CH₂); 7.12–7.33 (d, 2H, CHAr).

3.2.9. Sodium Salt of Benzoxazole-2-Yl-Mercapto- β -Propionic Acid (VII)

White, crystalline solid (4.50 g; yield, 92%); M.p. = 209–221 °C.
 Elemental analysis calculated for C₁₀H₈NO₃Na (%): C, 48.97; H, 3.26; N, 5.71; S, 13.16. Found: (%): C, 49.28; H, 3.43; N, 6.04; S, 13.34.
 IR; ν_{\max} (cm^{-1}): 790 (–CH₂–S); 1610 (COO⁻).
¹H-NMR (DMSO-d₆, 400 MHz), δ (ppm): 7.08–7.12 (m, 4H, 2CH₂); 7.26–7.62 (d, 2H, CHAr).

3.2.10. Di-(β -Chloroethyl)-Amides of the Benzoxazole-2-Yl-Mercapto-Formic, Acetic, β -Propionic Acids (VIII–X)

First, 0.02 mol of sodium salt (V–VII) were dissolved in 50 mL of anhydrous dichloromethane, cooled to 3–5 °C and, under stirring, 0.02 mol of freshly distilled pivalic chloride was added. The mixed anhydride formed was treated with 0.025 moles of di-(β -chloroethyl)-amine and then the stirring at 10–12 °C for 60 min was continued. Interrupting the cooling, the reaction mixture was stirred for 3 h, filtered, and recrystallized from the anhydrous dioxane precipitate. N-Mustards (VIII–X) were obtained.

3.2.11. Di-(β -Chloroethyl)-Amide of Benzoxazole-2-Yl-Mercapto-Formic Acid (VIII)

Solid white-yellow, crystalline (4.59 g; yield, 72%); M.p. = 195–197 °C.
 Elemental analysis calculated for C₁₂H₁₂N₂O₂SCl₂ (%): C, 45.14; H, 3.76; N, 8.77; S, 10.03; Cl, 22.25. Found: (%): C, 45.31; H, 3.98; N, 8.98; S, 10.37; Cl, 22.56.
 IR; ν_{\max} (cm^{-1}): 3095 (CHAr); 1491 (C = N); 1305 (C–N tertiary); 1623 (C = O amidic); 748, 789 (C–Cl).
¹H-NMR (DMSO-d₆, 400 MHz), δ (ppm): 3.16–3.19 (m, 4H, 2CH₂); 3.40–3.44 (m, 4H, 2CH₂); 7.39–7.41 (d, 2H, CHAr); 7.71–7.73 (d, 2H, CHAr).

3.2.12. Di-(β -Chloroethyl)-Amide of Benzoxazole-2-Yl-Mercapto-Acetic Acid (IX)

Yellow, crystalline solid (5.09 g; yield, 84%); M.p. = 178–180 °C.
 Elemental analysis calculated for C₁₃H₁₄N₂O₂SCl₂ (%): C, 46.84; H, 4.20; N, 8.40; S, 9.60; Cl, 21.32. Found: (%): C, 46.95; H, 4.44; N, 8.74; S, 9.99; Cl, 21.67.
 IR; ν_{\max} (cm^{-1}): 3097 (CHAr); 790 (S–CH₂); 1493 (C = N); 1283 (C–N tertiary); 1624 (C = O amidic); 749 (C–Cl).
¹H-NMR (DMSO-d₆, 400 MHz), δ (ppm): 3.35–3.37 (m, 4H, 2CH₂); 3.55–3.57 (m, 4H, 2CH₂); 4.62 (s, 2H, CH₂–S); 7.38–7.40 (d, 2H, CHAr); 7.60–7.61 (d, 2H, CHAr).

3.2.13. Di-(β -Chloroethyl)-Amide of Benzoxazole-2-Yl-Mercapto- β -Propionic Acid (X)

White-yellow, crystalline solid (4.71 g; yield, 68%); M.p. = 187–189 °C.
 Elemental analysis calculated for C₁₄H₁₆N₂O₂SCl₂ (%): C, 48.41; H, 4.61; N, 8.06; S, 9.22; Cl, 20.46. Found: (%): C, 48.70; H, 4.96; N, 8.47; S, 9.60; Cl, 20.82.
 IR; ν_{\max} (cm^{-1}): 3094 (CHAr); 785 (S–CH₂); 1490 (C = N); 1306 (C–N tertiary); 1623 (C = O amidic); 747, 788 (C–Cl).
¹H-NMR (DMSO-d₆, 400 MHz), δ (ppm): 2.55–2.57 (m, 2H, CH₂); 3.37–3.39 (m, 4H, 2CH₂); 3.60–3.62 (m, 4H, 2CH₂); 4.32–4.34 (m, 2H, CH₂–S); 7.71–7.73 (d, 2H, CHAr); 7.85–7.87 (d, 2H, CHAr).

3.3. Optimization of the Reactions

In the factorial experiments [31–33], the reaction yield is considered as being an indicator of the reaction optimization. It is markedly influenced by some conditions of the chemical reactions as temperature, time interval, solvent, solvent mixture, impuri-

ties, or pressure. These parameters are considered real variables. Some of these are significant variables.

The yield of the chemical reactions for obtaining the benzoxazoles derivatives VIII–X depends on two significant variables: temperature and time interval of reactions. Let us consider temperature (T , in °C, noted with X_1) and interval of time (t , in hours, noted with X_2) as being real variables of the experiment. In order to facilitate the calculations, dimensionless variables x_1 and x_2 are introduced instead of the real variables X_1 and X_2 by using the average value of the real variables, noted \bar{X}_i , $i = 1, 2$, and the half of the variation domain of the variables, noted ΔX_i , $i = 1, 2$, defined by relations (2) and (3):

$$\bar{X}_i = \frac{x_{i\min} + x_{i\max}}{2}, i = 1, 2 \quad (2)$$

$$\Delta X_i = \frac{x_{i\max} - x_{i\min}}{2}, i = 1, 2. \quad (3)$$

The dimensionless variables depend on the real variables as relation (4) indicates:

$$x_i = \frac{X_i - \bar{X}_i}{\Delta X_i}, i = 1, 2. \quad (4)$$

Let us propose a dependence (5) of the reaction yield [31–33], η , on the dimensionless variables, considering the individual influence and the conjugate effects of these variables:

$$\eta = a_0 + a_1x_1 + a_2x_2 + a_{12}x_1x_2 + a_{11}x_1^2 + a_{22}x_2^2, i = 1, 2. \quad (5)$$

The regression coefficients, a_i , can be determined using the values of η and of the dimensionless variables obtained in 3^2 experiments organized for the chemical reaction for obtaining benzoxazoles. The results are given in Tables 1–3 and in Figures 1–3 for the molecules VIII, IX and X, respectively.

Table 1. Experiment 3^2 for molecule VIII.

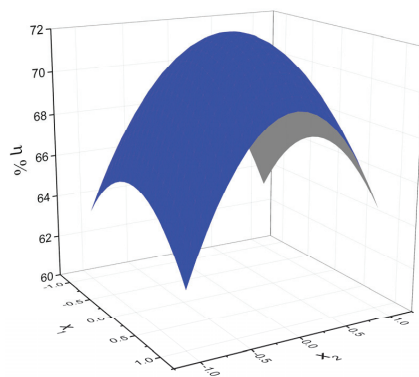
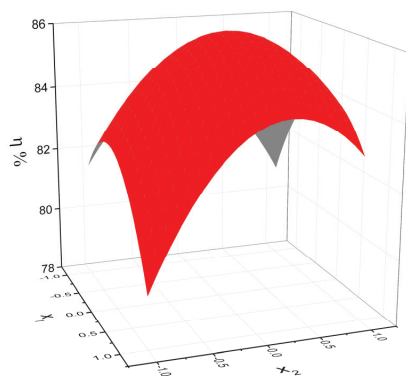
No.	x_1 (X_1 , °C)	x_2 (X_2 , h)	x_1x_2	$x_1^2-2/3$	$x_2^2-2/3$	η (%)
1	−1 (65)	−1 (2.5)	1	1/3	1/3	64
2	−1 (65)	0 (2.5)	0	1/3	−2/3	70
3	−1 (65)	1 (2.5)	−1	1/3	1/3	65
4	0 (70)	−1(3.0)	1	−2/3	1/3	68
5	0 (70)	0 (3.0)	0	−2/3	−2/3	73
6	0 (70)	1 (3.0)	−1	−2/3	1/3	67
7	1 (75)	−1 (3.5)	1	1/3	1/3	63
8	1 (75)	0 (3.5)	0	1.3	−2/3	71
9	1 (75)	1 (3.5)	−1	1/3	1/3	66
Σ	0	0	0	0	0	607

Table 2. Experiment 3^2 for molecule IX.

No.	x_1 (X_1 , °C)	x_2 (X_2 , h)	x_1x_2	$x_1^2-2/3$	$x_2^2-2/3$	η (%)
1	−1 (65)	−1 (2.5)	1	1/3	1/3	82
2	−1 (65)	0 (2.5)	0	1/3	−2/3	83
3	−1 (65)	1 (2.5)	−1	1/3	1/3	81
4	0 (70)	−1(3.0)	1	−2/3	1/3	82
5	0 (70)	0 (3.0)	0	−2/3	−2/3	87
6	0 (70)	1 (3.0)	−1	−2/3	1/3	84
7	1 (75)	−1 (3.5)	1	1/3	1/3	80
8	1 (75)	0 (3.5)	0	1.3	−2/3	84
9	1 (75)	1 (3.5)	−1	1/3	1/3	83
Σ	0	0	0	0	0	746

Table 3. Experiment 3^2 for molecule X.

No.	x_1 (X_1 , °C)	x_2 (X_2 , h)	x_1x_2	$x_1^2-2/3$	$x_2^2-2/3$	η (%)
1	-1 (65)	-1 (2.5)	1	1/3	1/3	64
2	-1 (65)	0 (2.5)	0	1/3	-2/3	68
3	-1 (65)	1 (2.5)	-1	1/3	1/3	63
4	0 (70)	-1(3.0)	1	-2/3	1/3	65
5	0 (70)	0 (3.0)	0	-2/3	-2/3	69
6	0 (70)	1 (3.0)	-1	-2/3	1/3	66
7	1 (75)	-1 (3.5)	1	1/3	1/3	65
8	1 (75)	0 (3.5)	0	1/3	-2/3	68
9	1 (75)	1 (3.5)	-1	1/3	1/3	67
Σ	0	0	0	0	0	595

**Figure 1.** Yield map obtained for molecule VIII.**Figure 2.** Yield map obtained for molecule IX.

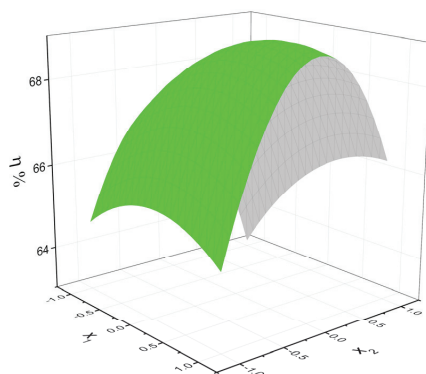


Figure 3. Yield map obtained for molecule IX.

The absolute values of the coefficients indicate the strength of the dependence of the reaction yield on the corresponding variables. The positive sign of these coefficients indicates the increasing in yield when the corresponding variables increase. The decrease of the reaction yield when the dimensionless variables increase is indicated by the negative sign of the corresponding coefficients.

Using the data from Tables 1–3, the regression coefficients from Table 4 were obtained for the three studied compounds.

Table 4. Regression coefficients for the analyzed molecules.

Molecule	a_0	a_1	a_2	a_{12}	a_{11}	a_{22}
VIII	72.218	0.167	0.5	0.5	−2.839	−5.833
IX	86.111	0.167	0.667	1	−2.166	−2.667
X	68.888	0.830	0.333	0.75	−0.833	−3.333

To decide the situations for which the reaction yield does not depend on a given variable, we must know the *t*-Student coefficients [32]. For this purpose, supplemental experiments were organized in the vicinity of the middle of the variation domain of the dimensionless variables (see Table 5).

Table 5. Yields for the experiments in the middle of the variation domain.

Molecule	η_1	η_2	η_3	η
VIII	71.0	73.5	74.0	72.83
IX	86.11	85.80	85.70	85.87
X	69.3	68.1	69.4	68.93

The precision of determination of the regression coefficients in relation (5) was estimated by using relation (6):

$$P = \sqrt{\frac{S_{\eta}^2}{N}}, \quad (6)$$

where

$$S_{\eta}^2 = \frac{\sum_1^3 (\eta_i - \eta)^2}{n - 1}. \quad (7)$$

In relations (6) and (7) N is the number of the experiments in 3^2 procedure and n is the number of the supplemental experiments organized for precision estimation. To compute the sum of quadratic deviations the data of Table 5 were used. The *t*-Student coefficients,

estimated on the basis of the values of the regression coefficients from Table 4, are given in Table 6.

Table 6. *t*-Student coefficients.

Molecule	t_0	t_1	t_2	t_{12}	t_{11}	t_{22}
VIII	830.14	18.93	5.67	5.67	32.13	66.13
IX	1209.42	2.35	9.37	14.04	30.42	37.46
X	285.67	3.46	1.38	3.11	3.46	13.83

If one supposes that the variables corresponding to the *t*-Student coefficients are smaller than 3.00, this does not exert a significant influence on the reaction yield, relation (5) can be written for the studied molecules in relations (8)–(10):

$$\eta_{VIII} = 72.22 + 0.17x_1 + 0.50x_2 + 0.50x_1x_2 - 2.84x_1^2 - 5.83x_2^2, \quad (8)$$

$$\eta_{IX} = 86.11 + 0.67x_2 + 1.00x_1x_2 - 2.17x_1^2 - 2.67x_2^2, \quad (9)$$

$$\eta_X = 68.89 + 0.83x_1 + 0.75x_1x_2 - 0.83x_1^2 - 3.33x_2^2. \quad (10)$$

3.4. Quantum Mechanical Analysis of N-Mustards

Since the N-mustards described above are new compounds, the quantum mechanical characterization is necessary because the provided results can help in obtaining information on the interaction mechanism of these molecules with living cells.

The optimized structures of the three molecules, performed by Spartan'14 software, are given in Figure 4a–c. In Figure 4a–c oxygen atom is red, nitrogen is blue, sulfur is yellow, chlorine is green, carbon is black, and hydrogen is white. Resulting from Figure 4a–c, the reciprocal orientation of the atomic groups in the optimized structure of N-mustards VIII–X and the change in the dipole moment orientation when CH₂ group is introduced in the structures IX and X. The arrow indicates the orientation of the electrical dipole moment of the molecule.

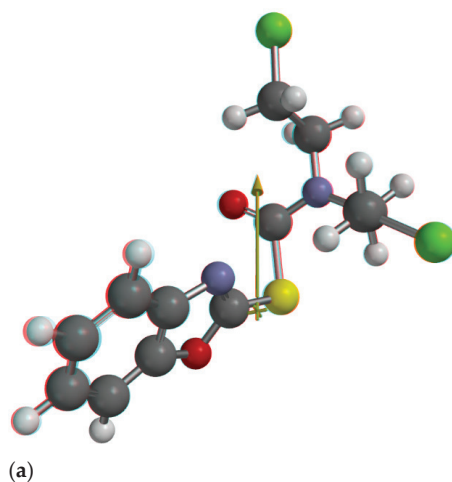


Figure 4. *Cont.*

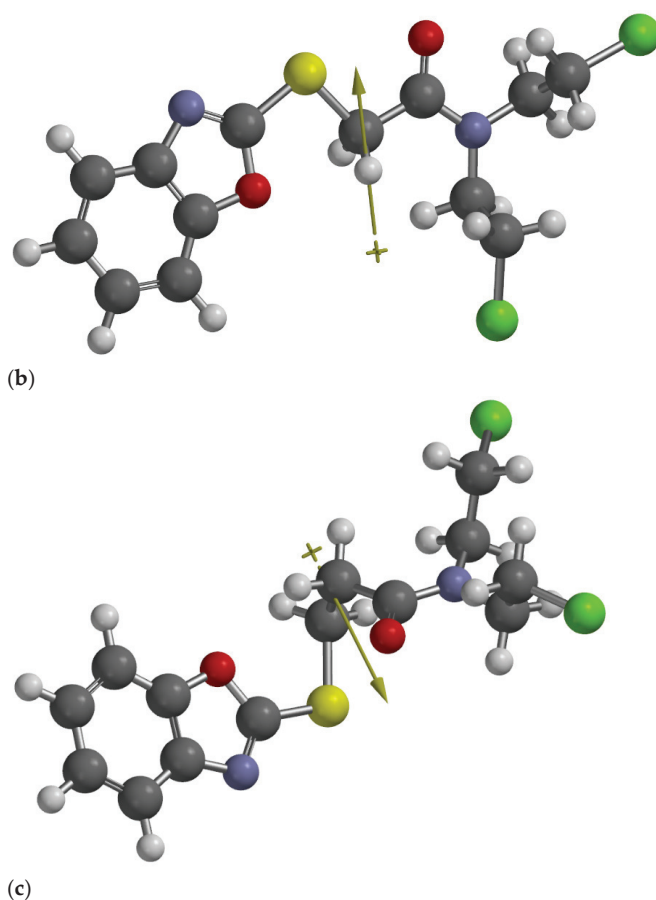


Figure 4. Optimized structure of molecules VIII (a), IX (b), and X (c).

The values of some electro-optical parameters computed using Spartan'14 for the studied molecules are given in Table 7.

Table 7. Molecular parameters computed by Spartan'14.

No.	Parameter	Molecule VIII	Molecule IX	Molecule X
1	Solvation energy (kcal/mol)	−35.60	−53.64	−61.09
2	E_{HOMO} (eV)	−6.28	−5.94	−5.90
3	E_{LUMO} (eV)	−1.29	−0.84	−0.77
4	$ \Delta E $ (eV)	4.99	5.10	4.13
5	Dipole moment (D)	1.53	4.40	4.33
6	Polarizability (\AA^3)	62.65	64.07	65.57
7	Area (\AA^2)	304.38	324.54	342.11
8	Volume (\AA^3)	276.89	294.66	313.21
9	PSA (\AA^2)	29.781	28.490	28.650
10	Log P	2.26	1.49	1.78
11	Ovality	1.48	1.52	1.53
12	Molecular radius (\AA)	2.7291	2.7238	2.7466
13	R^3 (\AA^3)	20.3253	20.2080	20.7192

The dipole moment, measuring the separation of the positive and negative electrical charges of the molecule, increases when passing from molecule VIII to molecule X, as results from Table 7. The molecular polarizability, giving information about the induced dipole moment in the molecule by the internal electric field acting in each point in solution, also increases from molecule VIII to molecule X.

The polar surface area (PSA) [47–51] defined as the sum of the polar atoms' surfaces in a molecule is a useful parameter for prediction of drug transport properties. The values of PSA are between 28.490 and 29.781 Å², these molecules being able to cross both the cell membranes and the blood-brain barrier.

The log P [47–51] value is a measure of lipophilicity or hydrophobicity. The chemical structures of the studied molecules are hydrophobic because the values of logP are positive.

The HOMO and LUMO maps of the studied N-mustards are illustrated in Figure 5a–c. HOMO and LUMO orbitals are involved in the chemical reactivity of the molecule, determining the chemical stability, the electrical and optical properties, and the interaction ability of the molecule with other species.

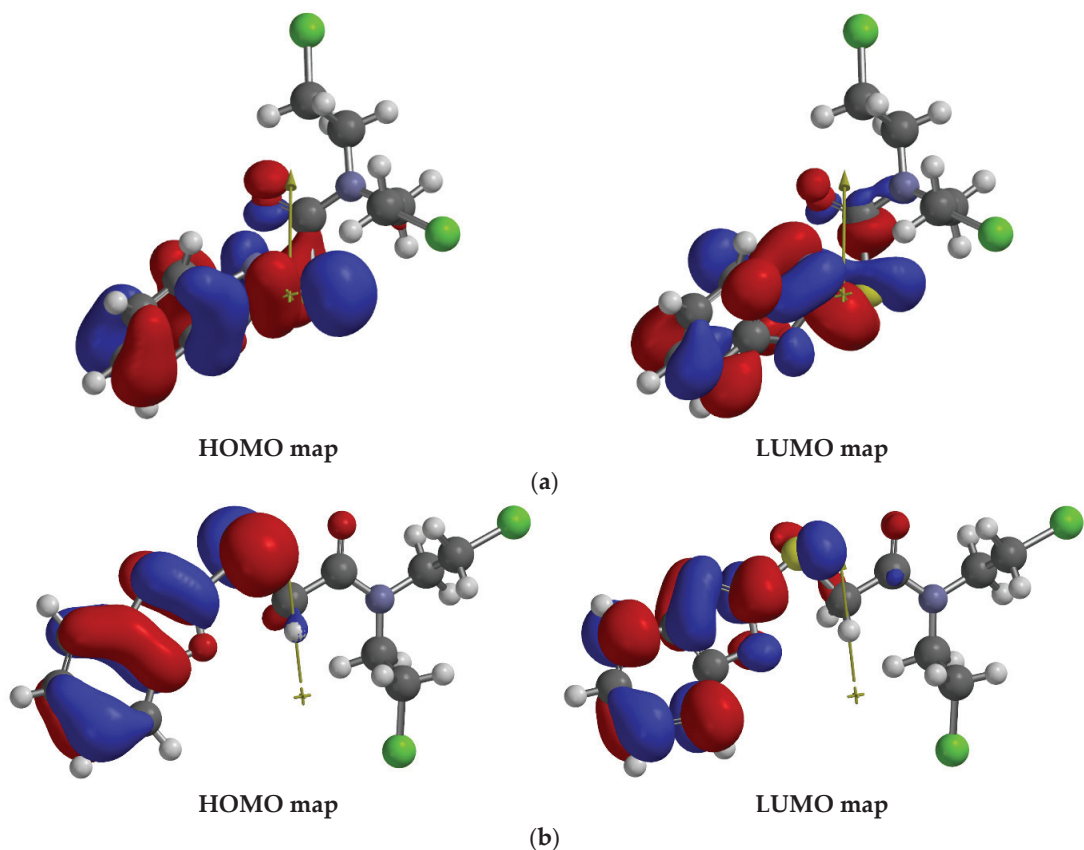


Figure 5. Cont.

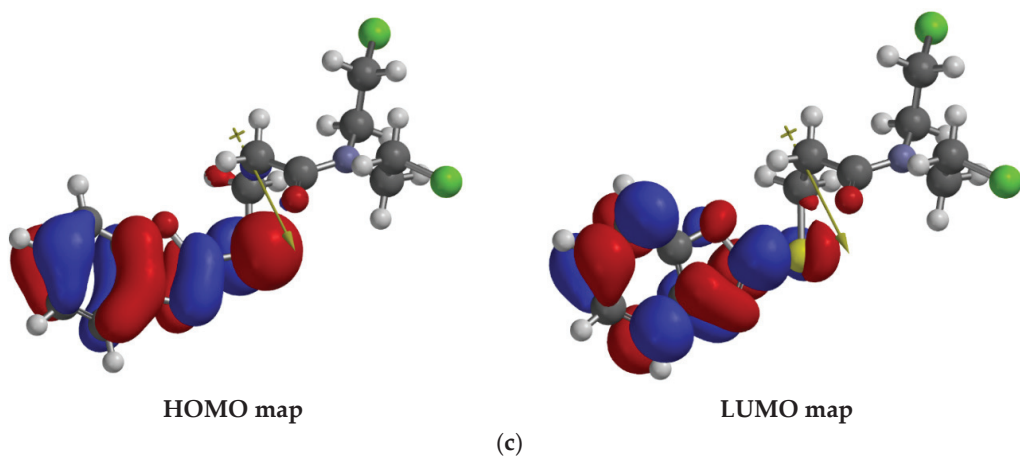


Figure 5. HOMO and LUMO maps of the molecules VIII (a), IX (b), and X (c).

Figure 5a–c illustrates the changes in the valence electron cloud distribution by excitation; these changes involve especially the heterocycle region. As results from the data of Table 7 referring to the energy gap $|\Delta E|$ (eV), the transitions between HOMO and LUMO are made under the UV photons. Figure 5a–c also emphasizes the atomic groups involved in the chemical reactions both in the ground and excited states of N-mustards molecules.

Some graphical representations provided by Spartan'14 program [34,35] are illustrated in Figures 6–8.

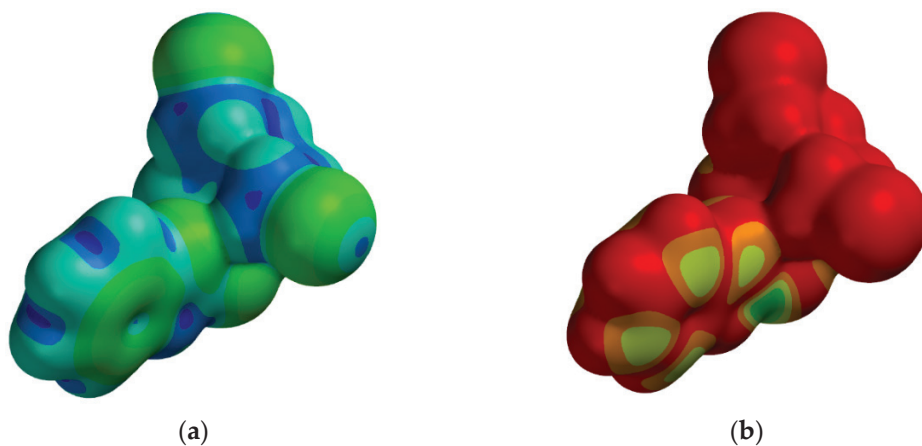


Figure 6. Local ionization map (a) and $|\text{LUMO}|$ map (b) for molecule VIII.

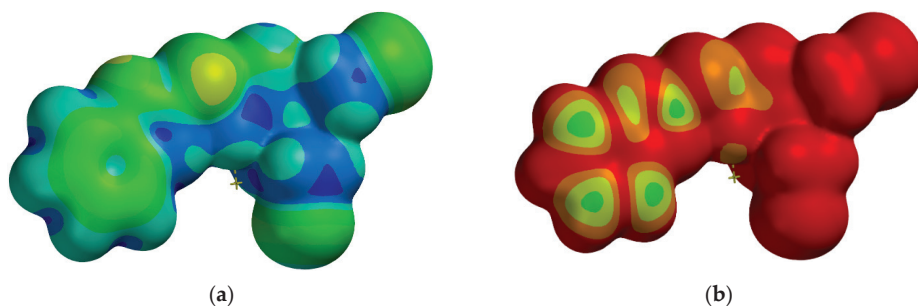


Figure 7. Local ionization map (a) and |LUMO| map (b) for molecule IX.

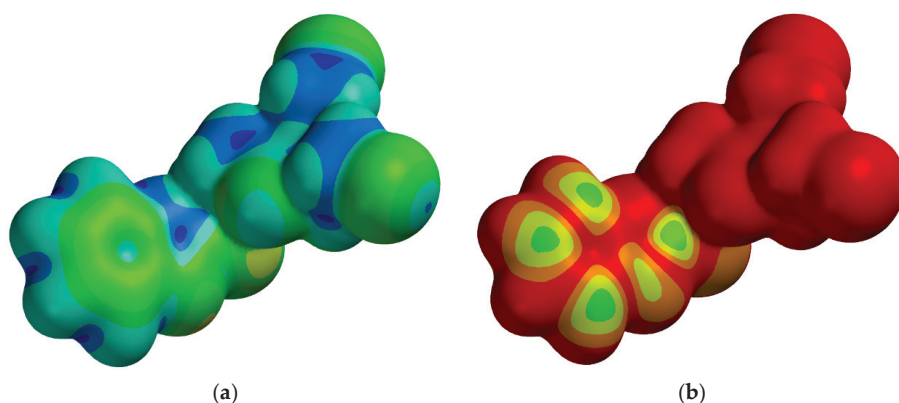


Figure 8. Local ionization map (a) and |LUMO| map (b) for molecule X.

Some information can be extracted from the analysis of Figures 6–8.

The local ionization potential map (Figures 6a, 7a and 8a) is an indicator of the electrophile addition. Colors in red correspond to small ionization potentials, while colors in blue correspond to high ionization potentials. The studied molecules are characterized by high and intermediate ionization potentials.

|LUMO| map (Figures 6b, 7b and 8b) is an indicator of nucleophilic addition. Colors in red indicate absolute low values of LUMO, while colors in blue indicate absolute high values of LUMO. For molecules VIII–X, the absolute values of LUMO are close to zero.

Figure 9a–c shows the electrostatic charges near the constituent atoms of the studied molecules, calculated using Spartan'14 program and expressed as a percentage of the elementary electric charge.

From Figure 9a–c, it results that the highest negative charges are localized near nitrogen atom belonging to the heterocycle and oxygen atom of the C = O group in all studied molecules.

The arrows in Figure 9a–c show the orientation of the electric dipole moment in the ground electronic states of the studied molecules. It is parallel to the CS bond for the molecule VIII and makes angles near 40–45 degrees with this bond in the other two molecules.

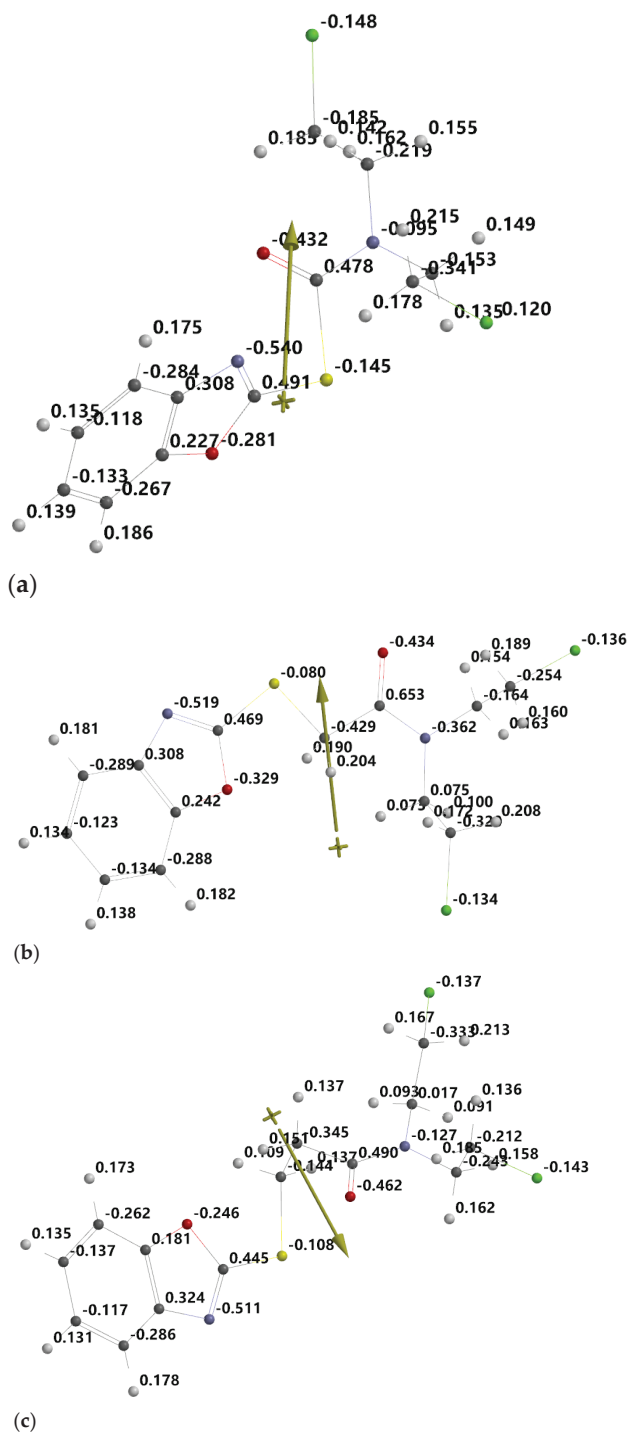


Figure 9. Electrostatic charges near the atoms composing the structures of molecules VIII (a), IX (b), and X (c), respectively.

3.5. Biological Properties

3.5.1. Assessment of Toxicity of Acids II–IV and N-Mustards VIII–X Compared to Di-(β -Chloroethyl)-Amine

The mice weighing 20 ± 2 g were used and the experimental groups consisted of 10 animals of both sexes. The substances were administered intraperitoneally as a suspension in Twen 80 and the mortality was recorded at 24 h, 48 h, and 7 days. The degree of toxicity (LD_{50}) was determined using the Spearman–Kärber method [36]. The obtained results are listed in Table 8.

Table 8. The LD_{50} values (mg/kg body weight) for the compounds II–IV, VIII–X.

Compound	LD_{50}			
	24 H	48 H	7 Days	Average
II	1695	1695	1682	1690
III	1830	1830	1790	1816
IV	1725	1725	1690	1713
VIII	1620	1620	1595	1611
IX	1790	1790	1740	1773
X	1685	1685	1650	1673
Di-(β -chloroethyl)-amine	378			

It is found that the N-mustards (VIII–X) present a very low toxicity compared to that of the di-(β -chloroethyl)-amine free base and a slightly increased toxicity compared to the support intermediates (II–IV). The results confirm the data from the literature according to which the use of heterocyclic structures as transport agents positively influences the decrease of cytotoxic group toxicity [1,52–54].

Thus, in the case of N-mustards, the toxicity is due to the support, which causes a decrease in the basicity of nitrogen atom by involvement in the amide conjugation system of its non-participating electrons.

3.5.2. Antitumor Activity of di-(β -Chloroethyl)-Amides VIII–X

In order to study the cytostatic action, the A_2G mice weighing 25–30 g (± 2 g) as experimental animals were used, and *Ascita Ehrlich* was used as an experimental tumor. The transplantation was performed intraperitoneally (10^6 cells dose). The substances were administered as suspensions in 1% methylcellulose, by single injections on the 7th day after transplantation. The concentrations of 400, 200, and 40 mg/kg body weight were used. The experimental groups included 20 animals for each concentration and the control groups had 10 tumored animals. The inhibition exerted by N-mustards VIII–X was calculated according to the methods from the literature [37], 7 days after the administration of the substances (Table 9), with an error of 1%.

Table 9. Inhibition (%) of N mustards VIII–X.

The Tested Compound	Experimental Animals	Route of Administration	Inhibition (%)		
			<i>Ehrlich Ascites</i>		
			mg/kg Body Weight		
			400	200	40
VIII	mice	i.p.	43	30	24
IX	mice	i.p.	74	66	53
X	mice	i.p.	52	46	39
I.O.B-82	mice	i.p.	88	79	68

From the experimental data it results:

- The tested N mustards presents appreciable antitumor activity; more selective is the N mustard IX: di-(β -chloroethyl)-amide of benzoxazole-2-yl-mercapto-acetic acid which inhibits *Ehrlich's Ascites* in a proportion close to that of the reference cytostatic, I.O.B.-82;
- In addition to the alkylating effect, the synthesized N-mustards may also have a specific antimetabolite effect;
- The selective transport of the di-(β -chloroethyl)-amine group performed by the benzoxazole heterocycle and the active group transforms it into a masked group (protected group);
- The relationship between the benzoxazole nucleus and the active group does not consist exclusively in transport, but also in their mutual potentiation (convenient or not, direct or indirect).

4. Conclusions

The paper presents results related to the extension of the grafting reaction of the di-(β -chloroethyl)-amine group on heterocyclic structures.

The technique of obtaining di-(β -chloroethyl)-amides with benzoxazole structure was applied for the first time using the activation of support acids derived from 2-mercaptobenzoxazole by transforming them into mixed pivalic anhydrides which, for electronic and steric reasons, can be cleaved by the aminic nitrogen to one of the two carbonyls in the desired direction.

The synthesized products were characterized by elemental and spectral analysis (IR, $^1\text{H-NMR}$).

The new compounds VIII–X were characterized by Spartan'14 and their electro-optical properties were established.

The importance of the synthesized N mustards among the biologically active products was highlighted by establishing the degree of toxicity and testing their antitumor activity on experimental animals.

Author Contributions: Conceptualization, C.C., V.S., D.G.D. and D.O.D.; methodology, C.C., V.S., D.G.D. and D.O.D.; software, A.C.M., D.G.D. and C.D.N.; validation, C.C., A.C.M., M.M.D.-O., M.-D.A., M.M. and R.N.M.; formal analysis, C.C., V.S., D.G.D. and D.O.D.; investigation, C.C., V.S., M.M.D.-O., M.-D.A., M.M. and R.N.M.; resources, V.S., D.O.D. and R.N.M.; data curation, V.S., D.G.D. and D.O.D.; writing—original draft preparation, C.C., V.S., D.G.D. and D.O.D.; writing—review and editing, D.G.D. and D.O.D.; visualization, A.C.M., M.M.D.-O., M.-D.A., M.M. and C.D.N.; supervision, V.S. and D.O.D.; project administration, V.S. and D.O.D.; funding acquisition, C.C. and R.N.M. All authors have read and agreed to the published version of the manuscript.

Funding: This research received no external funding.

Institutional Review Board Statement: The study was conducted according to the guidelines of the Declaration of Helsinki, and approved by the Ethics Committee of Faculty of Veterinary Medicine, “Ion Ionescu de la Brad” University of Agricultural Sciences and Veterinary Medicine (protocol code 224/10 March 2021).

Informed Consent Statement: Not applicable.

Data Availability Statement: The data presented in this study are available on request from the corresponding author.

Conflicts of Interest: The authors declare no conflict of interest.

References

1. Yakaiah, T.; Lingaiah, B.P.V.; Narsaiah, B.; Shireesha, B.; Ashok Kumar, B.; Gururaj, S.; Parthasarathy, T.; Sridhar, B. Synthesis and structure-activity relationships of novel pyrimido [1,2-b]indazoles as potential anticancer agents against A-549 cell lines. *Bioorg. Med. Chem. Lett.* **2007**, *17*, 3445–3453. [CrossRef]
2. Singh, R.K.; Kumar, S.; Prasad, D.N.; Bhardwaj, T.R. Therapeutic journey of nitrogen mustard as alkylating anticancer agents: Historic to future perspectives. *Eur. J. Med. Chem.* **2018**, *151*, 401–433. [CrossRef] [PubMed]

3. Ramadan, M.; Bremner-Hay, N.K.; Carlson, S.A.; Comstock, L.R. Synthesis and evaluation of N6-substituted azide- and alkyne-bearing N-mustard analogs of S-adenosyl-L-methionine. *Tetrahedron* **2014**, *70*, 5291–5297. [CrossRef]
4. Lee, C.-H.; Chou, T.-C.; Su, T.-L.; Yu, J.; Shao, L.-E.; Yu, A.L. BO-0742, a derivative of AHMA and N-mustard, has selective toxicity to drug sensitive and drug resistant leukemia cells and solid tumors. *Cancer Lett.* **2009**, *276*, 204–211. [CrossRef] [PubMed]
5. Kapuriya, N.; Kakadiya, R.; Dong, H.; Kumar, A.; Lee, P.-C.; Zhang, X.; Chou, T.-C.; Lee, T.-C.; Chen, C.-H.; Lam, K.; et al. Design, synthesis, and biological evaluation of novel water-soluble N-mustards as potential anticancer agents. *Bioorg. Med. Chem.* **2011**, *19*, 471–485. [CrossRef] [PubMed]
6. Hymbaugh Bergman, S.J.; Comstock, L.R. N-mustard analogs of S-adenosyl-L-methionine as biochemical probes of protein arginine methylation. *Bioorg. Med. Chem.* **2015**, *23*, 5050–5055. [CrossRef]
7. Acharya, P.C.; Bansal, R. Synthesis of androstene oxime-nitrogen mustard bioconjugates as potent antineoplastic agents. *Steroids* **2017**, *123*, 73–83. [CrossRef] [PubMed]
8. Cheptea, C.; Sunel, V.; Stan, C.; Dorohoi, D.O. New derivatives based 1,3-thiazolidine-2,3-disubstituted with support of 5-nitroindazole-1'-acetamidyl with mitodepressive activity. Reaction optimization in factorial experiment. *Rev. Roum. Chim.* **2012**, *57*, 229–234.
9. Holban, M.; Sunel, V.; Popa, M.; Lionte, C. Synthesis and characterization of a new starch ester with N-[(N'-tiazolylo)-p'-(benzenesulphone)] amide of N-(o-nitrobenzoyl)-D, L-asparagic acid. *Cellul. Chem. Technol.* **2007**, *45*, 191–196.
10. Samia, L.B.P.; Parrilha, G.L.; Bertoli, A.C.; Duarte, H.A.; Speziali, N.L.; Teixeira, S.F.; Kawamura, B.; Ferreira, A.K.; Beraldo, H. Investigation on the cytotoxic effects of nitrogen-mustard-derived Schiff bases. Studies on the reactivity of the N-mustard pharmacophoric group. *J. Mol. Struct.* **2019**, *1178*, 274–284. [CrossRef]
11. Stornetta, A.; Zimmermann, M.; Cimino, G.D.; Henderson, P.T.; Sturla, S.J. DNA adducts from anticancer drugs as candidate predictive markers for precision medicine. *Chem. Res. Toxicol.* **2017**, *30*, 388–409. [CrossRef]
12. Puyo, S.; Montaudon, D.; Pourquier, P. From old alkylating agents to new minor groove binders. *Crit. Rev. Oncol. Hematol.* **2014**, *89*, 43–61. [CrossRef] [PubMed]
13. Sunel, V.; Lionte, C.; Basu, C.; Cheptea, C. New antitumour alkylating compounds with N-[m-(arylthiocarbamoyl)-aminobenzoyl]-asparagic acids as supports. *Chem. Indian J.* **2005**, *2*, 1–6.
14. Sunel, V.; Popa, M.; Desbrières, J.; Profire, L.; Pintilie, O.; Lionte, C. New Di-(β-chloroethyl)-α-amides on N-(meta-Acylaminobenzoyl)-D,L-aminoacid supports with antitumoral activity. *Molecules* **2008**, *13*, 177–189. [CrossRef] [PubMed]
15. Sunel, V.; Cecal, A.; Soldea, C.; Asandei, N. Kinetic studies and analytical determinations on some derivatives of L-asparagic acid acting as antimetabolites and alkylating agents. *Rev. Roum. Chim.* **1995**, *40*, 773–778.
16. Popa, M.; Balaita Rusu, L.; Sunel, V. Immobilization of α-[di-(β-Chloroethyl)-Amide]-N-(m-Nitrobenzoyl)-D,L-Asparagic Acid on Xanthan. *J. Biomater. Appl.* **2003**, *18*, 83–94. [CrossRef]
17. Popa, M.; Sunel, V.; Dulea, N.; Popa, A.; Ottenbrite, R.M.; Uglea, C.V. Antitumoral activity induced by alkylating agents conjugated to Poly(maleic anhydride-alt-vinyl acetate). *J. Bioact. Compat. Polym.* **2007**, *22*, 651–666. [CrossRef]
18. Ritschel, W.A.; Ye, W.; Buhse, L.; Reepmeyer, J.C. Stability of the nitrogen mustard mechlorethamine in novel formulations for dermatological use. *Int. J. Pharm.* **2008**, *362*, 67–73. [CrossRef]
19. Sheng, C.; Xu, H.; Wang, W.; Cao, Y.; Dong, G.; Wang, S.; Che, X.; Ji, H.; Yao, J.; Zhang, W. Design, synthesis and antifungal activity of isosteric analogues of benzoheterocyclic N-myristoyltransferase inhibitors. *Eur. J. Med. Chem.* **2010**, *45*, 3531–3540. [CrossRef]
20. Desai, S.; Desai, V.; Shingade, S. In-vitro anti-cancer assay and apoptotic cell pathway of newly synthesized benzoxazole-N-heterocyclic hybrids as potent tyrosine kinase inhibitors. *Bioorg. Chem.* **2020**, *94*, 103382. [CrossRef]
21. Raman, N.; Kulandaisamy, A.; Jayasubramanian, K. Synthesis, structural characterization, redox, and antibacterial studies of 12-membered tetraaza macrocyclic Cu(II), Ni(II), Co(II), Zn(II), and VO(IV) complexes derived from 1,2-(Diimino-4'-antipyrinyl)-1,2-diphenylethane and o-Phenylenediamine. *Synth. React. Inorg. Met. Org. Chem.* **2004**, *34*, 17–43. [CrossRef]
22. Mishra, A.P. Physicochemical and antimicrobial studies on nickel (II) and copper (II) Schiff base complexes derived from 2-furfuraldehyde. *J. Indian Chem. Soc.* **1999**, *76*, 35–37.
23. Viaud, M.-C.; Jamoneau, P.; Flouzat, C.; Bizot-Espiard, J.-G.; Pfeiffer, B.; Renard, P.; Caignard, D.-H.; Adam, G.; Guillaumet, G. N-substituted oxazolo [5,4-b]pyridin-2(1H)-ones: A new class of non-opiate antinociceptive agents. *J. Med. Chem.* **1995**, *38*, 1278–1286. [CrossRef]
24. Gong, B.; Hong, F.; Kohm, C.; Bonham, L.; Klein, P. Synthesis and SAR of 2-arylbenzoxazoles, benzothiazoles and benzimidazoles as inhibitors of lysophosphatidic acid acyltransferase-β. *Bioorg. Med. Chem. Lett.* **2004**, *14*, 1455–1459. [CrossRef]
25. Courtois, M.; Mincheva, Z.; Andreu, F.; Rideau, M.; Viaud-Massuard, M.-C. Synthesis and biological evaluation with plant cells of new fosmidomycin analogues containing a benzoxazolone or oxazolopyridinone ring. *J. Enzyme Inhib. Med. Chem.* **2004**, *19*, 559–565. [CrossRef]
26. Bibian, M.; El-Habnoui, S.; Martinez, J.; Fehrentz, J.-A. Enantioselective synthesis of N-protected α-amino acid hydrazides. *Synthesis* **2009**, *2009*, 1180–1184. [CrossRef]
27. Sechi, M.; Azzena, U.; Delussu, M.P.; Dallochio, R.; Dessi, A.; Cosseddu, A.; Pala, N.; Neamati, N. Design and synthesis of bis-amide and hydrazide-containing derivatives of malonic acid as potential HIV-1 integrase inhibitors. *Molecules* **2008**, *13*, 2442–2461. [CrossRef] [PubMed]
28. Aparaschivei, R.; Holban, M.; Sunel, V.; Popa, M.; Desbrières, J. Synthesis and characterization of new heterocyclic compounds with potential antituberculosis activity and their immobilization on polymer supports. *Cellul. Chem. Technol.* **2012**, *46*, 301–306.

29. Hynes, N.E.; Lane, H.A. ERBB receptors and cancer: The complexity of targeted inhibitors. *Nat. Rev. Cancer* **2005**, *5*, 341–354. [CrossRef]
30. Sondhi, S.M.; Singhal, N.; Verma, R.P.; Arora, S.K.; Dastidar, S.G. Synthesis of hemin and porphyrin derivatives and their evaluation for anticancer activity. *Indian J. Chem. B* **2001**, *40*, 113–119.
31. Grebinisan, D.; Burlea, M.; Cheptea, C.; Lionte, C.; Dorohoi, D.O.; Sunel, V.; Popa, M.; Hurjui, I. Optimization reaction for obtaining some N-[p-R-benzoyl]-1-glutamine derivatives with pharmaceutical action. *Dig. J. Nanomater. Bios.* **2013**, *8*, 777–785.
32. Hurjui, I.; Cheptea, C.; Dascalu, C.F.; Hurjui, L.; Peptu, C.; Sunel, V.; Dorohoi, D.O. Optimization reaction of some 1,4-disubstituted thiocarbazides with tuberculostatic activity. *Dig. J. Nanomater. Bios.* **2012**, *7*, 1747–1756.
33. Gicu, T.A.; Nechifor, C.D.; Sunel, V.; Dorohoi, D.O.; Cheptea, C. Optimization reaction for obtaining new hydrazidones with biological activity. *Rev. Roum. Chim.* **2014**, *59*, 739–747.
34. Hehre, W.; Ohlinger, S. *Spartan'14 for Windows, Macintosh and Linux, Tutorial and User's Guide*; Wavefunction Inc.: Irvine, CA, USA, 2014.
35. Young, D. *Computational Chemistry: A Practical Guide for Applying Techniques to Real World Problems*; Wiley-Interscience: New York, NY, USA, 2001.
36. Hamilton, M.A.; Russo, R.C.; Thurston, R.V. Trimmed Spearman-Kärber method for estimating median lethal concentrations in bioassays. *Environ. Sci. Technol.* **1977**, *11*, 714–719. [CrossRef]
37. Winfield, A.J.; Richards, R.M.E. *Pharmaceutical Practice*, 3rd ed.; Elsevier: London, UK, 2004.
38. Ciugureanu, C.; Sunel, V.; Budeanu, C.H. Syntheses of anti-tumor substances. n-mustards derived from p-aminobenzoic acid and p-nitrophenol. *Rev. Chim.* **1985**, *36*, 990–993. [CrossRef]
39. Ciugureanu, C.; Sunel, V.; Budeanu, C.H. Synthesis of Azotyperites on 2, 5-Disubstituted 1, 3, 4-Thiadiazole Carriers. *Rev. Chim.* **1986**, *37*, 866–890.
40. Sassiver, M.L.; Lewis, A. Structure-activity relationships among semisynthetic cephalosporins. *Adv. Appl. Microbiol.* **1970**, *13*, 163–236. [CrossRef]
41. Kanafani, Z.A.; Corey, G.R. Ceftazolin: A cephalosporin with expanded Gram-positive activity. *Future Microbiol.* **2009**, *4*, 25–33. [CrossRef]
42. Pintilie, O.; Moise, M.; Profire, L.; Sunel, V. Synthesis and biological activities of some beta-lactamic derivatives. *Farmacia* **2006**, *54*, 61–66.
43. Jarrahpour, A.A.; Shekarriz, M.; Taslimi, A. Synthesis and antimicrobial activity of some new sugar-based monocyclic β -lactams. *Molecules* **2004**, *9*, 29–38. [CrossRef] [PubMed]
44. Heinisch, L.; Wittmann, S.; Stoiber, T.; Berg, A.; Ankel-Fuchs, D.; Möllmann, U. Highly antibacterial active aminoacyl penicillin conjugates with acylated bis-catecholate siderophores based on secondary diamino acids and related compounds. *J. Med. Chem.* **2002**, *45*, 3032–3040. [CrossRef]
45. Cottagnoud, P.H.; Täuber, M.G. New therapies for pneumococcal meningitis. *Expert Opin. Investig. Drugs* **2004**, *13*, 393–401. [CrossRef]
46. Cigu, T.A.; Vasiliu, S.; Racovita, S.; Lionte, C.; Sunel, V.; Popa, M.; Cheptea, C. Adsorption and release studies of new cephalosporin from chitosan-g-poly(glycidyl methacrylate) microparticles. *Eur. Polym. J.* **2016**, *82*, 132–152. [CrossRef]
47. Schlick, T. *Molecular Modeling and Simulation: An Interdisciplinary Guide*, 2nd ed.; Springer: New York, NY, USA, 2010.
48. Höltje, H.D.; Sippl, W.; Rognan, D.; Folkers, C. *Molecular Modeling: Basic Principles and Applications*, 3rd ed.; Wiley-VCH: Weinheim, Germany, 2008.
49. Dorohoi, D.O.; Creanga, D.E.; Dimitriu, D.G.; Morosanu, A.C.; Gritco-Todirascu, A.; Mariciuc, G.G.; Puica Melniciuc, N.; Ardelean, E.; Cheptea, C. Computational and spectral means for characterizing the intermolecular interactions in solutions and for estimating excited state dipole moment of solute. *Symmetry* **2020**, *12*, 1299. [CrossRef]
50. Morosanu, A.C.; Benchea, A.C.; Babusca, D.; Dimitriu, D.G.; Dorohoi, D.O. Quantum-mechanical and solvatochromic characterization of quercetin. *Anal. Lett.* **2017**, *50*, 2725–2739. [CrossRef]
51. Babusca, D.; Benchea, A.C.; Dimitriu, D.G.; Dorohoi, D.O. Solvatochromic characterization of Sudan derivatives in binary and ternary solutions. *Anal. Lett.* **2016**, *49*, 2615–2626. [CrossRef]
52. Sunel, V.; Ciovcia, S.; Asandei, N.; Soldea, C. Cellulose derivatives with antitumoral action. III: Δ 2-oxazolinones-5 derivatives from asparagic acid employed in the synthesis of modified celluloses. *Cellul. Chem. Technol.* **1995**, *29*, 11–16.
53. Bouissane, L.; El Kazzouli, S.; Léonce, S.; Pfeiffer, B.; Rakib, E.M.; Khoulil, M.; Guillaumet, G. Synthesis and biological evaluation of N-(7-indazolyl)benzenesulfonamide derivatives as potent cell cycle inhibitors. *Bioorg. Med. Chem.* **2006**, *14*, 1078–1088. [CrossRef] [PubMed]
54. Graff, A.; Biolka, H. *Experimental Oncology Topics*; Romanian Academy Publishing House: Bucharest, Romania, 1962. (In Romanian)



Article

Hexapod Assassins' Potion: Venom Composition and Bioactivity from the Eurasian Assassin Bug *Rhynocoris iracundus*

Nicolai Rügen¹, Timothy P. Jenkins², Natalie Wielsch³, Heiko Vogel⁴, Benjamin-Florian Hempel^{5,6}, Roderich D. Süßmuth⁵, Stuart Ainsworth⁷, Alejandro Cabezas-Cruz⁸, Andreas Vilcinskis^{1,9,10} and Miray Tonk^{9,10,*}

- ¹ Department of Bioresources, Fraunhofer Institute for Molecular Biology and Applied Ecology, Ohlebergsweg 12, 35392 Giessen, Germany; nicolai.ruegen@gmail.com (N.R.); Andreas.Vilcinskis@agr.uni-giessen.de (A.V.)
 - ² Department of Biotechnology and Biomedicine, Technical University of Denmark, 2800 Kongens Lyngby, Denmark; tpaje@dtu.dk
 - ³ Research Group Mass Spectrometry/Proteomics, Max Planck Institute for Chemical Ecology, Hans-Knoell-Strasse 8, 07745 Jena, Germany; nwielsch@ice.mpg.de
 - ⁴ Department of Entomology, Max Planck Institute for Chemical Ecology, Hans-Knöll-Straße 8, 07745 Jena, Germany; hvogel@ice.mpg.de
 - ⁵ Department of Chemistry, Technische Universität Berlin, Strasse des 17. Juni 124, 10623 Berlin, Germany; benjamin.hempel@charite.de (B.-F.H.); suessmuth@chem.tu-berlin.de (R.D.S.)
 - ⁶ BIH Center for Regenerative Therapies BCRT, Charité—Universitätsmedizin Berlin, 13353 Berlin, Germany
 - ⁷ Centre for Snakebite Research and Interventions, Department of Tropical Disease Biology, Liverpool School of Tropical Medicine, Liverpool L3 5QA, UK; stuart.ainsworth@lstm.ac.uk
 - ⁸ UMR BIPAR, Laboratoire de Santé Animale, Anses, INRAE, Ecole Nationale Vétérinaire d'Alfort, F-94700 Maisons-Alfort, France; alejandro.cabezas@vet-alfort.fr
 - ⁹ Institute for Insect Biotechnology, Justus Liebig University of Giessen, Heinrich-Buff-Ring 26-32, 35392 Giessen, Germany
 - ¹⁰ LOEWE Centre for Translational Biodiversity Genomics (LOEWE-TBG), Senckenberganlage 25, 60325 Frankfurt, Germany
- * Correspondence: miray.tonk@agr.uni-giessen.de

Citation: Rügen, N.; Jenkins, T.P.; Wielsch, N.; Vogel, H.; Hempel, B.-F.; Süßmuth, R.D.; Ainsworth, S.; Cabezas-Cruz, A.; Vilcinskis, A.; Tonk, M. Hexapod Assassins' Potion: Venom Composition and Bioactivity from the Eurasian Assassin Bug *Rhynocoris iracundus*. *Biomedicines* **2021**, *9*, 819. <https://doi.org/10.3390/biomedicines9070819>

Academic Editor: Leonardo Caputo

Received: 11 June 2021
Accepted: 8 July 2021
Published: 14 July 2021

Publisher's Note: MDPI stays neutral with regard to jurisdictional claims in published maps and institutional affiliations.



Copyright: © 2021 by the authors. Licensee MDPI, Basel, Switzerland. This article is an open access article distributed under the terms and conditions of the Creative Commons Attribution (CC BY) license (<https://creativecommons.org/licenses/by/4.0/>).

Abstract: Assassin bug venoms are potent and exert diverse biological functions, making them potential biomedical goldmines. Besides feeding functions on arthropods, assassin bugs also use their venom for defense purposes causing localized and systemic reactions in vertebrates. However, assassin bug venoms remain poorly characterized. We collected the venom from the assassin bug *Rhynocoris iracundus* and investigated its composition and bioactivity in vitro and in vivo. It caused lysis of murine neuroblastoma, hepatoma cells, and healthy murine myoblasts. We demonstrated, for the first time, that assassin bug venom induces neurolysis and suggest that it counteracts paralysis locally via the destruction of neural networks, contributing to tissue digestion. Furthermore, the venom caused paralysis and melanization of *Galleria mellonella* larvae and pupae, whilst also possessing specific antibacterial activity against *Escherichia coli*, but not *Listeria grayi* and *Pseudomonas aeruginosa*. A combinatorial proteo-transcriptomic approach was performed to identify potential toxins responsible for the observed effects. We identified neurotoxic Ptu1, an inhibitory cystin knot (ICK) toxin homologous to ω -conotoxins from cone snails, cytolytic redulysins homologous to trialysins from hematophagous kissing bugs, and pore-forming hemolysins. Additionally, chitinases and kininogens were found and may be responsible for insecticidal and cytolytic activities. We demonstrate the multifunctionality and complexity of assassin bug venom, which renders its molecular components interesting for potential biomedical applications.

Keywords: assassin bugs; venom; transcriptomics; proteomics; bioactivity; paralysis; cytotoxicity; antibacterial; neurolysis

1. Introduction

Venoms typically consist of a plethora of highly diverse toxins that affect a complex range of physiological targets [1]. Consequently, venom components have become highly specialized with the ability to perform complex and intricate biochemical tasks within their target organism [2]. This ability to precisely manipulate specific organismal functions presents a biochemical gold mine of bio-active compounds that can be developed towards therapeutic or biotechnological applications [3,4].

The repurposing of venom toxins has been highly successful in the development of novel analgesics [5], diabetes drugs [6], and blood pressure modulators [7]. Due to their potential applicability, venom toxins are receiving significant attention to discover candidates as therapeutics for many other diseases [8,9]. Particularly, the rich profile of active venom molecules, often found in diverse venoms, present promising molecules for oncological studies [10,11].

Toxins from venomous animals have also been investigated as therapeutic antibacterial candidates in the face of increasing antibiotic resistance and as alternatives for chemical insecticides [12,13]. However, to date, the focus of such investigations has primarily been on toxins from ‘classical’ venomous animals, such as snakes, scorpions, and spiders, with only few studies investigating diverse insect venoms [14,15].

The suborder heteroptera with more than 40,000 described species deserve further attention, since among these numerous species at least some possess potent venoms [16,17]. Notably, heteropterans’ saliva has evolved in response to different trophic specializations [18]. Kissing bugs (Heteroptera: *Triatominae*) are hematophagous species specialized on blood meals and their saliva possess local anesthetic effects enabling stealth feeding [19,20]. While phytophagous hemipteran have specialized to feed on various plant tissues (e.g., vascular fluids, cell contents, and seeds) [21,22], assassin bugs (Heteroptera: *Reduviidae*) are zoophagous and use their venom to paralyze and liquefy their invertebrate prey [23]. Their venom can also have severe effects on vertebrates, including pain, muscle paralysis, hemorrhage, and even death of mice due to respiratory paralysis [24,25]. Reduviids are generalistic predators and their venoms are not species-specific, making them an interesting source of bio-active compounds which could be used in a medical or agronomical context (e.g., as insecticides).

It was previously reported from the harpactorine assassin bug *Pristhesancus plagipennis* and the red-spotted assassin bug *Platymeris rhadamanthus* that their venom comprises numerous enzymes, putative pore-forming toxins, and peptides [26,27]. Moreover, venom gland reconstructions recently revealed three distinct venom gland compartments: posterior main gland (PMG), anterior main gland (AMG), and accessory gland (AG), each containing venom with distinct functions [25]. *P. plagipennis* PMG venom, which can be elicited by electrostimulation, paralyzed and killed their prey, whilst AMG venom, extracted via harassment, did not paralyze prey in the studied species [25]. However, paralytic effects of AMG venom were found in other assassin bug species [28]. AMG venom was suggested to serve defensive purposes and might deter common predators such as birds and small mammals [18,25]. Furthermore, despite the small size of assassin bugs, their venom is potent and medically significant to humans, causing symptoms such as sharp pain, edema, and fever [29]. Although assassin bugs specialized to feed on invertebrates, the cases reporting negative effects on humans demonstrate the bioactivity and complexity of their venom, making it an untapped and valuable source for biomedical applications.

Among reduviids, the assassin bug *Rhynocoris iracundus* has a particularly conspicuous behavior. Instead of hiding, *R. iracundus* is highly exposed to various predators since it ranges freely and prefers to ambush prey on flowers (personal observation). *R. iracundus* can use its proboscis to inject venom and for feeding purposes (Figure 1A) or defense (Figure 1B). During defense, *R. iracundus* displays similar behaviors and body position as typically observed in arachnids (Figure 1C). During feeding the main body segments are aligned in a position allowing an easy flow of liquefied prey content from the proboscis to the digestive organs (Figure 1D). During defense or prey attack, the thorax and abdomen

are lifted allowing the assassin bug to raise and strike with its proboscis. The segments of the latter are then aligned which allows the assassin bug to transfer the full striking energy emerging from the main body to the tip of the proboscis (Figure 1E). As a first line of defense, some assassin bug species have developed additional protective morphological features, such as dorsal crests as in *Arilus cristatus*, a thorn bush as in *Sinea diadema*, or a crown of prominent thorns as in *Platymeris biguttatus* and *Psytalla horrida*. The assassin bug *R. iracundus* shares aposematic coloration, but lacks these morphological features, and therefore relies on its venom for protection.

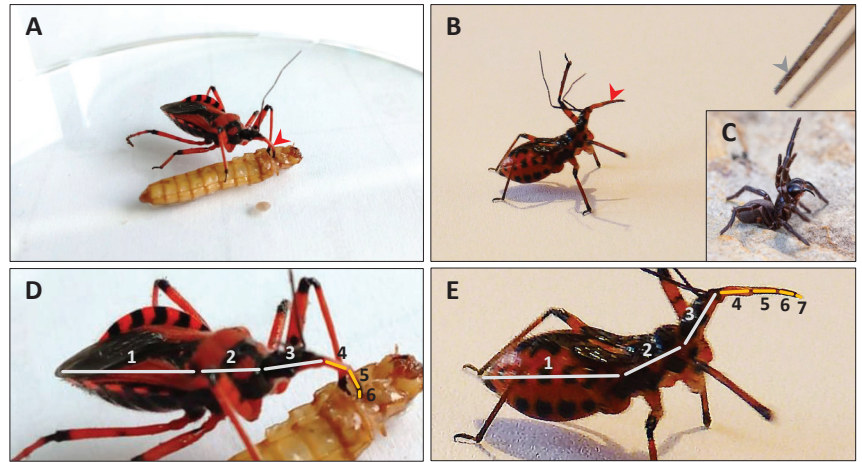


Figure 1. *Rhynocoris iracundus* using its proboscis for feeding or defense purposes. (A) *R. iracundus* using its proboscis (red arrowhead) to feed on a *Tenebrio molitor* larva. The front legs are used to grab and hold its prey. (B) *R. iracundus* in defense position with its elevated front legs and long proboscis (red arrowhead), ready to attack entomological forceps (gray arrowhead). (C) Defense position of a Blue Mountains funnel-web spider *Hadronyche versuta* with elevated front legs and chelicerae (Photo credits: with permission of Greg Bourke). (D,E) Alignment of main body and proboscis segments during feeding and defense, respectively. Body segments are shown with gray lines: abdomen (1), thorax (2), head (3), and proboscis segments are displayed as yellow lines (4–7).

Here, we study *R. iracundus* venom in detail and assess its molecular composition and functional characteristics for the first time. We tested the range of activity of *R. iracundus* venom on mammalian, insect, and bacterial cells, and we conducted in vivo studies in insects. To identify the compounds causing the observed effects, we performed a combinatorial proteo-transcriptomic analysis of the venom glands and the harvested venom. This study highlights the broad activity spectrum and potency of *R. iracundus* venom and identifies key candidates for potential therapeutic or insecticidal use.

2. Materials and Methods

2.1. Assassin Bug Collection, Rearing, and Venom Collection

R. iracundus nymphs were collected from North Rhine-Westphalia, Germany, with permission granted from the nature conservation authority as part of the County Government of Rhineland-Palatinate (Obere Naturschutzbehörde, permission No. 425-104.1713). *R. iracundus* used in this study were kept on a diet composed of meal worm *Tenebrio molitor* larvae and kept in laboratory conditions (24 ± 1 °C and 55–75% relative humidity), in ventilated boxes, partially filled with soil and dried wheat straw.

We used the recently established method to stimulate *R. iracundus* nymphs to display a defense posture and subsequently collected the venom as illustrated in Figure 2 [30]. This procedure performed with one individual assassin bug refers to one venom harvesting event.



Figure 2. *Rhynocoris iracundus* venom collection. (A) To stimulate defensive venom production, *R. iracundus* was tapped using forceps causing it to display a defense posture and to raise its proboscis. (B) Then, the assassin bug was gently pinched on a rear leg (yellow arrowhead) with forceps causing it to use its proboscis (red arrowhead) to stab through the Parafilm stretched over a microcentrifuge tube. (C) Small venom drop released by the assassin bug on the Parafilm (red arrow).

For cytotoxicity and antibacterial assays, the venom was collected from four individuals in four separate microcentrifuge tubes containing 100 μ L phosphate buffered saline (PBS) each. The venom harvesting event was repeated ten times for each individual with 2–3 day intervals. The content of all tubes was pooled to obtain a venom stock solution.

The venom concentration was directly determined with PBS diluted venom by measuring the total protein concentration using the Pierce BCA protein assay kit (Thermo Scientific, Frankfurt, Germany). The measured protein concentration was 3470 μ g/mL, which was used to determine the required venom concentrations for cytotoxicity and antibacterial assays.

For *in vivo* injections in *Galleria mellonella*, the venom harvesting event was repeated with four individuals in a total of either eight or 21 harvesting events, which corresponds to the low and high venom doses, respectively, used in subsequent experiments. Each microcentrifuge tube contained 75 μ L of PBS.

For proteome analysis, the venom was collected from a total of eight venom harvesting events from four individuals, in one microcentrifuge tube without PBS.

All venom harvesting events were performed with 2–3 day intervals. After each venom harvesting event, the microcentrifuge tubes were briefly centrifuged and kept in -20 $^{\circ}$ C until further use.

2.2. Cell Lines and Cell Viability Assay

The cytotoxic effects of *R. iracundus* venom was tested against 2D cell cultures using two cancerous cell lines (Hepa 1–6 mouse hepatoma and Neuro 2a mouse neuroblastoma), non-cancerous cells (C2C12 mouse myoblasts), and Schneider 2 cells (S2 *Drosophila melanogaster* cell line). The first three cell lines were maintained in Dulbecco's Modified Eagle's Medium (DMEM) (Thermo Fisher Scientific, Frankfurt, Germany) supplemented with 4.5 g/L glucose, 110 mg/L sodium pyruvate and 584 mg/L L-glutamine, and 10% heat-inactivated fetal bovine serum (FBS). Incubation was at 37 $^{\circ}$ C in a humidified atmosphere with 5% CO₂. S2 cells were cultured in Schneider's medium (Thermo Fisher Scientific, Frankfurt, Germany), supplemented with 10% heat inactivated FBS, 2 mM L-glutamine, penicillin (100 U/mL) and streptomycin (100 μ g/mL). Incubation was at 28 $^{\circ}$ C. Sub-culture was performed every 2–3 days, as soon as a confluency of 80–90% was reached.

The cytotoxic effects of assassin bug venom on the cell lines were evaluated using the resazurin-based alamarBlue assay (BioRad, Puchheim, Germany), which measures the cell viability after exposure to venom. Cells were seeded at a density of 2×10^4 cells/well for C2C12 cells, 8×10^4 cells/well for Hepa 1–6, and 1×10^5 cells/well for Neuro 2a in 96-well, and 1×10^7 cells/well for S2 cells. Incubation was for 48 h for the first three cell lines, with S2 cells incubated for 24 h. The cells were then exposed to assassin bug venom by incubating them for 4 h with final assassin bug venom concentrations of 43 μ g/mL, 79 μ g/mL, 174 μ g/mL, and 848 μ g/mL for the three cells and 174 μ g/mL for S2 cells. After incubation, venom was removed from the cells by rinsing with PBS. 10% *v/v* alamarBlue reagent was added to each well and the cells were incubated for 1.5 h at 37 $^{\circ}$ C for C2C12,

Neuro 2a and Hepa 1–6 cells, and for 1.5 h at 28 °C for S2 cells). The fluorescence of alamarBlue of the alive cells was measured in a Synergy H4 Hybrid Multi-Mode plate reader (BioTek Instruments, Vermont, United States) using excitation (528 nm) and emission (590 nm) filters. Cells incubated for the same period without venom (0 µg/mL venom) were used as negative controls (reference). The fitness of the control cells was verified by observing their shape using an inverted microscope Motic AE21 (Motic, Wetzlar, Germany). Respective media without cells were used as a blank. Two independent experiments were carried out for each concentration and performed in duplicates. The cell viability was calculated considering the reference as 100% viable cells and using Equation (1):

$$\text{Cell viability (\%)} = \frac{\text{Cell count venom}}{\text{Cell count reference}} \times 100 \quad (1)$$

For each cell line, statistical difference of cell viability between different concentrations of venom and the reference was evaluated using one-way ANOVA, with Dunnett's multiple comparison test in GraphPad 5 Prism program (GraphPad Software Inc., United States). Differences were considered significant when $p < 0.05$.

2.3. Antibacterial Assay

The effect of *R. iracundus* venom on bacterial growth was assessed using the Gram-positive bacterium *Listeria grayi* (DSM 20601), as well as the Gram-negative bacteria *Pseudomonas aeruginosa* (DSM 50071) and *Escherichia coli* (D31). Each strain was cultured overnight at 37 °C in a bacterial culture tube with 10 mL volume containing brain heart infusion broth (BHIB) liquid medium (Sigma-Aldrich, Darmstadt, Germany) for *L. grayi*, and lysogeny broth (LB) liquid medium (Sigma-Aldrich, Darmstadt, Germany) for *P. aeruginosa* and *E. coli*. Each bacterial suspension was then diluted in the respective media to reach an optical density at 600 nm (OD₆₀₀) of ~0.005. Venom stock solution was added to the bacterial suspension at final venom concentrations of 43 µg/mL, and 174 µg/mL. The subsequent incubation was performed for 16 h at 37 °C and the antibacterial activity was determined as previously reported [31]. Negative control cultures without venom (0 µg/mL) containing medium and bacteria only were also included. The assays were carried out twice with comparable results.

2.4. Injection of Venom in *Galleria Mellonella*

G. mellonella larvae at their sixth larval instar were obtained alive from a local pet shop (Fauna Topics Zoobedarf Zucht und Handels GmbH, Marbach am Neckar, Germany) and were maintained as previously described [32]. We used larval and fresh pupal stages for all in vivo injections.

The venom from the microcentrifuge tubes with 21 or 8 venom harvesting events (see Section 2.1) was directly used by injecting 5 µL of diluted venom into individual *G. mellonella* larvae or pupae. Injection was performed subcutaneously in the thorax region using Hamilton micro-syringes and 22 gauge needles. Pupae and larvae which received a single 5 µL PBS injection instead of venom, and also untreated pupae and larvae which did not receive any injection, were used as controls. The effect of the venom on the larvae and pupae was assessed by evaluating melanization on their bodies' surfaces 1 h, 4 h, and 24 h post injection. Paralysis was analyzed by observing their movements after a stimulation with tweezers 1 min, 30 min, 1 h, 4 h, 24 h after injection. *R. iracundus* releases varying quantities of venom in very small amounts, which does not allow precise quantification. Therefore, the venom dose injected in *G. mellonella* was calculated independently from the released amounts, as indicated in Equation (2):

$$\text{Venom dose (\%)} = \frac{\text{Venom harvesting event count}}{V_{\text{harvested venom + PBS}}} \times V_{\text{injection}} \quad (2)$$

with: venom harvesting event count: 8 or 21, $V_{\text{harvested venom+PBS}} = 75 \mu\text{L}$, and $V_{\text{injection}} = 5 \mu\text{L}$.

2.5. Venom Gland Transcriptome Analysis

2.5.1. RNA Isolation, Library Preparation and Illumina Sequencing

To prepare the samples for transcriptome analysis the assassin bugs were anaesthetized at $-20\text{ }^{\circ}\text{C}$ for 5 min, followed by dissection of the venom glands in pre-chilled ($+4\text{ }^{\circ}\text{C}$) PBS. The dissected material was placed in tubes containing 500 μL of TRIzol (Merck KGaA, Darmstadt, Germany) and stored at $-20\text{ }^{\circ}\text{C}$ until RNA extraction. Total RNA was isolated from pooled venom glands (VG), body residues (BO), and gut (GU) using TRIzol according to the manufacturer's instructions, followed by DNase treatment (Turbo DNase, Thermo Fisher Scientific, Schwerte, Germany) and further purification using RNA Clean and Concentrator 5 (Zymo Research, Irvine, United States). RNA quantity was determined using an Implen Nanophotometer and integrity of all RNA samples was verified using an Agilent 2100 Bioanalyzer and an RNA 6000 Nano Kit (Agilent Technologies, Palo Alto, United States). Transcriptome sequencing was carried out by GATC Biotech on an Illumina HiSeq3000 Genome Analyzer platform. Poly-A containing mRNAs were isolated from 1 μg total RNA using oligo-dT attached magnetic beads. The obtained mRNA was fragmented to an average of 260 bp and sequencing libraries were generated using the TruSeq RNA library preparation kit. Paired-end ($2 \times 150\text{ bp}$) read technology was used for sequencing the *R. iracundus* samples, and resulted in a total of 24 million reads for the venom gland samples. Quality control measures, including the filtering of high-quality reads based on the score provided in the fastq files, the removal of reads containing primer/adaptor sequences, and the trimming of the read length were carried out using CLC Genomics Workbench v11 (Qiagen, Hilden, Germany; <http://www.qiagenbioinformatics.com>).

2.5.2. Transcriptome Assembly, Annotation, and Venom Protein Prediction

The de novo transcriptome assembly was carried out using CLC Genomics Workbench v11 with standard settings and two additional CLC-based assemblies with different parameters and then selecting the presumed optimal consensus transcriptome, as described previously (Vogel et al., 2014). The resulting final de novo reference transcriptome assembly of *R. iracundus* contained 38,109 contigs for the venom gland RNAseq data, with an N50 contig size of 1448 bp and a maximum contig length of 26,864 bp. The de novo transcriptome assembly of the combined RNAseq datasets contained 67,588 contigs, with an N50 contig size of 1169 bp and a maximum contig length of 25,112 bp. The transcriptomes were annotated using BLAST, Gene Ontology and InterProScan with Blast2GO Pro version 5.2 [33]. For BLASTx searches against the nonredundant NCBI protein database (NR database; accessed on 13 November 2019), up to 20 best NR hits per transcript were retained, with an E-value cutoff of $\leq 10^{-1}$ and a minimum match length of 15 amino acids to obtain the best homolog for the predicted short polypeptides. To assess transcriptome completeness, we performed a BUSCO (Benchmarking Universal Single-Copy Orthologs; <http://busco.ezlab.org>) analysis by comparing our assembled transcriptome against a set of highly conserved single-copy orthologs. This was accomplished using the BUSCO v3 pipeline [34], comparing the predicted proteins of the *R. iracundus* transcriptome to the predefined set of 1658 Insecta single-copy orthologs from the OrthoDB v9.1 database. This resulted in 89.5% complete and 4.9% missing BUSCO genes for the combined transcriptome assembly. Digital gene expression analysis was carried out using CLC Genomics workbench v11 to generate binary alignment mapping (BAM) files, and finally by counting the sequences to estimate expression levels, using previously described parameters for read mapping and normalization [35]. Post annotation, contigs were manually curated and separated into three categories: (i) putative toxins (contigs with homology to sequences previously identified as pathogenic toxins), (ii) non-toxins (e.g., contigs matching sequences such as housekeeping genes), and (iii) unassigned (contigs where no matches were assigned or BLAST E-values $< 1 \times 10^{-5}$). Putative toxin contigs were subsequently curated in MEGA 7 by trimming to protein encoding regions only, (ii) removing contigs containing mutations which would interfere with expression of the encoded putative toxin (e.g., stop codons, frameshifts) and (iii) merging of identical sequences.

2.6. Venom Proteome Analysis

2.6.1. SDS-PAGE, Protein Digestion and LC-MS Analysis of *R. iracundus* Venom

Venom proteins were separated by sodium dodecylsulfate polyacrylamide gel electrophoresis (SDS-PAGE) on 4–12% Criterion™ XT gradient gels (BioRad, Kalsketal, Germany) with XT MES running buffer. Before loading, samples were mixed with XT sample buffer and reducing agent, and heated for 5 min at 95 °C. The Gel was run for 80 min at 120 V and stained using Coomassie Brilliant blue R250 (Imperial Protein stain, Thermo Scientific, Frankfurt, Germany). Molecular weights (kDa) of separated venom proteins were assessed using a pre-stained (Novex Sharp Pre-Stained Protein Standard, Invitrogen, Schwerte, Germany) and an unstained high mass precision protein marker (Broad Range Unstained Protein Standard, NEB, Frankfurt, Germany).

Two lanes of the SDS-PAGE gel were excised into 20 molecular weight fractions each, with the right lane containing twice the staining densities and twice the total protein amount compared to the left lane. Tryptic digestion was carried out as previously described [36].

For liquid chromatography-mass spectrometry (LC-MS) analysis, the extracted tryptic peptides were reconstituted in 30 µL aqueous 1% formic acid. Depending on staining intensity, 1 to 5 µL of sample were injected into the LC-MS/MS system consisting of an UPLC M-class system (Waters, Milford, United States) online coupled to a Synapt G2-si mass spectrometer (Waters, Milford, United States). Peptides were first on-line pre-concentrated and desalted using a UPLC M-Class Symmetry C18 trap column (100 Å, 180 µm × 20 mm, 5 µm particle size) at a flow rate of 15 µL min⁻¹ (0.1% aqueous formic acid) and then eluted onto a ACQUITY UPLC HSS T3 analytical column (100 Å, 75 µm × 200, 1.8 µm particle size) at a flow rate of 350 nL/min using following gradient: 3–10% B over 3 min, 10–20% B over 12 min, 20–30% B over 25 min, 30–70% B over 10 min, 70–95% B over 3 min, isocratic at 95% B for 1 min, and a return to 1%B (Buffers: A, 0.1% formic acid in water; B, 100% acetonitrile in 0.1% formic acid).

The eluted peptides were transferred into the mass spectrometer operated in V-mode with a resolving power of at least 20,000 full width at half height FWHM. All analyses were performed in a positive ESI mode. A 200 fmol/µL human Glu-Fibrinopeptide B in 0.1% formic acid/acetonitrile (1:1 *v/v*) was infused at a flow rate of 1 µL min⁻¹ through the reference sprayer every 45 s to compensate for mass shifts in MS and MS/MS fragmentation mode.

Data were acquired using data-dependent acquisition (DDA) and data-independent acquisition (DIA, referred to as enhanced MS^E). The acquisition cycle for DDA analysis consisted of a survey scan covering the range of *m/z* 400–2000 Da followed by MS/MS fragmentation of the 10 most intense precursor ions collected at 0.2 s intervals in the range of 50–2000 *m/z*. Dynamic exclusion was applied to minimize multiple fragmentations for the same precursor ions. LC-MS^E data were collected using alternating low energy (MS) and elevated energy (MSE) mode of acquisition over 0.5 s intervals in the range *m/z* 50–2000 with an interscan delay of 0.05 s. In low energy mode, data were collected at constant collision energy of 4 eV set on the trap T-wave device and ramped during scan from 20 to 45 eV in elevated MS^E mode. MS data were collected using MassLynx v4.1 software (Waters, Milford, United States).

2.6.2. Data Processing and Protein Identification

DDA raw data were processed and searched against a subdatabase containing common contaminants (human keratins and trypsin) using ProteinLynx Global Server (PLGS) version 2.5.2 (Waters, Milford, United States). The following searching parameters were applied: fixed precursor ion mass tolerance of 15 ppm for survey peptide, fragment ion mass tolerance of 0.02 Da, estimated calibration error of 0.002 Da, one missed cleavage, fixed carbamidomethylation of cysteines, and possible oxidation of methionine. Spectra remained unmatched by database searching were interpreted de novo to yield peptide sequences and subjected for homology-based searching using MS BLAST program [37] installed on a local server.

MS BLAST searches were performed against *R. iracundus* sub-database obtained from in silico translation of *R. iracundus* transcriptome and against insecta databases downloaded from <https://www.ncbi.nlm.nih.gov/>, accessed on 3 March 2020.

In parallel, pkl-files of MS/MS spectra were generated and searched against *R. iracundus* subdatabase combined with NCBI nr database (<https://www.ncbi.nlm.nih.gov/>, accessed on 24 May 2020; containing 285,796,321 sequences) using MASCOT software version 2.6.2. The acquired continuum LC-MSE data were processed using ProteinLynx Global Server (PLGS) version 2.5.2 (Waters, Milford, United States). The thresholds for low/high energy scan ions and peptide intensity were set at 150, 30 and 750 counts, respectively. The processed data were searched against *R. iracundus* protein sub-database combined with Swissprot database downloaded from <http://www.uniprot.org/>, accessed on 13 July 2020. The database searching was performed at a false discovery rate (FDR) of 4%, following searching parameters were applied for the minimum numbers of: product ion matches per peptide (3), product ion matches per protein (7), peptide matches (1), and maximum number of missed tryptic cleavage sites (1). Searches were restricted to tryptic peptides with a fixed carbamidomethyl modification for Cys residues.

2.7. Protein Sequence Alignment

Multiple sequence alignments were performed using MAFFT 7.0 with default parameters and the E-INS-i refinement method [38,39]. The sequence logo was generated using WebLogo tool (Version 2.8.2) [40].

2.8. Phylogenetic Tree

To create the phylogenetic trees for Pt1, hemolysin, and redulysin, we used the following approach: homologous sequences for each toxin family were obtained from Genbank. Sequences were aligned using MAFFT configured for highest accuracy [38] and non-aligned regions were removed with Gblocks (v 0.91b) [41]. The best-fit model was selected based on Akaike Information Criterion (AIC) and Bayesian Information Criterion (BIC) implemented in Molecular Evolutionary Genetics Analysis X (MEGA version X) [42]. MEGA was used for the following steps: obtaining the best tree topologies using the maximum likelihood (ML) method, estimation of the proportion of Gamma distributed sites (G), determination of the reliability of internal branches using the bootstrapping method (500 bootstrap replicates), and graphical representation and editing of the phylogenetic tree.

The percentage of trees in which the associated taxa clustered together is shown next to the branches. Initial tree(s) for the heuristic search were obtained automatically by applying Neighbor-Joining and BioNJ algorithms to a matrix of pairwise distances estimated using the JTT model (for redulysins and hemolysins), Le-Gascuel model (for Pt1 family peptides) and then selecting the topology with superior log likelihood value. The tree is drawn to scale, with branch lengths corresponding to the number of substitutions per site. This analysis involved 25, 14, and 17 amino acid sequences for redulysins, hemolysins, and Pt1 family peptides, respectively. All positions containing gaps and missing data were eliminated (complete deletion option). In the final dataset, there were a total of 112, 115, 21 positions for redulysins, hemolysins, and Pt1 family peptides, respectively. The phylogenetic trees were inferred using MEGA X [42].

Species and accession numbers used in phylogenetic trees and alignments are listed in Supplementary Data S5.

3. Results

3.1. Venom Activity Against Mouse Cancer Cells and Healthy Mouse Cells

To assess the activity of *R. iracundus* venom on different cell types, as well as its oncological potential, we performed viability assays with cancer cells, Hepa 1–6 (murine epithelial hepatoma cells), Neuro 2a (murine neuroblastoma cells) and C2C12 (healthy mouse myoblasts) using the resazurin-based alamarBlue assay. Exposure to the lowest

venom concentration (43 µg/mL) showed a significant and potent cytotoxic effect in all tested cell lines compared to the control (Figure 3).

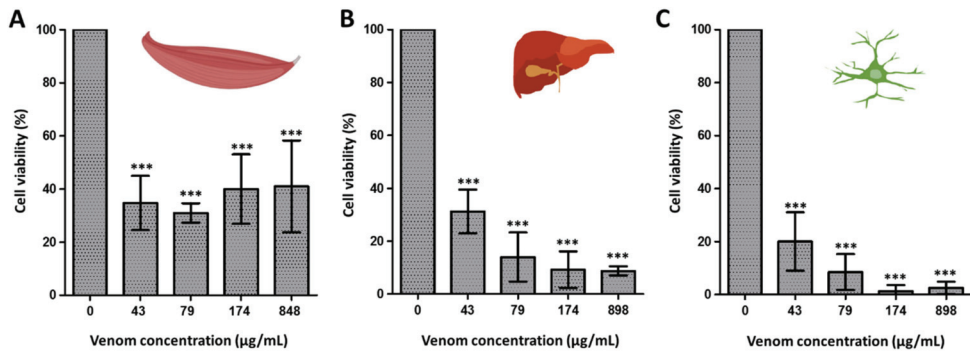


Figure 3. Cytotoxic effect of assassin bug venom. The effect of *Rhynocoris iracundus* venom was tested at different concentrations on healthy mouse myoblast cells C2C12 (A), on mouse hepatoma cells Hepa 1–6 (B), and on mouse neuroblastoma cells Neuro 2a (C). Shown are means and standard deviation values of the replicate samples. Statistical analysis was performed by one-way ANOVA with Tukey’s multiple comparison test applied for individual comparisons. Statistical significance of the differences of all venom concentrations against the control (0 µg/mL) are indicated with asterisks (***) $p < 0.0001$.

3.2. Venom Activity Against Bacteria

To evaluate the effect of *R. iracundus* venom against bacteria, we performed bacterial growth inhibition assays using Gram-positive *L. grayi* DSM 20601 and Gram-negative *P. aeruginosa* DSM 50071 and *E. coli* D31. No activity was observed on *L. grayi* and *P. aeruginosa* (Supplementary Figure S1). However, *E. coli* was susceptible to the highest venom concentration (174 µg/mL). A lower concentration of venom (43 µg/mL) delays the growth of *E. coli* (Figure 4).

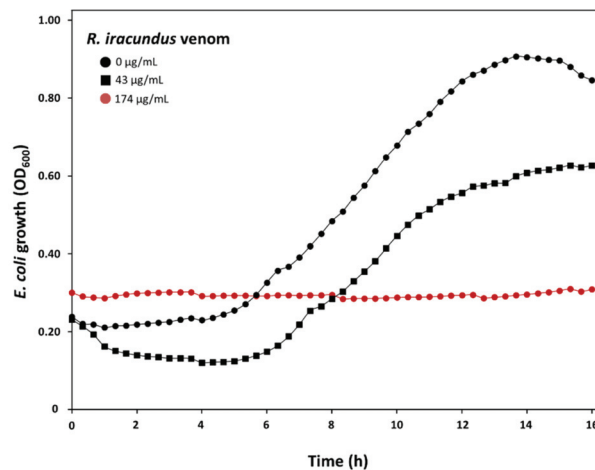


Figure 4. Effect of assassin bug *Rhynocoris iracundus* venom on *E. coli* D31 growth. Venom activity was tested using different concentrations of crude venom incubated together with *E. coli* D31. Bacterial growth was monitored by measuring OD₆₀₀ values at 20 min intervals for 16 h. The effective venom concentration of 174 µg/mL is shown as a red line, and the bacterial growth curve at lower venom concentrations (43 µg/mL), or without venom (0 µg/mL), are displayed as black lines.

3.3. Venom Activity Against Insect Cells and *G. mellonella* Pupae and Larvae

R. iracundus venom was tested for its cytotoxic effects on S2 cells using the resazurin based alamarBlue assay. Co-incubation of S2 cells with 174 µg/mL of venom strongly decreased the viability of S2 cells, causing 99% cell death during an incubation period of 4 h. S2 cells exposed to 174 µg/mL venom for as little as 30 s demonstrated morphological disruption by losing their shape, leading to lysis and cell death (Figure 5).

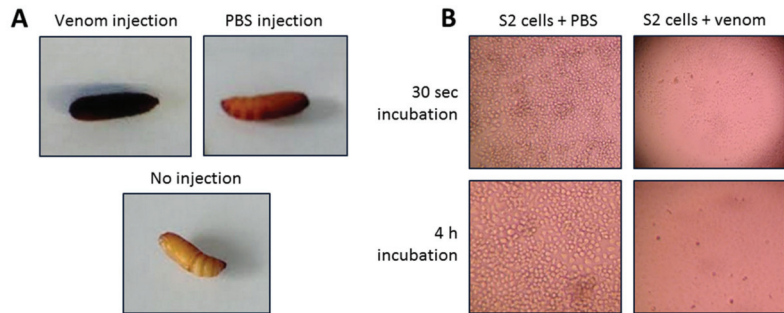


Figure 5. Effect of assassin bug *Rhynocoris iracundus* venom on insects. **(A)** Melanization of *G. mellonella* pupae in response to *R. iracundus* venom injection was assessed 4 h post injection. PBS injected and no injected pupae were used as controls. **(B)** Effect of venom on S2 cells after 30 s of co-incubation with venom. Morphological changes of S2 cells were monitored using an inverted microscope. Incubation of S2 cells together with 174 µg/mL venom for 30 s caused complete cell lysis. Incubation of S2 cells with PBS only (control) did not cause any visible cell lysis.

To investigate the effects of assassin bug venom on potential prey *in vivo*, we subcutaneously injected *R. iracundus* venom in *G. mellonella* larvae and pupae before evaluating the level of melanization and paralysis. Since the amount of venom during each envenomation can vary, we tested a low and a high dose of venom equivalent to 50% and 140% of the average venom dose, respectively (Table 1). For pupae and larvae, the first immobilization effects were already observed 1 min after post-injection. Strong melanization occurred after 4 h in larvae and pupae of *G. mellonella*. Three larvae were fully immobilized after 1 min, which progressively decreased after 4 h despite initiation of melanization. Furthermore, larvae became very soft 1 h post-injection. All tested *G. mellonella* pupae and larvae died, except one larva, which received only 50% of the average venom dose. This shows that the observed initial recovery in two out of three *G. mellonella* larvae was only temporary. Pupae and larvae, which were not injected remained healthy during the entire analysis and showed neither melanization responses nor a reduction in their mobility when stimulated with tweezers. PBS-injected pupae and larvae remained healthy as well but only slight and strictly localized melanization was observed at injection sites (Table 1).

3.4. Molecular Components of the Venom

3.4.1. Overview of *R. iracundus* Venom-Gland Transcriptome

Sequencing of *R. iracundus* venom gland transcriptome yielded ~16 Mio trimmed, paired-end reads. The reads were subsequently assembled into 38,109 distinct contigs. Post-annotation, contigs were assigned into three categories: venom toxins, non-toxins and unassigned. The venom toxin transcripts accounted for 29% of total relative expression despite being comprised of only 0.1% of total transcripts (292 venom toxin transcripts). Notably, a substantial portion of the relative venom toxin expression was due to just two toxin families; venom family 17 (3 transcripts representing ~11% total expression) and hemolysins (4 transcripts representing ~7% total expression) (Figure 6).

Table 1. Effect of *Rhynocoris iracundus* venom on *Galleria mellonella*. *G. mellonella* larvae and pupae were injected subcutaneously with low (50%) and high (140%) venom doses. Paralysis and melanization observations were recorded from 1 min until 24 h post injection.

<i>Galleria mellonella</i> Stages	Venom Dose (%)	Incubation after Injection								Replicates
		1 min Paralysis	30 min Paralysis	1 h Paralysis	1 h Melanization (%)	4 h Paralysis	4 h Melanization (%)	24 h Paralysis	24 h Melanization (%)	
Pupae	140	none	n.a.	none	0	full	70	full	100	4
	50	full	n.a.	full	0	full	70	full	100	1
	PBS only	full	n.a.	full	0	full	40	full	90	7
	No injection	none	none	none	0	none	<5	none	<5	12
Larvae	50	none	partial	n.a.	n.a.	full	60	full	100	5
		full	full	n.a.	n.a.	full	30	full	100	3
		full	full	n.a.	n.a.	partial	20	partial	100	1
		full	full	n.a.	n.a.	partial	20	full	100	1
	PBS only	none	none	n.a.	n.a.	none	<5	none	<5	12
	No injection	none	none	n.a.	n.a.	none	0	none	0	12

n.a. = not applicable (paralysis and/or melanization were not assessed).

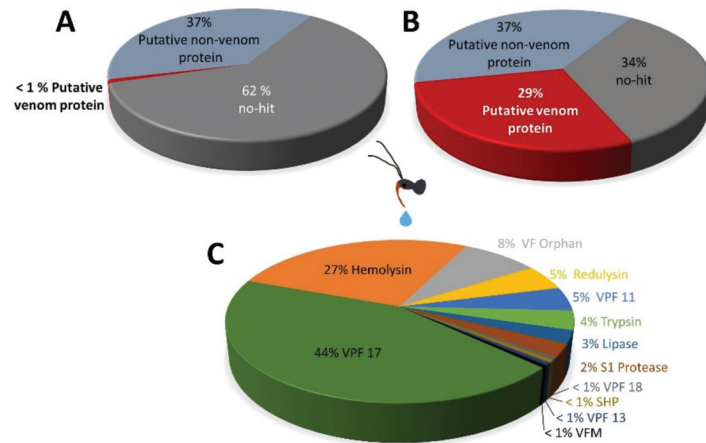


Figure 6. Types of transcripts found in *Rhynocoris iracundus* venom gland. (A) Relative proportion of venom protein encoding genes, non-venom protein encoding genes, and transcripts designated as “no-hit” (unknown). Venom protein genes account for <1% of the total transcripts (B) represents the relative transcript expression levels of the same categories. Among them, 29% of all sequence read counts of the transcripts are associated with the category “putative venom protein”. (C) Relative expression levels of toxin encoding genes only, displayed as % transcript expression of total putative venom protein encoding transcripts.

Curation of the *R. iracundus* venom toxin transcripts revealed 35 individual venom toxin families (including the two mentioned above) represented by full length or partial transcripts. A total of 71 venom toxin transcripts were removed due to the presence of mutations which would render resulting proteins non-functional.

The majority (>50%) of transcripts related to venom proteins belonged to the S1 protease (38 total, 10 full-length/28 fragment), trypsin (28, 15/33), orphan venom-family (25, 11/14), secreted hypothetical protein (14, 6/8), venom family 13 (11, 0/11) and chitinases (9, 3/6). However, the total relative expression of these families represented just 15% of total toxin transcript expression. In addition to venom family 17 and hemolysin already described above, other highly expressed toxin families include the orphan venom family (2% total expression), redulyisin (~1%), and venom family 11 (~1%) (Figure 6).

Nevertheless, it should be noted that our transcriptomic approach identifies putative toxin precursor transcripts, and that our subsequent proteomic analysis validates whether the toxins were expressed.

3.4.2. Venom Proteome of the Assassin Bug *R. iracundus*

Based on the assembled venom transcriptome of *R. iracundus*, we broadly characterized the venom proteome by two sample runs using a standard bottom-up proteomics workflow. Venom samples were separated by SDS-PAGE (Figure 7) and both lanes were divided into 20 gel slices and subjected to in-gel digestion [43,44]. Resulting tryptic peptides were analyzed by peptide spectrum matching (PSM) based on the translated toxin sequences of the assembled transcriptome. The selected workflow does not allow any precise quantitative statements, but qualitative correlation can be achieved by identical protein matches.

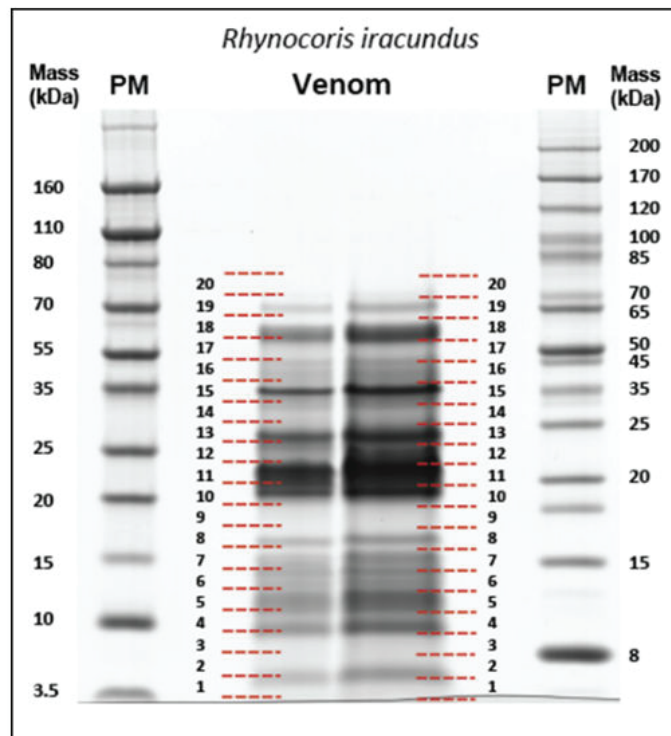


Figure 7. SDS-PAGE analysis of *Rhynocoris iracundus* venom proteins. Proteins collected from the venom glands of *R. iracundus* were separated by SDS-PAGE and stained with Coomassie Brilliant Blue R250. Numbers on the left and right of the lanes with venom indicate the 20 bands cut out from the gel and processed as individual samples for LC-MS/MS. PM = protein marker.

In total, the proteomic analysis resulted in 93 and 105 protein matches for run 1 and run 2, respectively (Supplementary Table S1). Among the 35 individual toxin families identified in the *R. iracundus* venom proteome, six abundant and 12 low abundant toxin families were represented. A direct comparison of the venom composition for both sample runs showed a high agreement of identical toxins (87% and 67% of the total toxins in run 1 and run 2 respectively were detected in both sample runs) (Figure 8, Supplementary Table S1). The majority of the assassin bug venom proteins, identified by specific peptide fingerprints, belong to the proteolytic toxin families S1 proteases (27 isoforms), S1 proteases with CUB

In the generated sequence logo, the overall height of each stack indicates the sequence conservation at that position (measured in bits) (Figure 9B). In the cytolytic region of redulysins and trialysins, Lys (K) residues are frequent and highly conserved. One Leu (L) is conserved in all sequences. We also aligned the complete sequences of the mentioned redulysins and trialysins and found that the C-terminal domain is stabilized by a pattern of eight conserved Cys (C) residues (Supplementary Data S1). To phylogenetically characterize *R. iracundus* redulysins, we used the same redulysin and trialysin sequences mentioned earlier together with trialysins from the broad-headed bug *Riptortus pedestris* (Hemiptera: Alydidae) (Figure 9C). The resulting phylogenetic tree is rooted with trialysins from *R. pedestris*. All redulysins and trialysins from *Reduviidae* fall into two main clades (roots highlighted in green and blue). Both of them display a clade expansion and have sequences from each assassin bug species. *R. iracundus* redulysins are more closely related to the redulysins from *P. plagipennis* than the redulysins from *P. rhadamanthus*.

3.5.2. Kininogens

In the *R. iracundus* proteome, we found a kininogen which belongs to the cystatin family. Kininogens are also found in *P. plagipennis* and *P. rhadamanthus*. We aligned the kininogen from *R. iracundus*, *P. plagipennis*, and *P. rhadamanthus* for comparison (Supplementary Data S2) and we found that, although the sequences align well, there are only 17% identical amino acids (Figure 10). We also found a conserved proteinase inhibitor cystatin site between Arg 72 and Glu 85, with 43% conserved amino acids. Four out of five putative protease inhibition sites are located within the proteinase inhibitor cystatin site.

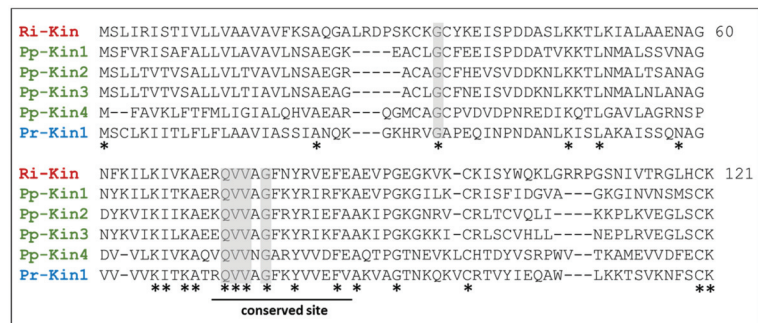


Figure 10. Sequence alignment of assassin bug kininogens. Kininogen sequences from *R. iracundus*, *P. plagipennis*, and *P. rhadamanthus* were aligned together. The conserved proteinase inhibitor cystatin site (Arg 72–Glu 85, Interproscan, IPR018073) is indicated with a line. Putative protease inhibition sites are highlighted in gray. Conserved amino acids are shown with asterisks (*).

3.5.3. Chitinases

In the *R. iracundus* proteome, we identified one chitinase. Based on the previously reported active domain motif for chitinases DxxDxDxE [47], we performed a motif search and aligned the identified active domain motifs from *R. iracundus* chitinase together with the chitinase-like protein from *P. plagipennis* (assassin bug) and the chitinases from *Halyomorpha halys* (stink bug), *Cimex lectularius* (bed bug), *Frankliniella occidentalis* (thrips), *Harpegnathos saltator* (ant), and *Apis cerana* (honey bee) (Figure 11). We found two conserved active domain motifs D₂₀₆xxD₂₀₉x D₂₁₁x E₂₁₃ (active domain 1) and N₆₂₉/D₆₂₉xxD₆₃₂x D₆₃₄x E₆₃₆ (active domain 2) (Figure 11, and Supplementary Data S3). To find out if other insect orders share Asn 629 (N₆₂₉), which was found in the active domain 2 of assassin bug chitinases, we aligned 86 chitinases from eight insect orders (Supplementary Table S2). Our findings revealed that assassin bugs share N₆₂₉ in the active domain 2 together with all insect orders, except for hymenopterans. The latter are the only representatives having Asp 629 (D₆₂₉) in active domain 2.

	206	629
Ri_Chi	DGLD VDWE	NGLD VDWE
Pp_Chi-like	DGLD VDWE	NGLD VDWE
Hh_Chi	DGLD VDWE	NGLD VDWE
Cl_Chi	DGLD MDWE	NGLD VDWE
Fo_Chi	DGLD MDWE	NGLD VDWE
Hs_Chi	DGLD IDWE	DGLD VDWE
Ac_Chi	DGLD IDWE	DGLD VDWE
	**** **	*****
	Active domain 1	
	DxxDxDxx	DxxDxDxx
		NxxDxDxx

Figure 11. Alignment of chitinases. Chitinase and chitinase-like protein sequences from order Hemiptera (red, *R. iracundus*, *P. plagipennis*, *Halyomorpha halys*, *Cimex lectularius*), Thysanoptera (yellow, *Frankliniella occidentalis*) and order Hymenoptera (green, *Harpegnathos saltator* and *Apis cerana*) aligned and two active regions were found using interproscan website using *R. iracundus* chitinase protein sequence. Conserved residues from the active site motifs known for the activity of glycosyl hydrolase family 18 (GH18) indicated with bold. * indicates conserved amino acid residues.

3.5.4. Hemolysins

Three full length hemolysin transcripts (Ri_Hly_1, Ri_Hly_2, and Ri_Hly_3) were identified in the *R. iracundus* transcriptome. We used pairwise identity matrix of hemolysin sequences from various Hemiptera, including the assassin bugs *R. iracundus* (Ri_Hly), *P. plagipennis* (Pp_Hly), and *P. rhadamanthus* (Pr_Hly), both kissing bugs *T. infestans* (Ti_Hly) and *Panstrongylus chinai* (Pc_Hly), the giant water bug *Lethocerus distinctifemur* (Ld_Hly) and the bacteria *E. coli* (Ec_Hly) together to assess their similarity. The analysis suggested that hemolysin from *E. coli* has a maximal identity of <18% to insect hemolysins. *R. iracundus* Ri_Hly1 showed ~79% and ~78% identity to *P. plagipennis* hemolysins Pp_Hly1 and Pp_Hly2, respectively. *R. iracundus* Ri_Hly2 presented 75.35% identity to *P. plagipennis* Pp_Hly3 (Figure 12A). We also build a phylogenetic tree using hemolysins from Hemiptera. Within insect hemolysins, there are two sub-clades of hemolysins; the first clade consists of assassin bugs including two sequences from *R. iracundus* and the giant water bug hemolysin, whereas the second one includes kissing bug and assassin bug hemolysins with one sequence from *R. iracundus* (Figure 12B).

3.5.5. Pt1 Family Peptides

Pt1 is a N-type calcium channel blocker [48] neurotoxin [26]. In our transcriptomics analysis, we identified two complete Pt1 family peptides in the venom gland assembly (Ri_Pt1_1 and Ri_Pt1_2) and four complete sequences in the combined assembly (Ri_Pt1_3-Ri_Pt1_6). We aligned the regions containing the knotting scaffold of Cys residues [48] from Pt1 family peptides from *R. iracundus* and other species of assassin bugs (*P. rhadamanthus*, *P. plagipennis*, *Peirates turpis*) and from ω -conotoxins, which are Pt1 homologues [48], from the cone snails *Conus magus* and *Conus moncuri* [49,50] (Figure 13A). We found that the Cys residues are highly conserved in *R. iracundus* Pt1 and present the typical inhibitor cystine knot (ICK) scaffold. However, all inter-cysteine loops show sequence diversities (Figure 13A). In the well characterized toxins Pt_Pt1 and MVIIA, we highlighted the residues in loop 2 which play a critical role in surface interactions [48]. Those residues are found in the same positions in Pt1 family peptides from *R. iracundus* (Ri_Pt1_3 and Ri_Pt1_4) (Figure 13A). However, for the remainder of Pt1, amino acids with different properties were found. The sequence similarities between Pt1 family peptides from *R. iracundus* and the previously characterized Pt_Pt1_1 and MVIIA [48] were below 45%.

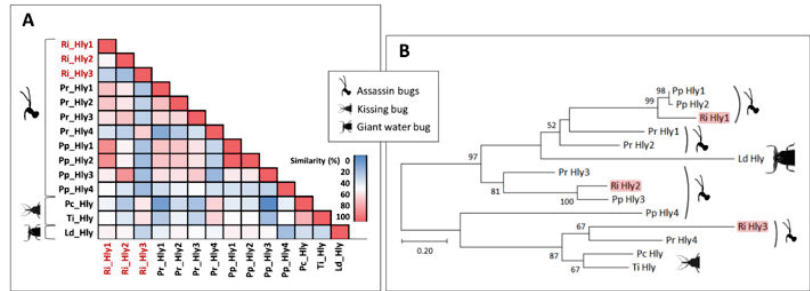


Figure 12. Characterization of hemolysins. **(A)** Pair-wise identity matrix of hemolysin sequences from insect order Hemiptera. Shown are hemolysins from the assassin bug *R. iracundus* (Ri_Hly), *P. plagipennis* (Pp_Hly), *P. rhadamanthus* (Pr_Hly), two kissing bugs *T. infestans* (Ti_Hly), and *Panstrongylus chinai* (Pc_Hly), and the giant water bug *Lethocerus distinctifemur* (Ld_Hly). **(B)** Phylogenetic tree of hemolysins. Hemolysin sequences from three assassin bugs *R. iracundus* (Ri_Hly) (highlighted in red), *P. plagipennis* (Pp_Hly), and *P. rhadamanthus* (Pr_Hly), two kissing bugs *T. infestans* (Ti_Hly), and *Panstrongylus chinai* (Pc_Hly), the giant water bug *Lethocerus distinctifemur* (Ld_Hly) were analyzed together. The phylogenetic tree was inferred by using the Maximum Likelihood method and Whelan and Goldman model (Whelan and Goldman, 2001). The tree with the highest log likelihood (−2664.67) is shown.

Using a pair-wise identity matrix we show that Ri_Ptu1_1 has 84% sequence similarity to Pp_Ptu1_1, and Ri_Ptu1_2 has 78% sequence similarity to Pp_Ptu1_2 (Supplementary Data S4). Interestingly, phylogenetic analysis revealed that *R. iracundus* Ri_Ptu1_4 and Ri_Ptu1_5 fall into a separate branch together with cone snail ω-conotoxins. The rest of the assassin bug Ptu1 family peptides form a separate clade (Figure 13B).

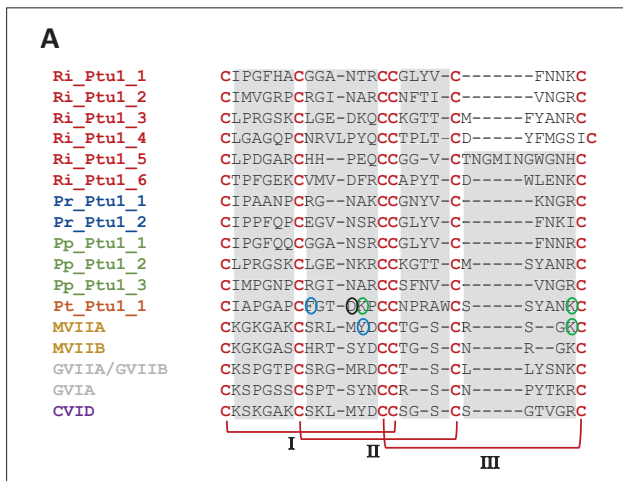


Figure 13. Cont.

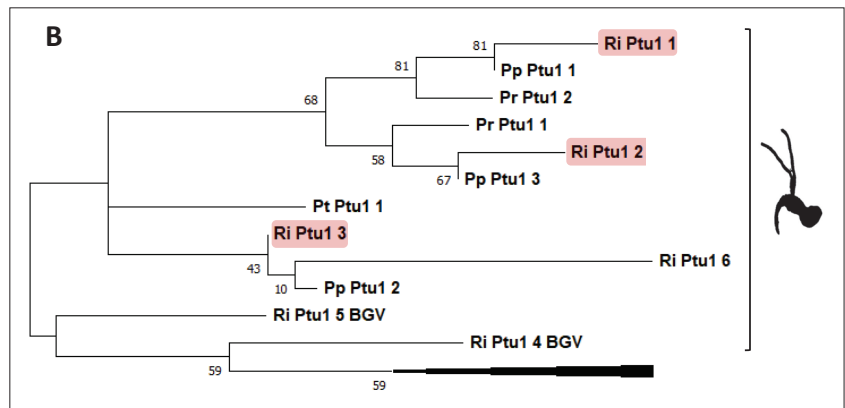


Figure 13. Characterization of Pt1 family peptides. (A) Alignment of Pt1 family peptides from *Rhynchocoris iracundus* (Ri_Ptu1_V1, Ri_Ptu1_V2, (Ri_Ptu1_BGV3-Ri_Ptu1_BGV6), *P. rhadamanthus* (Pr_Ptu1_1 and Pr_Ptu1_2), *P. plagipennis* (Pp_Ptu1_1, Pp_Ptu1_2, Pp_Ptu1_3), *P. turpis* (Pt_Ptu1_1), and their homolog ω -conotoxins (MVIIA, MVIIIB, GVIIA/GVIIIB, CVID) from cone snails. The structure of Pt1 family peptides includes three disulfide bridges (I, II, III) connecting six conserved cysteines, which are separated by four inter-cysteine loops. Residues playing a role in surface interaction such as aromatic residues (blue circle), acidic residues (black circle), and basic residues (green circle) are highlighted as published for Pt_Ptu1 and MVIIA. (B) Phylogenetic tree of Pt1 family peptides. Pt1 and ω -conotoxins mentioned above were used to generate a phylogenetic tree which was inferred by using the Maximum Likelihood method and Le-Gascuel model [46]. The tree with the highest log likelihood (-543.24) is presented. The cone snail image was created with Biorender.com.

4. Discussion

4.1. Primary Functions of Reduviid Venom: Capturing and Feeding on Arthropod Prey

Due to their abundance, arthropods represent a valuable food source for predators such as assassin bugs. However, arthropods have evolved to protect themselves from predatory attacks through the ability to quickly escape [51], possession of hard exoskeletons [52], the use of stingers [53] and venom [54]. Assassin bugs have learned and evolved to cope with these defense strategies. After a slow approach, reduviids ambush their prey, pin it down with their front legs, and quickly bite through soft body parts with a specialized straw-like proboscis. *R. iracundus* often feeds on honeybees *Apis* sp. and for such dangerous prey, *R. iracundus* prepares its proboscis in advance by elevating it towards the prey and in a sudden movement stabbing the prey with the proboscis and immediately pinning it down with the front legs at the same time (personal observation). A cocktail of venom with paralyzing components is injected through their particularly long proboscis [25]. Quick paralysis protects assassin bugs from injuries potentially caused by counterattacks from their prey and enables them to secure it for feeding purposes [25]. Since reduviids do not possess chewing mouth parts, components of the venom with liquefying properties are essential for feeding on their prey [25].

Notably, assassin bugs are able to modulate the composition of their venom in a context-dependent manner, either for defense or feeding purposes [25]. In our study, venom was collected after treating *R. iracundus* to display a defense posture. To understand its effects on their natural prey, we tested the venom on insects and insect cells. The injection of *R. iracundus* venom caused quick and full paralysis of *G. mellonella* larvae and pupae indicating the potency of the venom against insects, which is in line with the full paralysis observed on their natural preys such as honeybees; likely, the induced paralysis is a result of muscular or nervous dysfunction [55]. The earliest description of assassin bug venom effect on prey showing its paralytic activity, was described in 1773 [56] “once stung, the fly died immediately, which indicates that the assassin bug (*Reduvius personatus*)

probably delivers potent venom". In 1961, the paralysis observed in assassin bug prey was attributed to the disruption of cell membranes [23]. However, as it was observed with *R. personatus* and for other assassin bug species [25,57], *R. iracundus* venom also caused potent, quick and generalized paralysis in the entire insect body. This is in accordance with previous suggestions [25,27,57] that paralysis is not the result of localized cell membrane disruption, but it is due to molecular components of the venom targeting nerve cells. The neurotoxic effects on prey could be attributed, probably among other factors, to the presence of Pt1 [26]. However, the role of Pt1 family peptidases is controversial because previous publications mentioned that Pt1 family peptides are neurotoxins that blocks N-type voltage-sensitive calcium channels [26,48], while the toxicity of Pt1 family peptides could not be verified in vivo [58]. Further studies are required to understand its effects in vivo. Pt1 family peptides are part of the inhibitory cystin knot (ICK) family capable of blocking nerve conduction [26,48]. Here, we found six different Pt1 family peptides in the venom gland transcriptome of *R. iracundus*. In the well characterized Pt_Pt1 from the assassin bug *P. turpis* and in its homolog MVIIA from the cone snail *Conus magus*, the respective aromatic residues Phe13 and Tyr13, surrounded by basic residues in loop 2, are critical for the binding of the toxin to the channel [48]. Notably, we found two out of six Pt1 family peptides from *R. iracundus* clade together with cone snail ω -conotoxins. We have also observed, at the amino acid level, that one sequence of Pt1 family peptide from *R. iracundus* possesses two identical residues as MVIIA in the same positions in loop two, and another sequence of Pt1 family peptides from *R. iracundus* possesses one identical residue as Pt_Pt1_1 in the same position. These residues play critical roles in surface interaction [48]. The rest of the Pt1 family peptides have different amino acid residues at these positions. Potential candidates for sodium channel surface interaction residues with identical properties were found in different inter-cysteine loops in *R. iracundus* Pt1 family peptides. The residues present in the inter-cysteine loops of ICK toxins can be mutated without significantly affecting their 3D structure [59], but are known to have an impact on binding specificity [60]. The cone snail ω -conotoxins are used as analgesic drugs for severe and chronic pain [5,61] and due to their similarities, Pt1 family peptides could be interesting candidates for pharmaceutical applications. In addition, assassin bug venom Pt1 family peptides revealed high conservation between *R. iracundus* and the Australian *P. plagiipennis* (Ri_Pt1_1/Pp_Pt1_1: 84% similarity, Ri_Pt1_2/Pp_Pt1_3: 78% similarity), which suggests that these species share a relatively recent common ancestor of Pt1 family peptides in geographically distant assassin bug species.

Assassin bug venom contains a high proportion of molecular components with cytolytic and enzymatic activities involved in tissue liquefaction [26]. In vivo injected *G. mellonella* larvae and pupae with *R. iracundus* venom lost their bodies' rigidity and got soft to the touch. The addition of *R. iracundus* venom to S2 insect cells caused 99% cell lysis within 30 s, demonstrating the potency of *R. iracundus* venom to lyse and liquify their prey. In our transcriptome and proteome data we found digestive enzymes such as S1 proteases, S1 protease + CUB, and also chitinases which are, possibly among other molecular components, responsible for the observed insect softening and cell lysis [26,62].

In other zoophagous heteropterans, such as *P. plagiipennis* chitinase-like proteins were also detected. Chitinases are also present in salivary glands of phytophagous hemipterans, e.g., *Oncopeltus fasciatus* [63] but were not found in hematophagous kissing bugs such as *Rhodnius prolixus* [64]. Despite the phytophagy of *O. fasciatus*, the presence of chitinases in its salivary glands is probably important due to its occasional cannibalistic behavior [65], which is rare in kissing bugs [66]. Insect chitinases have the primary role to digest chitin during metamorphosis [67,68]. Their presence in salivary glands and venom glands of insects further suggests their importance toward feeding and defense purposes. We noticed that chitinases possess two active domains: active domain 1 (DxxDxDxx) present in all insects, while active domain 2 presented a sequence specific to hymenopterans (DxxDxDxx), which is different from all other insect orders (NxxDxDxx). The sequence DxxDxDxx was described essential for the enzymes' activity [47]. We suggest that in hymenopterans

Asn (N(1)) mutated to Asp (D(1)) in the active domain 2. The impact of this mutation in chitinases is not known yet. However, what is known is that chitinases have multifunctional roles, e.g., regulation of inflammation or intratumoral processes, potentially making them attractive candidates for cancer therapy and immunomodulation [69].

Beside paralysis, strong melanization of *G. mellonella* was also observed; however, it appeared a few hours post injection. Melanization could be a secondary response of the cell lysis, which was characterized by softening of the *G. mellonella* bodies. Melanization plays a vital role in various physiological processes in insects, including wound healing and immunity [70].

4.2. Versatility of Assassin Bug Venom towards Defense Purposes

Using their proboscis, assassin bugs are capable of inflicting painful bites to humans, with local and systemic symptoms, as reported from *Zelus* sp. [29]. This shows that assassin bugs can use their proboscis to stab and deliver venom for self-defense purposes, and that the venom has potent bioactivity on potential threats, such as predators. For example, mice can be severely affected by assassin bug venom, even resulting in their death due to venom-inflicted respiratory paralysis [24].

When harassed, *R. iracundus* immediately takes a defense posture, lifting its front legs, and displaying its venom delivery organ. We noticed that the defense posture of assassin bugs resembles those typically observed in arachnids [71]. This enables assassin bugs to raise up towards predators of greater size and the position of their proboscis prepares them for a direct attack. Furthermore, a small drop of venom sticking to the end of the proboscis was often released in a fashion similar to disturbed funnel web spiders [72].

Assassin bug *Holotrichius imesi* venom causes quick respiratory paralysis and leads to death in mice [24] which indicates that the venom is also potent against their natural enemies such as mice and potentially birds. To understand the effects of assassin bug venom on mammalian tissues, we tested *R. iracundus* venom on various cell types. The cytotoxicity assays performed with *R. iracundus* venom demonstrated significant lysis of all tested cell types: hepatoma cells, murine neuroblastoma, as well as on murine myoblasts demonstrating its activity on diverse cells. The activity of *R. iracundus* venom on neuroblastoma is especially interesting in regards of the observed paralysis in mice. Paralysis due to assassin bug venom was also noticed in insect preys which was first explained by cell membrane breakdown [23]. However, considering the similarity with ω -conotoxins, and the presence of conserved ICK motifs, Ptu1 family peptides block N-type voltage-sensitive calcium channels, which suggests that their presence in assassin bug venom could possibly be associated with pain [73] and paralysis [48]. However, Ptu1 was tested against a range of vertebrates and invertebrates, including insects, and it did not show toxicity [58]. All in all, this suggests that Ptu1 could be responsible for the relief of pain or counteract paralysis. Fast paralysis observed in insects in our experiment, and in insects and vertebrates in other studies [23–25,56] as well as sensations of numbness and tingling in human [29] can be associated with other yet undescribed neurotoxins.

The lysis of murine neuroblastoma, as shown for the first time in our study, and the observed murine respiratory paralysis [24] suggest that both neurolysis and paralysis are caused by assassin bug venom. Generalized and rapid paralysis in assassin bug prey enables assassin bugs to protect themselves from injuries. We suggest that neurolysis counteracts paralysis locally, in the region of the assassin bugs' sting, due to the destruction of neuronal networks and may serve for prey digestion and feeding purposes.

The observed cytotoxic effect against the tested cell types can be attributed, among other factors, to the presence of redulysins, hemolysins [74], and kininogen [75] which were found in our transcriptome data. Redulysins and kininogen were also found in the *R. iracundus* venom proteome.

Redulysins, homologs of trialysins [27] for which cytotoxic activity was demonstrated [45], were among the four protein families with highest relative expression levels. Alignment of the cytolytic domains of the four complete *R. iracundus* redulysins with

published sequences from other assassin bug species and from kissing bugs revealed a high proportion of Lys residues in all redulysins, which is required for their cytotoxic activity [45]. The remaining amino acid residues found within the cytolytic domain can be responsible for varying degrees of cytotoxic activity against mammalian cells [45].

Notably, one of the *R. iracundus* redulysins (Ri_Redulysin1) aligned well with the redulysin from *P. plagiipennis* (Pp_Redulysin5) and, when comparing both of them to all other redulysins and trialysins, they showed an additional Lys-rich region at the beginning of the cytolytic domain. Whether and how this insertion additional Lys-rich region affects the activity of the redulysins should be studied in more detail in regards of their cytolytic properties.

Hemolysins are known as pore-forming [76] exotoxins and are able to lyse erythrocytes [77]. One partial and three complete sequences were found in the *R. iracundus* venom transcriptome. Based on the pair-wise identity matrix and phylogenetic tree, *R. iracundus* hemolysins have sequence similarities with hemolysins from *P. plagiipennis*.

In our previous study we already discovered that *R. iracundus* venom causes only ~6% of hemolysis on porcine erythrocytes [30] and erythrocytes from different vertebrate species show different levels of hemolysis [57]. This suggests that assassin bug venom has selectivity on different erythrocyte types making assassin bug venom interesting for leukemia studies.

Finally, our third candidate for cytotoxic activity are kininogens, which are a family of cysteine protease inhibitors. They have similarities to histidine-rich glycoproteins and cystatin-related proteins [78,79]. We aligned kininogens from the assassin bugs *R. iracundus*, *P. plagiipennis*, and *P. rhadamanthus* and found a maximum sequence similarity (~58%) between the kininogens of *R. iracundus* Ri_Kin and *P. plagiipennis* Pp_Kin2. Kininogen inhibits migration and invasion of cancer cells in vitro [80], and overexpression of the kininogen KNG1 was shown to decrease tumor growth and to promote the apoptosis of glioma cells [75]. The observed cytotoxic activity on cancer cells in our study could therefore, possibly among other candidates, be attributed to kininogens. Therefore, kininogensA from assassin bugs kininogens are interesting to study in more detail regarding their antitumor activity. Interestingly, assassin bug venom did not negatively affect collagen tissues [23] and molecular components with cytolytic activities could therefore be interesting to study in cancer of bones and joints.

4.3. Keeping the Glands Clean: The Antibacterial Activity of Assassin Bug Venom

In their natural environment, and especially during feeding, assassin bugs are exposed to various microorganisms. Insects can carry entomopathogens such as bacteria, fungi, and viruses [81,82] which could potentially affect and kill their predatory insects [83,84] via toxemia, bacteremia, or septicemia [85]. To analyze whether *R. iracundus* venom protects the assassin bug from potential pathogens, we tested its venom against Gram-positive and Gram-negative bacteria and found venom-mediated bacterial growth inhibition on Gram-negative *E. coli* only. The selective antibacterial effect against *E. coli* highlights the potential of *R. iracundus* venom to identify molecular compounds, which could be used to treat human diseases caused by *E. coli* or other Gram-negative bacteria. Therefore, we suggest that *R. iracundus* venom can prevent microbial colonization of the glands, protecting the assassin bug against pathogens. Due to their similarity to trialysins [27], redulysins represent potential candidates for the observed growth inhibition of bacteria. Trialysins were shown to have pore forming activities in lipid bilayers [45]. Therefore, the identified redulysins in our *R. iracundus* venom are interesting candidates to investigate in more detail in regards to their potential antibacterial properties.

5. Conclusions

The need for novel biomedical tools is ever increasing, thus driving researchers to continuously explore novel and untapped opportunities. In this context, some focus has fallen on animal venoms since the toxins they are constituted of perform specialized physiological

functions within their prey or predators. The specificity as well as potency of animal venom toxins renders them highly interesting for biomedical research. However, whilst the venom cocktails of larger animals (e.g., snakes, spiders, and scorpions) have been investigated for decades, the ones from smaller animals remain poorly characterized. Only recently, assassin bugs and their multifunctional venom has entered the limelight. Therefore, in this study, we investigated the venom of the assassin bug *Rhynocoris iracundus* and discovered a diverse array of toxins and bioactivities. Indeed, we found that redulyisins, kininogens, chitinases, hemolysins, and Pt1 family peptides appear to be responsible for paralysis of arthropods and vertebrates, neurolysis and cytolysis of insect and mammalian cells, as well as insecticidal and antibacterial activities. Therefore, our study provides a promising basis for further investigation and characterization of specific *R. iracundus* toxins, and the candidate molecules presented here could, in future, serve as templates for novel biotherapeutics.

Supplementary Materials: The following are available online at <https://www.mdpi.com/article/10.3390/biomedicines9070819/s1>, Figure S1: *Rhynocoris iracundus* venom against *Listeria grayi* and *Pseudomonas aeruginosa* growth, Table S1: Venom proteome information of *Rhynocoris iracundus*, Table S2: Chitinase active domain 2 (DxxDxDxx), motif information from insect order Hemiptera, Lepidoptera, Coleoptera, Thysanoptera, Dictyoptera, Phthiraptera, and Hymenoptera, Data S1: Amino acid sequence alignment of assassin bug redulyisins together with homolog from kissing bug trialysins, Data S2: Pair-wise identity matrix of Kininogen sequences from the assassin bug *Rhynocoris iracundus*, Australian assassin bug *Pristhesancus plagipennis*, African assassin bug *Platymeris rhadamanthus*, Data S3: Alignment of Chitinases from order Hemiptera (assassin bugs, bed bugs, stink bugs), Thysanoptera (thrips) and order Hymenoptera (ant, bee), Data S4: Pair-wise identity matrix of Pt1 family peptides of the assassin bug *Rhynocoris iracundus*, Australian assassin bug *Pristhesancus plagipennis*, African assassin bug *Platymeris rhadamanthus*, Data S5: Accession numbers of the sequences which are used for the alignments and the phylogenetic analyses.

Author Contributions: Conceptualization and methodology, N.R. and M.T.; RNA isolation, transcriptomics and combined analyses, H.V. and S.A.; proteomic analyses, N.W. and B.-F.H.; data analysis, original draft preparation, writing, N.R. and M.T.; critical review and editing, N.R., M.T., A.C.-C., T.P.J., H.V., B.-F.H., S.A., R.D.S., and A.V.; All authors have read and agreed to the published version of the manuscript.

Funding: N.R., A.V., and M.T. acknowledge generous funding by the Hessian Ministry of Higher Education, Research, Science and the Arts (HMWK) via the LOEWE Centre for Translational Biodiversity Genomics (LOEWE-TBG) and the LOEWE Center for Insect Biotechnology and Bioresources. T.P.J. is the grateful recipient of funding from the European Union, Horizon 2020 research and innovation program under the Marie Skłodowska-Curie grant agreement no. 713683 (COFUNDfellowsDTU).

Data Availability Statement: The short read data described herein have been deposited in the EBI short read archive (SRA) with the following sample accession numbers: ERS6419927-ERS6419929. The complete study can also be accessed directly using the following URL: <http://www.ebi.ac.uk/ena/data/view/PRJEB44908>. Mass spectrometry proteomics data (.mgf and .raw files) have been deposited with the ProteomeXchange Consortium (<http://proteomecentral.proteomexchange.org>) via the MassIVE partner repository under project name “Eurasian assassin bug *Rhynocoris iracundus* venom proteome” with the data set identifier PXD 026055.

Acknowledgments: We thank the German nature conservation authority as part of the County Government of Rhineland-Palatinate for providing the insect collection permissions. We acknowledge Paul Bauer for maintaining the assassin bugs and Rabia Oezbek for injections in insects. We thank Bashir Hosseini, Kim Kirchoff, and Azka Jaffri for providing the cells. We are thankful to Robert Künast for the assassin bug picture used in the graphical abstract. We are grateful to Greg Bourke for providing the funnel web spider picture.

Conflicts of Interest: The authors declare no conflict of interest.

References

- Schendel, V.; Rash, L.D.; Jenner, R.A.; Undheim, E.A.B. The Diversity of Venom: The Importance of Behavior and Venom System Morphology in Understanding Its Ecology and Evolution. *Toxins* **2019**, *11*, 666. [CrossRef]

2. Zhang, Y. Why Do We Study Animal Toxins? *Zool. Res.* **2015**, *36*, 183–222. [CrossRef]
3. Da Silva, S.L.; Rowan, E.G.; Albericio, F.; Stábéli, R.G.; Calderon, L.A.; Soares, A.M. Animal Toxins and Their Advantages in Biotechnology and Pharmacology. *BioMed Res. Int.* **2014**, *2014*, 951561. [CrossRef]
4. McDermott, A. News Feature: Venom Back in Vogue as a Wellspring for Drug Candidates. *Proc. Natl. Acad. Sci. USA* **2020**, *117*, 10100–10104. [CrossRef]
5. McGivern, J.G. Ziconotide: A Review of Its Pharmacology and Use in the Treatment of Pain. *Neuropsychiatr. Dis. Treat.* **2007**, *3*, 69–85. [CrossRef]
6. Cai, Y.; Wei, L.; Ma, L.; Huang, X.; Tao, A.; Liu, Z.; Yuan, W. Long-Acting Preparations of Exenatide. *Drug Des. Devel. Ther.* **2013**, *7*, 963–970. [CrossRef]
7. Rosendorff, C. Captopril—An Overview. *South Afr. Med. J. Suid-Afr. Tydskr. Vir Geneesk.* **1982**, *62*, 593–599.
8. Waheed, H.; Moin, S.F.; Choudhary, M.I. Snake Venom: From Deadly Toxins to Life-Saving Therapeutics. *Curr. Med. Chem.* **2017**, *24*, 1874–1891. [CrossRef]
9. Yang, X.; Wang, Y.; Wu, C.; Ling, E.-A. Animal Venom Peptides as a Treasure Trove for New Therapeutics Against Neurodegenerative Disorders. *Curr. Med. Chem.* **2019**, *26*, 4749–4774. [CrossRef]
10. Calderon, L.A.; Sobrinho, J.C.; Zaqueo, K.D.; de Moura, A.A.; Grabner, A.N.; Mazzi, M.V.; Marcussi, S.; Nomizo, A.; Fernandes, C.F.C.; Zuliani, J.P.; et al. Antitumoral Activity of Snake Venom Proteins: New Trends in Cancer Therapy. *BioMed Res. Int.* **2014**, *2014*, 203639. [CrossRef]
11. Arruda Macêdo, J.K.; Fox, J.W.; de Souza Castro, M. Disintegrins from Snake Venoms and Their Applications in Cancer Research and Therapy. *Curr. Protein Pept. Sci.* **2015**, *16*, 532–548. [CrossRef] [PubMed]
12. Windley, M.J.; Herzog, V.; Dziemborowicz, S.A.; Hardy, M.C.; King, G.F.; Nicholson, G.M. Spider-Venom Peptides as Bioinsecticides. *Toxins* **2012**, *4*, 191–227. [CrossRef] [PubMed]
13. Juichi, H.; Miyashita, M.; Nakagawa, Y.; Miyagawa, H. Isolation and Characterization of the Insecticidal, Two-Domain Toxin LaIT3 from the *Liocheles Australasiae* Scorpion Venom. *Biosci. Biotechnol. Biochem.* **2019**, *83*, 2183–2189. [CrossRef]
14. Escoubas, P.; King, G.F. Venomics as a Drug Discovery Platform. *Expert Rev. Proteom.* **2009**, *6*, 221–224. [CrossRef]
15. Pennington, M.W.; Czerwinski, A.; Norton, R.S. Peptide Therapeutics from Venom: Current Status and Potential. *Bioorg. Med. Chem.* **2018**, *26*, 2738–2758. [CrossRef]
16. Sahayaraj, K.; Muthukumar, S. Zootoxic Effects of Reduviid *Rhynocoris Marginatus* (Fab.) (Hemiptera: Reduviidae) Venomous Saliva on *Spodoptera Litura* (Fab.). *Toxicon* **2011**, *58*, 415–425. [CrossRef]
17. Weirauch, C.; Schuh, R.T. Systematics and Evolution of Heteroptera: 25 Years of Progress. *Annu. Rev. Entomol.* **2011**, *56*, 487–510. [CrossRef]
18. Schuh, R.T.; Slater, J.A. *True Bugs of the World (Hemiptera:Heteroptera): Classification and Natural History*; Cornell University Press: Ithaca, NY, USA, 1995; ISBN 9780801420665.
19. Dan, A.; Pereira, M.H.; Pesquero, J.L.; Diotaiuti, L.; Beirão, P.S. Action of the Saliva of *Triatoma Infestans* (Heteroptera: Reduviidae) on Sodium Channels. *J. Med. Entomol.* **1999**, *36*, 875–879. [CrossRef]
20. Souza, R.; Soares, A.C.; Alves, C.L.; Lorosa, E.S.; Pereira, M.H.; Diotaiuti, L. Feeding Behavior of *Triatoma Vitticeps* (Reduviidae: Triatominae) in the State of Minas Gerais, Brazil. *Mem. Inst. Oswaldo Cruz* **2011**, *106*, 16–22. [CrossRef]
21. Santos, H.P.; Rost-Roszkowska, M.; Vilimova, J.; Serrão, J.E. Ultrastructure of the Midgut in Heteroptera (Hemiptera) with Different Feeding Habits. *Protoplasma* **2017**, *254*, 1743–1753. [CrossRef]
22. Wang, Y.; Li, L.; Dai, W. Fine Morphology of the Mouthparts in *Cheilocapsus Nigrescens* (Hemiptera: Heteroptera: Miridae) Reflects Adaptation for Phytophagous Habits. *Insects* **2019**, *10*, 143. [CrossRef]
23. Edwards, J.S.A. The Action and Composition of the Saliva of an Assassin Bug *Platymeris Rhadamanthus* Gaerst. (Hemiptera, Reduviidae). *J. Exp. Biol.* **1961**, *38*, 61–77. [CrossRef]
24. Zerachia, T.; Bergmann, F.; Shulov, A. Pharmacological Activities of the Venom of the Predaceous Bug *Holotrichius Innesi* (Heteroptera, Reduviidae). *Int. Symp. Anim. Plant Toxins 3d Darnstadt* **1972**, 143–146.
25. Walker, A.A.; Mayhew, M.L.; Jin, J.; Herzog, V.; Undheim, E.A.B.; Sombke, A.; Fry, B.G.; Meritt, D.J.; King, G.F. The Assassin Bug *Pristhesancus Plagipennis* Produces Two Distinct Venoms in Separate Gland Lumens. *Nat. Commun.* **2018**, *9*, 755. [CrossRef] [PubMed]
26. Walker, A.A.; Madio, B.; Jin, J.; Undheim, E.A.B.; Fry, B.G.; King, G.F. Melt With This Kiss: Paralyzing and Liquefying Venom of The Assassin Bug *Pristhesancus Plagipennis* (Hemiptera: Reduviidae). *Mol. Cell. Proteom. MCP* **2017**, *16*, 552–566. [CrossRef] [PubMed]
27. Walker, A.A.; Robinson, S.D.; Undheim, E.A.B.; Jin, J.; Han, X.; Fry, B.G.; Vetter, I.; King, G.F. Missiles of Mass Disruption: Composition and Glandular Origin of Venom Used as a Projectile Defensive Weapon by the Assassin Bug *Platymeris Rhadamanthus*. *Toxins* **2019**, *11*, 673. [CrossRef]
28. Haridass, E.T.; Ananthakrishnan, T.N. Functional Morphology of Pylorus and Rectal Glands in Reduviidae (Insecta—Heteroptera). *Proc. Anim. Sci.* **1981**, *90*, 483–493. [CrossRef]
29. Pereira Dos Santos, C.E.; de Souza, J.R.; Zanette, R.A.; da Silva, F.J.; Strussmann, C. Bite Caused by the Assassin Bug *Zelus Fabricius*, 1803 (Hemiptera; Heteroptera: Reduviidae) in a Human. *Wilderness Environ. Med.* **2019**, *30*, 63–65. [CrossRef]
30. Tonk, M.; Vilcinskas, A.; Grevelding, C.G.; Haerberlein, S. Anthelmintic Activity of Assassin Bug Venom against the Blood Fluke *Schistosoma Mansoni*. *Antibiotics* **2020**, *9*, 664. [CrossRef]

31. Tonk, M.; Cabezas-Cruz, A.; Valdés, J.J.; Rego, R.O.M.; Chrudimská, T.; Strnad, M.; Šima, R.; Bell-Sakyi, L.; Franta, Z.; Vilcinskas, A.; et al. Defensins from the Tick *Ixodes Scapularis* Are Effective against Phytopathogenic Fungi and the Human Bacterial Pathogen *Listeria Grayi*. *Parasit. Vectors* **2014**, *7*, 554. [CrossRef]
32. Mukherjee, K.; Hain, T.; Fischer, R.; Chakraborty, T.; Vilcinskas, A. Brain Infection and Activation of Neuronal Repair Mechanisms by the Human Pathogen *Listeria Monocytogenes* in the Lepidopteran Model Host *Galleria Mellonella*. *Virulence* **2013**, *4*, 324–332. [CrossRef]
33. Götz, S.; García-Gómez, J.M.; Terol, J.; Williams, T.D.; Nagaraj, S.H.; Nueda, M.J.; Robles, M.; Talón, M.; Dopazo, J.; Conesa, A. High-Throughput Functional Annotation and Data Mining with the Blast2GO Suite. *Nucleic Acids Res.* **2008**, *36*, 3420–3435. [CrossRef]
34. Waterhouse, R.M.; Seppey, M.; Simão, F.A.; Manni, M.; Ioannidis, P.; Klioutchnikov, G.; Kriventseva, E.V.; Zdobnov, E.M. BUSCO Applications from Quality Assessments to Gene Prediction and Phylogenomics. *Mol. Biol. Evol.* **2018**, *35*, 543–548. [CrossRef]
35. Jacobs, C.G.C.; Steiger, S.; Heckel, D.G.; Wielsch, N.; Vilcinskas, A.; Vogel, H. Sex, Offspring and Carcass Determine Antimicrobial Peptide Expression in the Burying Beetle. *Sci. Rep.* **2016**, *6*, 25409. [CrossRef]
36. Shevchenko, A.; Tomas, H.; Havli, J.; Olsen, J.V.; Mann, M. In-Gel Digestion for Mass Spectrometric Characterization of Proteins and Proteomes. *Nat. Protoc.* **2006**, *1*, 2856–2860. [CrossRef]
37. Shevchenko, A.; Sunyaev, S.; Loboda, A.; Shevchenko, A.; Bork, P.; Ens, W.; Standing, K.G. Charting the Proteomes of Organisms with Unsequenced Genomes by MALDI-Quadrupole Time-of-Flight Mass Spectrometry and BLAST Homology Searching. *Anal. Chem.* **2001**, *73*, 1917–1926. [CrossRef]
38. Katoh, K.; Standley, D.M. MAFFT Multiple Sequence Alignment Software Version 7: Improvements in Performance and Usability. *Mol. Biol. Evol.* **2013**, *30*, 772–780. [CrossRef]
39. Kuraku, S.; Zmasek, C.M.; Nishimura, O.; Katoh, K. ALeaves Facilitates On-Demand Exploration of Metazoan Gene Family Trees on MAFFT Sequence Alignment Server with Enhanced Interactivity. *Nucleic Acids Res.* **2013**, *41*, W22–W28. [CrossRef]
40. Crooks, G.E.; Hon, G.; Chandonia, J.-M.; Brenner, S.E. WebLogo: A Sequence Logo Generator. *Genome Res.* **2004**, *14*, 1188–1190. [CrossRef]
41. Castresana, J. Selection of Conserved Blocks from Multiple Alignments for Their Use in Phylogenetic Analysis. *Mol. Biol. Evol.* **2000**, *17*, 540–552. [CrossRef]
42. Kumar, S.; Stecher, G.; Li, M.; Niyaz, C.; Tamura, K. MEGA X: Molecular Evolutionary Genetics Analysis across Computing Platforms. *Mol. Biol. Evol.* **2018**, *35*, 1547–1549. [CrossRef] [PubMed]
43. Hempel, B.F.; Damm, M.; Göçmen, B.; Karis, M.; Oguz, M.A.; Nalbantsoy, A.; Süßmuth, R.D. Comparative Venomics of the *Vipera ammodytes transcaucasiana* and *Vipera ammodytes montandoni* from Turkey Provides Insights into Kinship. *Toxins* **2018**, *1*, 23. [CrossRef]
44. Petras, D.; Hempel, B.F.; Göçmen, B.; Karis, M.; Whiteley, G.; Wagstaff, S.C.; Heiss, P.; Casewell, N.R.; Nalbantsoy, A.; Süßmuth, R.D. Intact protein mass spectrometry reveals intraspecies variations in venom composition of a local population of *Vipera kaznakovi* in Northeastern Turkey. *J. Proteom.* **2019**, *199*, 31–50. [CrossRef]
45. Amينو, R.; Martins, R.M.; Procopio, J.; Hirata, I.Y.; Juliano, M.A.; Schenkman, S. Trialysin, a Novel Pore-Forming Protein from Saliva of Hematophagous Insects Activated by Limited Proteolysis. *J. Biol. Chem.* **2002**, *277*, 6207–6213. [CrossRef] [PubMed]
46. Le, S.Q.; Gascuel, O. An Improved General Amino Acid Replacement Matrix. *Mol. Biol. Evol.* **2008**, *25*, 1307–1320. [CrossRef] [PubMed]
47. Perrakis, A.; Tews, I.; Dauter, Z.; Oppenheim, A.B.; Chet, I.; Wilson, K.S.; Vorgias, C.E. Crystal Structure of a Bacterial Chitinase at 2.3 Å Resolution. *Structure* **1994**, *2*, 1169–1180. [CrossRef]
48. Bernard, C.; Corzo, G.; Mosbah, A.; Nakajima, T.; Darbon, H. Solution Structure of Ptu1, a Toxin from the Assassin Bug *Peirates Turpis* That Blocks the Voltage-Sensitive Calcium Channel N-Type. *Biochemistry* **2001**, *40*, 12795–12800. [CrossRef]
49. Sousa, S.R.; McArthur, J.R.; Brust, A.; Bhola, R.F.; Rosengren, K.J.; Ragnarsson, L.; Dutertre, S.; Alewood, P.F.; Christie, M.J.; Adams, D.J.; et al. Novel Analgesic ω -Conotoxins from the Vermivorous Cone Snail *Conus Moncuri* Provide New Insights into the Evolution of Conopeptides. *Sci. Rep.* **2018**, *8*, 13397. [CrossRef]
50. Adams, D.J.; Smith, A.B.; Schroeder, C.I.; Yasuda, T.; Lewis, R.J. ω -Conotoxin CVID Inhibits a Pharmacologically Distinct Voltage-Sensitive Calcium Channel Associated with Transmitter Release from Preganglionic Nerve Terminals. *J. Biol. Chem.* **2003**, *278*, 4057–4062. [CrossRef]
51. Evans, D.L.; Schmid, J.O. *Insect Defense: Adaptive Mechanisms and Strategies of Prey and Predators*; State University of New York Press: Albany, NY, USA, 1990; ISBN 9780887068966.
52. Moret, Y.; Moreau, J. The Immune Role of the Arthropod Exoskeleton. *Invertebr. Surviv. J.* **2012**, *9*, 200–206.
53. Moreau, S.J.M. “It Stings a Bit but It Cleans Well”: Venoms of Hymenoptera and Their Antimicrobial Potential. *J. Insect Physiol.* **2013**, *59*, 186–204. [CrossRef]
54. Villas-Boas, I.M.; Bonfá, G.; Tambourgi, D.V. Venomous Caterpillars: From Inoculation Apparatus to Venom Composition and Envenomation. *Toxicon* **2018**, *153*, 39–52. [CrossRef]
55. Shaik, H.A.; Mishra, A.; Kodrik, D. Beneficial Effect of Adipokinetic Hormone on Neuromuscular Paralysis in Insect Body Elicited by Braconid Wasp Venom. *Comp. Biochem. Physiol. Toxicol. Pharmacol. CBP* **2017**, *196*, 11–18. [CrossRef]
56. De Geer, C. *Memoires Pour Servir a l’Histoire Des Insectes*; Pierre Hesselberg: Stockholm, Sweden, 1773; Volume III.

57. Fischer, M.L.; Wielsch, N.; Heckel, D.G.; Vilcinskas, A.; Vogel, H. Context-Dependent Venom Deployment and Protein Composition in Two Assassin Bugs. *Ecol. Evol.* **2020**, *10*, 9932–9947. [CrossRef]
58. Corzo, G.; Adachi-Akahane, S.; Nagao, T.; Kusui, Y.; Nakajima, T. Novel Peptides from Assassin Bugs (Hemiptera: *Reduviidae*): Isolation, Chemical and Biological Characterization. *FEBS Lett.* **2001**, *499*, 256–261. [CrossRef]
59. Sollod, B.L.; Wilson, D.; Zhaxybayeva, O.; Gogarten, J.P.; Drinkwater, R.; King, G.F. Were Arachnids the First to Use Combinatorial Peptide Libraries? *Peptides* **2005**, *26*, 131–139. [CrossRef]
60. Balaji, R.A.; Ohtake, A.; Sato, K.; Gopalakrishnakone, P.; Kini, R.M.; Seow, K.T.; Bay, B.-H. λ -Conotoxins, a New Family of Conotoxins with Unique Disulfide Pattern and Protein Folding: Isolation and Characterization from the Venom of *Conus Marmoreus*. *J. Biol. Chem.* **2000**, *275*, 39516–39522. [CrossRef]
61. Deer, T.R.; Pope, J.E.; Hanes, M.C.; McDowell, G.C. Intrathecal Therapy for Chronic Pain: A Review of Morphine and Ziconotide as Firstline Options. *Pain Med. Off. J. Am. Acad. Pain Med.* **2019**, *20*, 784–798. [CrossRef]
62. Vijayakumar, N.; Nalini, M.; Rajkuberan, C.; Faruck, L.H.; Bakshi, H.; Sangilimuthu, A.Y. Genotoxic and Cytotoxic Effect of Chitinase against *Corcyra Cephalonica* Larvae under Laboratory Conditions. *Int. J. Trop. Insect Sci.* **2021**. [CrossRef]
63. Ribeiro, J.M.C.; Assumpção, T.C.; Francischetti, I.M.B. An Insight into the Sialomes of Bloodsucking Heteroptera. *Psyche* **2012**, *2012*, e470436. [CrossRef]
64. Ribeiro, J.M.C.; Genta, F.A.; Sorgine, M.H.F.; Logullo, R.; Mesquita, R.D.; Paiva-Silva, G.O.; Majerowicz, D.; Medeiros, M.; Koerich, L.; Terra, W.R.; et al. An Insight into the Transcriptome of the Digestive Tract of the Bloodsucking Bug, *Rhodnius Prolixus*. *PLoS Negl. Trop. Dis.* **2014**, *8*, e2594. [CrossRef]
65. Andre, F. Notes on the Biology of *Oncopeltus Fasciatus* (Dallas). *Iowa State Coll. J. Sci.* **1934**, *9*, 73–88.
66. Lazzari, C.R.; Fauquet, A.; Lahondère, C. Keeping Cool: Kissing Bugs Avoid Cannibalism by Thermoregulating. *J. Insect Physiol.* **2018**, *107*, 29–33. [CrossRef]
67. Royer, V.; Fraichard, S.; Bouhin, H. A Novel Putative Insect Chitinase with Multiple Catalytic Domains: Hormonal Regulation during Metamorphosis. *Biochem. J.* **2002**, *366*, 921–928. [CrossRef] [PubMed]
68. Arakane, Y.; Muthukrishnan, S. Insect Chitinase and Chitinase-like Proteins. *Cell. Mol. Life Sci.* **2010**, *67*, 201–216. [CrossRef] [PubMed]
69. Kzyshkowska, J.; Yin, S.; Liu, T.; Riabov, V.; Mitrofanova, I. Role of Chitinase-Like Proteins in Cancer. *Biol. Chem.* **2016**, *397*, 231–247. [CrossRef]
70. Nakhleh, J.; El Moussawi, L.; Osta, M.A. Chapter Three—The Melanization Response in Insect Immunity. In *Advances in Insect Physiology*; Ligoxygakis, P., Ed.; Insect Immunity; Academic Press: Salt Lake City, UT, USA, 2017; Volume 52, pp. 83–109.
71. Cabezas-Cruz, A.; Valdés, J.J. Are Ticks Venomous Animals? *Front. Zool.* **2014**, *11*, 47. [CrossRef]
72. Pineda, S.S.; Sollod, B.L.; Wilson, D.; Darling, A.; Sunagar, K.; Undheim, E.A.B.; Kely, L.; Antunes, A.; Fry, B.G.; King, G.F. Diversification of a Single Ancestral Gene into a Successful Toxin Superfamily in Highly Venomous Australian Funnel-Web Spiders. *BMC Genom.* **2014**, *15*, 177. [CrossRef]
73. Klint, J.K.; Senff, S.; Rupasinghe, D.B.; Er, S.Y.; Herzig, V.; Nicholson, G.M.; King, G.F. Spider-Venom Peptides That Target Voltage-Gated Sodium Channels: Pharmacological Tools and Potential Therapeutic Leads. *Toxicon* **2012**, *60*, 478–491. [CrossRef]
74. Hertle, R.; Hilger, M.; Weingardt-Kocher, S.; Walev, I. Cytotoxic Action of *Serratia Marcescens* Hemolysin on Human Epithelial Cells. *Infect. Immun.* **1999**, *67*, 817–825. [CrossRef]
75. Xu, J.; Fang, J.; Cheng, Z.; Fan, L.; Hu, W.; Zhou, F.; Shen, H. Overexpression of the Kininogen-1 Inhibits Proliferation and Induces Apoptosis of Glioma Cells. *J. Exp. Clin. Cancer Res.* **2018**, *37*, 180. [CrossRef] [PubMed]
76. Bhakdi, S.; Weller, U.; Walev, I.; Martin, E.; Jonas, D.; Palmer, M. A Guide to the Use of Pore-Forming Toxins for Controlled Permeabilization of Cell Membranes. *Med. Microbiol. Immunol.* **1993**, *182*, 167–175. [CrossRef]
77. Nayak, A.P.; Green, B.J.; Beezhold, D.H. Fungal Hemolysins. *Med. Mycol.* **2013**, *51*, 1–16. [CrossRef] [PubMed]
78. Rawlings, N.D.; Barrett, A.J. Evolution of Proteins of the Cystatin Superfamily. *J. Mol. Evol.* **1990**, *30*, 60–71. [CrossRef]
79. Turk, V.; Bode, W. The Cystatins: Protein Inhibitors of Cysteine Proteinases. *FEBS Lett.* **1991**, *285*, 213–219. [CrossRef]
80. Kamiyama, F.; Maeda, T.; Yamane, T.; Li, Y.H.; Ogukubo, O.; Otsuka, T.; Ueyama, H.; Takahashi, S.; Ohkubo, I.; Matsui, N. Inhibition of Vitronectin-Mediated Haptotaxis and Haptoinvasion of MG-63 Cells by Domain 5 (D5(H)) of Human High-Molecular-Weight Kininogen and Identification of a Minimal Amino Acid Sequence. *Biochem. Biophys. Res. Commun.* **2001**, *288*, 975–980. [CrossRef]
81. Vallet-Gely, I.; Lemaitre, B.; Boccard, F. Bacterial Strategies to Overcome Insect Defences. *Nat. Rev. Microbiol.* **2008**, *6*, 302–313. [CrossRef]
82. Sharma, L.; Bohra, N.; Rajput, V.D.; Quiroz-Figueroa, F.R.; Singh, R.K.; Marques, G. Advances in Entomopathogen Isolation: A Case of Bacteria and Fungi. *Microorganisms* **2020**, *9*, 16. [CrossRef]
83. Vilcinskas, A.; Stoecker, K.; Schmidtberg, H.; Röhrich, C.R.; Vogel, H. Invasive Harlequin Ladybird Carries Biological Weapons against Native Competitors. *Science* **2013**, *340*, 862–863. [CrossRef]
84. Baldiviezo, L.V.; Pedrini, N.; Santana, M.; Mannino, M.C.; Nieva, L.B.; Gentile, A.; Cardozo, R.M. Isolation of *Beauveria Bassiana* from the Chagas Disease Vector *Triatoma Infestans* in the Gran Chaco Region of Argentina: Assessment of Gene Expression during Host–Pathogen Interaction. *J. Fungi* **2020**, *6*, 219. [CrossRef]
85. Jurat-Fuentes, J.L.; Jackson, T.A. Bacterial Entomopathogens—Chapter 8. In *Insect Pathology*, 2nd ed.; Academic Press: Salt Lake City, UT, USA, 2012; pp. 265–349, ISBN 9780123849847.



Article

A Novel Competitive Binding Screening Assay Reveals Sennoside B as a Potent Natural Product Inhibitor of TNF- α

Lei Peng¹, Prasannavenkatesh Durai², Keunwan Park², Jeong Joo Pyo^{3,*} and Yongsoo Choi^{3,4,*}

¹ School of Chemistry and Chemical Engineering, Qiqihar University, Qiqihar 161006, China; 03555@qqhru.edu.cn

² Natural Product Informatics Research Center, Korea Institute of Science and Technology (KIST), Gangneung 25451, Korea; prasanna@kist.re.kr (P.D.); keunwan@kist.re.kr (K.P.)

³ Natural Product Research Center, Korea Institute of Science and Technology (KIST), Gangneung 25451, Korea

⁴ Department of Biological Chemistry, University of Science and Technology, Daejeon 34113, Korea

* Correspondence: brianpyo@kist.re.kr (J.J.P.); yongsoo.choi@kist.re.kr (Y.C.)

Abstract: Natural products (NPs) have played a significant role in drug discovery for diverse diseases, and numerous attempts have been made to discover promising NP inhibitors of tumor necrosis factor α (TNF- α), a major therapeutic target in autoimmune diseases. However, NP inhibitors of TNF- α , which have the potential to be developed as new drugs, have not been reported for over a decade. To facilitate the search for new promising inhibitors of TNF- α , we developed an efficient competitive binding screening assay based on analytical size exclusion chromatography coupled with liquid chromatography-tandem mass spectrometry. Application of this screening method to the NP library led to the discovery of a potent inhibitor of TNF- α , sennoside B, with an IC₅₀ value of 0.32 μ M in TNF- α induced HeLa cell toxicity assays. Surprisingly, the potency of sennoside B was 5.7-fold higher than that of the synthetic TNF- α inhibitor SPD304. Molecular docking was performed to determine the binding mode of sennoside B to TNF- α . In conclusion, we successfully developed a novel competition binding screening method to discover small molecule TNF- α inhibitors and identified the natural compound sennoside B as having exceptional potency.

Keywords: tumor necrosis factor α ; natural products; sennoside B; analytical size exclusion chromatography; liquid chromatography-tandem mass spectrometry

Citation: Peng, L.; Durai, P.; Park, K.; Pyo, J.J.; Choi, Y. A Novel Competitive Binding Screening Assay Reveals Sennoside B as a Potent Natural Product Inhibitor of TNF- α . *Biomedicines* **2021**, *9*, 1250. <https://doi.org/10.3390/biomedicines9091250>

Academic Editors: Laura Quintieri, Leonardo Caputo and Orazio Nicolotti

Received: 13 August 2021

Accepted: 10 September 2021

Published: 17 September 2021

Publisher's Note: MDPI stays neutral with regard to jurisdictional claims in published maps and institutional affiliations.



Copyright: © 2021 by the authors. Licensee MDPI, Basel, Switzerland. This article is an open access article distributed under the terms and conditions of the Creative Commons Attribution (CC BY) license (<https://creativecommons.org/licenses/by/4.0/>).

1. Introduction

Tumor necrosis factor-alpha (TNF- α), an important pleiotropic cytokine, is a well-known central biological mediator of critical pro-inflammatory and immunomodulatory effects [1,2]. Overexpression of TNF- α is widely associated with a series of autoimmune diseases, including rheumatoid arthritis [3], Crohn's disease [4], and psoriasis [5]. Because of its profound implications in various diseases, TNF- α has become one of the most promising molecular targets of interest and some therapeutic biologics, such as etanercept, infliximab, certolizumab, golimumab, and adalimumab, have been successfully developed to block the interaction between TNF- α and its receptors [1]. Nevertheless, biological drugs have inherent limitations pertaining to applications because of their immunogenicity, health economics, complexity in manufacturing, and inconvenient routes of administration [1,6,7]. In light of this, a small-molecule drug will have better applicability and be beneficial to more patients.

Suramin was the first small-molecule to demonstrate inhibitory effect on TNF- α through a direct action on the ligand rather than on its receptors [8]. Later, SPD304 was discovered as a small-molecule antagonist of TNF- α with an IC₅₀ value of 4.6 μ M. X-ray crystallography revealed that SPD304 displaces a subunit of the TNF- α trimer to form a complex with the resultant dimer [9]. Several small-molecule inhibitors that bind to TNF- α or tumor necrosis factor receptor (TNFR) have subsequently been reported. Utilizing a

ligand docking-based virtual screening method, Chan et al. discovered two compounds that show a similar binding modality to SPD304, quinuclidine and indoloquinolizidine [10]. Ma et al. applied computer-aided drug design combined with in vitro assays and identified C87 that directly binds to TNF- α [11]. Luzi et al. developed and improved the bicyclic peptide display method and discovered macrocyclic peptide M21, which could dissociate the active trimeric form of TNF- α [12]. Cao et al. used a novel surface plasmon resonance (SPR)-based screening method and identified TNFR1 antagonist physcion-8-O- β -D-monoglucoside (PMG) from complex herbal extracts [13]. Using TNF- α and TNFR crystal structures, Chen et al. performed a virtual screening method followed by SPR and biological validation and discovered T1 and R1, which could bind to TNF- α and TNFR1, respectively [14]. Despite several efforts, compounds' low potency and potential toxicity impeded further developments and no small molecule drug for TNF- α is currently available [15,16]. Therefore, the discovery of small-molecule TNF- α inhibitors with high efficacy, low toxicity, and potential clinical applications remains a challenging goal.

Natural products (NPs) have played a significant role in the drug discovery and development. According to a recent review paper, among 1394 small-molecule drugs approved over the last four decades, NPs and NP derivatives account for 441 drugs (32%) [17]. The contribution of NPs would be more significant when NP-inspired drugs, such as synthetic drugs with NP pharmacophores or those mimicking NPs, are included in NP drug classification. The virtues of chemical scaffold diversity, structural complexity, and potentially lower toxicity profiles of NPs continuously offers a great opportunity to discover novel bioactive compounds and contribute to drug development.

Encouraged by the fact that natural compounds with high potency and low toxicity that directly target TNF- α have rarely been reported, we developed a competitive binding screening assay coupled with analytical size exclusion chromatography (SEC) and liquid chromatography (LC) tandem mass spectrometry (MS) and applied the screening method to an in-house NP compound library to discover of novel small-molecule TNF- α antagonists. In vitro cell-based assays were performed to validate the inhibitory effect of the NPs and in silico modeling was performed to predict their interactions. Collectively, we observed that sennoside B, a NP small-molecule, effectively inhibited TNF- α and its downstream signaling pathways. Moreover, the binding mode of sennoside B with the TNF- α crystal structure was analyzed using molecular docking, and the key residue interactions between sennoside B and TNF- α were predicted.

2. Materials and Methods

2.1. Chemicals, Reagents, and Cell Lines

All HPLC grade solvents were purchased from Fisher Scientific (Thermo Fisher Scientific, Hanover Park, IL, USA). Centrifugal ultrafiltration filters (Microcon YM10) were obtained from Millipore (MilliporeSigma, Burlington, MA, USA). Human recombinant TNF- α was obtained from PeproTech (PeproTech, Rocky Hill, NJ, USA). Fetal bovine serum (FBS) was purchased from the American Type Culture Collection (ATCC, Manassas, VA, USA). Prostaglandin D₂ (PGD₂) and prostaglandin E₂ (PGE₂), and internal standards (IS) of d₄-prostaglandin D₂ (d₄-PGD₂) and d₄-prostaglandin E₂ (d₄-PGE₂) were purchased from Cayman Chemical (Cayman Chemical, Ann Arbor, MI, USA). Dimethyl sulfoxide (DMSO), actinomycin D (AMD), and SPD304 were purchased from Sigma-Aldrich (MilliporeSigma, Burlington, MA, USA). L929 and HeLa cells were purchased from ATCC and maintained in Dulbecco's Modified Eagle Medium (DMEM) supplemented with 10% FBS.

2.2. Method Development

2.2.1. Competitive Binding Screening Assay Using Analytical SEC

To develop a competitive binding screening assay, the known TNF- α inhibitor SPD304 and the NP compound were incubated with TNF- α in 70 μ L buffer (pH 7.5) consisting of 100 mM Tris, 10% glycerol, 50 mM KCl, and 1 mM EDTA at room temperature for 20 min. The final concentration of SPD304 and the NP compound was 3.5 μ M each, and of TNF- α

was 0.1 μM . After incubation, the mixture solution was loaded into an SP-6 Bio-gel SEC column (Bio-Rad, Hercules, CA, USA), followed by spin-down at 1000 g for 4 min at 4 °C. The eluted solution containing the ligand and TNF- α complex was washed three times with 50 mM ammonium acetate (pH 7.5), followed by another centrifugation at 13,000 g for 10 min. Then, the ligands were dissociated using 400 μL of methanol. The ultrafiltrate containing the ligand was dried using a SpeedVac (Thermo Fisher Scientific, Hanover Park, IL, USA). The sample was reconstituted with 100 μL of 50% methanol, and 2 μL of the sample was injected into the LC–tandem MS system.

2.2.2. LC–Tandem MS Analysis

The samples were analyzed using an Agilent 1290 HPLC system (Agilent Technologies, Santa Clara, CA, USA) interfaced with a triple quadrupole mass spectrometer (SCIEX API 4000, Foster City, CA, USA) with multiple reaction monitoring (MRM) scan in electrospray ionization positive mode. The separation was achieved using a Waters ACQUITY BEH (Waters Corporation, Milford, MA, USA) C18 column (2.1 \times 100 mm, 1.7 μm) fitted to a Waters ACQUITY UHPLC BEH C18 Vanguard pre-column (2.1 \times 5 mm, 1.7 μm). The mobile phase consisted of mixtures A (95% water and 5% acetonitrile, 0.1% formic acid) and B (95% acetonitrile and 5% water, 0.1% formic acid). The flow rate was set to 0.6 mL/min. The following gradient program was employed: 0–10 min, 5–100% B. Re-equilibration was applied for 3 min between analyses. The oven temperature was set to 40 °C. The mass spectrometer parameters were as follows: voltage, 5.5 kV; probe temperature, 400 °C; gas 1, 35; gas 2, 40; curtain gas, 40; and dwell time, 200 ms. The MRM parameters for the SPD304 were set up as follows: Q1 (548.4), Q3 (274.3), DP (100), EP (10), CE (43), and CXP (15).

2.3. Cell Viability Assay

A cell viability assay was performed using Cell Counting Kit-8 (CCK-8, Dojindo, Kumamoto, Japan) according to the manufacturer's instruction. Briefly, mouse L929 and human HeLa cells were seeded in 96-well plates at a density of 2.0×10^4 cells/well and cultured overnight. Prepared DMEM containing different concentrations of sennoside B was added to the cells and incubated for 18 h. Subsequently, cells were washed with phosphate-buffered saline three times and cell viability was assessed by adding CCK-8 solution to the treated cells and incubating for 2 h. The optical density in the CCK-8 assay was measured at 450 nm using a microplate reader (BioTek, Winooski, VT, USA).

2.4. TNF- α Dependent L929 Cytotoxicity Assay

Treating mouse L929 cells with TNF- α induces cytotoxicity, and the susceptibility of L929 to TNF- α is greatly increased when cells are exposed to AMD [18,19]. This assay has been successfully used to characterize the in vitro efficacy of TNF- α biologics [11,20]. L929 cells were seeded in 96-well plates at a density of 2.0×10^4 cells/well and cultured overnight. Prepared DMEM containing different concentrations of sennoside B (6.25–100 μM), 10 ng/mL of TNF- α , and 1 $\mu\text{g}/\text{mL}$ of AMD was added to the cells, and incubated for 18 h. The cell viability was assessed by microscopic examination and CCK-8 assay. SPD304 was used as a positive control.

2.5. Western Blot Analysis

L929 and HeLa cell lines were used for western blotting analyses. After the treatment, the cells were lysed and the total protein concentration was determined using Bradford reagent (Bio-Rad, Hercules, CA, USA). Total protein samples (20 μg) were separated using sodium dodecyl polyacrylamide gel electrophoresis and transferred to polyvinylidene difluoride (MilliporeSigma, Burlington, MA, USA) membranes. The membranes were blocked with 5% BSA in TBST and the protein levels of caspase 3, cleaved caspase 3, inhibitor of kappa B- α (I κ B- α), and glyceraldehyde-3-phosphate dehydrogenase (GAPDH) were determined using anti-caspase 3 primary antibody (#9662, Cell Signaling Technology), anti-cleaved caspase 3 primary antibody (#9661, Cell Signaling Technology), anti-I κ B- α

primary antibody (#4812, Cell Signaling Technology), and anti-GAPDH primary antibody (#2118, Cell Signaling Technology), respectively. Densitometric analysis of the bands was performed using the LAS4000 system (Fujifilm, Tokyo, Japan).

2.6. Measurement of PGD₂ and PGE₂ by LC-high Resolution MS

L929 cells were seeded in 6-well plates at a density of 5.0×10^5 cells/well and cultured overnight. Prepared DMEM containing different concentrations of sennoside B (25–100 μ M), 10 ng/mL TNF- α , and 1 μ g/mL AMD was added to the cells and incubated for 18 h. The collected cell medium was centrifuged at 13,000 g at 4 °C to remove dead cells. Then, 2 μ L of d₄-PGE₂ and d₄-PGD₂ (10 μ g/mL, IS) were added to the collected supernatant. The supernatant was cleaned using solid-phase extraction cartridges (Phenomenex, Torrance, CA, USA). The filtrate was dried under nitrogen flow and reconstituted with 100 μ L of 50% aqueous methanol, and 2 μ L of the reconstituted filtrate was injected directly into the LC-high resolution MS system.

Analysis of PGD₂ and PGE₂ was performed according to a previous report [21] using a Vanquish pump and Q-Exactive Hybrid Quadrupole-Orbitrap Mass Spectrometer (Thermo Fischer Scientific, Bremen, Germany). Briefly, the separation was achieved using a Waters ACQUITY BEH (Waters Corporation, Milford, MA, USA) C18 column (2.1 \times 100 mm, 1.7 μ m) fitted to a Waters ACQUITY UHPLC BEH C18 Vanguard pre-column (2.1 \times 5 mm, 1.7 μ m). The mobile phase consisted of mixtures A (95% water and 5% acetonitrile, 0.1% formic acid) and B (95% acetonitrile and 5% water, 0.1% formic acid). The flow rate was set to 0.5 mL/min. The following gradient program was employed: 0–10 min, 5–100% B. Re-equilibration was applied for 3 min between analyses. The oven temperature was maintained at 35 °C. The Orbitrap Mass Spectrometer was operated in full scan mode (m/z 200–500) in negative ion mode at a mass resolving power of 70,000 (FWHM at m/z 200). The electrospray ion source parameters were as follows: spray voltage, 3.5 kV; sheath gas (N₂ > 95%), 40; auxiliary gas (N₂ > 95%), 10; sweep gas (N₂ > 95%), 1; capillary temperature, 320 °C; heater temperature, 300 °C; and S-lens RF level, 50. The full scan mass spectra were acquired using the following parameters: automatic gain control (AGC), 5×10^5 and maximum accumulation time, 100 ms.

2.7. Molecular Docking and Dynamic Simulations

The crystal structure TNF- α was retrieved from the Protein Data Bank (ID: 2AZ5). TNF- α and its dimeric form were used as the receptors and sennoside B as the ligand. Molecular docking was performed using the AutoDock 4 [22]. Proteins were prepared by removing water molecules, and the number of rotatable bonds in the ligand was left unmodified. The grid box was set to perform blind docking to cover almost the entire protein structure with a grid spacing of 0.375 Å. Ten docking runs were set with the genetic algorithm, and the maximum number of energy evaluations was changed to 25,000,000 using the Lamarckian genetic algorithm to score the energy. The docking complex of sennoside B with the positive control SPD304 crystal complex structure was scored against TNF- α using the DSX online server [23] to compare interaction scores. Molecular docking interactions and figures were generated using BIOVIA Discovery Studio 2018. GROMACS-2018 [24] was used for molecular dynamics (MD) simulations. The PRODRG server [25] was used to determine the GROMOSA1 force field for the ligand molecules. The proteins and the ligands were solvated with the SPC water model, periodic boundary conditions were applied in all directions, and the total charge of the system was neutralized. Energy minimization steps were carried out using the steepest descent algorithm. For long-range interactions, the particle mesh Ewald method was used with a Fourier spacing of 0.16 nm. The electrostatic cutoff was set to 1.4 nm, and the van der Waals cutoff was set to 1.4 nm. The bond angles were restrained using the LINCS algorithm. The Parrinello–Rahman method was used to set the pressure (1 atm) of the system, and the V-rescale weak coupling method was used to regulate the temperature (310 K). The position restraints in the MD simulations for the NVT and NPT were carried out for 100 ps, with a production run of

30 ns for each protein–ligand complex, and a time step of 2 fs. The structural coordinates were saved every 1 ps, and final snapshots of the complexes were extracted using the GROMACS analysis tool.

2.8. Statistical Analysis

All results are presented as the mean \pm standard error of the mean (SEM). Statistical analysis was performed using GraphPad Prism 7.0 software (GraphPad Software Inc., San Diego, CA, USA). Statistical significance was considered at $p < 0.05$, after one-way analysis of variance (ANOVA) with Tukey multiple comparison test.

3. Results

3.1. Development of Competitive Binding Screening Assay

The scheme illustrating the overall screening method described in the Materials and Methods section is shown in Figure 1A. The known TNF- α inhibitor SPD304 was selected as a positive control or competitive ligand to validate the competitive binding screening assay using analytical SEC LC–tandem MS. First, sample of SPD304 incubated without TNF- α was analyzed as shown in Figure 1B, indicating that the small molecule SPD304 was efficiently removed after SEC and 10 kDa ultrafiltration. Next, when SPD304 was incubated with fresh TNF- α , a strong signal of SPD304 was detected at a retention time of 5.0 min after the process of analytical SEC (Figure 1C). However, no SPD304 signal was detected when SPD304 was incubated with denatured TNF- α (Figure 1D). This result confirmed that signal detection of SPD304 occurred only when it successfully bound to intact TNF- α .

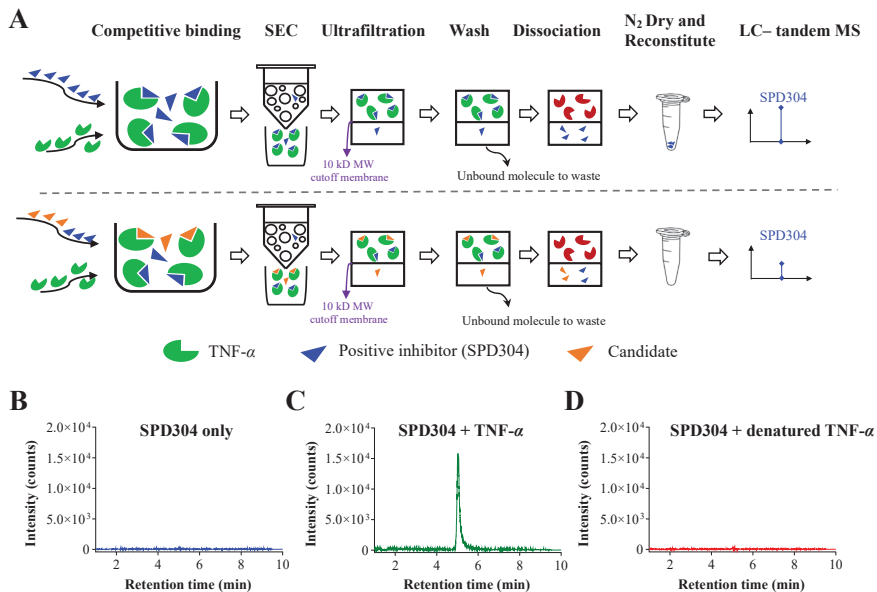


Figure 1. Method development and validation of competitive binding screening assay. (A) Schematic overview of competitive binding screening assay. After sample incubation for competitive binding, samples were processed through size exclusion chromatography, washed, and dissociated. The final eluent was N₂ dried and reconstituted. Samples were analyzed with liquid chromatography–tandem mass spectrometry. The signal intensity of SPD304 when (B) SPD304 was incubated without TNF- α ; (C) SPD304 was incubated with fresh TNF- α ; (D) SPD304 was incubated with denatured TNF- α .

3.2. Natural Product Compound Library Screening

Using the validated method, a competitive binding screening assay was performed with the natural product compound library listed in Table 1. Thirty-five prescreened

candidate compounds from the library were chemically diverse and included alkaloids, phenolic acids, and flavonoids. These compounds presented at least one of the following bioactivities: anti-inflammatory, anticancer, and antiviral activities. Using SPD304 as a positive control, the competitive binding ability of the library compounds was calculated, and the results are presented in Table 1. Signal reduction of SPD304 suggested competitive binding of a screened compound to TNF- α . In general screening assays, the threshold activity should be determined by making a few considerations, such as test concentration, desired potency, and system sensitivity. In this study, compounds with an inhibition level of SPD304 signal higher than 70% were set as the moderate inhibitors, giving a 5.7% hit rate with two primary hits among the 35 phytochemicals (Table 1). The two hits, sennoside B (#23) and acutumidine (#27), were found to be the most potent inhibitors with inhibition percentages of SPD304 signal at 89.4% and 71.4%, respectively (structures shown in Figure 2).

Table 1. Natural product compound library list used in the screening and corresponding signal inhibition percentages.

Sample #	Signal Inhibition ^a	Name	Sample #	Signal Inhibition ^a	Name
1	18.7	(23)-Hydroxyursolic acid	19	1.3	Gomisin N
2	29.3	Fraxinellone	20	-1.3	Harpagoside
3	20.2	Limonin	21	21.1	(+)-Matrine
4	33.3	Obacunone	22	32.5	Paoniflorin
5	14.7	Heraclenol	23	89.4	Sennoside B
6	44	Imperatorin	24	25	Tanshinone IIA
7	25.9	Dioscin	25	22.6	Hexahydrocurcumin
8	20	Amygdalin	26	21	Acutumine
9	14.7	Betaine	27	71.4	Acutumidine
10	17.3	Decursin	28	35	Isoliquiritigenin
11	6.9	6,7-Dimethylesculetin	29	12.5	Liquiritin
12	-1.3	Ephedrine	30	17.4	(8)-Demethoxyrunanine
13	15	Eugenol	31	32.5	Chlorogenic acid
14	20	Evodiamine	32	31.2	Caffeine
15	28	(6)-Gingerol	33	0	Dihydrofolic acid
16	33.9	Ginsenoside Rb1	34	23.5	N-(1-Naphthyl)ethylenediamine dihydrochloride
17	17.4	Ginsenoside Rg1	35	15.2	Myricetin
18	25.3	Gomisin A			

^a: Inhibition percentage (%) of SPD304 signal intensity; # denotes “number”.

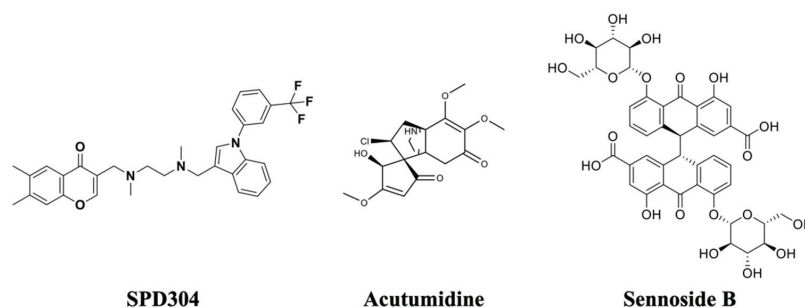


Figure 2. The chemical structures of SPD304, acutumidine, and sennoside B.

To further validate whether the two hits, acutumidine and sennoside B, competitively bind to TNF- α with SPD304, a competition binding assay with the two compounds was performed and the final eluate was analyzed using UPLC-Q Exactive hybrid quadrupole-orbitrap MS. As shown in Figure 3, when SPD304 was incubated with TNF- α alone, the signal of SPD304 was approximately 7×10^4 at a retention time of 7.2 min. However, when sennoside B was added to the mixture of SPD304 and TNF- α , the signal of SPD304 was significantly attenuated to 0.8×10^4 . Additionally, the peak of sennoside B was simultaneously detected at a retention time of 2.8 min. These results showed that sennoside

B competes with SPD304 for binding to TNF- α . In the case of acutumidine, the result was not reproducible, which led us to focus on sennoside B for further validation.

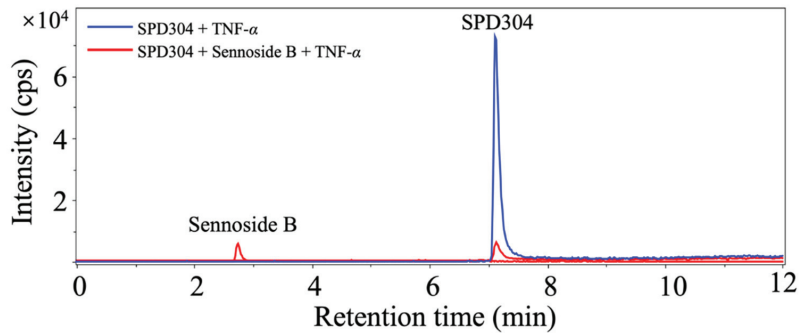


Figure 3. Confirmation of competitive binding of sennoside B with SPD304 against TNF- α . After the competitive binding assay and the subsequent follow-up steps, the samples were analyzed using UPLC-Q Exactive hybrid quadrupole-orbitrap MS. Blue line indicates the signal intensity from SPD304 + TNF- α sample. Red line indicates the signal intensity from SPD304 + sennoside B + TNF- α sample.

3.3. Sennoside B Inhibits TNF- α -Induced L929 Cell Death

Next, we evaluated the efficacy of sennoside B using a TNF- α dependent L929 cell cytotoxicity assay [6,20,26]. In the presence of sub-lethal concentrations of AMD, TNF- α can induce apoptosis in L929 cells. As expected, the positive control SPD304 significantly reduced L929 cell death induced by TNF- α up to 37.33% at 100 μ M (Figure 4A,B). Sennoside B showed significant dose-dependent inhibition of TNF- α -mediated cytotoxicity in L929 cells, inhibiting 80.3% at 100 μ M concentration (Figure 4A,C). Surprisingly, the efficacy of sennoside B was much better than that of positive control SPD304. When L929 cells were treated with sennoside B alone, a minimal effect on cell proliferation was observed (Supplementary Figure S1), thus excluding the possibility that the TNF- α inhibition efficacy of sennoside B did not result from direct biological effect on L929 cells.

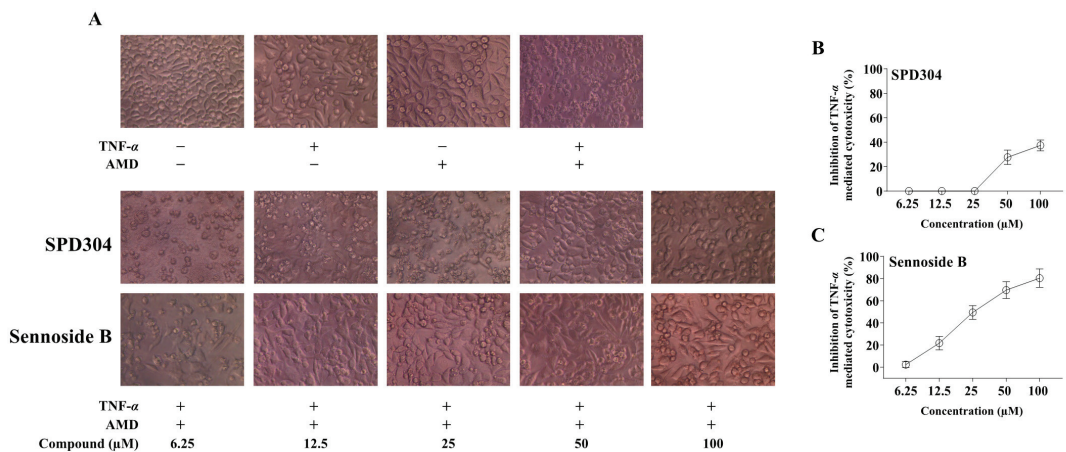


Figure 4. Sennoside B inhibits TNF- α -induced L929 cell death. (A) L929 cells were treated with 10 ng/mL TNF- α and 1 μ g/mL actinomycin D for 18 h in the presence of the indicated concentrations of SPD304 and sennoside B. SPD304 was used as the positive control. Cell viability was examined under a microscope (\times 200). Inhibition of TNF- α -mediated cytotoxicity by (B) SPD304 and (C) sennoside B on L929 cells was measured using the CCK-8 assay. Data were obtained from three independent experiments performed in triplicate and presented as mean \pm standard error of the mean (SEM).

3.4. Sennoside B Blocks TNF- α -Induced Signaling Pathways in Mouse L929 Cells

Having confirmed that sennoside B potently inhibits TNF- α -induced cell death, we next tested the effects of sennoside B on the signaling pathways induced by TNF- α . First, we explored whether sennoside B could block the degradation of I κ B- α and the activation of caspase-3, a common downstream signaling process of TNF- α [27,28]. As expected, SPD304 successfully antagonized the downstream signaling pathways of TNF- α in L929 cells (Figure 5). Indeed, sennoside B also significantly inhibited the degradation of I κ B- α and the activation of caspase 3 induced by TNF- α in a dose-dependent manner (Figure 5A,B). Eicosanoid lipid mediators, PGD₂ and PGE₂, are involved in diverse cellular responses, including cell proliferation, apoptosis, angiogenesis, and inflammation [29]. We found that treatment of L929 cells with TNF- α dramatically increased the secretion of PGD₂ and PGE₂ compared with the control group. This effect was significantly inhibited after treatment with 25, 50, and 100 μ M of sennoside B (Figure 5C). In line with previous assays, sennoside B showed greater efficacy in blocking the activation of caspase 3 and inhibiting the secretion of pro-inflammatory mediators, compared to SPD304. These data indicate that sennoside B successfully inhibited the inflammatory response induced by TNF- α in mouse L929 cells.

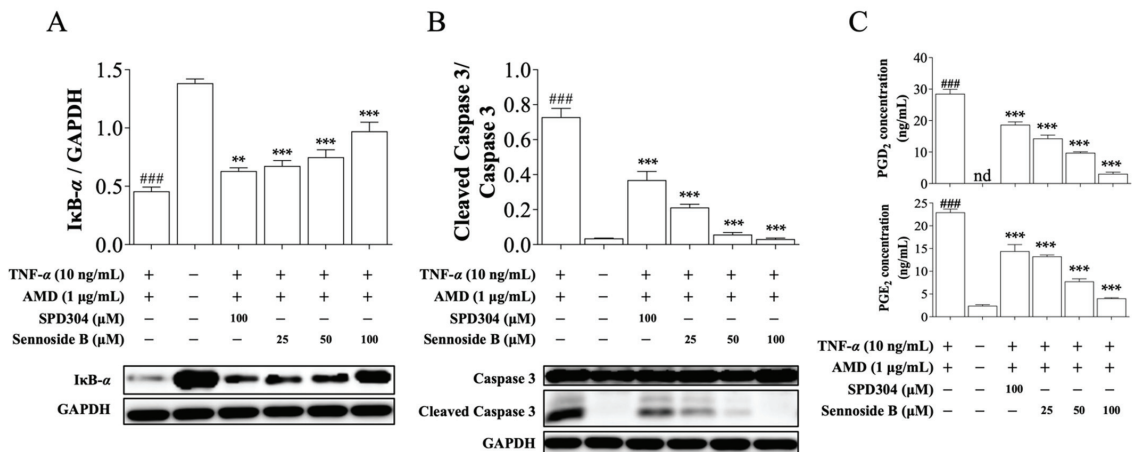


Figure 5. Sennoside B blocks TNF- α -induced signaling pathways in mouse L929 cells. L929 cells were treated with the positive control SPD304 or sennoside B and the protein levels of (A) I κ B- α , (B) caspase 3 and cleaved caspase 3 were measured. GAPDH was used as the internal control. (C) After the cell treatment, PGD₂ and PGE₂ levels were quantified in the cell medium ($n = 3$). All data are expressed as the mean \pm SEM. ** $p < 0.01$ and *** $p < 0.001$ indicate significant difference from the TNF- α -induced group and ### $p < 0.001$ indicates significant difference from the control group. nd indicates not detected.

3.5. Sennoside B Blocks Degradation of I κ B- α in HeLa Cells

After confirming the TNF- α inhibitory effect of sennoside B in a mouse cell line, the inhibitory effect of sennoside B on human cells was investigated. In HeLa cells, SPD304 inhibited TNF- α -mediated I κ B- α degradation, and showed a comparable IC₅₀ value (1.82 μ M), as observed earlier (Figure 6A) [9,10]. Consistently, sennoside B significantly inhibited the degradation of I κ B- α induced by TNF- α in HeLa cells and was found to be much more potent than SPD304 with an IC₅₀ value of 0.32 μ M (Figure 6B), which is 5.69 times lower than that of SPD304. No signs of cytotoxicity or cell proliferation were observed when HeLa cells were treated with sennoside B alone (Supplementary Figure S2). These results suggest that sennoside B can inhibit TNF- α -induced I κ B- α degradation in human HeLa cells very well.

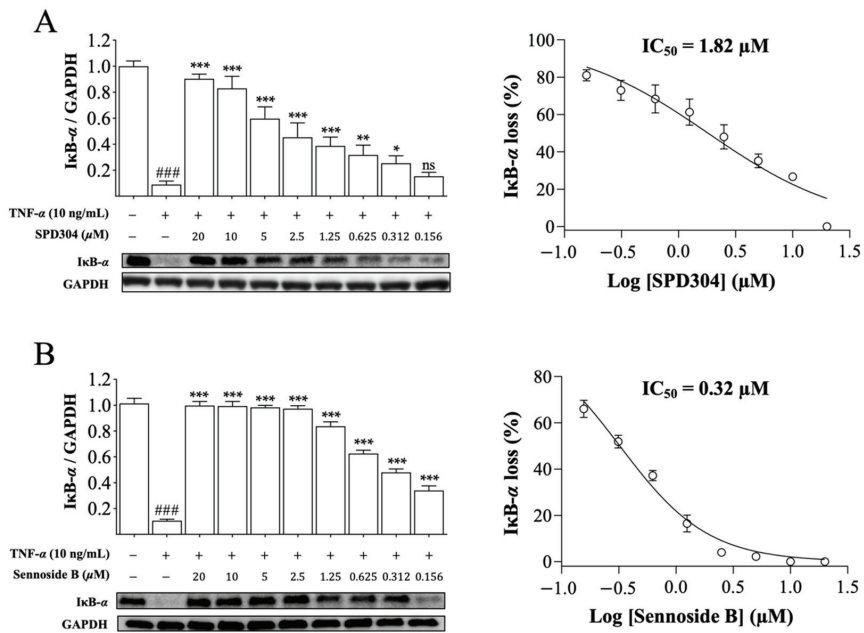


Figure 6. Sennoside B blocks TNF- α induced degradation of I κ B- α in human HeLa cells. Cells were treated with the indicated concentrations of (A) SPD304 and (B) sennoside B in the presence of TNF- α , and the protein level of I κ B- α was measured. GAPDH was used as the internal control. The IC_{50} values were calculated based on the inhibition percentage. All data are expressed as the mean \pm SEM ($n = 3$). ### $p < 0.001$ indicates significant difference from the control group, and * $p < 0.05$; ** $p < 0.01$, and *** $p < 0.001$ indicate significant difference from the TNF- α -induced group. ns indicates not significant.

3.6. Sennoside B-TNF- α Binding Interactions and Stability

The binding interactions of SDP304 with the TNF- α dimer include L57, Y59, S60, Q61, Y119, L120, G121, G122, and Y151 from chain A and L57*, Y59*, S60*, Y119*, L120*, G121*, and Y151* from chain B of the dimer (asterisks indicate the TNF- α B chain residues) [9]. Using the TNF- α dimer PDB crystal structure (PDB code 2AZ5), molecular docking was performed to investigate the binding mode of sennoside B to TNF- α . Sennoside B was stably positioned in the hydrophobic cavity of TNF- α and was predicted to have numerous hydrophobic interactions with residues, such as Y119, L57*, Y119*, and L120* (Figure 7). These interactions are also part of the key interactions between TNF- α and the SPD304 complex. Moreover, the significant residues Q61 and Y151 are proposed to form hydrogen bonds with the hydroxyl oxygen atoms in sennoside B, and G121* is proposed to form a hydrogen bond with a carbonyl oxygen atom in sennoside B (Figure 7C). Furthermore, to evaluate the binding energy between TNF- α and sennoside B, binding energy was calculated using the DSX online server and MD simulations. The interaction scores obtained from the DSX online server were -20.730 and -122.948 for SPD304 and sennoside B, respectively. The total interaction energy values obtained using GROMACS 2018 after 30 ns of MD simulations were -246.8415 kJ/mol for SPD304 and -367.8971 kJ/mol for sennoside B. The consistent lowest binding affinity scores of TNF- α /sennoside B suggest that sennoside B is a promising inhibitor of TNF- α . In short, sennoside B may not only fit well in the SPD304 binding site of the TNF- α dimer, but it also forms a complex that appears to be stable in molecular dynamics simulations.

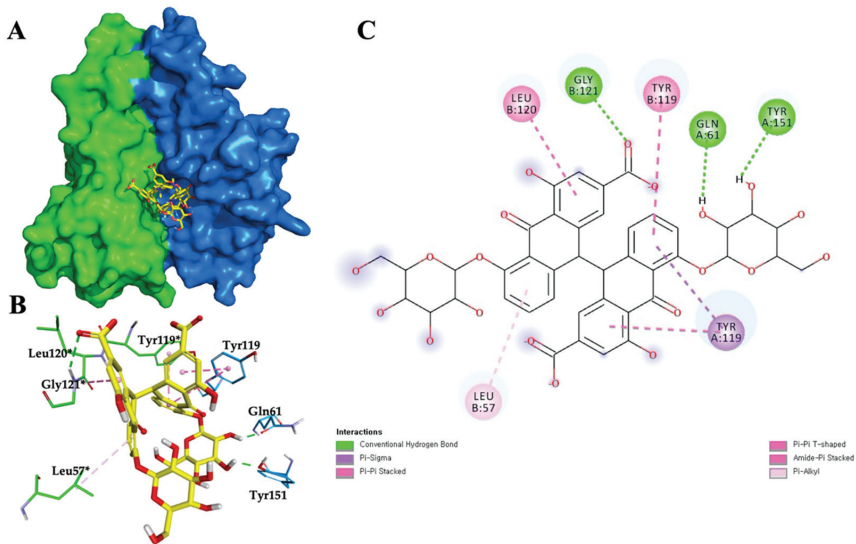


Figure 7. Sennoside B/TNF- α binding interactions and stability. (A) Sennoside B binding to the crystal structure of TNF- α (2AZ5). Blue color indicates chain A and green color indicates chain B. (B) Three-dimensional representation of sennoside B/TNF- α interactions. Residues of TNF- α and sennoside B are represented as sticks. The carbon and oxygen of ligands are presented in yellow and red colors, respectively. Hydrogen bond and hydrophobic interactions are shown as dotted lines. Asterisks indicate the B chain residues. (C) Two-dimensional representation of sennoside B/TNF- α interactions. Carbons of sennoside B are presented in black color.

4. Discussion

There are several viable strategies to antagonize TNF- α using small molecules. SPD304 directly binds to the inner pocket of the homotrimer of TNF- α and disassembles the homotrimer, resulting in a dimer that has no signaling activity against TNFR [9]. The natural product-derived compound, PMG directly binds to TNFR1, blocking the interaction between TNF- α and TNFR1 [13]. The synthetic compound UCB-9260 uniquely interacts with the homotrimer of TNF- α and stabilizes the asymmetric form of the trimer, which has no signal transduction activity [6]. Resveratrol has been proposed to inhibit TNF- α activity by modulating NF- κ B translocation, the downstream signaling of TNF- α [30].

Here, we developed a screening assay based on analytical SEC LC–tandem MS to identify small molecule inhibitors of TNF- α , that can compete for the active site with the known inhibitor SPD304. In silico molecular docking-based virtual screening method offers a fast and cost-effective way to screen diverse chemical libraries against the target of interests, although it requires rigorous validation steps. In vitro protein evolution methods, such as phage display, bacterial display, or mRNA display are powerful methods to screen peptides or proteins that have strong affinities against the desired target, but their utilization for small-molecule screening is limited. Other in vitro affinity-based assays, such as ELISA or SPR, can be used for small molecule screening, but require specific antibodies against the target or target immobilization. Our analytical SEC LC–tandem MS screening method utilizes an intact TNF- α homotrimer in solution without any chemical derivatization on the surface, which allows a much more straightforward and high-throughput screening. In our study, application of this screening method to in-house prescreened NP library compounds led to the identification of sennoside B, which showed higher efficacy than the known inhibitor SPD304.

Sennoside B, a dianthrone glycoside, is one of the main compounds extracted from *Cassia angustifolia*, which has been widely used as a natural laxative in traditional medicines [31]. Additionally, it has been reported that sennoside B can block platelet-derived growth factor

receptor signaling in human osteosarcoma cells [32] and inhibit SARS-CoV-2 main protease activity as well [33]. We discovered that sennoside B is a potent inhibitor of TNF- α with an IC₅₀ value of 0.32 μ M in human HeLa cells. To date, the most potent NP TNF- α inhibitor was quinuclidine, as reported by Chan et al. [10]. Quinuclidine showed an IC₅₀ value of 5 μ M in TNF- α -induced cell toxicity assays. Although the assayed platform was different, they used SPD304 as a positive control, and upon comparing the biological efficacy of compounds using SPD304, sennoside B showed an IC₅₀ value approximately 5.7 times lower than SPD304, whereas quinuclidine had an IC₅₀ value 1.6 times higher than SPD304. To our knowledge, sennoside B is by far the most potent NP TNF- α inhibitor known to date. The potency of sennoside B is comparable to that of UCB-9060, the most potent synthetic compound TNF- α inhibitor, with an IC₅₀ value of 116 nM in the L929 cell-based assay [6].

Sennoside B is believed to directly bind to the active site of TNF- α , as evidenced by LC-MS detection of both SPD304 and sennoside B. When sennoside B was added to the incubation mixture consisting of SPD304 and TNF- α , and the analytical SEC assay was further processed, the signal of sennoside B appeared, whereas the signal of the positive compound SPD304 was attenuated due to the competitive binding of sennoside B with SPD304 against TNF- α . Molecular docking using the crystal structure (PDB code 2AZ5) of the TNF- α dimer also indicated the possible hydrophobic interactions and hydrogen bonds between sennoside B and the binding site of TNF- α , suggesting that sennoside B effectively binds to and inhibits TNF- α , as specifically described in the results of Figure 7.

5. Conclusions

In this study, we developed and validated a competition binding screening method based on analytical SEC coupled with LC-tandem mass spectrometry for the discovery of small-molecule TNF- α inhibitors. Among the screened natural product library compounds, sennoside B showed an exceptional effect on TNF- α inhibition and is probably the most potent natural product TNF- α inhibitor identified to date. The activity of sennoside B was further validated by a series of in vitro cell assays that showed that sennoside B successfully inhibited TNF- α induced cell death and subsequent downstream signaling pathways in both mouse and human cell lines. Finally, the binding mode of sennoside B with the TNF- α crystal structure was analyzed using AutoDock 4, and the key residue interactions between sennoside B and TNF- α were predicted. Currently, the optimization of sennoside B to enhance its pharmacokinetic and metabolic properties is in progress for drug development.

Supplementary Materials: The following are available online at <https://www.mdpi.com/article/10.3390/biomedicines9091250/s1>. Figure S1: Effects of sennoside B on the cell viability of mouse L929 cells. L929 cells were seeded in 96-well plates at a density of 2.0×10^4 cells/well and cultured overnight. Prepared DMEM containing different concentrations of sennoside B (1.56–100 μ M) was treated to the cells. After incubating for 18 h, cell viability was measured using the CCK-8 assay, Figure S2: Effects of sennoside B on the cell viability of human HeLa cells. HeLa cells were seeded in 96-well plates at a density of 2.0×10^4 cells/well and cultured overnight. Prepared DMEM containing different concentrations of sennoside B (0.62–40 μ M) was treated to the cells. After incubating for 18 h, cell viability was measured using the CCK-8 assay.

Author Contributions: Conceptualization, L.P. and Y.C.; methodology—instrument analysis, L.P., J.J.P. and Y.C.; methodology—biological experiment, L.P. and J.J.P.; methodology—molecular docking, P.D. and K.P.; validation, L.P., J.J.P. and Y.C.; formal analysis, L.P., J.J.P. and Y.C.; writing—original draft preparation, L.P. and J.J.P.; writing—review and editing, J.J.P. and Y.C.; visualization, L.P. and J.J.P.; funding acquisition, Y.C. All authors have read and agreed to the published version of the manuscript.

Funding: This work was financially supported by the Korea Institute of Science and Technology (KIST) under grant (2Z06481).

Institutional Review Board Statement: Not applicable.

Informed Consent Statement: Not applicable.

Data Availability Statement: Not applicable.

Conflicts of Interest: The authors declare no conflict of interest.

References

- Kallioli, G.D.; Ivashkiv, L.B. TNF biology, pathogenic mechanisms and emerging therapeutic strategies. *Nat. Rev. Rheumatol.* **2016**, *12*, 49–62. [CrossRef] [PubMed]
- Tracey, D.; Klareskog, L.; Sasso, E.H.; Salfeld, J.G.; Tak, P.P. Tumor necrosis factor antagonist mechanisms of action: A comprehensive review. *Pharmacol. Ther.* **2008**, *117*, 244–279. [CrossRef] [PubMed]
- Taylor, P.C.; Feldmann, M. Anti-TNF biologic agents: Still the therapy of choice for rheumatoid arthritis. *Nat. Rev. Rheumatol.* **2009**, *5*, 578–582. [CrossRef]
- Levin, A.D.; Wildenberg, M.E.; van den Brink, G.R. Mechanism of Action of Anti-TNF Therapy in Inflammatory Bowel Disease. *J. Crohns. Colitis.* **2016**, *10*, 989–997. [CrossRef]
- Lowes, M.A.; Bowcock, A.M.; Krueger, J.G. Pathogenesis and therapy of psoriasis. *Nature* **2007**, *445*, 866–873. [CrossRef]
- O’Connell, J.; Porter, J.; Kroepfli, B.; Norman, T.; Rapecki, S.; Davis, R.; McMillan, D.; Arakaki, T.; Burgin, A.; Fox Iii, D.; et al. Small molecules that inhibit TNF signalling by stabilising an asymmetric form of the trimer. *Nat. Commun.* **2019**, *10*, 5795. [CrossRef]
- Rider, P.; Carmi, Y.; Cohen, I. Biologics for Targeting Inflammatory Cytokines, Clinical Uses, and Limitations. *Int. J. Cell Biol.* **2016**, *2016*, 9259646. [CrossRef]
- Alzani, R.; Cozzi, E.; Corti, A.; Temponi, M.; Trizio, D.; Gigli, M.; Rizzo, V. Mechanism of suramin-induced deoligomerization of tumor necrosis factor alpha. *Biochemistry* **1995**, *34*, 6344–6350. [CrossRef]
- He, M.M.; Smith, A.S.; Oslob, J.D.; Flanagan, W.M.; Braisted, A.C.; Whitty, A.; Cancilla, M.T.; Wang, J.; Lugovskoy, A.A.; Yoburn, J.C.; et al. Small-molecule inhibition of TNF-alpha. *Science* **2005**, *310*, 1022–1025. [CrossRef]
- Chan, D.S.; Lee, H.M.; Yang, F.; Che, C.M.; Wong, C.C.; Abagyan, R.; Leung, C.H.; Ma, D.L. Structure-based discovery of natural-product-like TNF-alpha inhibitors. *Angew. Chem. Int. Ed. Engl.* **2010**, *49*, 2860–2864. [CrossRef]
- Ma, L.; Gong, H.; Zhu, H.; Ji, Q.; Su, P.; Liu, P.; Cao, S.; Yao, J.; Jiang, L.; Han, M.; et al. A novel small-molecule tumor necrosis factor alpha inhibitor attenuates inflammation in a hepatitis mouse model. *J. Biol. Chem.* **2014**, *289*, 12457–12466. [CrossRef]
- Luzi, S.; Kondo, Y.; Bernard, E.; Stadler, L.K.; Vaysburd, M.; Winter, G.; Holliger, P. Subunit disassembly and inhibition of TNFalpha by a semi-synthetic bicyclic peptide. *Protein Eng. Des. Sel.* **2015**, *28*, 45–52. [CrossRef] [PubMed]
- Cao, Y.; Li, Y.H.; Lv, D.Y.; Chen, X.F.; Chen, L.D.; Zhu, Z.Y.; Chai, Y.F.; Zhang, J.P. Identification of a ligand for tumor necrosis factor receptor from Chinese herbs by combination of surface plasmon resonance biosensor and UPLC-MS. *Anal. Bioanal. Chem.* **2016**, *408*, 5359–5367. [CrossRef] [PubMed]
- Chen, S.; Feng, Z.; Wang, Y.; Ma, S.; Hu, Z.; Yang, P.; Chai, Y.; Xie, X. Discovery of Novel Ligands for TNF-alpha and TNF Receptor-1 through Structure-Based Virtual Screening and Biological Assay. *J. Chem. Inf. Model.* **2017**, *57*, 1101–1111. [CrossRef] [PubMed]
- McGeary, R.P.; Bennett, A.J.; Tran, Q.B.; Cosgrove, K.L.; Ross, B.P. Suramin: Clinical uses and structure-activity relationships. *Mini. Rev. Med. Chem.* **2008**, *8*, 1384–1394. [CrossRef] [PubMed]
- Sun, H.; Yost, G.S. Metabolic activation of a novel 3-substituted indole-containing TNF-alpha inhibitor: Dehydrogenation and inactivation of CYP3A4. *Chem. Res. Toxicol.* **2008**, *21*, 374–385. [CrossRef]
- Newman, D.J.; Cragg, G.M. Natural Products as Sources of New Drugs over the Nearly Four Decades from 01/1981 to 09/2019. *J. Nat. Prod.* **2020**, *83*, 770–803. [CrossRef]
- Rubin, B.Y.; Smith, L.J.; Hellermann, G.R.; Lunn, R.M.; Richardson, N.K.; Anderson, S.L. Correlation between the anticellular and DNA fragmenting activities of tumor necrosis factor. *Cancer Res.* **1988**, *48*, 6006–6010.
- Trost, L.C.; Lemasters, J.J. A cytotoxicity assay for tumor necrosis factor employing a multiwell fluorescence scanner. *Anal. Biochem.* **1994**, *220*, 149–153. [CrossRef]
- Nesbitt, A.; Fossati, G.; Bergin, M.; Stephens, P.; Stephens, S.; Foulkes, R.; Brown, D.; Robinson, M.; Bourne, T. Mechanism of action of certolizumab pegol (CDP870): In vitro comparison with other anti-tumor necrosis factor alpha agents. *Inflamm. Bowel. Dis.* **2007**, *13*, 1323–1332. [CrossRef]
- Shin, J.S.; Peng, L.; Kang, K.; Choi, Y. Direct analysis of prostaglandin-E2 and -D2 produced in an inflammatory cell reaction and its application for activity screening and potency evaluation using turbulent flow chromatography liquid chromatography-high resolution mass spectrometry. *J. Chromatogr. A* **2016**, *1463*, 128–135. [CrossRef]
- Morris, G.M.; Huey, R.; Lindstrom, W.; Sanner, M.F.; Belew, R.K.; Goodsell, D.S.; Olson, A.J. AutoDock4 and AutoDockTools4: Automated docking with selective receptor flexibility. *J. Comput. Chem.* **2009**, *30*, 2785–2791. [CrossRef]
- Gohlke, H.; Hendlich, M.; Klebe, G. Knowledge-based scoring function to predict protein-ligand interactions. *J. Mol. Biol.* **2000**, *295*, 337–356. [CrossRef]
- Pronk, S.; Pall, S.; Schulz, R.; Larsson, P.; Bjelkmar, P.; Apostolov, R.; Shirts, M.R.; Smith, J.C.; Kasson, P.M.; van der Spoel, D.; et al. GROMACS 4.5: A high-throughput and highly parallel open source molecular simulation toolkit. *Bioinformatics* **2013**, *29*, 845–854. [CrossRef]
- Schuttelkopf, A.W.; van Aalten, D.M. PRODRG: A tool for high-throughput crystallography of protein-ligand complexes. *Acta Crystallogr. D* **2004**, *60*, 1355–1363. [CrossRef] [PubMed]

26. Humphreys, D.T.; Wilson, M.R. Modes of L929 cell death induced by TNF-alpha and other cytotoxic agents. *Cytokine* **1999**, *11*, 773–782. [CrossRef]
27. Faustman, D.; Davis, M. TNF receptor 2 pathway: Drug target for autoimmune diseases. *Nat. Rev. Drug Discov.* **2010**, *9*, 482–493. [CrossRef] [PubMed]
28. Van Herreweghe, F.; Festjens, N.; Declercq, W.; Vandenamee, P. Tumor necrosis factor-mediated cell death: To break or to burst, that's the question. *Cell Mol. Life Sci. CMLS* **2010**, *67*, 1567–1579. [CrossRef] [PubMed]
29. Nakanishi, M.; Rosenberg, D.W. Multifaceted roles of PGE2 in inflammation and cancer. *Semin. Immunopathol.* **2013**, *35*, 123–137. [CrossRef] [PubMed]
30. Silva, A.M.; Oliveira, M.I.; Sette, L.; Almeida, C.R.; Oliveira, M.J.; Barbosa, M.A.; Santos, S.G. Resveratrol as a natural anti-tumor necrosis factor-alpha molecule: Implications to dendritic cells and their crosstalk with mesenchymal stromal cells. *PLoS ONE* **2014**, *9*, e91406. [CrossRef]
31. Wu, H.; Feng, F.; Jiang, X.; Hu, B.; Qiu, J.; Wang, C.; Xiang, Z. Pharmacokinetic and metabolic profiling studies of sennoside B by UPLC-MS/MS and UPLC-Q-TOF-MS. *J. Pharm. Biomed. Anal.* **2020**, *179*, 112938. [CrossRef] [PubMed]
32. Chen, Y.C.; Chang, C.N.; Hsu, H.C.; Chiou, S.J.; Lee, L.T.; Hseu, T.H. Sennoside B inhibits PDGF receptor signaling and cell proliferation induced by PDGF-BB in human osteosarcoma cells. *Life Sci.* **2009**, *84*, 915–922. [CrossRef]
33. Abdallah, H.M.; El-Halawany, A.M.; Sirwi, A.; El-Araby, A.M.; Mohamed, G.A.; Ibrahim, S.R.M.; Koshak, A.E.; Asfour, H.Z.; Awan, Z.A.; Elfaky, M.A. Repurposing of Some Natural Product Isolates as SARS-COV-2 Main Protease Inhibitors via In Vitro Cell Free and Cell-Based Antiviral Assessments and Molecular Modeling Approaches. *Pharmaceuticals* **2021**, *14*, 213. [CrossRef] [PubMed]



Article

Molecular Docking Simulations on Histone Deacetylases (HDAC)-1 and -2 to Investigate the Flavone Binding

Bernardina Scafuri ^{1,†}, Paola Bontempo ^{2,†}, Lucia Altucci ², Luigi De Masi ^{3,*} and Angelo Facchiano ^{4,*}

¹ Department of Chemistry and Biology “A. Zambelli”, University of Salerno, Via Giovanni Paolo II, 132, Fisciano, 84084 Salerno, Italy; bscafuri@unisa.it

² Department of Precision Medicine, University of Campania “Luigi Vanvitelli”, via L. De Crecchio 7, 80138 Naples, Italy; paola.bontempo@unicampania.it (P.B.); lucia.altucci@unicampania.it (L.A.)

³ National Research Council (CNR), Institute of Biosciences and BioResources (IBBR), via Università 133, Portici, 80055 Naples, Italy

⁴ National Research Council (CNR), Institute of Food Science (ISA), via Roma 64, 83100 Avellino, Italy

* Correspondence: luigi.demasi@ibbr.cnr.it (L.D.M.); angelo.facchiano@isa.cnr.it (A.F.)

† These authors contributed equally to this research work.

Received: 18 October 2020; Accepted: 2 December 2020; Published: 4 December 2020

Abstract: Histone modifications through acetylation are fundamental for remodelling chromatin and consequently activating gene expression. The imbalance between acetylation and deacetylation activity causes transcriptional dysregulation associated with several disorders. Flavones, small molecules of plant origin, are known to interfere with class I histone deacetylase (HDAC) enzymes and to enhance acetylation, restoring cell homeostasis. To investigate the possible physical interactions of flavones on human HDAC1 and 2, we carried out *in silico* molecular docking simulations. Our data have revealed how flavone, and other two flavones previously investigated, i.e., apigenin and luteolin, can interact as ligands with HDAC1 and 2 at the active site binding pocket. Regulation of HDAC activity by dietary flavones could have important implications in developing epigenetic therapy to regulate the cell gene expression.

Keywords: epigenetics; histone deacetylase inhibitors; flavones; molecular simulations

1. Introduction

The fine remodelling of the chromatin structure by post-translational covalent modifications (acetylation, methylation, phosphorylation, and clipping) of histone tails is a key mechanism for epigenetic regulation of gene expression [1,2]. In this context, histone acetyltransferases (EC 2.3.1.48, HAT) and histone deacetylases (EC 3.5.1.98, HDAC) are essential enzymes in adding and removing, respectively, the acetyl moiety on the amino acid lysine [1]. N-terminal tails of histones deacetylated by HDAC have positive charges that interact with the negatively charged phosphate groups of DNA. Consequently, the chromatin is condensed into a compact structure (heterochromatin) associated with low levels of gene transcription. This structural condition can be reversed by HAT activity to a relaxed and transcriptionally active DNA (euchromatin). Therefore, the levels of histone acetylation are the result of the HAT/HDAC activity balance that plays a crucial role in the regulation of gene transcription through modulation of epigenetic changes. Alterations of this tightly coordinated molecular system have been implicated in a range of diseases including inflammation, cardiovascular and neurodegenerative disorders, diabetes, and cancer [3,4].

To date, 18 eukaryotic HDAC are known and grouped into four classes on the basis of their structural and catalytic similarity [3]. Class I with HDAC1, 2, 3, and 8 is subdivided into the three

subclasses Ia (HDAC1 and 2), Ib (HDAC3), and Ic (HDAC8). Class II is formed by the two subclasses IIa (HDAC4, 5, 7, 9) and IIb (HDAC6 and 10). Class III consists of NAD⁺ dependent HDAC homologous to the yeast Sir2 protein (Sir2-like or sirtuins: Sirt1-7). Class IV only includes HDAC11. The common characteristic to classes I, II, and IV is a catalytic domain with one histidine (His) and two aspartate (Asp) residues associated with Zn²⁺ ion cofactor responsible for Zn²⁺-dependent hydrolysis of ε-N-acetylated lysine residues to yield deacetylated histone by a charge-relay mechanism [5]. Overall, HDACs have a conserved domain belonging to the open alpha/beta fold class. This central core consists of alpha-helices alternating with parallel beta-strands that build a central beta-sheet. From here, large loops associate to form a binding pocket where, in depth, the Zn²⁺ ion participates in the enzyme active site.

HDAC activity can be regulated at different levels by transcriptional regulation, post-translational modifications, subcellular localization, protein–protein interactions, proteolytic regulation, and small-molecules acting as HDAC inhibitors (HDACi). Thus, HDAC are attractive targets for the development of novel drugs, and HDACi may constitute potential therapeutic agents. Based on their structural characteristics, HDACi of natural origin are subdivided in hydroxamates, benzamides, cyclic peptides, and short-chain fatty acids [2]. Among the inhibitors acting on classes I-II HDACs, the anticancer agents Vorinostat (suberoylanilide hydroxamic acid or SAHA, Figure 1) and the structurally related Trichostatin A (TSA) exert multiple biological effects by interfering with the cell cycle, inducing apoptosis, autophagy, oxidative stress, and inhibiting angiogenesis [6,7]. SAHA and TSA reversibly bind to the HDAC active site, where chelate the cofactor Zn²⁺ by their hydroxamic acid group. NAD⁺ dependent HDAC belonging to class III (sirtuins) are not inhibited by conventional HDACi such as TSA and SAHA [8].

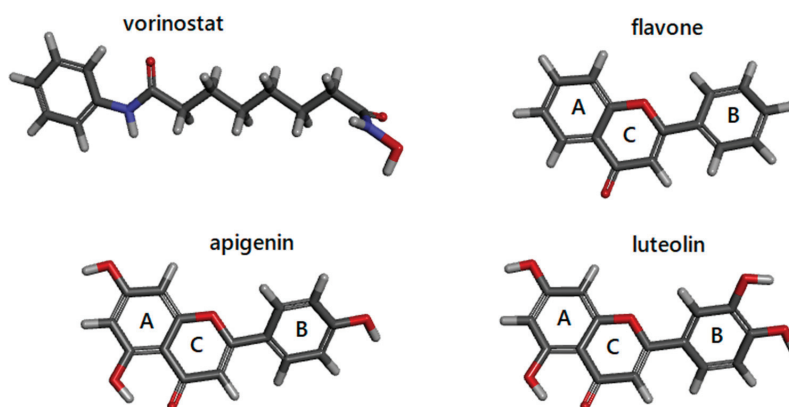


Figure 1. Molecular structures of vorinostat, flavone, apigenin, and luteolin are from the PubChem database. A, B, and C indicate the different rings of flavones. Images are generated by DiscoveryStudio4.5.

Since clinically used HDACi still experience adverse effects, to identify novel, more potent and specific inhibitors, plant-derived compounds have been screened and tested against human diseases, including cancers, for their ability to restore gene expression alterations [2,6,9,10]. A previous study on the acetonic extract from fruits of *Feijoa sellowiana* O. Berg has identified the bioactive component 2-phenyl-1,4-benzopyrone (known as flavone) to show anti-cancer action on solid and haematological cancer cells via HDAC inhibition [9]. This natural inhibitor, together with apigenin and luteolin, belongs to the subclass of flavonoids called flavones and is structurally different from known HDACi. Flavonoids have a backbone of 15 carbon atoms formed by two phenyl rings (A and B) and a heterocyclic ring with oxygen (C) abbreviated C6-C3-C6 (Figure 1). They are characterized by a double bond in position 2–3 and a ketone in position 4 of the ring C. Luteolin and apigenin have additional hydroxyl groups on the A and B rings. Flavonoids are chemopreventive molecules, ubiquitously present in

different plant organs [2,10–12]. However, the exact action mechanism at the molecular level of inhibitory effects is still not fully understood [9].

The observation that the apoptotic activities of flavones are correlated with the same targets of HDACi [9,13,14] inspired us to carry out an *in silico* molecular characterization of underlying inhibition mechanism on HDAC of flavone and its derivatives apigenin and luteolin. In fact, the activity of these flavones has been already observed by experimental results reported in the literature [9,13,14], but it is not known how these molecules bind and inhibit their protein targets. We investigated their possible interactions on subclass Ia HDAC1 and 2 in comparison with the better known HDACi vorinostat. In more detail, we used docking simulations to check the suitability of the three molecules to mimic the interaction occurring between HDAC2 and vorinostat, described by the structural model obtained by X-ray diffraction studies [1]. We simulated by molecular docking the ligand-protein interaction, showing that the flavonic ligands can bind HDAC1 and 2 at the active site, as the vorinostat does with HDAC2. Consequently, HDAC activity could be directly regulated by dietary flavones with important implications on global gene expression regulation.

2. Materials and Methods

The structures of human HDAC1 and HDAC2 were selected from RCSB PDB [15], file code 4BKX and 4LXZ, respectively. The HDAC2 structure 4LXZ is complexed with vorinostat, an hydroxamic acid that inhibits HDACs. By selecting this structure, we have an experimental reference of HDAC2-inhibitor binding for our study. We selected the highest-resolution structure available of the entire HDAC1, i.e., the structure 4BKX in complex with the dimeric ELM2-SANT domain of MTA1 from the NuRD complex, in the absence of an HDAC1 structure complexed with vorinostat; the dimeric domain has been removed to perform the docking simulation. Although the sequences of HDAC1 and HDAC2 are very similar and can be aligned with the shift of one position at the N-terminus and few gaps in the C-terminal portion (see Supplementary Figure S1), we used the amino acid numbers with a difference of 5 positions in agreement with the numbers in the PDB structures.

Docking simulations were performed between the two enzymes and vorinostat, flavone, apigenin, and luteolin, with AutoDock 4.2 and AutoDockTools4 [16], to verify the suitability of the molecular structure of flavone, apigenin, and luteolin to interact with HDAC1 and HDAC2 at the same binding site occupied by vorinostat.

The crystallographic structure of HDAC2 with vorinostat from the PDB was used to perform a redocking test in order to check the correctness of the parameters used and to evaluate the binding energy. In this way, the value of the predicted binding energy was used to compare the docking results between HDAC1/2 and ligands.

The 3D structures of flavones were downloaded in .sdf format from the PubChem database (<https://pubchem.ncbi.nlm.nih.gov>) [17] and converted in .pdb format using UCSF Chimera (<http://www.rbvi.uscf.edu/chimera>) [18].

Two different docking approaches were performed: the blind docking, by setting a grid box to include the entire protein surface, and the focused docking, by setting the grid box only on the binding site of the protein, as reported by the PDB file annotations. For each docking simulation, we simulated three protein-ligand systems: (i) the protein structures without water molecules, as suggested by AutoDock 4.2 protocol; (ii) the protein structures with two water molecules in binding site; (iii) the ligand decorated with an ensemble of water molecules, which may then contribute to the interaction (hydration condition).

For all systems, the molecular docking was performed with flexible ligands and both by keeping the entire protein rigid and by making flexible the residues involved in the catalytic channel, selected by visual inspection of the structure and on the basis of AutoDock limits in a flexibility setting. For HDAC1, the flexible residues were His140, His141, Phe205, Asp264, Tyr303, and additionally Asp176 for apigenin and luteolin. For HDAC2, the flexible residues were His145, His146, Asp181, Phe210, Asp269, Tyr308, and additionally Phe155 for flavone. According to docking simulation protocols already in use in

our laboratory [19,20], the ligands and the proteins were prepared using AutoDockTools, by adding hydrogens and partial charges in agreement with Gasteiger. The dimensions of the grid box were set according to the protein's dimension. The Lamarckian Genetic Algorithm was employed, setting 100 independent Genetic Algorithm runs for each ligand; the other parameters were kept at default values. Detailed settings are reported in Supplementary Table S1.

Cluster analysis was performed on the docked results using a root mean square deviation (RMSD) tolerance of 2 Å, and the initial coordinates of the ligand were used as the reference structure. Subsequently, we selected for each ligand the result with the best binding energy value. To further investigate the cluster population, we selected the best five results in terms of binding energy, and evaluated their mean value with standard deviation.

Analysis of the ligand–protein interaction has been performed with DiscoveryStudio4.5 (Biovia, San Diego, CA, USA), used also to generate the 2D schemes of ligand-protein binding and 3D molecular images.

3. Results and Discussion

3.1. Docking Simulations of Inhibitor Vorinostat Interaction with HDAC1 and HDAC2

In this work, docking simulations were performed to explore the capability of flavone, luteolin, and apigenin to interact with HDAC1 and HDAC2 proteins. The availability of the crystal structure of HDAC2 in complex with the inhibitor vorinostat allowed us to use vorinostat as a reference point for settings of the docking procedure and comparison of binding energy values obtained with the natural compounds under study. Firstly, we re-docked vorinostat in the binding site of HDAC2. This procedure is useful to verify that the simulation protocol is able to reproduce an experimental proof. The result of the simulation showed that vorinostat is correctly positioned into the active site binding pocket of HDAC2 (see Figure 2) and gave favourable energy values of interaction (Table 1). The comparison of the vorinostat conformation from the experimental structure and from redocking procedure is also reported as a molecular superimposition image with RMSD in Supplementary Figure S2.

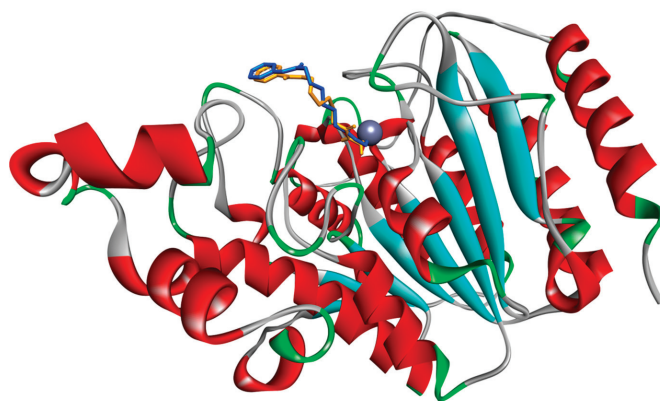


Figure 2. Interaction of the inhibitor vorinostat with HDAC2 from a crystallographic structure and re-docking simulations. The complex HDAC2-vorinostat obtained by redocking simulation has been superimposed to the crystallographic complex. Vorinostat from redocking (orange molecule in stick representation) occupies the same site as in the crystallographic complex (blue molecule). HDAC2 backbone is represented as a ribbon, with red helices and cyan strands. Grey sphere indicates the Zinc atom in the site. Image is generated by DiscoveryStudio4.5.

Table 1. Predicted energies of interaction from molecular docking simulations of HDAC1/2 with flavones as ligands and inhibitor vorinostat as a reference.

Protein–Ligand Complex	Free Energy of Interaction (Kcal/mol)	Explicit Interaction with Zn ²⁺ Ion	Rigid/Flexible Docking	Notes
Blind docking				
HDAC1-flavone	−8.50	yes	Rigid	
HDAC1-luteolin	−7.09	yes	Rigid	
HDAC1-apigenin	−7.61	yes	Rigid	
HDAC1-vorinostat	−7.23	yes	Rigid	
HDAC2-flavone	−7.94	yes	Rigid	
HDAC2-luteolin	−6.84	no	Rigid	
HDAC2-apigenin	−8.98	yes	flexible	hydrated with 3 water molecules
HDAC2-vorinostat	−7.45	yes	Rigid	Hydrated
Focused docking				
HDAC1-flavone	−10.25	Yes	flexible	
HDAC1-luteolin	−9.41	Yes	flexible	
HDAC1-apigenin	−9.25	Yes	flexible	
HDAC1-vorinostat	−8.46	Yes	rigid	hydrated
HDAC2-flavone	−8.90	Yes	rigid	
HDAC2-luteolin	−9.26	Yes	flexible	
HDAC2-apigenin	−9.32	Yes	flexible	
HDAC2-vorinostat	−8.45	Yes	rigid	2 water molecules involved

The simulation has been performed under different conditions (see Section 2) and the best interaction energy value obtained, i.e., −8.45 Kcal/mol (Table 1), referred to the focused docking in the presence of the crystallographic water molecules. Binding to the cofactor Zn²⁺ in HDAC2 is given by the hydroxamic acid group (Supplementary Figure S3), as expected [7]. Then, we also performed docking simulations between HDAC1 and vorinostat, and obtained a very similar interaction energy value, i.e., −8.46 Kcal/mol (Table 1). However, at the lowest energy the orientation of vorinostat into the HDAC1 catalytic site allows that the oxygen bound to C8 coordinates the cofactor Zn²⁺ (Supplementary Figure S4), different to HDAC2. By exploring the other conformations obtained in the docking simulations of vorinostat-HDAC1, the interaction of the hydroxamic acid group with the cofactor Zn²⁺ is also possible, though with higher energy, i.e., −6.71 Kcal/mol (data not shown), thus suggesting that two different binding modes may exist with HDAC1.

It is worth noting that, while the conformation at the lowest energy value represents the best interaction obtained, the docking simulations generate 100 conformations, clustered on the basis of their structural similarity. Therefore, we performed a deeper analysis of the results by comparing the best 3 conformations from the cluster containing the conformation with the lowest binding energy. The table with mean energy values and standard deviation (Supplementary Table S2) confirms the capability of flavone, luteoline, and apigenin to interact with HDAC1 and 2 with binding energy values similar to the value of vorinostat, or better.

3.2. Docking Simulations of Flavones Interaction with HDAC1 and HDAC2

To explore the possibility that flavone, luteolin, and apigenin bind to HDACs, we applied the same docking simulation protocol to HDAC1 and HDAC2 as target proteins and these three molecules as ligands, by testing different conditions. The best energy values obtained for each pair of protein-ligands are reported in Table 1.

Blind docking was performed to explore the entire surface of protein, searching for possible binding sites to be further investigated in more detail. In our case, the target active site of the protein is known, being already identified by crystallographic structure of HDAC2 in complex with the vorinostat inhibitor. However, in any case, the blind simulation is useful in finding alternative binding sites, as it helps to have a preliminary screening of the surface. Next, focused docking was performed on the preliminary sites resulting from the blind search, by setting a higher resolution screening. The blind docking identified in all cases the known active site pocket as the most reliable binding site for the ligands. The energy values of blind docking are commonly considered not optimized, being performed

by searching grids with low definition. It is interesting to note that the blind docking suggested that flavone and apigenin might interact with better energy values than vorinostat, in both HDAC1 and HDAC2 (Table 1, higher part). On the contrary, the blind docking conditions suggested that luteolin might interact with HDAC1 in a worse way than vorinostat.

The results of blind docking have been further investigated by focusing on the binding site of HDACs. The results are shown in Table 1 (lower part). As expected, in all cases interaction energy values obtained with focused docking are lower than in blind docking, because the higher definition of the simulation allows to optimize the docking and find protein–ligand interactions with lower energies. Previous docking simulations reported better docking scores for givinostat, another known inhibitor of HDACs, than apigenin and luteolin [21]. Interestingly, the energy values of our focused docking indicate that flavone, luteolin, and apigenin may interact with both HDAC1 and HDAC2 better than vorinostat. The differences in energy values are evident in both cases, but more relevant with HDAC1. The low values of energy obtained in our simulations strongly support the possibility that flavone, luteolin, and apigenin may interact with HDAC1 and HDAC2, thus confirming the experimental evidence [9,13,14,22].

3.3. Molecular Interactions of Flavones with HDAC1 and HDAC2

Bontempo et al. (2007) [9] demonstrated that the anti-cancer pharmacological potential of the *Feijoa* fruits is due to the secondary metabolite flavone, which showed to inhibit HDAC1, thus hyper-acetylating histones and non-histone targets in leukaemia cell lines. To investigate the details of molecular interactions of flavone with HDAC1 and HDAC2, as also suggested by the energy values of our in silico simulations, we analysed the interactions of flavone in the active site binding pockets of HDAC1 and HDAC2 (see Figures 3 and 4, respectively). A schematic 2D view is also reported in Supplementary Materials (Figures S5 and S6). Schematic 2D images for apigenin and luteolin are under Supplementary Figures S7–S8 and S9–S10, respectively. Apigenin and luteolin present additional hydroxyl groups that make possible different binding modes (not shown).

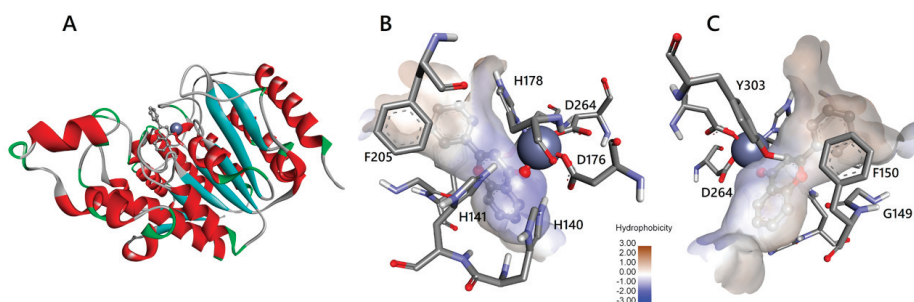


Figure 3. Interaction of flavone with HDAC1. (A) HDAC1 (ribbon with red helices and cyan strands) with flavone (grey molecule, in a ball and stick representation) in the interaction resulting from docking simulation. Zinc ion is represented as a sphere. (B) flavone (ball and stick) in the catalytic channel (surface coloured by hydrophobicity scale) of HDAC1. Amino acids (sticks) involved in the interaction with flavone are labelled with a one-letter code and number in the sequence. Zinc ion, represented as a sphere, is coordinated with the carbonyl oxygen atom of flavone ring C and D176, H178, D264. Atoms are coloured in grey (Carbon), red (Oxygen), white (Hydrogen), and blue (Nitrogen). (C) the opposite view of panel B shows the position of amino acids not visible in the other panel. Images are generated by DiscoveryStudio4.5.

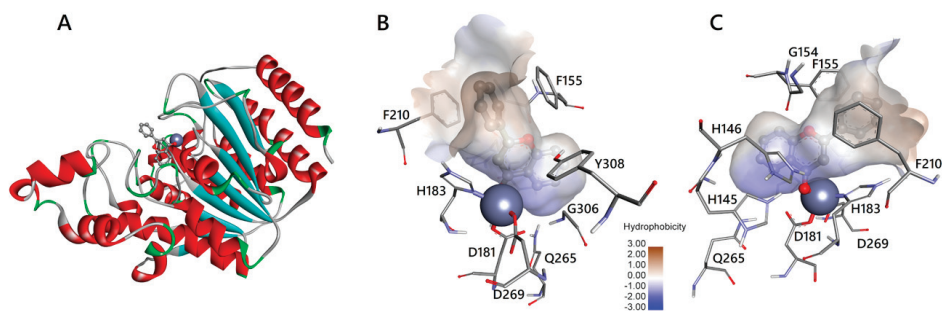


Figure 4. Interaction of flavone with HDAC2. (A) HDAC2 with flavone in the interaction with zinc ion resulting from docking simulation. Colours and representations are as in Figure 3. (B) flavone in the catalytic channel of HDAC2. Amino acids are labelled as in Figure 3. Zinc ion, represented as a sphere, is coordinated by the carbonyl oxygen of flavone ring C and D181, H183, D269. Atoms and bonds are coloured and represented as in Figure 3. (C) the opposite view of panel B shows the position of amino acids not visible in the other panel. Images are generated by DiscoveryStudio4.5.

Overall, the three flavones are able to bind to the HDACs by completely inserting their aromatic rings into the active site pocket with multiple contacts to the tubular channel. Similar to the subclass benzamides of HDAC inhibitors, flavones are located in the active site pocket, more in depth than vorinostat belonging to the inhibitor's subclass hydroxamic acids [23]. Indeed, as initially supposed by Bontempo et al. (2007) [9], flavone occupies in depth the catalytic channel of HDACs, binding the cofactor Zn^{2+} (Figures 3 and 4 and Supplementary Video S1). HDACs deacetylate the ϵ -N-acetyl lysines of histones and non-histone targets in the active site channel of binding pocket about 11 Å deep, where the cofactor Zn^{2+} ion is located, by activating bound water for nucleophilic addition and subsequent hydrolysis [23,24]. The alkoxide zinc tetrahedral intermediate, stabilized by enzyme residues, releases the acetate and the lysine residue of target protein as reaction products. The tubular internal cavity about 14 Å deep is located below the active site and has been suggested to be an exit way for the acetate [23]. The first crystallographic structures of the human HDACs complexed with inhibitors support the mechanism of action of HDACi through binding to active site channels and steric hindrance preventing substrate hydrolysis [25]. In this regard, Bontempo et al. (2007) [9] hypothesized that flavone (and its derivatives) may similarly interact with the active site of HDAC occupying the same channel. According to the biochemical and structural characteristics of HDAC enzymes, a prototypical HDACi can be structurally subdivided into three functional regions: a polar tail (such as hydroxamic acid) chelates the catalytic Zn^{2+} ion located deep into the active site tunnel; a hydrophobic cap (aromatic group) is responsible for molecular recognition and selectivity of HDAC type closing the active site gate by interaction with the amino acid residues of the binding pocket rim; lastly, a central linker region places the two functional groups at the correct distance and interacts with the residues of the tunnel wall. Flavones do not structurally resemble canonical HDACi, lacking a true cap, but they can be considered to have a zinc binding group (carbonyl oxygen of ring C) and a linker (ring B). Nowadays, however, the classic inhibitor structure is questionable, because in most cases HDACis are profoundly different and cannot be dissected into the canonical zinc binding-linker-cap structure [26].

The amino acids of HDACs involved in the interaction with flavone, apigenin, luteolin, and vorinostat, are reported in Supplementary Table S3. First of all, we note that all residues involved at least in one of the interactions are conserved in HDAC1 and HDAC2. It is relevant to note that all ligands interact with the cofactor Zn^{2+} of both HDAC proteins. In fact, as already shown in Figures 3 and 4, the atom of carbonyl oxygen of flavone, belonging to the heterocyclic ring C, can coordinate with the active site Zn^{2+} ion. The carbonyl carbon C4 of flavone should mime the carbonyl carbon of the acetyl moiety in the acetylated lysine residue of the substrate. The aromatic

configuration of flavone hinders the nucleophilic attack by a water molecule. The chelation of the zinc ion by flavone differs from the bidentate binding mode proposed for class I HDAC (HDAC1, 2, 3, 8), based on the different structure of vorinostat, which binds the Zn^{2+} ion with two oxygen atoms in the hydroxamic acid group [27]. Flavone binding is possibly strengthened by an aromatic interaction with Tyr303/308 in HDAC1/2. Previous findings on in silico triple mutants indicate that this tyrosine residue, when present together with two phenylalanines, is essential to determine the chelation mode with vorinostat [27]. Our simulations confirm that two conserved phenylalanine residues (Phe150/155 and Phe205/210 in HDAC1/2) are located around the gateway of the binding pocket. Their phenyl groups are orientated in parallel to bind the ring B of flavone with a stacking configuration in both HDACs (Figures 3 and 4). As proposed by Wu et al. (2011) [27], this “sandwich-like” conformation, when the two phenylalanines bind the linker region of vorinostat, blocks the binding pocket entrance and prevents water molecules from entering the channel.

All ligands interact with Gly149/154 and Gly301/306 of HDAC1/2 by van der Waals forces. Although no evidence of a key role is reported for these two amino acids, we note that Gly149/154 is spatially located right at the entrance of the binding pocket between the two conserved phenylalanines (the aforementioned Phe150/155 and Phe205/210), contributing to making the channel wall take its shape. Therefore, the space made available by the absence of a side chain for this glycine is needed to create an appropriate entrance for the substrate, as for the inhibitor flavone. Gly301/306 is located in a stretch of glycine residues (positions 299–302/304–307) of a loop region that, in the same way, generates an internal cavity adjacent to the binding pocket (data not shown).

Moreover, in all ligand-protein complexes with HDAC1/2, there is an interaction with Asp176/181 and His178/183. These two amino acids play an important role, because the coordination of Zn^{2+} is given by Asp176/181, His178/183, and Asp264/269. The latter amino acid interacts with ligands only in some complexes.

The proposed catalytic mechanism for deacetylation assigns also an important role to His140/145, His141/146, and Tyr303/308 [5], in particular with the histidines contributing to the charge-relay system of the active site. It is worth noting that our results show that these amino acids are involved in the interaction with vorinostat as well as with flavones in both HDACs (Supplementary Table S3).

Finally, four residues of HDAC1, i.e., Met30, Leu139, Cys151, and Gly300, such as two residues in HDAC2, i.e., Asp104 and Gln265, are always involved in ligand–protein binding. Although no evidence of a key role is reported, based on their location, they could contribute to shaping the binding pocket.

The dietary flavones apigenin and luteolin showed profiles of interaction similar to that of flavone. Overall, the position of flavones (having direct interactions with amino acids involved in relevant activities) midway between the active site channel and the tubular cavity, and their direct binding with the catalytic Zn^{2+} ion are suitable to prevent the interaction of HDACs with acetylated lysine residues as a substrate.

4. Conclusions

The aim of our work was to verify whether the three flavones, which were the object of our study (flavone, apigenin, luteolin), already known for their inhibitory activity on HDACs, can physically interact with HDAC1 and 2 similar to the known inhibitor vorinostat. Therefore, we used docking simulations for checking the ability of these three molecules to occupy the same binding site. The similar or better binding energy values for flavones suggest that it is possible. In more details, flavones are able to interact with HDAC1 and HDAC2 with energies similar to the known inhibitor vorinostat by occupying the catalytic site and creating interactions with Zn^{2+} ion and amino acids in the binding pocket. The present study contributed to shedding light on the molecular basis of the pharmacological potential of flavones as naturally occurring and no canonical HDACi. These plant secondary metabolites could be an important weapon against several diseases by epigenetic therapy. In the future, new “smart” drugs to fight cancer could have a natural origin and, thanks to the knowledge of their action mechanism, present reduced adverse effects by exerting anti-cancer activities

via epigenetic modulation on responsive cells, such as HDAC inhibition. We would experimentally verify these data to further understand the selectivity of the flavones for the inhibitor effects on the different HDACs. Our findings could stimulate further investigations on these inhibitors by in vitro and in vivo model systems and be a support for the development of more selective and potent therapeutic molecules.

Supplementary Materials: The following are available online at <http://www.mdpi.com/2227-9059/8/12/568/s1>, Supplementary File S1 containing Tables S1–S3 and Figures S1–S10. Supplementary Video S1: 3D view of the catalytic site of HDAC1 with flavone.

Author Contributions: Conceptualization, A.F., L.A., L.D.M. and P.B.; methodology, A.F. and B.S.; software, A.F. and B.S.; validation, A.F., B.S. and L.D.M.; formal analysis, A.F. and B.S.; investigation, A.F., B.S., L.D.M. and P.B.; resources, A.F.; data curation, A.F., B.S. and L.D.M.; writing—original draft preparation, A.F., B.S., L.D.M. and P.B.; writing—review and editing, A.F., B.S., L.D.M. and P.B.; visualization, A.F. and B.S.; supervision, A.F. and L.D.M.; project administration, A.F. All authors have read and agreed to the published version of the manuscript.

Funding: This research was funded by VALERE: Vanvitelli per la Ricerca; Campania Regional Government Technology Platform Lotta alle Patologie Oncologiche: iCURE-B21C17000030007; Campania Regional Government FASE2: IDEAL; MIUR, Proof of Concept-EPICUREPOC01_00043-B64I19000290008.

Acknowledgments: Research activity of A.F. is in the framework of the CNR project NUTR-AGE (FOE-2019, DSB.AD004.271) and ELIXIR-IIB infrastructure. Research infrastructure of L.D.M. was supported by the CNR project “Green & Circular Economy” (GECE, DBA.AD003.139) from the Italian Ministry of University and Research (FOE-2019).

Conflicts of Interest: The authors declare no conflict of interest.

References

1. Lauffer, B.E.L.; Mintzer, R.; Fong, R.; Mukund, S.; Tam, C.; Zilberleyb, I.; Flicke, B.; Ritscher, A.; Fedorowicz, G.; Vallero, R.; et al. Histone deacetylase (HDAC) inhibitor kinetic rate constants correlate with cellular histone acetylation but not transcription and cell viability. *J. Biol. Chem.* **2013**, *288*, 26926–26943. [CrossRef] [PubMed]
2. Miceli, M.; Bontempo, P.; Nebbioso, A.; Altucci, L. Natural compounds in epigenetics: A current view. *Food Chem. Toxicol.* **2014**, *73*, 71–83. [CrossRef] [PubMed]
3. Yoon, S.; Eom, G.H. HDAC and HDAC inhibitor: From cancer to cardiovascular diseases. *Chonnam Med. J.* **2016**, *52*, 1–11. [CrossRef] [PubMed]
4. Yoon, S.; Kang, G.; Eom, G.H. HDAC inhibitors: Therapeutic potential in fibrosis-associated human diseases. *Int. J. Mol. Sci.* **2019**, *20*, 1329. [CrossRef] [PubMed]
5. Seto, E.; Yoshida, M. Erasers of Histone Acetylation: The Histone Deacetylase Enzymes. *Cold. Spring Harb. Perspect. Biol.* **2014**, *6*, a018713. [CrossRef] [PubMed]
6. Singh, P.; Singh, R.; Srikanta, T.; Rath, K. Anticancer potential of the histone deacetylase inhibitor-like effects of flavones, a subclass of polyphenolic compounds: A review. *Mol. Biol. Rep.* **2015**, *42*, 1515–1531. [CrossRef] [PubMed]
7. Richon, V.M. Cancer biology: Mechanism of antitumour action of vorinostat (suberoylanilide hydroxamic acid), a novel histone deacetylase inhibitor. *Br. J. Cancer* **2006**, *95*, S2–S6. [CrossRef]
8. West, A.C.; Johnstone, R.W. New and emerging HDAC inhibitors for cancer treatment. *J. Clin. Investig.* **2014**, *124*, 30–39. [CrossRef]
9. Bontempo, P.; Mita, L.; Miceli, M.; Doto, A.; Nebbioso, A.; De Bellis, F.; Conte, M.; Minichiello, A.; Manzo, F.; Carafa, V.; et al. *Feijoa sellowiana* derived natural Flavone exerts anti-cancer action displaying HDAC inhibitory activities. *Int. J. Biochem. Cell Biol.* **2007**, *39*, 1902–1914. [CrossRef]
10. Bontempo, P.; Rigano, D.; Doto, A.; Formisano, C.; Conte, M.; Nebbioso, A.; Carafa, V.; Caserta, G.; Sica, V.; Molinari, A.M.; et al. *Genista sessilifolia* DC. extracts induce apoptosis across a range of cancer cell lines. *Cell Proliferat.* **2013**, *46*, 183–192. [CrossRef]
11. Magri, A.; Adiletta, G.; Petriccione, M. Evaluation of antioxidant systems and ascorbate-glutathione cycle in *Feijoa* edible flowers at different flowering stages. *Foods* **2020**, *9*, 95. [CrossRef] [PubMed]
12. Zhu, F. Chemical and biological properties of feijoa (*Acca sellowiana*). *Trends Food Sci. Technol.* **2018**, *81*, 121–131. [CrossRef]

13. Pandey, M.; Kaur, P.; Shukla, S.; Abbas, A.; Fu, P.; Gupta, S. Plant flavone apigenin inhibits HDAC and remodels chromatin to induce growth arrest and apoptosis in human prostate cancer cells: In vitro and in vivo study. *Mol. Carcinog.* **2012**, *51*, 952–962. [CrossRef] [PubMed]
14. Attoub, S.; Hassan, A.H.; Vanhoecke, B.; Iratni, R.; Takahashi, T.; Gaben, A.M.; Bracke, M.; Awad, S.; John, A.; Kamalboor, H.A.; et al. Inhibition of cell survival, invasion, tumor growth and histone deacetylase activity by the dietary flavonoid luteolin in human epithelioid cancer cells. *Eur. J. Pharmacol.* **2011**, *651*, 18–25. [CrossRef] [PubMed]
15. Berman, H.M.; Westbrook, J.; Feng, Z.; Gilliland, G.; Bhat, T.N.; Weissig, H.; Shindyalov, I.N.; Bourne, P.E. The Protein Data Bank. *Nucleic Acids Res.* **2000**, *28*, 235–242. [CrossRef] [PubMed]
16. Morris, G.M.; Huey, R.; Lindstrom, W.; Sanner, M.F.; Belew, R.K.; Goodsell, D.S.; Olson, A.J. AutoDock4 and AutoDockTools4: Automated docking with selective receptor flexibility. *J. Comput. Chem.* **2009**, *30*, 2785–2791. [CrossRef]
17. Kim, S.; Thiessen, P.A.; Bolton, E.E.; Chen, J.; Fu, G.; Gindulyte, A.; Han, L.; He, J.; He, S.; Shoemaker, B.A.; et al. PubChem Substance and Compound databases. *Nucleic Acids Res.* **2016**, *44*, D1202–D1213. [CrossRef]
18. Pettersen, E.F.; Goddard, T.D.; Huang, C.C.; Couch, G.S.; Greenblatt, D.M.; Meng, E.C.; Ferrin, T.E. UCSF Chimera—A visualization system for exploratory research and analysis. *J. Comput. Chem.* **2004**, *25*, 1605–1612. [CrossRef]
19. Scafuri, B.; Marabotti, A.; Carbone, V.; Minasi, P.; Dotolo, S.; Facchiano, A. A theoretical study on predicted protein targets of apple polyphenols and possible mechanisms of chemoprevention in colorectal cancer. *Sci. Rep.* **2016**, *6*, 32516. [CrossRef]
20. Scafuri, B.; Varriale, A.; Facchiano, A.; D’Auria, S.; Raggi, M.E.; Marabotti, A. Binding of mycotoxins to proteins involved in neuronal plasticity: A combined in silico/wet investigation. *Sci. Rep.* **2017**, *7*, 15156. [CrossRef]
21. Ganai, S.A.; Farooq, Z.; Banday, S.; Altaf, M. In silico approaches for investigating the binding propensity of apigenin and luteolin against class I HDAC isoforms. *Future Med. Chem.* **2018**, *10*, 1925–1945. [CrossRef] [PubMed]
22. Busch, C.; Burkard, M.; Leischner, C.; Lauer, U.M.; Frank, J.; Venturelli, S. Epigenetic activities of flavonoids in the prevention and treatment of cancer. *Clin. Epigenet.* **2015**, *7*, 64. [CrossRef] [PubMed]
23. Wang, D.F.; Wiest, O.; Helquist, P.; Lan-Hargest, H.Y.; Wiech, N.L. On the function of the 14 Å long internal cavity of histone deacetylase-like protein: Implications for the design of histone deacetylase inhibitors. *J. Med. Chem.* **2004**, *47*, 3409–3417. [CrossRef] [PubMed]
24. Biel, M.; Wascholowski, V.; Giannis, A. Epigenetics—An epicenter of gene regulation: Histones and histone-modifying enzymes. *Angew. Chem. Int. Ed. Engl.* **2005**, *44*, 3186–3216. [CrossRef] [PubMed]
25. Vannini, A.; Volpari, C.; Filocamo, G.; Caroli Casavoli, E.; Brunetti, M.; Renzoni, D.; Chakravarty, P.; Paolini, C.; De Francesco, R.; Gallinari, P.; et al. Crystal structure of a eukaryotic zinc-dependent histone deacetylase, human HDAC8, complexed with a hydroxamic acid inhibitor. *Proc. Natl. Acad. Sci. USA* **2004**, *101*, 15064–15069. [CrossRef] [PubMed]
26. Wang, F.; Wang, C.; Wang, J.; Zou, Y.; Chen, X.; Liu, T.; Li, Y.; Zhao, Y.; Li, Y.; He, B. N^ε-acetyl lysine derivatives with zinc binding groups as novel HDAC inhibitors. *R. Soc. Open Sci.* **2019**, *6*, 190338. [CrossRef]
27. Wu, R.; Lu, Z.; Cao, Z.; Zhang, Y. Zinc Chelation with Hydroxamate in Histone Deacetylases Modulated by Water Access to the Linker Binding Channel. *J. Am. Chem. Soc.* **2011**, *133*, 6110–6113. [CrossRef]

Publisher’s Note: MDPI stays neutral with regard to jurisdictional claims in published maps and institutional affiliations.



© 2020 by the authors. Licensee MDPI, Basel, Switzerland. This article is an open access article distributed under the terms and conditions of the Creative Commons Attribution (CC BY) license (<http://creativecommons.org/licenses/by/4.0/>).



Article

Computationally Assisted Lead Optimization of Novel Potent and Selective MAO-B Inhibitors

Vedanjali Gogineni^{1,2}, Manal A. Nael^{3,4,†}, Narayan D. Chaurasiya^{5,6,†}, Khaled M. Elokely^{3,4}, Christopher R. McCurdy^{1,7}, John M. Rimoldi¹, Stephen J. Cutler^{1,8}, Babu L. Tekwani^{5,6,*} and Francisco León^{1,8,*}

- ¹ Department of BioMolecular Sciences, Division of Medicinal Chemistry, University of Mississippi, Oxford, MS 38677, USA; gogineni@musc.edu (V.G.); cmccurdy@cop.ufl.edu (C.R.M.); jrimoldi@olemiss.edu (J.M.R.); sjcutler@cop.sc.edu (S.J.C.)
 - ² Department of Drug Discovery, Biomedical Sciences and Public Health, College of Pharmacy, Medical University of South Carolina, Charleston, SC 29425, USA
 - ³ Department of Chemistry, Institute for Computational Molecular Science, Temple University, Philadelphia, PA 19122, USA; manal.nael@temple.edu (M.A.N.); kelokely@temple.edu (K.M.E.)
 - ⁴ Department of Pharmaceutical Chemistry, Faculty of Pharmacy, Tanta University, Tanta 31527, Egypt
 - ⁵ Division of Drug Discovery, Southern Research, Birmingham, AL 35205, USA; nchaurasiya@southernresearch.org
 - ⁶ National Center for Natural Products Research, Research Institute of Pharmaceutical Sciences, University of Mississippi, Oxford, MS 38677, USA
 - ⁷ Department of Medicinal Chemistry, College of Pharmacy, University of Florida, Gainesville, FL 32610, USA
 - ⁸ Department of Drug Discovery and Biomedical Sciences, College of Pharmacy, University of South Carolina, Columbia, SC 29208, USA
- * Correspondence: btekwani@southernresearch.org (B.L.T.); jleon@mailbox.sc.edu (F.L.)
† These authors contributed equally to this study.

Citation: Gogineni, V.; Nael, M.A.; Chaurasiya, N.D.; Elokely, K.M.; McCurdy, C.R.; Rimoldi, J.M.; Cutler, S.J.; Tekwani, B.L.; León, F. Computationally Assisted Lead Optimization of Novel Potent and Selective MAO-B Inhibitors.

Biomedicines **2021**, *9*, 1304. <https://doi.org/10.3390/biomedicines9101304>

Academic Editors: Leonardo Caputo, Laura Quintieri and Orazio Nicolotti

Received: 9 August 2021

Accepted: 18 September 2021

Published: 24 September 2021

Publisher's Note: MDPI stays neutral with regard to jurisdictional claims in published maps and institutional affiliations.



Copyright: © 2021 by the authors. Licensee MDPI, Basel, Switzerland. This article is an open access article distributed under the terms and conditions of the Creative Commons Attribution (CC BY) license (<https://creativecommons.org/licenses/by/4.0/>).

Abstract: A series of dietary flavonoid acacetin 7-O-methyl ether derivatives were computationally designed aiming to improve the selectivity and potency profiles against monoamine oxidase (MAO) B. The designed compounds were evaluated for their potential to inhibit human MAO-A and -B. Compounds **1c**, **2c**, **3c**, and **4c** were the most potent with a K_i of 37 to 68 nM against MAO-B. Compounds **1c–4c** displayed more than a thousand-fold selectivity index towards MAO-B compared with MAO-A. Moreover, compounds **1c** and **2c** showed reversible inhibition of MAO-B. These results provide a basis for further studies on the potential application of these modified flavonoids for the treatment of Parkinson's Disease and other neurological disorders.

Keywords: flavonoids; Parkinson's Disease; monoamine oxidases A and B; acacetin; docking

1. Introduction

Parkinson's Disease (PD) is one of the most prevalent neurodegenerative disorders [1], affecting over four million people worldwide. The causes of PD remain unknown. However, the disease is known to arise from interaction between environmental and genetic factors, resulting in progressive degeneration of neurons in the brain. Despite decades of research, the molecular pathways involved in neurodegeneration, the nature of the interaction, and the identity of the factors are poorly understood [2]. PD is characterized by the progressive loss of dopaminergic neurons. Most of the PD cases are sporadic, but rare familial forms have also been recognized. The common pathways underlying the pathogenesis of PD include oxidative stress, mitochondrial quality control, and protein degradation processes. Understanding the possible reasons behind these common processes provides various targets, which are therapeutically relevant to the discovery of disease-modifying treatments [1].

The etiology of PD remains obscure, but oxidative stress is thought to play a significant role in dopaminergic neurotoxicity. At the cellular level, PD is associated with

excessive production of reactive oxygen species (ROS), resulting in metabolic alteration of catecholamine, the mitochondrial electron-transporter chain (METC), or enhancement of the deposition of iron in the substantia nigra pars compacta (SNpc) [3]. Recently, special focus has been directed to the role of oxidative stress in neurological abnormalities, including PD. Excessive production of ROS has been considered to be a significant cause of neuronal death [4]. The most effective pharmacological treatment to date is levodopa–dopamine substitution therapy. Recently, attention has been shifted towards the enzyme monoamine oxidase B (MAO-B) as a secondary drug target in PD [5].

MAO-B is one of the two subtypes of the monoamine oxidases (MAO-A and MAO-B). It is a major monoamine-metabolizing enzyme that is known to oxidize the neurotransmitter dopamine, along with other amines. MAO-B is primarily localized in astrocytes, while MAO-A is largely located in the neurons of the brain [5]. Selective, irreversible MAO-B inhibitors are devoid of the severe side effect called the “cheese effect” resulting from the non-selective MAOs that potentiate the effects of tyramine. Since MAO-B is significantly involved in the degradation of dopamine, it is considered to be a first-line therapy for PD [6]. Selegiline [5], rasagiline [5], and safinamide [7] are the only approved MAO-B inhibitors used in the treatment of PD [5–8]. Selegiline and rasagiline are examples of irreversible MAO-B inhibitors [8], while safinamide is a potent reversible MAO-B inhibitor [6]. Therefore, there is a need to develop novel selective MAO-B inhibitors as PD drugs.

Our previous research on the Central American medicinal plant, *Calea urticifolia*, yielded acacetin, a prominent dietary flavonoid [9,10] as a bioactive compound using bioassay-guided fractionation [9]. Acacetin exhibited good inhibitory activities against MAO-A (0.121 μ M) and -B (0.049 μ M). Later, acacetin 7-*O*-methyl ether proved to be a selective MAO-B inhibitor with a selectivity index (SI) of 505-fold for MAO A/B [11], which inspired further exploration of new MAO-B inhibitors using acacetin 7-*O*-methyl ether as the lead compound. Flavonoids are known for their admirable safety profile with no known notable adverse effects. Flavonoids possess various pharmacological properties, including anticancer, antioxidant, antimicrobial, cardioprotective, anti-inflammatory, and hepatoprotective activity [12].

In the current study, a series of acacetin 7-*O*-methyl ether derivatives were computationally designed using fragment-based drug design [13], synthesized, and evaluated as monoamine oxidase B inhibitors. Furthermore, molecular modeling studies were performed to understand the binding interactions.

2. Materials and Methods

2.1. General

^1H and ^{13}C NMR spectra were obtained using Bruker model AMX 400 and 500 NMR spectrometers operating at 400 and 500 MHz in ^1H and 100 and 125 MHz in ^{13}C , respectively. The chemical shift values were reported from tetramethylsilane (TMS) in parts per million (ppm) using known solvent chemical shifts. Standard pulse sequences were used for DEPT, COSY, HSQC, HMBC, NOESY, and TOCSY. Coupling constants are documented in hertz (Hz). The high-resolution mass spectra (HRMS) were recorded on a Waters Micromass Q-ToF Micro mass spectrometer with a lock spray source. The mass spectra (MS) were recorded on a WATERS ACQUITY Ultra Performance LC with a ZQ detector in ESI mode. If needed, the purity was determined using high-performance liquid chromatography (HPLC). The purity of all the final compounds was greater than 95%. Column chromatography was carried out on Sephadex LH-20 (GE Healthcare, Uppsala, Sweden) and silica gel (70–230 mesh, Merck, Billerica, MA, USA). The fractions from column chromatography were monitored using TLC (silica gel 60 F254, Merck, Billerica, MA, USA). Preparative TLC was carried out with silica gel 60 PF254 + 366 plates (20 × 20 cm, 1 mm thick, Analtech, Newark, DE, USA). Human recombinant monoamine oxidase A and monoamine oxidase B enzymes were obtained from BD Biosciences (Bedford, MA, USA). Kynuramine, clorgyline, deprenyl, acacetin, and DMSO were purchased from Sigma Chemical (St. Louis, MO, USA). All the acacetin 7-*O*-methyl ether analogs were synthesized in the Department of

BioMolecular Sciences, Division of Medicinal Chemistry, School of Pharmacy, University of Mississippi, Oxford, MS, USA.

2.2. Synthesis of Derivatives

2.2.1. Procedure for Preparation of Compounds 1–4

Synthesis of (E)-4-Propyloxy-4',6'-Dimethoxy-2'-Hydroxychalcone (**1a**)

IUPAC.: (E)-1-(2-Hydroxy-4,6-dimethoxyphenyl)-3-(4-propoxyphenyl)prop-2-en-1-one. A mixture of equimolar amounts of 2'-hydroxy-4',6'-dimethoxyacetophenone (300 mg, 1.53 mmol) and 4-*n*-propoxybenzaldehyde (251 mg, 1.53 mmol) was taken in a round-bottomed flask (RBF) and 10 mL of 50% NaOH in ethanol for 16 h at rt. The resulting yellow precipitate was filtered and washed with Hex and CH₂Cl₂ to yield **1a** (342 mg, 65%). ¹H NMR (400 MHz, CDCl₃) δ_H 14.41 (s, C-2'-OH), 7.79 (s br, 2H, H-α and H-β), 7.55 (d, *J* = 8.5 Hz, 1H, H-2 and H-6), 6.91 (d, *J* = 8.5 Hz, 2H, H-3 and H-5), 6.10 (d, *J* = 1.8 Hz, 1H, H-3'), 5.96 (d, *J* = 1.8 Hz, 1H, H-5'), 3.97 (t, *J* = 6.5, 2H, H₂-1'), 3.93 (s, 3H, OCH₃), 3.85 (s, 3H, OCH₃), 1.83 (dt, *J* = 6.5, 7.4 Hz, 2H, H₂-2''), 1.05 (t, *J* = 7.4 Hz, 3H, CH₃-3''). ¹³C NMR (100 MHz, CDCl₃) δ_C 192.6 (C=O), 168.3 (C-2'), 166.0 (C-4'), 162.4 (C-6'), 161.0 (C-4), 142.6 (C-β), 130.1 (C-2 and C-6), 128.1 (C-1), 124.9 (C-α), 114.8 (C-3 and C-5), 106.3 (C-1'), 93.8 (C-3'), 91.2 (C-5'), 69.6 (C-1''), 55.8 (OCH₃), 55.5 (OCH₃), 22.5 (C-2''), 10.5 (C-3''). HRESIMS *m/z* 343.0897 [M+H]⁺ (calcd C₂₀H₂₂O₅ 342.1467).

Synthesis of 5,7-Dimethoxy-4'-Propyloxyflavone (**1b**)

IUPAC.: 5,7-Dimethoxy-2-(4-propoxyphenyl)-4*H*-chromen-4-one. The chalcone **1a** (200 mg, 0.584 mmol) was treated with 3–4 mol% of iodine crystals with a minimal amount of DMSO at 140 °C for 4–6 h. The resulting white precipitate was extracted with CH₂Cl₂ and was removed by filtration. The filtrate was transferred into a separatory funnel where the layers were separated as aqueous and organic. The organic layer was washed with sodium thiosulfate (Na₂S₂O₃), dried with sodium sulfate (Na₂SO₄), and concentrated. The intermediate flavonoid **1b** was then purified in a silica column using 100% CH₂Cl₂, 50:1 CH₂Cl₂-MeOH, 9:1 CH₂Cl₂-MeOH, 1:1 CH₂Cl₂-MeOH, and 100% MeOH (128 mg, 64%). ¹H NMR (400 MHz, CDCl₃) δ_H 7.80 (d, *J* = 8.9 Hz, 2H, H-2' and H-6'), 6.98 (d, *J* = 8.9 Hz, 2H, H-3' and H-5'), 6.59 (s, 1H, H-3), 6.57 (d, *J* = 2.3 Hz, 1H, H-6), 6.37 (d, *J* = 2.3 Hz, 1H, H-8), 3.99 (t, *J* = 6.6 Hz, 2H, H₂-1''), 3.96 (s, OCH₃), 3.91 (s, OCH₃), 1.84 (dt, *J* = 6.5, 7.4 Hz, 2H, H₂-2''), 1.06 (t, *J* = 7.4 Hz, 3H CH₃-3''). ¹³C NMR (100 MHz, CDCl₃) δ_C 177.7 (C-4), 163.9 (C-2), 161.6 (C-5), 160.9 (C-4'), 160.7 (C-9), 159.8 (C-7), 127.5 (C-2' and C-6'), 123.5 (C-1'), 114.8 (C-3' and C-5'), 109.2 (C-10), 107.6 (C-3), 96.0 (C-8), 92.8 (C-6), 69.7 (C-1''), 56.4 (OCH₃), 55.7 (OCH₃), 22.5 (C-2''), 10.5 (C-3''). HRESIMS *m/z* 341.0738 [M+H]⁺ (calcd C₂₀H₂₀O₅ 340.1311).

Synthesis of 7-Methoxy-4'-Propyloxy-5-Hydroxyflavone (**1c**)

IUPAC.: 5-Hydroxy-7-methoxy-2-(4-propoxyphenyl)-4*H*-chromen-4-one. The intermediate **1b** (128 mg, 0.377 mmol) was treated with 1N boron tribromide (189 mg, 0.754 mmol) in the presence of CH₂Cl₂ at rt for 1–3 h. The reactant solution was diluted with 10:1 CH₂Cl₂:MeOH and then washed with brine and water. Na₂SO₄ was added to the solution and left overnight. The solution was then filtered, dried, and concentrated. The flavonoid **1c** was purified in a silica column using 30:1 CH₂Cl₂-MeOH (35 mg, 29%). ¹H NMR (400 MHz, CDCl₃) δ_H 12.83 (s, C-5-OH), 7.82 (d, *J* = 8.9 Hz, 2H, H-2' and H-6'), 7.00 (d, *J* = 8.9 Hz, 2H, H-3' and H-5'), 6.56 (s, 1H, H-3), 6.47 (d, *J* = 2.2 Hz, 1H, H-6), 6.35 (d, *J* = 2.2 Hz, 1H, H-8), 4.00 (t, *J* = 6.6 Hz, 2H, H₂-1''), 3.88 (s, OCH₃), 1.86 (ddd, *J* = 6.6, 7.4 Hz, 2H, H₂-2''), 1.08 (t, *J* = 7.4 Hz, 3H, CH₃-3''). ¹³C NMR (100 MHz, CDCl₃) δ_C 182.4 (C-4), 165.4 (C-7), 164.0 (C-2), 162.2 (C-4'), 162.1 (C-5), 157.6 (C-9), 127.7 (C-2' and C-6'), 123.5 (C-1'), 115.0 (C-3' and C-5'), 105.5 (C-10), 104.2 (C-3), 98.0 (C-8), 92.5 (C-6), 69.8 (C-1''), 55.8 (OCH₃), 22.5 (C-2''), 10.5 (C-3''). HRESIMS *m/z* 327.1038 [M+H]⁺ (calcd C₁₉H₁₈O₅ 326.1154).

Synthesis of (E) 4-Isopropoxy-4',6'-Dimethoxy-2'-Hydroxychalcone (2a)

IUPAC.: (E)-1-(2-Hydroxy-4,6-dimethoxyphenyl)-3-(4-isopropoxyphenyl)prop-2-en-1-one. The procedure for the preparation of the chalcone **2a** is similar to that for the preparation of the chalcone **1a** except for the use of 4-isopropoxybenzaldehyde (251 mg, 1.53 mmol). The chalcone **2a** was purified in a silica column using 4:1 Hex-EtOAc, 3:1 Hex-EtOAc, 4:1 EtOAc-Hex, 100% EtOAc, and 100% MeOH (411 mg, 79%). ¹H NMR (400 MHz, CDCl₃) δ_H 14.43 (s, C-2'-OH), 7.80 (s br, 2H, H-α and H-β), 7.55 (d, *J* = 8.7 Hz, 2H, H-2 and H-6), 6.91 (d, *J* = 8.7 Hz, 2H, H-3 and H-5), 6.12 (d, *J* = 2.3, 1H, H-3'), 5.97 (d, *J* = 2.3, 1H, H-5'), 4.62 (sept, *J* = 6.0 Hz, 1H, H-1''), 3.93 (s, 3H, OCH₃), 3.84 (s, 3H, OCH₃), 1.37 (d, *J* = 6.0 Hz, 6H, CH₃-2'' and CH₃-3''). ¹³C NMR (100 MHz, CDCl₃) δ_C 192.6 (C=O), 168.3 (C-2'), 166.0 (C-4'), 162.4 (C-6'), 159.8 (C-4), 142.6 (C-β), 130.1 (C-2 and C-6), 127.9 (C-1), 124.9 (C-α), 115.9 (C-3 and C-5), 106.4 (C-1'), 93.8 (C-3'), 91.2 (C-5'), 70.0 (C-1''), 55.8 (OCH₃), 55.6 (OCH₃), 22.0 (C-2'' and C-3''). HRESIMS *m/z* 343.0876 [M+H]⁺ (calcd C₂₀H₂₂O₅ 342.1467).

Synthesis of 5,7-Dimethoxy-4'-Isopropoxyflavone (2b)

IUPAC.: 2-(4-Isopropoxyphenyl)-5,7-dimethoxy-4H-chromen-4-one. This procedure is similar to that for the preparation of the intermediate flavonoid **1b**. The intermediate flavonoid **2b** was purified in a silica column using 1:1 Hex-EtOAc, 100% EtOAc, 20:1 EtOAc-MeOH, and 100% MeOH (78 mg, 52%). ¹H NMR (400 MHz, CDCl₃) δ_H 7.78 (d, *J* = 8.9 Hz, 2H, H-2' and H-6'), 6.95 (d, *J* = 8.9, 2H, H-3' and H-5'), 6.56 (s, 1H, H-3), 6.53 (d, *J* = 2.3, 1H, H-6), 6.34 (d, *J* = 2.3, 1H, H-8), 4.62 (sept, *J* = 6.0 Hz, 1H, H-1''), 3.93 (s, 3H, OCH₃), 3.89 (s, 3H, OCH₃), 1.36 (d, *J* = 6.0 Hz, 6H, CH₃-2'' and CH₃-3''). ¹³C NMR (100 MHz, CDCl₃) δ_C 177.6 (C-4), 163.8 (C-2), 160.8 (C-5), 160.7 (C-4'), 160.5 (C-9), 159.8 (C-7), 127.6 (C-2' and C-6'), 123.3 (C-1'), 115.8 (C-3' and C-5'), 109.2 (C-3), 109.2 (C-10), 107.5 (C-3), 96.0 (C-8), 92.8 (C-6), 70.1 (C-1''), 56.4 (OCH₃), 55.7 (OCH₃), 21.9 (C-2'' and C-3''). HRESIMS *m/z* 341.0796 [M+H]⁺ (calcd C₂₀H₂₀O₅ 340.1311).

Synthesis of 7-Methoxy-4'-Isopropoxy-5-Hydroxyflavone (2c)

IUPAC.: 5-Hydroxy-2-(4-isopropoxyphenyl)-7-methoxy-4H-chromen-4-one. This procedure is similar to that for the preparation of the final flavonoid **1c**. The final flavonoid **2c** was purified in a silica column using 7:3 Hex-EtOAc and 1:1 Hex-EtOAc (6 mg, 10%). ¹H NMR (400 MHz, CDCl₃) δ_H 12.83 (s, C-5-OH), 7.83 (d, *J* = 8.9 Hz, 2H, H-2' and H-6'), 6.99 (d, *J* = 8.9 Hz, 2H, H-3' and H-5'), 6.58 (s, 1H, H-3), 6.49 (d, *J* = 2.2 Hz, 1H, H-6), 6.37 (d, *J* = 2.2 Hz, 1H, H-8), 4.66 (sept, *J* = 6.0 Hz, 1H, H-1''), 3.89 (s, 3H, OCH₃), 1.40 (d, *J* = 6.0 Hz, 6H, CH₃-2'' and CH₃-3''). ¹³C NMR (100 MHz, CDCl₃) δ_C 182.4 (C-4), 165.4 (C-7), 164.1 (C-2), 162.2 (C-4'), 161.1 (C-5), 157.3 (C-9), 128.0 (C-2' and C-6'), 123.1 (C-1'), 115.9 (C-3' and C-5'), 105.5 (C-10), 104.2 (C-3), 98.0 (C-8), 92.6 (C-6), 70.2 (C-1''), 55.8 (OCH₃), 21.9 (C-2'' and C-3''). HRESIMS *m/z* 327.1038 [M+H]⁺ (calcd C₁₉H₁₈O₅ 326.1154).

Synthesis of (E) 4-Isobutyloxy-4',6'-Dimethoxy-2'-Hydroxychalcone (3a)

IUPAC.: (E)-1-(2-Hydroxy-4,6-dimethoxyphenyl)-3-(4-isobutoxyphenyl)prop-2-en-1-one. This procedure is similar to that for the preparation of the chalcone **1a** except for the use of 4-isobutoxy benzaldehyde (273 mg, 1.53 mmol). The chalcone **3a** was purified in a silica column using CH₂Cl₂ (436 mg, 80%). ¹H NMR (500 MHz, CDCl₃) δ_H 14.45 (s, C-2'-OH), 7.82 (s br, 2H, H-α and H-β), 7.57 (d, *J* = 8.8 Hz, 2H, H-2 and H-6), 6.94 (d, *J* = 8.8 Hz, 2H, H-3 and H-5), 6.13 (d, *J* = 2.4 Hz, 1H, H-3'), 5.99 (d, *J* = 2.4 Hz, 1H, H-5'), 3.94 (s, 3H, OCH₃), 3.86 (s, 3H, OCH₃), 3.79 (d, *J* = 6.6 Hz, 2H, H-1''), 2.13 (sept, *J* = 6.7 Hz, 1H, H-2''), 1.06 (d, *J* = 6.7 Hz, 6H, CH₃-3'' and CH₃-4''). ¹³C NMR (125 MHz, CDCl₃) δ_C 192.6 (C=O), 168.4 (C-2'), 166.0 (C-4'), 162.4 (C-6'), 161.1 (C-4), 142.6 (C-β), 130.1 (C-2 and C-6), 128.0 (C-1), 124.9 (C-α), 114.9 (C-3 and C-5), 106.4 (C-1'), 93.8 (C-3'), 91.2 (C-5'), 74.5 (C-1''), 55.8 (OCH₃), 55.6 (OCH₃), 28.2 (C-2''), 19.2 (C-3'' and C-4''). HRESIMS *m/z* 357.0610 [M+H]⁺ (calcd C₂₁H₂₄O₅ 356.1624).

Synthesis of 5,7-Dimethoxy-4'-Isobutyloxyflavone (3b)

IUPAC.: 2-(4-Isobutoxyphenyl)-5,7-dimethoxy-4H-chromen-4-one. This procedure is similar to that for the preparation of the intermediate flavonoid **1b**. The intermediate flavonoid **3b** was purified in a silica column using 1:1 Hex-EtOAc, 8:2 EtOAc-Hex, 100% EtOAc, 20:1 EtOAc, and 9:1 EtOAc-MeOH (113 mg, 57%). ¹H NMR (400 MHz, CDCl₃) δ_H 7.73 (d, *J* = 8.6 Hz, 2H, H-2' and H-6'), 6.92 (d, *J* = 8.4 Hz, 2H, H-3' and H-5'), 6.52 (s, 1H, H-3), 6.48 (d, *J* = 1.4 Hz, 1H, H-6), 6.29 (d, *J* = 1.6 Hz, 1H, H-8), 3.89 (s, 3H, OCH₃), 3.85 (s, 3H, OCH₃), 3.73 (d, *J* = 6.5 Hz, 2H, H₂-1''), 2.07 (sept, *J* = 6.7 Hz, 1H, H-2''), 1.00 (d, *J* = 6.7 Hz, 6H, CH₃-3'' and CH₃-4''). ¹³C NMR (100 MHz, CDCl₃) δ_C 177.6 (C-4), 163.8 (C-2), 161.7 (C-5), 160.7 (C-4' and C-9), 159.7 (C-7), 127.4 (C-2' and C-6'), 123.4 (C-1'), 114.8 (C-3' and C-5'), 109.0 (C-10), 107.4 (C-3), 96.0 (C-8), 92.8 (C-6), 74.5 (C-1''), 56.3 (OCH₃), 55.7 (OCH₃), 28.2 (C-2''), 19.2 (C-3'' and C-4''). HRESIMS *m/z* 355.0958 [M+H]⁺ (calcd C₂₁H₂₂O₅ 354.1467).

Synthesis of 7-Methoxy-4'-Isobutyloxy-5-Hydroxyflavone (3c)

IUPAC.: 5-Hydroxy-2-(4-Isobutoxyphenyl)-7-methoxy-4H-chromen-4-one. This procedure is similar to that for the preparation of the final flavonoid **1c**. The final flavonoid **3c** was purified in a silica column using 7:3 EtOAc-Hex and 100% EtOAc (40 mg, 44%). ¹H NMR (400 MHz, CDCl₃) δ_H 12.79 (s, C-5-OH), 7.81 (d, *J* = 8.9 Hz, 2H, H-2' and H-6'), 7.00 (d, *J* = 8.9 Hz, 2H, H-3' and H-5'), 6.56 (s, 1H, H-3), 6.47 (d, *J* = 2.2 Hz, 1H, H-6), 6.36 (d, *J* = 2.2 Hz, 1H, H-8), 3.88 (s, 3H, OCH₃), 3.80 (d, *J* = 6.6 Hz, 2H, H₂-1''), 2.14 (sept, *J* = 6.6 Hz, 1H, CH₃-2''), 1.07 (d, *J* = 6.7 Hz, 6H, CH₃-3'' and CH₃-4''). ¹³C NMR (100 MHz, CDCl₃) δ_C 182.4 (C-4), 165.4 (C-7), 164.1 (C-2), 162.3 (C-4'), 162.1 (C-5), 157.6 (C-9), 127.9 (C-2' and C-6'), 123.1 (C-1'), 114.9 (C-3' and C-5'), 105.5 (C-10), 104.1 (C-3), 98.0 (C-8), 92.5 (C-6), 74.6 (C-1''), 55.7 (OCH₃), 28.2 (C-2''), 19.2 (C-3'' and C-4''). HRESIMS *m/z* 341.0737 [M+H]⁺ (calcd C₂₀H₂₀O₅ 340.1311).

Synthesis of (E) 4-Propargyloxy-4',6'-Dimethoxy-2'-Hydroxychalcone (4a)

IUPAC.: (E)-1-(2-Hydroxy-4,6-dimethoxyphenyl)-3-(4-(prop-2-yn-1-yloxy)phenyl)prop-2-en-1-one. This procedure is similar to that for the preparation of the chalcone **1a** except for the use of 4-(prop-2-ynyloxy)benzaldehyde (245 mg, 1.53 mmol). The chalcone **4a** was purified in a silica column using 100% CH₂Cl₂ (326 mg, 63%). ¹H NMR (500 MHz, CDCl₃) δ_H 14.38 (s, C-2'-OH), 7.84 (d, *J* = 15.6 Hz, 1H, H-β), 7.79 (d, *J* = 15.6 Hz, 1H, H-α), 7.60 (d, *J* = 8.8 Hz, 2H, H-2 and H-6), 7.03 (d, *J* = 8.8 Hz, 2H, H-3 and H-5), 6.14 (d, *J* = 2.3 Hz, 1H, H-3'), 5.99 (d, *J* = 2.3 Hz, 1H, H-5'), 4.76 (d, *J* = 2.4 Hz, 2H, H₂-1''), 3.94 (s, 3H, OCH₃), 3.86 (s, 3H, OCH₃), 2.57 (t, *J* = 2.4 Hz, 1H, H-3''). ¹³C NMR (125 MHz, CDCl₃) δ_C 192.6 (C=O), 168.4 (C-2'), 166.1 (C-4'), 162.5 (C-6'), 159.1 (C-4), 142.1 (C-β), 130.0 (C-2 and C-6), 129.2 (C-1), 125.7 (C-α), 115.3 (C-3 and C-5), 106.4 (C-1'), 93.8 (C-3'), 91.3 (C-5'), 78.1 (C-2''), 75.9 (C-3''), 55.9 (2C, OCH₃, C-1''), 55.6 (OCH₃). HRESIMS *m/z* 339.0599 [M+H]⁺ (calcd C₂₀H₁₈O₅ 338.1154).

Synthesis of 5,7-Dimethoxy-4'-Propargyloxyflavone (4b)

IUPAC.: 5,7-Dimethoxy-2-(4-(prop-2-yn-1-yloxy)phenyl)-4H-chromen-4-one. This procedure is similar to that for the preparation of the intermediate flavonoid **1b**. The intermediate flavonoid **4b** was purified in a silica column using 1:1 Hex-EtOAc, 100% EtOAc, 20:1 EtOAc-MeOH, 9:1 EtOAc-MeOH, 1:1 EtOAc-MeOH, and 100% MeOH (87 mg, 54%). ¹H NMR (400 MHz, CDCl₃) δ_H 7.82 (d, *J* = 8.9 Hz, 2H, H-2' and H-6'), 7.07 (d, *J* = 8.9 Hz, 2H, H-3' and H-5'), 6.58 (s, 1H, H-3), 6.54 (d, *J* = 2.3 Hz, 1H, H-6), 6.36 (d, *J* = 2.3 Hz, 1H, H-8), 4.76 (d, *J* = 2.4 Hz, 2H, H₂-1''), 3.94 (s, 3H, OCH₃), 3.90 (s, 3H, OCH₃), 2.57 (t, *J* = 2.4 Hz, 1H, H-3''). ¹³C NMR (100 MHz, CDCl₃) δ_C 177.6 (C-4), 163.9 (C-2), 160.9 (C-5), 160.4 (C-4'), 159.8 (C-9), 159.8 (C-7), 127.5 (C-2' and C-6'), 124.7 (C-1'), 115.2 (C-3' and C-5'), 109.2 (C-10), 107.9 (C-3), 96.1 (C-8), 92.8 (C-6), 77.9 (C-2''), 76.1 (C-3''), 56.4 (C-1''), 55.9 (OCH₃), 55.7 (OCH₃). HRESIMS *m/z* 337.0495 [M+H]⁺ (calcd C₂₀H₁₆O₅ 336.0998).

Synthesis of 7-Methoxy, 4'-Propargyloxy-5-Hydroxyflavone (4c)

IUPAC.: 5-Hydroxy-7-methoxy-2-(4-(prop-2-yn-1-yloxy)phenyl)-4H-chromen-4-one. This procedure is similar to that for the preparation of the final flavonoid 1c. The final flavonoid 4c was purified in a silica column with 7:3 Hex-EtOAc, 1:1 Hex-EtOAc, 100% EtOAc, 20:1 EtOAc-MeOH, and 9:1 EtOAc-MeOH (14 mg, 28%). ¹H NMR (400 MHz, CDCl₃) δ_H 12.79 (s, C-5-OH), 7.88 (d, *J* = 8.9 Hz, 2H, H-2' and H-6'), 7.12 (d, *J* = 8.9 Hz, 2H, H-3' and H-5'), 6.60 (s, 1H, H-3), 6.50 (d, *J* = 2.2 Hz, 1H, H-6), 6.39 (d, *J* = 2.2 Hz, 1H, H-8), 4.80 (d, *J* = 2.3 Hz, 2H, H₂-1''), 3.90 (s, 3H, OCH₃), 2.59 (t, *J* = 2.3 Hz, 1H, H-3''). ¹³C NMR (100 MHz, CDCl₃) δ_C 182.4 (C-4), 165.5 (C-7), 163.8 (C-2), 162.2 (C-4'), 160.4 (C-5), 157.7 (C-9), 128.0 (C-2' and C-6'), 124.4 (C-1'), 115.4 (C-3' and C-5'), 105.6 (C-10), 104.6 (C-3), 98.1 (C-8), 92.6 (C-6), 77.7 (C-2''), 76.2 (C-3''), 55.9 (C-1''), 55.8 (OCH₃). HRESIMS *m/z* 323.0767 [M+H]⁺ (calcd C₁₉H₁₄O₅ 322.0841).

2.2.2. Procedure for Preparation of Compounds 5

Synthesis of 4-(Cyclopropyl Methoxy)Benzaldehyde (Compound IV)

IUPAC.: 4-(Cyclopropylmethoxy)benzaldehyde. (Bromomethyl)cyclopropane (400 mg, 2.96 mmol) was added to 4-hydroxy benzaldehyde (724 mg, 5.92 mmol) and was dissolved in 15 mL of acetone and potassium carbonate (1.6 g, 11.9 mmol). The mixture was then refluxed for 36 h, then diluted with EtOAc and washed with water. This compound IV was purified in a silica column using 95:5 Hex-EtOAc (380 mg, 73%). ¹H NMR (400 MHz, CDCl₃) δ_H 9.82 (s, 1H, CHO), 7.76 (d, *J* = 8.8 Hz, 2H, H-2 and H-6), 6.94 (d, *J* = 8.8 Hz, 2H, H-3 and H-5), 3.84 (dd, *J* = 8.1, 10.9 Hz, 2H, H₂-1'), 1.27–1.21 (m, 1H, H-2'), 0.64–0.61 (m, 2H, H-3'a and H-4'a), 0.34–0.32 (m, 2H, H-3'b and H-4'b). ¹³C NMR (100 MHz, CDCl₃) δ_C 190.7 (CHO), 164.0 (C-4), 131.9 (C-2 and C-6), 129.8 (C-1), 114.8 (C-3 and C-5), 73.0 (C-1'), 10.0 (C-2'), 3.2 (C-3' and C-4').

Synthesis of (E) 4-(Cyclopropyl Methoxy)-4',6'-Dimethoxy-2'-Hydroxychalcone (5a)

IUPAC.: (E)-3-(4-(Cyclopropylmethoxy)phenyl)-1-(2-hydroxy-4,6-dimethoxyphenyl)prop-2-en-1-one. This procedure is similar to that for the preparation of the chalcone 1a except for the use of 4-(Cyclopropylmethoxy)benzaldehyde (compound IV) (270 mg, 1.53 mmol). The chalcone 5a was purified in a silica column with 4:1 CH₂Cl₂-Hex, 100% CH₂Cl₂, 20:1 CH₂Cl₂-MeOH, and 9:1 CH₂Cl₂-MeOH (287 mg, 53%). ¹H NMR (400 MHz, CDCl₃) δ_H 14.42 (s, C-2'-OH), 7.84 (s, br, 2H, H-α and H-β), 7.55 (d, *J* = 8.7 Hz, 2H, H-2 and H-6), 6.93 (d, *J* = 8.7 Hz, 2H, H-3 and H-5), 6.11 (d, *J* = 2.3 Hz, 1H, H-3'), 5.97 (d, *J* = 2.3 Hz, 1H, H-5'), 3.86 (s, 2H, H₂-1''), 3.92 (s, 3H, OCH₃), 3.84 (s, 3H, OCH₃), 1.31–1.27 (m, 1H, H-2''), 0.67 (dd, *J* = 4.9, 12.9 Hz, 2H, H-3''a and H-4''a), 0.38 (dd, *J* = 4.9, 10.3 Hz, 2H, H-3''b and H-4''b). ¹³C NMR (100 MHz, CDCl₃) δ_C 192.6 (C=O), 168.3 (C-2'), 166.0 (C-4'), 162.4 (C-6'), 160.8 (C-4), 142.5 (C-β), 130.1 (C-2 and C-6), 128.2 (C-1), 125.0 (C-α), 114.9 (C-3 and C-5), 106.3 (C-1'), 93.8 (C-3'), 91.2 (C-5'), 72.9 (C-1''), 55.8 (OCH₃), 55.5 (OCH₃), 10.2 (C-2''), 3.2 (C-3'' and C-4''). HRESIMS *m/z* 355.0575 [M+H]⁺ (calcd C₂₁H₂₂O₅ 354.1467).

Synthesis of 5,7-Dimethoxy-4'(Cyclopropyl Methoxy)Flavone (5b)

IUPAC.: 2-(4-(Cyclopropylmethoxy)phenyl)-5,7-dimethoxy-4H-chromen-4-one. This procedure is similar to that for the preparation of the intermediate flavonoid 1b. The intermediate flavonoid 5b was purified in a silica column using 1:1 Hex-EtOAc, 100% EtOAc, 20:1 EtOAc-MeOH, 9:1 EtOAc-MeOH, and 1:1 EtOAc-MeOH (120 mg, 78%). ¹H NMR (400 MHz, CDCl₃) δ_H 7.78 (d, *J* = 9.0 Hz, 2H, H-2' and H-6'), 6.97 (d, *J* = 9.0 Hz, 2H, H-3' and H-5'), 6.56 (s, 1H, H-3), 6.53 (d, *J* = 2.3 Hz, 1H, H-6), 6.34 (d, *J* = 2.3 Hz, 1H, H-8), 3.93 (s, 3H, OCH₃), 3.89 (s, 3H, OCH₃), 3.85 (d, *J* = 6.9 Hz, 2H, H₂-1''), 1.25 (t, *J* = 7.2, 1H, H-2''), 0.66 (dd, *J* = 4.8, 12.9 Hz, 2H, H-3''a and H-4''a), 0.37 (dd, *J* = 4.8, 10.6 Hz, 2H, H-3''b and H-4''b). ¹³C NMR (100 MHz, CDCl₃) δ_C 177.6 (C-4), 163.9 (C-2), 161.5 (C-5), 160.8 (C-4'), 160.7 (C-9), 159.8 (C-7), 127.5 (C-2' and C-6'), 123.6 (C-1'), 114.9 (C-3' and C-5'), 109.1 (C-10), 107.5 (C-3), 96.0 (C-8), 92.8 (C-6), 72.9 (C-1''), 56.4 (OCH₃), 55.7 (OCH₃), 10.1 (C-2''), 3.2 (C-3'' and C-4''). HRESIMS *m/z* 353.0805 [M+H]⁺ (calcd C₂₁H₂₀O₅ 352.1311).

2.2.3. Procedure for Preparation of Compounds 6–8

Synthesis of (E) 4-Bromo-4',6'-Dimethoxy-2'-Hydroxychalcone (6a)

IUPAC.: (E)-3-(4-Bromophenyl)-1-(2-hydroxy-4,6-dimethoxyphenyl)prop-2-en-1-one. A mixture of equimolar amounts of 2'-hydroxy-4',6'-dimethoxyacetophenone (300 mg, 1.53 mmol) and 4-bromobenzaldehyde (285 mg, 1.53 mmol) was taken in a RBF and 10 mL of 50% NaOH in ethanol was added and left for 16 h at rt. The resulting yellow precipitate was then suction filtered and washed with hexanes and CH₂Cl₂. The brominated chalcone **6a** was then purified in a silica column using 10% EtOAc and hexanes (361 mg, 65%). ¹H NMR (400 MHz, CDCl₃) δ_H 14.23 (s, C-2'-OH), 7.89 (d, *J* = 15.6 Hz, 1H, H-β), 7.71 (d, *J* = 15.6 Hz, 1H, H-α), 7.55 (d, *J* = 8.4 Hz, 2H, H-2 and H-6), 7.47 (d, *J* = 8.4 Hz, 2H, H-3 and H-5), 6.13 (d, *J* = 2.2 Hz, 1H, H-3'), 5.98 (d, *J* = 2.2 Hz, 1H, H-5'), 3.93 (s, 3H, OCH₃), 3.86 (s, 3H, OCH₃). ¹³C NMR (100 MHz, CDCl₃) δ_C 192.3 (C=O), 168.4 (C-4'), 166.4 (C-6'), 162.5 (C-2'), 140.8 (C-β), 134.5 (C-1), 132.1 (C-3 and C-5), 129.7 (C-2 and C-6), 128.1 (C-α), 124.2 (C-4), 106.3 (C-1'), 93.8 (C-3'), 91.3 (C-5'), 55.9 (OCH₃), 55.6 (OCH₃). HRESIMS *m/z* 363.1418 [M+H]⁺ (calcd C₁₇H₁₅BrO₄ 362.0154).

Synthesis of 5,7-Dimethoxy-4'-Bromoflavone (6b)

IUPAC.: 2-(4-Bromophenyl)-5,7-dimethoxy-4H-chromen-4-one. The brominated chalcone (**6a**) (200 mg, 0.551 mmol) was treated with 3–4 mol% of iodine crystals with a minimal amount of DMSO at 140 °C for 4–6 h. The resulting white precipitate was extracted with CH₂Cl₂ and was removed by filtration. The filtrate was transferred into a separatory funnel, where the layers were separated as aqueous and organic. The organic layer was washed with Na₂S₂O₃, dried with Na₂SO₄, and concentrated. The intermediate flavonoid **6b** was purified in a silica column with 1:1 Hex-EtOAc, 3:2 EtOAc-Hex, 4:1 EtOAc-Hex, and 9:1 EtOAc-Hex (134 mg, 67%). ¹H NMR (400 MHz, CDCl₃) δ_H 7.72 (d, *J* = 8.7 Hz, 2H, H-3' and H-5'), 7.62 (d, *J* = 8.7 Hz, 2H, H-2' and H-6'), 6.64 (s, 1H, H-3), 6.55 (d, *J* = 2.3 Hz, 1H, H-6), 6.37 (d, *J* = 2.3 Hz, 1H, H-8), 3.95 (s, 3H, OCH₃), 3.91 (s, 3H, OCH₃). ¹³C NMR (100 MHz, CDCl₃) δ_C 177.3 (C-4), 164.2 (C-2), 160.9 (C-5), 159.8 (C-9), 159.5 (C-7), 132.2 (C-3' and C-5'), 130.4 (C-1'), 127.3 (C-2' and C-6'), 125.8 (C-4'), 109.2 (C-10 and C-3), 96.3 (C-8), 92.8 (C-6), 56.4 (OCH₃), 55.8 (OCH₃). HRESIMS *m/z* 361.1324 [M+H]⁺ (calcd C₁₇H₁₃BrO₄ 359.9997).

Synthesis of 5,7-Dimethoxy-4'-Aminopropylflavone (6c)

IUPAC.: 5,7-Dimethoxy-2-(4-(propylamino)phenyl)-4H-chromen-4-one. Sodium *tert*-butoxide (17 mg, 0.18 mmol), tris(dibenzylideneacetone)dipalladium (11 mg, 0.012 mmol), and 1,1'-binaphthalene-2,2'-diylbis(diphenylphosphine) (8 mg, 0.012 mmol) were dissolved in 5 mL of toluene. To this, the brominated intermediate flavonoid **6b** (50 mg, 0.138 mmol) and propylamine (11 mg, 0.18 mmol) were added dropwise with stirring at rt, and the mixture was refluxed at 80 °C for 48 h. The nitrogenated intermediate flavonoid was purified in a silica column using 7:3 EtOAc-Hex, 9:1 EtOAc-Hex, 100% EtOAc, and 9:1 EtOAc-MeOH (24 mg, 52%). ¹H NMR (500 MHz, CDCl₃) δ_H 7.67 (d, *J* = 10.9 Hz, 2H, H-2' and H-6'), 6.61 (d, *J* = 10.9 Hz, 2H, H-3' and H-5'), 6.52 (d, *J* = 2.6 Hz, 1H, H-6), 6.50 (s, 1H, H-3), 6.33 (d, *J* = 2.5 Hz, 1H, H-8), 3.92 (s, 3H, OCH₃), 3.88 (s, 3H, OCH₃), 3.13 (t, *J* = 9.0 Hz, 2H, H₂-1''), 1.66 (ddd, *J* = 9.2, 18.2, 9.0 Hz, 2H, H₂-2''), 1.00 (t, *J* = 9.2 Hz, 3H, CH₃-3''). ¹³C NMR (125 MHz, CDCl₃) δ_C 177.8 (C-4), 163.6 (C-2), 161.6 (C-5), 160.7 (C-4'), 159.7 (C-9), 150.9 (C-7), 127.5 (C-2' and C-6'), 119.0 (C-1'), 112.1 (C-3' and C-5'), 109.2 (C-10), 105.8 (C-3), 95.8 (C-8), 92.8 (C-6), 56.3 (OCH₃), 55.7 (OCH₃), 45.2 (C-1''), 22.5 (C-2''), 11.5 (C-3''). HRESIMS *m/z* 340.2991 [M+H]⁺ (calcd C₂₀H₂₁NO₄ 339.1471).

Synthesis of 7-Methoxy-4'-Aminopropyl-5-Hydroxyflavone (6d)

IUPAC.: 5-Hydroxy-7-methoxy-2-(4-(propylamino)phenyl)-4H-chromen-4-one. The nitrogenated intermediate flavonoid **6c** (15 mg, 0.044 mmol) was treated with double the moles of 1N boron tribromide (22 mg, 0.088 mmol) in the presence of CH₂Cl₂ at rt for 1–3 h. The reactant solution was diluted with 10:1 CH₂Cl₂:MeOH and then washed with brine and water. Na₂SO₄ was added to the solution and left overnight. The solution was

then filtered into a RBF, dried, and concentrated. The final compound **6d** was purified in a silica column using 1:1 Hex-EtOAc (11 mg, 77%). ¹H NMR (500 MHz, CDCl₃) δ_H 12.90 (s, C-5-OH), 7.65 (d, *J* = 8.8 Hz, 2H, H-2' and H-6'), 6.58 (d, *J* = 8.7 Hz, 2H, H-3' and H-5'), 6.43 (s, 1H, H-3), 6.39 (d, *J* = 2.2 Hz, 1H, H-6), 6.27 (d, *J* = 2.2 Hz, 1H, H-8), 3.80 (s, 3H, OCH₃), 3.10 (t, *J* = 7.2 Hz, 2H, H₂-1''), 1.62 (ddd, *J* = 7.4, 7.2, 7.3 Hz, 2H, H₂-2''), 0.96 (t, *J* = 7.4 Hz, 3H, CH₃-3''). ¹³C NMR (125 MHz, CDCl₃) δ_C 182.3 (C-4), 165.2 (C-7), 164.4 (C-2), 162.1 (C-5 and C-4'), 157.6 (C-9), 128.0 (C-2' and C-6'), 127.5 (C-1'), 114.0 (C-3' and C-5'), 105.4 (C-10), 103.0 (C-3), 97.9 (C-8), 92.5 (C-6), 55.8 (OCH₃), 29.7 (C-1''), 22.1 (C-2''), 11.5 (C-3''). HRESIMS *m/z* 326.2691 [M+H]⁺ (calcd C₁₉H₁₉NO₄ 325.1314).

Synthesis of 5,7-Dimethoxy-4'-Aminoisopropylflavone (7c)

IUPAC.: 2-(4-(Isopropylamino)phenyl)-5,7-dimethoxy-4H-chromen-4-one. This procedure is similar to that for the preparation of the intermediate flavonoid **6c** except for the use of isopropylamine (11 mg, 0.18 mmol). The intermediate flavonoid **7c** was purified in a silica column using 9:1 EtOAc-Hex (37 mg, 79%). ¹H NMR (400 MHz, CDCl₃) 7.65 (d, *J* = 8.7 Hz, 2H, H-2' and H-6'), 6.58 (d, *J* = 8.7 Hz, 2H, H-3' and H-5'), 6.50 (d, *J* = 2.2 Hz, 1H, H-6), 6.48 (s, 1H, H-3), 6.31 (d, *J* = 2.2 Hz, 1H, H-8), 3.90 (s, 3H, OCH₃), 3.86 (s, 3H, OCH₃), 3.67 (sept, *J* = 6.4 Hz, 1H, H-1''), 1.22 (d, *J* = 6.4 Hz, 6H, H-2'' and H-3''). ¹³C NMR (100 MHz, CDCl₃) δ_C 177.7 (C-4), 163.6 (C-2), 161.5 (C-5), 160.7 (C-4'), 159.7 (C-9), 150.0 (C-7), 127.5 (C-2' and C-6'), 118.8 (C-1'), 112.5 (C-3' and C-5'), 109.1 (C-10), 105.7 (C-3), 95.8 (C-8), 92.8 (C-6), 56.3 (OCH₃), 55.6 (OCH₃), 43.9 (C-1''), 22.7 (C-2'' and C-3''). HRESIMS *m/z* 340.3005 [M+H]⁺ (calcd C₂₀H₂₁NO₄ 339.1471).

Synthesis of 7-Methoxy-4'-Aminoisopropyl-5-Hydroxyflavone (7d)

IUPAC.: 5-Hydroxy-2-(4-(Isopropylamino)phenyl)-7-methoxy-4H-chromen-4-one. This procedure is similar to that for the preparation of the final compound **6d**. The final compound **7d** was purified in a silica column with 9:1 Hex-EtOAc (16 mg, 83%). ¹H NMR (500 MHz, CDCl₃) 13.00 (s, C-5-OH), 7.74 (d, *J* = 8.9 Hz, 2H, H-2' and H-6'), 6.64 (d, *J* = 8.9 Hz, 2H, H-3' and H-5'), 6.52 (s, 1H, H-3), 6.48 (d, *J* = 2.3 Hz, 1H, H-6), 6.37 (d, *J* = 2.3 Hz, 1H, H-8), 3.90 (s, 3H, OCH₃), 3.75 (sept, *J* = 6.3 Hz, 1H, H-1''), 1.29 (d, *J* = 6.3 Hz, 6H, CH₃-2'' and CH₃-3''). ¹³C NMR (125 MHz, CDCl₃) δ_C 182.4 (C-4), 165.1 (C-7), 164.9 (C-2), 162.1 (C-4'), 157.6 (C-5), 150.5 (C-9), 128.1 (C-2' and C-6'), 118.6 (C-1'), 112.6 (C-3' and C-5'), 105.5 (C-10), 102.4 (C-3), 97.8 (C-8), 92.5 (C-6), 55.7 (OCH₃), 44.1 (C-1''), 22.8 (C-2'' and C-3''). HRESIMS *m/z* 326.2691 [M+H]⁺ (calcd C₁₉H₁₉NO₄ 325.1314).

Synthesis of 5,7-Dimethoxy-4'-(Cyclopropyl Methylamino)Flavone (8c)

IUPAC.: 2-(4-((Cyclopropylmethyl)amino)phenyl)-5,7-dimethoxy-4H-chromen-4-one. This procedure is similar to that for the preparation of the intermediate flavonoid **6c** except for the use of (aminomethyl)cyclopropane (13 mg, 0.18 mmol). The intermediate flavonoid **8c** was purified in a silica column using 7:3 EtOAc-Hex, 100% EtOAc, 10:1 EtOAc-MeOH, and 100% MeOH (40 mg, 83%). ¹H NMR (500 MHz, CDCl₃) 7.66 (d, *J* = 8.5 Hz, 2H, H-2' and H-6'), 6.66 (d, *J* = 8.7 Hz, 2H, H-3' and H-5'), 6.56 (s, 1H, H-3), 6.41 (d, *J* = 2.2 Hz, 1H, H-6), 6.38 (d, *J* = 2.2 Hz, 1H, H-8), 3.97 (s, 3H, OCH₃), 3.92 (s, 3H, OCH₃), 3.05 (d, *J* = 6.9 Hz, 2H, H₂-1''), 1.12 (m, 1H, H-2''), 0.61 (dd, *J* = 6.0, 13.6 Hz, 2H, H-3''a and H-4''a), 0.30 (dd, *J* = 5.5, 10.5 Hz, 2H, H-3''b and H-4''b). ¹³C NMR (125 MHz, CDCl₃) δ_C 177.8 (C-4), 163.7 (C-2), 161.5 (C-5), 160.8 (C-4'), 160.9 (C-9), 159.8 (C-7), 127.5 (C-2' and C-6'), 119.3 (C-1'), 112.3 (C-3' and C-5'), 109.3 (C-10), 106.0 (C-3), 96.3 (C-8), 92.8 (C-6), 56.5 (OCH₃), 55.7 (OCH₃), 48.5 (C-1''), 10.7 (C-2''), 3.6 (C-3'' and C-4''). HRESIMS *m/z* 352.2586 [M+H]⁺ (calcd C₂₁H₂₁NO₄ 351.1471).

Synthesis of 7-Methoxy-4'-(Cyclopropyl Methylamino)-5-Hydroxyflavone (8d)

2-(4-((Cyclopropylmethyl)amino)phenyl)-5-hydroxy-7-methoxy-4H-chromen-4-one. This procedure is similar to that for the preparation of the final compound **6d**. The final compound **8d** was purified in a sephadex column with 1:1 Hex-EtOAc (2 mg, 7%). ¹H NMR (500 MHz,

CDCl₃) 13.00 (s, C-5-OH), 7.75 (d, $J = 8.8$ Hz, 2H, H-2' and H-6'), 6.67 (d, $J = 8.8$ Hz, 2H, H-3' and H-5'), 6.53 (s, 1H, H-3), 6.48 (d, $J = 2.1$ Hz, 1H, H-6), 6.37 (d, $J = 2.1$ Hz, 1H, H-8), 3.90 (s, 3H, OCH₃), 3.07 (d, $J = 6.9$ Hz, 2H, H₂-1''), 1.14 (m, 1H, H-2''), 0.63 (dd, $J = 5.9, 13.0$ Hz, 2H, H-3''a and H-4''a), 0.31 (dd, $J = 4.9, 9.9$ Hz, 2H, H-3''b and H-4''b). ¹³C NMR (125 MHz, CDCl₃) δ_C 182.4 (C-4), 165.1 (C-7), 164.9 (C-2), 162.1 (C-4'), 157.6 (C-5), 151.3 (C-9), 128.1 (C-2' and C-6'), 118.9 (C-1'), 112.3 (C-3' and C-5'), 105.5 (C-10), 102.5 (C-3), 97.8 (C-8), 92.5 (C-6), 55.7 (OCH₃), 48.4 (C-1''), 10.7 (C-2''), 3.6 (C-3'' and C-4''). HRESIMS m/z 338.2880 [M+H]⁺ (calcd C₂₀H₁₉NO₄ 337.1314).

2.3. Evaluation of Pan Assay Interference Compounds (PAINS)

All the designed MAO-B inhibitors were analyzed per the recently published editorial [14] using the False Positive Remover [15] and the ZINC Pattern Identifier [16]. All compounds passed the filter and were not reported as covalent inhibitors or potential PAINS by any of these algorithms.

2.4. Monoamine Oxidase Inhibition Assay and Determination of IC₅₀ Values for Synthesized Compounds

To investigate the inhibitory effect of the acacetin 7-*O*-methyl ether analogs on human recombinant MAO-A and MAO-B, the kynuramine oxidation deamination assay was performed in 384-well plates as previously reported, with minor modifications [17]. A fixed single concentration of kynuramine substrate and varying concentrations of the test inhibitor were used to determine the IC₅₀ values. The kynuramine concentrations for MAO-A and -B were 80 μM and 50 μM, respectively. These concentrations of kynuramine were twice the apparent K_M value for substrate binding [9,18]. The acacetin 7-*O*-methyl ether analogs were tested at the concentrations ranging from 0.001 μM to 100 μM for MAO-A and -B inhibition assays. Enzymatic reactions were performed in 50 μL of the assay mixture containing 0.1 M potassium phosphate buffer, pH 7.4. The inhibitors and acacetin 7-*O*-methyl ether analogs were dissolved in DMSO, diluted in the buffer solution, and pre-incubated at 37 °C for 10 min (the final concentration of DMSO was <1.0%). Reactions were initiated by the addition of 12.50 μL of MAO-A (to 5 μg/mL) or -B (to 10 μg/mL). The plate was incubated for 20 min at 37 °C, and the enzymatic reaction was terminated by the addition of 18.8 μL of 2N NaOH. Formation of the enzyme product, 4-hydroxyquinoline, was measured fluorometrically using a SpectraMax M5 fluorescence plate reader (Molecular Devices, Sunnyvale, CA, USA) with excitation (320 nm) and emission (380 nm) wavelengths and the Soft Max Pro program. The inhibition effects of enzyme activity were calculated as percent of product formation compared to the corresponding control (enzyme–substrate reaction) without inhibitors. Controls included the assays where the enzyme or the substrate was added after terminating the reaction to determine the interference with the fluorescence measurements. The IC₅₀ values for MAO-A and -B inhibition were calculated from the concentration-dependent inhibition curves using XLFit[®] software.

The enzyme assay was performed at a fixed concentration of the substrate kynuramine (80 μM for MAO-A and 50 μM for MAO-B) and varying concentrations of the inhibitor /test analogs (0.01 μM to 100 μM) for MAO-A and (0.01 μM to 100 μM) for MAO-B. The dose–response curves were generated using Microsoft[®] Excel and the IC₅₀ values were calculated using XLfit software [9].

2.5. Enzyme Kinetics, Mechanism Studies, Analysis of Reversibility, and Binding Assays of Acacetin 7-*O*-Methyl Ether Analogs

For determination of the binding affinity of the inhibitor (*K_i*) with MAO-B, the enzyme assays were carried out at different concentrations of kynuramine substrate (1.90 μM to 500 μM) and varying concentrations of the test compound. Acacetin 7-*O*-methyl ether analogs: **1c**, **2c**, **3c**, and **4c** were tested at 0.015–0.500 μM for MAO-B to determine the *K_m* and *V_{max}* values of the enzymes in the presence of the inhibitor. The controls without inhibitor were also run simultaneously. Three sets of assays were performed at varying

concentrations of the substrate for each experiment: one control without inhibitor and the others at two fixed concentrations of the inhibitor. The data were analyzed by double reciprocal Lineweaver–Burk plots to determine K_i (i.e., inhibition/binding affinity) values and the kinetic data, namely K_m , V_{max} , and K_i values, were computed by SigmaPlot 12 [9].

Most of the inhibitors produce inhibition of the target enzyme activity through formation of an enzyme–inhibitor complex. Formation of the enzyme–inhibitor complex may be accelerated in the presence of a high concentration of the inhibitor. The reversibility/irreversibility of binding of acacetin 7-*O*-methyl ether analogs with MAO-B was determined from the formation of the complex by incubating the enzyme with a high concentration of the inhibitor followed by extensive equilibrium-dialysis of the enzyme–inhibitor complex. Recovery of the catalytic activity of the enzyme was determined by assay of the enzyme activity before and after equilibrium-dialysis. MAO-B (0.2 mg/mL protein) enzyme was incubated with each analog, namely acacetin (0.5 μ M), **1c** (1.5 μ M), **2c** (1.5 μ M), **3c** (1.5 μ M), **4c** (1.5 μ M), and deprenyl (0.5 μ M), in a total volume of 1 mL of potassium phosphate buffer (100 mM, pH 7.4). After 20 min of incubation at 37 °C, the reaction was stopped by chilling the tubes in the ice bath. All the samples were dialyzed against potassium phosphate buffer (25 mM; pH 7.4) at 4 °C for 14–18 h (with three buffer changes). The control enzyme (without inhibitor) was also run simultaneously using the same procedure and the activity of the enzyme was determined before and after the dialysis.

To analyze if the nature of MAO-B binding to the inhibitor was time-dependent, the enzyme was pre-incubated for different time periods (0–15 min) with the inhibitor concentrations, which exhibited approximately 70–80% inhibition. The inhibitor concentrations used to test time-dependent inhibition were acacetin (0.080 μ M), **1c** (0.100 μ M), **2c** (0.300 μ M), **3c** (0.300 μ M), **4c** (0.400 μ M), and deprenyl (0.080 μ M) with MAO-B (12.5 μ g/mL). The controls, without inhibitors, were also run simultaneously. Activities of the enzyme were determined as described above, and the percentage of the remaining enzyme activity was plotted against the pre-incubation time to determine time-dependent inhibition.

2.6. Molecular Modeling Studies

The crystal structures of MAO-A (PDB ID: 2Z5Y with an atomic resolution of 2.17 Å) and MAO-B (PDB ID: 4A79 with an atomic resolution of 1.89 Å) were downloaded from the protein databank (www.rcsb.org, accessed on 12 January 2017). The protein structural files were prepared using the protein preparation wizard of Schrödinger suite [19]. Standard procedures were followed for protein preparation through assigning bond orders, adding hydrogens and removing original ones, creating zero-order bonds to metals, filling in the missing side chains, and deleting waters beyond 5 Å from the ligand. The ionization states were generated at pH 7.4 using Epik [20–22]. The next step was sampling water orientations and checking for possible protonation and tautomerization states at pH 7.4. Water molecules that did not display at least two hydrogen bonds with no-water residues were deleted. Finally, the structure was relaxed to remove all atomic clashes using OPLS3 force field [23].

The receptor grid was generated using Glide [24–27]. The binding pocket was identified by the ligand coordinates. Because of the importance of the FAD cofactor in directing the right pose in the substrate binding pocket [28–30], it was kept during the construction of the docking grids. The dimensions of the docking grid of MAO-A are: a grid center of $-40.89 \times -26.66 \times -14.85$, an inner box of $10 \times 10 \times 10$, and an outer box of $22.59 \times 22.59 \times 22.59$ (Å). The dimensions of the MAO-B grid are: a grid center of $14.02 \times 130.51 \times 25.58$, an inner box of $10 \times 10 \times 10$, and an outer box of $26.74 \times 26.74 \times 26.74$ (Å). The soft docking protocol was followed by softening the potential of nonpolar parts of the receptor (i.e., decreasing the van der Waals radius of nonpolar atoms to accommodate ligands). Ligands were prepared for docking using LigPrep [31]. This step was performed for acacetin 7-*O*-methyl ether and for the designed compounds as well. Possible protonation and tautomerization states were generated at a pH of 7.4 and

the specified chiralities were retained. The lowest energy conformer of each ligand was kept. OPLS force field was employed in the preparation step. Acacetin 7-*O*-methyl ether and the designed compounds were docked into the receptor grids of MAO-A/B. The soft docking protocol [32] was followed by using flexible ligand sampling and the soft receptor grid. Standard docking precision was used to generate the best five poses for acacetin 7-*O*-methyl ether and the best pose for the other compounds.

The two most diverse poses of acacetin 7-*O*-methyl ether were used for molecular dynamics simulations and mapping of the active site water molecules. Each complex was prepared and solvated in an orthorhombic box of the TIP4P water solvation model using Desmond system builder [33,34]. The net charge on the protein was neutralized by adding the appropriate number of sodium ions. MD simulations were conducted using OPLS3 force field. The FAD cofactor was included in the MD studies and it was prepared by OPLS3 force field and charges. The cofactor showed a state penalty of 0.65 kcal/mol and a hydrogen bond count of 16 at a negative charge of -2 . Desmond's minimization algorithm was used to relax the MD system for 2000 iterations. Desmond's algorithm involves a series of energy minimizations and short MD simulations to further relax the solvated protein before the MD production step, including two minimization steps and 4 short MD simulation steps for 12 ps, 12 ps, 24 ps, and 24 ps at 10 K, 10 K, 300 K, and 300 K, respectively, using the NPT ensemble. For the production step of the MD simulations, the NPT ensemble, the Nose–Hoover chain thermostat, and the Martyna–Tobias–Klein barostat [33,34] were used. The coordinates were saved at intervals of 25 ps, ending with 8000 frames, and the MD simulations were sampled over 200 ns. The active site water structure and thermodynamic stability were examined for the protein–ligand complexes using SZMAP [35–37]. Positive (unfavorable) and negative (favorable) free energy hydration sites of the protein–ligand complexes were identified by implementing the semi-continuous solvation model of SZMAP to map the surface of the protein-binding pocket.

3. Results and Discussion

3.1. Comparison of Acacetin and Acacetin 7-*O*-Methyl Ether with Known Flavonoids

The structural requirements of the flavonoid skeleton are provided in Figure 1 and a simple comparison of the IC₅₀ values of the related flavonoids (Table 1) gave more insight into our computational approach.

Table 1. Comparison of the IC₅₀ values of acacetin and acacetin 7-*O*-methyl ether with known flavonoids.

Flavonoids	MAO-A (IC ₅₀ , μM) *	MAO-B (IC ₅₀ , μM) *	Selectivity Index MAO-A/B
Naringenin [38]	955 ± 129	288 ± 18	3.32
Chrysin [39]	0.25 ± 0.04	1.04 ± 0.17	0.24
Rhamnocitrin [40]	0.051 ± 0.001	2.97 ± 2.97	0.02
4'- <i>O</i> -Methyl kaempferol [38]	1.350 ± 0.198	>100	0.01
3,4'-Di- <i>O</i> -methyl kaempferol [41]	0.033 ± 0.042	9.667 ± 2.39	0.03
Quercetin [39]	1.52 ± 0.09	28.39 ± 5.41	0.05
Isorhamnetin [42]	6.42 ± 7.69	21.2 ± 4.99	0.30
Luteolin [43]	8.57 ± 0.47	>100	0.08
Vetulin [11]	18.79 ± 0.29	0.44 ± 0.01	42.70
Diosmetin [42]	5.74 ± 0.57	1.58 ± 0.88	3.63
Apigenin [44]	0.64 ± 0.11	1.12 ± 0.27	0.30
Genkwanin [40]	0.14 ± 0.01	0.35 ± 0.03	0.40
Acacetin [9]	0.121 ± 0.001	0.049 ± 0.0007	4.28
Acacetin 7- <i>O</i> -methyl ether [11]	>100	0.198 ± 0.001	>505.05

* The IC₅₀ values computed from the dose–response inhibition curves are mean ± S.D. of triplicate observations. Luteolin data were obtained by chemiluminescent assays using a MAO-Glo kit. All other flavonoid IC₅₀ data were obtained by spectrometric/fluorometric techniques similar to those followed here using kynuramine as a substrate and human recombinant MAO A/B (see Section 2.4), except for naringenin where a chromogenic solution was used and MAO A/B where a rat liver mitochondrial fraction was used.

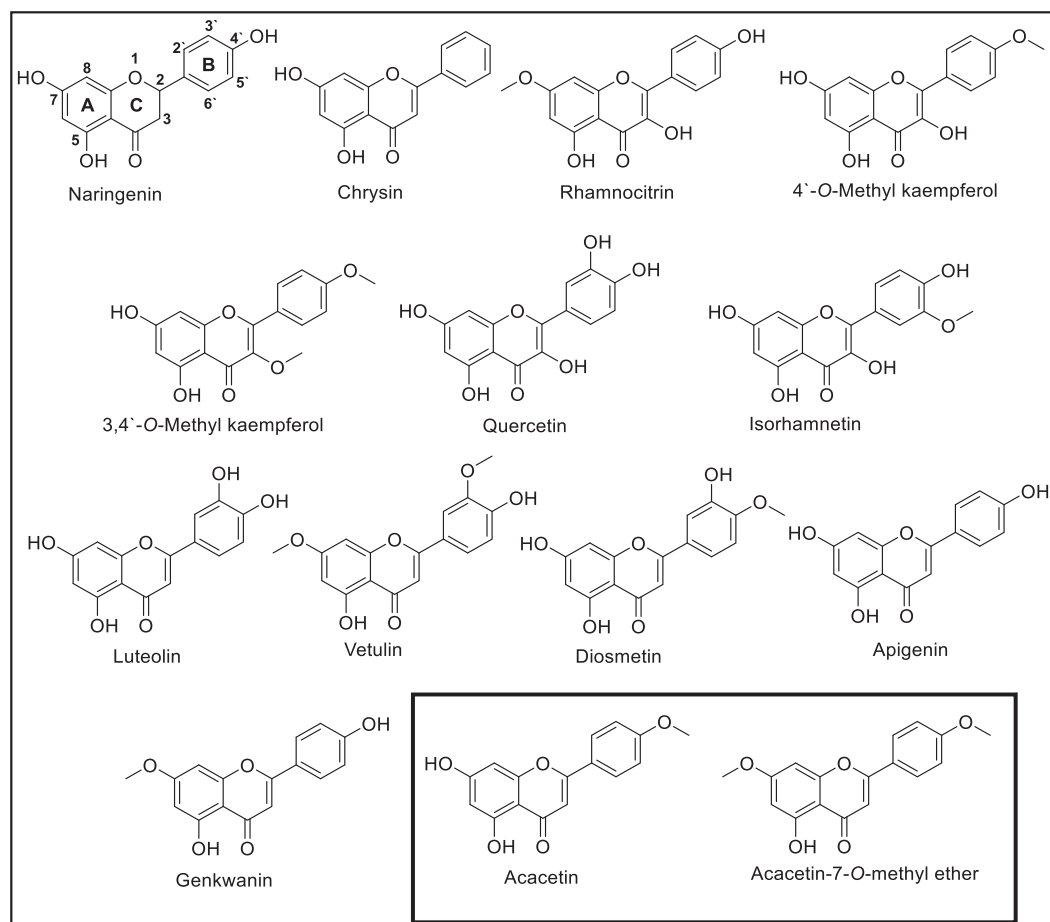


Figure 1. Comparison of acacetin and acacetin 7-O-methyl ether with known flavonoids.

The lack of a double bond between the C-2 and C-3 positions resulted in the depletion of MAO inhibition as seen in the flavanone naringenin [38]. The absence of substituents on ring B showed a slight preference for MAO-A in a manner similar to the flavone chrysin [39]. Monosubstitution on ring B of the flavonol scaffold decreased the SI of MAO-A versus MAO-B, improving the activity towards MAO-A in a manner comparable to the flavonols rhamnocitrin [40], 4'-O-methyl kaempferol, and 3, 4'-O-methyl kaempferol [41], while disubstitution of ring B resulted in the loss of MAO-A activity as seen with the flavonols quercetin [39] and isorhamnetin [42]. Dioxygenation at positions C-3' and C-4' on ring B resulted in the loss of selectivity towards MAO-B in a manner similar to the flavone luteolin [43], while methoxylation of the same positions gained MAO-B selectivity in a manner similar to vetulin [11] and diosmetin [42], respectively. Monosubstitution of ring B on the flavone scaffold at C-4' resulted in no selectivity towards any MAO as seen with apigenin [44], genkwanin [40], and acacetin [9]. Methylation of the C-7 position increased selectivity towards MAO-B in a manner similar to acacetin-7-O-methyl ether [11]. Based on this SAR analysis, oxygenation at the C-5 and C-7 positions of ring A is significant for MAO inhibition. Oxygenation of the C-3 position resulted in MAO-A selectivity, while substitution on C-4' resulted in MAO-B selectivity.

3.2. In Silico Optimization and Design

3.2.1. Molecular Dynamics (MD) Simulations of the Binding Modes of Acacetin and Acacetin 7-*O*-Methyl Ether

Acacetin 7-*O*-methyl ether was recently discovered to be a selective MAO-B inhibitor with 0.198 μM inhibition of MAO-B versus MAO-A (>100 μM) [11]. The binding characteristics of acacetin 7-*O*-methyl ether were studied to understand the basis of target selectivity. Molecular constraints were imposed on the system during docking simulations based on our previous investigations [9]. The chemistry of the acacetin 7-*O*-methyl ether was mapped with the binding site environment using molecular dynamics (MD) simulations and thermodynamic calculations to better define the most abundant binding mode. The same analysis was carried out for acacetin (Figures S1–S73, see Supplementary Materials).

Acacetin 7-*O*-methyl ether demonstrated a very strong binding interaction with MAO-B and a very weak binding to MAO-A. Figure 2 shows the binding of acacetin 7-*O*-methyl ether with and without constraints to MAO-A and -B. Acacetin 7-*O*-methyl ether was docked preferentially with a docking score of -8.9 kcal/mol into MAO-B and a docking score of -6.7 kcal/mol into MAO-A, without forcing the constraints. The benzopyranone was located between the aromatic cages (Tyr residues) in both cases, and the terminal phenyl group interacted with the aromatic gating amino acids (Phe208 for MAO-A, and Tyr326 for MAO-B). Keeping the water molecules close to the gating amino acids clashed with the phenyl group in the case of MAO-A, while it allowed two possible poses for MAO-B.

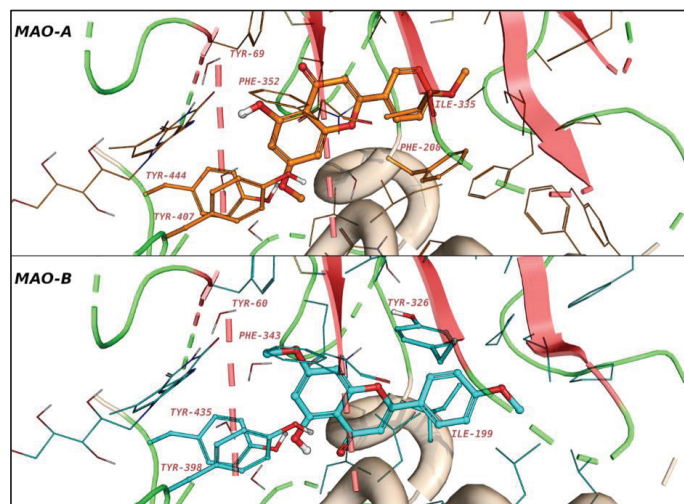


Figure 2. The predicted binding modes of acacetin ether in MAO-A and MAO-B. The gating amino acids (Ile335 and Phe208 of MAO-A, Ile199 and Tyr326 of MAO-B) and the aromatic cages (Tyr407 and Tyr444 of MAO-A, Tyr398 and Ty435 of MAO-B) are shown as sticks.

The two possible binding modes for acacetin 7-*O*-methyl ether in the case of MAO-B were visualized and are shown in Figure 3. The first pose of acacetin 7-*O*-methyl ether has benzopyranone facing the cofactor (referred to as pose 1, Figure 3A) and in the second pose, the methoxyphenyl group is facing the cofactor (referred to as pose 2, Figure 3B). Pose 1 has a better docking score compared with pose 2. The average root mean square deviation (RMSD) of pose 1 was 3.2 Å with respect to 1.6 Å for the protein backbone over the course of the MD simulations.

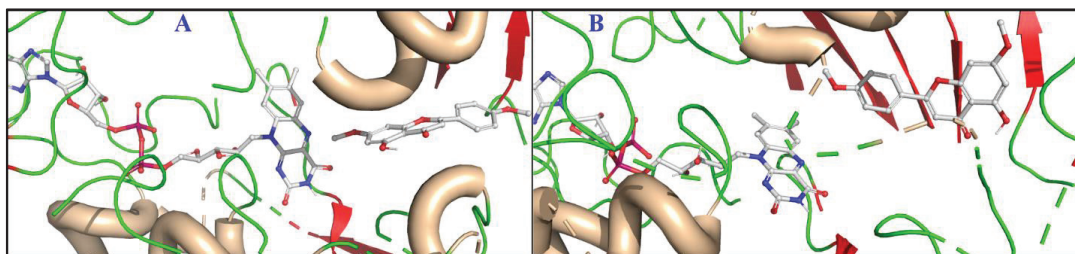


Figure 3. The two binding modes of acetaminophen 7-O-methyl ether. **(A)** Pose 1 with benzopyranone facing the FAD. **(B)** Pose 2 with the methoxyphenyl group facing the FAD. The protein is shown as a cartoon (helices are colored wheat, strands are colored red, and loops are colored green) and the ligands as sticks.

Pose 2 exhibited a RMSD value of ~ 1.6 Å, while the RMSD of the protein backbone was ~ 2.3 Å. Large local changes were observed along the protein chains between amino acids 99–102, particularly in the case of pose 2 (Figure S74). These local changes could be attributed to ligand binding (Figures 4 and S75) leading to high fluctuations in the RMSD values (Figure S74).

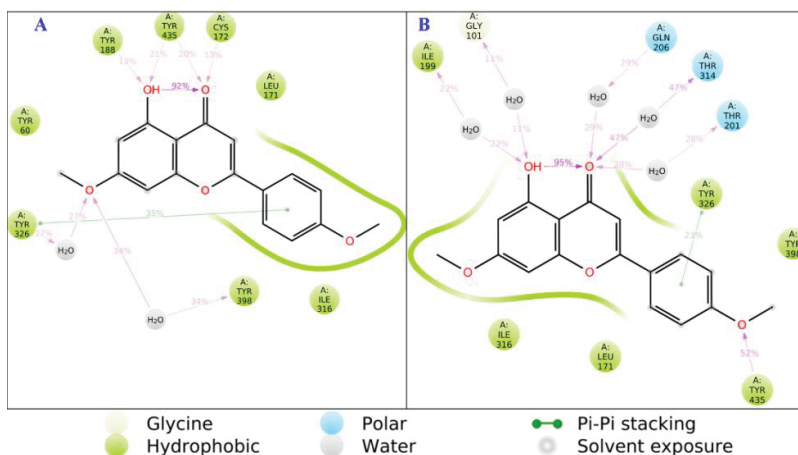


Figure 4. The 2D protein–ligand contacts for pose 1 **(A)** and pose 2 **(B)** for acetaminophen 7-O-methyl ether.

3.2.2. Active Site Hydration of MAO-B: MD Simulations, Thermodynamics, and Ligand Designs

There are 10 crystallographic water molecules in the binding pocket of MAO-B, which would have significant effects on ligand recognition and ligand design. The exact location of active site water molecules was confirmed by thermodynamic calculations to assess their contributions in ligand binding and target selectivity. Analysis of the MD simulations revealed that an average of three water molecules were fluctuating near the cofactor. In the case of pose 1, the ligand interacts with the hydrogen bond to Pro 102 through a water molecule for $\sim 5\%$ of the MD simulation time. On the other hand, pose 2 showed hydrogen bonds through water molecules to Phe 99 (less than 5%), Gly 101 (11%), and Pro 102 ($\sim 5\%$). More hydrophobic contacts were observed for pose 1, while more hydrogen bonds and water bridges were traced for pose 2 (Figure S75).

In conclusion, water molecules are more involved in the binding of pose 2 (Figures 4–6). Several other important protein–ligand contacts for both poses were sampled over the course of MD simulations, including hydrophobic contacts, π - π stacking, hydrogen bond-

ing, and interactions through water bridges with Leu 171, Leu 316, Tyr 326, Tyr 398, and Tyr 435 (Figure 4).

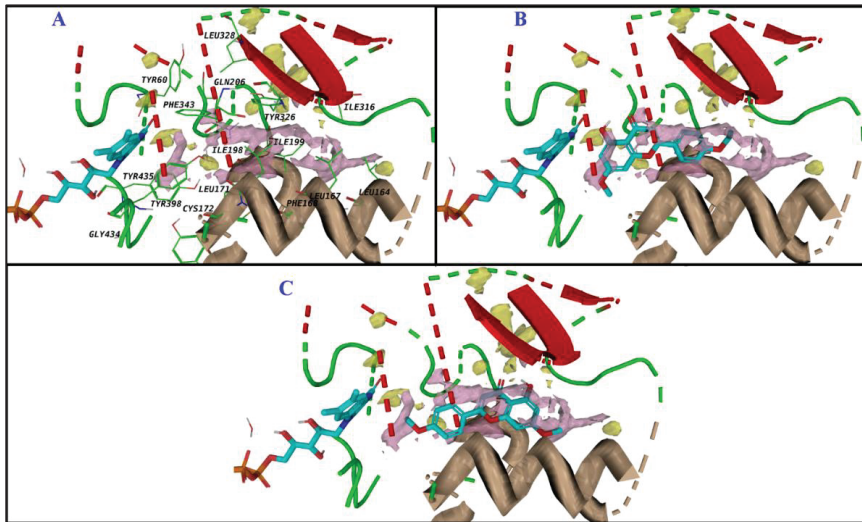


Figure 5. Water map of the MAO-B active site (A) and fitting of pose 1 (B) and pose 2 (C) with site hydration properties. Favorable regions for water molecules and polar groups are shown as yellow surfaces; hydrophobic regions are shown in purple.

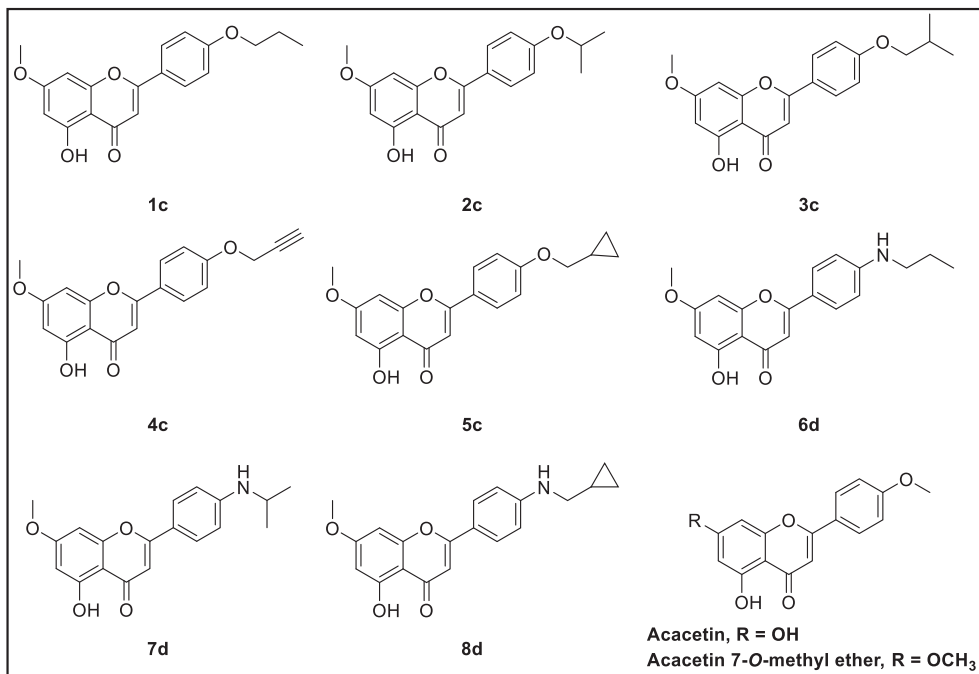


Figure 6. Designed acacetin 7-O-methyl ether analogs.

The active site water molecules (Figure 5A) were also investigated by water mapping calculations to compute their free energy and predict their effect on target selectivity.

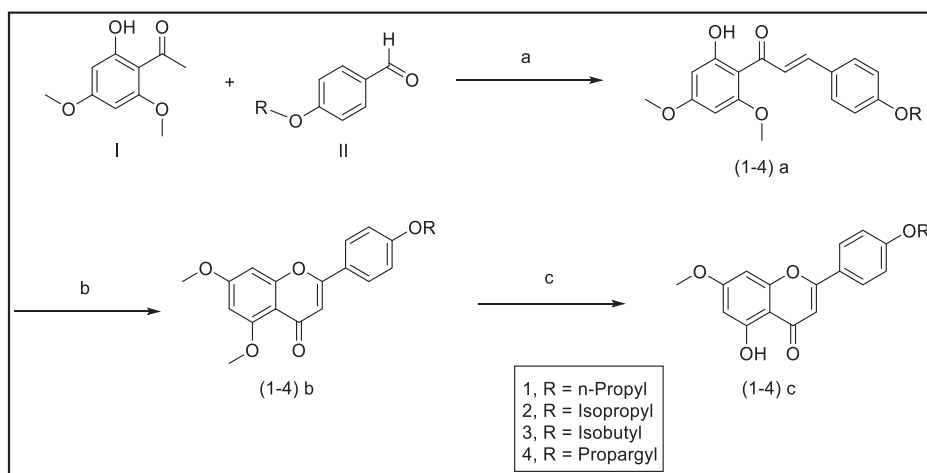
The binding pocket of MAO-B has a hydration shell near the cofactor (which is similar to what was found during the MD) that overlaps well with the hydroxyl group of the benzopyranone of pose 1 (Figure 5B). Therefore, to design high-affinity ligands, we should keep the hydroxyl group or modify the structure to have more polarity at the same position. A hydrophobic region (a positive free energy region) was noticed at the opposite site of FAD; and it covers the methoxyphenyl group of acacetin 7-*O*-methyl ether. To improve ligand binding, the polarity should be decreased at this position. The ligand chemistry of pose 2 did not fit well with the active site hydration map, while pose 1 showed a perfect match (Figure 5C).

Based on the interaction profile of acacetin 7-*O*-methyl ether as well as the thermodynamic properties of MAO-B's active site, eight analogs were virtually designed to have small ether and/or amine modifications at C-4' of the acacetin 7-*O*-methyl ether scaffold (Figure 6) and docked into the active sites of MAO-A and -B using Glide (Table S1).

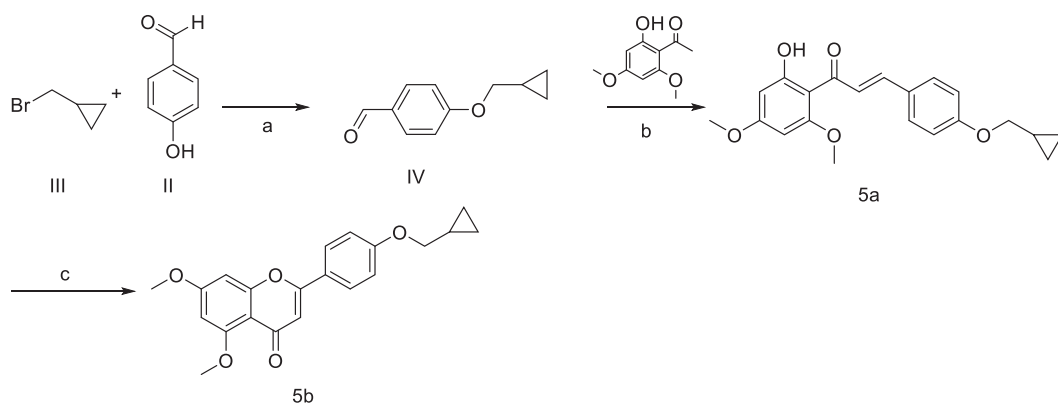
The designed compounds were evaluated for their absorption, distribution, metabolism, and excretion (ADME) properties. They did not show any violation of the rules of five or three; they have a good balance of lipophilicity/hydrophilicity, and are expected to be orally bioavailable (Table S2). The compounds mapped well with the hydrophobic regions of the binding pocket while their polar chemistry fits with the small hydrophilic regions. Consequently, syntheses of five small ether derivatives were planned: propyl-ether (1c), isopropyl-ether (2c), isobutyl-ether (3c), propargylic-ether (4c), and methyl (cyclopropyl)-ether (5c). The role of the bioisosteric change of nitrogen from oxygen was also scrutinized. Thus, propyl amine (6d), isopropyl amine (7d), and methyl (cyclopropyl)-amine (8d) were synthesized.

3.3. Chemistry

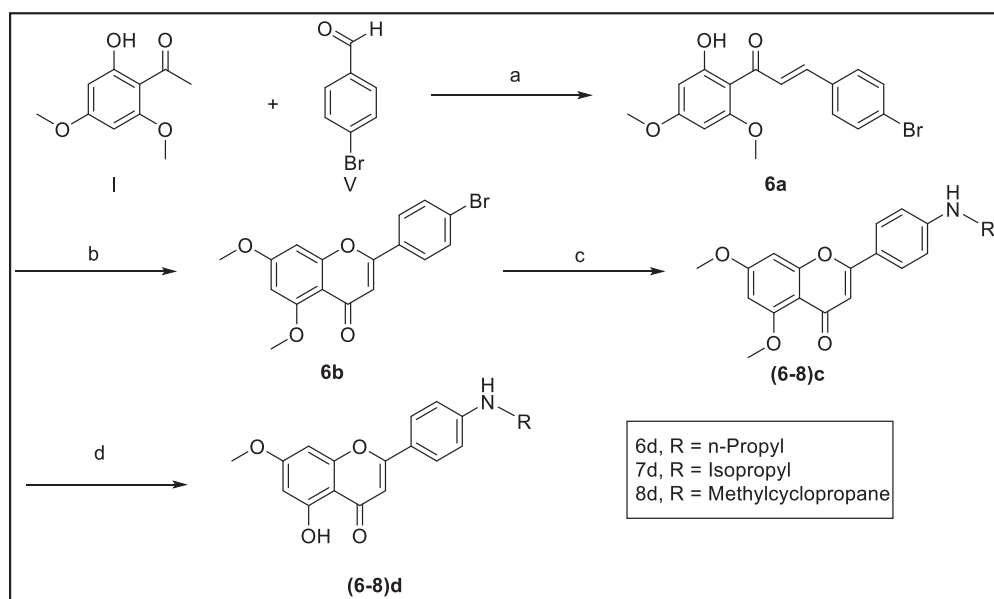
The synthetic routes to access the target compounds (1–5) c and (6–b) d were based on reported synthetic procedures [45] (Schemes 1–3).



Scheme 1. Reagents and conditions: (a) NaOH 50%, EtOH, rt, 16–20 h; (b) I₂, DMSO, 140 °C, 4–6 h; (c) 1N BBr₃, CH₂Cl₂, rt, 1–3 h.



Scheme 2. Reagents and conditions: (a) K_2CO_3 , acetone, reflux; (b) NaOH 50%, EtOH, rt, 16–20 h; (c) I_2 , DMSO, 140 °C, 4–6 h.



Scheme 3. Reagents and conditions: (a) NaOH 50%, EtOH, rt, 16–20 h; (b) I_2 , DMSO, 140 °C, 4–6 h; (c) NaOtBu, $Pd_2(dba)_3$, corresponding amines (propylamine, isopropylamine, and (aminomethyl)cyclopropane), BINAP, toluene, 80 °C, 48 h; (d) 1N BBr_3 , CH_2Cl_2 , rt, 1–2 h.

3.3.1. Synthesis of Modified Flavonoids 1–5

Chalcones (**1–4**) **a** were afforded through Schmidt condensation by reacting 2'-hydroxy-4',6'-dimethoxyacetophenone **I** and the corresponding 4-benzaldehydes **II** with 50% sodium hydroxide in ethanol. Treatment of the chalcones (**1–4**) with iodine crystals in a minimal amount of DMSO underwent cyclization to yield the dimethoxylated flavonoids (**1–4**) **b**. To obtain the target flavonoids (**1–4**) **c**, selective demethylation of position C-5 of (**1–4**) **b** was accomplished using boron tribromide (BBr_3) in CH_2Cl_2 (Scheme 1).

Compound **5** was prepared as seen in Scheme 2. 4-(cyclopropylmethoxy) benzaldehyde **IV** was synthesized by reacting (bromomethyl) cyclopropane **III** with 4-hydroxybenzaldehyde **II** in acetone and potassium carbonate. Chalcone **5a** was prepared through Schmidt condensation by treatment of the cyclopropyl aldehyde **IV** with 2'-hydroxy-4',6'-dimethoxyacet-

ophenone I and 50% NaOH in ethanol. The intermediate flavonoid **5b** was obtained from the treatment of the chalcone with iodine crystals in a minimal amount of DMSO by undergoing cyclization. Several attempts to demethylate position C-5 were unsuccessful, thereby preventing the demethylation at C-5 and releasing the alkyl group to form the hydroxyl group at C-4'.

3.3.2. Synthesis of Modified Flavonoids 6–8

Compounds **6–8** were prepared as shown in Scheme 3 with an extra step involved in the formation of the brominated flavonoid at C-4'. Thus, the brominated chalcone **6a** was produced by treating 2'-hydroxy-4',6'-dimethoxyacetophenone I with 4-bromobenzaldehyde V through Schmidt condensation with 50% sodium hydroxide in ethanol. The brominated flavonoid **6b** was prepared from the treatment of the chalcone with iodine crystals in a minimal amount of DMSO by cyclization. The flavonoids (**6–8**) c were prepared by treating compound **6b** with sodium *tert*-butoxide, tris(dibenzylideneacetone) dipalladium, 1,1'-binaphthalene-2,2'-diylbis(diphenylphosphine), and the corresponding amines such as propylamine, isopropylamine, and (aminomethyl)cyclopropane in toluene. Finally, the selective demethylated flavonoids at position 5 (**6–8**) d were prepared with boron tribromide in dichloromethane (Scheme 3). With the exception of compound **5c**, the evaluation of MAO-A and -B inhibition was performed on the final and intermediate compounds.

3.4. Biological Assays

3.4.1. Determination of Inhibitory Effects of Modified Flavonoids and Intermediates on MAO-A and -B

The synthesized acacetin 7-*O*-methyl ether analogs and their intermediates were evaluated against MAO-A and -B inhibition assays. The IC₅₀ values of acacetin 7-*O*-methyl ether analogs were prominent against MAO-B compared with MAO-A. Flavonoid **3c** showed > 3000-fold selective inhibition for MAO-B over MAO-A (Table 2). The significant selectivity obtained for the oxygenated analogs clearly validated our design. Bioisosteric replacement of oxygen with nitrogen at position C-4' diminished the selectivity of MAO-B considerably (see Table 2). The presence of the hydroxyl group at C-5 showed increased selectivity towards MAO-B. Thus, the activity and selectivity are increased for the series as follows: hydroxyls at C-5 (**1c–4c**) > protected-methylated flavonoids at C-5 (**1b–6b**) > chalcones (**1a–6a**) > amine flavonoids at C-4' (**6c,d–8c,d**). Compounds (**1–4**) c exhibited more than a thousand-fold SI (Table 2), equal to or more potent than safinamide (Table 2), and were considered for further studies to understand their mechanisms of inhibition. Figure S76 shows the inhibition dose–response for the potent analogs (**1–4**) c.

3.4.2. Evaluation of MAO-B Inhibition Kinetics and Analysis of Binding and Time-Dependent Inhibition of Modified Flavonoids (**1–4**) c

Modified flavonoids (**1–4**) c were evaluated against MAO-B at varying concentrations of kynuramine, a nonselective substrate, to investigate the nature of inhibition of the enzymes. Based on dose–concentration inhibition, three to five concentrations (below and above the concentration of IC₅₀ values) were selected for the inhibition kinetics experiment. Modified flavonoids (**1–4**) c inhibited the enzymatic activity of MAO-B with considerably high affinity *K_i* at nanomolar units with a range from 43 to 68 nM (Table 3).

Binding of modified flavonoids (**1–4**) c with human MAO-B affected *K_m* (i.e., the affinity of the substrate for the enzyme) as well as *V_{max}* (maximum enzyme activity) values, indicating the type of MAO-B inhibition by the analogs: flavonoid **1c** (mixed/partially reversible), **2c** (mixed/partially reversible), **3c** (mixed/irreversible), and **4c** (mixed/irreversible) (Table 3, Figure 7).

Table 2. Inhibition (IC_{50} values) of recombinant human monoamine oxidases A and B by acacetin 7-*O*-methyl ether analogs and intermediates.

Synthesized Analogs	MAO-A (IC_{50} , μ M) *	MAO-B (IC_{50} , μ M) *	Selectivity Index MAO-A/B
1a	0.515 \pm 0.024	0.40 \pm 0.024	1.3
2a	0.117 \pm 0.05	0.049 \pm 0.0035	2.4
3a	0.42 \pm 0.002	0.22 \pm 0.0211	1.9
4a	9.42 \pm 1.78	8.33 \pm 0.7871	1.1
5a	1.30 \pm 0.09	0.90 \pm 0.035	1.4
1b	>100	1.70 \pm 0.076	>58.8
2b	>100	2.64 \pm 0.0880	>37.9
3b	>100	7.23 \pm 2.1438	>13.8
4b	>100	>100	>1
4a	9.42 \pm 1.78	8.33 \pm 0.7871	1.1
4b	>100	>100	>1
5b	>100	22.82 \pm 2.098	>4.4
1c	48.78 \pm 2.01	0.033 \pm 0.0042	1478.2
2c	30.74 \pm 0.023	0.016 \pm 0.0070	1921.3
3c	>100	0.031 \pm 0.0070	>3225.8
4c	62.70 \pm 5.21	0.049 \pm 0.0014	1279.6
6a	12.349 \pm 0.249	>100	>0.1
6b	87.830 \pm 5.449	28.407 \pm 2.639	3.1
6c	>100	22.097 \pm 2.479	>4.5
7c	37.492 \pm 0.476	9.447 \pm 0.113	4.0
8c	39.095 \pm 5.144	12.727 \pm 0.290	3.1
6d	85.484 \pm 1.585	1.554 \pm 0.137	55.0
7d	40.500 \pm 2.374	0.417 \pm 0.012	97.1
8d	39.114 \pm 0.555	2.185 \pm 0.088	17.9
Acacetin	0.105 \pm 0.0014	0.042 \pm 0.0021	2.5
Acacetin 7- <i>O</i> -methyl ether [11]	>100	0.198 \pm 0.001	>505.05
Clorgyline	0.0039 \pm 0.0002	2.15 \pm 0.212	0.002
Deprenyl	33.00 \pm 1.411	0.046 \pm 0.0014	717.4
Safinamide [46]	90.00 \pm 2.470	0.060 \pm 0.005	1500.0
Harmine	0.0031 \pm 0.0003	39.000 \pm 1.412	0.00008

* The IC_{50} values computed from the dose–response inhibition curves are the mean \pm S.D. of triplicate observations.

Table 3. Inhibition/binding affinity constant (K_i) values for inhibition of recombinant human MAO-B by modified flavonoids (1–4) c, acacetin, acacetin 7-*O*-methyl ether, and deprenyl.

Compound	Monoamine Oxidase A		Monoamine Oxidase B	
	K_i (nM) *	Type of Inhibition	K_i (nM) *	Type of Inhibition
1c	-	-	43 \pm 3.8	mixed/partially reversible
2c	-	-	52 \pm 3.1	mixed/reversible
3c	-	-	37 \pm 9.5	mixed/irreversible
4c	-	-	68 \pm 7.1	mixed/irreversible
Acacetin	30 \pm 1.8	competitive/reversible	21 \pm 1.8	competitive/reversible
Acacetin 7- <i>O</i> -methyl ether [11]	-	-	45 \pm 3.0	competitive/partially reversible
Deprenyl	-	-	43 \pm 4.0	mixed/irreversible

* Values are the mean \pm S.D. of triplicate experiments.

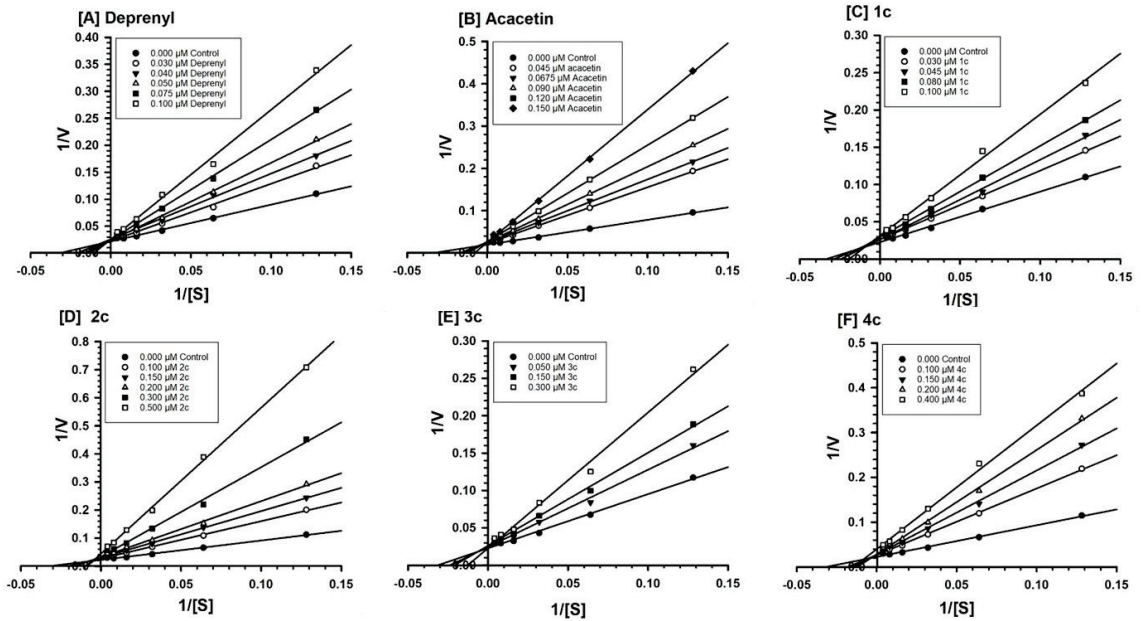


Figure 7. Kinetic characteristics of inhibition of recombinant human MAO-B with [A] deprenyl [B] acetatin, [C] 1c, [D] 2c, [E] 3c, and [F] 4c; V = nmoles/min/mg protein and S = substrate kynuramine concentration (μM).

The binding characteristics of the modified flavonoids (1–4) *c* with MAO-B were examined by equilibrium dialysis to measure the dissociation of the enzyme–inhibitor complex (Figure 8). MAO-B enzyme was incubated with the highest concentration of the analogs for 20 min at 37 °C to allow for binding of the inhibitor with the enzyme and formation of the enzyme–inhibitor complex. Then, the mixtures of the enzyme–inhibitor complex were dialyzed overnight at 4 °C using 25 mM KHPO_4 (pH 7.4) buffer. The enzyme activities were examined before and after dialysis. Incubation of MAO-B with 1.5 μM of modified flavonoids (1–4) *c* caused more than 70% inhibition of activity and only the enzyme activities of 1c (30%) and 2c (66%) were recovered after dialysis. Thus, the binding of 1c was partially reversible, while 2c was reversible with MAO-B (Figure 8, Table 3).

To inspect the time-dependent binding inhibition of MAO-B, the enzyme was pre-incubated with the analog for 0 to 15 min at concentrations that caused nearly 40–80% inhibition depending on the analog (Figure S77). For compounds 1c, 3c, and 4c, 70–80% inhibition was seen at the concentrations given in Figure S77. Meanwhile, compound 2c showed 30–50% of MAO-B enzyme inhibition. The control enzyme without inhibitor was also run concurrently. For validation, the MAO-B standards were run simultaneously for the time-dependent assay.

3.5. Computational Analysis of Enzyme–Inhibitor Interactions for Modified Flavonoids (1–4) *c*

Based on the remarkable experimental selectivity of MAO-B towards the designed compounds (1–4) *c*, further computational analysis was conducted. These analogs did not show good docking poses in MAO-A due to the clashes between the R group and the amino acids in the substrate binding site. The size and nature of the R group are essential for selective targeting. In general, these four acetatin 7-*O*-methyl ether analogs exploited the hydrophobic nature of the amino acids in the binding pocket of MAO-B, particularly Tyr 398 and Tyr 435, near the FAD cofactor by forming π - π stacking with their aromatic functionalities. The non-polar nature of the R group matches the hydrophobic nature of the Leu and Ile amino acids on the other side of the binding site. Considerable hydrophobic contacts were observed between the ligands and Leu 167, Leu 171, Ile 199, Tyr 236, and

Phe 343. The ligands placed properly their polar chemistry to form strong hydrogen bonds with the backbones of Leu 171, Ile 199, and the side chain of Gln 206 (Figure 9). There is room in the binding pocket for water molecules to bridge the interactions between the ligands and amino acids, principally near the FAD.

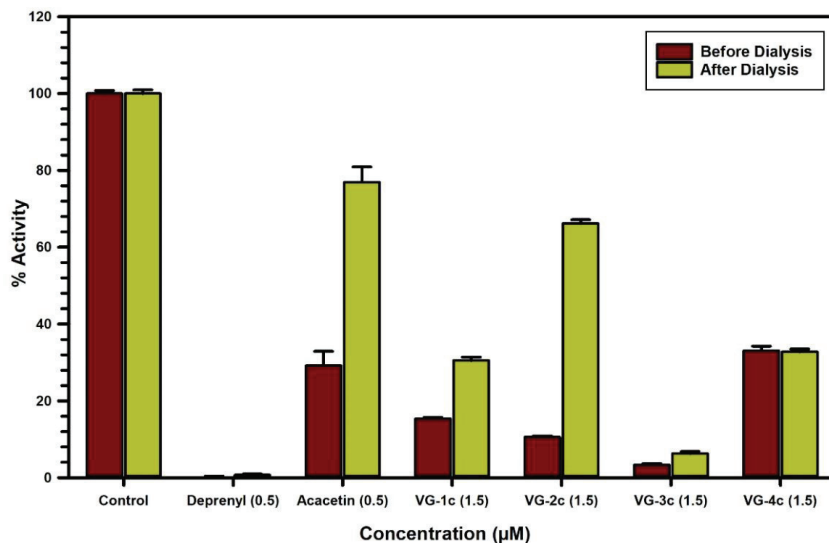


Figure 8. Analysis of the nature of binding of deprenyl (0.5 µM), acacetin (0.5 µM), 1c (1.5 µM), 2c (1.5 µM), 3c (1.5 µM), and 4c (1.5 µM) with recombinant human MAO-B by recovery of catalytic activity of the enzyme after equilibrium dialysis dissociation. Each bar shows the mean ± S.D. of triplicate values.

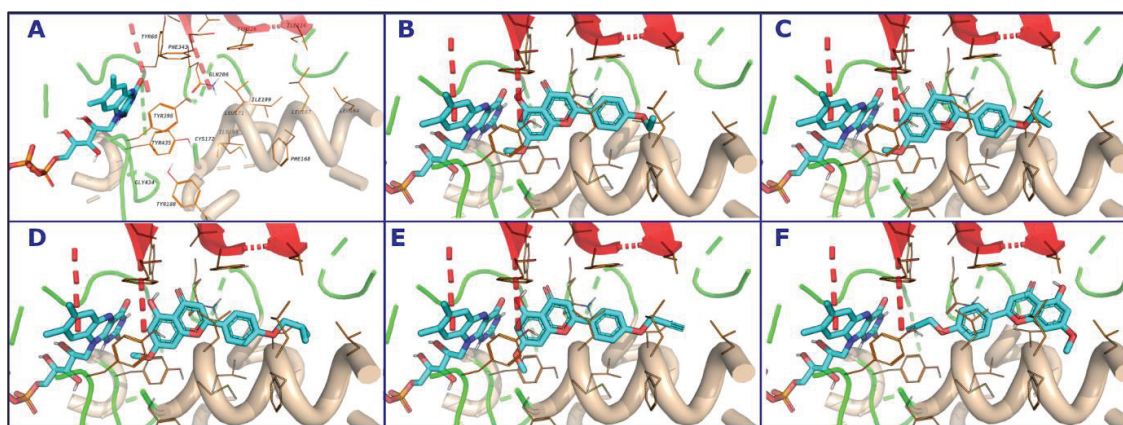


Figure 9. Binding modes of acacetin 7-*O*-methyl ether derivatives and surrounding amino acids. The amino acids that interact with the ligand are shown as lines (A), Compounds 1c (B), 2c (C), 3c (D), and 4c (E,F). There are two possible orientations for 4c in the binding site.

4. Conclusions

Based on our understanding of the SAR of the flavonoid skeleton and the molecular modeling studies, eight flavonoid analogs were designed. All the analogs did not demonstrate acceptable docking poses in the active site of MAO-A but they had good binding

scores in MAO-B (Table S1). They also fitted well with the thermodynamic properties of the MAO-B active site. The flavonoid compounds with *O*-propyl, *O*-isopropyl, *O*-isobutyl, and *O*-propargyl substituents showed excellent selectivity towards MAO-B, in the range of a 1200- to 3200-fold difference from MAO-A.

Rasagiline and selegiline are FDA-approved irreversible MAO-B inhibitors that exhibited a selectivity of 103- and 127-fold against MAO-A, while safinamide is a reversible MAO-B inhibitor with a selectivity of 1000–1500-fold towards MAO-B [8,9,46]. The synthesized flavonoids *O*-propyl and *O*-isopropyl are reversible MAO-B inhibitors with a selectivity of 1478- and 1921-fold against MAO-A, respectively. *O*-isobutyl was the most selective of all the synthesized compounds with 3225-fold selectivity towards MAO-B, while *O*-propargyl exhibited 1279-fold selectivity. *O*-isobutyl and *O*-propargyl were both irreversible MAO-B inhibitors. *O*-propyl, *O*-isopropyl, *O*-isobutyl, and *O*-propargyl substituents are potential candidates worth pursuing. Based on the results of these derivatives, (1–4) **c** with *O*-alkyl (a short chain with three to four carbon atoms) substituents at position C-4' yield high selectivity toward MAO-B. The nitrogen amine series did not display any significant selectivity towards MAO-B. This could be attributed to the high electronegativity of oxygen compared with nitrogen. The study of the longer alkyl chain on C-4' should be explored. It is also worth pursuing the introduction of halogens at position 7, which might help improve the ADMET properties. Introduction of an electronegative atom such as nitrogen at position 8 would be interesting to understand the SAR of ring A in MAO activity. Another chemical modification that would help us to understand the activity of MAO-B versus MAO-A in the flavonoid scaffold that is worth exploring is the substitution of the B ring, introducing *O*-substituent groups at position C-3' or C-4' as on vetulin or diosmetin (see Table 1), which both show a slight preference towards MAO-B. Flavonoids have limited clinical use due to their significant challenges related to the pharmacokinetic and pharmacodynamic profiles. They have poor oral absorption along with extensive hepatic metabolism and low solubility, thereby resulting in poor bioavailability [12]. Modifying the chemical structure by substituting the flavonoid rings can help overcome the solubility issue. For example, the C-7 position on the A ring can be replaced with fluorine to improve its solubility and bioavailability.

Supplementary Materials: The following are available online at <https://www.mdpi.com/article/10.3390/biomedicines9101304/s1>, Figures S1–S77, and Tables S1 and S2. Additional data, such as ¹H-NMR spectra, ¹³C-NMR spectra, HRMS spectra, and HPLC analysis of compounds 1–8, computational interactions of acacetin and acacetin 7-*O*-methyl ether and MAO-A and MAO-B, and docking scores and ADME predictions for acacetin 7-*O*-methyl ether analogs (PDF).

Author Contributions: Synthesis, structural characterization, and manuscript writing, V.G. and F.L.; computational approach and ligand design, M.A.N. and K.M.E.; enzymatic monoamine oxidase inhibition and statistical analysis, N.D.C. and B.L.T.; academic supervision, J.M.R. and S.J.C.; manuscript editing, C.R.M. and S.J.C.; conceptualization, study coordination, and manuscript editing, B.L.T. and F.L. All authors have read and agreed to the published version of the manuscript.

Funding: This research was funded in part by grant numbers P20GM104932 and P30GM122733 from the National Institute of General Medical Sciences (NIGMS), a component of the National Institutes of Health (NIH), and was conducted in part in a facility constructed with support from the Research Facilities Improvements Program (C06RR14503) from the NIH National Center for Research Resources; its contents are solely the responsibility of the authors and do not necessarily represent the official view of the NIGMS or the NIH.

Institutional Review Board Statement: Not applicable.

Informed Consent Statement: No human assay was performed in the present study.

Data Availability Statement: All supporting results are reported in the manuscript.

Acknowledgments: The authors acknowledge the free academic license granted by Openeye Scientific Software. Some of the results reported in this paper were included in the dissertation submitted by V.G for a Ph.D. in Pharmaceutical Sciences at the School of Graduate Studies, University of Mississippi, University MS 38677. F.L. thanks the College of Pharmacy, University of South Carolina for start-up funds.

Conflicts of Interest: The authors declare no conflict of interest.

References

1. Scott, L.; Dawson, V.L.; Dawson, T.M. Trumping Neurodegeneration: Targeting Common Pathways Regulated by Autosomal Recessive Parkinson's Disease Genes. *Exp. Neurol.* **2017**, *298*, 191–201. [CrossRef] [PubMed]
2. Pringsheim, T.; Jette, N.; Frolkis, A.; Steeves, T.D.L. The Prevalence of Parkinson's Disease: A Systematic Review and Meta-Analysis. *Mov. Disord.* **2014**, *29*, 1583–1590. [CrossRef]
3. Blesa, J.; Trigo-Damas, I.; Quiroga-Varela, A.; Jackson-Lewis, V.R. Oxidative Stress and Parkinson's Disease. *Front. Neuroanat.* **2015**, *9*, 91. [CrossRef]
4. Sarrafchi, A.; Bahmani, M.; Shirzad, H.; Rafieian-Kopaei, M. Oxidative Stress and Parkinson's Disease: New Hopes in Treatment with Herbal Antioxidants. *Curr. Pharm. Des.* **2016**, *22*, 238–246. [CrossRef] [PubMed]
5. Tong, J.; Rathitharan, G.; Meyer, J.H.; Furukawa, Y.; Ang, L.-C.; Boileau, I.; Guttman, M.; Hornykiewicz, O.; Kish, S.J. Brain Monoamine Oxidase B and A in Human Parkinsonian Dopamine Deficiency Disorders. *Brain* **2017**, *140*, 2460–2474. [CrossRef] [PubMed]
6. Szökő, É.; Tábi, T.; Riederer, P.; Vécsei, L.; Magyar, K. Pharmacological Aspects of the Neuroprotective Effects of Irreversible MAO-B Inhibitors, Selegiline and Rasagiline, in Parkinson's Disease. *J. Neural Transm.* **2018**, *125*, 1735–1749. [CrossRef]
7. Liguori, C.; Stefani, A.; Mercuri, N.B.; Pierantozzi, M. Effective Treatment of Restless Legs Syndrome by Safinamide in Parkinson's Disease Patients. *Sleep Med.* **2018**, *41*, 113–114. [CrossRef]
8. Guglielmi, P.; Carradori, S.; Ammazalorso, A.; Secci, D. Novel Approaches to the Discovery of Selective Human Monoamine Oxidase-B Inhibitors: Is There Room for Improvement? *Expert Opin. Drug Discov.* **2019**, *14*, 995–1035. [CrossRef]
9. Chaurasiya, N.D.; Gogineni, V.; Elokely, K.M.; León, F.; Núñez, M.J.; Klein, M.L.; Walker, L.A.; Cutler, S.J.; Tekwani, B.L. Isolation of Acacetin from *Calea urticifolia* with Inhibitory Properties against Human Monoamine Oxidase-A and -B. *J. Nat. Prod.* **2016**, *79*, 2538–2544. [CrossRef] [PubMed]
10. Semwal, R.B.; Semwal, D.K.; Combrinck, S.; Trill, J.; Gibbons, S.; Viljoen, A. Acacetin—A Simple Flavone Exhibiting Diverse Pharmacological Activities. *Phytochem. Lett.* **2019**, *32*, 56–65. [CrossRef]
11. Chaurasiya, N.D.; Zhao, J.; Pandey, P.; Doerksen, R.J.; Muhammad, I.; Tekwani, B.L. Selective Inhibition of Human Monoamine Oxidase B by Acacetin 7-Methyl Ether Isolated from *Turnera diffusa* (Damiana). *Molecules* **2019**, *24*, 810. [CrossRef]
12. Amawi, H.; Ashby, C.R., Jr.; Tiwari, A.K. Cancer Chemoprevention Through Dietary Flavonoids: What's Limiting? *Chin. J. Cancer* **2017**, *36*, 1–13. [CrossRef]
13. Jin, C.-F.; Wang, Z.-Z.; Chen, K.-Z.; Xu, T.-F.; Hao, G.-F. Computational Fragment-Based Design Facilitates Discovery of Potent and Selective Monoamine Oxidase-B (MAO-B) Inhibitor. *J. Med. Chem.* **2020**, *63*, 15021–15036. [CrossRef] [PubMed]
14. Aldrich, C.; Bertozzi, C.; Georg, G.I.; Kiessling, L.; Lindsley, C.; Liotta, D.; Merz, K.M., Jr.; Schepartz, A.; Wang, S. The Ecstasy and Agony of Assay Interference Compounds. *J. Med. Chem.* **2017**, *60*, 2165–2168. [CrossRef]
15. Baell, J.B.; Holloway, G.A. New Substructure Filters for Removal of Pan Assay Interference Compounds (PAINS) from Screening Libraries and for Their Exclusion in Bioassays. *J. Med. Chem.* **2010**, *53*, 2719–2740. [CrossRef] [PubMed]
16. Sterling, T.; Irwin, J.J. ZINC 15—Ligand Discovery for Everyone. *J. Chem. Inf. Model.* **2015**, *55*, 2324–2337. [CrossRef]
17. Chaurasiya, N.D.; León, F.; Ding, Y.; Gómez-Betancur, I.; Benjumea, D.; Walker, L.A.; Cutler, S.J.; Tekwani, B.L. Interactions of Desmethoxyyangonin, a Secondary Metabolite from *Renealmia alpinia*, with Human Monoamine Oxidase-A and Oxidase-B. *Evid. Based Complement. Altern. Med.* **2017**, *2017*, 4018724. [CrossRef]
18. Parikh, S.; Hanscom, S.; Gagne, P.; Crespi, C.; Patten, C. A Fluorescent-Based, High-Throughput Assay for Detecting Inhibitors of Human Monoamine Oxidase A and B. *BD Biosci. Discov. Labware* **2002**, S02T081R2. [CrossRef]
19. *Small-Molecule Drug Discovery Suite 2017-4*; Schrödinger, LLC.: New York, NY, USA, 2017.
20. Greenwood, J.R.; Calkins, D.; Sullivan, A.P.; Shelley, J.C. Towards the Comprehensive, Rapid, and Accurate Prediction of the Favorable Tautomeric States of Drug-Like Molecules in Aqueous Solution. *J. Comput. Aided Mol. Des.* **2010**, *24*, 591–604. [CrossRef]
21. Shelley, J.C.; Cholleti, A.; Frye, L.L.; Greenwood, J.R.; Timlin, M.R.; Uchimaya, M. Epik: A Software Program for pK_a Prediction and Protonation State Generation for Drug-Like Molecules. *J. Comput. Aided Mol. Des.* **2007**, *21*, 681–691. [CrossRef] [PubMed]
22. *Schrödinger Release 2017-4: Epik*; Schrödinger, LLC.: New York, NY, USA, 2017.
23. Harder, E.; Damm, W.; Maple, J.; Wu, C.; Reboul, M.; Xiang, J.Y.; Wang, L.; Lupyan, D.; Dahlgren, M.K.; Knight, J.L.; et al. OPLS3: A Force Field Providing Broad Coverage of Drug-like Small Molecules and Proteins. *J. Chem. Theory Comput.* **2016**, *12*, 281–296. [CrossRef] [PubMed]
24. Friesner, R.A.; Murphy, R.B.; Repasky, M.P.; Frye, L.L.; Greenwood, J.R.; Halgren, T.A.; Sanschagrin, P.C.; Mainz, D.T. Extra Precision Glide: Docking and Scoring Incorporating a Model of Hydrophobic Enclosure for Protein-Ligand Complexes. *J. Med. Chem.* **2006**, *49*, 6177–6196. [CrossRef]

25. Halgren, T.A.; Murphy, R.B.; Friesner, R.A.; Beard, H.S.; Frye, L.L.; Pollard, W.T.; Banks, J.L. Glide: A New Approach for Rapid, Accurate Docking and Scoring. 2. Enrichment Factors in Database Screening. *J. Med. Chem.* **2004**, *47*, 1750–1759. [CrossRef] [PubMed]
26. Friesner, R.A.; Banks, J.L.; Murphy, R.B.; Halgren, T.A.; Klicic, J.J.; Mainz, D.T.; Repasky, M.P.; Knoll, E.H.; Shelley, M.; Perry, J.K.; et al. Glide: A New Approach for Rapid, Accurate Docking and Scoring. 1. Method and Assessment of Docking Accuracy. *J. Med. Chem.* **2004**, *47*, 1739–1749. [CrossRef]
27. *Schrödinger Release 2017-4: Glide*; Schrödinger, LLC.: New York, NY, USA, 2017.
28. Arul Murugan, N.; Chiotis, K.; Rodriguez-Vieitez, E.; Lemoine, L.; Ågren, H.; Nordberg, A. Cross-interaction of tau PET tracers with monoamine oxidase B: Evidence from in silico modelling and in vivo imagining. *Eur. J. Nucl. Med. Mol. Imaging* **2019**, *46*, 1369–1382. [CrossRef] [PubMed]
29. Arul Murugan, N.; Zalesny, R. Multiscale modeling of two-photon probes for Parkinson's diagnostics based on monoamine oxidase B biomarker. *J. Chem. Inf. Model.* **2020**, *60*, 3854–3863. [CrossRef]
30. Arul Murugan, N.; Muvva, C.; Jeyarajandian, C.; Jeyakanthan, J.; Subramanian, V. Performance of force-field and machine learning-based scoring functions in ranking MAO-B protein-inhibitor complexes in relevance to developing Parkinson's therapeutics. *Int. J. Mol. Sci.* **2020**, *21*, 7648. [CrossRef]
31. *Schrödinger Release 2017-4: LigPrep*; Schrödinger, LLC.: New York, NY, USA, 2017.
32. Elokely, K.M.; Doerksen, R.J. Docking Challenge: Protein Sampling and Molecular Docking Performance. *J. Chem. Inf. Model.* **2013**, *53*, 1934–1945. [CrossRef]
33. Bowers, K.J.; Chow, D.E.; Xu, H.; Dror, R.O.; Eastwood, M.P.; Gregersen, B.A.; Klepeis, J.L.; Kolossvary, I.; Moraes, M.A.; Sacerdoti, F.D.; et al. Scalable Algorithms for Molecular Dynamics Simulations on Commodity Clusters. In Proceedings of the SC '06: Proceedings of the 2006 ACM/IEEE Conference on Supercomputing, Tampa, FL, USA, 11–17 November 2006. [CrossRef]
34. Desmond Molecular Dynamics System, D.E. Shaw Research, New York, NY, 2021. Maestro-Desmond Interoperability Tools, Schrödinger, New York, NY, 2021. Available online: <https://www.schrodinger.com/citations> (accessed on 12 December 2017).
35. SZMAP 1.2.1.4; OpenEye Scientific Software: Santa Fe, NM, USA. Available online: <http://www.eyesopen.com> (accessed on 12 December 2017).
36. Bayden, A.S.; Moustakas, D.T.; Joseph-McCarthy, D.; Lamb, M.L. Evaluating Free Energies of Binding and Conservation of Crystallographic Waters Using SZMAP. *J. Chem. Inf. Model.* **2015**, *55*, 1552–1565. [CrossRef] [PubMed]
37. Elokely, K.; Velisetty, P.; Delemotte, L.; Palovcak, E.; Klein, M.L.; Rohacs, T.; Carnevale, V. Understanding TRPV1 Activation by Ligands: Insights from the Binding Modes of Capsaicin and Resiniferatoxin. *Proc. Natl. Acad. Sci. USA.* **2016**, *113*, E137–E145. [CrossRef]
38. Olsen, H.T.; Stafford, G.I.; van Staden, J.; Christensen, S.B.; Jäger, A.K. Isolation of the MAO-Inhibitor Naringenin from *Mentha aquatica* L. *J. Ethnopharmacol.* **2008**, *117*, 500–502. [CrossRef]
39. Larit, F.; Elokely, K.M.; Chaurasiya, N.D.; Benyahia, S.; Nael, M.A.; León, F.; Abu-Darwish, M.S.; Efferth, T.; Wang, Y.-H.; Belouahem-Abed, D.; et al. Inhibition of Human Monoamine Oxidase A and B by Flavonoids Isolated from Two Algerian Medicinal Plants. *Phytomedicine* **2018**, *40*, 27–36. [CrossRef]
40. Baek, S.C.; Park, M.H.; Ryu, H.W.; Lee, J.P.; Kang, M.-G.; Park, D.; Park, C.M.; Oh, S.-R.; Kim, H. Rhamnocitrin Isolated from *Prunus padus* var. *seoulensis*: A Potent and Selective Reversible Inhibitor of Human Monoamine Oxidase A. *Bioorg. Chem.* **2019**, *83*, 317–325. [CrossRef] [PubMed]
41. Chaurasiya, N.D.; Midiwo, J.; Pandey, P.; Bwire, R.N.; Doerksen, R.J.; Muhammad, I.; Tekwani, B.L. Selective Interactions of O-Methylated Flavonoid Natural Products with Human Monoamine Oxidase-A and -B. *Molecules* **2020**, *25*, 5358. [CrossRef] [PubMed]
42. Carradori, S.; Gidaro, M.C.; Petzer, A.; Costa, G.; Guglielmi, P.; Chimenti, P.; Alcaro, S.; Petzer, J.P. Inhibition of Human Monoamine Oxidase: Biological and Molecular Modeling Studies on Selected Natural Flavonoids. *J. Agric. Food Chem.* **2016**, *64*, 9004–9011. [CrossRef]
43. Park, S.E.; Paudel, P.; Wagle, A.; Seong, S.H.; Kim, H.R.; Fauzi, F.M.; Jung, H.A.; Choi, J.S. Luteolin, a Potent Human Monoamine Oxidase-A Inhibitor and Dopamine D₄ and Vasopressin V_{1A} Receptor Antagonist. *J. Agric. Food Chem.* **2020**, *68*, 10719–10729. [CrossRef] [PubMed]
44. Chaurasiya, N.D.; Ibrahim, M.A.; Muhammad, I.; Walker, L.A.; Tekwani, B.L. Monoamine Oxidase Inhibitory Constituents of Propolis: Kinetics and Mechanism of Inhibition of Recombinant Human MAO-A and MAO-B. *Molecules* **2014**, *19*, 18936–18952. [CrossRef] [PubMed]
45. Chen, H.; Mrzcek, A.A.; Wang, X.; Ding, C.; Ding, Y.; Porro, L.J.; Liu, H.; Chao, C.; Hellmich, M.R.; Zhou, J. Design, Synthesis, and Characterization of Novel Apigenin Analogues that Suppress Pancreatic Stellate Cell Proliferation In vitro and Associated Pancreatic Fibrosis In vivo. *Bioorg. Med. Chem.* **2014**, *22*, 3393–3404. [CrossRef]
46. Pandey, P.; Chaurasiya, N.D.; Tekwani, B.L.; Doerksen, R.J. Interactions of endocannabinoid virodhamine and related analogs with human monoamine oxidase-A and -B. *Biochem. Pharmacol.* **2018**, *155*, 82–91. [CrossRef]



Article

Identification of CDK7 Inhibitors from Natural Sources Using Pharmacoinformatics and Molecular Dynamics Simulations

Vikas Kumar ^{1,†}, Shraddha Parate ^{2,†}, Gunjan Thakur ^{3,†}, Gihwan Lee ², Hyeon-Su Ro ⁴, Yongseong Kim ⁵, Hong Ja Kim ⁶, Myeong Ok Kim ^{6,*} and Keun Woo Lee ^{1,*}

- ¹ Department of Bio & Medical Big Data (BK4 Program), Division of Life Sciences, Research Institute of Natural Science (RINS), Gyeongsang National University (GNU), 501 Jinju-daero, Jinju 52828, Korea; vikaspathania777@gmail.com
 - ² Plant Molecular Biology and Biotechnology Research Center (PMBBRC), Division of Applied Life Science, Gyeongsang National University (GNU), 501 Jinju-daero, Jinju 52828, Korea; parateshraddha@gmail.com (S.P.); pika890131@gmail.com (G.L.)
 - ³ Department of Veterinary Medicine, Institute of Animal Medicine, Gyeongsang National University (GNU), Jinju 52828, Korea; thakur.gunjan.123@gmail.com
 - ⁴ Department of Bio & Medical Big Data (BK4 Program), Research Institute of Life Sciences, Gyeongsang National University (GNU), Jinju 52828, Korea; rohyeon@gnu.ac.kr
 - ⁵ School of Cosmetics and Food Development, Kyungnam University, Masan 631-701, Korea; kimys@kyungnam.ac.kr
 - ⁶ Division of Life Sciences and Applied Life Science (BK21 Four), Research Institute of Natural Science (RINS), Gyeongsang National University (GNU), 501 Jinju-daero, Jinju 52828, Korea; hongjaac@gnu.ac.kr
- * Correspondence: mokim@gnu.ac.kr (M.O.K.); kwlee@gnu.ac.kr (K.W.L.); Tel.: +82-55-772-1360 (K.W.L.)
† These authors contributed equally.

Citation: Kumar, V.; Parate, S.; Thakur, G.; Lee, G.; Ro, H.-S.; Kim, Y.; Kim, H.J.; Kim, M.O.; Lee, K.W. Identification of CDK7 Inhibitors from Natural Sources Using Pharmacoinformatics and Molecular Dynamics Simulations. *Biomedicines* **2021**, *9*, 1197. <https://doi.org/10.3390/biomedicines9091197>

Academic Editor: Leonardo Caputo

Received: 12 July 2021

Accepted: 7 September 2021

Published: 10 September 2021

Publisher's Note: MDPI stays neutral with regard to jurisdictional claims in published maps and institutional affiliations.



Copyright: © 2021 by the authors. Licensee MDPI, Basel, Switzerland. This article is an open access article distributed under the terms and conditions of the Creative Commons Attribution (CC BY) license (<https://creativecommons.org/licenses/by/4.0/>).

Abstract: The cyclin-dependent kinase 7 (CDK7) plays a crucial role in regulating the cell cycle and RNA polymerase-based transcription. Overexpression of this kinase is linked with various cancers in humans due to its dual involvement in cell development. Furthermore, emerging evidence has revealed that inhibiting CDK7 has anti-cancer effects, driving the development of novel and more cost-effective inhibitors with enhanced selectivity for CDK7 over other CDKs. In the present investigation, a pharmacophore-based approach was utilized to identify potential hit compounds against CDK7. The generated pharmacophore models were validated and used as 3D queries to screen 55,578 natural drug-like compounds. The obtained compounds were then subjected to molecular docking and molecular dynamics simulations to predict their binding mode with CDK7. The molecular dynamics simulation trajectories were subsequently used to calculate binding affinity, revealing four hits—ZINC20392430, SN00112175, SN00004718, and SN00262261—having a better binding affinity towards CDK7 than the reference inhibitors (CT7001 and THZ1). The binding mode analysis displayed hydrogen bond interactions with the hinge region residues Met94 and Glu95, DFG motif residue Asp155, ATP-binding site residues Thr96, Asp97, and Gln141, and quintessential residue outside the kinase domain, Cys312 of CDK7. The *in silico* selectivity of the hits was further checked by docking with CDK2, the close homolog structure of CDK7. Additionally, the detailed pharmacokinetic properties were predicted, revealing that our hits have better properties than established CDK7 inhibitors CT7001 and THZ1. Hence, we argue that proposed hits may be crucial against CDK7-related malignancies.

Keywords: CDK7; cancer; pharmacophore; molecular docking; MD simulation; MM-PBSA; pharmacokinetic properties

1. Introduction

Cancer is one of the leading causes of death in the 21st century and the most critical obstruction for the upsurge of the global lifespan [1]. As a result, the pharmaceutical industry and scientific communities have all focused on reducing the cancer-related death

rate, with the expectation of rapid development of effective and safe cancer treatment. Generally, the genetic alteration in signaling pathways that control cell-cycle progression, apoptosis, and cell growth is the common hallmark of the disease progression [2]. Among the reasons mentioned above, the abnormal cell cycle is one of the most protruding features of tumor cells. Anomalous expression of cell-cycle-related proteins provides tumor cells their invasive, metastatic, drug-resistant, and anti-apoptotic properties [3]. The cell cycle is a highly regulated process managed by numerous checkpoints to safeguard the division and proliferation in an ideal way. The central machines that drive the cell-cycle progression are mediated by cyclin-dependent kinases (CDKs) and partner cyclins [4,5]. The CDKs are a family of approximately 20 serine/threonine kinases that regulate the fundamental processes [6]. CDKs are primarily divided into two main groups; the first ones are the cell-cycle linked CDKs (CDK1, 4, and 6) that directly regulate the cell-cycle progression, and the second ones are the transcription-linked CDKs (CDK7, 8, 9, 12, and 13) [7]. CDK7 is a unique member of the CDK family among transcription-associated kinases due to its dual function in cell-division control and transcription [8]. CDK7 forms a dimeric complex with MAT1, which is an element of various chromatin remodeling complexes. Furthermore, the dimeric complex with additional involvement of cyclin H is known as CDK-activating kinase (CAK), which phosphorylates the T-loop of corresponding CDK members (CDKs 1, 2, 4, and 6) to regulate the cell cycle [9,10]. The transcriptional regulation by CDK7 or CAK is performed by phosphorylating the carboxy-terminal domain (CTD) of RNA polymerase II at serine 5 and 7, as well as other transcription factors [11–13]. Bartkova et al., have identified the expression of CDK7 in normal and tumor cells for the first time [14]. According to recent studies, CDK7 overexpression is reported in various malignancies such as hepatocellular carcinoma, gastric cancer, oral squamous cell carcinoma, breast cancer, ovarian cancer, high-grade glioma, cholangiocarcinoma, pancreatic cancer, and colorectal cancer with aggressive clinicopathological features and poor prognosis [15–25]. As a result of CDK7's direct involvement in numerous cancers, it has become an attractive target in cancer therapy [26–28]. To date, only one ATP-bound human CDK7 crystal structure is known [29]. The structure reveals that the ATP-binding site is located in the cleft between the residues of the N-terminal and C-terminal lobes. Interestingly, CDK7 has a 44% sequence similarity with CDK2 with a reported root mean square deviation of 1.25 Å [29]. The available structural and functional information of CDK7 was exploited previously by researchers to develop inhibitors that can bind to the ATP-binding site of CDK7 [28,30–32]. The literature survey confirms that great progress has been made over the past few years in discovering and developing CDK inhibitors during the last decade. Still, unfortunately, very few inhibitors were reported effective against CDK7 due to adverse effects and low efficacy [30,31]. The CDK7 inhibitors are classified either as reversible or irreversible. The first selective, reversible small-molecule inhibitor identified against CDK7 was BS-181, inhibiting CDK7 with a half-maximal inhibitory concentration (IC₅₀) of 21 nM [33]. Interestingly, BS-181 was derived using computer-aided drug designing from roscovitine. Further studies based on BS-181 led to the identification of ICE0942 (CT7001) which inhibited CDK7 with an IC₅₀ of 40 nM and is currently under Phase I clinical trials [30,34,35]. The inhibitors mentioned above have demonstrated nanomolar potency against CDK7 while inhibiting numerous other CDK family members, limiting their usage as selective inhibitors [31]. Intriguingly, Nathanael's group identified THZ1, a phenylaminopyrimidine derivative, as the first irreversible ATP-competitive (covalent) inhibitor, inhibiting CDK7 with an IC₅₀ of 3.2 nM and showing less affinity towards other CDK members [36]. To further improve the potency and selectivity of THZ1, Syros Pharmaceuticals developed SY-1365 which inhibits CDK7 with an IC₅₀ of 84 nM and is currently under Phase I clinical trials [30]. Apart from small success in inhibiting CDK7, there is a continuous need for research in the design of selective inhibitors due to the dual role of CDK7 in cell-cycle regulation and transcription. A survey of literature reported numerous studies for inhibiting CDK7 considering in vitro or in silico strategies. However, a ligand- and structure-based pharmacophore study has not reported for CDK7 to date.

Therefore, the present study was undertaken to explore the molecular mechanism of the selective binding of inhibitors with CDK7 over CDK2. In the current study, ligand- and structure-based pharmacophore models were generated to obtain the key features responsible for CDK7 inhibition. The generated pharmacophore models were validated and used as 3D queries to screen a drug-like database of natural compounds. The obtained compounds were subsequently subjected to molecular docking for the identification of the binding mode with CDK7. Furthermore, molecular dynamics simulations were performed on individual complexes to study the stability and binding affinity of the potential inhibitors with CDK7 under physiological conditions. The identified hit compounds were then checked for their *in silico* selectivity towards CDK7 over CDK2, using molecular docking studies. Finally, the detailed *in silico* pharmacokinetic properties were predicted for the identified hits, which may be helpful for their optimization or synthesis for further studies.

2. Materials and Methods

2.1. Ligand-Based Pharmacophore Generation

The ligand-based pharmacophore can be built as either a qualitative (common feature pharmacophore) or quantitative (3D-QSAR) model [37]. Owing to the lesser number of inhibitors reported against CDK7 to date, a reliable 3D-QSAR model cannot be generated. Therefore, in the present study, a ligand-based common feature pharmacophore approach was selected. In the literature, two types of inhibitors were reported for CDK7 inhibition, *viz.* selective or non-selective [28,30,31]. Rationally, a small set of well-known selective inhibitors was selected as a training set for hypothesis generation [31]. The training set compounds were downloaded from the PubChem database in SDF format and checked manually in *Discovery Studio* (DS) v18 (www.accelrys.com (accessed on 25 March 2021)) Accelrys Inc. San Diego, CA, USA). The compounds were then energy minimized using the *Steepest Descent* algorithm with CHARMM force field in DS. Before pharmacophore generation, the *Feature Mapping* module of the DS was used to identify the most common features of the training set compounds. The pharmacophore model generation was then carried out with the Common Feature Pharmacophore Generation module of DS. This module is based on the Hip-Hop algorithm, which identifies the three-dimensional (3D) spatial arrangements of chemical *features* common to training set molecules. A maximum of 255 hypothesis conformations were generated using the *BEST* algorithm with an energy threshold of 20 kcal/mol. Ten pharmacophore models were generated with various parameters such as the rank of the hypothesis, features, direct hit, partial hit, and max fit. During the hypothesis generation, special weightage was given to well-known CDK7 inhibitors—CT7001 and THZ1—by applying Principal and Max Omit feat values 2 and 0, respectively, to ensure that the inhibitor's chemical features are considered in building pharmacophore space [38]. At the same time, other training set compounds were regarded as reasonably active, where all but one feature must map to the compound.

2.2. Structure-Based Pharmacophore Generation

To build a reliable structure-based pharmacophore model, a protein's 3D structural complex with a highly active ligand is a prerequisite. Lolli *et al.*, reported the first X-ray crystal structure in 2004 for CDK7 in complex with ATP [29]. Thenceforth, no other ligand-bound X-ray crystal structure was reported with CDK7. Interestingly, electron microscopy (EM)-derived CDK7 structure, bound with the highly selective covalent inhibitor, THZ1, was deposited recently in Protein Data Bank (PDB) (PDB ID: 6XD3) [39]. The structure was downloaded and prepared in DS using the Clean Protein module. The unwanted molecules were removed, and the Receptor-Ligand Pharmacophore Generation module was used to generate the pharmacophore model. This module develops selective pharmacophore models based on protein–ligand interactions [40]. The *BEST* algorithm was opted for the conformation generation with the flexible fitting method, which generates ten hypotheses with different feature sets and selectivity scores. The best hypothesis was selected based on validation parameters and key interacting features with active site residues.

2.3. Validation of the Pharmacophore

Validation of the pharmacophore model is an essential step for its selection and evaluation. In the present study, two commonly used validation approaches, mainly, the receiver operating characteristic (ROC) curve and the Güner–Henry (GH) approach, were used [41,42]. The ROC curve analysis was performed during hypothesis generation in both ligand- and structure-based procedures. First, a small dataset was prepared with known active and inactive compounds. The four compounds used for pharmacophore generation were considered as known actives, and the other eight were taken as inactive. The top three hypotheses from each approach were selected and further validated with a second validation technique, the GH or decoy set method. A decoy set of 110 compounds was generated with 6 already known active inhibitors of CDK7 ($IC_{50} < 100$ nm) [30,31] and 104 inactive compounds. The Ligand Pharmacophore Mapping module in DS was used to screen the decoy dataset. The resulting mapping data were used for assessment of the pharmacophore quality by evaluating the following equation:

$$GF = \left(\frac{Ha}{4HtA} \right) (3A + Ht) \times \left\{ 1 - \frac{Ht - Ha}{D - A} \right\}$$

The selected and validated hypotheses from the ligand- and structure-based pharmacophore procedures were exploited as 3D queries to screen four natural compound databases in DS.

2.4. Drug-like Database Generation and Virtual Screening

Four natural compound libraries (ZINC, SuperNatural2, ExiMed, and InterBioScreen) were considered in the present study. To retrieve the drug-like small-molecule compounds from these libraries, it is recommended to filter the huge number of compounds during early steps to save time and unnecessary effort at a later stage in drug discovery [43,44]. Therefore, the libraries were filtered at first with Lipinski's rule of five (Ro5) and then for their ADMET (absorption, distribution, metabolism, excretion, and toxicity) properties in DS [45,46]. The validated hypotheses from the ligand- and structure-based approaches were then used to map the compounds using the Ligand Pharmacophore Mapping protocol in DS, with the FAST algorithm for generating the conformations with the flexible fitting method. The obtained compounds were then checked manually aligning with the generated models, and the most appropriate ones were selected for the molecular docking study.

2.5. Molecular Docking

Molecular docking is a productive and cost-effective technique in computational drug design to identify and assess molecular interactions between the ligands and receptors [47]. In the present work, the aforementioned drug-like database constructed from natural sources was used for docking with the active site of CDK7 using the Genetic Optimization for Ligand Docking (GOLD v5.2.2) program [48]. The only available inhibitor-bound structure of CDK7 (PDB ID: 6XD3) was used for the molecular docking study. The active site for molecular docking was defined within a 13.10 Å radius around the THZ1, using DS's Define and Edit Binding Site module. The docking sphere's X, Y, and Z coordinates were 116.84, 95.12, and 79.66, respectively. In general, ten docking runs/ligand were performed for consensus generation. For the scoring of ligands, the commonly used scoring function-GoldScore fitness was used. The GoldScore fitness function is a molecular mechanics-like function optimized for predicting the ligand-binding site considering hydrogen bonding energy, van der Waals energy, metal interactions, and torsion deformations [49]. Higher GoldScore than reference (REF) inhibitors were used as a cut-off criterion for the selection of potential CDK7 binders. The compounds were further filtered based on their binding mode and vital residual interactions with active site residues reported as necessary for inhibiting CDK7 in the cell.

2.6. Molecular Dynamics Simulation

Molecular dynamics (MD) simulations were conducted using the Groningen Machine for Chemical Simulations (GROMACS v5.1.5) to understand better the molecular interaction mechanism of protein and potential hit chemicals under physiological settings in a better way [50]. The simulation parameters and coordinates of CDK7 and potential hit compounds were generated using CHARMM27 force field in GROMACS and SwissParam, respectively [51,52]. The TIP3P water model was used for hydration during the simulation run, and the prepared system was energy minimized with a force of 10 kJ/mol to avoid steric hindrance. The equilibration step was performed under NVT and NPT ensembles for 500 ps at 300 K, using a V-rescale thermostat and Parrinello–Rahman barostat, respectively [53,54]. All the simulations were run under periodic boundary conditions for 50 ns. The MD simulation trajectories were analyzed using DS and visual molecular dynamics (VMD) [55].

2.7. Binding Free Energy Calculations

The docking studies used to calculate the binding affinity for the target protein ignores the flexibility of the protein. Despite the advantage of screening large libraries of ligands in a short time, the docking scoring functions often lead to inconsistent results [56]. Therefore, a more reliable method, molecular mechanics Poisson–Boltzmann surface area (MM-PBSA), is generally used to rank the simulated complexes. The combined MD simulations and MM-PBSA calculations can incorporate the conformational fluctuations and entropic contributions to the binding energy [57]. The *g_mmpbsa* plugin tool in GROMACS was used to calculate the binding free energy from MD simulation trajectories [58]. The precise method used to calculate the binding free energy can be found elsewhere [59]. In general terms, the binding free energy of the protein–ligand complex in the solvent can be calculated as

$$\Delta G_{bind} = G_{complex} - (G_{protein} + G_{ligand})$$

where $G_{complex}$ is the total free energy of the protein–ligand complex whereas $G_{protein}$ and G_{ligand} are the total free energies of the protein and ligand alone in the solvent, respectively. The final ΔG_{bind} value for the CDK7–ligand complex was computed as the average value from the last 40 to 50 ns of the MD simulation trajectories.

2.8. In Silico Specificity over CDK2

Designing small-molecule inhibitors with selectivity profiles that will ultimately be successful in the clinic is a huge concern in kinase drug research due to higher similarities among the family members [60,61]. The literature survey reveals that CDK7 shares high similarities with one of its family members, CDK2 [29]. Therefore, to select a specific inhibitor for CDK7, we performed molecular docking of the selected hits from MD simulation analysis with CDK2. The crystal structure of CDK2 in complex with CT7001 was obtained from PDB (PDB ID: 5JQ5) [62]. As mentioned earlier, the structure was prepared in DS, and the GOLD program was used for molecular docking with similar docking parameters. The results were analyzed based on docking scores and fundamental residual interactions.

2.9. In Silico Prediction of Pharmacokinetic Properties

Predicting the pharmacokinetic properties (PK) using in silico tools is a common step in drug discovery to identify novel inhibitors [38,63,64]. The PK properties, including sub-categories in absorption, distribution, metabolism, excretion, and toxicity of a particular compound, were considered. The detailed in silico prediction of the PK properties might be helpful for further optimization of the selected hit as a successful leader. Therefore, in the present study, PK properties were predicted using an online webserver, *pkCSM* [65]. The selected hits were converted to their SMILES format in BIOVIA Draw and used as input for assessing their properties (<http://biosig.unimelb.edu.au/pkcsm/> (accessed on

30 May 2021)). The output results were analyzed according to the threshold values and compared with REF inhibitors CT7001 and THZ1 used in the study.

3. Results

The identification of prospective and specific inhibitors of CDK7 was conducted in the present study using several computational methodologies. A general overview of the study is depicted (Figure 1).

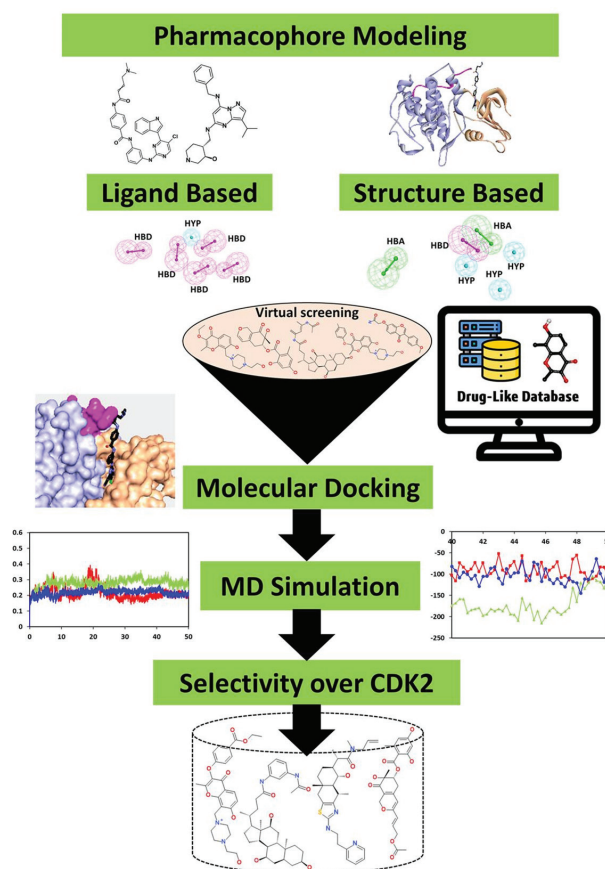


Figure 1. Schematic workflow for ligand and structure-based drug design used in the present study.

3.1. Ligand-Based Pharmacophore Generation

A qualitative common feature pharmacophore model was generated using a small group of selective inhibitors known against CDK7 (Figure 2).

The Feature Mapping module in DS was used to select the most common features present in the training set compounds, which revealed a higher number of hydrogen bond donor (HBD), hydrogen bond acceptor (HBA), ring aromatic (RA), hydrophobic (HYP), and positive ionizable (PI) features. The obtained information was then used as input for the pharmacophore generation. A total of ten hypotheses (Hypo) were generated with a narrow range of ranking scores (67.71 to 69.73), indicating that all ten models' features were spatially ordered. A deeper insight revealed that a minimum of 3–5 HBD features was present in all the hypotheses. A detailed overview of the generated hypothesis is given (Table 1).

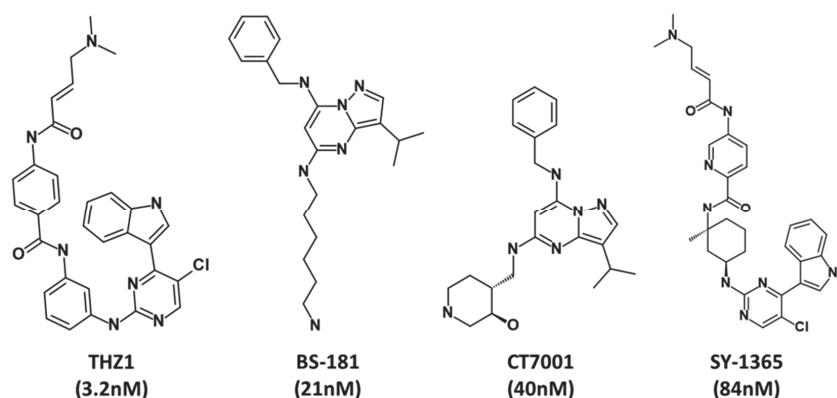


Figure 2. The two-dimensional structures of the compounds used as a training set for ligand-based common feature pharmacophore generation.

Table 1. The chemical features of 10 hypotheses that were generated for CDK7 using the *Hip-Hop* algorithm.

Sr. No.	Features ^a	Rank ^b	Direct Hit ^c	Partial Hit ^d	Max Fit ^e
Hypo1	HYA, HBD, HYP, HBD, HBD, HBD	69.73	1111	0000	6
Hypo2	HYA, HYA, HBD, HYP, HBD, HBD, HBD	69.51	1111	0000	7
Hypo3	HYA, HBD, HYP, HBD, HBD, HBD	68.80	1111	0000	6
Hypo4	RA, HYA, HYP, HBD, HBD, HBD	68.72	1111	0000	6
Hypo5	RA, HYA, HYP, HBD, HBD, HBD	68.39	1111	0000	6
Hypo6	RA, HYA, HYP, HBD, HBD	68.39	1111	0000	6
Hypo7	HYA, HBD, HBD, HBD, HBD, HBD	68.18	1111	0000	6
Hypo8	HYA, HBD, HYP, HBD, HBD, HBD	67.86	1111	0000	6
Hypo9	HYA, HBD, HYP, HBD, HBD, HBD	67.79	1111	0000	6
Hypo10	HYA, HBD, HYP, HBD, HBD, HBD	67.71	1111	0000	6

^a Features: HBA—hydrogen bond acceptor, HBD—hydrogen bond donor, HYP—hydrophobic, RA—ring aromatic. ^b Rank: Higher the ranking score, probability of chance correlation is less. ^c Direct hit: Indicates whether (1 or 0) a training set molecule mapped every feature in hypothesis. ^d Partial hit: A training set molecule mapped every but one feature in hypothesis. ^e Max fit: Maximum number of features in a hypothesis.

As mentioned in the Section 2, a validation step with ROC was performed simultaneously during the generation of the hypothesis. The ROC results revealed that Hypo1, Hypo2, and Hypo7 showed the highest specificity score of 0.75, 0.87, and 0.87, respectively (Table S1). The specificity score is the fraction of the genuinely inactive compounds being correctly recognized, and its value ranges from zero to one [66]. Therefore, the hypotheses mentioned above were selected for further analysis based on ROC analysis (Figure S1).

3.2. Structure-Based Pharmacophore Generation

The CDK7 structure consists of an N- and C-terminal, which includes the kinase domain of the protein ranges from 12 to 295 amino acids (Figure 3A,B). The ATP-binding region of the protein primarily contains residues 90 to 170 (Figure 3C,D).

The *Receptor-Ligand Pharmacophore Generation* protocol generated a total of ten hypotheses with five to six features. A minimum of three to four features was hydrophobic in all the hypotheses, and the selectivity score ranged from 8.79 to 10.31. A detailed summary of the hypothesis, such as the number and types of features, and selectivity score, is given (Table 2). The ROC analysis further revealed Hypo1, Hypo3, and Hypo4 displayed a specificity value of 0.75, 0.75, and 0.87 in terms of identifying inactive compounds; therefore, these hypotheses were initially selected for further study (Table S2 and Figure S1).

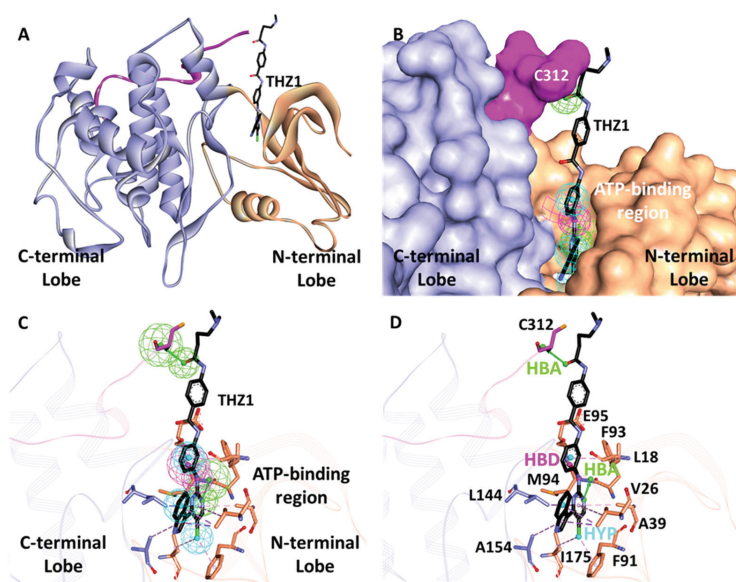


Figure 3. Generation of the structure-based pharmacophore. (A) CDK7 in complex with THZ1 was used to generate pharmacophore hypothesis. The N- and C-terminal of CDK7 are shown in tan and purple color, respectively. The region outside of the kinase domain is shown in pink. THZ1 is shown as a black stick. (B) The 3D representation of the pharmacophore inside the ATP-binding pocket of CDK7. (C,D) Mapping of pharmacophore hypothesis with the ATP-binding site residues and residue located outside the kinase domain Cys312 of CDK7. The surrounding residues are shown as sticks, and the hypothesis features are represented as hydrogen bond donor (HBD, magenta), hydrophobic (HYP, cyan), and hydrogen bond acceptor (HBA, green).

Table 2. The chemical features of 10 hypotheses that were generated for CDK7, using structure-based pharmacophore modeling.

Sr. No.	Number of Features	Features Set	Selectivity Score
Hypo1	6	HBA, HBA, HBD, HYP, HYP, HYP	10.31
Hypo2	6	HBA, HBD, HYP, HYP, HYP, HYP	10.31
Hypo3	6	HBA, HBD, HYP, HYP, HYP, HYP	10.31
Hypo4	6	HBA, HBA, HBD, HYP, HYP, HYP	10.31
Hypo5	6	HBA, HBA, HBD, HYP, HYP, HYP	10.31
Hypo6	6	HBA, HBA, HBD, HYP, HYP, HYP	10.31
Hypo7	6	HBA, HBA, HYP, HYP, HYP, HYP	9.39
Hypo8	5	HBA, HBD, HYP, HYP, HYP	8.79
Hypo9	5	HBA, HBD, HYP, HYP, HYP	8.79
Hypo10	5	HBA, HBD, HYP, HYP, HYP	8.79

3.3. Pharmacophore Validation

Hypothesis validation is an essential step in pharmacophore modeling to check the performance of the hypothesis generated. The two commonly used approaches, ROC and GH, were used to validate the generated hypotheses [41,42]. Based on ROC, we initially selected the top three hypotheses from both pharmacophore approaches as mentioned in the above sections (Figure S1). Then, selected hypotheses were further subjected to validation by the GH approach. A test set of 106 inactive and 6 active ($IC_{50} < 100$) compounds were compiled and named as decoy set [30,31]. The mapping analysis revealed that in the ligand-based approach, Hypo7 was found to have the highest GH score of 0.75, followed by Hypo2 and Hypo1. On the other hand, in the structure-based approach, Hypo4 displayed

a GH score of 0.83, followed by Hypo3 and Hypo1. A detailed analysis of the GH method for both approaches is shown (Table 3).

Table 3. Pharmacophore validation of ligand- and structure-based hypotheses by the Güner-Henry approach.

Sr. No.	Parameters	Ligand-Based			Structure-Based		
		Hypo1	Hypo2	Hypo7	Hypo1	Hypo3	Hypo4
1	Total number of compounds in the database (D)	110	110	110	110	110	110
2	Total number of active compounds in the database (A)	6	6	6	6	6	6
3	Total number of hits retrieved by pharmacophore model from the database (Ht)	11	8	5	3	4	2
4	Total number of active compounds in the hit list (Ha)	5	5	4	2	3	2
5	% Yield of active ((Ha/Ht) × 100)	45.45	62.5	80	66.66	75	100
6	% Ratio of actives ((Ha/A) × 100)	83.33	83.33	66.66	33.33	50	33.33
7	False negatives (A-Ha)	1	1	1	4	3	4
8	False positives (Ht-Ha)	5	3	3	1	1	0
9	Goodness of fit score (GF)	0.51	0.65	0.75	0.57	0.68	0.83

Hypothesis Comparison

The validation results confirmed that Hypo7 (Pharm-A) and Hypo4 (Pharm-B) from ligand- and structure-based approaches, respectively, have the potential to differentiate between the active and inactive compounds of a given dataset. Therefore, these hypotheses can be further utilized for the process of virtual screening. Furthermore, the detailed inspection reveals that Pharm-A includes five HBD and one HYP feature (Figure 4A). On the other hand, Pharm-B has one HBD, two HBA, and three HYP characteristics (Figure 4C). Thus, it can be seen that the structure-based hypothesis includes more diverse features than the ligand-based hypothesis.

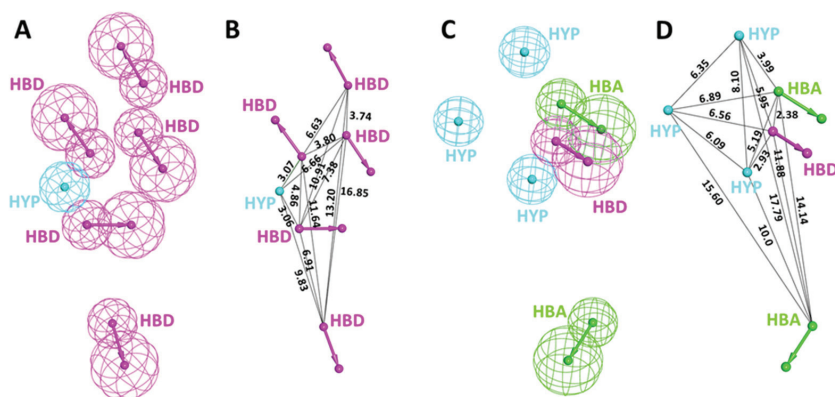


Figure 4. The selected pharmacophore models from the (A) ligand-based and (C) structure-based approach with the (B,D) interfeature distance between individual features of both models, respectively.

Interestingly, the superimposition of the Pharm-B in the active site reveals that the HBA feature situated outside of the cluster is responsible for interaction with Cys312, which is reported to provide selectivity and a covalent nature for interaction with CDK7 inhibitors (Figure 3C,D). On the contrary, this is mimicked by HBD in the case of Pharm-A. The interfeature distance was also calculated for both hypotheses, displaying the distance between individual features in Å (Figure 4B,D).

3.4. Drug-like Database and Virtual Screening

To reduce the cost and time of the screening process, we first filtered the compound libraries based on their Lipinski's Ro5 and ADMET properties (Figure 5 and Table S3), as suggested in previous reports [43,44]. Ro5 states that compounds have drug-like characteristics

when the AlogP value ≤ 5 , while HBD and HBA numbers are ≤ 5 and 10, respectively. The molecular weight of the compounds was extended beyond $Ro5 \leq 600$ Da to obtain a greater number of compounds for the screening process. In ADMET descriptors, the properties encompassing blood–brain barrier (BBB) permeability (BBBp), solubility, absorption, hepatotoxicity, and CYP2D6 were considered. The compounds were evaluated as drug-like only if they had an absorption level of 0, with solubility and BBBp level of 3. Furthermore, the compounds which predicted false value in CYP2D6 and hepatotoxicity properties were considered. The application of filters resulted in a database of 57,578 drug-like compounds (Figure 5).

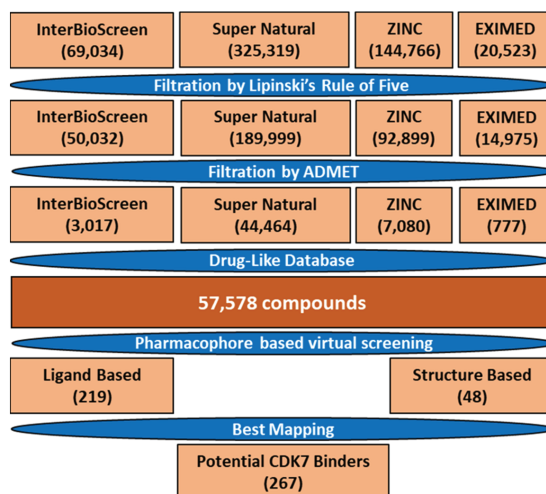


Figure 5. Generation and virtual screening of the natural drug-like database. Four natural compound libraries—InterBioScreen, SuperNatural2, ZINC, and ExiMed were used in the present study.

Selected pharmacophore models were then used to screen the database, and the analysis revealed that Pharm-A and Pharm-B mapped a total of 219 and 48 compounds, respectively (Figure 5). Additional manual inspection of the obtained 267 compounds resulted in 195 compounds that mapped correctly on the hypothesis. The selected compounds were then subjected to molecular docking with CDK7.

3.5. Molecular Docking

The THZ1-bound structure (PDB ID: 6XD3) revealed that it could target both the ATP-binding site as well as the site outside the kinase domain (Figure S2). A deeper inspection of the active site revealed hydrophobic interactions with residues Gly21, Lys41, Phe91, Leu144, Ala154, and hydrogen bonding with residues Met94, Glu95, Asp155, and Cys312 are essential for THZ1 interactions with CDK7. Before the docking experiment, the validation of the docking program GOLD was performed by re-docking the bound inhibitor THZ1. The results displayed a root mean square deviation $< 2 \text{ \AA}$ between the docking pose and co-crystallized THZ1 pose, confirming that GOLD is suitable for our docking study (Figure S3). The REF inhibitor, CT7001, an ATP-competitive CDK7 inhibitor, displayed a GoldScore of 56.48, and THZ1, the first covalent CDK7 inhibitor, displayed a GoldScore of 55.80 (Tables S4 and S5). During the docking experiment, the compounds with better scores than both the REF inhibitors were selected initially. Finally, the compounds were filtered based on fundamental molecular interactions with the active site residues mentioned above. Our analysis revealed that the docked compounds obtained from Pharm-A followed a non-competitive mode for binding similar to CT7001. In contrast, compounds obtained from Pharm-B showed a competitive binding mode similar to THZ1. The GoldScores and SMILES IDs of the selected compounds are shown (Tables S4 and S5).

3.6. Molecular Dynamics Simulations

The docking results were further validated using MD simulations. A total of 24 CDK7 bound inhibitor complexes were simulated individually for 50 ns in the present study. For comparative analysis, REF inhibitors (CT7001 and THZ1) were also simulated under similar conditions. The stability of the simulated complexes during the MD run was scrutinized by analyzing the root mean square deviation (RMSD) and root mean square fluctuation (RMSF) plots. The binding affinity of the compounds towards CDK7 was calculated through MM-PBSA. Compounds and inhibitors were ranked according to the binding free energy (Tables S4 and S5). The compounds which failed to show stability during the simulation and desirable binding free energy (ΔG) values were removed from the analysis. Lastly, based on the stable binding mode, four molecules were selected and considered as hits against CDK7 (Table S6). It is noteworthy that Hit1 and Hit2 are obtained from the ligand-based approach, while Hit3 and Hit4 are from the structure-based approach.

3.6.1. Root Mean Square Deviation and Fluctuations

The residual deviations and fluctuations were determined using backbone RMSD and RMSF analyses [67]. The backbone RMSD for CT7001, Hit1, and Hit2 demonstrated that simulated systems displayed steady-state stability after 10 ns of run time (Figure 6A). A slight bump was observed for CT7001 near 20 ns. Hit1 showed an average RMSD value of 0.27 nm, whereas a similar average value of 0.21 nm was observed for Hit2 and CT7001 (Table S6). Although the RMSD for Hit3, Hit4, and THZ1 showed stable RMSD after 5 ns, only a tiny bump was observed in the case of Hit3 near 30 ns (Figure 6C). The average RMSD value for Hit3 was 0.24 nm, whereas Hit4 and THZ1 displayed a similar value of 0.22 nm (Table S5). The RMSD values of all the simulated compounds declined after 40 ns and remained constant until the endpoint (Figure 6A,C). The RMSF is another essential parameter for the identification of the rigid and flexible region of the protein. It can be used to assess the flexibility of the backbone elements of the protein structure. The backbone RMSF was measured for all four hits and REF inhibitors (Figure 6B,D). The average RMSF value for Hit1, Hit2, Hit3, and Hit4 was 0.11, 0.09, 0.10, and 0.09 nm, respectively (Table S6). The REF inhibitors also showed similar average RMSF values of 0.09 and 0.11 for THZ1 and CT7001, respectively (Table S6). Significant fluctuations were observed for Hit1 at residues 15 and 167, Hit2 at residue 303, and CT7001 at residue 312 (Figure 6B). The observed residues are not part of the ATP-binding pocket; except these, no significant fluctuations were observed. Broadly, all simulated systems displayed <0.3 nm of RMSD and RMSF values, indicating no substantial deviations and changes, which can influence the structural stability of CDK7.

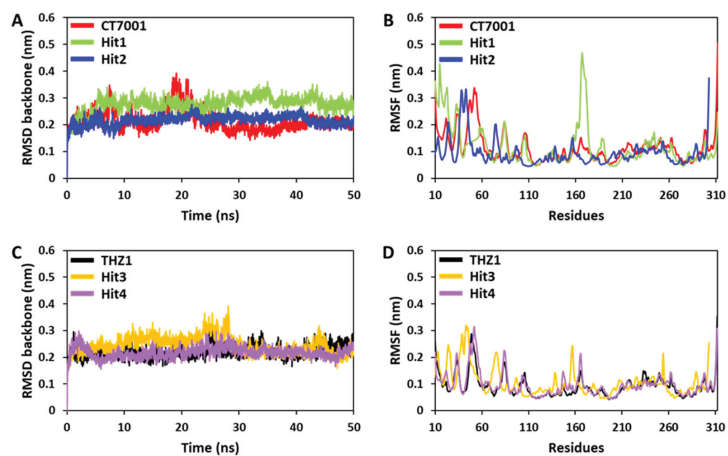


Figure 6. MD simulation analyses display the backbone RMSD and RMSF for (A,B) CT7001, Hit1, and Hit2, respectively, and (C,D) THZ1, Hit3, and Hit4.

3.6.2. Binding Free Energy Analysis

The MD simulation trajectories were used for the binding free energy (ΔG) calculations. A total of 40 snapshots were taken from the last 10 ns of stable trajectories. The REF inhibitors, CT7001 and THZ1, showed an average ΔG value of -90.58 and -91.48 kJ/mol, respectively (Figure 7 and Table 4).

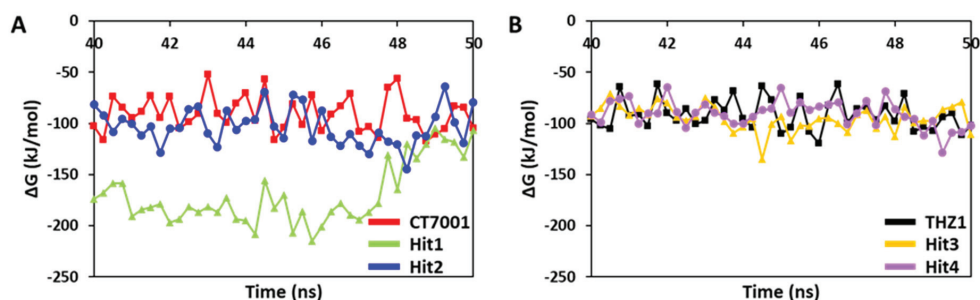


Figure 7. Binding free energy (ΔG) analysis for (A) CT7001, Hit1, and Hit2, and (B) THZ1, Hit3, and Hit4.

Table 4. The distribution of the total binding free energy scores for reference inhibitors and identified hits with CDK7 calculated through MM-PBSA methodology.

Inhibitors	van der Waals (kJ/mol)	Electrostatic (kJ/mol)	Polar Solvation (kJ/mol)	SASA Energy (kJ/mol)	Binding Energy ΔG_{bind} (kJ/mol)
Hit1	-191.19 ± 14.45	-309.22 ± 30.04	355.74 ± 44.97	-25.34 ± 1.40	-170.01 ± 29.50
Hit2	-164.36 ± 14.68	-47.28 ± 20.40	128.50 ± 26.24	-20.02 ± 1.73	-103.17 ± 17.65
Hit3	-167.45 ± 10.86	-22.27 ± 7.28	115.57 ± 17.06	-20.50 ± 1.07	-94.66 ± 12.26
Hit4	-147.54 ± 11.28	-17.71 ± 9.15	91.10 ± 13.54	-16.44 ± 1.65	-90.59 ± 12.80
THZ1	-151.40 ± 11.25	-22.06 ± 15.20	98.27 ± 18.60	-16.29 ± 1.06	-91.48 ± 14.79
CT7001	-181.13 ± 13.51	-44.09 ± 16.30	154.73 ± 31.72	-20.09 ± 1.20	-90.58 ± 17.08

The ΔG values of REF inhibitors can be considered as threshold values for the selection and ranking of hits. Our results demonstrated that a total of four compounds showed better ΔG than REF inhibitors (Table 4). The average ΔG for Hit1, Hit2, Hit3, and Hit4 was -170.01 , -103.17 , -94.66 , and -90.59 kJ/mol, respectively. Interestingly, Hit1 displayed a significantly better binding affinity towards CDK7 than other hits and REF inhibitors. The ΔG values were further decomposed into individual components (Table 4). The decomposition showed that van der Waals interaction contributed significantly to the binding of hits with CDK7, followed by electrostatic and SASA energy. In addition, the polar solvation contributed positively to the binding and therefore opposed the complex formation.

3.6.3. Binding Mode Analysis

The binding mode of the selected hits with CDK7 was evaluated using the average structure calculated from the last 10 ns of MD simulation trajectories. All the CDK7/ligand structures were superimposed in DS (Figure S4). Accordingly, the superimposition revealed that Hit1 and Hit2 occupied the ATP-binding pocket of CDK7, similar to that of CT7001 (Figure 8). A deeper insight into the molecular interactions revealed that CT7001 forms three hydrogen bonds with the ATP-binding site's hinge region residues Met94 and Asp97, and DFG (Asp-Phe-Gly) motif residue, Asp155 (Figure 8A). The binding of CT7001 in the active site is also strengthened by van der Waals interactions with Leu18, Gly19, Glu20, Gly21, Thr25, Ile40, Asp92, Phe93, Glu95, Thr96, Asn141, Asn142, and π -alkyl interactions with Ala24, Val26, Ala39, Ile75, Phe91, Leu144, Ala154 (Figure 8D). Our Hit1 formed one hydrogen bond with hinge region residue Met94 (Figure 8B), van der Waals interactions with Leu18, Gly19, Glu20, Gly21, Thr25, Lys28, Phe93, Thr96, and Leu144, and π -alkyl

interactions with Ala24, Val26, and Lys41 (Figure 8E). Hit2 forms a hydrogen bond with hinge region residue Met94 and DFG motif residue Asp155 (Figure 8C). Additionally, the van der Waals interactions with Gly19, Glu20, Gly21, Ala39, Lys41, Phe91, Glu95, Thr96, Asp97, Lys139, Asn141, Asn142, and π -alkyl interactions with Leu18, Val26, Phe93, Leu144, Cys312 were also observed (Figure 8F). Table S7 exhibits the detailed overview of H-bond distances and atoms involved in interactions with CT7001, Hit1, and Hit2.

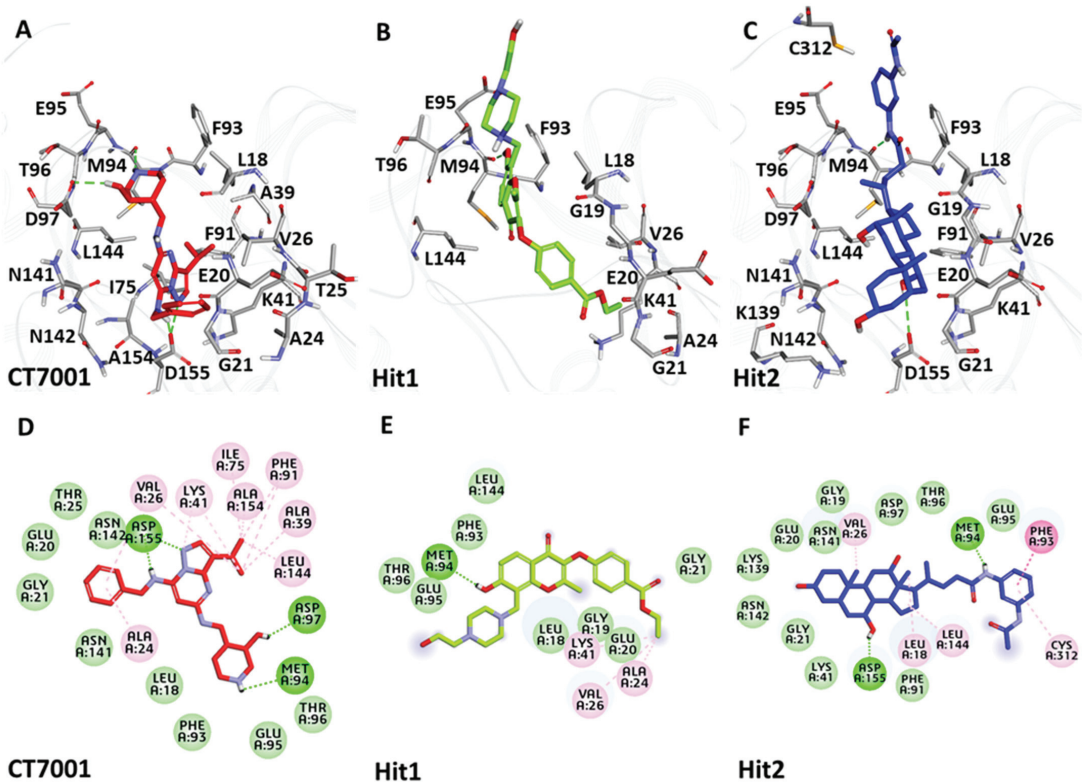


Figure 8. Binding mode and intermolecular interactions of CT7001 (A,D), Hit1 (B,E), and Hit2 (C,F) with CDK7. Upper and lower panel represents the interactions in 3D and 2D, respectively. The protein in the background is shown with grey lines, whereas interacting residues are shown as grey sticks. Dark green dashed lines indicate hydrogen bonds, light green: van der Waals, while the π - π and π -alkyl interactions are shown in pink.

The superimposition of the hits inside the CDK7 active site revealed that Hit3 and Hit4 followed binding mode as seen for THZ1, indicating the hits' covalent nature (Figure S4). Detailed inspection of molecular interactions revealed that THZ1 forms hydrogen bonds with hinge region residues Met94, Glu95, and Ala154, and DFG motif residue Asp155 (Figure 9A). Unfortunately, a hydrogen bond with Cys312 was not observed during MD simulation, which was observed in the crystal structure of CDK7 with THZ1 (PDB ID: 6XD3). THZ1 also forms van der Waals interactions with active site residues, Glu20, Gly21, Phe91, Phe93, Thr96, Arg309, Pro310, Asn311, Cys312, and alkyl interactions with Leu18, Val26, Ala39, Lys41, Ile75, Leu144 (Figure 9D). Hit3 formed hydrogen bonds with residues Glu95 and Asn141 (Figure 9B). The van der Waals interactions for Hit3 with CDK7 were observed with Gly19, Lys41, Ile75, Phe91, Phe93, Met94, Asp97, Leu144, Ala154, Asn311, whereas alkyl interactions were observed with Leu18, Val26, Ala39, Pro310, Cys312 (Figure 9E). Hit4 formed hydrogen bonds with residues Glu95, Asp97, and Cys312 (Figure 9C). Additionally, the van der Waals interactions for Hit4 with CDK7 were observed

HBA feature of CDK2, Leu83 (Figure S5B). Moreover, Hit2 also exhibited unfavorable bonds with Gln131 and Leu134 of CDK2 (Figure S5C). Furthermore, hit molecules from a structure-based approach establish only hydrophobic and van der Waals interactions with CDK2 residues, whereas no hydrogen bond was observed (Figure S5E,F). Hydrogen bonds with essential CDK2 residues Ile10, Leu83, Asp86, Lys89, and Asp145 were not observed for our identified hits with CDK2 [68,69]. On the other hand, our hits display interactions with CDK7 hinge residue Met94 through hydrogen bonds as maintained during MD simulation analysis (Figure 8). Additionally, our hits target crucial CDK7 residues, Pro310 and Cys312 (Figure 9), which are not observed in CDK2 (Figure S6). These residues, along with additional CDK7 residues Val100 and Thr96 are selective for CDK7 [68]. Our docking analysis indicated interactions with the residues mentioned above via van der Waals and hydrophobic π -bonds (Table S7). While the co-crystallized CDK2 inhibitor CT7001 established hydrogen bonds with residues Leu83 and Asp145, our docking results suggested that identified hits could not follow a similar binding pattern (Figure S5). Therefore, we argue that our identified hits may be selective for CDK7 over CDK2.

3.8. *In Silico Prediction of Pharmacokinetic Properties*

In the present study, PK properties were analyzed using the *pkCSM* webserver (Table 5). In absorption properties, the water solubility of the hits was predicted as being more soluble than the REF inhibitors, CT7001 and THZ1. According to the literature, a compound that exhibits a value >0.90 may have a high absorption rate in Caco-2 cell lines. The results indicated that CT7001 has higher permeability, whereas THZ1 has a moderate absorption rate. Interestingly, Hit2 and Hit3 also showed high absorption levels, whereas Hit4 may have a reasonable absorption level. Unfortunately, Hit1 failed to cross the Caco-2 cell line. The hits and REF inhibitors displayed an intestinal absorption rate of $>30\%$, which indicated that all might have high intestinal absorption. The skin permeability for the compounds was found below the threshold value >-2.5 , which confirmed that all compounds could easily cross the skin barriers. P-glycoprotein I, also known as multi-drug resistance protein 1 (MDR1), functions as a biological barrier by extruding toxins and xenobiotics outside of the cell. P-gp II or MDR2 functions as a phospholipid translocator. Results indicated that all the hits and REF inhibitors are P-gp substrates. The accumulation of these compounds can be reduced in specific tissues. P-gp I/II inhibition results showed that Hit2, Hit3, and THZ1 are predicted to inhibit both the variants studied. Hit1 was not predicted to inhibit P-gp II, whereas CT7001 was not predicted to inhibit P-gp I. Hit4 was not predicted to be a P-gp I/II inhibitor. In the distribution the following properties: volume of distribution (VDss), blood–brain barrier permeability (BBBp), and central nervous system (CNS) permeability (CNSp) were considered. VDss below 0.71 L/kg is considered low, and above 2.81 L/kg is considered high. The higher the VDss, more the drug is distributed in tissues. Here, CT7001 showed higher VDss, followed by Hit1, Hit3, and Hit2. Hit4 and THZ1 showed the least values of VDss. If a compound showed a value of >0.3 for BBBp and >-2 for CNSp, they can cross the BBB and CNS. Interestingly, all the hits and REF inhibitors were not predicted to be permeable for both the parameters; hence, chances of brain-related toxicities are negligible. Cytochrome P450 (CYP450) is a vital detoxification enzyme found in the liver. It oxidizes the xenobiotics to facilitate their excretion. The two main isoforms of cytochrome responsible for drug metabolism are 2D6 and 3A4, which were studied. The results indicate that none of the hits and REF inhibitors were predicted as substrates or inhibitors for the 2D6 isoform of CYP450. Unfortunately, Hit1, Hit3, and both REF inhibitors were predicted as 3A4 substrates and inhibitors. Hit2 and Hit4 were not predicted to be 3A4 inhibitors. Additionally, Hit4 was not predicted as a 3A4 substrate. Clearance can be used to calculate the rate at which drugs must be added to the circulation to maintain the steady-state plasma concentration. The clearance results showed that Hit1, CT7001, and Hit4 might have a higher clearance rate than Hit2, Hit3, and THZ1, which may have an increased half-life. The critical parameters of pharmacokinetic toxicity were

also studied. None of the hits and the REF inhibitors were predicted to be mutagenic in AMES toxicity prediction. The maximum tolerated dose and oral rat toxicity properties were also predicted for hits and REF inhibitors, and are reported in our study (Table 5). The inhibition of human ether-a-go-go-related gene (hERG), which encodes a potassium ion (K) channel with two subtypes, hERG I and hERG II, was also predicted. The hERG I inhibitors may lead to cardiotoxicity-related effects. Hit compounds were not predicted to be hERG I inhibitors. hERG II is known to play a role in insulin secretion; all hits, except Hit4, were predicted to be hERG II inhibitors, and therefore may affect the glucose level. The *pkCSM* hepatotoxicity results showed that all hits and REF inhibitors might have hepatotoxic effects, but the results predicted using DS showed that hits could not be hepatotoxic. Nevertheless, these effects can be further cleared via in vitro studies. Our results showed that none of the hits and REF inhibitors were involved in skin sensitization allergic reactions.

Table 5. In silico prediction of ADMET properties for reference inhibitors and identified hits.

ADMET Properties		Hit 1	Hit 2	Hit 3	Hit 4	CT7001	THZ1	Unit
Absorption	Water solubility	−3.57	−4.40	−5.18	−3.70	−3.18	−3.26	log mol/L
	Caco-2 permeability	0.01	1.00	1.09	0.45	1.26	0.86	log Papp in 10 ^{−6} cm/s
	IA (human)	64.37	84.75	95.29	60.14	89.43	93.01	% Absorbed
	Skin permeability	−2.74	−2.73	−3.14	−2.79	−2.73	−2.73	log Kp
	P-gp substrate	Yes	Yes	Yes	Yes	Yes	Yes	Yes/No
	P-gp I inhibitor	Yes	Yes	Yes	No	No	Yes	Yes/No
	P-gp II inhibitor	No	Yes	Yes	No	Yes	Yes	Yes/No
Distribution	VDss (human)	1.49	0.04	0.50	−0.08	2.13	−0.64	log L/kg
	BBBp	−1.33	−0.67	−0.83	−1.40	−0.84	−1.26	logBB
	CNSp	−3.69	−2.12	−2.92	−3.50	−2.66	−2.2	log PS
Metabolism	CYP2D6 substrate	No	No	No	No	No	No	Yes/No
	CYP2D6 inhibitor	No	No	No	No	No	No	Yes/No
	CYP3A4 substrate	Yes	Yes	Yes	No	Yes	Yes	Yes/No
	CYP3A4 inhibitor	Yes	No	Yes	No	Yes	Yes	Yes/No
Excretion	TC	1.08	0.10	0.18	0.77	0.88	0.48	log mL/min/kg
Toxicity	AMES toxicity	No	No	No	No	No	No	Yes/No
	Max. tolerated dose (human)	0.14	−1.47	−0.3	0.32	0.15	0.43	log mg/kg/day
	hERG I inhibitor	No	No	No	No	No	No	Yes/No
	hERG II inhibitor	Yes	Yes	Yes	No	Yes	Yes	Yes/No
	Oral rat acute toxicity	2.70	3.72	2.60	3.46	2.82	2.84	LD ₅₀ mol/kg
	Hepatotoxicity	Yes	Yes	Yes	Yes	Yes	Yes	Yes/No
Skin sensitization	No	No	No	No	No	No	Yes/No	

Abbreviation: IA—intestinal absorption, P-gp—P-glycoprotein, VDss—volume of distribution, BBBp—blood–brain barrier permeability, CNSp—central nervous system permeability, TC—total clearance, AMES—*Salmonella typhimurium* reverse mutation assay, hERG—human ether-a-go-go-related gene.

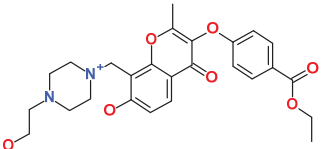
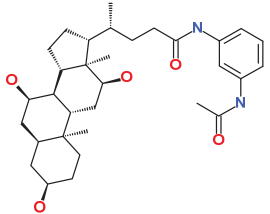
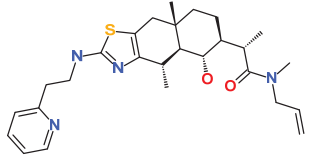
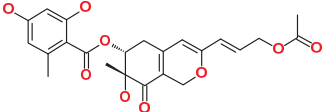
4. Discussion

Cyclin-dependent kinase 7 (CDK7) regulates the cell cycle and transcription and, therefore, plays a key role in cancer development and progression [70]. The role of CDK7 has been reported in multiple human cancers and, therefore, is considered a promising therapeutic target [30]. Several investigations have found CDK7 inhibitors so far; however, first-generation inhibitors have shown considerable adverse effects, limiting their usage in clinical trials [71]. Another reason reported for the failure of first-generation inhibitors is the higher level of structural similarity among CDK family members. In the case of CDK7, it shares a 44% sequence identity with its family member, CDK2 [29]. Therefore, many of the CDK7 inhibitors have been reported to target CDK2 [32]. However, only a few inhibitors with high selectivity for CDK7 have been identified in recent years, and they are now in the early stages of clinical studies [31]. Hence, the inhibitors which can selectively inhibit CDK7 are of primary importance. Since CDK7 plays such a critical role in cell proliferation and transcription, there is a constant need for research to find effective inhibitors that can

control overexpression and combat emerging cancer resistance. Therefore, we employed a ligand- and structure-based pharmacophore modeling approach complexed with a series of other computational methods as a valuable strategy for targeting CDK7 inhibition (Figure 1). The combination approach can retrieve more drug-like compounds from databases as both works on different principles [72,73]. To our knowledge, this is the first pharmacophore-based study to search for novel and selective CDK7 inhibitors. In the ligand-based approach, due to the small number of inhibitors known to date against CDK7 [31], a common feature approach was selected where a limited number of inhibitors are required as the training set (Figure 2) [43]. The only available covalent inhibitor, THZ1-bound structure (PDB ID: 6DX3), was used in the structure-based approach (Figure 3) [39]. Both approaches generated a total of ten hypotheses each (Tables 1 and 2). The hypotheses were validated with two well-known methods- ROC and GH approach [41,42]. According to our hypothesis validation outcomes Hypo7 and Hypo4 from the ligand- and structure-based approach, respectively, can filter out known active and inactive compounds (Table 3, Figure 4). As a result, both hypotheses were used for virtual drug-like database screening. The mapping resulted in 267 drug-like compounds showing the potential to interact with CDK7 (Figure 5). The binding potential of obtained compounds was then studied by a molecular docking study [74,75]. Two well-known selective CDK7 inhibitors, CT7001 and THZ1, were used in the docking studies for comparative analysis. Recently, Wang et al., reviewed the inhibitor design studies of CDK7 and concluded that one or more hydrogen bonds with ATP-binding site residues, Gly21, Phe91, Met94, Asp155, Thr170, and Cys312, located outside the kinase domain are responsible for the inhibition [30]. Therefore, we selected only those compounds that displayed a similar binding mode as CT7001 and THZ1, greater docking scores than both REF inhibitors, and key molecular interactions with residues mentioned above. The representative pose of THZ1 and CT7001 in the docking study displayed a GoldScore value of 55.8 and 56.48, respectively. The molecular docking results further revealed that 13 compounds from the ligand-based approach and 11 from the structure-based approach have a greater docking score than CT7001 and THZ1 (Tables S4 and S5). One of the major limitations of the docking study is that they do not consider real-time dynamics of the protein–ligand interaction [47]. To study the real-time dynamics, we employed MD simulation studies. The selected protein–ligand complexes were prepared and subjected to MD simulations [43,44,59]. For comparative study, the known inhibitors THZ1 and CT7001 were also simulated. The MD study revealed that all the simulated systems showed stable RMSD and RMSF < 0.3 nm (Figure 6 and Table S6), which are the criteria generally used in the stability assessment of simulated complexes [67,76]. We were further interested in studying the binding affinity of the simulated compounds compared to known inhibitors. For this purpose, a well-known method, MM-PBSA, was employed using the *g_mmpbsa* tool [58]. The analysis revealed that CT7001 showed average binding free energy of -90.58 kJ/mol, and THZ1 displayed -91.48 kJ/mol (Figure 7, Table 5). The previous reports confirm that the lower the binding free energy values, the higher the affinity of the molecules towards the protein [43,75,76]. A similar relationship was also observed in some combined in silico and in vitro studies [77,78]. Our analysis found that Hit1 displayed significantly better binding free energy, -170.01 kJ/mol compared to REF inhibitors; this was followed by Hit2 -103.17 , Hit3 94.66 , and Hit4 -90.58 . All the hits displayed better binding free energies than CT7001, whereas THZ1 showed slightly better binding affinity than Hit4. Although four other compounds demonstrated better binding energies than THZ1 and CT7001 (Table S5), they were not considered for further analysis because they displayed a slightly different binding mode than REF inhibitors with CDK7. The binding mode of the compounds was assessed using the average structure extracted from the last 10 ns MD simulation trajectories. CT7001 is known to inhibit CDK7 with an IC_{50} of 40 nM and CDK2 with an IC_{50} of 620 nM via an in vitro kinase assay [35]. The study by Hazel et al., demonstrated that MD simulation of CT7001/CDK7 could form hydrogen bonds with hinge region residue Met94, and G-rich loop residues Gly21, Asp137, and Asp155. Additionally, using the Asp155 mutant, it has been confirmed that interaction with

Asp155 is key for the selectivity of the CT7001 towards CDK7 [62]. Our study observed that Hit1 and Hit2 obtained a similar binding mode as CT7001 (Figure 8). Hit1 forms a hydrogen bond with hinge region residue Met94; unfortunately, molecular interaction with Asp155 was not observed. Hit2 was observed to form hydrogen bond interactions with Met94 and Asp155, which enhances the selectivity towards CDK7. Interestingly, Hit2 also forms alkyl interactions outside the kinase domain with Cys312, which is reported to provide a covalent nature to THZ1. The phenylaminopyrimidine derivative THZ1 is reported as the first covalent inhibitor for CDK7 with an IC_{50} of 3.2 nM [36]. The docking studies indicated that THZ1 targets the CDK7 kinase domain and outside the domain via interacting with Cys312 through a hydrogen bond. The study also indicated that mutation of Cys312 to Ser312 prevented the THZ1 binding with CDK7 in a covalent fashion. This confirms the role of Cys312 interaction in covalent inhibition [36]. However, there is no MD simulation study reported to date for THZ1 dynamics. Here, we obtained a similar binding mode as reported, but instead of a hydrogen bond, a van der Waals interaction was observed for THZ1 with Cys312 (Figure 9). This may happen due to the position of Cys312 as it is present at the last position or maybe due to a change in dynamics, as docking studies do not consider the protein flexibility. Our analysis revealed that THZ1 forms a hydrogen bond with hinge region residues Met94, Glu95, Ala154, and Asp155. Hit3 was observed to form hydrogen bonds with Glu95 and Asn141. Unfortunately, a hydrogen bond with Cys312 was not observed in the case of Hit3 but it formed a π -alkyl interaction with the Cys312, suggesting the compound may act as a covalent inhibitor. Hit4 binding mode revealed that it forms a hydrogen bond with Glu95, Asp97, and Cys312 located outside the kinase domain, important for covalent inhibition (Figure 9). As mentioned earlier, CDK7 has similarities with CDK2; we next investigated for selectivity of the identified hits. For this purpose, a molecular docking study was performed with the CDK2 crystal structure, using similar parameters. The docking results confirmed that the docking scores were less than the co-crystal ligand CT7001 of CDK2 (Table S8). The structural details reveal that residues Lys33, Asp86, Gln131, and Asp145 are responsible for the polar interactions [68]. The hydrogen bond with Leu83 of CDK2 was reported in more than 90% of the CDK2 inhibitor interactions [68]. Our docking results followed the same interactions for the REF inhibitors CT7001 and THZ1. Interestingly, hits were not found to interact with the polar interaction site of CDK2 via hydrogen bond. Hit1 formed one hydrogen bond with Thr14, and Hit2 formed a hydrogen bond with Asn132, and both the residues are not reported to contribute much to inhibitor interactions. Additionally, our hits formed various interactions with CDK7 residues, which are not similar in CDK2. The sequence alignment of CDK7 with CDK2 revealed that ATP-binding site residues (Leu18, Ala24, Thr25, Glu95, Thr96, Val100, and Gln141) and residues outside the kinase domain (Arg309, Pro310, Asn311, and Cys312) are aligned with different CDK2 residues (Figure S6). Interestingly, our hits were found targeting these residues via various types of interactions (Table S7). This indicates that identified hits might show selectivity for CDK7 (Figures 8 and 9). As part of the final assessment strategy, the detailed PK properties were assessed for REF inhibitors and hits, using the well-known tool *pkCSM* (Table 5). Results indicated that our hits showed slightly better PK properties than REF inhibitors. Among all, Hit4 was observed to be the best candidate in terms of absorption, distribution, metabolism, and toxicity parameters. Lastly, we provided the scaffolds comprised of the hits, IUPAC names, and database IDs (Table 6). Hit1 (ZINC20392430) and Hit4 (SN00262261) were observed to encompass benzoate scaffolds, while Hit2 (SN00112175) and Hit3 (SN00004718) were perceived to be pentamide and propanamide, respectively.

Table 6. The database ID, IUPAC name, and 2D representation of the final identified hits.

Inhibitor	Database ID	IUPAC Name	2D Representation
Hit1	ZINC20392430	ethyl 4-[7-hydroxy-8-[[4-(2-hydroxyethyl)piperazin-1-ium-1-yl]methyl]-2-methyl-4-oxo-chromen-3-yl]oxybenzoate	
Hit2	SN00112175	(4R)-N-(3-acetamidophenyl)-4-[(3R,5S,7R,8R,9S,10S,12S,13R,14S,17R)-3,7,12-trihydroxy-10,13-dimethyl-2,3,4,5,6,7,8,9,11,12,14,15,16,17-tetradecahydro-1H-cyclopenta[a]phenanthren-17-yl]pentanamide	
Hit3	SN00004718	(2S)-2-[(4S,4aS,5S,6S,8aS)-5-hydroxy-4,8a-dimethyl-2-[2-(2-pyridyl)ethylamino]-4a,5,6,7,8,9-hexahydro-4H-benzo[f][1,3]benzothiazol-6-yl]-N-allyl-N-methylpropanamide	
Hit4	SN00262261	[(6R,7R)-3-[(E)-3-acetoxyprop-1-enyl]-7-hydroxy-7-methyl-8-oxo-5,6-dihydro-1H-isochromen-6-yl] 2,4-dihydroxy-6-methyl-benzoate	

5. Conclusions

To identify new potential scaffolds against CDK7, two commonly used pharmacophore modeling approaches, ligand and structure-based, were used to generate hypotheses. The generated hypotheses were used for virtual screening of a drug-like database prepared from four natural compound databases. The filtered compounds were then subjected to molecular docking and subsequent molecular dynamics simulations for identification of their binding mode with CDK7. Additional ΔG calculations confirmed that four hits display a better binding affinity for CDK7 when compared with CT7001 and THZ1. Moreover, the selectivity of the identified hits was checked using molecular docking against CDK2, a close homolog of CDK7. Our results confirmed that the identified hits form polar and non-polar interactions with the residues unique to CDK7 (Ala24, Glu95, Thr96, Val100, Gln141, Pro310, Asn311, and Cys312), reported to enhance the selectivity. As a result, we recommend that future drug design studies focus on these residues in order to develop covalent inhibitors of CDK7, in line with earlier reports. Finally, the pharmacokinetic (PK) properties were investigated, and analyses revealed that hits have better PK properties when compared with CT7001 and THZ1. We argue that our identified hits will help to design novel drugs for CDK7.

Supplementary Materials: The following are available online at <https://www.mdpi.com/article/10.3390/biomedicines9091197/s1>, Figure S1. The pharmacophore models from both the approaches obtained after ROC validation. Figure S2. Molecular docking site used in the present study. The bound ligand THZ1 was used to define the docking sphere. Figure S3. Validation of docking parameters using co-crystallized ligand THZ1 (grey) and docked pose (black). Figure S4. Binding patterns of the reference inhibitors and the hits in the active site of CDK7. Superimposition (left) of THZ1, CT7001, Hit1, Hit2, Hit3, and Hit4 (left) and its enlarged view (right). The protein is shown as

grey color ribbon representation, and the ligands are shown with stick representation. Only polar hydrogen atoms are shown for clear visualization. Figure S5. The 2D molecular interactions of the reference inhibitors and identified hits with CDK2 crystal structure bound with CT7001 (PDB ID: 5JQ5). The dark green dashed lines indicating hydrogen bonds, light green: van der Waals, purple: π -sigma, red: unfavorable acceptor–acceptor, orange: π -cation, while the π - π and π -alkyl interactions are shown in pink. Figure S6. Sequence alignment of CDK7 (PDB ID: 6XD3) and CDK2 (PDB ID: 5JQ5) resulted in 44.4% identity and 67.1% similarity. The red boxes are used to show the differences between the active site and outside the active site residues (309–312) of both the proteins. The degree of identity ranges from dark cyan color (identical) to white color (non-identical). Table S1. Ligand-based pharmacophore validation using receiver operating characteristic (ROC) curve. Table S2. Structure-based pharmacophore validation using receiver operating characteristic (ROC) curve. Table S3. Details of different properties used for generation of drug-like database. Table S4. List of potential compounds obtained after molecular docking. A total of 13 compounds show a better GoldScore than reference (REF) inhibitor. The binding free energies obtained after MD simulation are also shown. Table S5. List of potential compounds obtained after molecular docking. A total of 11 compounds show better GoldScore than REF inhibitor. The binding free energies obtained after MD simulation are also shown. Table S6. Molecular docking and molecular dynamics simulation analysis of hits and reference inhibitors against CDK7. Table S7. Molecular interactions of reference inhibitors and hits with CDK7 active site residues acquired from stable molecular dynamics simulation trajectories. Table S8. The molecular docking scores of hits and reference inhibitors with CDK2 and CDK7.

Author Contributions: Conceptualization, V.K. and S.P.; methodology, V.K., S.P. and G.T.; software, V.K. and G.L.; validation, V.K. and S.P.; formal analysis, G.T., G.L. and H.-S.R.; investigation, V.K., S.P. and G.T.; resources, K.W.L.; data curation, V.K., S.P. and G.T.; writing—original draft preparation, V.K. and S.P.; writing—review and editing, V.K., S.P., G.T. and H.J.K.; visualization, V.K. and S.P.; supervision, K.W.L.; project administration, K.W.L., H.-S.R. and M.O.K.; funding acquisition, H.J.K., M.O.K. and Y.K. All authors have read and agreed to the published version of the manuscript.

Funding: This research was supported by the Neurological Disorder Research Program of the National Research Foundation (NRF) funded by the Korean Government (MSIT) (2020M3E5D9080660).

Institutional Review Board Statement: Not applicable.

Informed Consent Statement: Not applicable.

Data Availability Statement: Data are contained within the article.

Conflicts of Interest: The authors declare no conflict of interest.

References

1. Cui, W.; Aouidate, A.; Wang, S.; Yu, Q.; Li, Y.; Yuan, S. Discovering Anti-Cancer Drugs via Computational Methods. *Front. Pharmacol.* **2020**, *11*, 733. [CrossRef] [PubMed]
2. Sanchez-Vega, F.; Mina, M.; Armenia, J.; Chatila, W.K.; Luna, A.; La, K.C.; Dimitriadoy, S.; Liu, D.L.; Kantheti, H.S.; Saghafinia, S.; et al. Oncogenic Signaling Pathways in The Cancer Genome Atlas. *Cell* **2018**, *173*, 321–337.e10. [CrossRef] [PubMed]
3. Liu, K.; Zheng, M.; Lu, R.; Du, J.; Zhao, Q.; Li, Z.; Li, Y.; Zhang, S. The role of CDC25C in cell cycle regulation and clinical cancer therapy: A systematic review. *Cancer Cell Int.* **2020**, *20*, 1–16. [CrossRef] [PubMed]
4. Lim, S.; Kaldis, P. Cdks, cyclins and CKIs: Roles beyond cell cycle regulation. *Development* **2013**, *140*, 3079–3093. [CrossRef] [PubMed]
5. Barnum, K.J.; O’Connell, M.J. Cell Cycle Regulation by Checkpoints. *Methods Mol. Biol.* **2014**, *1170*, 29–40. [CrossRef] [PubMed]
6. Malumbres, M.; Harlow, E.; Hunt, T.; Hunter, T.; Lahti, J.M.; Manning, G.; Morgan, D.O.; Tsai, L.H.; Wolgemuth, D.J. Cy-clin-dependent kinases: A family portrait. *Nat. Cell Biol.* **2009**, *11*, 1275–1276. [CrossRef] [PubMed]
7. Galbraith, M.D.; Bender, H.; Espinosa, J.M. Therapeutic targeting of transcriptional cyclin-dependent kinases. *Transcription* **2019**, *10*, 118–136. [CrossRef]
8. Fisher, R.P. Secrets of a double agent: CDK7 in cell-cycle control and transcription. *J. Cell Sci.* **2005**, *118*, 5171–5180. [CrossRef] [PubMed]
9. Tassan, J.P.; Jaquenoud, M.; Fry, A.M.; Frutiger, S.; Hughes, G.J.; Nigg, E. In vitro assembly of a functional human CDK7-cyclin H complex requires MAT1, a novel 36 kDa RING finger protein. *EMBO J.* **1995**, *14*, 5608–5617. [CrossRef] [PubMed]
10. Martinez, A.-M.; Afshar, M.; Martin, F.; Cavadore, J.; Labbé, J.; Dorée, M. Dual phosphorylation of the T-loop in cdk7: Its role in controlling cyclin H binding and CAK activity. *EMBO J.* **1997**, *16*, 343–354. [CrossRef]

11. Cao, K.; Shilatfard, A. Inhibit Globally, Act Locally: CDK7 Inhibitors in Cancer Therapy. *Cancer Cell* **2014**, *26*, 158–159. [CrossRef] [PubMed]
12. Ramanathan, Y.; Rajpara, S.M.; Reza, S.M.; Lees, E.; Shuman, S.; Mathews, M.B.; Pe’Ery, T. Three RNA Polymerase II Carboxyl-terminal Domain Kinases Display Distinct Substrate Preferences. *J. Biol. Chem.* **2001**, *276*, 10913–10920. [CrossRef] [PubMed]
13. Glover-Cutter, K.; Larochele, S.; Erickson, B.; Zhang, C.; Shokat, K.; Fisher, R.P.; Bentley, D.L. TFIIH-Associated Cdk7 Kinase Functions in Phosphorylation of C-Terminal Domain Ser7 Residues, Promoter-Proximal Pausing, and Termination by RNA Polymerase II. *Mol. Cell. Biol.* **2009**, *29*, 5455–5464. [CrossRef] [PubMed]
14. Bartkova, J.; Zemanova, M.; Bartek, J. Expression of CDK7/CAK in normal and tumour cells of diverse histogenesis, cell-cycle position and differentiation. *Int. J. Cancer* **1996**, *66*, 732–737. [CrossRef]
15. Kim, J.; Cho, Y.-J.; Ryu, J.-Y.; Hwang, I.; Han, H.D.; Ahn, H.J.; Kim, W.Y.; Cho, H.; Chung, J.-Y.; Hewitt, S.M.; et al. CDK7 is a reliable prognostic factor and novel therapeutic target in epithelial ovarian cancer. *Gynecol. Oncol.* **2020**, *156*, 211–221. [CrossRef] [PubMed]
16. Zhang, Z.; Peng, H.; Wang, X.; Yin, X.; Ma, P.; Jing, Y.; Cai, M.-C.; Liu, J.; Zhang, M.; Zhang, S.; et al. Preclinical Efficacy and Molecular Mechanism of Targeting CDK7-Dependent Transcriptional Addiction in Ovarian Cancer. *Mol. Cancer Ther.* **2017**, *16*, 1739–1750. [CrossRef]
17. Greenall, S.A.; Lim, Y.C.; Mitchell, C.B.; Ensbey, K.S.; Stringer, B.W.; Wilding, A.L.; O’Neill, G.M.; McDonald, K.L.; Gough, D.J.; Day, B.W.; et al. Cyclin-dependent kinase 7 is a therapeutic target in high-grade glioma. *Oncogenesis* **2017**, *6*, e336. [CrossRef]
18. Lu, P.; Geng, J.; Zhang, L.; Wang, Y.; Niu, N.; Fang, Y.; Liu, F.; Shi, J.; Zhang, Z.-G.; Sun, Y.-W.; et al. THZ1 reveals CDK7-dependent transcriptional addictions in pancreatic cancer. *Oncogene* **2019**, *38*, 3932–3945. [CrossRef] [PubMed]
19. Patel, H.; Abduljabbar, R.; Lai, C.-F.; Periyasamy, M.; Harrod, A.; Gemma, C.; Steel, J.H.; Patel, N.; Busonero, C.; Jerjees, D.; et al. Expression of CDK7, Cyclin H, and MAT1 Is Elevated in Breast Cancer and Is Prognostic in Estrogen Receptor-Positive Breast Cancer. *Clin. Cancer Res.* **2016**, *22*, 5929–5938. [CrossRef]
20. Wang, Q.; Li, M.; Zhang, X.; Huang, H.; Huang, J.; Ke, J.; Ding, H.; Xiao, J.; Shan, X.; Liu, Q.; et al. Upregulation of CDK7 in gastric cancer cell promotes tumor cell proliferation and predicts poor prognosis. *Exp. Mol. Pathol.* **2016**, *100*, 514–521. [CrossRef]
21. Naseh, G.; Mohammadifard, M.; Mohammadifard, M. Upregulation of cyclin-dependent kinase 7 and matrix metalloproteinase-14 expression contribute to metastatic properties of gastric cancer. *IUBMB Life* **2016**, *68*, 799–805. [CrossRef] [PubMed]
22. Tsang, F.H.; Law, C.; Tang, T.C.; Cheng, C.L.; Chin, D.W.; Tam, W.V.; Wei, L.; Wong, C.C.L.; Ng, I.O.; Wong, C. Aberrant Super-Enhancer Landscape in Human Hepatocellular Carcinoma. *Hepatology* **2019**, *69*, 2502–2517. [CrossRef] [PubMed]
23. Jiang, L.; Huang, R.; Wu, Y.; Diao, P.; Zhang, W.; Li, J.; Li, Z.; Wang, Y.; Cheng, J.; Yang, J. Overexpression of CDK7 is associated with unfavourable prognosis in oral squamous cell carcinoma. *Pathology* **2019**, *51*, 74–80. [CrossRef] [PubMed]
24. Huang, T.; Ding, X.; Xu, G.; Chen, G.; Cao, Y.; Peng, C.; Shen, S.; Lv, Y.; Wang, L.; Zou, X. CDK7 inhibitor THZ1 inhibits MCL1 synthesis and drives cholangiocarcinoma apoptosis in combination with BCL2/BCL-XL inhibitor ABT-263. *Cell Death Dis.* **2019**, *10*, 602. [CrossRef] [PubMed]
25. Zhou, Y.; Lu, L.; Jiang, G.; Chen, Z.; Li, J.; An, P.; Chen, L.; Du, J.; Wang, H.-S. Targeting CDK7 increases the stability of Snail to promote the dissemination of colorectal cancer. *Cell Death Differ.* **2019**, *26*, 1442–1452. [CrossRef]
26. Ding, L.; Cao, J.; Lin, W.; Chen, H.; Xiong, X.; Ao, H.; Yu, M.; Lin, J.; Cui, Q. The Roles of Cyclin-Dependent Kinases in Cell-Cycle Progression and Therapeutic Strategies in Human Breast Cancer. *Int. J. Mol. Sci.* **2020**, *21*, 1960. [CrossRef] [PubMed]
27. Fisher, R.P. Cdk7: A kinase at the core of transcription and in the crosshairs of cancer drug discovery. *Transcription* **2018**, *10*, 47–56. [CrossRef] [PubMed]
28. Sava, G.P.; Fan, H.; Coombes, R.C.; Buluwela, L.; Ali, S. CDK7 inhibitors as anti-cancer drugs. *Cancer Metastasis Rev.* **2020**, *39*, 805–823. [CrossRef]
29. Lolli, G.; Lowe, E.D.; Brown, N.R.; Johnson, L.N. The Crystal Structure of Human CDK7 and Its Protein Recognition Properties. *Structure* **2004**, *12*, 2067–2079. [CrossRef] [PubMed]
30. Wang, M.; Wang, T.; Zhang, X.; Wu, X.; Jiang, S. Cyclin-dependent kinase 7 inhibitors in cancer therapy. *Futur. Med. Chem.* **2020**, *12*, 813–833. [CrossRef]
31. Diab, S.; Yu, M.; Wang, S. CDK7 Inhibitors in Cancer Therapy: The Sweet Smell of Success? *J. Med. Chem.* **2020**, *63*, 7458–7474. [CrossRef]
32. Sánchez-Martínez, C.; Lallena, M.J.; Sanfeliciano, S.G.; de Dios, A. Cyclin dependent kinase (CDK) inhibitors as anticancer drugs: Recent advances (2015–2019). *Bioorganic Med. Chem. Lett.* **2019**, *29*, 126637. [CrossRef]
33. Ali, S.; Heathcote, D.A.; Kroll, S.H.B.; Jogalekar, A.S.; Scheiper, B.; Patel, H.; Brackow, J.; Siwicka, A.; Fuchter, M.; Periyasamy, M.; et al. The Development of a Selective Cyclin-Dependent Kinase Inhibitor That Shows Antitumor Activity. *Cancer Res.* **2009**, *69*, 6208–6215. [CrossRef]
34. Clark, K.; Ainscow, E.; Peall, A.; Thomson, S.; Leishman, A.; Elaine, S.; Ali, S.; Coombes, R.; Barrett, A.; Bahl, A.K. CT7001, a Novel Orally Bio-Available CDK7 Inhibitor, Is Highly Active in in-Vitro and in-Vivo Models of AML. *Blood* **2017**, *130*, 2645. [CrossRef]
35. Patel, H.; Periyasamy, M.; Sava, G.; Bondke, A.; Slafer, B.W.; Kroll, S.H.B.; Barbazanges, M.; Starkey, R.; Ottaviani, S.; Harrod, A.; et al. ICEC0942, an Orally Bioavailable Selective Inhibitor of CDK7 for Cancer Treatment. *Mol. Cancer Ther.* **2018**, *17*, 1156–1166. [CrossRef] [PubMed]
36. Kwiatkowski, N.; Zhang, T.; Rahl, P.B.; Abraham, B.J.; Reddy, J.; Ficarro, S.B.; Dastur, A.; Amzallag, A.; Ramaswamy, S.; Tesar, B.; et al. Targeting transcription regulation in cancer with a covalent CDK7 inhibitor. *Nature* **2014**, *511*, 616–620. [CrossRef] [PubMed]

37. Chandrasekaran, B.; Agrawal, N.; Kaushik, S. Pharmacophore Development. In *Encyclopedia of Bioinformatics and Computational Biology: ABC of Bioinformatics*; Elsevier: Amsterdam, The Netherlands, 2019; Volume 1–3, pp. 677–687.
38. Kumar, V.; Kumar, R.; Parate, S.; Yoon, S.; Lee, G.; Kim, D.; Lee, K.W. Identification of ACK1 Inhibitors as Anticancer Agents by using Computer-Aided Drug Designing. *J. Mol. Struct.* **2021**, *1235*, 130200. [CrossRef]
39. Greber, B.J.; Perez-Bertoldi, J.M.; Lim, K.; Iavarone, A.T.; Toso, D.B.; Nogales, E. The cryoelectron microscopy structure of the human CDK-activating kinase. *Proc. Natl. Acad. Sci. USA* **2020**, *117*, 22849–22857. [CrossRef]
40. Parate, S.; Kumar, V.; Hong, J.; Lee, K. Identification of Flavonoids as Putative ROS-1 Kinase Inhibitors Using Pharmacophore Modeling for NSCLC Therapeutics. *Molecules* **2021**, *26*, 2114. [CrossRef]
41. Zou, K.H.; O'Malley, A.J.; Mauri, L. Receiver-Operating Characteristic Analysis for Evaluating Diagnostic Tests and Predictive Models. *Circulation* **2007**, *115*, 654–657. [CrossRef]
42. Guner, O.F. History and Evolution of the Pharmacophore Concept in Computer-Aided Drug Design. *Curr. Top. Med. Chem.* **2002**, *2*, 1321–1332. [CrossRef] [PubMed]
43. Parate, S.; Kumar, V.; Hong, J.C.; Lee, K.W. Computational Investigation Identified Potential Chemical Scaffolds for Hepa-*ranase* as Anticancer Therapeutics. *Int. J. Mol. Sci.* **2021**, *22*, 5311. [CrossRef] [PubMed]
44. Kumar, V.; Parate, S.; Yoon, S.; Lee, G.; Lee, K.W. Computational Simulations Identified Marine-Derived Natural Bioactive Compounds as Replication Inhibitors of SARS-CoV-2. *Front. Microbiol.* **2021**, *12*, 647295. [CrossRef] [PubMed]
45. Lipinski, C.A.; Lombardo, F.; Dominy, B.W.; Feeney, P.J. Experimental and computational approaches to estimate solubility and permeability in drug discovery and development settings. *Adv. Drug Deliv. Rev.* **2001**, *46*, 3–26. [CrossRef]
46. Van de Waterbeemd, H.; Gifford, E. ADMET in silico modelling: Towards prediction paradise? *Nat. Rev. Drug Discov.* **2003**, *2*, 192–204. [CrossRef]
47. Meng, X.-Y.; Zhang, H.-X.; Mezei, M.; Cui, M. Molecular Docking: A Powerful Approach for Structure-Based Drug Discovery. *Curr. Comput. Drug Des.* **2011**, *7*, 146–157. [CrossRef]
48. Jones, G.H.; Willett, P.; Glen, R.C.; Leach, A.R.; Taylor, R. Development and validation of a genetic algorithm for flexible docking. *J. Mol. Biol.* **1997**, *267*, 727–748. [CrossRef] [PubMed]
49. Sapundzhi, F.; Prodanova, K.; Lazarova, M. Enhanced sampling in molecular dynamics. *J. Chem. Phys.* **2019**, *2172*, 70902. [CrossRef]
50. Pronk, S.; Páll, S.; Schulz, R.; Larsson, P.; Bjelkmar, P.; Apostolov, R.; Shirts, M.R.; Smith, J.C.; Kasson, P.M.; Van Der Spoel, D.; et al. GROMACS 4.5: A high-throughput and highly parallel open source molecular simulation toolkit. *Bioinformatics* **2013**, *29*, 845–854. [CrossRef] [PubMed]
51. Sapay, N.; Tieleman, D.P. Combination of the CHARMM27 force field with united-atom lipid force fields. *J. Comput. Chem.* **2010**, *32*, 1400–1410. [CrossRef] [PubMed]
52. Zoete, V.; Cuendet, M.A.; Grosdidier, A.; Michielin, O. SwissParam: A fast force field generation tool for small organic molecules. *J. Comput. Chem.* **2011**, *32*, 2359–2368. [CrossRef]
53. Bussi, G.; Donadio, D.; Parrinello, M. Canonical sampling through velocity rescaling. *J. Chem. Phys.* **2007**, *126*, 014101. [CrossRef]
54. Parrinello, M.; Rahman, A. Polymorphic transitions in single crystals: A new molecular dynamics method. *J. Appl. Phys.* **1981**, *52*, 7182–7190. [CrossRef]
55. Humphrey, W.; Dalke, A.; Schulten, K. VMD: Visual molecular dynamics. *J. Mol. Graph.* **1996**, *14*, 33–38. [CrossRef]
56. Berry, M.; Fielding, B.; Gamielien, J. Practical Considerations in Virtual Screening and Molecular Docking. In *Emerging Trends in Computational Biology, Bioinformatics, and Systems Biology: Algorithms and Software Tools*; Elsevier Inc.: Amsterdam, The Netherlands, 2015; pp. 487–502.
57. Genheden, S.; Ryde, U. The MM/PBSA and MM/GBSA methods to estimate ligand-binding affinities. *Expert Opin. Drug Discov.* **2015**, *10*, 449–461. [CrossRef] [PubMed]
58. Kumari, R.; Kumar, R.; Lynn, A.; Open Source Drug Discovery Consortium. G-mmpbsa -A GROMACS tool for high-throughput MM-PBSA calculations. *J. Chem. Inf. Model.* **2014**, *54*, 1951–1962. [CrossRef] [PubMed]
59. Verma, A.K.; Kumar, V.; Singh, S.; Goswami, B.C.; Camps, I.; Sekar, A.; Yoon, S.; Lee, K.W. Repurposing potential of Ayurvedic medicinal plants derived active principles against SARS-CoV-2 associated target proteins revealed by molecular docking, molecular dynamics and MM-PBSA studies. *Biomed. Pharmacother.* **2021**, *137*, 111356. [CrossRef] [PubMed]
60. Maddox, S.; Hecht, D.; Gustafson, J.L. Enhancing the selectivity of kinase inhibitors in oncology: A chemical biology perspective. *Future Med. Chem.* **2016**, *8*, 241–244. [CrossRef]
61. Norman, R.A.; Toader, D.; Ferguson, A.D. Structural approaches to obtain kinase selectivity. *Trends Pharmacol. Sci.* **2012**, *33*, 273–278. [CrossRef]
62. Hazel, P.; Kroll, S.H.B.; Bondke, A.; Barbazanges, M.; Patel, H.; Fuchter, M.J.; Coombes, R.C.; Ali, S.; Barrett, A.G.M.; Freemont, P.S. Inhibitor Selectivity for Cyclin-Dependent Kinase 7: A Structural, Thermodynamic, and Modelling Study. *ChemMedChem* **2017**, *12*, 372–380. [CrossRef]
63. Han, Y.; Zhang, J.; Hu, C.Q.; Zhang, X.; Ma, B.; Zhang, P. In silico ADME and Toxicity Prediction of Ceftazidime and Its Impurities. *Front. Pharmacol.* **2019**, *10*, 434. [CrossRef] [PubMed]
64. Lagorce, D.; Douguet, D.; Miteva, M.; Villoutreix, B.O. Computational analysis of calculated physicochemical and ADMET properties of protein-protein interaction inhibitors. *Sci. Rep.* **2017**, *7*, srep46277. [CrossRef] [PubMed]

65. Pires, D.E.V.; Blundell, T.L.; Ascher, D.B. pkCSM: Predicting Small-Molecule Pharmacokinetic and Toxicity Properties Using Graph-Based Signatures. *J. Med. Chem.* **2015**, *58*, 4066–4072. [CrossRef] [PubMed]
66. Triballeau, N.; Acher, F.; Brabet, I.; Pin, J.-P.; Bertrand, H.-O. Virtual Screening Workflow Development Guided by the “Receiver Operating Characteristic” Curve Approach. Application to High-Throughput Docking on Metabotropic Glutamate Receptor Subtype 4. *J. Med. Chem.* **2005**, *48*, 2534–2547. [CrossRef] [PubMed]
67. Martinez, L. Automatic Identification of Mobile and Rigid Substructures in Molecular Dynamics Simulations and Fractional Structural Fluctuation Analysis. *PLoS ONE* **2015**, *10*, e0119264. [CrossRef]
68. Chohan, T.A.; Pan, Y.-L.; Qian, H.-Y.; Chen, J.-Z. Molecular simulation studies on the binding selectivity of 2-anilino-4-(thiazol-5-yl)-pyrimidines in complexes with CDK2 and CDK7. *Mol. BioSyst.* **2015**, *12*, 145–161. [CrossRef]
69. Tripathi, S.K.; Muttineni, R.; Singh, S.K. Extra precision docking, free energy calculation and molecular dynamics simulation studies of CDK2 inhibitors. *J. Theor. Biol.* **2013**, *334*, 87–100. [CrossRef]
70. Whittaker, S.; Mallinger, A.; Workman, P.; Clarke, P.A. Inhibitors of cyclin-dependent kinases as cancer therapeutics. *Pharmacol. Ther.* **2017**, *173*, 83–105. [CrossRef]
71. Asghar, U.; Witkiewicz, A.K.; Turner, N.C.; Knudsen, E.S. The history and future of targeting cyclin-dependent kinases in cancer therapy. *Nat. Rev. Drug Discov.* **2015**, *14*, 130–146. [CrossRef]
72. Arooj, M.; Sakkiah, S.D.; Kim, S.; Arulalapperumal, V.; Lee, K.W. A Combination of Receptor-Based Pharmacophore Modeling & QM Techniques for Identification of Human Chymase Inhibitors. *PLoS ONE* **2013**, *8*, e63030. [CrossRef]
73. Maganti, L.; Grandhi, P.; Ghoshal, N. Integration of ligand and structure based approaches for identification of novel MbtI inhibitors in Mycobacterium tuberculosis and molecular dynamics simulation studies. *J. Mol. Graph. Model.* **2016**, *70*, 14–22. [CrossRef]
74. Bhowmick, S.; AlFaris, N.A.; Altamimi, J.Z.; Allothman, Z.A.; Aldayel, T.S.; Wabaidur, S.M.; Islam, A. Screening and analysis of bioactive food compounds for modulating the CDK2 protein for cell cycle arrest: Multi-cheminformatics approaches for anticancer therapeutics. *J. Mol. Struct.* **2020**, *1216*, 128316. [CrossRef]
75. Zeb, A.; Son, M.; Yoon, S.; Kim, J.H.; Park, S.J.; Lee, K.W. Computational Simulations Identified Two Candidate Inhibitors of Cdk5/p25 to Abrogate Tau-associated Neurological Disorders. *Comput. Struct. Biotechnol. J.* **2019**, *17*, 579–590. [CrossRef] [PubMed]
76. Kumar, R.; Kumar, V.; Lee, K.W. A computational drug repurposing approach in identifying the cephalosporin antibiotic and anti-hepatitis C drug derivatives for COVID-19 treatment. *Comput. Biol. Med.* **2021**, *130*, 104186. [CrossRef] [PubMed]
77. Cheng, Z.-Q.; Zhu, K.-K.; Zhang, J.; Song, J.-L.; Muehlmann, L.A.; Jiang, C.-S.; Liu, C.-L.; Zhang, H. Molecular-docking-guided design and synthesis of new IAA-tacrine hybrids as multifunctional AChE/BChE inhibitors. *Bioorganic Chem.* **2019**, *83*, 277–288. [CrossRef]
78. Silva, L.R.; Guimarães, A.S.; Nascimento, J.D.; Nascimento, I.J.D.S.; da Silva, E.B.; McKerrow, J.H.; Cardoso, S.H.; da Silva-Júnior, E.F. Computer-aided design of 1,4-naphthoquinone-based inhibitors targeting cruzain and rhodesain cysteine proteases. *Bioorganic Med. Chem.* **2021**, *41*, 116213. [CrossRef]



Article

Development of New Meridianin/Leucettine-Derived Hybrid Small Molecules as Nanomolar Multi-Kinase Inhibitors with Antitumor Activity

Mohamed H. Elsherbeny^{1,2,3}, Ahmed Elkamhawy^{4,5,*}, Hossam Nada^{4,6}, Magda H. Abdellattif⁷, Kyeong Lee⁴ and Eun Joo Roh^{1,2,*}

- ¹ Chemical Kinomics Research Center, Korea Institute of Science and Technology (KIST), Seoul 02792, Korea; mohamed.alsherbeny@pharma.asu.edu.eg
 - ² Division of Bio-Medical Science & Technology, KIST School, University of Science and Technology, Seoul 02792, Korea
 - ³ Pharmaceutical Chemistry Department, Faculty of Pharmacy, Ahran Canadian University, Giza 12566, Egypt
 - ⁴ College of Pharmacy, Dongguk University-Seoul, Goyang 10326, Korea; hossam_hammouda@dgu.ac.kr (H.N.); kaylee@dongguk.edu (K.L.)
 - ⁵ Department of Pharmaceutical Organic Chemistry, Faculty of Pharmacy, Mansoura University, Mansoura 35516, Egypt
 - ⁶ Pharmaceutical Chemistry Department, Faculty of Pharmacy, Badr University, Cairo 11829, Egypt
 - ⁷ Department of Chemistry, College of Science, Taif University, P.O. Box 11099, Taif 21944, Saudi Arabia; m.hasan@tu.edu.sa
- * Correspondence: a_elkamhawy@mans.edu.eg or a.elkamhawy@dongguk.edu (A.E.); r8636@kist.re.kr (E.J.R.)

Citation: Elsherbeny, M.H.; Elkamhawy, A.; Nada, H.; Abdellattif, M.H.; Lee, K.; Roh, E.J. Development of New Meridianin/Leucettine-Derived Hybrid Small Molecules as Nanomolar Multi-Kinase Inhibitors with Antitumor Activity. *Biomedicines* **2021**, *9*, 1131. <https://doi.org/10.3390/biomedicines9091131>

Academic Editors: Leonardo Caputo, Laura Quintieri and Orazio Nicolotti

Received: 8 June 2021

Accepted: 27 August 2021

Published: 1 September 2021

Publisher's Note: MDPI stays neutral with regard to jurisdictional claims in published maps and institutional affiliations.



Copyright: © 2021 by the authors. Licensee MDPI, Basel, Switzerland. This article is an open access article distributed under the terms and conditions of the Creative Commons Attribution (CC BY) license (<https://creativecommons.org/licenses/by/4.0/>).

Abstract: Although the sea ecosystem offers a broad range of bioactivities including anticancer, none of the FDA-approved antiproliferative protein kinase inhibitors are derived from a marine source. In a step to develop new marine-inspired potent kinase inhibitors with antiproliferative activities, a new series of hybrid small molecules (**5a–5g**) was designed and synthesized based on chemical moieties derived from two marine natural products (Meridianin E and Leucettamine B). Over a panel of 14 cancer-related kinases, a single dose of 10 μ M of the parent hybrid **5a** possessing the benzo[*d*][1,3]dioxole moiety of Leucettamine B was able to inhibit the activity of FMS, LCK, LYN, and DAPK1 kinases with 82.5 ± 0.6 , 81.4 ± 0.6 , 75.2 ± 0.0 , and $55 \pm 1.1\%$, respectively. Further optimization revealed the most potent multiple kinase inhibitor of this new series (**5g**) with IC_{50} values of 110, 87.7, and 169 nM against FMS, LCK, and LYN kinases, respectively. Compared to imatinib (FDA-approved multiple kinase inhibitor), compound **5g** was found to be ~9- and 2-fold more potent than imatinib over both FMS and LCK kinases, respectively. In silico docking simulation models of the synthesized compounds within the active site of FMS, LCK, LYN, and DAPK1 kinases offered reasonable explanations of the elicited biological activities. In an in vitro anticancer assay using a library of 60 cancer cell lines that include blood, lung, colon, CNS, skin, ovarian, renal, prostate, and breast cancers, it was found that compound **5g** was able to suppress 60 and 70% of tumor growth in leukemia SR and renal RXF 393 cell lines, respectively. Moreover, an ADME study indicated a suitable profile of compound **5g** concerning cell permeability and blood-brain barrier (BBB) impermeability, avoiding possible CNS side effects. Accordingly, compound **5g** is reported as a potential lead towards novel antiproliferative marine-derived kinase modulators.

Keywords: meridianins; leucettine; marine-inspired kinase inhibitors; DAPK1; FMS; LCK; LYN; molecular modeling; ADME studies

1. Introduction

The process of drug development from marine organisms is a prehistoric praxis. To date, more than 20,000 marine natural products (MNP) have been isolated from ocean life-forms. The discovery of novel small molecules based on a natural heterocyclic scaffold

has always attracted the attention of medicinal chemists worldwide. This fact was driven by the broad range of bioactivities that the sea ecosystem offers such as anticancer, anti-inflammatory, antibacterial, antiviral, antifungal, antifouling, antiprotozoal, anticoagulant, immunosuppressive, and neuroprotective activities [1–4]. However, to date, only eight anticancer drugs of marine origin were approved by the US Food and Drug Administration (FDA), the European Medicines Evaluation Agency (EMA), or the Australian Therapeutic Goods Administration (TGA), as well as a few in phases I, II, and III clinical pipelines [5,6].

Over the past two decades, drug development has shifted from the random screening of large compound libraries of synthetic origin using high-throughput cell-based cytotoxicity assays to screening against clinically validated molecular targets [7–9]. This new target-based discovery aims to enhance the efficacy and selectivity of treatment by offering new drug candidates that block disease mechanisms in a defined and specific way. This new approach is widely driven by the rapidly expanding knowledge of disease biology and pathology at the molecular level. This approach has been particularly successful in oncology [10,11]. Among these targets, protein kinases are involved in various cellular functions including metabolism, cell cycle regulation, survival, and differentiation.

Dysregulation of protein kinases is implicated in various processes of carcinogenesis [12]. Moreover, overexpression of various types of protein kinases is found in different types of cancer, which encouraged medicinal chemists worldwide to develop numerous receptor tyrosine kinases inhibitors (RTKIs). In addition, the advent of protein kinase inhibitors in cancer research and therapy has led to a paradigm shift in how cancer is currently treated [13–29]. As a result, the FDA has approved many protein kinase inhibitors in the last few decades. Surprisingly, none of them are derived from a marine source [1,30].

Searching the literature reveals interesting kinase inhibitory activities of two MNPs (Meridianin E and Leucettamine B). Meridianins are indole alkaloids, isolated from tunicate *Aplidium meridianum*, inhibit various protein kinases associated with neurodegenerative and cancer diseases. These compounds also showed promising antiproliferative activity in several cancer cell lines. Amongst natural meridianins, meridianin E (Figure 1) attracted our attention since it exhibited significant cytotoxicity against murine tumor cell lines [31]. Moreover, it demonstrated potent and selective inhibition of CDK-1 and CDK-5 kinases. Furthermore, several synthetic meridianin analogs showed potent and selective inhibitory effects over glycogen synthase-3 (GSK-3) and dual-specificity tyrosine-phosphorylation regulated kinase 1A (DYRK-1A), which are known to be implicated in the progression of Alzheimer's disease [2,32]. On the other hand, Leucettamine B (Figure 1) is a natural product found in marine sponge *Leucetta microraphis*. Several analogs of its family such as aplysinopsine and clathridine are medicinally active molecules that have applications in many pharmaceuticals and healthcare products. A recent study also reported the potential anticancer activity of a series of Leucettamine B synthesized derivatives [33]. However, leucettamine B and its analog leucettine L41 have not been well studied for their kinase inhibitory activity. Only a few reports in the literature indicated the ability of leucettamine B to inhibit “dual-specificity” kinases DYRK-1A, DYRK-2, CLK-1, and CLK-3 with high IC_{50} values of 2.8, 1.5, 0.40, and 6.4 μ M, respectively [34–37]. Accordingly, with the great potential of these two MNPs (Meridianin E and Leucettamine B) to afford new more potent kinase inhibitors, further investigations in this field are highly needed. Thus, this encouraged us to apply a structure-based drug design strategy towards the development of a new marine-inspired potential kinase inhibitor (5a, Figure 1).

As shown in Figure 1, a structural hybridization approach was carried out by incorporating the pyrimidine scaffold of Meridianin E with the benzo[d][1,3]dioxole moiety of Leucettamine B via a backbone amide linker. The pyrimidine nucleus was also substituted at positions 2 and 4 with 4-morpholinophenylamino and 4-methoxyphenoxy moieties, respectively. These two substituents, widely found as solvent exposure moieties in the chemical structures of many kinase inhibitors, were introduced to enhance the binding interaction of the synthesized hybrid inhibitor with the binding site of the potential kinase target(s). The performed hybridization strategy led to the design and synthesis of the new

hybrid small molecule **5a** which was assessed for its biological activity over a panel of 14 cancer-related kinases in a step to identify a potential kinase inhibitory activity. Optimization of the chemical structure of compound **5a** afforded new derivatives **5b–5g** which were further biologically evaluated for their kinase inhibitory and antiproliferative activities. Compounds that showed inhibition > 50% over any tested kinase were further assessed for their IC₅₀ on the corresponding kinase. Moreover, the target compounds were tested for their in vitro cytotoxic activity against the NCI 60 cell lines panel. Molecular docking studies were also carried out for the designed compounds with the target kinases to study their binding modes and their interactions with the key amino acids in the ATP-binding pocket. Accordingly, we report our rational design, optimization, synthetic routes, in vitro and in silico biological evaluation of the newly synthesized marine-derived compounds **5a–5g**.

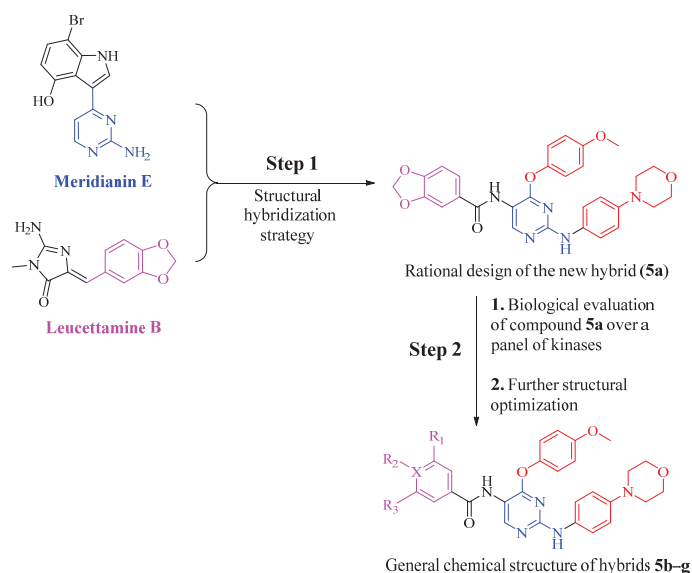


Figure 1. Rational design steps of the new set of Meridianin E and Leucettamine B hybrids (**5a–5g**).

2. Materials and Methods

2.1. Chemistry

General

All reagents and solvents were purchased from TCI, Sigma-Aldrich, and Alfa Aesar, and were used without further purification. Biotage Initiator+ apparatus was used to carry out microwave-assisted reactions (Biotage AB, Uppsala, Sweden). Sealed vessels with magnetic stirrers were used to perform the reactions under controlled temperature for a programmed duration. The chemical synthesis, column chromatography, NMR identification, purity, and HRMS experiments were carried out following the previously reported general methods [38,39] (for details, see Supplementary File).

Synthesis of 2-chloro-4-(4-methoxyphenoxy)-5-nitropyrimidine (2). A solution of 4-methoxyphenol (10 mmol) dissolved in a mixture of 1N aqueous sodium bicarbonate (10 mL) and water (40 mL) was added dropwise using an addition funnel to a 250 mL rounded-bottom flask containing a prepared solution of 2,4-dichloro-5-nitro-pyrimidine (10 mmol) dissolved in acetone (50 mL) and cooled to 0 °C. The flask was then allowed to return to room temperature and kept under stirring for 3 h until TLC showed the reaction completion. The reaction mixture was evaporated under vacuum, and the residue was washed sequentially with EA, 1N NaOH (aq.), and brine. The organic layer was then dried over anhydrous Na₂SO₄ and purified using flash chromatography (20% EA/Hex) to obtain

compound **2**. Yellowish white solid, yield: 87%, $^1\text{H NMR}$ (400 MHz, $\text{DMSO}-d_6$): δ 9.39 (s, 1H), 7.24 (d, $J = 9.2$ Hz, 2H), 7.05 (d, $J = 9.2$ Hz, 2H), 3.81 (s, 3H). Reported [18].

Synthesis of 4-(4-methoxyphenoxy)-N-(4-morpholinophenyl)-5-nitropyrimidin-2-amine (3). A clean and efficient reported reaction condition was employed [22], where 4-morpholinoaniline (5 mmol) was added to a solution of 2-chloro-4-(4-methoxyphenoxy)-5-nitropyrimidine (**2**, 5 mmol) dissolved in acetonitrile. The reaction was then stirred at room temperature overnight. The mixture was then evaporated *in vacuo*, washed with water, NaHCO_3 , and brine. The organic layer was dried over Na_2SO_4 and purified by flash column chromatography (EA:Hex, 1:1) to yield compound **3** as an orange solid. Orange solid, yield: 43%, $^1\text{H NMR}$ (400 MHz, $\text{DMSO}-d_6$): δ 10.61 (s, 1H), 9.13 (s, 1H), 7.22 (d, $J = 9.0$ Hz, 2H), 7.13 (d, $J = 8.7$ Hz, 2H), 7.08 (d, $J = 8.9$ Hz, 2H), 6.58 (d, $J = 8.8$ Hz, 2H), 3.85 (s, 3H), 3.72 (t, $J = 4.9$ Hz, 4H), 2.98 (t, $J = 4.4$ Hz, 4H). Reported [40].

Synthesis of 4-(4-methoxyphenoxy)-N2-(4-morpholinophenyl)pyrimidine-2,5-diamine (4). A solution of 4-(4-methoxyphenoxy)-N-(4-morpholinophenyl)-5-nitropyrimidin-2-amine (**3**, 1 mmol) was prepared using 50 mL of a 10% MC/MeOH mixture as a solvent, followed by adding 0.1 mmol of Pd/C under nitrogen, and the mixture was then stirred under hydrogen overnight. The metal was then filtered using celite, and the filtrate was evaporated under reduced pressure to give compound **4**. Grey solid, yield: 69%, $^1\text{H NMR}$ (400 MHz, $\text{DMSO}-d_6$): δ 8.58 (s, 1H), 7.82 (s, 1H), 7.28 (d, $J = 9.0$ Hz, 2H), 7.14–7.17 (m, 2H), 7.02–7.05 (m, 2H), 6.64 (d, $J = 9.0$ Hz, 2H), 4.51 (s, 2H), 3.81 (s, 3H), 3.71 (t, $J = 4.8$ Hz, 4H), 2.93 (t, $J = 4.7$ Hz, 4H). Reported [40].

General procedure of final amide derivatives 5a–5d. A small flask containing 0.3 mmol of the pre-final amine (**4**) and DIPEA (0.3 mmol) dissolved in dichloromethane (DCM, 5 mL) was cooled to 0 °C, and an equivalent amount of the appropriate benzoyl chloride was added. The reaction mixture was allowed to warm to room temperature and stirred overnight. The reaction mixture was then evaporated *in vacuo* and purified by flash column chromatography (20–50% EA/Hex) to obtain the final amides **5a–5d**.

N-(4-(4-Methoxyphenoxy)-2-((4-morpholinophenyl)amino)pyrimidin-5-yl)benzo[d][1,3]dioxole-5-carboxamide (5a). Yellow solid, yield: 56%, mp: 205.9–206.9 °C, HPLC purity: 6.43 min, 95.12%, $^1\text{H NMR}$ (400 MHz, CDCl_3): δ 9.13 (s, 1H), 7.82 (s, 1H), 7.36 (dd, $J = 8.1$, 1.5 Hz, 1H), 7.32 (d, $J = 1.4$ Hz, 1H), 7.14 (d, $J = 8.8$ Hz, 2H), 7.03 (d, $J = 8.9$ Hz, 2H), 6.88 (d, $J = 8.9$ Hz, 2H), 6.85 (s, 1H), 6.80 (d, $J = 8.0$ Hz, 1H), 6.64 (d, $J = 8.8$ Hz, 2H), 5.97 (s, 2H), 3.76–3.78 (m, 7H), 2.97 (t, $J = 4.6$ Hz, 4H). $^{13}\text{C NMR}$ (100 MHz, CDCl_3) δ 164.58, 160.39, 157.39, 155.41, 150.87, 150.65, 148.26, 146.73, 145.60, 132.56, 128.38, 123.07, 121.92, 119.94, 116.51, 114.59, 112.89, 108.23, 107.76, 101.90, 66.98, 55.71, 50.16. HRMS (ESI) m/z calculated for $\text{C}_{17}\text{H}_{17}\text{N}_3\text{O}_3$ $[\text{M}+\text{H}]^+$: 542.2040. Found: 542.2040.

3,4-Dimethoxy-N-(4-(4-methoxyphenoxy)-2-((4-morpholinophenyl)amino)pyrimidin-5-yl)benzamide (5b). Yellow solid, yield: 73%, mp: 119.1–120.1 °C, HPLC purity: 6.24 min, 97.24%, $^1\text{H NMR}$ (400 MHz, CDCl_3) δ 9.26 (s, 1H), 8.01 (s, 1H), 7.57 (d, $J = 1.7$ Hz, 1H), 7.45 (dd, $J = 8.3$, 1.8 Hz, 1H), 7.25 (d, $J = 8.8$ Hz, 2H), 7.14 (d, $J = 9.0$ Hz, 2H), 6.99 (d, $J = 9.0$, 2H), 6.93 (d, $J = 8.2$ Hz, 2H), 6.75 (d, $J = 8.8$ Hz, 2H), 3.99 (s, 3H), 3.97 (s, 3H), 3.86–3.89 (m, 7H). $^{13}\text{C NMR}$ (100 MHz, CDCl_3) δ 164.94, 160.40, 157.38, 155.39, 152.29, 150.63, 149.31, 146.74, 145.63, 132.56, 126.83, 123.07, 119.97, 119.5, 116.51, 114.59, 112.98, 110.87, 110.40, 66.98, 56.14, 56.11, 50.16. HRMS (ESI) m/z calculated for $\text{C}_{17}\text{H}_{17}\text{N}_3\text{O}_3$ $[\text{M}+\text{H}]^+$: 558.2353. Found: 558.2352.

3,4,5-Trimethoxy-N-(4-(4-methoxyphenoxy)-2-((4-morpholinophenyl)amino)pyrimidin-5-yl)benzamide (5c). Yellow solid, yield: 69%, mp: 179.5–180.5 °C, $^1\text{H NMR}$ (400 MHz, CDCl_3) δ 9.21 (s, 1H), 7.94 (s, 1H), 7.25 (d, $J = 8.8$ Hz, 2H), 7.14–7.16 (m, 4H), 7.01–6.98 (m, 3H), 6.75 (d, $J = 8.8$ Hz, 2H), 3.96 (s, 6H), 3.93 (s, 3H), 3.86–3.89 (m, 7H). $^{13}\text{C NMR}$ (100 MHz, CDCl_3) δ 165.23, 160.57, 157.41, 155.59, 153.42, 150.99, 146.81, 145.60, 141.56, 132.45, 129.68, 123.04, 120.04, 116.49, 114.60, 112.67, 104.74, 66.98, 60.99, 56.50, 55.71, 50.13. HRMS (ESI) m/z calculated for $\text{C}_{17}\text{H}_{17}\text{N}_3\text{O}_3$ $[\text{M}+\text{H}]^+$: 588.2458. Found: 588.2458.

3,5-Diethoxy-N-(4-(4-methoxyphenoxy)-2-((4-morpholinophenyl)amino)pyrimidin-5-yl)benzamide (5d). Yellow solid, yield: 59%, mp: 113.1–114.1 °C, $^1\text{H NMR}$ (400 MHz,

CDCl₃): δ 9.16 (s, 1H), 7.90 (s, 1H), 7.14 (d, J = 8.4 Hz, 2H), 7.02 (d, J = 8.5 Hz, 2H), 6.86–6.92 (m, 5H), 6.64 (d, J = 8.0 Hz, 2H), 6.54 (s, 1H), 3.97 (q, J = 6.7 Hz, 4H), 3.78 (s, 7H), 2.98 (s, 4H), 1.33 (t, J = 6.8 Hz, 6H). ¹³C NMR (100 MHz, CDCl₃) δ 165.22, 160.38, 157.39, 155.45, 150.61, 146.74, 145.59, 136.30, 132.54, 123.10, 119.97, 116.50, 114.58, 112.84, 105.58, 104.72, 66.98, 63.91, 55.70, 50.15, 14.76. HRMS (ESI) m/z calculated for C₁₇H₁₇N₃O₃ [M+H]⁺: 586.2666. Found: 586.2665.

General procedure of final amide derivatives 5e–5g. The appropriate carboxylic acid (1.15 eq.) and HATU (1.15 eq.) were first dissolved in DMF and stirred for 10 min, DIPEA (2.5 eq.) was then added, and the mixture stirred for another 5 min. The pre-final amine was finally added, and the reaction mixture was microwaved at 120 °C for 1 h. The reaction mixture was then washed several times using ethyl acetate and brine. The organic layer was then dried over Na₂SO₄ and purified by flash column chromatography (20–50% EA/Hex) to afford the final amides 5e–5g.

2-(3,5-Dimethoxyphenyl)-N-(4-(4-methoxyphenoxy)-2-((4-morpholinophenyl)amino)pyrimidin-5-yl)acetamide (5e). Yellow solid, yield: 51%, mp: 152.7–153.7 °C, HPLC purity: 6.61 min, 98.92%, ¹H NMR (400 MHz, CDCl₃): δ 8.92 (s, 1H), 7.31 (s, 1H), 7.12 (d, J = 8.6 Hz, 2H), 6.95 (d, J = 8.8 Hz, 2H), 6.84 (d, J = 8.8 Hz, 2H), 6.81 (s, 1H), 6.63 (d, J = 8.3 Hz, 2H), 6.43 (s, 2H), 6.32 (s, 1H), 3.75–3.77 (m, 7H), 3.68 (s, 6H), 3.64 (s, 2H), 2.97 (s, 4H). ¹³C NMR (100 MHz, CDCl₃) δ 168.82, 161.42, 160.35, 157.23, 155.63, 150.88, 146.77, 145.54, 136.466, 132.49, 122.80, 120.02, 116.49, 114.44, 112.36, 107.43, 99.72, 66.97, 55.68, 55.39, 50.14, 44.71. HRMS (ESI) m/z calculated for C₁₇H₁₇N₃O₃ [M+H]⁺: 572.2509. Found: 572.2509.

N-(4-(4-Methoxyphenoxy)-2-((4-morpholinophenyl)amino)pyrimidin-5-yl)-2-nitroisonicotinamide (5f). Orange solid, yield: 62%, mp: 170–171 °C, ¹H NMR (400 MHz, CDCl₃): δ 9.16 (s, 1H), 8.84 (d, J = 3.8 Hz, 1H), 8.71 (s, 1H), 8.25 (s, 1H), 8.18 (s, 1H), 7.24 (d, J = 7.4 Hz, 2H), 7.13 (d, J = 8.1 Hz, 2H), 6.99–7.04 (m, 3H), 6.75 (d, J = 7.8 Hz, 2H), 3.88 (s, 7H), 3.09 (s, 4H). ¹³C NMR (100 MHz, CDCl₃) δ 161.02, 160.81, 157.56, 157.37, 156.31, 151.51, 150.12, 147.11, 145.69, 145.23, 131.90, 126.72, 122.97, 120.35, 116.36, 115.67, 114.67, 111.41, 66.94, 55.71, 49.97, 31.60, 22.66, 14.13. HRMS (ESI) m/z calculated for C₁₇H₁₇N₃O₃ [M+H]⁺: 544.1945. Found: 544.1945.

N-(4-(4-Methoxyphenoxy)-2-((4-morpholinophenyl)amino)pyrimidin-5-yl)-3-(methylthio)benzamide (5g). Yellow solid, yield: 54%, mp: 106–107 °C, HPLC purity: 6.67 min, 99.29%, ¹H NMR (400 MHz, CDCl₃): δ 9.26 (s, 1H), 8.03 (s, 1H), 7.83 (s, 1H), 7.63 (d, J = 7.0 Hz, 1H), 7.40–7.46 (m, 2H), 7.25 (d, J = 8.8 Hz, 2H), 7.14 (d, J = 8.9 Hz, 2H), 6.99–7.01 (m, 3H), 6.75 (d, J = 8.9 Hz, 2H), 3.86–3.89 (m, 7H), 3.07 (t, J = 4.72 Hz, 4H), 2.57 (s, 3H). ¹³C NMR (100 MHz, CDCl₃) δ 164.99, 160.48, 157.40, 155.58, 150.83, 146.79, 145.57, 140.19, 134.92, 132.48, 129.75, 129.09, 125.07, 123.15, 123.07, 120.02, 116.49, 114.59, 112.68, 66.98, 55.71, 50.14, 15.64. HRMS (ESI) m/z calculated for C₁₇H₁₇N₃O₃ [M+H]⁺: 544.2019. Found: 544.2018.

2.2. Biological Evaluation

2.2.1. In Vitro Kinase Inhibition Assay

The in vitro kinase inhibition assay was carried out by Reaction Biology Corp. (Reaction Biology Corp., Chester, PA, USA) Kinase HotSpotSM service (<http://www.reactionbiology.com>, accessed on 15 January 2021), following the previously reported methods [16,40]. (For details, see Supplementary Material).

2.2.2. In Vitro Antitumor Activity towards 60 Cancer Cell Lines

The antitumor assay was performed according to the protocol of the Drug Evaluation Branch, NCI, Bethesda [41]. A 48 h drug exposure protocol was adopted, and sulforhodamine B (SRB) assay was utilized to assess the cell growth and viability, as reported earlier [42,43].

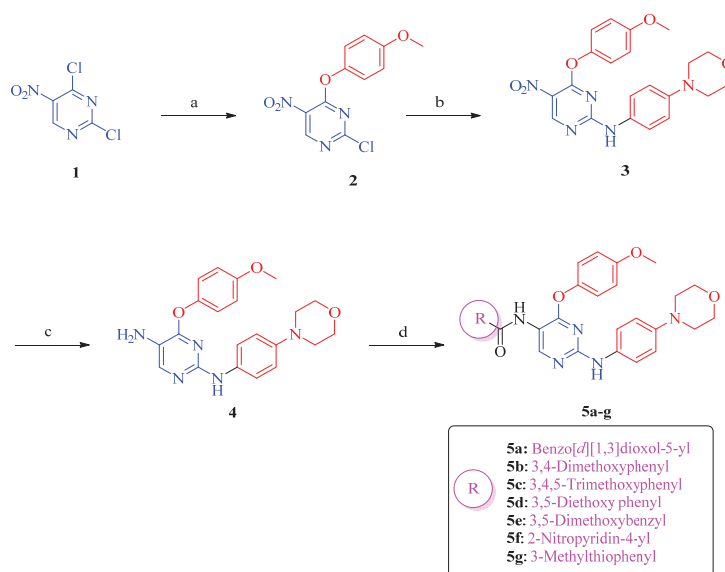
2.2.3. Molecular Modeling Study

Crystal structure of LCK (PDB ID: 3KMM), DAPK1 (PDB code: 4TXC), FMS (PDB ID: 6N33), and LYN (PDB ID: 2ZVA) were downloaded from the protein data bank (www.pdb.org, accessed on 20 March 2021). LCK, FMS, and DAPK1 structures are all respectively complexed with small molecule inhibitors. Protein structures were prepared using the protein preparation wizard of the Schrodinger 2020 suite of the package at the default setting and 7.4 pH value. All ligands were sketched using ChemDraw Professional 16.0, saved as structure data file format, and imported to Ligprep module. Ligprep module of Schrodinger was used for preparing all ligands and geometry optimization. Re-docking X-ray ligands confirmed the reproducibility of the docking program (data not shown). All minimized conformations of ligands were docked into their own respective binding site using Glide's standard precision module and produced 10 poses for each ligand. The docking figures were produced using the Discovery Studio Client 2020 package. We selected the docked poses with more negative docking scores and significant interactions.

3. Results and Discussion

3.1. Chemical Synthesis

The newly synthesized target compounds (**5a–5g**) were prepared as outlined in Scheme 1. Starting from the commercially available 2,4-dichloro-5-nitropyrimidine (**1**). A solution of 4-methoxyphenol in a mixture of aqueous sodium bicarbonate and water was added to compound **1** in acetone to give compound **2** which was stirred with 4-morpholinoaniline in acetonitrile overnight to afford compound **3** as an orange solid. Compound **3** was reduced by stirring in a mixture of DCM/methanol (1:9) under hydrogen gas in the presence of a catalytic amount of palladium on carbon. The reduced pre-final amine (**4**) was then used to afford the final amide derivatives **5a–5g** either by stirring overnight with the corresponding benzoyl chloride in DCM solvent and DIPEA base to yield derivatives **5a–5d**, or by reacting it with the appropriate carboxylic acid in dimethylformamide and in the presence of HATU and DIPEA to afford compounds **5e–5g**. The structure elucidation and identification of the synthesized target hybrids were done with the aid of NMR and HRMS spectroscopy. The synthesis of compound **2** was confirmed through the presence of a signal corresponding to the methoxy group of the 4-methoxyphenoxy moiety at 3.81 ppm. ¹H NMR chart of compounds **3** was characterized by the appearance of eight hydrogens attributable the morpholine ring and three hydrogens of the methoxy group of the 4-methoxyphenoxy moiety. The subsequent reduction of the nitro group to produce compound **4** was confirmed through the appearance of a new signal attributable to two new exchangeable protons of the newly generated amino group. The ¹H NMR spectra of compounds **5a–5g** were all characterized by the presence of two peaks at 3.00–4.00 ppm attributable to the eight hydrogens of the morpholine ring and the three hydrogens of the methoxy group. In addition, the amide group of compounds **5a–5g** always displayed signals resonating in the range of 8.8–9.3 ppm of the ¹H NMR spectra. Moreover, their ¹³C NMR spectra showed signals resonating in the range of 161–168 ppm characteristic to C = O carbons.



Scheme 1. Reagents and conditions: (a) 4-Methoxyphenol, aq. NaHCO_3 , acetone, 0 °C to rt, 3 h; (b) 4-morpholinoaniline, MeCN, rt, overnight; (c) H_2 , 10% Pd/C, 10% DCM/methanol, rt, 12 h; (d) (i) for derivatives **5a–5d**: Appropriate acyl chloride, DIPEA, DCM, 0 °C to rt, overnight; (ii) for derivatives **5e–5g**: Appropriate carboxylic acid, DIPEA, HATU, DMF, MW, 120 °C, 1 h.

3.2. Biological Evaluation

3.2.1. Assessment of Kinase Inhibitory Activity of Compound **5a** against a Panel of Kinases

As mentioned in the introduction, to get insights about the kinase inhibition profile of the hybrid small molecule **5a**, an in vitro screening over a panel of 14 cancer-related kinases was carried out. Accordingly, 10 μM concentrations of compound **5a** were used in a kinase inhibition assay over various kinase groups and families in the presence of 10 M ATP using HotSpotSM technology. To get a comprehensive picture of the inhibitory activities of the tested compound (**5a**) against the kinase panel, data are illustrated in Table 1. Interestingly, compound **5a** displayed promising inhibitory activities of more than 50% inhibition against four kinases: Colony-stimulating factor-1 receptor (FMS), lymphocyte-specific protein tyrosine kinase (LCK), tyrosine-protein kinase LYN, and death-associated protein kinase 1 (DAPK1) with inhibition values of 82.5 ± 0.6 , 81.4 ± 0.6 , 75.2 ± 0.0 , and $55 \pm 1.1\%$, respectively. Compound **5a** was also able to suppress the kinase activity of the epidermal growth factor receptor (EGFR), platelet-derived growth factor receptor-alpha (PDGFR α), and cyclin-dependent kinase 2 (CDK2) with modest inhibition values of 26.99 ± 0.9 , 24.0 ± 0.4 , and $20.1 \pm 0.1\%$, respectively. Other kinases showed very little to no inhibition. Several studies have confirmed direct relationships between the most affected kinases (FMS, LCK, LYN, and DAPK1) and different human disorders including cancer [40,44–49]. Accordingly, these four kinases were selected to be included in further biological assays for the optimized hybrids **5b–5g** in a step to identify more active kinase inhibitors and to get structure-activity relationship (SAR) insights for this new marine-derived series.

Table 1. In vitro inhibition screening results of compound **5a** against a panel of 17 kinases at a single dose of 10 μ M.

Type of Kinase	Family	Kinase	Percent Inhibition
Receptor Tyrosine Kinases	TAM family	c-MER	4.4 \pm 0.1
	EGF receptor family	EGFR	26.99 \pm 0.9
		FMS	82.5 \pm 0.6
	PVR family	PDGFR α	24.0 \pm 0.4
		FLT1/VEGFR1	-2.4 \pm 1.7
		KDR/VEGFR2	7.9 \pm 1.4
HGF receptor	c-MET	12.0 \pm 13.7	
Non-Receptor Tyrosine Kinases	SRC-B family	LCK	81.4 \pm 0.6
		LYN	75.2 \pm 0.0
	JAK family	JAK3	11.2 \pm 1.2
Tyrosine Kinase-Like kinases	RAF family	BRAF	4.1 \pm 10.5
Calcium/Calmodulin-dependent kinases (CAMKs)	DAPK family	DAPK1	55 \pm 1.1
CMGC serine/threonine kinases	Cyclin-dependent kinase family	CDK2/cyclin A	20.1 \pm 0.1
P21-activated serine/threonine kinases	PAK Family	PAK1	-29.1 \pm 3.4

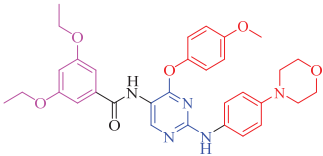
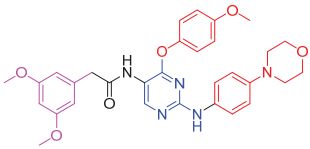
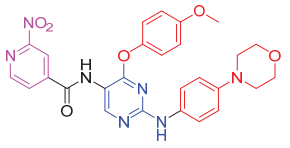
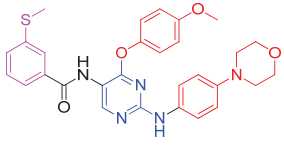
3.2.2. Assessment of Kinase Inhibitory Activity of Compounds **5b–5g** against FMS, LCK, LYN, and DAPK1 Kinases

The four protein kinases inhibited by the hybrid small molecule **5a** with more than 50% inhibition (FMS, LCK, LYN, and DAPK1) were selected to run an assessment for the optimized derivatives **5b–5g** at 10 μ M concentration of each compound. Table 2 shows the percent inhibition values of the optimized compounds **5b–5g** over the four selected kinases in comparison to the results obtained for compound **5a**.

Table 2. Percent inhibition values of the synthesized compounds **5a–5g** over the selected kinases at a single dose concentration of 10 μ M.

Cpd	Chemical Structure	Percent Inhibition ^a			
		DAPK1	FMS	LCK	LYN
5a		55 \pm 1.1	82.5 \pm 0.6	81.4 \pm 0.6	75.2 \pm 0.0
5b		65 \pm 1.2	44.1 \pm 0.2	62.3 \pm 0.8	36.9 \pm 4.5
5c		50 \pm 0.1	69.9 \pm 0.4	19.4 \pm 0.9	-1.6 \pm 0.3

Table 2. Cont.

Cpd	Chemical Structure	Percent Inhibition ^a			
		DAPK1	FMS	LCK	LYN
5d		51.6 ± 0.5	95.1 ± 0.3	38.3 ± 4.2	31.5 ± 5.8
5e		47.1 ± 0.7	75.5 ± 0.8	39.5 ± 0.4	7.9 ± 0.4
5f		65.5 ± 1.4	65.4 ± 0.1	72.6 ± 0.6	34.1 ± 2.2
5g		54.6 ± 0.8	90.6 ± 0.8	96.9 ± 0.3	96.4 ± 0.1

^a Percent inhibition values of different kinases at a single dose of 10 µM of the prepared compound.

Replacement of the benzo[*d*][1,3]dioxole moiety in compound **5a** with 3,4,5-trimethoxyphenyl (**5c**) or 3,5-dimethoxyphenyl (**5e**) led to a noticeable decrease of the kinase inhibition against all four kinases (DAPK1, FMS, LCK, and LYN) with percent inhibition values of 50 ± 0.1 , 69.9 ± 0.4 , 19.4 ± 0.9 , and $-1.6 \pm 0.3\%$ for compound **5c** and 47.1 ± 0.7 , 75.5 ± 0.8 , 39.5 ± 0.4 , and $7.9 \pm 0.4\%$ for compound **5e**, respectively. While compounds possessing 3,4-dimethoxyphenyl (**5b**) and 2-nitropyridin-4-yl (**5f**) showed a similar decrease pattern of the kinase inhibitory activity over FMS, LCK, and LYN kinases with percent inhibition values ranging from 34.1 ± 2.2 to $72.6 \pm 0.6\%$, surprisingly, both compounds were able to elicit higher inhibitory activities against DAPK1 kinase compared to the parent hybrid compound **5a** with 65 ± 1.2 and $65.5 \pm 1.4\%$ inhibition, respectively. Interestingly, compound **5d** possessing 3,5-diethoxyphenyl moiety displayed the highest inhibitory activity over FMS kinase ($95.1 \pm 0.3\%$ inhibition), while it demonstrated moderate inhibitory activities against DAPK1, LCK, and LYN kinases with 51.6 ± 0.5 , 38.3 ± 4.2 , and $31.5 \pm 5.8\%$, respectively. As illustrated in Figure 2, the most broad-spectrum active compound in this series was compound **5g** possessing 3-methylthiophenyl moiety. While **5g** displayed a modest inhibitory activity against DAPK1 kinase with percent inhibition value of $54.6 \pm 0.8\%$, it showed more than 90% inhibition against the other three tested kinases (90.6 ± 0.8 , 96.9 ± 0.3 , and $96.4 \pm 0.1\%$ over FMS, LCK, and LYN kinases, respectively). Based on these results, compounds **5d** and **5g** were subjected to further evaluation.

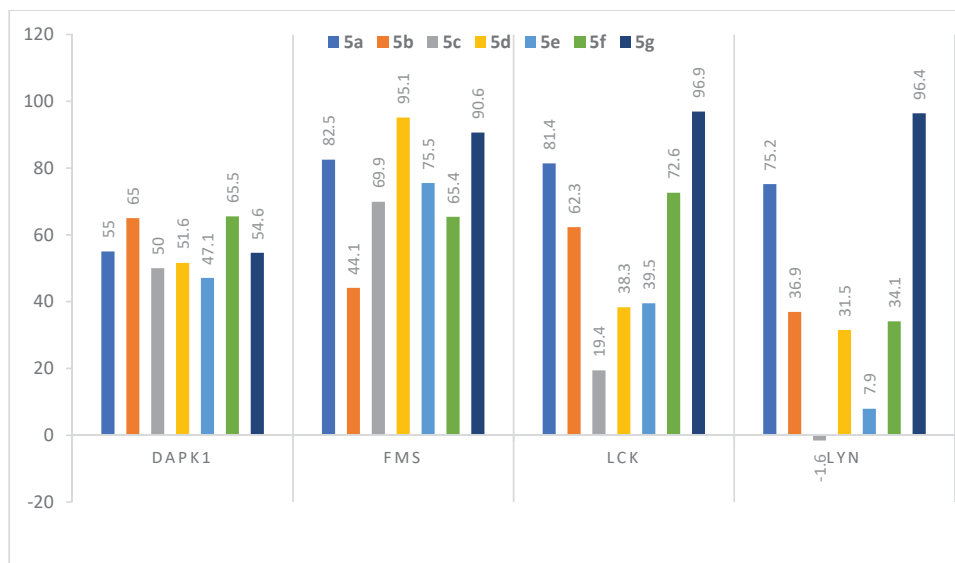


Figure 2. Schematic chart for percent enzyme inhibition (relative to DMSO controls) of all synthesized analogs at a concentration of 10 μM over DAPK1, FMS, LCK, and LYN kinases.

3.2.3. Dose-Dependent Assay of the Most Active Analogs 5d and 5g over FMS, LCK, and LYN Kinases

Since only compounds 5d and 5g were able to inhibit FMS, LCK, and/or LYN kinases with percent inhibition of more than 90%, both compounds were selected for a further dose-dependent assay to determine their IC_{50} values over the corresponding kinases(s) in a 10-dose IC_{50} duplicate mode with a 3-fold serial dilution starting at 100 μM. The results were compared with the FDA-approved multiple kinase inhibitor imatinib [50]. As summarized in Table 3, compound 5d was only assessed over FMS kinase where it demonstrated an IC_{50} value of 213 ± 1 nM, which is almost 5-fold more potent than imatinib. Compound 5g was also able to show potent IC_{50} values of 110 ± 8 , 87.7 ± 8.3 , and 169 ± 31 nM against FMS, LCK, and LYN kinases, respectively. Compared to imatinib, compound 5g was found to be ~ 9- and 2-fold more potent than imatinib over FMS and LCK kinases, respectively.

Table 3. IC_{50} of most active compounds 5d and 5g.

Compound	FMS IC_{50} (nM)	LCK IC_{50} (nM)	LYN IC_{50} (nM)
5d	213 ± 1	NT	NT
5g	110 ± 8	87.7 ± 8.3	169 ± 31
Imatinib	1000	160	190

3.2.4. Efficacy and Spectrum against Diverse Cancer Cells in Growth Inhibition (GI) Assays

The inhibition results of tumor cell growth by the newly synthesized compounds (5a–5g) are described in Table 4. The reported measurements have been performed at the NIH National Cancer Institute, USA by a standardized assay including a panel of 60 different tumor cell lines (Supplementary Data) [51]. The following cancer cell types were included in these assays: Leukemia, non-small cell lung cancer, colon cancer, CNS cancer, melanoma, ovarian cancer, renal cancer, prostate, and breast cancer. The data provided in Table 4, as well as the graphical representation of the inhibitory activity of the synthesized compounds on the different cell lines (Figure 3), revealed that the dimethoxy substitution

of the phenyl ring reduced the anti-cancer activity, as in the 3,5-dimethoxy substituted compound (**5e**) which totally lost the inhibitory activity. Additionally, the 3,4-dimethoxy substituted compound (**5b**) also suffered poor activity against the cancer cell lines. Replacing the dimethoxy substitutions with a 3,5-diethoxy substitution (**5d**) significantly increased the inhibitory activity, while the incorporation of an ortho-substituted nitro group on the phenyl ring did not cause a significant improvement of the activity. While the parent marine-derived compound **5a** was only able to inhibit the RXF 393 cell line of renal cancer with 50.5% growth inhibition, both derivatives **5c** and **5g** showed a significant antiproliferative activity against the SR cell line of leukemia (64.4 and 60.5% growth inhibition, respectively) as well as the RXF 393 cell line of renal cancer with 50.6 and 70.1% growth inhibition, respectively. The other synthesized analogs **5b**, **5d**, **5e**, and **5f** exhibited moderate to poor inhibitory effects on the different cancer cell lines.

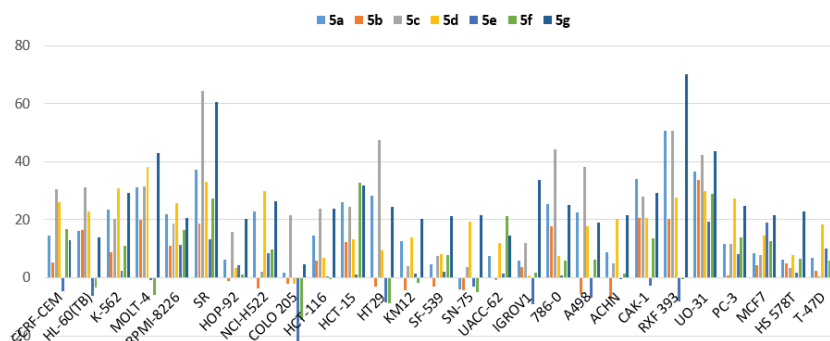


Figure 3. Schematic chart of percent inhibition of all synthesized compounds **5a–5g** against a panel of cancer cell lines.

Table 4. The growth inhibition percentages of the synthesized compounds over the most sensitive cell lines at a single dose concentration of 10 μ M.

Cancer Type	Cell Line	Percent Growth Inhibition (GI)						
		5a	5b	5c	5d	5e	5f	5g
Leukemia	CCRF-CEM	14.46	5.37	30.5	26.1	−4.73	16.66	12.96
	HL-60(TB)	16.16	16.41	31.0	22.8	−6.34	−3.19	13.94
	K-562	23.4	8.76	20.4	30.7	2.31	10.89	29.1
	MOLT-4	31.1	19.9	31.6	38.2	−0.81	−5.98	43.1
	RPMI-8226	21.8	11.12	18.76	25.6	11.31	16.32	20.5
	SR	37.1	18.75	64.4	33.2	13.21	27.4	60.5
Non-Small Cell Lung Cancer	HOP-92	6.16	−1.19	15.76	3.34	4.46	1.12	20.2
	NCI-H522	22.7	−3.5	2.25	29.8	8.4	9.77	26.4
Colon Cancer	COLO 205	1.75	−2.21	21.6	−2.11	−22.42	−14.56	4.7
	HCT-116	14.57	6.01	23.9	6.73	0.34	−0.19	23.7
	HCT-15	26.0	12.32	34.4	13.24	1.13	32.8	31.7
	HT29	28.3	−2.93	47.4	9.54	−8.47	−8.86	24.3
CNS Cancer	KM12	12.72	−4.34	3.99	14	1.32	−1.85	20.2
	SF-539	4.73	−3.17	7.64	8.01	2.09	7.72	21.1
	SNB-75	−3.98	−4.29	3.59	19.2	−3.1	−4.975	21.5

Table 4. Cont.

Cancer Type	Cell Line	Percent Growth Inhibition (GI)						
		5a	5b	5c	5d	5e	5f	5g
Melanoma	UACC-62	7.38	0.1	−0.63	11.99	1.34	21.4	14.69
Ovarian Cancer	IGROV1	5.92	3.6	11.87	0.72	−9.02	1.91	33.9
Renal Cancer	786-0	25.3	17.64	44.2	7.41	0.75	5.78	25.0
	A498	22.4	−5.56	38.3	17.86	−6.85	6.39	18.93
	ACHN	8.91	−7.28	4.83	20.4	−0.26	1.61	21.4
	CAKI-1	33.9	20.6	28.1	20.6	−2.58	13.69	29.4
	RXF 393	50.5	20.4	50.6	27.5	−8.16	−0.36	70.1
	UO-31	36.7	33.6	42.3	29.9	19.36	29	43.7
Prostate Cancer	PC-3	11.71	0.75	11.58	27.3	8.05	13.85	24.9
Breast Cancer	MCF7	8.51	4.24	7.94	14.43	18.87	12.54	21.5
	HS 578T	6.26	5.09	3.23	7.96	1.64	6.7	22.7
	T-47D	6.78	2.41	0.52	18.4	10.16	5.93	28.2

3.2.5. Molecular Docking Studies

A molecular docking study was performed on the active binding regions of LCK, FMS, DAPK1, and LYN proteins. This study was conducted to provide a deeper view of how the changes of the functional groups may affect the activity of the compounds. The docking models over each enzyme are discussed separately in the following subsections.

Molecular Docking Models within the LCK Binding Site

As shown in Table 5, the docked poses of all synthesized compounds showed a direct correlation between the predicted binding affinity of the tested compounds to the active site and their respective LCK inhibition. Compounds with the highest docking scores **5a** (−9.75), **5f** (−9.62), and **5g** (−9.32) correspondingly demonstrated the highest LCK inhibition (81.4, 72.6, and 96.9%, respectively). On the contrary, compounds with lower docking scores **5c** (−7.39) and **5d** (−6.84) exhibited only 19.4 and 38.3% inhibition of LCK, respectively. The inhibitory activity of compounds **5a**, **5b**, **5f**, and **5g** against LCK could be explained due to their ability to establish a minimum of two hydrogen bonds with Met319. Compound **5c**, on the other hand, was able to establish only one hydrogen bond with Met319 in addition to a weak π - π stacking with the pyridine ring, which explains the reason for its weak binding affinity to the binding site of the LCK receptor leading to a weak inhibitory activity. The binding mode of compound **5g** that possesses the highest LCK effect is compared to that of the least active compound **5c** in Figure 4.

Table 5. Computational analysis of all synthesized compounds against LCK.

Compound	Docking Score	Ligand Atoms	Receptor Atoms	Interaction Type	Percent Inhibition
5a	−9.75	N3	Met319	HBA	81.4 ± 0.6
		N7	Met319	HBD	
		O38	Asp382	HBA	
5b	−8.15	N3	Met319	HBA	62.3 ± 0.8
		N7	Met319	HBD	
5c	−7.39	N7 Pyridine ring	Met319 Lys273	HBD π - π stacking	19.4 ± 1.0
5d	−6.84	O31	Ser329	HBA	38.3 ± 4.2
		O27	Asp382	HBA	

Table 5. Cont.

Compound	Docking Score	Ligand Atoms	Receptor Atoms	Interaction Type	Percent Inhibition
5e	−8.96	O31	Met319	HBA	37.5 ± 0.3
		O27	SER323	HBA	
5f	−9.62	N3	Met319	HBA	72.6 ± 0.6
		N7	Met319	HBD	
		Pyridine ring	Lys273	π - π stacking	
		N38	Glu288	Salt bridge	
		O39	Phe383	HBA	
5g	−9.32	O40	Asp382	HBA	96.9 ± 0.3
		N3	Met319	HBA	
		N7	Met319	HBD	
		Pyridine ring	Lys273	π - π stacking	

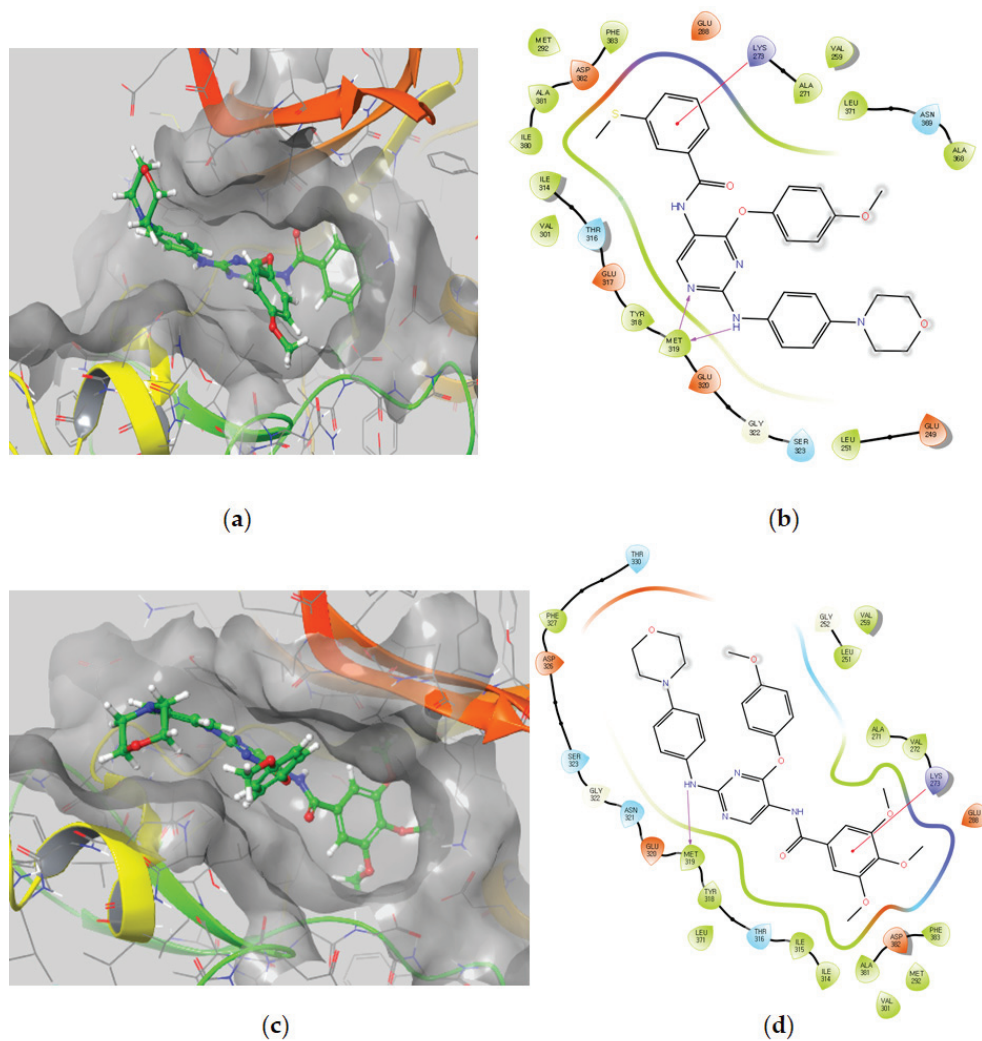


Figure 4. Docked complexes of compounds **5g** and **5c** with LCK. (a,c) 3D docking models of compounds **5g** and **5c** into LCK binding pocket, respectively. (b,d) 2D interaction diagrams of compounds **5g** and **5c** with LCK, respectively.

Molecular Docking Models within the FMS Binding Site

Compounds **5a**, **5b**, **5f**, and **5g** had the highest docking scores of -7.57 , -6.81 , -6.38 , and -6.23 , respectively, while compounds **5c**, **5d**, and **5e** demonstrated comparatively weaker docking scores of -3.26 , -4.47 , and -5.63 , respectively. Despite the relative difference of these docking scores, several characteristics were elucidated through the docking study. One such feature is the amide group responsible for establishing a hydrogen bond between the amide group of the ligand and GLU633. Thus, the amide group was found to be essential for FMS inhibitory activity. To understand the difference in binding activity and identify the important binding groups, an energy-optimized pharmacophore (e-pharmacophore) hypothesis using “Develop a Pharmacophore from Receptor Cavity” option in the phase module was developed. Six pharmacophore sites were predicted, and the final hypothesis consisted of four aromatic rings (R13, 14, 15, and R16) and two H-bond acceptors (A8 and A4) as shown in Figure 5. The SAR diagram of the synthesized compounds, the top score docking model of compound **5a**, and its e-pharmacophore hypothesis are illustrated in Figure 5.

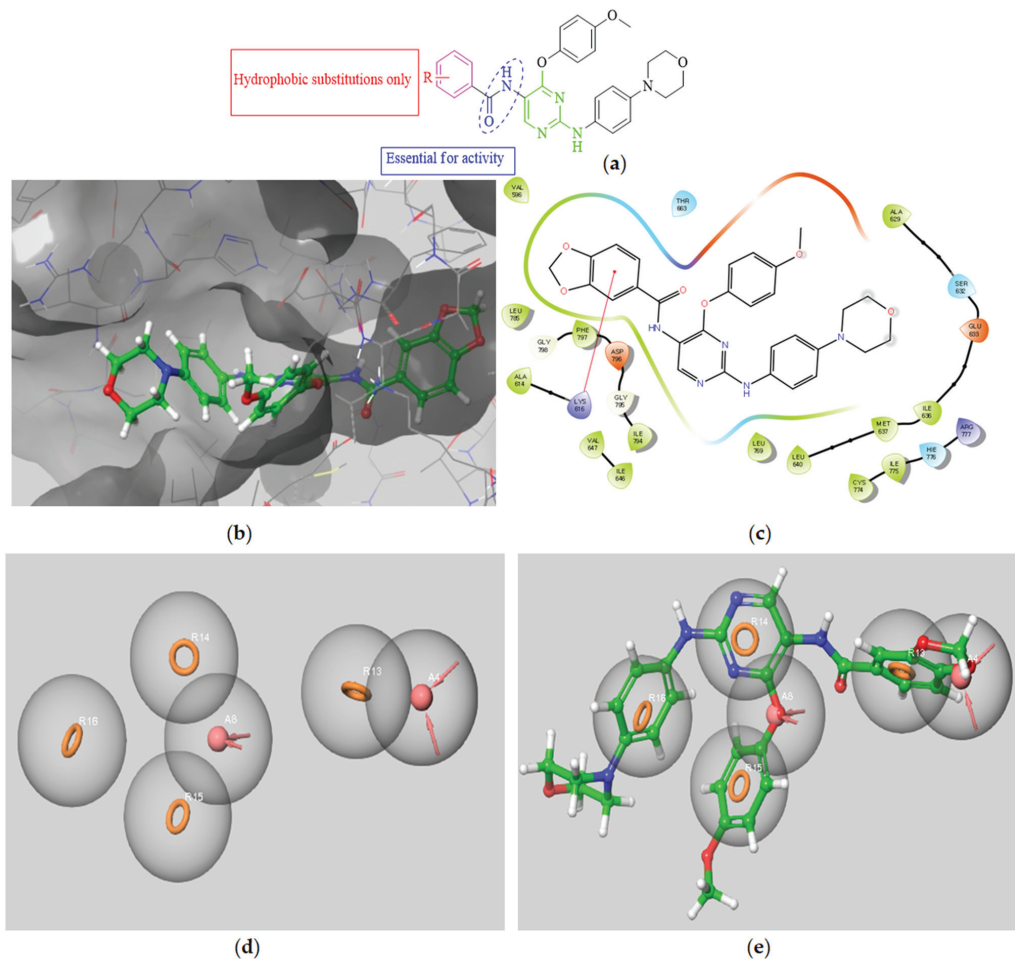


Figure 5. (a) General SAR of the synthesized compounds against FMS kinase. (b) 3D docking model of compound **5a** into the FMS pocket. (c) 2D interaction diagram of compound **5a** with FMS. (d) predicted hypothesis of the essential binding interactions using compound **5a** as a reference. (e) compound **5a** overlaid on the generated e-pharmacophore hypothesis.

Molecular Docking Models within the DAPK1 Binding Site

All synthesized compounds displayed almost similar inhibitory activity over DAPK1, with a range of percent inhibition varying from 65.5% (**5f**) to 47.1% (**5e**). This difference in activity could be explained due to the difference of their binding modes to the active site residue. Compound **5f** formed one salt bridge and four hydrogen bonds, two of these hydrogen bonds were formed via the oxygen of the morpholine ring with Asp161 and Phe162, while the other two hydrogen bonds were established via the nitro group which acted as a hydrogen bond acceptor for Glu100 and Asp103. On the other hand, the least active compound **5e** was only able to form one hydrogen bond through the NH of the morpholino moiety with GLU143. The 2D predicted interaction diagram comparing both compounds **5f** and **5e** is demonstrated in Figure 6.

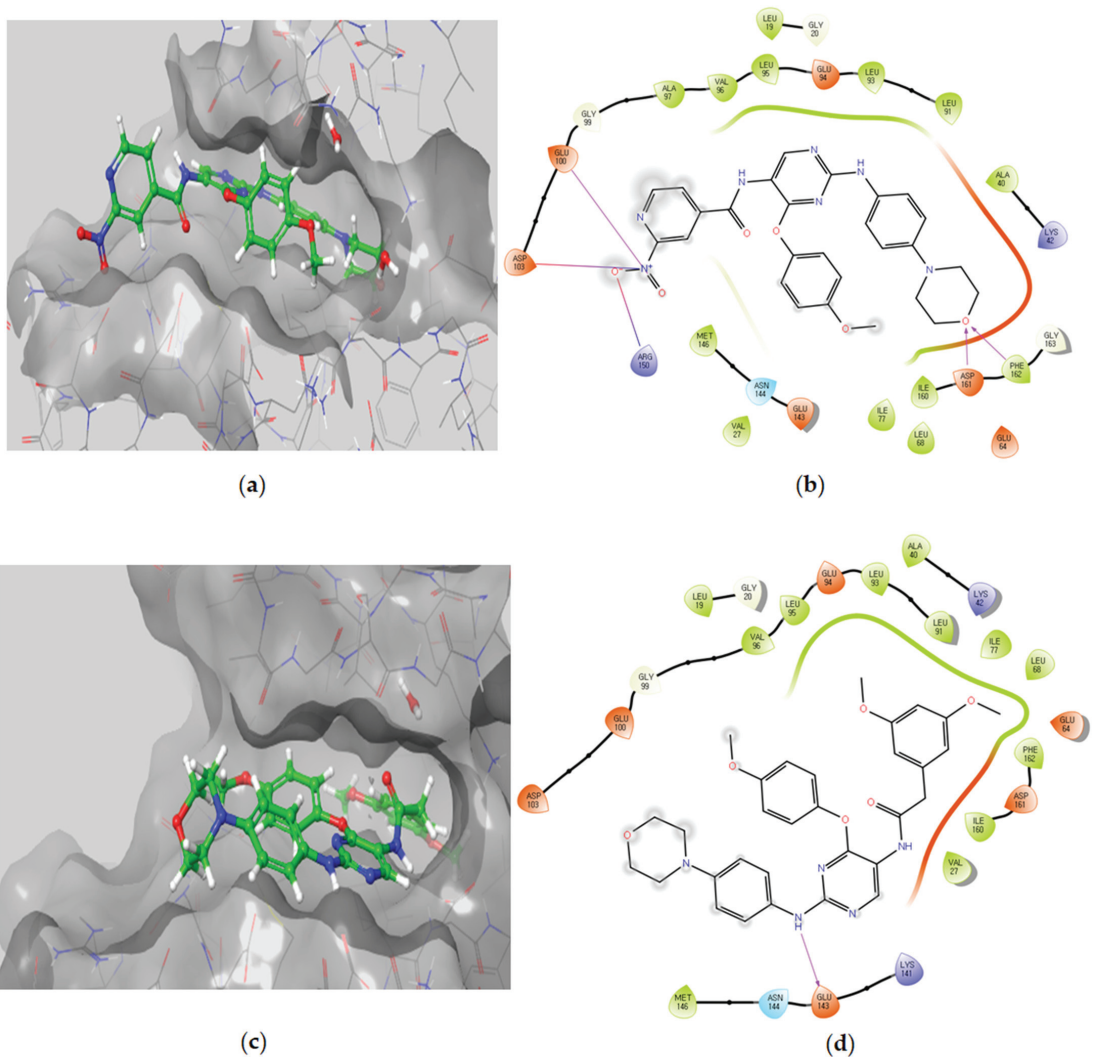


Figure 6. Docked complexes of compounds **5f** and **5e** with DAPK1. (a,c) 3D docking models of compounds **5f** and **5e** into DAPK1 binding pocket, respectively. (b,d) 2D interaction diagrams of compounds **5f** and **5e** with DAPK1, respectively.

Table 6. Predicted pharmacokinetic properties of compounds 5a–5g.

Compound	TPSA	Solubility in Water	BBB Permeability	Intestinal Absorption
5a	116.3	Moderately soluble	no	high
5b	116.3	Moderately soluble	no	high
5c	125.5	Moderately soluble	no	low
5d	116.3	Poorly soluble	no	low
5e	116.3	Moderately soluble	no	high
5f	156.5	Moderately soluble	no	low
5g	123.1	Poorly soluble	no	low

The polar surface area (PSA) or topological polar surface area (TPSA) is characterized as the surface sum over every polar atom or molecule, predominantly oxygen and nitrogen, comprising their attached hydrogen atoms. PSA is frequently used as a medicinal chemistry metric for enhancing the drug's capability to permeate cells. Molecules with a polar surface area of higher than 140 Å² are likely to be inadequate at permeating cell membranes. For a molecule to possess the ability to infiltrate BBB (and thereby be able to exert its effects on the receptors of the central nervous system), a PSA less than 90 angstroms squared is usually considered necessary [57]. Accordingly, among the synthesized compounds, only compound 5f (TPSA of 156.2 Å²) is predicted to be unable to penetrate the cellular membrane easily.

On the other hand, compounds 5a–5e and 5g were found to possess appropriate TPSA values (higher than 90 and below 140 Å²) predicting their ability to penetrate the cells and exert their effects without any possible CNS side effects. Nevertheless, all the synthesized compounds were predicted to suffer from poor to moderate solubility. This, coupled with the fact that compounds 5c, 5d, 5f, and 5g were predicted to have low intestinal absorption. This means that further future modifications of the structures should be carried out to improve the oral bioavailability for this series and maximize their effectiveness.

4. Conclusions

A new series of hybrid small molecules (5a–5g) was developed based on chemical moieties originating from two marine natural products (Meridianin E and Leucettamine B). A single dosage of 10 µM of the parent hybrid 5a, which contains the benzo[*d*][1,3]dioxole moiety of Leucettamine B, inhibited the activity of FMS, LCK, LYN, and DAPK1 kinases by 82.5 ± 0.6, 81.4 ± 0.6, 75.2 ± 0.0, and 55 ± 1.1%, respectively. Further optimizations led to compound 5g (the most potent multi-kinase inhibitor of this new series) with IC₅₀ values of 110, 87.7, and 169 nM against FMS, LCK, and LYN kinases, respectively, which is 9- and 2-fold more potent than the multi-kinase inhibitor imatinib over both FMS and LCK kinases, respectively. Compound 5g also showed promising antitumor activities against leukemia SR and renal RXF 393 cell lines with 60 and 70% inhibition. Supported by the computational studies including docking and ADME simulations, compound 5g is reported as a promising marine-derived multi-kinase potent inhibitor worthy of further investigation.

Supplementary Materials: The following are available online at <https://www.mdpi.com/article/10.3390/biomedicines9091131/s1>. General methods and instruments of Chemistry; charts of NMR, HPLC, and HRMS; biology protocols and raw data for kinase inhibition IC₅₀ determination; original anticancer data obtained from NCI (USA) and Swiss ADME.

Author Contributions: Conceptualization, A.E. and E.J.R.; methodology, M.H.E. and H.N.; software, H.N.; validation, A.E., M.H.A. and K.L.; formal analysis, A.E.; investigation, E.J.R. and K.L.; resources, E.J.R. and K.L.; data curation, A.E.; writing—original draft preparation, M.H.E., A.E. and H.N.; writing—review and editing, A.E. and M.H.A.; visualization, H.N.; supervision, E.J.R.; project

administration, A.E.; funding acquisition, A.E., K.L. and E.J.R. All authors have read and agreed to the published version of the manuscript.

Funding: This study was supported by the KIST Institutional programs (grant no. 2E31140) from the Korea Institute of Science and Technology, the Creative Fusion Research Program through the Creative Allied Project funded by the National Research Council of Science & Technology (CAP-12-1-KIST). This work was also supported by the National Research Foundation of Korea (NRF) grant funded by the Korean government (MSIT) (no. NRF-2018R1A5A2023127).

Institutional Review Board Statement: Not applicable.

Informed Consent Statement: Not applicable.

Acknowledgments: A.E. extends his appreciation to the Korea Institute of Science and Technology (KIST) for supporting this work through “2021 KIST School partnership project” and in the accomplishment of this project. A.E. would like to thank the Technology Innovation Commercial Office (TICO) at Mansoura University for their highly effective contribution. M.H.A thanks Taif University Researchers Supporting Project number (TURSP-2020/91), Taif University, Taif, Saudi Arabia.

Conflicts of Interest: The authors declare no conflict of interest.

References

1. Bharate, S.B.; Sawant, S.D.; Singh, P.P.; Vishwakarma, R.A. Kinase Inhibitors of Marine Origin. *Chem. Rev.* **2013**, *113*, 6761–6815. [CrossRef]
2. Bharate, S.B.; Yadav, R.R.; Battula, S.; Vishwakarma, R.A. Meridianins: Marine-derived potent kinase inhibitors. *Mini Rev. Med. Chem.* **2012**, *12*, 618–631. [CrossRef] [PubMed]
3. Eldehna, W.M.; Hassan, G.S.; Al-Rashood, S.T.; Alkahtani, H.M.; Almehezia, A.A.; Al-Ansary, G.H. Marine-Inspired Bis-indoles Possessing Antiproliferative Activity against Breast Cancer; Design, Synthesis, and Biological Evaluation. *Mar. Drugs* **2020**, *18*, 190. [CrossRef]
4. Gerwick, W.H.; Fenner, A.M. Drug discovery from marine microbes. *Microb. Ecol.* **2013**, *65*, 800–806. [CrossRef] [PubMed]
5. Wang, E.; Sorolla, M.A.; Krishnan, P.D.G.; Sorolla, A. From Seabed to Bedside: A Review on Promising Marine Anticancer Compounds. *Biomolecules* **2020**, *10*, 248. [CrossRef]
6. Pereira, F. Have marine natural product drug discovery efforts been productive and how can we improve their efficiency? *Expert Opin. Drug Discov.* **2019**, *14*, 717–722. [CrossRef] [PubMed]
7. Wang, X.; Song, K.; Li, L.; Chen, L. Structure-Based Drug Design Strategies and Challenges. *Curr. Top. Med. Chem.* **2018**, *18*, 998–1006. [CrossRef] [PubMed]
8. Nagasaka, M.; Gadgeel, S.M. Role of chemotherapy and targeted therapy in early-stage non-small cell lung cancer. *Expert Rev. Anticancer Ther.* **2018**, *18*, 63–70. [CrossRef]
9. Hughes, J.P.; Rees, S.; Kalindjian, S.B.; Philpott, K.L. Principles of early drug discovery. *Br. J. Pharmacol.* **2011**, *162*, 1239–1249. [CrossRef]
10. Hoelder, S.; Clarke, P.A.; Workman, P. Discovery of small molecule cancer drugs: Successes, challenges and opportunities. *Mol. Oncol.* **2012**, *6*, 155–176. [CrossRef] [PubMed]
11. Elkamhawy, A.; Viswanath, A.N.I.; Pae, A.N.; Kim, H.Y.; Heo, J.C.; Park, W.K.; Lee, C.O.; Yang, H.; Kim, K.H.; Nam, D.H.; et al. Discovery of potent and selective cytotoxic activity of new quinazoline-ureas against TMZ-resistant glioblastoma multiforme (GBM). *Eur. J. Med. Chem.* **2015**, *103*, 210–222. [CrossRef]
12. Bhullar, K.S.; Lagarón, N.O.; McGowan, E.M.; Parmar, I.; Jha, A.; Hubbard, B.P.; Rupasinghe, H.P.V. Kinase-targeted cancer therapies: Progress, challenges and future directions. *Mol. Cancer* **2018**, *17*, 48. [CrossRef]
13. Madhusudan, S.; Ganesan, T.S. Tyrosine kinase inhibitors in cancer therapy. *Clin. Biochem.* **2004**, *37*, 618–635. [CrossRef]
14. Cicenás, J.; Cicenás, E. Multi-kinase inhibitors, AURKs and cancer. *Med. Oncol.* **2016**, *33*, 43. [CrossRef]
15. Nada, H.; Elkamhawy, A.; Lee, K. Structure Activity Relationship of Key Heterocyclic Anti-Angiogenic Leads of Promising Potential in the Fight against Cancer. *Molecules* **2021**, *26*, 553. [CrossRef] [PubMed]
16. Elkamhawy, A.; Farag, A.K.; Viswanath, A.N.I.; Bedair, T.M.; Leem, D.G.; Lee, K.-T.; Pae, A.N.; Roh, E.J. Targeting EGFR/HER2 tyrosine kinases with a new potent series of 6-substituted 4-anilinoquinazoline hybrids: Design, synthesis, kinase assay, cell-based assay, and molecular docking. *Bioorg. Med. Chem. Lett.* **2015**, *25*, 5147–5154. [CrossRef] [PubMed]
17. Elkamhawy, A.; Park, J.-e.; Cho, N.-C.; Sim, T.; Pae, A.N.; Roh, E.J. Discovery of a broad spectrum antiproliferative agent with selectivity for DDR1 kinase: Cell line-based assay, kinase panel, molecular docking, and toxicity studies. *J. Enzym. Inhib. Med. Chem.* **2016**, *31*, 158–166. [CrossRef] [PubMed]
18. Elkamhawy, A.; Paik, S.; Hassan, A.H.E.; Lee, Y.S.; Roh, E.J. Hit discovery of 4-amino-N-(4-(3-(trifluoromethyl)phenoxy)pyrimidin-5-yl)benzamide: A novel EGFR inhibitor from a designed small library. *Bioorganic Chem.* **2017**, *75*, 393–405. [CrossRef] [PubMed]

19. Elkamhawy, A.; Kim, N.y.; Hassan, A.H.E.; Park, J.-e.; Yang, J.-E.; Oh, K.-S.; Lee, B.H.; Lee, M.Y.; Shin, K.J.; Lee, K.-T.; et al. Design, synthesis and biological evaluation of novel thiazolidinedione derivatives as irreversible allosteric IKK- β modulators. *Eur. J. Med. Chem.* **2018**, *157*, 691–704. [CrossRef] [PubMed]
20. Elkamhawy, A.; youn Kim, N.; Hassan, A.H.E.; Park, J.-e.; Yang, J.-E.; Elsherbeny, M.H.; Paik, S.; Oh, K.-S.; Lee, B.H.; Lee, M.Y.; et al. Optimization study towards more potent thiazolidine-2,4-dione IKK- β modulator: Synthesis, biological evaluation and in silico docking simulation. *Bioorg. Chem.* **2019**, *92*, 103261. [CrossRef] [PubMed]
21. Al-Sanea, M.M.; Elkamhawy, A.; Paik, S.; Lee, K.; El Kerdawy, A.M.; Syed Nasir Abbas, B.; Joo Roh, E.; Eldehna, W.M.; Elshemy, H.A.H.; Bakr, R.B.; et al. Sulfonamide-based 4-anilinoquinoline derivatives as novel dual Aurora kinase (AURKA/B) inhibitors: Synthesis, biological evaluation and in silico insights. *Bioorg. Med. Chem.* **2020**, *28*, 115525. [CrossRef]
22. Zhao, J.; Huang, Y.; Ma, G.; Lin, L.; Feng, P. One-Pot Protocol To Synthesize 2-Aminophenols from Anilines via Palladium-Catalyzed C–H Acetoxylation. *Organometallics* **2019**, *38*, 2084–2091. [CrossRef]
23. Ellis, H.; Ma, C.X. PI3K Inhibitors in Breast Cancer Therapy. *Curr. Oncol. Rep.* **2019**, *21*, 110. [CrossRef]
24. Wang, M.; Wang, T.; Zhang, X.; Wu, X.; Jiang, S. Cyclin-dependent kinase 7 inhibitors in cancer therapy. *Future Med. Chem.* **2020**, *12*, 813–833. [CrossRef]
25. Otto, T.; Sicinski, P. Cell cycle proteins as promising targets in cancer therapy. *Nat. Rev. Cancer* **2017**, *17*, 93–115. [CrossRef] [PubMed]
26. Degirmenci, U.; Wang, M.; Hu, J. Targeting Aberrant RAS/RAF/MEK/ERK Signaling for Cancer Therapy. *Cells* **2020**, *9*, 198. [CrossRef]
27. Wang, P.F.; Qiu, H.Y.; He, Y.; Zhu, H.L. Cyclin-dependent kinase 4/6 inhibitors for cancer therapy: A patent review (2015–2019). *Expert Opin. Ther. Pat.* **2020**, *30*, 795–805. [CrossRef] [PubMed]
28. Roskoski, R., Jr. Small molecule inhibitors targeting the EGFR/ErbB family of protein-tyrosine kinases in human cancers. *Pharmacol. Res.* **2019**, *139*, 395–411. [CrossRef]
29. Zhong, L.; Li, Y.; Xiong, L.; Wang, W.; Wu, M.; Yuan, T.; Yang, W.; Tian, C.; Miao, Z.; Wang, T.; et al. Small molecules in targeted cancer therapy: Advances, challenges, and future perspectives. *Signal Transduct. Target. Ther.* **2021**, *6*, 201. [CrossRef]
30. Li, T.; Wang, N.; Zhang, T.; Zhang, B.; Sajeevan, T.P.; Joseph, V.; Armstrong, L.; He, S.; Yan, X.; Naman, C.B. A Systematic Review of Recently Reported Marine Derived Natural Product Kinase Inhibitors. *Mar. Drugs* **2019**, *17*, 493. [CrossRef]
31. Franco, L.H.; Joffé, E.B.d.K.; Puricelli, L.; Tatian, M.; Seldes, A.M.; Palermo, J.A. Indole Alkaloids from the Tunicate *Aplidium meridianum*. *J. Nat. Prod.* **1998**, *61*, 1130–1132. [CrossRef]
32. Gompel, M.; Leost, M.; De Kier Joffe, E.B.; Puricelli, L.; Franco, L.H.; Palermo, J.; Meijer, L. Meridianins, a new family of protein kinase inhibitors isolated from the ascidian *Aplidium meridianum*. *Bioorg. Med. Chem. Lett.* **2004**, *14*, 1703–1707. [CrossRef]
33. Hsu, M.-H.; Hsieh, C.-Y.; Kapoor, M.; Chang, J.-H.; Chu, H.-L.; Cheng, T.-M.; Hsu, K.-C.; Lin, T.E.; Tsai, F.-Y.; Homg, J.-C. Leucettamine B analogs and their carborene derivative as potential anti-cancer agents: Design, synthesis, and biological evaluation. *Bioorg. Chem.* **2020**, *98*, 103729. [CrossRef]
34. Chan, G.W.; Mong, S.; Hemling, M.E.; Freyer, A.J.; Offen, P.H.; DeBrosse, C.W.; Sarau, H.M.; Westley, J.W. New Leukotriene B4 Receptor Antagonist: Leucettamine A and Related Imidazole Alkaloids from the Marine Sponge *Leucetta microraphis*. *J. Nat. Prod.* **1993**, *56*, 116–121. [CrossRef] [PubMed]
35. Debdab, M.; Carreaux, F.; Renault, S.; Soundararajan, M.; Fedorov, O.; Filippakopoulos, P.; Lozach, O.; Babault, L.; Tahtouh, T.; Baratte, B.; et al. Leucettines, a Class of Potent Inhibitors of cdc2-Like Kinases and Dual Specificity, Tyrosine Phosphorylation Regulated Kinases Derived from the Marine Sponge Leucettamine B: Modulation of Alternative Pre-RNA Splicing. *J. Med. Chem.* **2011**, *54*, 4172–4186. [CrossRef]
36. Debdab, M.; Renault, S.; Lozach, O.; Meijer, L.; Paquin, L.; Carreaux, F.; Bazureau, J.-P. Synthesis and preliminary biological evaluation of new derivatives of the marine alkaloid leucettamine B as kinase inhibitors. *Eur. J. Med. Chem.* **2010**, *45*, 805–810. [CrossRef] [PubMed]
37. Tahtouh, T.; Elkins, J.M.; Filippakopoulos, P.; Soundararajan, M.; Burgy, G.; Durieu, E.; Cochet, C.; Schmid, R.S.; Lo, D.C.; Delhomme, F.; et al. Selectivity, Cocrystal Structures, and Neuroprotective Properties of Leucettines, a Family of Protein Kinase Inhibitors Derived from the Marine Sponge Alkaloid Leucettamine B. *J. Med. Chem.* **2012**, *55*, 9312–9330. [CrossRef] [PubMed]
38. Park, J.-e.; Elkamhawy, A.; Hassan, A.H.E.; Pae, A.N.; Lee, J.; Paik, S.; Park, B.-G.; Roh, E.J. Synthesis and evaluation of new pyridyl/pyrazinyl thiourea derivatives: Neuroprotection against amyloid- β -induced toxicity. *Eur. J. Med. Chem.* **2017**, *141*, 322–334. [CrossRef] [PubMed]
39. Elkamhawy, A.; Hassan, A.H.E.; Paik, S.; Sup Lee, Y.; Lee, H.H.; Shin, J.S.; Lee, K.T.; Roh, E.J. EGFR inhibitors from cancer to inflammation: Discovery of 4-fluoro-N-(4-(3-(trifluoromethyl)phenoxy)pyrimidin-5-yl)benzamide as a novel anti-inflammatory EGFR inhibitor. *Bioorg. Chem.* **2019**, *86*, 112–118. [CrossRef]
40. Farag, A.K.; Elkamhawy, A.; Londhe, A.M.; Lee, K.T.; Pae, A.N.; Roh, E.J. Novel LCK/FMS inhibitors based on phenoxy pyrimidine scaffold as potential treatment for inflammatory disorders. *Eur. J. Med. Chem.* **2017**, *141*, 657–675. [CrossRef]
41. Skehan, P.; Storeng, R.; Scudiero, D.; Monks, A.; McMahon, J.; Vistica, D.; Warren, J.T.; Bokesch, H.; Kenney, S.; Boyd, M.R. New colorimetric cytotoxicity assay for anticancer-drug screening. *JNCI J. Natl. Cancer Inst.* **1990**, *82*, 1107–1112. [CrossRef] [PubMed]
42. Elkamhawy, A.; Al-Sanea, M.M.; Song, C.; Sim, T.; Roh, E.J. Design and Synthesis of New [1,2,3]Triazololo[4,5-d]pyrimidine Derivatives as Potential Antiproliferative Agents. *Bull. Korean Chem. Soc.* **2015**, *36*, 1863–1873. [CrossRef]

43. Al-Sanea, M.M.; Elkamhawy, A.; Zakaria, A.; Park, B.S.; Kwon, Y.; Lee, S.H.; Lee, S.W.; Kim, I.T. Synthesis and in Vitro Screening of Phenylbipyridinylpyrazole Derivatives as Potential Antiproliferative Agents. *Molecules* **2015**, *20*, 1031–1045. [CrossRef] [PubMed]
44. El-Gamal, M.I.; Anbar, H.S.; Yoo, K.H.; Oh, C.H. FMS Kinase Inhibitors: Current Status and Future Prospects. *Med. Res. Rev.* **2013**, *33*, 599–636. [CrossRef]
45. Sun, Y.; Yang, Y.; Zhao, Y.; Li, X.; Zhang, Y.; Liu, Z. The role of the tyrosine kinase Lyn in allergy and cancer. *Mol. Immunol.* **2021**, *131*, 121–126. [CrossRef]
46. Chen, D.; Zhou, X.Z.; Lee, T.H. Death-Associated Protein Kinase 1 as a Promising Drug Target in Cancer and Alzheimer’s Disease. *Recent Pat. Anti-Cancer Drug Discov.* **2019**, *14*, 144–157. [CrossRef]
47. Singh, P.; Ravanan, P.; Talwar, P. Death Associated Protein Kinase 1 (DAPK1): A Regulator of Apoptosis and Autophagy. *Front. Mol. Neurosci.* **2016**, *9*, 46. [CrossRef] [PubMed]
48. Agodi, A.; Barchitta, M.; Quattrocchi, A.; Maugeri, A.; Vinciguerra, M. DAPK1 Promoter Methylation and Cervical Cancer Risk: A Systematic Review and a Meta-Analysis. *PLoS ONE* **2015**, *10*, e0135078. [CrossRef] [PubMed]
49. Elkamhawy, A.; Ali, E.M.H.; Lee, K. New horizons in drug discovery of lymphocyte-specific protein tyrosine kinase (Lck) inhibitors: A decade review (2011–2021) focussing on structure-activity relationship (SAR) and docking insights. *J. Enzym. Inhib. Med. Chem.* **2021**, *36*, 1574–1602. [CrossRef] [PubMed]
50. Kitagawa, D.; Yokota, K.; Gouda, M.; Narumi, Y.; Ohmoto, H.; Nishiwaki, E.; Akita, K.; Kirii, Y. Activity-based kinase profiling of approved tyrosine kinase inhibitors. *Genes Cells* **2013**, *18*, 110–122. [CrossRef]
51. Teicher, B.A. *Anticancer Drug Development Guide: Preclinical Screening, Clinical Trials, and Approval*; Springer Science & Business Media: Berlin/Heidelberg, Germany, 2013.
52. Di, L.; Kerns, E.H. *Drug-Like Properties: Concepts, Structure Design and Methods from ADME to Toxicity Optimization*; Academic Press: Cambridge, MA, USA, 2015.
53. Zhang, P.; Xu, S.; Zhu, Z.; Xu, J. Multi-target design strategies for the improved treatment of Alzheimer’s disease. *Eur. J. Med. Chem.* **2019**, *176*, 228–247. [CrossRef] [PubMed]
54. Daina, A.; Michielin, O.; Zoete, V. SwissADME: A free web tool to evaluate pharmacokinetics, drug-likeness and medicinal chemistry friendliness of small molecules. *Sci. Rep.* **2017**, *7*, 42717. [CrossRef] [PubMed]
55. Daina, A.; Zoete, V. A BOILED-Egg to Predict Gastrointestinal Absorption and Brain Penetration of Small Molecules. *ChemMed-Chem* **2016**, *11*, 1117–1121. [CrossRef] [PubMed]
56. Alavijeh, M.S.; Chishty, M.; Qaiser, M.Z.; Palmer, A.M. Drug metabolism and pharmacokinetics, the blood-brain barrier, and central nervous system drug discovery. *NeuroRx* **2005**, *2*, 554–571. [CrossRef] [PubMed]
57. Pajouhesh, H.; Lenz, G.R. Medicinal chemical properties of successful central nervous system drugs. *NeuroRx* **2005**, *2*, 541–553. [CrossRef]



Article

N-Alkylation of Anthracycline Antibiotics by Natural Sesquiterpene Lactones as a Way to Obtain Antitumor Agents with Reduced Side Effects

Margarita Neganova, Alexey Semakov, Yulia Aleksandrova, Ekaterina Yandulova, Sergey Pukhov, Lada Anikina and Sergey Klochkov *

Institute of Physiologically Active Compounds, Russian Academy of Sciences, 142432 Chernogolovka, Russia; neganova83@mail.ru (M.N.); l_vok@list.ru (A.S.); yulia.aleks.97@mail.ru (Y.A.); yandulovacaterina@gmail.com (E.Y.); pukhov.sergey@gmail.com (S.P.); anikina1970@gmail.com (L.A.)

* Correspondence: klochkov@ipac.ac.ru; Tel.: +7-(496)5242525

Abstract: Anthracycline antitumor antibiotics are one of the promising classes of chemotherapeutic agents for cancer treatment. The main deterrent to their use is high toxicity to a healthy environment, including cumulative cardiotoxicity. In our work, bipharmacophore molecules containing in their structure a fragment of the known anthracycline antibiotics daunorubicin and doxorubicin and natural sesquiterpene lactones were obtained for the first time. When studying the biological activity of the synthesized compounds, it was found that with equal and, in some cases, higher cytotoxicity and glycolysis inhibition by anthracycline antibiotics conjugates with sesquiterpene lactones in comparison with doxo- and daunorubicin, a reduced damaging effect on the functioning of rat heart mitochondria was observed. The results obtained allow us to confirm the assumption that the chemical modification of the anthracycline antibiotics molecules doxo- and daunorubicin by natural sesquiterpene lactones can be a promising strategy for creating potential antitumor chemotherapeutic drugs with a pronounced cytotoxic effect on tumor cells and a reduced damaging effect on healthy cells of the human organism.

Keywords: doxorubicin; daunorubicin; sesquiterpene lactones; conjugates; cancer; cardiotoxicity; glycolysis; rat heart mitochondria

Citation: Neganova, M.; Semakov, A.; Aleksandrova, Y.; Yandulova, E.; Pukhov, S.; Anikina, L.; Klochkov, S. N-Alkylation of Anthracycline Antibiotics by Natural Sesquiterpene Lactones as a Way to Obtain Antitumor Agents with Reduced Side Effects. *Biomedicines* **2021**, *9*, 547. <https://doi.org/10.3390/biomedicines9050547>

Academic Editors: Leonardo Caputo, Laura Quintieri and Orazio Nicolotti

Received: 18 March 2021

Accepted: 11 May 2021

Published: 13 May 2021

Publisher's Note: MDPI stays neutral with regard to jurisdictional claims in published maps and institutional affiliations.



Copyright: © 2021 by the authors. Licensee MDPI, Basel, Switzerland. This article is an open access article distributed under the terms and conditions of the Creative Commons Attribution (CC BY) license (<https://creativecommons.org/licenses/by/4.0/>).

1. Introduction

Anthracycline antibiotics have pronounced antitumor properties. The clinical use of representatives of this class as antineoplastic agents dates to the 60s of the last century. Notable examples are doxorubicin, which is an important component of therapy aimed at the treatment of various solid tumors, soft tissue sarcomas, and aggressive lymphomas, and daunorubicin, which is active against acute lymphoblastic and myeloblastic leukemias [1]. Despite the fact that anthracyclines undoubtedly play one of the key roles in the treatment of malignant neoplasms, their use is limited due to their low selectivity of action and high toxicity in relation to healthy tissues, mainly of the cardiovascular system. Thus, chronic administration of substances of this class leads to the development of cardiomyopathy and treatment-resistant congestive heart failure, which is caused by damage to the cell myocardium membranes [2]. In this regard, for more than 40 years, scientists have been making numerous attempts to identify new anthracycline antitumor antibiotics that could surpass doxo- and daunorubicin in terms of activity and/or tolerance to the development of cardiovascular pathologies. To date, more than two thousand analogs of anthracycline antibiotics are known, which were created by various chemical modifications, substitutions, and/or conjugations, both in the tetracyclic nucleus and in the side chain or amino sugar [1], but only a few of them have become commercially successful and remain in use. Epirubicin, a semisynthetic derivative of doxorubicin obtained as a result of the hydroxyl group

epimerization at the 4-position of daunosamine, and idarubicin, one of the first synthetic derivatives of daunorubicin, formed by the removal of the methoxy group in aglycone, are very popular chemotherapeutic agents, which show improvements in efficacy and cardiotoxicity [3–5]. This confirms the promise of the search for antitumor agents in analogs of this class of compounds.

It is known that the cytotoxicity of anthracycline antibiotics is caused by DNA damage, mediated mainly by the inhibition of topoisomerase II [6], as well as the excessive formation of reactive oxygen species [7] (Figure 1). Thus, one of the main causes of oxidative stress caused by this class of compounds is a violation of mitochondrial function, affecting the electron transport chain complexes of organelles, leading to their deactivation and overproduction of ROS [8,9]. Ca^{2+} homeostasis disruption triggered by anthracycline antibiotics causes the opening of the mitochondrial membrane permeability transition pore (mPTP) and a decrease in the transmembrane potential along with an increase in the permeability of the outer mitochondrial membrane for the release of apoptotic factors [10]. In addition, it has been shown that doxo- and daunorubicin are capable of inhibiting the glycolytic pathway of energy production [11], disrupting the work of the endogenous antioxidant system of cell defense [12], and also directly interacting with iron ions, forming reactive anthracycline-iron complexes, which leads to cyclic transition of Fe^{3+} and Fe^{2+} , energy collapse, and additionally stimulates the ROS formation [13].

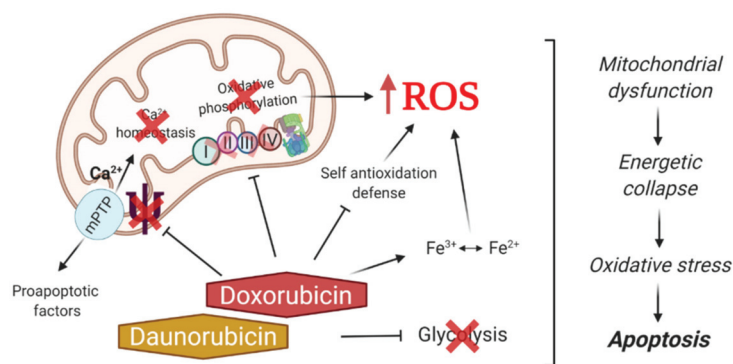


Figure 1. Mechanisms of antitumor action of anthracycline antibiotics associated with hyperproduction of reactive oxygen species (ROS) and inhibition of glycolysis.

The development of anthracycline analogues is still actively continuing to reduce the risk of cardiotoxicity and improve the therapeutic index. An interesting object used for their modification can be natural origin products—sesquiterpene lactones, which contain activated double bonds in their structure and exhibit a wide range of biological activity. The antitumor potential of this class of compounds is confirmed by their ability to modulate a number of mechanisms involved in the development of oncological diseases, in particular, the processes associated with oxidative stress [14–16], the mitochondria functioning [17], and the glycolytic profile of transformed cells [18,19].

In this work, a number of anthracycline antibiotics conjugates with natural sesquiterpene lactones of *Inula helenium* L. (*Asteraceae*) were first obtained and studied. The anthracycline antibiotics doxorubicin (a) and daunorubicin (b) were modified with sesquiterpene lactones—isoalantholactone (1), alantolactone (2), alloalantholactone (3), epoxyisovalantholactone (4), epoxyalantholactone (5), epoxyalloalantholactone (6), 6-hydroxyxanthodiene (7), alanthodiene (8). Conjugates 1–6a–b were obtained in our previous works [20–22]; compounds 7a, b and 8a, b were first obtained and studied. Their cytotoxic and antiproliferative properties in relation to tumor cell lines were evaluated and their influence on key aspects of formation of cytotoxicity—mitochondrial functional character-

istics (mitochondrial swelling, membrane potential, and mitochondrial respiratory chain complexes) as well as the glycolytic function parameters of HeLa tumor cells— was studied.

2. Materials and Methods

2.1. Chemistry

^1H and ^{13}C NMR spectra were recorded on Bruker AVANCE III instruments (operating frequency 500.13 and 125.78 MHz) and Bruker DPX-200 (200.13 and 50.32 MHz). In CDCl_3 , the internal standard is the residual solvent signal; subscripts “alpha” and “beta” denote nonequivalent protons at one carbon atom. To refine the multiplicity in the proton spectra analysis, we used the multiplication by the TRAF function. For some weakly intense ^{13}C spectra, the convolution difference was used to increase the signal-to-noise ratio. High-resolution mass spectra were recorded using a Sciex QStar quadrupole time-of-flight mass spectrometer with orthogonal ion input and a Thermo Fisher Exactive mass spectrometer with an electrospray ionization source and Orbitrap mass analyzer. For ionization, solutions of the starting substances in acetonitrile with a concentration of $\sim 10^{-5}$ M were taken. When calculating the molecular masses, the following atomic masses were used: H—1.007825, O—15.994915, C—12.000000, N—14.003074. The compounds were purified by silica gel column chromatography. If necessary, the individual components were purified by semi-preparative HPLC (Turbo LC 200 chromatograph, Perkin Elmer, Germany), diode matrix detector, UV 254 nm; analytical column 4×100 mm with Kromasil C18, 5 μm ; preparative column 10×250 mm with Kromasil C18, 5 μm ; gradient elution: eluent A was 0.1% trifluoroacetic acid in distilled water (pH 2.0), eluent B was acetonitrile, and the elution rates were 1 and 4 $\text{mL} \cdot \text{min}^{-1}$ for the analytical and preparative columns, respectively. The melting points were measured by a Kruss M3000 apparatus. TLC was performed by Alugram Xtra Sil G/UV254 plates; compounds were detected without additional treatment, as well as after treatment with anisaldehyde reagent. The reaction of the obtained compounds was monitored using TLC on Alugram Xtra SIL D/UV254 plates in the $\text{CHCl}_3:\text{MeOH} = 10:1$ system, the conversion degree of the initial lactone was controlled by ^1H NMR (the disappearance of proton signals of the exomethylene group in the 4–5 ppm).

In chemical experiments, we used reagents from Acros Organics, Catrosa, Panreac, and Sigma–Aldrich; doxo- and daunorubicin were obtained from OSEIB (OSEIB, Kirov, Russia).

The natural sesquiterpene lactones (1) and (2) were isolated from the roots of elecampane *Inula helenium* L. according to the method we developed earlier [23]. Alloalantholactone (3) was obtained by isomerization of isolantholactone (1) under the action of a 5-fold excess of trifluoroacetic acid (in chloroform) [22]. Epoxylactones (4), (5), (6) were obtained from them by the action of peracetic acid according to the procedures from [23]. 6-Hydroxyxanthodiene (7) and alanthodiene (8) were obtained as we described earlier under the conditions of acid isomerization of epoxyalantolactone. The spectral characteristics were consistent with the literature data [23] (Figure 2).

2.2. Preparation of Daunorubicin and Doxorubicin Conjugates

Anthracycline antibiotics conjugates (1a), (2a), (4a), (5a), (6a), (1b), (3b), (4b), (5b), (6b) were obtained as described earlier; the spectral characteristics corresponded to the literature data [20–22].

2.3. General Procedure for the Preparation of Doxorubicin Conjugates

In a mixture of 2 mL of methanol and 2 mL of chloroform, 0.431 mmol of the respective lactone (1)–(8) was dissolved, then 250 mg of doxorubicin hydrochloride and 120 μL (2 eq.) of triethylamine were added and left at room temperature for seven days. The reaction was monitored by TLC in the $\text{CHCl}_3:\text{MeOH} = 10:1$ system. The reaction mixture was evaporated under reduced pressure on a rotary evaporator, purified by column chromatography on silica gel, washed first with CHCl_3 , then $\text{CHCl}_3:\text{AcOEt} = 10:2$ and $\text{CHCl}_3:\text{MeOH} = 10:1$,

and the product was eluted from the column with a narrow zone. If necessary, additional HPLC purification was carried out.

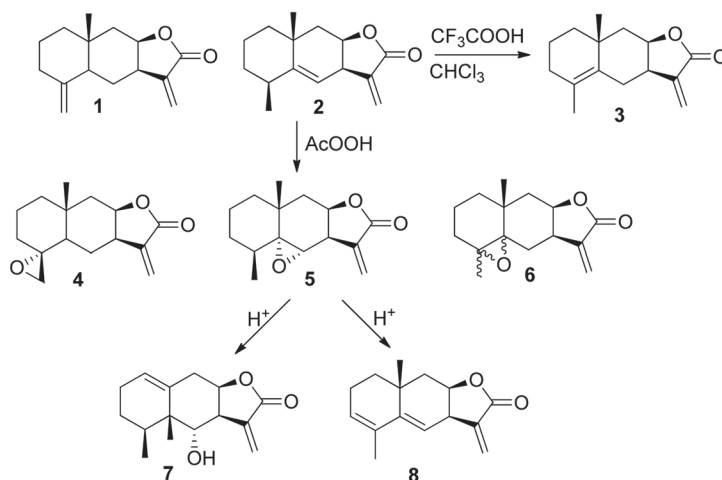


Figure 2. Scheme for obtaining of sesquiterpene lactones used to modify anthracycline antibiotics.

2.4. Preparation of Daunorubicin as a Base

In a separatory funnel, 1 g of daunorubicin hydrochloride was dissolved in 200 mL of water; 100 mL of chloroform and 1–5 mL of methanol were added, and NaHCO_3 was added until the main part of the colored anthracycline was transferred to the organic layer. The lower layer was poured off and evaporated, and the remaining daunorubicin was extracted from the aqueous phase three times with 50 mL of chloroform. The sum of the chloroform extracts was evaporated to yield daunorubicin base powder.

2.5. General Procedure for the Preparation of Daunorubicin Conjugates

In a mixture of 2 mL of methanol and 2 mL of chloroform, 0.43 mmol of the corresponding lactone (1)–(8) was dissolved, and then 250 mg of daunorubicin was added in the form of a free amine and left at room temperature for seven days. The progress of the reaction was monitored by TLC in the $\text{CHCl}_3:\text{MeOH} = 10:1$ system. The reaction mixture was evaporated under reduced pressure on a rotary evaporator, purified by column chromatography on silica gel, washed first with CHCl_3 (until a low-polarity colored aglycone daunorubicin emerged), then with $\text{CHCl}_3:\text{AcOEt} = 10:2$ and $\text{CHCl}_3:\text{MeOH} = 10:1$, and the colored product was eluted from the column in a narrow zone (unreacted daunorubicin remained at the start). Fractions with the target product were evaporated from the solvent, and the product was evaporated once again together with ether. If necessary, additional HPLC purification was carried out.

Characterization of compounds **7a**, **7b**, **8a**, **8b** (see Supplementary Materials).

(8*S*,10*S*)-6,8,11-Trihydroxy-10-(((2*R*,4*S*,5*S*,6*S*)-5-hydroxy-4-(((3*S*,3*aS*,4*S*,4*aR*,5*S*,9*aR*)-4-hydroxy-4*a*,5-dimethyl-2-oxo-2,3,3*a*,4,4*a*,5,6,7,9,9*a*-decalhydronaphtho[2,3-*b*]furan-3-yl)methyl)amino)-6-methyltetrahydro-2*H*-pyran-2-yl)oxy)-8-(2-hydroxyacetyl)-1-methoxy-7,8,9,10-tetrahydrotetracene-5,12-dione (**7a**). A red solid (127 mg, 37.2%); m.p. = 170–175 °C; TLC Rf = 0.39 ($\text{CHCl}_3:\text{MeOH} = 10:1$); HRMS (ESI): $m/z = 792.3252$ ($\text{M}+\text{H}^+$). $\text{C}_{42}\text{H}_{49}\text{NO}_{14}$. Calculated, $m/z = [\text{M}+\text{H}]^+ = 792.3226$. $^1\text{H-NMR}$ (500 MHz, CDCl_3 , δ , ppm) 0.86 (3H, d, $J = 6.8$ Hz, H-42), 0.99 (3H, s, H-41), 1.29–1.40 (2H, m, H-36*a*, H-36*b*), 1.36 (3H, d, $J = 6.6$ Hz, H-27), 1.69–1.87 (2H, m, H-23*a*, H-23*b*), 1.93 (1H, m, H-37), 1.93–2.00 (2H, m, H-35*a*, H-35*b*), 2.14–2.19 (m, H-12*a*), 2.16 (dd, $J = 15.6, 4.2$ Hz, H-32*a*), 2.22–2.33 (1H, m, H-32*b*), 2.37 (1H, br.d, $J = 14.6$ Hz, H-12*b*), 2.55 (1H, m, H-29), 2.62 (1H, d, $J = 7.0$ Hz, H-28*a*), 2.81–2.96 (3H, m, H-28*b*, H-24, H-30), 3.03 (1H, dd, $J = 18.6, 3.1$ Hz, H-10*a*), 3.26 (1H, d, $J = 18.8$ Hz, H-10*b*),

3.65 (1H, br.s, H-25), 3.84 (1H, d, $J = 5.0$ Hz, H-39), 4.00–4.12 (1H, m, H-26), 4.08 (3H, s, H-21), 4.60 (1H, dt, $J = 11.0, 7.5$ Hz, H-31), 4.76 (2H, s, H-20), 5.32 (1H, br.s, H-13), 5.52 (1H, d, $J = 3.1$ Hz, H-22), 5.62 (1H, br.s, H-34), 7.39 (1H, d, $J = 8.2$ Hz, H-2), 7.78 (1H, dd, $J = 7.5, 8.2$ Hz, H-3), 8.02 (1H, d, $J = 7.5$ Hz, H-4), 13.24 (1H, br.s, hydroquinone OH), 13.95 (1H, br.s, hydroquinone OH); $^{13}\text{C-NMR}$ (126 MHz, CDCl_3 , δ , ppm) 16.4 (C-42), 17.3 (C-27), 19.4 (C-41), 25.7 (C-35), 26.9 (C-36), 30.3 (C-23), 32.7 (C-37), 34.1 (C-10), 35.3 (C-12), 35.6 (C-32), 42.0 (C-38), 42.9 (C-30), 45.8 (C-28), 52.8 (C-24), 56.8 (C-21), 65.6 (C-20), 66.0 (C-11), 67.2 (C-25, C-26), 69.6 (C-13), 74.4 (H-39), 77.4 (C-31), 101.0 (C-22), 111.6 (C-7), 111.8 (C-16), 118.6 (C-2), 120.0 (C-4), 121.0 (C-18), 128.1 (C-34), 135.0 (C-33), 135.6 (C-5), 135.9 (C-3), 155.8 (C-8), 156.3 (C-15), 161.2 (C-1), 178.0 (C-40), 186.9 (C-6), 187.2 (C-17), 213.8 (C-19).

(8*S*,10*S*)-10-(((2*R*,4*S*,5*S*,6*S*)-4-(((3*S*,3*aR*,8*aR*,9*aR*)-5,8*a*-Dimethyl-2-oxo-2,3,3*a*,7,8,8*a*,9,9*a*-octahydronaphtho[2,3-*b*]furan-3-yl)methyl)amino)-5-hydroxy-6-methyltetrahydro-2*H*-pyran-2-yl)oxy)-6,8,11-trihydroxy-8-(2-hydroxyacetyl)-1-methoxy-7,8,9,10-tetrahydrotetracene-5,12-dione (**8a**).

A red solid (77 mg, 23.1%): m.p. = 166–170 °C; TLC Rf = 0.54 (CHCl_3 :MeOH = 10:1); HRMS (ESI): $m/z = 774.3148$ ($\text{M}+\text{H}^+$). $\text{C}_{42}\text{H}_{47}\text{NO}_{13}$. Calculated, $m/z = [\text{M}+\text{H}]^+ = 774.3120$. $^1\text{H-NMR}$ (500 MHz, CDCl_3 , δ , ppm) 1.03 (3H, s, H-41), 1.32 (1H, m, H-34a), 1.37 (3H, d, $J = 6.6$ Hz, H-27), 1.50 (1H, dd, $J = 9.1, 2.4$ Hz, H-32a), 1.51 (1H, d, $J = 18.4$ Hz, H-34b), 1.71 (3H, br.s, H-42), 1.76 (2H, m, H-23a, H-23b), 2.01 (1H, dt, $J = 18.8, 5.6$ Hz, H-35a), 2.16 (1H, dd, $J = 13.1, 3.8$ Hz, H-12a), 2.18 (1H, dd, $J = 14.8, 3.2$ Hz, H-32b), 2.25 (1H, br.d, $J = 15.7$ Hz, H-35b), 2.37 (1H, dt, $J = 14.4, 2.2$ Hz, H-12b), 2.82 (1H, dd, $J = 11.0, 5.9$ Hz, H-28a), 2.87 (1H, ddd, $J = 11.7, 5.7, 2.6$ Hz, H-24), 2.95 (1H, m, H-29), 2.98 (1H, m, H-28b), 3.00 (1H, d, $J = 18.9$ Hz, H-10a), 3.24 (1H, m, H-30), 3.25 (1H, dd, $J = 18.6, 1.8$ Hz, H-10b), 3.65 (1H, br.s, H-25), 4.0–4.09 (1H, m, H-26), 4.07 (3H, s, H-21), 4.75 (2H, s, H-20), 4.77 (1H, m, H-31), 5.21 (1H, d, $J = 3.5$ Hz, H-39), 5.31 (1H, dd, $J = 3.7, 2.2$ Hz, H-13), 5.52 (1H, br.d, $J = 2.6$ Hz, H-22), 5.58 (1H, br.d, $J = 3.4$ Hz, H-36), 7.39 (1H, dd, $J = 8.6, 1.1$ Hz, H-2), 7.77 (1H, dd, $J = 7.8, 8.4$ Hz, H-3), 8.01 (1H, dd, $J = 7.8, 1.0$ Hz, H-4), 13.22 (1H, br.s, hydroquinone OH), 13.24 (1H, br.s, hydroquinone OH); $^{13}\text{C-NMR}$ (126 MHz, CDCl_3 , δ , ppm) 17.3 (C-27), 20.3 (C-42), 22.3 (C-35), 24.8 (C-41), 30.6 (C-33), 30.9 (C-23), 34.1 (C-10), 35.6 (C-12), 37.3 (C-34), 38.3 (C-30), 39.6 (C-32), 42.6 (C-28), 45.8 (C-29), 52.4 (C-24), 56.8 (C-21), 65.6 (C-20), 67.2 (C-26), 67.4 (C-25), 69.7 (C-13), 76.8 (C-11), 77.4 (C-31), 101.2 (C-22), 111.6 (C-7), 111.7 (C-16), 113.0 (C-39), 118.6 (C-2), 120.0 (C-4), 121.0 (C-18), 126.9 (C-36), 130.4 (C-37), 133.6 (C-9), 134.0 (C-14), 135.6 (C-5), 135.9 (C-3), 145.0 (C-38), 155.8 (C-8), 156.3 (C-15), 161.2 (C-1), 177.8 (C-40), 186.9 (C-6), 187.2 (C-17), 213.8 (C-19).

(8*S*,10*S*)-8-Acetyl-6,8,11-trihydroxy-10-(((2*R*,4*S*,5*S*,6*S*)-5-hydroxy-4-(((3*S*,3*aS*,4*S*,4*aR*,5*S*,9*aR*)-4-hydroxy-4*a*,5-dimethyl-2-oxo-2,3,3*a*,4,4*a*,5,6,7,9,9*a*-decahydronaphtho[2,3-*b*]furan-3-yl)methyl)amino)-6-methyltetrahydro-2*H*-pyran-2-yl)oxy)-1-methoxy-7,8,9,10-tetrahydrotetracene-5,12-dione (**7b**). A red solid (183 mg, 54.7%): m.p. = 155–162 °C; TLC Rf = 0.78 (CHCl_3 :MeOH = 10:1); HRMS (ESI): $m/z = 776.3291$ ($\text{M}+\text{H}^+$). $\text{C}_{42}\text{H}_{49}\text{NO}_{13}$. Calculated, $m/z = [\text{M}+\text{H}]^+ = 776.3277$. $^1\text{H-NMR}$ (500 MHz, CDCl_3 , δ , ppm) 0.86 (3H, d, $J = 6.8$ Hz, H-42), 0.98 (3H, s, H-41), 1.36 (3H, d, $J = 6.6$ Hz, H-27), 1.29–1.42 (2H, m, H-36a, H-36b), 1.69–1.77 (2H, m, H-23a, H-23b), 1.90–1.99 (2H, m, H-35a, H-35b), 1.93 (1H, m, H-37), 2.06–2.12 (1H, m, H-12a), 2.10 (1H, dd, $J = 14.8, 4.1$ Hz, H-32a), 2.23–2.32 (1H, m, H-32b), 2.35 (1H, br.d, $J = 15.0$ Hz, H-12b), 2.42 (3H, s, 3H, H-20), 2.53 (1H, m, H-29), 2.66 (1H, m, H-28a), 2.86 (1H, m, H-30), 2.91 (1H, m, H-28b), 2.96 (1H, d, $J = 18.6$ Hz, H-10a), 3.22 (1H, dt, $J = 18.7, 2.4$ Hz, H-10b), 3.65 (1H, br.d, $J = 6.8$ Hz, H-25), 3.83 (1H, d, $J = 6.8$ Hz, H-39), 4.03–4.10 (1H, m, H-26), 4.08 (3H, s, H-21), 4.60 (1H, dt, $J = 10.8, 7.3$ Hz, H-31), 5.29 (1H, dd, $J = 3.9, 2.1$ Hz, H-13), 5.50 (1H, br.d, $J = 3.5$ Hz, H-22), 5.62 (1H, dt, $J = 3.9, 1.8$ Hz, H-34), 7.38 (1H, dd, $J = 8.6, 0.9$ Hz, H-2), 7.78 (1H, dd, $J = 7.8, 8.4$ Hz), 8.02 (1H, dd, $J = 7.7, 1.1$ Hz, H-4), 13.27 (1H, br.s, hydroquinone OH), 13.96 (1H, br.s, hydroquinone OH); $^{13}\text{C-NMR}$ (126 MHz, CDCl_3 , δ , ppm) 16.4 (C-42), 17.2 (C-27), 19.4 (C-41), 24.9 (C-20), 25.6 (C-35), 26.9 (C-36), 30.4 (C-23), 32.7 (C-32), 33.5 (C-10), 35.0 (C-37), 35.3 (C-12), 42.0 (C-30), 42.9 (C-38), 45.7 (C-28), 45.8 (C-29), 52.8 (C-24), 56.8 (C-21), 67.1 (C-26), 67.3 (C-25), 69.8 (C-13), 74.4 (C-39), 77.0 (C-31), 77.1 (C-11), 100.9 (C-22), 111.4 (C-7), 111.6 (C-16), 118.5 (C-2), 119.9 (C-4),

121.1 (C-18), 128.0 (C-34), 134.4 (C-9), 134.5 (C-14), 135.0 (C-33), 135.7 (C-5), 135.9 (C-3), 156.0 (C-8), 156.5 (C-15), 161.2 (C-1), 178.0 (C-40), 186.9 (C-6), 187.2 (C-17), 211.9 (C-19). (8*S*,10*S*)-8-Acetyl-10-(((2*R*,4*S*,5*S*,6*S*)-4-(((3*S*,3*aR*,8*aR*,9*aR*)-5,8*a*-dimethyl-2-oxo-2,3,3*a*,7,8,8*a*,9,9*a*-octahydronaphtho[2,3-*b*]furan-3-yl)methyl)amino)-5-hydroxy-6-methyltetrahydro-2*H*-pyran-2-yl)oxy)-6,8,11-trihydroxy-1-methoxy-7,8,9,10-tetrahydrotetracene-5,12-dione (**8b**). A red solid (191 mg, 57.2%): m.p. = 152–158 °C; TLC R_f = 0.81 (CHCl₃:MeOH = 10:1); HRMS (ESI): m/z = 758.3197 (M+H⁺). C₄₂H₄₇NO₁₂. Calculated, m/z = [M+H]⁺ = 758.3171. ¹H-NMR (500 MHz, CDCl₃, δ, ppm) 1.03 (3H, s, H-41), 1.36 (3H, d, J = 6.6 Hz, H-27), 1.32 (1H, m, H-34a), 1.50 (2H, d, J = 18.3 Hz, H-34b + br.d, J = 11.8 Hz, H-32a), 1.71 (3H, br.s, H-42), 1.75 (2H, m, H-23a, H-23b), 2.00 (1H, dt, J = 18.7, 5.2 Hz, H-35a), 2.10 (1H, dd, J = 14.8, 4.1 Hz, H-12a), 2.18 (1H, dd, J = 14.6, 3.1 Hz, H-32b), 2.25 (1H, br.d, J = 15.7 Hz, H-35b), 2.35 (1H, dt, J = 14.9, 2.7 Hz, H12b), 2.41 (3H, s, H-20), 2.82 (1H, m, H-28a), 2.89 (1H, m, H-24), 2.94 (1H, m, H-29), 2.93 (1H, d, J = 19.0 Hz, H-10a), 2.97 (1H, m, H-28b), 3.20 (1H, dd, J = 18.8, 2.0 Hz, H-10b), 3.24 (1H, m, H-30), 3.64 (1H, d, J = 1.5 Hz, H-25), 4.05–4.10 (1H, m) H-26, 4.07 (3H, br.s, H-21), 4.75 (1H, dt, J = 5.6, 2.7 Hz, H-31), 5.20 (1H, d, J = 3.2 Hz, H-39), 5.28 (1H, dd, J = 3.8, 2.0 Hz, H-13), 5.52 (1H, t, J = 2.5 Hz, H-22), 5.57 (1H, d, J = 4.0 Hz, H-36), 7.38 (1H, dd, J = 8.5, 0.8 Hz, H-2), 7.77 (1H, dd, J = 8.4, 7.8 Hz, H-3), 8.01 (1H, dd, J = 7.7, 0.8 Hz, H-4), 13.26 (1H, br.s, hydroquinone OH), 13.94 (1H, br.s, hydroquinone OH); ¹³C-NMR (126 MHz, CDCl₃, δ, ppm) 17.2 (C-27), 20.3 (C-42), 22.3 (C-35), 24.8 (C-41), 24.9 (C-20), 30.5 (C-33), 30.9 (C-23), 33.5 (C-10), 35.0 (C-12), 37.3 (C-34), 38.4 (C-30), 39.6 (C-32), 42.5 (C-28), 45.9 (C-29), 52.4 (C-24), 56.8 (C-21), 67.0 (C-26), 67.5 (C-25), 70.0 (C-13), 77.0 (C-11), 77.3 (C-31), 101.2 (C-22), 111.4 (C-7), 111.6 (C-16), 113.0 (C-39), 118.5 (C-2), 119.9 (C-4), 121.1 (C-18), 126.8 (C-36), 130.5 (C-37), 134.4 (C-9), 134.5 (C-14), 135.6 (C-5), 135.8 (C-3), 144.9 (C-38), 156.0 (C-8), 156.5 (C-15), 161.2 (C-1), 177.8 (C-40), 186.8 (C-6), 187.1 (C-17), 211.9 (C-19).

2.6. Cell Lines and Cultivation

Human cell cultures of tumor origin (A549 (lung carcinoma), HCT116 (colon adenocarcinoma), MCF7 (breast cancer), RD (embryonic rhabdomyosarcoma)), and the line of non-transformed cells HEK293 (embryonic kidney) provided by the Laboratory of Tumor Cell Genetics at the N.N. Blokhin Russian Cancer Research Institute, as well as by the Institute of Cytology of the Russian Academy of Sciences, were grown in DMEM (Gibco, Scotland, UK) and MEM (Gibco, Scotland, UK) containing fetal calf serum (10% by volume) (ThermoFisher Scientific, Paisley, UK), L-glutamine (2 mM) (Gibco, Scotland, UK), and penicillin-streptomycin (1% by volume) (PanEco, Moscow, Russia). The cultivation was carried out at 37 °C in a humidified CO₂ atmosphere (5%).

2.7. Determination of Cell Viability

Cellular viability was determined by the MTT test [24]. The cells were seeded in a 96-well plate in the amount of 1 × 10⁴ cells/200 μL of complete culture medium and cultured at 37 °C in a CO₂ atmosphere (5%). After 24 h of incubation, various concentrations of the test compounds dissolved in DMSO (≤1%) were added to the cell cultures, the solvent was added to the control wells in an equal volume, and then the cells were cultured under the same conditions for 72 h. After the incubation time, MTT (3-(4,5-dimethylthiazol-2-yl)-2,5-diphenyltetrazolium bromide, 5 mg/mL) was added to each well, and the plates were further incubated for 2 h (until a characteristic color appeared). Then, the formazan granules were dissolved in DMSO.

Using a plate analyzer (Cytation3, BioTech Instruments Inc., USA), the optical density was determined at λ = 530 nm. The concentration value causing 50% inhibition of cell population growth (IC₅₀) was determined from dose-response curves using GraphPad Prism 9.0 software.

2.8. Animals

The experiments used male nonlinear outbred rats weighing 200–220 g. The animals were kept in a standard vivarium with a 12-hour light regime and free access to water and food. All manipulations with animals were carried out in accordance with the decisions of the IPAC RAS Bioethics Commission.

2.9. Rat Brain Homogenate and Heart Mitochondria

To obtain a brain homogenate, decapitation of rats anesthetized in advance with CO₂ was performed using a guillotine. The brain was homogenized in a buffer containing KCl (120 mM) and HEPES (20 mM) (Gibco, Scotland, UK), pH = 7.4, at 4 °C and centrifuged at 1500 rpm to obtain a supernatant.

Rat heart mitochondria were isolated by differential centrifugation using ice-cold buffer containing KCl (120 mM) and HEPES (20 mM), pH = 7.4, and a trypsin inhibitor. The mitochondrial yield ranged from 5 to 10 mg/mL of protein in the heart sediment. Mitochondria were stored in plastic containers at 4 °C.

The quantitative determination of protein was carried out according to the standard technique using the microbiuret method [25].

2.10. Lipid Peroxidation

To study the effect of compounds on the process of lipid peroxidation (LPO) of rat brain homogenate, we used a modified version of the TBA test [26], which is based on the reaction of 2-thiobarbituric acid with the final LPO product—malonic dialdehyde (MDA). According to the experimental scheme, the well of the plate contained the studied compounds (100 µM), rat brain homogenate (2 mg/mL), as well as 500 µM ferrous iron ions (FeSO₄ × 10H₂O). After 30 min of incubation at 37 °C, TBA reagent was added to all samples, incubated for 90 min at 90 °C, and centrifuged at 6000 rpm for 15 min. The optical density of the selected supernatant was measured on a Victor 3 plate analyzer (Perkin Elmer, Germany city, abbreviated state (for USA/Canada), country) at λ = 540 nm.

2.11. Mitochondrial Swelling

Mitochondrial swelling was recorded by the light transmission of the rat heart mitochondrial suspension at λ = 540 nm using a Victor 3 plate analyzer (Perkin Elmer, Germany). The swelling rate was estimated as ΔA₅₄₀/min and was calculated as the tangent of the angle of the steepest dependence curve part ΔA₅₄₀ versus time.

2.12. Mitochondrial Membrane Potential

The transmembrane potential of rat heart mitochondria was measured by a Victor 3 plate analyzer (Perkin Elmer, Germany) using a potential-dependent indicator Safranin A [27]. The mitochondrial preparation was diluted in a buffer containing mannitol (225 mM) (Dia-M, Moscow, Russia), sucrose (75 mM) (Sigma Aldrich, Saint Louis, USA), HEPES (10 mM) (Gibco, Scotland, UK), EGTA (20 µM) (Dia-M, Moscow, Russia), KH₂PO₄ (1 mM), pH = 7.4, at the rate of 0.5 mg of protein in 1 mL of medium. Safranin A (5 µM) was added to the suspension immediately before the start of the measurement. The organelles were energized with a solution of potassium succinate and rotenone, against which the studied compounds were added at a concentration of 100 µM. The mitochondrial pore was induced by the addition of CaCl₂ (25 µM).

2.13. The Work of Mitochondrial Respiratory Chain Complexes

The effect of the compounds on the functioning of the electron transport chain complexes was carried out using an Agilent Seahorse XF96e Analyzer (Seahorse Bioscience, Billerica, MA, USA) according to their ability to change the rate of oxygen uptake by isolated rat heart mitochondria (10 µg/well). The following modulators were used: activators of complex I of the electron transport chain, NADH dehydrogenase,—glutamate/malate; rotenone (2 µM) (Sigma Aldrich, Saint Louis, USA)—a tissue respiration blocker that stops

the transfer of electrons from the reduced form of NADH to cytochrome b, was used as complex I inhibitor; potassium succinate (2 μ M) (Dia-M, Moscow, Russia), which is a substrate of complex II of the electron transport chain, made it possible to assess mitochondrial respiration mediated by succinate dehydrogenase; complex III (ubiquinol-cytochrome c-oxidoreductase) inhibitor—a blocker of cellular respiration antimycin A (Sigma Aldrich, Saint Louis, USA), as well as ascorbate/TMPD (0.5 μ M) (Sigma Aldrich, Saint Louis, USA), allowed us to evaluate the cytochrome-c-oxidase mediated respiration of organelles.

2.14. Parameters of the Glycolytic Function of the Tumor Cells HeLa

The ability of the studied compounds to modulate anaerobic glycolysis was investigated using the Agilent Seahorse XF96e Analyzer (Seahorse Bioscience, Billerica, MA, USA) according to the level of hydrogen proton production in the samples on the HeLa cervical tumor cell line by the glycolysis stress test [28].

HeLa cells in the exponential growth phase were plated into a 96-well cell culture microplate Seahorse (the density of the cell culture was 3×10^4 /well). After 24 h, the rate of medium extracellular acidification by cells treated with the test compounds was recorded in real time during the sequential injection of modulators: glucose (10 mM) (Dia-M, Moscow, Russia), oligomycin (1 μ M) (Sigma Aldrich, Saint Louis, USA), 2-fluoro-2-deoxy-D-glucose (25 mM) (Sigma Aldrich, Saint Louis, USA). This allowed us to estimate the glycolysis intensity in cells by three main parameters of glycolytic function: glycolysis by adding saturating amounts of glucose to the system, glycolytic capacity by the introduction of oligomycin, and glycolytic reserve by using the inhibitor of this glycolysis 2-fluoro-2-deoxy-D-glucose.

3. Results & Discussion

3.1. Chemical Synthesis

All used lactones contain an exocyclic electron-deficient double bond in the lactone cycle and can enter into the aza-Michael reaction with amines. Anthracycline antibiotics containing an amino group in the carbohydrate fragment, doxorubicin (**a**), and daunorubicin (**b**) were used as such amines. Before carrying out the aza-Michael reaction, daunorubicin hydrochloride was converted to a base. The resulting amine is more reactive and is easily isolated in pure form by extraction with chloroform from an aqueous solution. Doxorubicin is more hydrophilic, and its base is not extracted from the aqueous solution by chloroform. In this case, to carry out the aza-Michael reaction with sesquiterpene lactones, doxorubicin was used in the form of hydrochloride, and the process was carried out in the presence of a base (triethylamine), under the action of which, in the reaction medium, doxorubicin was released in situ as a free amine and directly reacted with the lactone (Figure 3).

Sesquiterpene lactones (**1**)–(**8**) react both with daunorubicin and doxorubicin under mild conditions, but at a low rate. As a result, a number of previously undescribed conjugates containing two pharmacophore fragments, natural sesquiterpene lactone and anthracycline antibiotics daunorubicin or doxorubicin, were obtained. The degree of conversion of the starting lactones was monitored by TLC and ^1H NMR (disappearance of signals from the protons of the exomethylene group—doublets at 5.4 and 6.16 ppm). The structure of the synthesized compounds was established using a set of physicochemical methods: NMR spectroscopy (including two-dimensional COZY and NOESY experiments) and high-resolution mass spectrometry. The ^1H NMR spectra contains signals of protons appearing in the products at the C-29 atom in the range of 2.5–2.8 ppm in the form of a quartet with a spin-spin coupling (SSC) constant of 6.6–6.9 Hz. The signals and their multiplicity of the remaining protons of both the initial lactone and daunorubicin or doxorubicin are retained, which corresponds to the proposed structures, as well as the configuration of all asymmetric centers of the initial molecules. In addition, a new chiral center with a certain configuration is formed in the conjugates [20]. The stereoconfiguration of the new asymmetric center (atom C-29) was established based on two-dimensional experiments H—H COZY and NOESY (Figure 4).

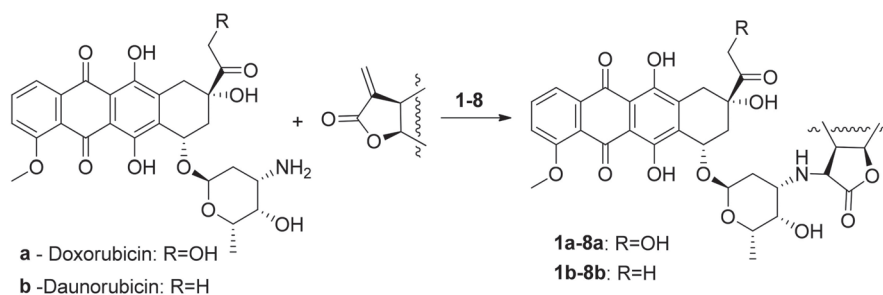


Figure 3. Scheme for the preparation of conjugates of daunorubicin and doxorubicin with sesquiterpene lactones.

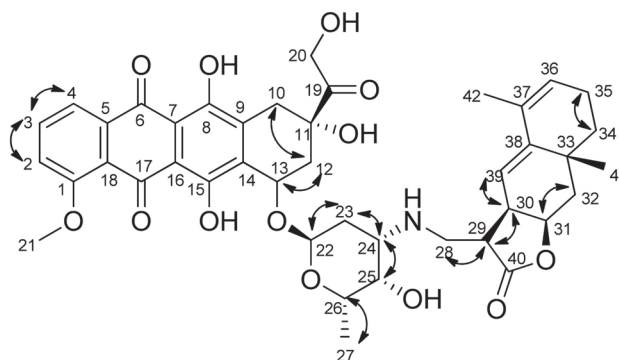


Figure 4. Main correlations H-H-COZY and numbering of carbons, for example, compound **8a**.

3.2. The Study of Biological Activity

Antitumor drugs that are planned to be used as chemotherapy for the treatment of neoplasms should have a number of specific properties, one of which is the cytotoxicity presence towards tumor cells. Therefore, at the first stage of the biological activity study of the doxorubicin and daunorubicin synthesized conjugates with sesquiterpene lactones, the cytotoxic profile was analyzed in cell cultures, including cell lines of tumor origin and the line of non-transformed cells in order to assess the compound selectivity in relation to malignant cells.

According to the obtained data, presented in Table 1, in relation to all lines of tumor cells, pronounced cytotoxic properties were found, comparable to the action of doxo- and daunorubicin, without increasing the toxic effect on normal cells for most of the conjugates. Moreover, for a number of tested compounds, an increased viability of normal human renal epithelium cells was recorded. Thus, the IC_{50} for HEK293 for doxorubicin (**a**) was $6.78 \pm 0.76 \mu\text{M}$, in turn, for its derivatives containing isoalantholactone (**1a**), alantolactone (**2a**), and alanthodiene (**8a**), values of IC_{50} more than double that of the initial cytostatic agent were shown: $19.82 \pm 0.42 \mu\text{M}$, $29.83 \pm 0.18 \mu\text{M}$, and $16.42 \pm 1.07 \mu\text{M}$, respectively. A similar situation was found for the daunorubicin conjugate with epoxyalantolactone (**5b**). The IC_{50} (**b**) value of $12.31 \pm 1.17 \mu\text{M}$, (**5b**) shows a value exceeding $18 \mu\text{M}$.

It is also important to note that lactones themselves do not have a pronounced cytotoxic effect on tumor cells, while for modified doxorubicin derivatives, for example, (**6a**), the IC_{50} value of cytotoxicity was $0.25 \pm 0.04 \mu\text{M}$, and for daunorubicin conjugates (**4b**) the IC_{50} value was $0.02 \pm 0.001 \mu\text{M}$. This is an order of magnitude higher than the activity of the original pharmacophores. Thus, the combination of an anthracycline antibiotic with sesquiterpene lactone in one molecule makes it possible to obtain a cytotoxic effect comparable to the initial anthracyclines in relation to tumor origin cells and a reduced damaging effect on a healthy cell culture (HEK293). To understand this effect, we studied

the influence of the synthesized compounds on oxidative stress (accumulation of free radicals), mitochondrial function, and glycolysis as the main metabolic pathway for obtaining energy by transformed tumor cells.

Table 1. In vitro cytotoxicity daunorubicin and doxorubicin conjugates with sesquiterpene lactones.

Compound	IC ₅₀ , μM				
	A549	HCT116	MCF7	RD	HEK293
1	32.04 ± 3.24	11.31 ± 0.27	17.51 ± 0.60	10.37 ± 0.79	74.03 ± 0.51
2	36.73 ± 1.43	10.57 ± 0.04	13.15 ± 0.93	5.48 ± 0.20	36.47 ± 0.07
3	23.12 ± 1.18	34.52 ± 3.51	17.92 ± 0.68	8.82 ± 0.14	35.87 ± 0.48
4	83.51 ± 0.26	21.40 ± 0.32	31.87 ± 0.14	18.60 ± 0.21	105.68 ± 4.13
5	21.49 ± 0.75	5.12 ± 0.05	11.41 ± 0.32	4.81 ± 0.12	38.10 ± 1.08
6	50.28 ± 1.11	9.75 ± 0.57	24.03 ± 0.80	8.77 ± 0.01	18.47 ± 0.20
6	61.71 ± 2.40	10.80 ± 0.18	38.55 ± 0.86	16.78 ± 0.28	29.77 ± 0.05
8	59.86 ± 2.26	4.99 ± 0.06	4.31 ± 0.02	4.94 ± 0.09	9.07 ± 0.25
a	0.38 ± 0.02	0.14 ± 0.01	0.46 ± 0.03	0.29 ± 0.02	6.78 ± 0.76
1a	2.21 ± 0.06	2.81 ± 0.05	11.11 ± 0.17	2.41 ± 0.03	19.82 ± 0.42
2a	3.29 ± 0.11	4.55 ± 0.03	26.76 ± 0.65	2.67 ± 0.11	29.83 ± 0.18
4a	1.86 ± 0.12	1.07 ± 0.01	5.65 ± 0.22	2.76 ± 0.02	11.73 ± 0.10
5a	4.52 ± 0.57	2.52 ± 0.02	3.03 ± 0.07	2.47 ± 0.07	4.50 ± 0.32
6a	0.88 ± 0.11	0.25 ± 0.04	2.94 ± 0.02	1.18 ± 0.01	0.98 ± 0.23
7a	5.43 ± 0.16	0.92 ± 0.00	6.03 ± 0.11	4.22 ± 0.10	10.49 ± 0.88
8a	1.87 ± 0.07	0.43 ± 0.02	2.34 ± 0.01	1.03 ± 0.02	16.42 ± 1.07
b	0.33 ± 0.01	0.12 ± 0.00	0.84 ± 0.17	0.63 ± 0.03	12.31 ± 1.17
1b	0.93 ± 0.06	0.28 ± 0.00	3.95 ± 0.03	0.96 ± 0.02	3.43 ± 0.04
3b	1.42 ± 0.05	1.01 ± 0.01	1.24 ± 0.23	0.59 ± 0.05	6.37 ± 0.24
4b	0.27 ± 0.01	0.02 ± 0.00	1.99 ± 0.27	0.63 ± 0.02	11.41 ± 0.53
5b	1.19 ± 0.02	1.30 ± 0.02	1.84 ± 0.06	0.80 ± 0.00	18.19 ± 0.18
6b	0.56 ± 0.01	0.26 ± 0.01	1.47 ± 0.04	0.41 ± 0.02	3.68 ± 0.16
7b	2.01 ± 0.09	0.20 ± 0.01	1.90 ± 0.07	1.95 ± 0.01	6.42 ± 0.21

Values were obtained by averaging three repeated measurements for each concentration.

Oxidative stress and, in particular, the process of lipid peroxidation are among the main causes for cellular defect accumulation as a result of the overproduction of free radicals [29]. This can lead to tumor cell transformation and uncontrolled proliferation [30,31]. The study of the effect of the synthesized compounds on the lipid peroxidation process of the rat brain homogenate used as a model system was carried out by the TBA test. Ions of bivalent iron were used as an initiator to accelerate the reaction time for the formation of MDA. They are able to trigger the Fenton reaction with hydroxyl radical formation. A high prooxidant effect was observed for anthracycline antibiotics—doxo- and daunorubicin (the percentage of MDA was 236.68 ± 13.06 and 226.05 ± 6.60, respectively). In turn, an increase in the MDA level was not observed or did not exceed 139.08 ± 0.64% for the synthesized derivatives (Figure 5).

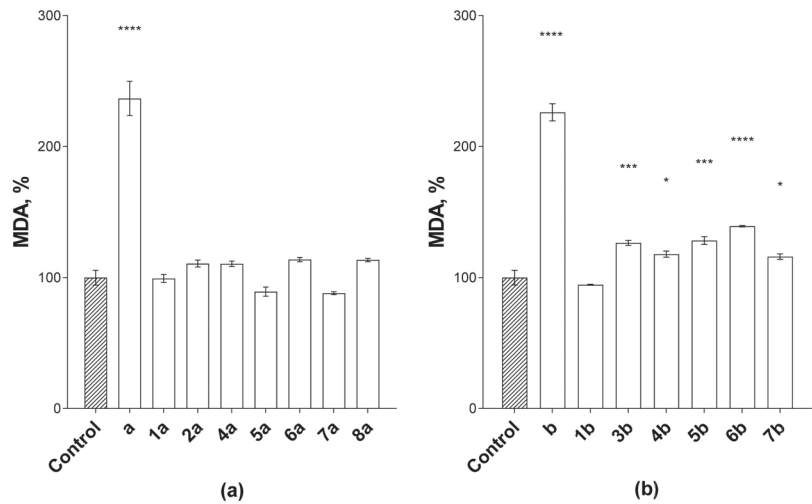


Figure 5. Effect of doxorubicin (a) and daunorubicin (b) conjugates with sesquiterpene lactones on the lipid peroxidation process of rat brain homogenate (2 mg/mL) initiated by ferrous iron ions (500 μ M). The test compound concentration was 100 μ M. Data are presented as % of MDA relative to control (DMSO \leq 1%); as mean \pm SEM (three repeated measurements for each compound). Asterisks (*, ***, ****) indicate a statistically significant ($p < 0.05$, $p < 0.001$, $p < 0.0001$) difference between the control and the studied compounds (one-way ANOVA, Dunnett's test).

Mitochondria are the main free radical sources in the cell. Defects in the functioning of these organelles are manifested in electron transport chain disruption, the induction of the permeability transition pore opening, and depolarization of the mitochondrial membrane. For example, a pathological change in the activity of even one of the mitochondria electron-transport chain complexes can lead to overproduction of superoxide radicals and other reactive oxygen species. In turn, this contributes to the development of oxidative stress and permanent damage to cell components [32]. Heart mitochondria were chosen as the study object since cumulative cardiotoxicity is the main side effect of anthracycline antibiotics.

The study of the effect of synthesized compounds on the mitochondria functional characteristics was carried out by analyzing three parameters: the measurement of mitochondrial swelling, which characterizes the process of permeability transition pore opening, the transmembrane potential, and the work of the respiratory chain complexes. The results obtained are presented in the form of summarized quantitative data in Table 2 for a comparative analysis of "structure–activity". Figure 6 shows the kinetic curves of the studied processes for high-quality visualization.

As described earlier [10], doxo- and daunorubicin provoke the permeability transition pore opening and mitochondrial membrane depolarization. These data were confirmed by us in experiments on isolated rat heart mitochondria. When the initial anthracyclines were added to the isolated organelles, swelling was induced, which was comparable to the mitochondrial permeability pore formation under the action of a standard trigger of this process—calcium ions at a concentration of 25 μ M (Figure 6A). Such a concentration allowed us to observe the maximum swelling rate in isolated rat heart mitochondria under our experimental conditions. However, no effect on mitochondrial swelling was observed for most conjugates (Table 2). The situation is similar to the effect on the mitochondria transmembrane potential. Doxo- and daunorubicin have a pronounced depolarizing effect, exceeding the action of conjugates in this process by more than three times (Table 2, Figures 6B and 7B).

Table 2. Effect of daunorubicin and doxorubicin conjugates with sesquiterpene lactones on the functional characteristics of rat heart mitochondria.

Compound	Work of Respiratory Chain Complexes, % Decrease in OCR of Control		Mitochondrial Swelling, % of Ca ²⁺ -Induced Swelling	Mitochondrial Membrane Depolarization, % of Control
	II	IV		
a	70.54 ± 0.64	37.73 ± 0.34	116.20 ± 10.98	61.55 ± 4.49
1a	27.61 ± 5.71	24.52 ± 7.61	—	—
2a	39.11 ± 4.05	20.45 ± 5.85	31.51 ± 8.35	—
4a	38.58 ± 1.05	27.69 ± 2.93	—	14.04 ± 1.48
5a	—	23.99 ± 4.41	—	—
6a	53.34 ± 6.31	40.50 ± 4.05	54.22 ± 5.49	15.39 ± 0.42
7a	33.21 ± 3.84	38.16 ± 0.84	—	17.72 ± 0.69
8a	27.58 ± 4.30	25.95 ± 4.43	47.84 ± 4.99	13.34 ± 1.72
b	72.12 ± 0.96	—	40.98 ± 3.86	56.81 ± 3.19
1b	—	—	—	15.77 ± 0.20
3b	57.77 ± 1.75	—	26.45 ± 7.14	17.99 ± 0.57
4b	46.22 ± 9.50	—	27.75 ± 4.25	24.82 ± 2.52
5b	—	21.56 ± 3.66	—	21.55 ± 1.04
6b	26.74 ± 4.56	41.69 ± 2.13	—	27.55 ± 1.54
7b	21.04 ± 4.22	46.08 ± 3.42	—	36.76 ± 2.90

Data in the table are presented as mean ± SEM (three repeated measurements for each compound in any experiment). “—” indicates activity absence for compounds (≤10%) in a particular test.

The functioning of the respiratory chain complexes of isolated rat heart mitochondria was studied using a cellular metabolism analyzer Agilent Seahorse XF96e Analyzer (Seahorse Bioscience, USA) in real time. The investigation of the oxygen consumption rate (OCR) was carried out under the influence of tissue respiration modulators.

It was found that both doxorubicin and daunorubicin had a pronounced inhibitory effect on complex II of the electron transport chain, which was expressed as a decrease in OCR by organelles by more than 70% (Table 2, Figure 6C and Figure 7C). A similar effect was recorded for doxorubicin with respect to the cytochrome-c-oxidase complex of the mitochondrial respiratory chain: OCR was reduced by 37.73 ± 0.34%. In turn, either no effect on the respiratory complex functioning or a decrease in OCR by mitochondria by no more than 40% was found for most of the synthesized conjugates. Only two compounds exhibited inhibitory activity, exceeding 50% (**6a** and **3b**) against respiratory chain complexes II and IV.

Thus, the results of studying the effect of the synthesized conjugates on the functional characteristics of rat heart mitochondria suggest that doxo- and daunorubicin modification with natural sesquiterpene lactones carried out by us may be a prerequisite for reducing the toxic effect on healthy cells, in particular, cardiomyocytes, against the background of similar cytotoxicity with the original anthracyclines.

As is known, cancerogenesis occurs in a hypoxic microenvironment, while a distinctive feature of neoplastic cells already at the earliest stages of the disease development is a high anaerobic glycolysis rate, characterized by intense glucose absorption followed by conversion to lactic acid in the absence of oxygen [33]. Thus, tumor cells receive the main part of the energy from this metabolic pathway, while no more than 10% of ATP is formed during glycolysis in physiologically healthy cells. This reprogrammed metabolism of neoplastic cells plays an important role in the development of malignant neoplasms, due to which this cell type has unlimited division ability, metastasis, and reduction of their death by avoiding apoptosis [34].

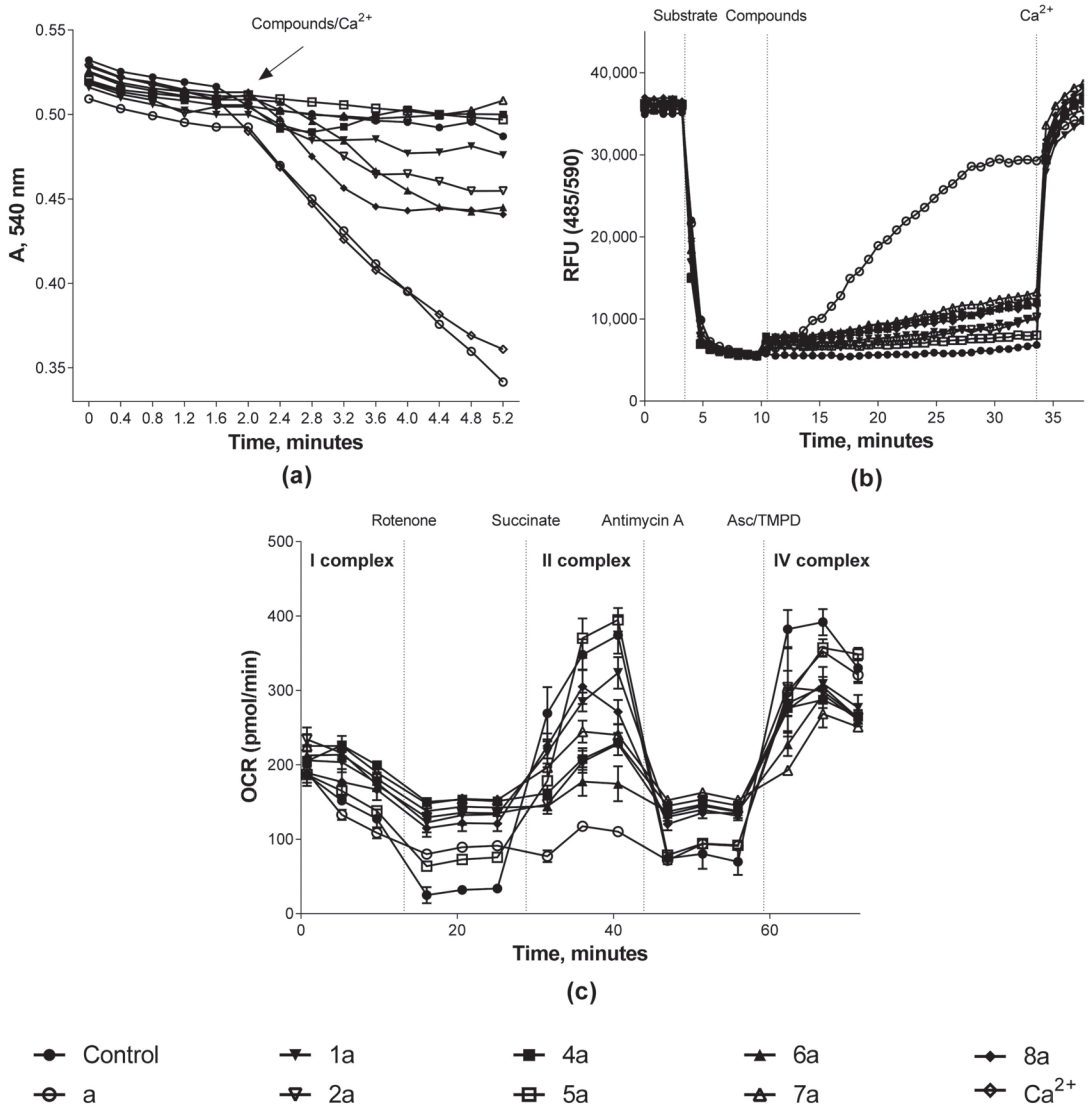


Figure 6. Effect of doxorubicin conjugates with sesquiterpene lactones on the functional characteristics of rat heart mitochondria. Kinetic curves of (a)—mitochondrial swelling and (b)—changes in the transmembrane potential of organelles (0.5 mg/mL) under the influence of the test compounds at 100 μ M; the concentration of Ca²⁺ ions was 25 μ M; (c)—changes in the OCR by organelles (10 μ g/well) treated with the test compounds at 30 μ M with the addition of modulators: rotenone (2 μ M), potassium succinate (2 μ M), antimycin A (4 μ M), and ascorbate/TMPD (0.5 μ M). Data for any experiment were obtained by averaging three repeated measurements for each compound.

In our work, information about the glycolytic activity of the tumor cell culture HeLa under the action of the studied compounds was obtained by measuring the extracellular acidification rate during the sequential injection of metabolic modulators by the glycolysis stress test.

It was found that all studied substances inhibited the process of anaerobic glycolysis (Figure 8), which is expressed in their suppression of glycolytic function parameters such as glycolysis, glycolytic capacity, and glycolytic reserve. At the same time, the

doxorubicin derivative with epoxy-alantolactone (5a) and the daunorubicin conjugate with alantolactone (3b) had the most pronounced ability to reduce the acidification rate of the medium by cells.

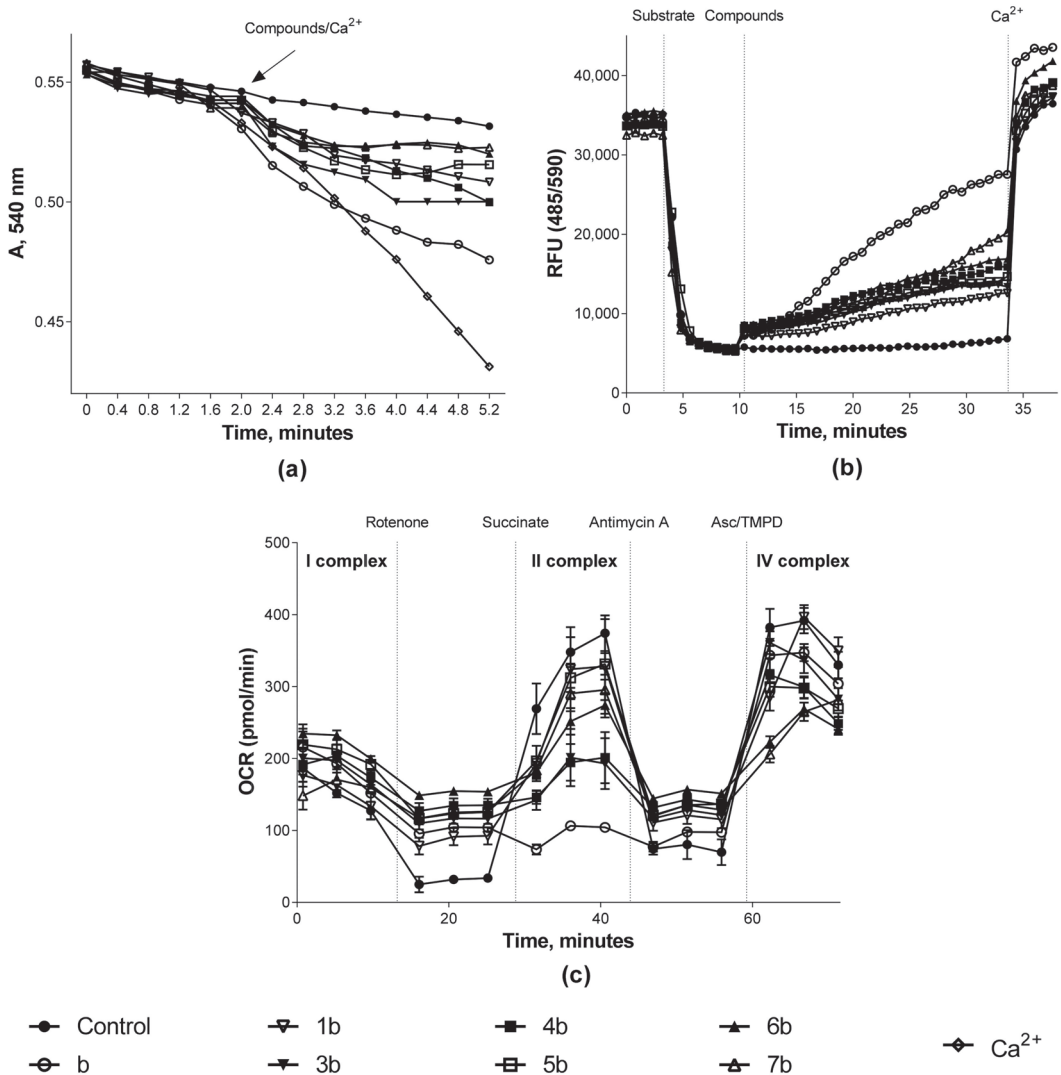


Figure 7. Effect of daunorubicin conjugates with sesquiterpene lactones on the functional characteristics of rat heart mitochondria. Kinetic curves of (a)—mitochondrial swelling and (b)—changes in the transmembrane potential of organelles (0.5 mg/mL) under the influence of the test compounds at 100 µM; the concentration of Ca²⁺ ions was 25 µM; (c)—changes in the OCR by organelles (10 µg/well) treated with the test compounds at 30 µM with the addition of modulators: rotenone (2 µM), potassium succinate (2 µM), antimycin A (4 µM), and ascorbate/TMPD (0.5 µM). Data for any experiment were obtained by averaging three repeated measurements for each compound.

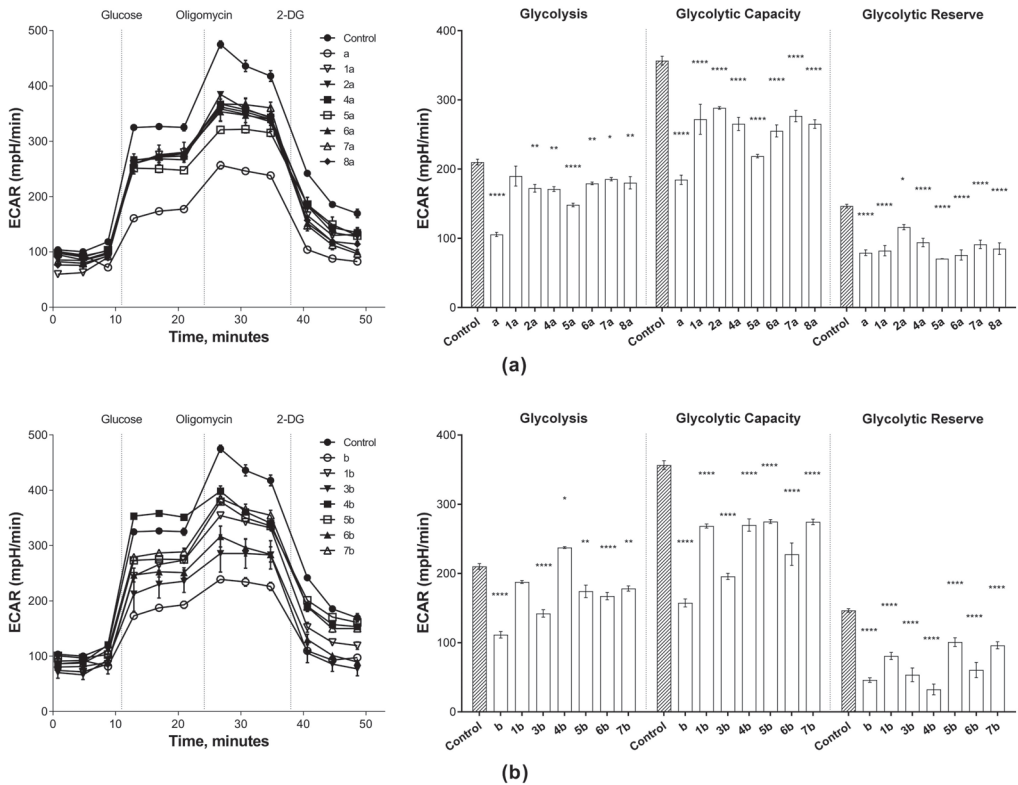


Figure 8. Effect of doxorubicin (a) and daunorubicin (b) conjugates with sesquiterpene lactones on the glycolytic profile of HeLa cells (density was 3×10^6 cells/well). The concentration of the test substances was 30 μ M, glucose—10 mM, oligomycin—1 μ M, 2-fluoro-2-deoxy-D-glucose—25 mM. Data are presented as the mean \pm SEM (three repeated measurements for each compound). Asterisks (*, **, ****) indicate a statistically significant ($p < 0.05$, $p < 0.01$, $p < 0.0001$) difference between the control and the studied compounds (one-way ANOVA, Dunnett’s test).

Thus, we were the first to obtain biparmacophore molecules containing in their structure a fragment of the known anthracycline antibiotics—daunorubicin and doxorubicin—with natural sesquiterpene lactones. When studying the biological activity of the synthesized compounds, a reduced damaging effect on the rat heart mitochondria functioning was observed with equal and, in some cases, higher cytotoxicity and glycolysis inhibition by anthracycline antibiotic conjugates with sesquiterpene lactones in comparison with doxo- and daunorubicin. These results allow us to confirm the assumption that the chemical modification of the anthracycline antibiotic doxo- and daunorubicin molecules by sesquiterpene lactones can be a promising strategy for creating potential antitumor chemotherapeutic drugs with a pronounced cytotoxic effect on tumor cells and a reduced damaging effect on healthy cells of the human organism.

Supplementary Materials: The following are available online at <https://www.mdpi.com/article/10.3390/biomedicines9050547/s1>.

Author Contributions: Conceptualization, M.N. and S.K.; investigation, M.N., A.S., Y.A., E.Y., S.P. and L.A.; methodology, M.N. and S.K.; supervision, S.K.; writing—original draft, M.N., A.S., Y.A., S.P. and S.K.; writing—review & editing, M.N. and S.K. All authors have read and agreed to the published version of the manuscript.

Funding: The work was supported by the Russian Science Foundation (project no. 19-73-00343) within the framework of State Assignment 0090-2019-0006.

Institutional Review Board Statement: All manipulations requiring the use of animals were approved by the Bioethics Commission (IPAC RAS), project 19-73-00343, protocol 43, 18.12.2020.

Informed Consent Statement: Not applicable.

Data Availability Statement: The following are available online at Supplementary Materials containing NMR spectra for compounds.

Acknowledgments: The authors are grateful to the Center for the Collective Use (IPAC RAS) for providing the opportunity to conduct experiments using laboratory animals.

Conflicts of Interest: The authors declare no conflict of interest.

References

1. Minotti, G.; Menna, P.; Salvatorelli, E.; Cairo, G.; Gianni, L. Anthracyclines: Molecular advances and pharmacologic developments in antitumor activity and cardiotoxicity. *Pharmacol. Rev.* **2004**, *56*, 185–229. [CrossRef] [PubMed]
2. Semeraro, G.C.; Lamantia, G.; Cipolla, C.M.; Cardinale, D. How to identify anthracycline-induced cardiotoxicity early and reduce its clinical impact in everyday practice. *Kardiol. Pol.* **2021**, *79*, 114–122. [PubMed]
3. Khasraw, M.; Bell, R.; Dang, C. Epirubicin: Is it like doxorubicin in breast cancer? A clinical review. *Breast* **2012**, *21*, 142–149. [CrossRef] [PubMed]
4. Binaschi, M.; Bigioni, M.; Cipollone, A.; Rossi, C.; Goso, C.; Maggi, C.A.; Capranico, G.; Animati, F. Anthracyclines: Selected new developments. *Curr. Med. Chem. Anticancer Agents* **2001**, *1*, 113–130. [CrossRef]
5. Menna, P.; Minotti, G.; Salvatorelli, E. In vitro modeling of the structure-activity determinants of anthracycline cardiotoxicity. *Cell Biol. Toxicol.* **2007**, *23*, 49–62. [CrossRef]
6. Perego, P.; Corna, E.; De Cesare, M.; Gatti, L.; Polizzi, D.; Pratesi, G.; Supino, R.; Zunino, F. Role of apoptosis and apoptosis-related genes in cellular response and antitumor efficacy of anthracyclines. *Curr. Med. Chem.* **2001**, *8*, 31–37. [CrossRef]
7. Myers, C. The role of iron in doxorubicin-induced cardiomyopathy. *Semin. Oncol.* **1998**, *25* (Suppl. S10), 10–14.
8. Xiong, Y.; Liu, X.; Lee, C.P.; Chua, B.H.; Ho, Y.S. Attenuation of doxorubicin-induced contractile and mitochondrial dysfunction in mouse heart by cellular glutathione peroxidase. *Free Radic. Biol. Med.* **2006**, *41*, 46–55. [CrossRef]
9. Yen, H.C.; Oberley, T.D.; Gairola, C.G.; Szwed, L.I.; St Clair, D.K. Manganese superoxide dismutase protects mitochondrial complex I against adriamycin-induced cardiomyopathy in transgenic mice. *Arch. Biochem. Biophys.* **1999**, *362*, 59–66. [CrossRef]
10. Moutagne, D.; Hurt, C.; Neviere, R. Mitochondria death/survival signaling pathways in cardiotoxicity induced by anthracyclines and anticancer-targeted therapies. *Biochem. Res. Int.* **2012**, *2012*, 951539. [CrossRef]
11. Capeloa, T.; Benyahia, Z.; Zampieri, L.X.; Blackman, M.; Sonveaux, P. Metabolic and non-metabolic pathways that control cancer resistance to anthracyclines. *Semin. Cell Dev. Biol.* **2020**, *98*, 181–191. [CrossRef]
12. Sterba, M.; Popelova, O.; Vavrova, A.; Jirkovsky, E.; Kovarikova, P.; Gersl, V.; Simunek, T. Oxidative stress, redox signaling, and metal chelation in anthracycline cardiotoxicity and pharmacological cardioprotection. *Antioxid. Redox Signal.* **2013**, *18*, 899–929. [CrossRef]
13. Gorini, S.; De Angelis, A.; Berrino, L.; Malara, N.; Rosano, G.; Ferraro, E. Chemotherapeutic Drugs and Mitochondrial Dysfunction: Focus on Doxorubicin, Trastuzumab, and Sunitinib. *Oxid. Med. Cell Longev.* **2018**, *2018*, 7582730. [CrossRef]
14. Itoh, T.; Ohguchi, K.; Nozawa, Y.; Akao, Y. Intracellular glutathione regulates sesquiterpene lactone-induced conversion of autophagy to apoptosis in human leukemia HL60 cells. *Anticancer Res.* **2009**, *29*, 1449–1457.
15. Scarponi, C.; Butturini, E.; Sestito, R.; Madonna, S.; Cavani, A.; Mariotto, S.; Albanesi, C. Inhibition of inflammatory and proliferative responses of human keratinocytes exposed to the sesquiterpene lactones dehydrocostuslactone and costunolide. *PLoS ONE* **2014**, *9*, e107904.
16. Neganova, M.E.; Afanas'eva, S.V.; Klochkov, S.G.; Shevtsova, E.F. Mechanisms of antioxidant effect of natural sesquiterpene lactone and alkaloid derivatives. *Bull. Exp. Biol. Med.* **2012**, *152*, 720–722. [CrossRef]
17. Carlisi, D.; Buttitta, G.; Di Fiore, R.; Scerri, C.; Drago-Ferrante, R.; Vento, R.; Tesoriere, G. Parthenolide and DMAPT exert cytotoxic effects on breast cancer stem-like cells by inducing oxidative stress, mitochondrial dysfunction and necrosis. *Cell Death Dis.* **2016**, *7*, e2194. [CrossRef]
18. Gaspar, A.R.; Potgieter, D.J.; Vermeulen, N.M. The effect of the sesquiterpene lactones from *Geigeria* on glycolytic enzymes. *Biochem. Pharmacol.* **1986**, *35*, 493–497.
19. Klochkov, S.G.; Neganova, M.E.; Pukhov, S.A.; Afanas'eva, S.V.; Aleksandrova, Y.R.; Yandulova, E.Y. New Arteannuin B derivatives and their cytotoxic activity. *Chem. Nat. Compd.* **2020**, *56*, 445–451. [CrossRef]
20. Semakov, A.V.; Anikina, L.V.; Pukhov, S.A.; Afanasieva, S.V.; Klochkov, S.G. Conjugates of alantolactone with anthracycline antibiotics. *Chem. Nat. Compd.* **2016**, *52*, 695–696. [CrossRef]
21. Anikina, L.V.; Semakov, A.V.; Afanas'eva, S.V.; Pukhov, S.A.; Klochkov, S.G. Synthesis and antiproliferative activity of Daunorubicin conjugates with sesquiterpene lactones. *Pharm. Chem. J.* **2018**, *52*, 308–311. [CrossRef]

22. Semakov, A.V.; Anikina, L.V.; Afanasyeva, S.V.; Pukhov, S.A.; Klochkov, S.G. Synthesis and antiproliferative activity of conjugates of anthracycline antibiotics with sesquiterpene lactones of the elecampane. *Russ. J. Bioorg. Chem.* **2018**, *44*, 538–546. [CrossRef]
23. Klochkov, S.G.; Afanasyeva, S.V.; Pushin, A.N. Acidic isomerization of alantolactone derivatives. *Chem. Nat. Compd.* **2006**, *42*, 400–406. [CrossRef]
24. Prabst, K.; Engelhardt, H.; Ringgeler, S.; Hubner, H. Basic Colorimetric Proliferation Assays: MTT, WST, and Resazurin. *Methods Mol. Biol.* **2017**, *1601*, 1–17.
25. Gornall, A.G.; Bardawill, C.J.; David, M.M. Determination of serum proteins by means of the biuret reaction. *J. Biol. Chem.* **1949**, *177*, 751–766. [CrossRef]
26. Klochkov, S.G.; Neganova, M.E.; Afanas'eva, S.V.; Shevtsova, E.F. Synthesis and antioxidant activity of securinine derivatives. *Pharm. Chem. J.* **2014**, *48*, 15–17. [CrossRef]
27. Akerman, K.E.; Wikstrom, M.K. Safranin as a probe of the mitochondrial membrane potential. *FEBS Lett.* **1976**, *68*, 191–197. [CrossRef]
28. Zhang, J.; Zhang, Q. Using Seahorse Machine to Measure OCR and ECAR in Cancer Cells. *Methods Mol. Biol.* **2019**, *1928*, 353–363. [PubMed]
29. Zhu, L.; Lu, Z.; Song, Y.Y. Advances in the Association between Apolipoprotein (a) Gene Polymorphisms and Coronary Heart Disease. *Zhongguo Yi Xue Ke Xue Yuan Xue Bao* **2015**, *37*, 482–488. [PubMed]
30. Chio, I.I.C.; Tuveson, D.A. ROS in Cancer: The Burning Question. *Trends Mol. Med.* **2017**, *23*, 411–429. [CrossRef] [PubMed]
31. Moloney, J.N.; Cotter, T.G. ROS signalling in the biology of cancer. *Semin. Cell Dev. Biol.* **2018**, *80*, 50–64. [CrossRef]
32. Annesley, S.J.; Fisher, P.R. Mitochondria in Health and Disease. *Cells* **2019**, *8*, 890. [CrossRef]
33. Warburg, O. On respiratory impairment in cancer cells. *Science* **1956**, *124*, 269–270.
34. Bonner, M.Y.; Arbiser, J.L. The antioxidant paradox: What are antioxidants and how should they be used in a therapeutic context for cancer. *Future Med. Chem.* **2014**, *6*, 1413–1422. [CrossRef]

MDPI AG
Grosspeteranlage 5
4052 Basel
Switzerland
Tel.: +41 61 683 77 34

Biomedicines Editorial Office
E-mail: biomedicines@mdpi.com
www.mdpi.com/journal/biomedicines



Disclaimer/Publisher's Note: The statements, opinions and data contained in all publications are solely those of the individual author(s) and contributor(s) and not of MDPI and/or the editor(s). MDPI and/or the editor(s) disclaim responsibility for any injury to people or property resulting from any ideas, methods, instructions or products referred to in the content.



Academic Open
Access Publishing

[mdpi.com](https://www.mdpi.com)

ISBN 978-3-7258-1874-7